Status of R-parity Conserving Supersymmetry after the LHC Run 2 and Other Experiments

Dissertation
zur Erlangung des Doktorgrades
an der Fakultät für Mathematik, Informatik und
Naturwissenschaften
Fachbereich Physik
der Universität Hamburg

vorgelegt von

Malte Mrowietz
Hamburg

2023

Gutachter/innen der Dissertation:

Prof. Dr. Peter Schleper
Prof. Dr. Gregor Kasieczka

Zusammensetzung der Prüfungskommission:

Prof. Dr. Peter Schleper
Prof. Dr. Christian Schwanenberger
Prof. Dr. Dieter Horns
Prof. Dr. Georg Weiglein
Prof. Dr. Gregor Kasieczka

Vorsitzender der Prüfungskommission:	Prof. Dr. Dieter Horns
Datum der Disputation:	04.12.2023
Vorsitzender Fach-Promotionsausschuss:	Prof. Dr. Günter Sigl
Leiter des Fachbereichs Physik:	Prof. Dr. Wolfgang Parak
Dekan der Fakultät MIN:	Prof. Dr.-Ing. Norbert Ritter

Acknowledgments

I would like to extend my gratitude to my PhD supervisor Prof. Peter Schleper for the opportunity to work on not just one, but three, interesting and fulfilling research topics throughout my Bachelors, Masters, and now PhD studies, and for his mentorship throughout. It is hard to imagine a more kind, patient, and insightful person, whose insights have helped to shape this analysis into a consistent work that I can be proud of. I would also like to thank Prof. Gregor Kasieczka for agreeing to act as secondary referee for this thesis, and for suggesting the excellent new coffee machine in the office.

I also wholeheartedly thank Sam Bein for his insight and friendship, and for being the bouncing board for any good, and bad, ideas that have come up in these years of working on this project, and in general. It is hard to overstate his importance to this work and to me during this time, often helping me overcome phases of crippling perfectionism.

Furthermore, I would like to thank the particle physics group at the University of Hamburg, Alexandra, Moritz, Viktor, and Yuval, Torben, and Tobias.

I want to thank my family and friends for their continuous support, and for being the kind of persons they are.

Finally, I cannot thank Maren enough for always being there for me, and for sharing my life with me. Lastly, I want to thank my dog Boomer, who provides me comfort and joy, and who manages to make me go outside during the hot summer months.

Abstract

Supersymmetry, if it describes our universe, may provide an explanation for some of the most vexing puzzles in particle physics and cosmology. Despite arguments that support supersymmetry (SUSY) as a general hypothesis, direct evidence for SUSY is yet to be observed. Decades of searches for SUSY at the energy frontier, including 12 years of searches performed at the LHC, have failed to turn up a positive signal. However, it is an open question to what extent the general hypothesis has been constrained by all of the data collected so far, and it is an open possibility that SUSY has manifested in these analyses but was not identified, either because its signal strength is small or because its signatures are challenging or spread out rather than confined to a single analysis strategy. This thesis presents a study of the viability of the Minimal Supersymmetric Standard Model (MSSM) given a wide variety of experimental results. It makes use of the phenomenological MSSM (pMSSM) as a proxy model for the MSSM. The pMSSM is sampled by means of Markov chain Monte Carlo (McMC), steered by measurements of the Higgs mass, constraints from LEP on the mass of the charginos and on the branching ratio BR(Z $\rightarrow$ invisible), and a suite of measurements from the flavor sector. The resulting pMSSM scan is a discrete representation of the posterior density with respect to the measurements included in the McMC, consisting of 27 million pMSSM models. The ensemble of model scenarios procured from this McMC are confronted with Run 2 data from ATLAS and CMS searches at the CERN LHC, as well as with data from dark matter measurements and searches interpreted within the standard model of cosmology, and with considerations from naturalness and fine tuning.

The LHC impact is evaluated on the basis of five direct SUSY searches, covering the 0-lepton p_T^{miss}+jets final state [1, 2], the di-lepton final state [3], the soft-di-lepton final state [4], the multi-lepton final state [5], and the final state featuring disappearing tracks [6, 7]. Within the considered parameter space, approximately 47% of the pMSSM scan is excluded by the LHC, with the largest impact coming from the p_T^{miss}+jets search, followed by the search for disappearing tracks.

The LHC is directly sensitive to the mass of the lightest supersymmetric particle (LSP) of $m(\widetilde{\chi}_1^0) \simeq 700\,\text{GeV}$, with $m(\widetilde{\chi}_1^0) \lesssim 500\,\text{GeV}$ significantly disfavored by the data, particularly for wino-like LSPs. All LSP masses remain viable in some parts of the pMSSM. A small excess in the data seen by the multi-lepton search is well fit by the pMSSM at $\Delta m(\widetilde{\chi}_1^\pm, \widetilde{\chi}_1^0) \simeq 100\,\text{GeV}$. Left-chiral selectrons and smuons with masses below 600 GeV are severely disfavored, with masses below 400 GeV almost entirely excluded. Sensitivity to right-chiral sleptons is significantly smaller, with surviving models featuring slepton masses as small as 100 GeV. Mass-compressed slepton-LSP scenarios remain particularly viable even for very small slepton masses of order 100 GeV. Colored superpartners with masses below 1 TeV are strongly disfavored, but not completely excluded. Significant suppression is evident up to $m(\widetilde{g}) \simeq 2\,\text{TeV}$, and to a lesser degree for $m(\widetilde{u}_R, \widetilde{c}_R)$, $m(\widetilde{u}_L, \widetilde{c}_L)$, and $m(\widetilde{d}_L, \widetilde{s}_L) \lesssim 2\,\text{TeV}$. A significant population of models with light stop survive in the compressed model space, namely where the LSP mass is only a few hundred GeV or less below the stop mass.

Direct detection constraints are found to exclude approximately 15% of both the LHC prior and posterior densities. They are most constraining on models with a higgsino-like LSP or a wino-like LSP, especially mixed wino-higgsino scenarios. A fraction of models are excluded in the whole range of scanned LSP masses, including large LSP masses that are currently out of reach for the LHC.

Constraints from indirect dark matter detection exclude a very small fraction of the LHC prior, and no part of the LHC posterior density. Higher-order corrections not included in this study may lead to a significant strengthening of the constraint.

Constraints in the form of upper bounds on the dark matter relic density Ωh^2 exclude most bino-like LSP, most higgsino-like LSP with $m(\widetilde{\chi}_1^0) \gtrsim 1.2\,\text{TeV}$, and wino-like LSP with $m(\widetilde{\chi}_1^0) \gtrsim 1.8\,\text{TeV}$, complementing the LHC well. Lower bounds on Ωh^2 progressively exclude models with larger $m(\widetilde{\chi}_1^0)$ for wino-like and higgsino-like LSP, with $\Omega h^2 > 0.1\,\Omega h^2_{\text{Planck}}$ [8] excluding $m(\widetilde{\chi}_1^0) \lesssim 600\,\text{GeV}$, and $m(\widetilde{\chi}_1^0) \lesssim 300\,\text{GeV}$ for wino-like and higgsino-like LSP, respectively. These mass ranges are within the reach of LHC sensitivity. For $\Omega h^2 \in [0.9, 1.1]\,\Omega h^2_{\text{Planck}}$, surviving models include higgsino-like LSPs at $m(\widetilde{\chi}_1^0) \simeq 1.1\,\text{TeV}$, wino-like LSPs at $m(\widetilde{\chi}_1^0) \simeq 1.7\,\text{TeV}$, and wino-higgsino mixed LSPs in between. Some models with mixed-bino LSP, or pure bino LSP inside the A-funnel region, survive. Constraints from direct detection complement these constraints, particularly for models with wino-higgsino mixed LSPs.

Low fine tuning is largely incompatible with LHC data if additionally requiring that the LSP account for all dark matter. However, so-called natural models with low fine tuning remain viable in regions of the pMSSM with lower Ωh^2 saturation, and a small sliver of models with $m(\widetilde{\chi}_1^0) \simeq 350\,\text{GeV}$ and $\Delta m(\widetilde{\chi}_1^\pm, \widetilde{\chi}_1^0) \simeq 1\,\text{GeV}$ survives all constraints.

Interpretations and limits within simplified model limits are compared with conclusions drawn from the MSSM study. It is found that, with a small number of exceptions, the intuition garnered

from simplified models is in stark contrast with the full model analysis, and are thus potentially misleading. The only subsets of the pMSSM for which conclusions coincide with simplified model limits are subsets with a bino-like LSP for which colored superpartner cross sections dominate over electroweak cross sections.

Zusammenfassung

Wenn Supersymmetrie existiert, könnte sie eine Erklärung für einige der größten Rätsel der Teilchenphysik und Kosmologie liefern. Trotz Argumenten, die für Supersymmetrie (SUSY) sprechen, ist ein direkter Nachweis für SUSY noch nicht erbracht worden. Die jahrzehntelange Suche nach SUSY an der Energiegrenze, einschließlich der 12 Jahre dauernden Suche am LHC, hat kein positives Signal erbracht. Es ist jedoch eine offene Frage, inwieweit die allgemeine Hypothese durch alle bisher gesammelten Daten eingeschränkt wurde, und es besteht die Möglichkeit, dass sich SUSY in diesen Analysen manifestiert hat, aber nicht identifiziert wurde, entweder weil seine Signalstärke gering ist, oder weil seine Signaturen schwer detektierbar oder verstreut sind und nicht auf eine einzige Analysestrategie beschränkt sind. In dieser Arbeit wird das Minimal Supersymmetrische Standardmodell (MSSM) anhand einer Vielzahl von experimentellen Ergebnissen untersucht. Dabei wird das phänomenologische MSSM (pMSSM) als Ersatzmodell für das MSSM verwendet. Ein Ensemble aus pMSSM Modellen wird mittels Markov-Chain-Monte-Carlo (McMC) erzeugt, gesteuert durch Messungen der Higgs-Masse, beschränkungen durch LEP auf die Masse der Charginos und des Verzweigungsverhältnisses BR(Z $\rightarrow$ unsichtbar), sowie eine Reihe von Messungen aus dem Flavor-Sektor. Der sich daraus ergebende pMSSM-Scan ist eine diskrete Darstellung der posterioren Wahrscheinlichkeitsdichte in Bezug auf die im McMC enthaltenen Messungen und besteht aus etwa 27 Millionen pMSSM-Modellen. Das Ensemble von Modellszenarien, das aus diesem McMC gewonnen wurde, wird mit Run-2-Daten von ATLAS- und CMS-Suchen am CERN LHC, sowie mit Daten von Suchen nach dunkler Materie konfrontiert, die im Rahmen des Standardmodells der Kosmologie interpretiert werden, und mit Überlegungen zur Natürlichkeit und fine-tuning.

Die Auswirkungen des LHC werden auf der Grundlage von fünf direkten SUSY-Suchen bewertet, die den 0-Lepton p_T^{miss}+jets Endzustand [1, 2], den di-Lepton-Endzustand [3], den soft-di-Lepton-Endzustand [4], den multi-Lepton-Endzustand [5], und den Endzustand mit verschwindenden Spuren [6, 7] abdecken.

Innerhalb des untersuchten parameterraums sind ungefähr 47% des pMSSM-Scans vom LHC ausgeschlossen, wobei der größte Beitrag von der Suche nach p_T^{miss}+jets kommt, gefolgt von der Suche nach verschwindenden Spuren.

Der LHC ist direkt sensitiv auf das leichteste supersymmetrische Teilchen (LSP) bis zu Massen von $m(\widetilde{\chi}_1^0) \simeq 700\,\text{GeV}$, wobei $m(\widetilde{\chi}_1^0) \lesssim 500\,\text{GeV}$, insbesondere für Wino-artige LSP, deutlich durch die LHC Daten unterdrückt sind. Alle LSP-Massen bleiben in einigen Teilen des pMSSM möglich. Ein kleiner Überschuss in den Daten der multi-Lepton-Suche kann im pMSSM bei $\Delta m(\widetilde{\chi}_1^\pm, \widetilde{\chi}_1^0) \simeq 100\,\text{GeV}$ realisiert werden.

Links-chirale Selektronen und Smuonen mit Massen unter 600 GeV sind stark unterdrückt, wobei Massen unter 400 GeV fast vollständig ausgeschlossen sind. Die Sensitivität gegenüber rechts-chiralen Sleptonen ist deutlich geringer und einige Modelle mit Sleptonmassen von nur 100 GeV überleben. Insbesondere massenkomprimierte Slepton-LSP-Szenarien sind auch bei sehr kleinen Sleptonmassenin der Größenordnung von 100 GeV möglich.

Farbgeladene Superpartner mit Massen unter 1 TeV sind stark unterdrückt, aber nicht völlig ausgeschlossen. Gluino-Massen bis zu $m(\widetilde{g}) \simeq 2\,\text{TeV}$ werden stark unterdrückt, Squark-Massen von sowohl $m(\widetilde{u}_R, \widetilde{c}_R)$, $m(\widetilde{u}_L, \widetilde{c}_L)$, als auch $m(\widetilde{d}_L, \widetilde{s}_L) \lesssim 2\,\text{TeV}$ werden in etwas geringerem Maße unterdrückt. Ein bedeutender Anteil von Modellen mit leichten $\widetilde{t}_1$ überlebt die LHC Daten im massenkomprimierten Parameterraum, wo das LSP nur einige Hundert GeV oder weniger leichter ist als das Stop.

Direkte Suchen nach dunkler Materie schließen etwa 15% des pMSSM scan aus. Am stärksten betroffen sind Modelle mit Higgsino- oder wino-artigen LSP, als auch gemische Wino-Higgsino LSP. Direkte Suchen nach dunkler Materie schließen einer Teil der Modelle im gesamten Bereich der abgedeckten LSP-Massen aus, einschließlich großer LSP-Massen, die derzeit für den LHC unerreichbar sind.

Indirekte Suchen nach dunkler Materie schließen einen sehr kleinen Teil des pMSSM Scans aus, und kein Modell dass die LHC Daten überlebt. Korrekturen höherer Ordnung, die in dieser Studie nicht berücksichtigt wurden, können zu einer erheblichen Verstärkung der Einschränkung führen.

Oberen Schranken auf die Reliktdichte der dunklen Materie Ωh^2 schließen die meisten Bino-artigen LSP, die meisten Higgsino-artigen LSP mit $m(\widetilde{\chi}_1^0) \gtrsim 1.2\,\text{TeV}$ und Wino-artigen LSP mit $m(\widetilde{\chi}_1^0) \gtrsim 1.8\,\text{TeV}$ aus, was den LHC gut ergänzt. Untere Schranken für Ωh^2 schließen sukzessiv Modelle mit größerem $m(\widetilde{\chi}_1^0)$ von Wino- und Higgsino-artigen LSPs aus, wobei $\Omega h^2 > 0.1\,\Omega h^2_{\text{Planck}}$ [8] zum Ausschluss von $m(\widetilde{\chi}_1^0) \lesssim 600\,\text{GeV}$, und $m(\widetilde{\chi}_1^0) \lesssim 300\,\text{GeV}$ für Wino- bzw. Higgsino-artige LSP führt. Diese Massenbereiche liegen innerhalb der Reichweite des LHC. Für $\Omega h^2 \in [0.9, 1.1]\,\Omega h^2_{\text{Planck}}$ überleben Modelle mit Higgsino-artige LSPs bei $m(\widetilde{\chi}_1^0) \simeq 1.1\,\text{TeV}$, Wino-artige LSPs bei $m(\widetilde{\chi}_1^0) \simeq 1.7\,\text{TeV}$, und Wino-Higgsino-gemischte LSPs dazwischen. Einige Modelle

mit einem gemischten Bino-LSP oder reinen Bino-LSP innerhalb der A-Trichter-Region bleiben möglich. Die Einschränkungen aus der direkten Suche nach dunkler Materie ergänzen die Einschränkungen durch Ωh^2, insbesondere bei Modellen mit gemischten Wino-Higgsino-LSPs.

Niedriges fine-tuning is größtenteils unvereinbar mit den LHC Daten falls zusätzlich verlangt wird dass das LSP die gesamte dunkle Materie ausmacht. Allerdings bleiben sogenannte natürliche Szenarien mit geringem fine-tuning in Regionen des pMSSM mit geringerer Ωh^2-Sättigung möglich und ein kleiner Teil der Modelle mit $m(\widetilde{\chi}_1^0) \simeq 350\,\text{GeV}$ und $\Delta m(\widetilde{\chi}_1^\pm, \widetilde{\chi}_1^0) \simeq 1\,\text{GeV}$ überlebt alle Einschränkungen.

Die Interpretationen und Limits von vereinfachten Modellen werden mit den Schlussfolgerungen aus der MSSM-Studie verglichen. Es zeigt sich, dass die aus den vereinfachten Modellen gewonnene Intuition mit wenigen Ausnahmen in krassem Gegensatz zur Analyse des vollständigen Modells steht und daher potenziell irreführend ist. Die einzigen Unterräume des pMSSM, für die die Schlussfolgerungen mit den Limits des vereinfachten Modells übereinstimmen, sind Unterräume mit einem bino-artigen LSP, für die farbige Superpartner die Wirkungsquerschnitte gegenüber elektroschwachen dominieren.

Contents

1 Introduction **1**

2 Theoretical Foundation: The Standard Model and Beyond **3**
2.1 The Standard Model . . . 3
2.1.1 Local gauge symmetries . . . 3
2.1.2 Particles and interactions . . . 3
2.1.3 Electroweak unification and particle masses via spontaneous symmetry breaking 6
2.1.4 Shortcomings of the Standard Model . . . 8
2.1.4.1 Gravity . . . 8
2.1.4.2 Dark matter . . . 8
2.1.4.3 Matter-antimatter asymmetry . . . 8
2.1.4.4 Neutrino masses . . . 9
2.1.4.5 Grand unification . . . 9
2.1.4.6 The hierarchy problem . . . 9
2.2 Supersymmetry . . . 11
2.2.1 Supersymmetry breaking . . . 11
2.2.2 Supersymmetric solutions to open questions . . . 11
2.3 The MSSM and pMSSM . . . 13
2.3.1 The pMSSM-19 . . . 14
2.3.2 Electroweak fine tuning . . . 15
2.3.3 Simplified Models . . . 15
2.4 Natural units . . . 16

3 Observations and experiments **17**
3.1 Dark matter detection . . . 17
3.1.1 Direct detection of dark matter . . . 17
3.1.2 Indirect detection of dark matter . . . 18
3.1.3 Production and detection of dark matter at particle colliders . . . 18
3.1.4 Cosmological implications on dark matter . . . 19
3.2 Anomalous magnetic moment of the muon . . . 20
3.2.1 The muon g-2 experiment at Fermilab . . . 20
3.3 Flavor physics experiments . . . 21
3.3.1 Belle . . . 21
3.3.2 BaBar . . . 22
3.3.3 LHCb . . . 23
3.4 The Large Hadron Collider and its Detectors . . . 25
3.4.1 The CMS detector . . . 25
3.4.2 The ATLAS detector . . . 29
3.4.3 Trigger systems at ATLAS and CMS . . . 30

4 Scientific goals and methodology **33**

5 The pMSSM scan **36**
5.1 Construction of the LHC prior . . . 36
5.1.1 McMC Algorithm Impact . . . 39
5.1.2 Model-inherent constraints . . . 40
5.1.3 Impact of the Higgs mass constraint . . . 50
5.1.4 Impact of the LEP chargino and Z to invisible constraints . . . 54
5.1.4.1 Non-convergence in μ in small Markov chains . . . 54
5.1.5 Impact of included flavor observables . . . 56
5.1.6 BR($b \to s\gamma$) . . . 57
5.1.7 BR($B_s \to \mu\mu$) . . . 61
5.1.7.1 Remaining low-energy observables . . . 65
5.2 Summary and presentation of the low-energy posterior . . . 65
5.2.0.1 Electroweakinos . . . 66
5.2.0.2 Sleptons . . . 68
5.2.0.3 Colored sector . . . 70

5.2.0.4 Higgs sector . . . 74
5.3 McMC convergence . . . 76
5.3.1 Burn-in . . . 76
5.3.2 Rubin-Gelman heuristic . . . 76
5.4 Known biases of the prior . . . 78

6 Including the LHC data **79**
6.1 Variable sampling of subset for LHC results . . . 79
6.1.1 Over-sampled regions . . . 79
6.1.2 Under-sampled regions . . . 80
6.1.3 Reweighting validation . . . 80
6.2 Signal simulation . . . 83
6.2.1 `MadAnalysis5` workflow . . . 83
6.2.2 CMS workflow . . . 83
6.3 Included LHC analyses . . . 85
6.3.1 ATLAS_SUSY_2018_06 (*multi-lepton*) . . . 85
6.3.2 ATLAS_SUSY_2018_32 (*di-lepton*) . . . 85
6.3.3 CMS_SUS_18_004 (*di-lepton SOS*) . . . 85
6.3.4 CMS_SUS_19_006 (p_T^{miss}+*jets*) . . . 85
6.3.5 CMS_SUS_21_006 (*disappearing tracks*) . . . 85
6.3.6 Summary of covered final states . . . 85

7 Statistical methods and displays **87**
7.1 LHC likelihoods . . . 87
7.1.1 Full likelihood . . . 87
7.1.2 Simplified likelihood . . . 87
7.1.3 Bayes factor and Z significance . . . 88
7.2 Impact plots . . . 88
7.3 Survival probabilities . . . 90
7.4 Bayes factor quantiles . . . 90
7.5 Credibility intervals . . . 92
7.6 Most significant models . . . 93
7.7 2D panels . . . 93

8 Results **95**
8.1 Summary table on search complementarity . . . 95
8.2 Impact on particle properties . . . 99
8.2.1 Electroweak SUSY . . . 99
8.2.2 Sleptons . . . 116
8.2.3 Colored SUSY . . . 119
8.2.3.1 LCSP . . . 119
8.2.3.2 Gluino . . . 124
8.2.3.3 Stop & sbottom . . . 124
8.2.3.4 Sup and sdown . . . 128
8.3 Impact on the pMSSM parameters . . . 132
8.3.1 Colored SUSY . . . 132
8.3.2 Electroweak SUSY . . . 136
8.3.3 Slepton sector . . . 143
8.3.4 Higgs sector . . . 144
8.4 Dark matter . . . 146
8.4.1 Direct detection . . . 146
8.4.2 Relic density . . . 153
8.4.2.1 LHC impact on relic density . . . 153
8.4.2.2 Relic density impact on pMSSM . . . 156
8.4.3 Indirect Detection . . . 168
8.4.4 Combined dark matter direct detection and relic density . . . 171
8.5 Fine tuning . . . 175
8.5.1 Small fine tuning regions . . . 179
8.5.1.1 Tight ΔEW region . . . 182

8.5.2 Combined fine tuning and dark matter constraints . . . 184
8.6 Anomalous magnetic moment of the muon . . . 190
8.7 Simplified model limit compatibility . . . 194
8.7.1 Jets + p_T^{miss} . . . 194
8.7.2 Di-lepton . . . 201
8.7.3 Di-lepton soft-opposite sign . . . 204
8.7.4 Multi-lepton . . . 207
8.7.5 Disappearing tracks . . . 208

9 Summary **215**

A McMC algorithm shaping solutions **220**

B Tachyons and SPheno error codes **221**

C Low-energy observable impact **232**
C.1 BR(B $\to \tau\nu$) . . . 232
C.2 BR(B $\to$ Xsee) and BR(B $\to$ Xs$\mu\mu$) . . . 235
C.3 BR($B^0 \to K^{*0}\gamma$) . . . 236
C.4 $\Delta(\rho)$ . . . 240
C.5 BR($D_s \to \tau\nu$) . . . 244
C.6 BR($D_s \to \mu\nu$) . . . 247
C.7 BR($B_d \to \mu\mu$) and $\Delta_{0+}(K^*\gamma)$ . . . 251

1 Introduction

Known fundamental physics today rests on two as of yet irreconcilable pillars – General Relativity (GR) describing gravity at large scales, and Quantum Field Theory (QFT) describing interactions on small scales. While GR can generally be understood as the consequences of curved geometry, and intuition is available in two dimensional geometries, both QFT and actual four-dimensional GR continue to defy our evolved capacity for intuitions even a century after their inception. In this unintuitive landscape of quantum fields and particles, progress has been made steadily by the creative advancement of mathematics and its diligent application, culminating in the formulation of the Standard Model of particle physics (SM) and its central building block, the Higgs mechanism. The SM today describes all discovered fundamental particles and their interactions at small scales with remarkable precision, and, with the discovery of the Higgs boson at the LHC in 2012 [9, 10], no further fields or particles are necessary for the consistency of the SM up to large energy scales. Similarly, our quest for understanding the origin and early evolution of the universe have brought us to the *Standard Model of Cosmology*, or Λ_{CDM}, where Λ refers to the cosmological constant of GR and CDM to a mysterious and not yet fundamentally understood form of matter – cold dark matter.

Furthermore, GR is not reconcilable with QFT at small scales and there is incontrovertible evidence that the SM does not provide a complete description of the universe, and is not valid up to arbitrarily large energies. Among the most compelling reasons is evidence for the existence of dark matter, which is believed to make up a dominant part of the matter content of the universe. In this context, irreconcilable tension also exists between the SM and Λ_{CDM}. Dark matter is at the same time an instrumental ingredient in Λ_{CDM}, but there exists no explanation for it in the context of the SM. Other problems of a more aesthetic nature can be found in the so-called hierarchy problem, which, without the introduction of new fields or a new paradigm, imply a large degree of fine tuning among unrelated model parameters. As a last example, while unification of the weak and electromagnetic forces is a core feature of the SM, grand unification with the strong force is not possible at any energy scale in the SM, and would require the presence of new physics beyond the SM.

To solve these problems, new theories for physics are needed. These new theories need to remain compatible with the huge set of observations and experiments that have been carried out over the past hundreds of years, which tremendously constrain them from the beginning. Thus, in this seemingly infinite but heavily constrained space of conceivable theories, it has often proved useful in the past to expand and slightly modify previously acceptable theoretical structures, rather than build up a completely new one. Arguably the best example of this approach is the lead-up to the SM itself, where the notion of symmetries has guided our increasing understanding of particle physics. With that in mind, supersymmetric extensions of the SM are a promising subject to explore and constrain, as they are the only possible extensions of the space-time symmetry group the SM is based on, the Poincaré group [11], that remain compatible with gauge theory. Additionally, they allow the known physics of the Standard Model to re-emerge as a low-energy effective field theory, thus conforming to previous observations. For this reason, many state-of-the-art experiments have extensively searched for supersymmetry.

The study of supersymmetry in even its minimal complete application, the Minimal Supersymmetric Standard Model (MSSM), comes with a huge parameter space that needs to be constrained. Therein lies a significant challenge for theorists and experimentalists alike, as considering high-dimensionality parameter spaces is another task for which our evolved intuitions fail. To nevertheless make progress, a strategy of simplification is adopted, in which the need for understanding the impact of observations on supersymmetry is balanced against the need to completely study the richness in phenomenology and complexity that supersymmetry offers. While the standard has been to maximize the intuitiveness of the interpretation of results in the form of simplified models, there remains a desire to give an account of current constraints on supersymmetry in as complete a model as possible. Additionally, evaluating constraints from different types of experiments, such as direct and indirect searches for dark matter, low-energy observables, and LHC data, necessarily requires more complete models than what simplified models offer.

This thesis aims to provide an account of the consistency of as much relevant data as possible with the R-parity conserving MSSM. As a proxy of the full MSSM, a phenomenological sub-model is considered, called the phenomenological MSSM, or pMSSM-19. The pMSSM-19 (pMSSM for short) preserves most of the phenomenology of the MSSM, while drastically reducing the model space. To this end, a scan of the pMSSM parameter space is created using Markov chain Monte Carlo, and the impact of a large set of various kinds of data on the pMSSM is evaluated. These include direct

searches for supersymmetry at the LHC covering the most relevant final states, constraints from previous generations of particle colliders, from experiments studying the flavor sector of the Standard Model, from astrophysical and cosmological constraints on dark matter, from measurements of the anomalous magnetic moment of the muon, and from considerations of naturalness. The results are presented in a Bayesian statistical framework as a discrete representation of the posterior density in the pMSSM, as well as in terms of measures that are intelligible in a frequentist context. In addition, a study of the viability and reach of the interpretation of LHC results in terms of simplified models in the MSSM is presented.

2 Theoretical Foundation: The Standard Model and Beyond

To understand the value of this work, it is important to introduce the framework in which to make sense of the results. This is the aim of this section, by giving a short description of the Standard Model of particle physics, its shortcomings, followed by strategies to alleviate some of these shortcomings. We focus specifically on the concept of supersymmetry, its minimal application in the form of the Minimal Supersymmetric Standard Model (MSSM), as well as practical concepts of making scientific progress on constraining the MSSM, given its large dimensionality. In particular, two solutions to the problem of large dimensionality are introduced: simplified models and the phenomenological MSSM (pMSSM). We highlight the general motivation and the differences between these two approaches.

2.1 The Standard Model

The Standard Model of particle physics (SM) is a relativistic quantum field theory with interactions based on local gauge symmetries. Observed particles herein are the excitations of fundamental fields, which interact via fundamental forces. The SM describes three out of the four known fundamental forces and all currently discovered particles. Incidentally, with the discovery of the Higgs boson in 2012 [9, 10], all particles predicted by the SM have been discovered. The following is meant to be a refresher and is not an educational or groundbreaking endeavor. Comprehensive descriptions of the SM are abundant, and are given, for example, in [12] and [13].

2.1.1 Local gauge symmetries

The SM contains two different sets of symmetries – space-time conforms to the Poincaré symmetry group, the SM field content additionally conforms to a group of gauge symmetries.

Gauge symmetries are an important foundation of modern particle physics. Symmetries can either be global symmetries, which means that they do not depend on the underlying space-time coordinates, or they can be local, which means that they do depend on the space-time coordinates. In local gauge symmetries, such as they exist in the SM, the dependence of the symmetry transformation on space-time coordinates results in the need for a co-variant derivative. This is because in applying a gauge transformation to a Lagrangian that contains, for example, spinor fields Ψ, terms of the form $\sim [\delta_\mu, U]$ appear and do not generally vanish, which need to be compensated for by a change to the derivative operator. This change necessarily introduces new *gauge* fields, whose characteristics are defined by the generators of the gauge transformation. In addition to the new gauge field, Noether's theorem tells us that continuous local gauge symmetries result in conserved charges. To shortly summarize, a Lagrangian symmetric under local gauge transformations made up of spinor fields Ψ automatically contains gauge fields pertaining to the symmetry, which mediate interactions of the fields Ψ and contain conserved charges.

The SM gauge group consists of three symmetry groups, $\mathrm{SU(3)_c} \times \mathrm{SU(2)_L} \times \mathrm{U(1)_Y}$, with c referring to three *color* charges called red, blue, and green, L to the left-chiral component of the *weak isospin* charge T, and Y refers to the hypercharge. The gauge fields of the $\mathrm{SU(3)_c}$ symmetry are the eight gluons g. The gauge fields of the $\mathrm{SU(2)_L}$ are W^1, W^2, and W^3, and the gauge field of the $\mathrm{U(1)_Y}$ is the field B. Electroweak symmetry breaking, discussed in more detail below, leads to a mixing of the $\mathrm{SU(2)_L} \times \mathrm{U(1)_Y}$ symmetries and results in electric charge $Q = Y + T_3$, where T_3 is the third component of the weak isospin, and the better known physical states, the massive weak bosons $W^\pm$ and Z^0, as well as the massless photon γ.

An important road block to this endeavor has been that the usual mass terms of the form $\mathcal{L} \sim -m^2 B_\mu B^\mu$ for gauge bosons B break any SU(N) gauge symmetry and can thus not be included ad-hoc in the SM. Similarly, mass terms for fermionic fields Ψ, $\mathcal{L} \sim -m\bar{\Psi}\Psi$, are not invariant under the combined $\mathrm{SU(2)_L} \times \mathrm{U(1)_Y}$ symmetry group and can also not be included ad-hoc in the SM. The solution to generating the observed masses of these particles in the SM is given by the Brout-Englert-Higgs mechanism, which is introduced below in Section 2.1.3.

2.1.2 Particles and interactions

Having introduced the foundational symmetries of the SM, we move to give its full field content and interactions. This field or particle content is shown in Figure 1, their interactions are shown as

transparently shaded areas that encompass the groups of particles that interact with each other. These particles can be divided according to their mass and quantum numbers – spin, electric charge, weak isospin, and color charge. Starting with the spin, we can differentiate between the spin-$\frac{1}{2}$ fermions, the spin-1 gauge bosons already mentioned in the previous section, and the spin-0 Higgs boson. The fermions can be further subdivided into those that carry color charge, the quarks, and the leptons, which do not. Of the bosons, only the gluon carries color charge, which interacts via the strong force with quarks and itself, but not with leptons. Next, the fermions are separated according to their electric charge Q and weak isospin I into *up*-type with $Q = \frac{2}{3}$ and *down*-type quarks with $Q = -\frac{1}{3}$, as well as the charged leptons with $Q = 1$ and electrically neutral neutrinos with $Q = 0$. Each of these exist as left-chiral doublets and right-chiral singlets of the weak isospin, with the exception of the neutrinos, for which no right-chiral version exists in the original version of the SM. The weak isospin of the left-chiral up-type and down-type quarks is $I = \pm\frac{1}{2}$, respectively, and $I = \pm\frac{1}{2}$, for the neutrinos and charged lepton, respectively. The left-chiral quarks and the charged leptons interact with both the electric and weak isospin parts of the W and Z bosons, as well as electrically with the photon. Due to their electric neutrality, the neutrinos only interact with the weak isospin components of the W and Z bosons. Because the right-chiral fermions have a weak isospin $I = 0$, they only interact with the Z boson and the photon according to their hypercharge and electric charge, respectively. The final subdivision for the fermions is into three generations that only differ with respect to their mass. Conventionally, the masses increase with each generation. Each generation contains an up-type quark, a down-type quark, a charged lepton, and a neutrino. In this order, the first generation is made up of the up quark (u), the down quark (d), the electron (e), and the electron neutrino (ν_e). The second generation contains the charm quark (c), the strange quark (s), the muon (μ), and the muon neutrino (ν_μ). Finally, the third generation is made up of the top quark (t), the bottom quark (b), the tau lepton (τ), and the tau neutrino (ν_τ).

The masses of the quarks range from $m(\mathrm{u}) = (2.16\,^{+0.49}_{-0.26})\,\frac{\mathrm{MeV}}{\mathrm{c}^2}$ [14] for the up-quark to $m(\mathrm{t}) = (172.69 \pm 0.30)\,\frac{\mathrm{GeV}}{\mathrm{c}^2}$ [14], for the charged leptons they range from $m \simeq 0.511\,\frac{\mathrm{MeV}}{\mathrm{c}^2}$ for the electron to $m \simeq 1.78\,\frac{\mathrm{GeV}}{\mathrm{c}^2}$ for the tauon. The neutrinos do not have a mass in the original version of the SM, contrary to strong evidence that they are massive in nature.

Finally, the SM also contains a copy of each fermion with the same mass as the original, called anti-particles, whose charges are inverted. The fermions and anti-fermions are individually described by Weyl-spinors, but need to be described as a whole by Dirac spinors made up of particle and antiparticle. A potential exception to this can again be found for the neutrinos, for which it is unknown whether they are Dirac fermions or Majorana fermions.

There is an additional feature of the strong interaction that has significant phenomenological consequences, in that its strength increases the larger the distance. As a consequence, colored particles only exist for significant time scales in color-neutral, *confined*, bound states, called hadrons. Color neutrality here means that all three color charges must be zero, and can be realized in the form of pairs of opposite-color quarks (mesons), or trimers of quarks of all different colors (baryons).

This concludes the introduction of the fermion sector of the SM. For the bosons of the SM, there are a couple of charactistics to add. First, the photon is the only gauge boson that does not carry a charge, and does not interact with itself due to the abelian nature of the gauge symmetry. In contrast, due to the non-abelian nature of the $\mathrm{SU(2)_L}$ gauge group, the W and Z bosons interact with each other. The eight gluons carry color charge, one color and one anti-color, with the eight gluons each realizing one of the possible permutations of color and anti-color. Like the W and Z bosons, gluons interact with each other due to the non-abelian nature of the $\mathrm{SU(3)_c}$ gauge group.

The nature of the Higgs boson is explained in the following section.

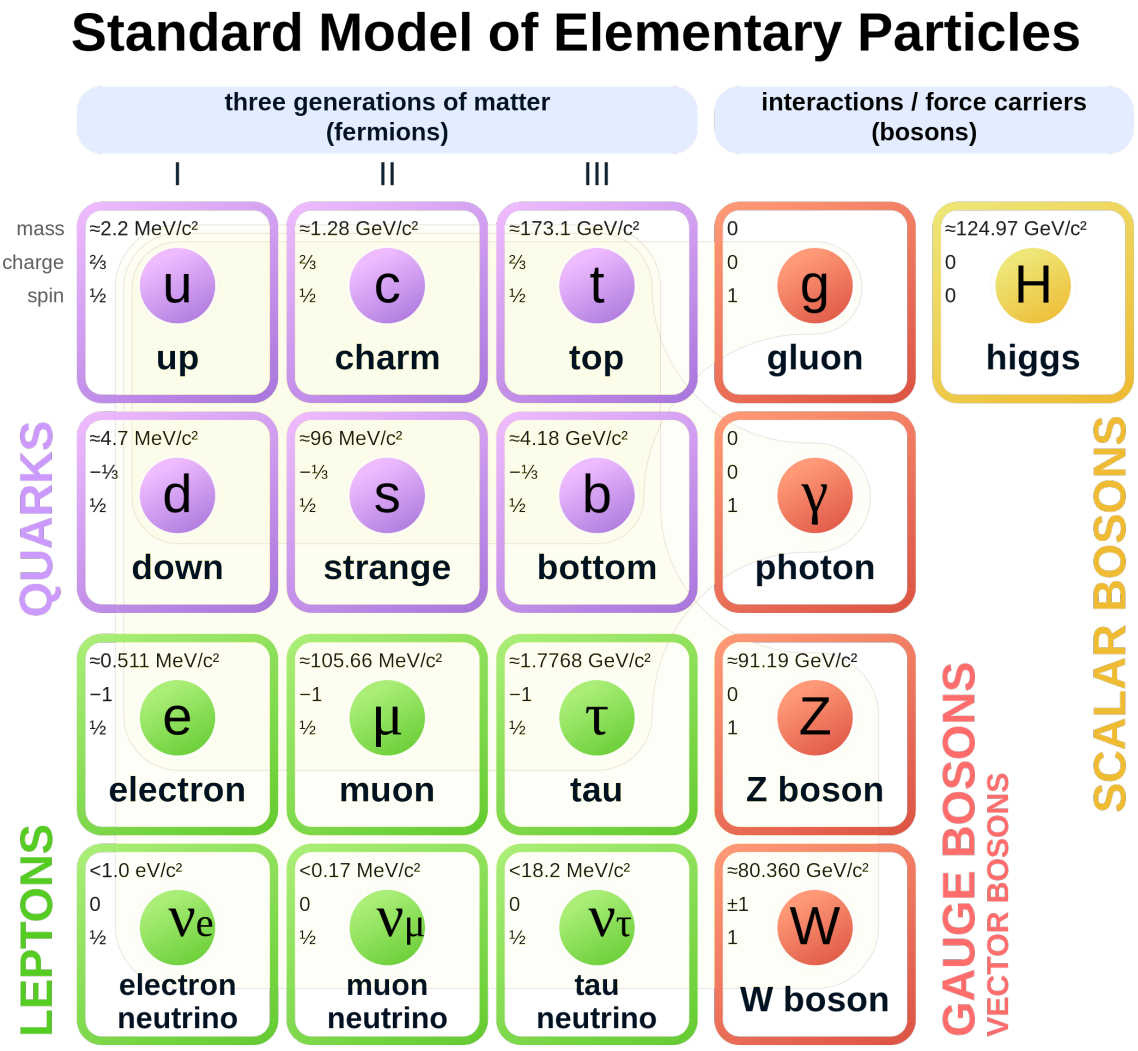

Figure 1: Summary of the particle content of the Standard Model [15]. It includes the possibility of neutrino masses which are not formally part of the Standard Model.

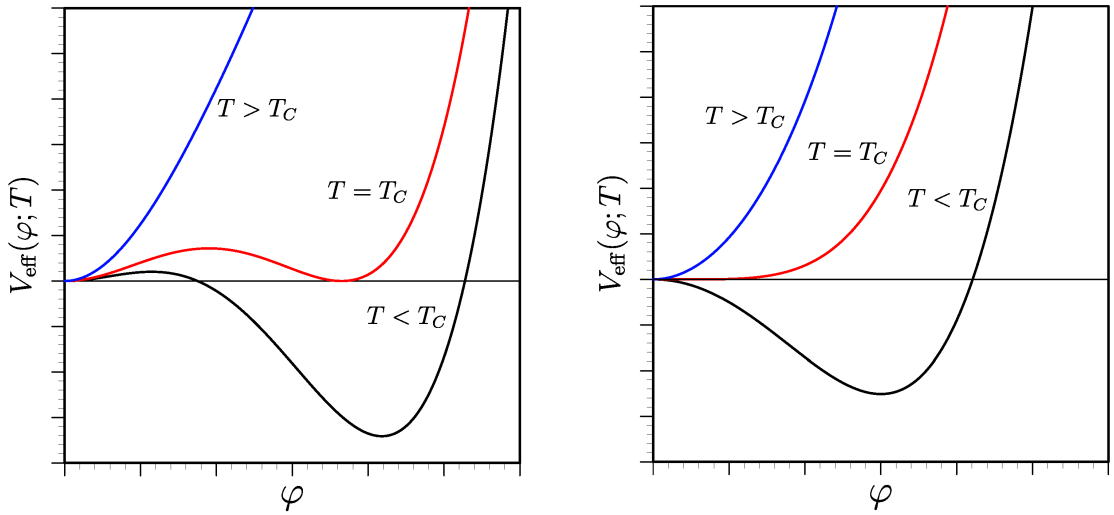

Figure 2: Illustration of the temperature dependence of the effective Higgs potential for first-order (left) and second order (right) electroweak phase transitions. Figure taken from [20], removed not needed sub-figures and rearranged remaining sub-figures.

2.1.3 Electroweak unification and particle masses via spontaneous symmetry breaking

The SM gauge group, specifically the $\mathrm{SU(2)_L} \times \mathrm{U(1)_Y}$ part, is spontaneously broken by the Brout-Englert-Higgs (BEH) mechanism [16, 17]. A new complex scalar $\mathrm{SU(2)_L}$ field doublet Φ is postulated, together with a scalar potential that conforms to the $\mathrm{SU(2)_L}$ symmetry at the zero field value, but whose minimum, the vacuum expectation value (*vev* or v), is not symmetric with respect to $\mathrm{SU(2)_L}$ transformations. The simplest form of such a potential is postulated for the SM:

$$V(\Phi) = -\mu^2 \Phi^\dagger \Phi + \lambda (\Phi^\dagger \Phi)^2, \tag{1}$$

where $\mu^2 > 0$ and $\lambda > 0$. At large temperatures present in the very early universe, temperature dependent contributions to this potential [18, 19] lead to an effective potential where the minimum is at $|\Phi|^2 = 0$, such that the effective potential is completely symmetric with respect to a gauge transformation. In this regime, the $\mathrm{SU(2)_L} \times \mathrm{U(1)_Y}$ symmetry is intact and the gauge bosons and fermions are massless. As the temperature decreases with the expansion of the early universe below a critical temperature $\mathrm{T_c}$, the minima in the potential develop and the symmetry is spontaneously broken. This behavior is illustrated in Figure 2.

As the universe transitions into the newly formed potential minimum, the original fields of the $\mathrm{SU(2)_L}$, W^1, W^2, W^3, as well as the $\mathrm{U(1)_Y}$ gauge field B mix into the more well known W, Z, and γ bosons. Three of the four degrees of freedom of Φ are absorbed to provide the longitudinal polarizations and masses of W^+, W^-, and Z^0. The photon γ remains massless due to a residual symmetry after the breaking, which is the well-known $\mathrm{U(1)_Q}$ symmetry of quantum electrodynamics with the electric charge Q. The remaining degree of freedom in Φ is retained in a new physical, electrically neutral spin-0 boson – the Higgs boson $\mathrm{h^0}$ (sometimes also labeled $\mathrm{H^0}$ or simply H). The symmetries and field content of the SM before and after electroweak symmetry breaking is shown in Figure 3.

This concept of electroweak symmetry breaking unifies the low-energy weak and electromagnetic forces into the electroweak force, while at the same time providing the prediction of the Higgs boson within the Higgs mechanism. The fermions obtain their masses through Yukawa interactions with the Higgs field. Yukawa interactions relate the left- and right-chiral components for a given fermion Ψ:

$$\mathcal{L} = -y \bar{\Psi}_R \Phi \Psi_L + \text{hermetian conjugate}, \tag{2}$$

with the Yukawa coupling y and the Higgs field Φ. Perturbative expansion of Φ around the vacuum expectation value v then leads to

$$\mathcal{L} = -\frac{yv}{\sqrt{2}} \bar{\Psi}_R \Psi_L - \frac{yh^0}{\sqrt{2}} \bar{\Psi}_R \Psi_L, \tag{3}$$

where $-\frac{yv}{\sqrt{2}}$ in the first term can be identified with the fermion mass, and $-\frac{yh^0}{\sqrt{2}}$ describes the vertex factor for the interaction of the Higgs boson with the fermion.

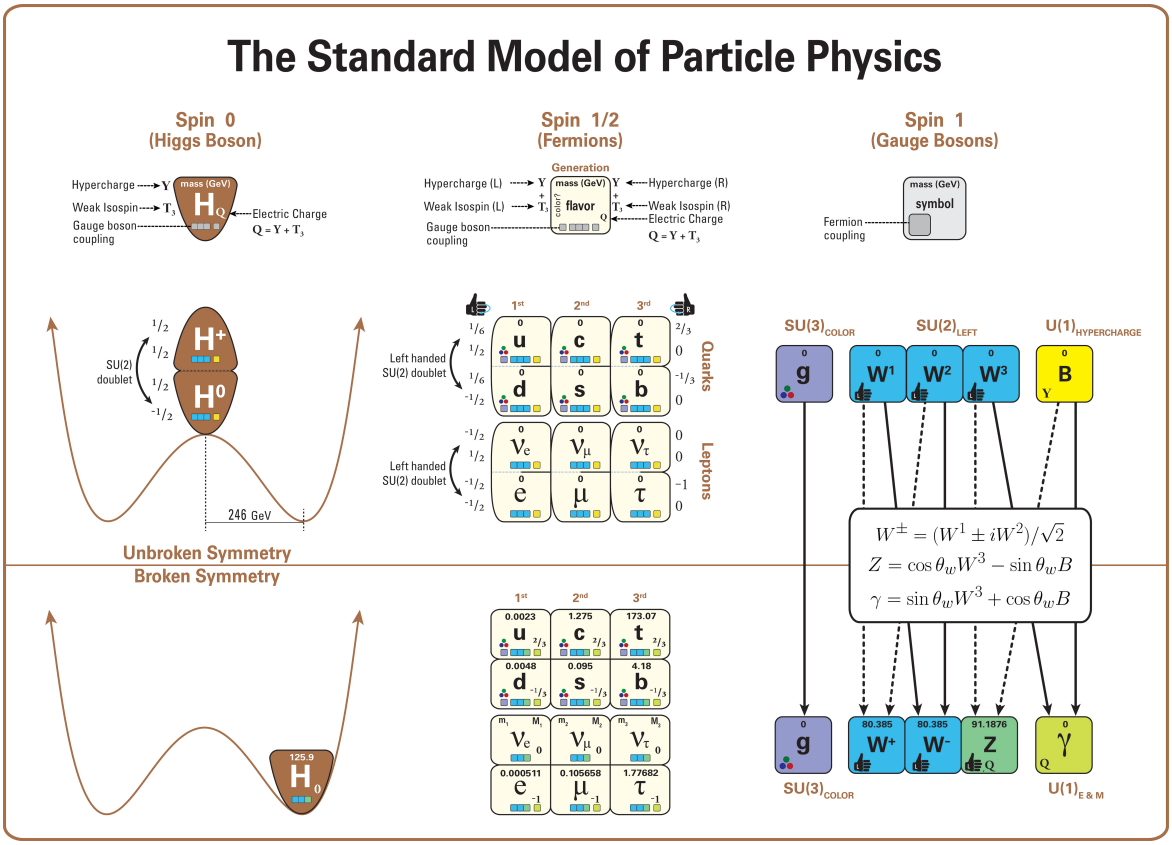

Figure 3: Summary of the particle content of the Standard Model and their interaction structure before and after electroweak symmetry breaking [21]. Includes the possibility of neutrino masses which are not formally part of the Standard Model.

2.1.4 Shortcomings of the Standard Model

There a number of reasons to believe that the Standard Model is an effective rather than a fundamental theory, and that it is incomplete. Some of these shortcomings are based on observations, such as gravity, dark matter, and neutrino flavor oscillations, while others pertain to apparent patterns among the parameters of the model, such as the hierarchy problem and other areas of excessive fine tuning. Additionally, there is a lack of unification among the strong and electroweak forces at any energy scale.

2.1.4.1 Gravity

To start, the SM only contains three out of the four known fundamental interactions, gravity is not included. Attempts to quantize gravity, with a corresponding mediating boson called a graviton, have not been successful yet. This is mostly due to the fact that spin-2 fields are not renormalizable in a four-dimensional space-time. Efforts to quantize gravity, such as superstring theory, or to geometrize particle physics, have yielded interesting solutions, but have fallen short of certain scientific criteria, such as falsifiability. Quantum theories and gravity must reconcile, at the latest, at the Planck energy scale of approximately $E_P \simeq 10^{19}\,\text{GeV}$. At these energy scales, the current version of the SM cannot be valid anymore.

2.1.4.2 Dark matter

Evidence for dark matter comes exclusively from astrophysical and cosmological observations. These include deviations of the rotation curves of disc galaxies from the expected Keplerian decline of $v_{rot} \sim r^{-\frac{1}{2}}$, whereas observations show that the rotation velocity remains flat towards large distances from the galactic centers [22, 23]. Additional evidence comes from measurements of gravitational lensing by galaxy clusters, where the luminous matter is insufficient to account for the amount of gravitational lensing observed [23]. A more recent type of astrophysical evidence comes from colliding galaxy clusters, in which the majority of the baryonic matter is located inside the intergalactic gas. In these collisions, the gas is shock-heated, resulting in a very large signal of X-rays. Comparing the baryonic mass distribution, inferred from this X-ray signal, to the distribution of the total mass, inferred from weak gravitational lensing, reveals a discrepancy that can be resolved by the presence of dark matter [23]. Finally, there is evidence from cosmology in the form of baryon nucleo-synthesis (BBN), which shows that baryons only makes up approximately 20% of the total matter in the universe, and from measurements of the cosmic microwave background radiation (CMB). The CMB is the residue of photons existing within an epoch of the universe where no neutral atoms existed, which means that the universe was opaque to photons. Around 380,000 years after the Big Bang, neutral atoms first formed and became stable, and the universe became transparent to photons, which released the previously contained photons into the universe. These photons are still visible today as the CMB. Computer simulations for the evolution of the universe show that existence of non-baryonic dark matter is essential in explaining structure formation in the universe that results in today's distribution [23]. Astronomical surveys of dark baryonic matter using microlensing, as well as the aforementioned measurement of the CMB, have also shown that known sources of baryonic matter, such as brown dwarfs, can only make up a small fraction of the measured dark matter density [23].

Three general approaches to solving the dark matter question have been considered – modifications of gravity, new configurations of existing types of matter, like primordial black holes, and the existence of a new type of particle, for example a weakly interacting massive particle (WIMP). The only conceivable dark matter candidate in the SM is the neutrino. However, even in the SM with neutrino masses, due to their extremely small mass, neutrinos move at relativistic velocities and thus would be *hot* dark matter. If they made up all of the dark matter in the early universe, cosmological structure formation would have occurred from large structures first, to small structures later, which is incompatible with observations of galaxies that existed less than a billion years after the big bang [23]. Thus, the SM does not contain a suitable candidate for dark matter and solutions to the dark matter question must lie outside the SM.

2.1.4.3 Matter-antimatter asymmetry

The universe today contains far more matter than antimatter. To achieve this state, three conditions must have been satisfied at some point in the early universe [24]:

- processes exist that violate the Baryon number;

- C- and CP-symmetry is violated;
- the relevant interactions occur outside thermal equilibrium.

A promising candidate to answer this question can be found in the context of the SM, which contains sources of C- and CP-violation, and where the conditions may have been met during the electroweak phase transition in the early universe. However, besides requiring a first-order phase transition [25] (compare Figure 2), the level of CP-violation that is present in the SM is far too small to result in the apparent matter-antimatter asymmetry. One step towards a resolution of this problem would be the existence of new physics, with additional sources of CP-violation.

2.1.4.4 Neutrino masses

The observation of neutrino flavor oscillation [26] shows that, contrary to what the original version of the SM states, neutrinos have masses. This is because the flavor oscillation comes about from a misalignment of the mass and flavor eigenstates of the three neutrino types. While interactions giving rise to the production of neutrinos occur in the flavor eigenstates, the propagation of the neutrino fields is based on their mass eigenstates. The misalignment of mass and flavor eigenstates results in an oscillating phase shift, which means that the initial neutrino flavor can interact as a different neutrino flavor at different places. This phase shift can only occur if there is a non-zero difference between the squares of the neutrino mass states and therefore observations of neutrino oscillations prove that at least two out of the three neutrinos are massive. A straightforward inclusion of neutrino masses into the SM is the introduction of right-chiral Dirac neutrinos and Yukawa couplings of the left-chiral and right-chiral neutrinos to the Higgs boson, generating their very small masses. Alternative mechanisms for the origin of the neutrino mass have been proposed, such as the Seesaw mechanism [27], which involve the postulation that neutrinos are in fact Majorana fermions, and not Dirac fermions. Part of the motivation for these alternative mechanisms lie in the fact that if the neutrino masses are generated by simple Yukawa interactions, there would be a very large hierarchy in the Yukawa coupling strengths in the SM of at least 11 orders of magnitude between the neutrinos and the top quark. Such large hierarchies are deemed unnatural by parts of the physics community.

2.1.4.5 Grand unification

The program of force unification has yielded very important results in the past, with the unification of quantum electrodynamics and weak interaction theory giving us the Standard Model as we know it today. The prospect of the unification of quantum chromodynamics and electroweak theory is a tantalizing prospect that has served as motivation for many papers and theses. This so-called grand unification does not naturally occur in the Standard Model, which is evident from the renormalization group equation (RGE) evolution of the coupling constants, shown in Figure 4. Grand unification would require the three couplings to meet at some large scale, which evidently does not happen in the SM. The appearance of new physics can alter the RGE evolution of the couplings and might lead to grand unification. The energy scale associated with grand unification is referred to as the GUT scale, and is believed to be of order $E_{GUT} \simeq 10^{16}\,\mathrm{GeV}$.

2.1.4.6 The hierarchy problem

As mentioned above, it is clear that the SM is not the final high-energy theory that describes the universe. In order to describe gravity, some new yet-unobserved physics must manifest at very high energy, and effectively replace the SM. The value associated with this energy scale, referred to as the UV cut-off scale Λ_{UV}, could, for example, be somewhere between the GUT and Planck scales. It is a fundamental property of scalar particles like the Higgs boson that the square of their masses receive radiative corrections $\Delta m^2_{\mathrm{h}^0}$ through interactions with other particles, e.g., via Yukawa and triboson interactions, such that

$$m^2_{\mathrm{h}^0,\mathrm{obs}} = m^2_{\mathrm{h}^0,\mathrm{bare}} + \Delta m^2_{\mathrm{h}^0}, \tag{4}$$

where $m^2_{\mathrm{h}^0,\mathrm{bare}}$ is the fundamental, bare, Higgs mass, and $m^2_{\mathrm{h}^0,\mathrm{obs}}$ is the square of the measured Higgs mass, $m(\mathrm{h}^0)$= (125.25±0.17) GeV [14]. In the SM, these corrections to $\Delta m^2_{\mathrm{h}^0}$ scale quadratically with Λ_{UV}, and the sign of the bosonic and fermionic contributions is opposite. If the SM were valid up to large scales like the Planck scale $\simeq 10^{19}\,\mathrm{GeV}$, the corresponding cutoff scale would mean that $\Delta m^2_{\mathrm{h}^0}$ is of similar magnitude. It directly follows from Equation 4 that the bare Higgs mass and its radiative corrections, potentially numbers of order 10^{19}, cancel to within two orders of magnitude to result in the measured Higgs mass. Because there is no mechanism in the SM that requires $m^2_{\mathrm{h}^0,\mathrm{bare}} \simeq \Delta m^2_{\mathrm{h}^0}$,

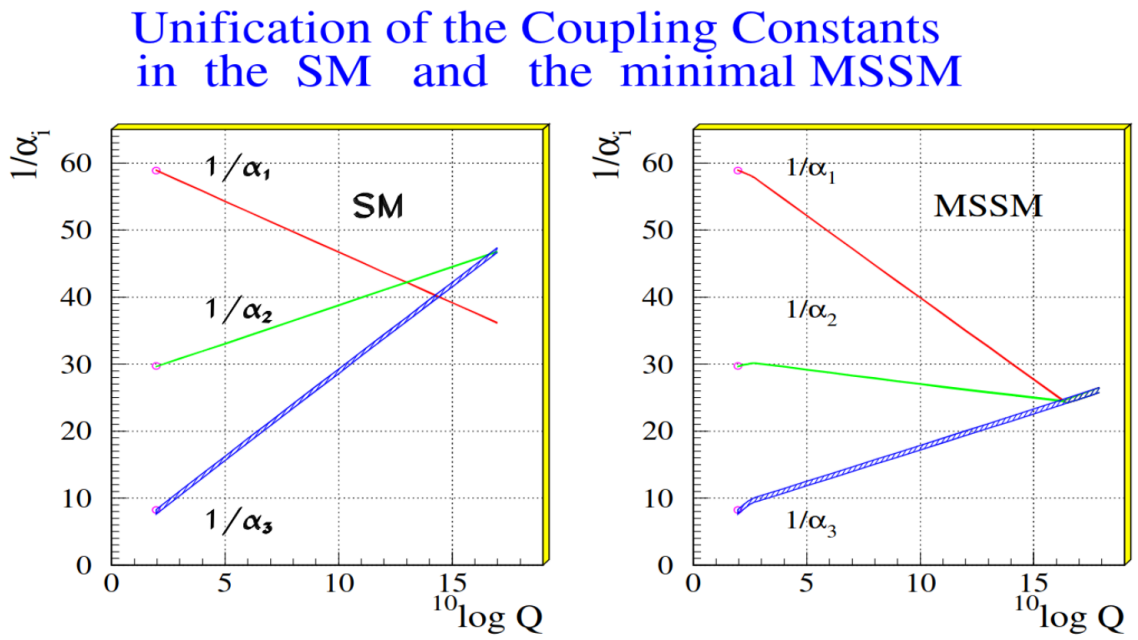

Figure 4: Scale evolution of the inverse couplings in the Standard Model (left) and potential scale evolution of the inverse couplings in suitable configurations of the MSSM (right). Figure taken from [28].

the large hierarchy between the observed Higgs mass and its radiative corrections is regarded by many (but not all) physicists as unnaturally fine-tuned. There are a number of conceivable resolutions for this problem.

1. The universe is simply fine-tuned to a large degree, the SM is valid up to very large scales such as the GUT or Planck scales, and it turns out that the problem is only an aesthetic one;
2. there is a yet-unknown connection between and reason why $m^2_{\mathrm{h^0,bare}} \simeq \Delta m^2_{\mathrm{h^0}}$;
3. Equation 4 is fundamentally flawed, with large consequences for quantum field theory in general;
4. the calculation of $\Delta m^2_{\mathrm{h^0}}$ is flawed in such a way that $\Delta m^2_{\mathrm{h^0}}$ is actually of order $m^2_{\mathrm{h^0,obs}}$;
5. new physics appears at relatively small energy scales, such that $\Lambda_{\mathrm{UV}} \simeq 10^2 - 10^4\,\mathrm{GeV}$, and which results in additional contributions to $\Delta m^2_{\mathrm{h^0}}$ that naturally cancel or significantly reduce the quadratic dependence on the scale for $\Lambda > \Lambda_{\mathrm{UV}}$. If the scale of new physics is too large, the hierarchy problem is only partially resolved, and a residual *little* hierarchy problem remains.

2.2 Supersymmetry

Supersymmetry (SUSY) is the only possible extension of the SM space-time symmetry group, the Poincaré group [29, 30], that is compatible with gauge theory. This new space-time symmetry requires that the fermionic and bosonic degrees of freedom are symmetric, by introducing a new fermionic partner field, called bosino, for each boson of the SM, and a new bosonic partner field, called sfermion, for each fermion of the SM. The spin of these new fields differs by $\frac{1}{2}$ from their SM partners. These new fields are connected with the SM fields by new operators Q, such that [31]

$$Q\,|\text{Boson}\rangle = |\text{Fermion}\rangle,\; Q\,|\text{Fermion}\rangle = |\text{Boson}\rangle. \tag{5}$$

If supersymmetry holds, these new supersymmetric particles have the same mass and charges as their SM partners. The following discussion of SUSY is based on [31, 32].

2.2.1 Supersymmetry breaking

Because additional particles with the same mass and charges as in the SM are experimentally ruled out, SUSY, if it exists, must be a broken symmetry at low energies. Furthermore, if SUSY is to solve the hierarchy problem, then the symmetry must be softly broken, meaning that the Langrangian can be written as [31]

$$\mathcal{L} = \mathcal{L}_{\text{SUSY}} + \mathcal{L}_{\text{soft}}, \tag{6}$$

where $\mathcal{L}_{\text{SUSY}}$ preserves supersymmetry invariance and $\mathcal{L}_{\text{soft}}$ breaks supersymmetry, but only contains mass terms and couplings with positive mass dimension – it must not contain dimensionless couplings. A number of interesting mechanisms of supersymmetry breaking have been proposed, such as gravity-mediated SUSY breaking [33, 34, 35, 36, 37, 38, 39], AMSB [40, 41], and gauge-mediated SUSY breaking [42, 43, 44, 45, 46, 47], and their respective model spaces have been constrained by various experiments. However, in the absence of a positive signal for supersymmetry, it makes sense to also interpret our experiments in models that are agnostic about the breaking mechanism, and which thus better reflect our (lack of) knowledge. One such model of supersymmetry is the minimal version of a supersymmetric extension of the Standard Model, called the Minimal Supersymmetric Standard Model (MSSM). It comes about by parameterizing our lack of knowledge of $\mathcal{L}_{\text{soft}}$ and the SUSY breaking mechanism, by collecting all possible terms that break supersymmetry softly. The MSSM is introduced in more detail in Section 2.3.

2.2.2 Supersymmetric solutions to open questions

Supersymmetric theories offer solutions to some of the shortcomings of the SM, the most important of which are the need for a dark matter candidate and a solution to the hierarchy problem.

The hierarchy problem

The most striking of these solutions is that to the hierarchy problem. Because bosons and fermions contribute with opposite signs to loop contributions of the Higgs mass, the introduction of a sfermion for each fermion exactly cancels the loop contribution of the fermion to the Higgs mass. This solution to the hierarchy problem is valid above the SUSY breaking scale and remains valid below, provided the mass of the supersymmetric particles is not too large. If they are large, the hierarchy problem re-emerges as the so-called *little hierarchy problem* due to the new dependence of the Higgs mass correction on the squared mass of the supersymmetric particles $m(\text{SUSY})^2$ of the form [31]

$$\Delta m(h^0)^2 \sim m(\text{SUSY})^2\, ln\left(\frac{\Lambda_{\text{UV}}}{m(\text{SUSY})}\right). \tag{7}$$

The absence of supersymmetric particles shown by the LHC results thus far put a strain on supersymmetry providing a complete solution to the hierarchy problem, as lower bounds on the masses of the sfermions, especially the top squark, start to push supersymmetry into a regime where the little hierarchy problem becomes relevant.

Dark matter

While not all supersymmetric models provide a candidate for dark matter, there is a general class of models that do. These models invoke a conserved quantity called R-parity, defined as

$$R = (-1)^{3\mathrm{B}+\mathrm{L}+2\mathrm{S}}, \tag{8}$$

where B is the baryon number, L is the lepton number, and S is the particle spin. If this quantity is conserved, then all particles with $R = -1$ can only be created or annihilated in pairs. As a result of this, the lightest $R = -1$ state does not decay and is thus stable. Once produced in the early universe, its number density is preserved unless effective pair-annihilation processes occur. If this lightest particle is at the same time massive, color-less and electrically neutral, it can serve as a dark matter candidate called a weakly interacting massive particle (WIMP). It turns out that supersymmetry can accommodate WIMPs of a mass and coupling strength that is compatible with the observations of the current dark matter density, assuming the freeze-out mechanism and the cosmological standard model Λ_{CDM} [8, 48, 49]. It is noted that the desire for a suitable dark matter candidate is not the only, or even main, reason to believe that R-parity exists, as it is also needed to prevent proton decay in supersymmetric models.

Matter-antimatter asymmetry

Supersymmetry adds additionaly sources of CP violation and can explain the baryon asymmetry. However, these new sources of CP violation are so abundant in supersymmetric model spaces that large parts are ruled out by overabundant CP violation in excess of what is required to explain the baryon content of todays universe. In particular, the supersymmetric model used in this work, the phenomenological MSSM, explicitly removes these new sources of CP violation. Thus, addressing the question of the matter-antimatter asymmetry as a constraint is not within the scope of this work.

Grand unification

Grand unification requires that the gauge coupling RGE evolution for strong and electroweak couplings results in their convergence at large scales. This is possible within supersymmetric models, by introducing new physics at smaller scales, as sketched in Figure 4. Note that there are no explicit theories of grand unification given within current theories of supersymmetry – the alteration of the gauge coupling RGE evolution and their eventual convergence is merely a prerequisite for grand unification. As such, the possibility of grand unification is not taken into account as a constraint in this work.

2.3 The MSSM and pMSSM

The Minimal Supersymmetric Standard Model (MSSM) is a collection of all soft breaking terms that come with the minimal supersymmetric extension of the SM, making no assumptions about the mechanism responsible for breaking SUSY. This extension makes the following modifications to the field content.

- The Standard Model Higgs sector is extended by a second complex Higgs doublet, since the conjugation of the Higgs field that is possible in the SM, and which enables one $\mathrm{SU}(2)_L$ Higgs doublet to give masses to both up- and down-type fermions, is not possible in a supersymmetric model. The four additional degrees of freedom that come with the new Higgs doublet result in four new Higgs particles: an electrically neutral heavy scalar H^0, a neutral pseudoscalar A^0, and two charged scalars $\mathrm{H}^{\pm}$. These new Higgs bosons have an R-parity of $R = 1$.
- Each field in the SM gets a supersymmetric partner field with a different mass and a spin that differs by $\frac{1}{2}$, but has otherwise identical quantum numbers. The superpartners of the SM fermions are spin-0 bosons called sfermions. The partners of the SM bosons are spin-$\frac{1}{2}$ fermions called bosinos. The R-parity for these particles is $R = -1$.

The full field content is given in Table 1.

	Spin-1 bosons	Spin-$\frac{1}{2}$ bosinos
Gauge fields	B (B boson) W^i (W bosons) g_a^i (gluons)	$\widetilde{B}$ (bino) $\widetilde{W}^i$ (winos) $\widetilde{g}_a^i$ (gluinos)
	Spin-$\frac{1}{2}$ fermions	Spin-0 sfermions
Colored matter fields	u_L, u_R (up) d_L, d_R (down) c_L, c_R (charm) s_L, s_R (strange) t_L, t_R (top) b_L, b_R (bottom)	$\widetilde{u}_L, \widetilde{u}_R$ (sup) $\widetilde{d}_L, \widetilde{d}_R$ (sdown) $\widetilde{c}_L, \widetilde{c}_R$ (scharm) $\widetilde{s}_L, \widetilde{s}_R$ (sstrange) $\widetilde{t}_L, \widetilde{t}_R$ (stop) $\widetilde{b}_L, \widetilde{b}_R$ (sbottom)
Leptonic matter fields	e_L, e_R (electron) ν_e (electron neutrino) μ_L, μ_R (muon) ν_μ (muon neutrino) τ_L, τ_R (tauon) ν_τ (tau neutrino)	$\widetilde{e}_L, \widetilde{e}_R$ (selectron) $\widetilde{\nu}_e$ (electron sneutrino) $\widetilde{\mu}_L, \widetilde{\mu}_R$ (smuon) $\widetilde{\nu}_\mu$ (muon sneutrino) $\widetilde{\tau}_L, \widetilde{\tau}_R$ (stau) $\widetilde{\nu}_\tau$ (tau sneutrino)
	Spin-0 Higgs	Spin-$\frac{1}{2}$ higgsinos
Higgs fields	H_u^+, H_u^0 H_d^+, H_d^0	$\widetilde{H}_u^+, \widetilde{H}_u^0$ $\widetilde{H}_d^+, \widetilde{H}_d^0$

Table 1: Field content of the MSSM.

The neutral components of the electroweak states of the bino, the wino and the higgsino fields

mix into four mass states called **neutralinos** $\widetilde{\chi}^0_{1,2,3,4}$, connected by the mass matrix [31]

$$M_{\widetilde{\chi}^0_{1,2,3,4}} = \begin{pmatrix} \mathrm{M}_1 & 0 & -c_\beta\, s_W\, m_Z & s_\beta\, s_W\, m_Z \\ 0 & \mathrm{M}_2 & c_\beta\, s_W\, m_Z & -s_\beta\, s_W\, m_Z \\ -c_\beta\, s_W\, m_Z & c_\beta\, cos(\theta_W)\, m_Z & 0 & -\mu \\ s_\beta\, s_W\, m_Z & -s_\beta\, cos(\theta_W)\, m_Z & -\mu & 0 \end{pmatrix} M_{\widetilde{B},\widetilde{W}^0,\widetilde{H}^0_u,\widetilde{H}^0_d}, \quad (9)$$

where $c_\beta = \cos(\beta)$ and $s_\beta = \sin(\beta)$, β is the angle in the Higgs vacuum expectation values, $s_W = \sin(\theta_W)$, where θ_W is the Weinberg angle, and m_Z is the Z boson mass. By convention they are ordered by mass, meaning that $\widetilde{\chi}^0_1$ is the lightest neutralino. The charged electroweak states of the wino and the higgsino mix to form two mass states called **charginos** $\widetilde{\chi}^\pm_{1,2}$, which are again ordered by their mass. Their mass matrix, in 2×2 block form, is [31]

$$M_{\widetilde{\chi}^\pm_{1,2}} = \begin{pmatrix} 0 & X^T \\ X & 0 \end{pmatrix} M_{\widetilde{W}^\pm,\widetilde{H}^\pm_{u,d}}, \qquad \text{with } X = \begin{pmatrix} \mathrm{M}_2 & \sqrt{2}\, s_\beta\, m_W \\ \sqrt{2}\, c_\beta\, m_W & \mu \end{pmatrix}, \quad (10)$$

where m_W is the W boson mass.

Mixing also occurs in the sfermion sector, with the left- and right-chiral flavor states $\widetilde{f}_L$ and $\widetilde{f}_R$ forming mass-ordered states $\widetilde{f}_1$ and $\widetilde{f}_2$. The mixing in the sfermion sector is often neglected for the first two generations, which makes their flavor state identical to their mass eigenstates. Mixing of the third generation sfermions is not usually neglected, such that there exist mass eigenstates $\widetilde{\mathrm{t}}_1$ and $\widetilde{\mathrm{t}}_2$, $\widetilde{\mathrm{b}}_1$ and $\widetilde{\mathrm{b}}_2$, as well as $\widetilde{\tau}_1$ and $\widetilde{\tau}_2$, that differ from the flavor eigenstates.

In addition to this, we here require that R-parity is conserved, which means that bosinos and sfermions can only be pair-produced and pair-annihilated. The lightest supersymmetric particle does not decay, as this would violate R-parity conservation.

2.3.1 The pMSSM-19

The MSSM introduces an large number of over 100 new *free* parameters to parameterize our ignorance about the breaking of supersymmetry. Constraining such a large parameter space is enormously challenging, and in the absence of specific, positive evidence for supersymmetry, it makes sense to first simplify the MSSM model space to the phenomenologically most relevant part. A popular version of a simplified but phenomenologically rich model is the phenomenological MSSM – the **pMSSM** [50]. It preserves most of the phenomenology of the MSSM, given our current experiments, and reduces the number of new parameters to 19, by making 5 sets of assumptions on the structure of the MSSM. These assumptions are:

- There are no tree level flavor changing neutral currents – all terms in the Lagrangian that would lead to them are removed.
- There are no new sources of CP-violation in addition to what is allowed by the CKM matrix – the complex parts in the Lagrangian that contain such sources are treated as real.
- The first and second generation of sfermions are mass degenerate.
- The trilinear couplings to the first and second generation are neglected, as our experiments are not sensitive to them.
- The lightest supersymmetric particle is the lightest neutralino, $\widetilde{\chi}^0_1$.

Note that as a consequence of requiring that there are no flavor changing neutral currents, and no trilinear couplings to the first and second sfermion generations, the left- and right-chiral field do not mix. This means that they are not expressed as mass-ordered states, but rather as the original flavor eigenstates.

The pMSSM then contains the following 19 new parameters, which are defined at the SUSY scale. To achieve an acceptable uncertainty on the light Higgs boson mass after RGE evolution, the SUSY scale is chosen to be the geometric mean of the stop mass parameters, $\mathrm{Q_{SUSY}} = \sqrt{m_{\widetilde{t},1} \times m_{\widetilde{t},2}}$. The 19 parameters of the pMSSM are the following:

- three gaugino parameters: the bino mass parameter M_1, the wino mass parameter M_2, and the gluino mass parameter M_3;

- six squark mass parameters for the squarks corresponding to the left- and right-chiral quarks: $M_{q,1}(=M_{q,2})$, $M_{q,3}$, $M_{u,1}(=M_{u,2})$, $M_{u,3}$, $M_{d,1}(=M_{d,2})$, and $M_{d,3}$;
- four slepton mass parameters for the sleptons corresponding to the left- and right-chiral leptons: $M_{l,1}(=M_{l,2})$, $M_{l,3}$, $M_{r,1}(=M_{r,2})$, and $M_{r,3}$;
- three trilinear sfermion-Higgs couplings: A_t, A_b, and A_l;
- three further Higgs related parameters: the higgsino mass parameter μ, the ratio of the vacuum expectation values of the Higgs doublets $\tan(\beta)$, and the mass of the pseudoscalar Higgs boson m_A.

A couple of additional constraints are applied on the pMSSM in this thesis, namely:

- the mass of the lightest (scalar) Higgs boson is compatible with the discovered Higgs boson;
- the particle spectrum does not contain tachyons.

These constraints are implemented within the sampling procedure, detailed in Section 5.

2.3.2 Electroweak fine tuning

The little hierarchy problem can be qualified in terms of fine tuning from the electroweak sector of the MSSM. Minimizing the MSSM super potential gives the following equation [51]:

$$\frac{m_Z^2}{2} = \frac{m_{H_d}^2 + \sum_d^d - \left(m_{H_u}^2 + \sum_u^u\right)\tan^2\beta}{\tan^2\beta - 1} - \mu^2, \tag{11}$$

where m_{H_d} and m_{H_u} are the soft mass terms of the two MSSM Higgs doublets, and $\sum_d^d$ and $\sum_u^u$ are a collection of independent radiative corrections involving particles with sizable Yukawa or gauge couplings to the Higgs sector for down-type and up-type sfermions, respectively. The sum in Equation 11 is expanded to its individual terms C_i, such that $\frac{m_Z^2}{2} = \sum_i C_i$ with $C_{H_d} = \frac{m_{H_d}^2}{\tan^2\beta - 1}$, $C_{\sum_d^d} = \frac{\sum_d^d}{\tan^2\beta - 1}$, $C_{H_u} = -\frac{m_{H_u}^2 \tan^2\beta}{\tan^2\beta - 1}$, $C_{\sum_u^u} = -\frac{\sum_u^u \tan^2\beta}{\tan^2\beta - 1}$, and $C_\mu = -\mu^2$. The electroweak fine tuning measure ΔEW can then be defined as

$$\Delta EW = max_i \frac{|C_i|}{\frac{m_Z^2}{2}}. \tag{12}$$

If any one C_i in Equation 11 becomes large, there needs to be fine tuning among the other contributors for the equation to hold, with the degree of fine tuning proportional to the maximum of terms C_i. ΔEW thus serves as a measure of the fine tuning necessary for Equation 11 to hold.

2.3.3 Simplified Models

One of the main challenges in searches for supersymmetry is the high dimensionality of the super-symmetric model space. In the MSSM, there is an overabundance of configurations that might fit potential signals from new physics at the LHC, and as many ways in which constraints from the LHC can be evaded. To both provide a first characterization of possible measured deviations from the SM and to provide an intuitive interpretation of any null-results, simplified models [52] can be constructed with just one or two variable parameters, such as masses, which can represent ultra constrained sub-models of the MSSM. To this purpose, they usually contain 2 or 3 parameters, like new particles and their masses, and the branching ratios of their decay channels. All other supersymmetric particles are assumed to be decoupled and to have no influence on the observables. It is then possible to constrain this rather limited and *simplified* model space using null-results of the LHC in an intuitive way. In the presence of results that deviate from SM expectation, they can provide simple example topologies that may fit the data, from which a realistic and full model may be built. These simplified models are not intended to provide a solution to fundamental problems of the SM, such as achieving grand unification or low fine tuning. Most searches for supersymmetry at the LHC interpret their results in terms of simplified models, by placing upper limits on the signal cross section in parameter planes of the respective simplified model space. One of the goals of this thesis is to overcome these restrictions by interpreting in the full pMSSM, and by comparing the result to those obtained for simplified models.

2.4 Natural units

Natural unit systems are defined using constants of nature. We use a natural unit system throughout this thesis in which $\hbar = c = 1$, where $\hbar$ is the reduced Planck constant, and c is the speed of light. We do **not** use these natural units on occasions where the respective constant is explicitly stated, such as for the proper decay length $c\tau$.

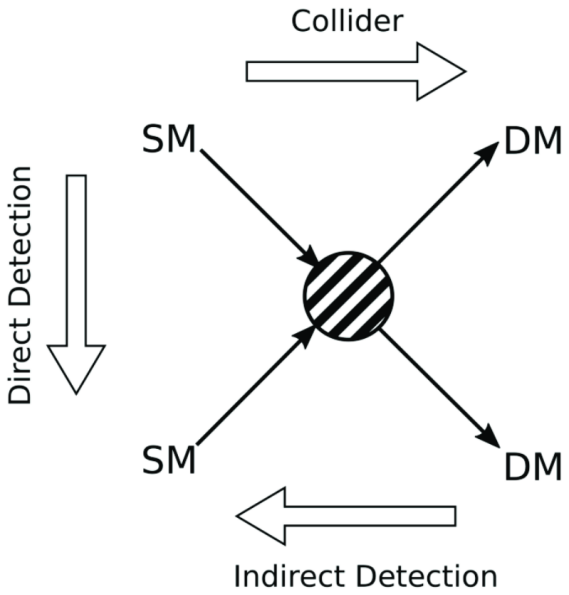

Figure 5: Potential interactions of dark matter with the Standard Model and associated search strategies. Figure taken from [53].

3 Observations and experiments

3.1 Dark matter detection

Current efforts for dark matter searches fall in three categories, which can be summarized alongside the generalized Feynman diagram shown in Figure 5. Reading the diagram from top to bottom describes scattering of dark matter on SM particles, the associated search strategy is called direct detection of dark matter. Reading the diagram from left to right results in on-shell production of dark matter, whose search strategy involves particle colliders such as the LHC. Reading the diagram from right to left describes the annihilation of dark matter, with the associated search strategy of indirect detection of dark matter by searching for the SM final state of the annihilation processes.

3.1.1 Direct detection of dark matter

Direct detection experiments aim to detect the elastic or inelastic scattering of dark matter particles on nuclei or nucleons in the molecules of an active detector element. In elastic scattering, the signal consists of the recoil of the nucleus from the dark matter scattering. In inelastic processes, the active detector element is excited, and the signal comes in the form of the relaxation of the exited state. These experiments, similar to neutrino detectors, are built to produce as little background noise as possible. There are two contributions of dark matter nucleon or dark matter nuclei interactions that are relevant to dark matter consisting of WIMPs. These are spin-dependent (SD) interactions from higher order couplings of the dark matter spin to the spin of the nucleons, and spin-independent (SI) interactions with the nucleons.

These interactions scale differently with the properties of the active detector material. The SI interactions prefer nuclei with a large number of nucleons, and because the detector volume needs to be chemically inert to reduce background noise, heavy noble gases such as xenon are used. To detect SD interactions, detector materials with an odd number of protons or neutrons are required [22].

Observed data from four experiments and detectors are used in this thesis.

- The XENON1T experiment and detector [54, 55] was situated in the Laboratori Nazionali del Gran Sasso (LNGS) in Italy and took data from 2015 to 2018. It used a dual-phase time projection chamber, filled with 3.2 tonnes of liquid xenon as the active detection material, with a gaseous xenon phase at the top. An electric field is created inside the detector to facilitate the drifting of charges from the liquid to the gaseous phase. This allows for the independent measurement of primary light signals from the WIMP-xenon interaction, and the delayed signals

from electrons, created in the primary interaction, transitioning from the liquid to the gaseous phase.

- The DarkSide-50 experiment and detector [56] was situated at LNGS and took data from 2015 to 2018. Similarly to the XENON experiments, it uses a dual-phase time projection chamber with a liquid and gaseous phase, but uses approximately 46.4 kg of liquid argon instead of xenon as the active detector element.

- The CRESST-III experiment and detector [57] is situated at LNGS, producing first results in 2019. It is made up of detection modules consisting of cryogenically cooled $CaWO_4$ scintillating calorimeters, which measure both phonons from potential dark matter interactions, as well as the accompanying scintillation light signal.

- The PICO-60 experiment and detector [58, 59] was situated at SNOLAB in Canada. It was a super-heated bubble chamber that took data from 2013 to 2014 using 25 liters of CF_3I, and from 2016 to 2017 using 54 liters of C_3F_8 as the active detector material. The detector achieves the low background noise required for sensitivity to dark matter by tuning the ionization thresholds using different thermodynamic conditions, and calibrating the backgrounds on them.

Of these four experiments, the XENON1T detector achieves the largest sensitivity to the range of WIMP masses relevant to the pMSSM. More recent results with larger sensitivity, in particular from the LUX-ZEPLIN experiment [60], could not be considered in this work due to time constraints. The upper limits on the SI cross sections are stronger by a factor of approximately 3 in the relevant WIMP mass region.

Because neutrinos are an irreducible background for the dark matter signal, the sensitivity of direct detection experiments is fundamentally limited by the interaction rate of neutrinos with the detectors. This transition to a much more background dominated regime, called the neutrino floor, lies approximately 3 orders of magnitude below the current best upper limits on the spin-independent dark matter nucleon interaction cross section for a xenon target [61].

3.1.2 Indirect detection of dark matter

Indirect detection aims to measure signals from dark matter annihilation into Standard Model particles. These final states include high-energy neutrinos, positrons, anti-protons and heavier anti-nuclei, as well as high-energy photons. Because the annihilation flux increases with the square of the dark matter density, the most promising sources for this are regions of space with a large local dark matter density, such as the galactic center of the Milky Way, or galaxy clusters and dwarf galaxies [62]. Of particular interest in this thesis are gamma-ray searches performed by the `MAGIC` Cherenkov telescopes [63] and the `FERMI-LAT` space telescope [64]. The `MAGIC` telescopes measure the Cherenkov light emitted by gamma rays and other cosmic particles interacting with the Earth atmosphere. The `MAGIC` telescopes are able to detect photons with energies between approximately 50 GeV and 50 TeV [62]. The Fermi-LAT is a pair-conversion telescope on board the Fermi Gamma-ray Space Telescope. It measures the pair-conversion of cosmic high-energy photons into electron-positron pairs [64]. It is sensitive to photons with energies between approximately 20 MeV and more than 300 GeV [62]. Measurements of the differential rate of cosmic photons enables to place upper limits on the annihilation cross section of dark matter into SM final states that contain photons.

3.1.3 Production and detection of dark matter at particle colliders

Dark matter can potentially be produced at particle colliders, provided that it interacts strongly enough with SM particles, and that its mass is not greater than the center-of-mass energy of the respective particle collisions. Because a dark matter particle will not annihilate or scatter inside the detector, it is not reconstructed. Therefore, the presence of dark matter in events must be inferred from missing energy and momentum. This in turn requires that something else must be produced inside the signal events, such as hadron jets from initial state radiation. Knowing the initial values for energy and momentum, or at least their transverse components, then allows to infer the invisible system that recoils of the measured visible system from initial state radiation. Standard Model final states that contain neutrinos are an irreducible background in most search for dark matter at particle colliders.

3.1.4 Cosmological implications on dark matter

Measurements of the cosmic microwave background put constraints on the total matter density, as well as the baryonic and dark matter relic densities, in the context of the Λ_{CDM} cosmological standard model. The most recent constraints on the relic density are from the Planck satellite observatory, which constrains the cold dark matter relic density to [8]

$$\Omega_C \mathrm{h}^2 = 0.12 \pm 0.001, \tag{13}$$

where Ω_C is the fraction of the critical density ρ_c that results in a geometrically flat universe. Note that $\Omega_C \mathrm{h}^2$ is abbreviated to $\Omega \mathrm{h}^2$ throughout this thesis. Because the neutralinos present in the MSSM are a form of cold dark matter, these constraints directly apply to the MSSM models in question in this work, assuming the Λ_{CDM} model as described in [8].

3.2 Anomalous magnetic moment of the muon

The anomalous magnetic moment of the muon a_μ is the degree to which the gyromagetic ratio g of the magnetic dipole moment of the muon deviates from 2 (also called *g-2*). It is sensitive to higher order corrections, which can potentially include contributions from sources beyond the SM. Because a_μ can both be measured and predicted in the SM with extreme precision, its measurement constitutes one of the most sensitive tests of the SM that exists today.

To measure a_μ, polarized muons are introduced into a storage ring. Two frequencies are then measured: the frequency with which the polarization turns relative to the momentum ω_p and the value of the magnetic field normalized to the Larmor frequency of the proton, ω_p [65]. The anomalous magnetic moment is then calculated as [65]

$$a_\mu = \frac{\omega_a/\omega_p}{\lambda_+ - \omega_a/\omega_p}, \tag{14}$$

where $\lambda_+ = \frac{\mu_{\mu^+}}{\mu_p}$ is the ratio of magnetic moments of the muon and proton.

3.2.1 The muon g-2 experiment at Fermilab

The most recent and most accurate measurements of a_μ have recently been performed by the muon g-2 experiment at Fermilab. The experiment consists of an accelerator complex, a muon storage ring, and a detector.

The accelerator collides 8 GeV protons with a target, resulting in pions with a momentum of approximately 3.1 GeV. The pions subsequently decay into muons, which are first brought into the so-called Delivery Ring to remove residual pion impurities of the beam. Finally, the muons are ejected from the Delivery Ring and injected into the storage ring [65].

The storage ring consists of one continuous superconducting di-pole magnet, which is extensively shimmed to provide a highly uniform magnetic field. The magnet geometry is a C-shape that is open towards the inside of the storage ring. The injected muons are *kicked* to the so-called *magic* momentum of $p = m/\sqrt{a_\mu} \simeq 3.09\,\text{GeV}$, at which electric field contributions to the precession frequency ω_a vanish at first order. The muons subsequently decay into positrons, whose momentum is correlated to the muon spin direction. This allows the measurement of the muon spin through measurement of the positron momenta, which is performed by 24 electromagnetic calorimeters using lead flouride Cherenkov crystals to absorb the positron energy. Read-out occurs via silicon photomultipliers [65].

The measurement of the positron energies over time constitutes a measurement of the muon spin over time, from which the precession frequency ω_a is extracted. Using this precise measurement of ω_a together with a precise measurement of the magnetic field has resulted in the currently most precise measurement of $a_\mu = 116592055(24) \times 10^{-11}$ [66].

3.3 Flavor physics experiments

Precision measurements in the flavor sector of the SM, especially of rare decays of B-mesons and D-mesons, can put significant constraints on supersymmetry. These measurements have been performed by a number of experiments, the most important of which are shortly introduced here. These are two very similar experiments, Belle and BaBar, located at the KEKB collider in Japan and the PEP-II collider at SLAC National Laboratory at Stanford University, respectively. We also introduce the LHCb detector, located at the Large Hadron Collider at CERN.

3.3.1 Belle

The Belle detector was a particle collision experiment specialized in the study of b-physics. It was placed in the KEKB collider and took data from 1999 to 2010, with a number of data events collected corresponding to an integrated luminosity of $L_{int} = 710\,\text{fb}^{-1}$. The KEKB collider was an asymmetric electron-positron collider in Tsukuba, Japan. Electron and positrons with energies of 8 GeV and 3.5 GeV, respectively, were collided inside the Belle detector with a center-of-mass energy equal to the $\Upsilon(4S)$ resonance, which subsequently decays into pairs of B-mesons. Because of the asymmetry of the collisions, the interaction final state is boosted, which allows for lifetime dependent measurements.

A schematic view of the Belle detector is shown in Figure 6. The Belle detector itself is cylindrically symmetric around the beam pipe, with the different detector subsystems built in layers around the interaction point. The detector is immersed in a longitudinal 1.5 T magnetic field, created by a cryogenic solenoid magnet.

The innermost component is a silicon vertex detector (SVD), made of double-sided silicon strip detectors, and whose purpose is the measurement of both primary and secondary vertices and the reconstruction of particle momenta whose tracks are bent by the magnetic field. Directly outside the vertex detector, a drift tube system (CDC) is installed, which assists in the measurement of the particle momenta, in addition to measuring their energy loss $\frac{dE}{dx}$.

To facilitate particle identification, Belle also employs aerogel Cherenkov counters (ACC), made up of distinct aerogel modules with varying refractive indices, and time-of-flight counters (TOF) using plastic scintillators. Read-out for both systems is performed using photo-multiplier tubes.

An electromagnetic calorimeter (ECL) is positioned outside the previously described systems, which consists of a barrel portion and an end cap for each the forward and backward regions. The calorimeter is highly segemented into modules made up of scintillating thallium-doped cesium iodide (CsI(Tl)) crystals, which are read-out by silicon photodiodes. In the very forward regions, Belle contains an additional particularly radiation hard extreme forward calorimeter (EFC), which uses Bismuth Germanate Oxide crystals. Its main purpose was to assist the measurement of the instantaneous luminosity.

The final subsystems are the solenoid magnet, placed outside the electromagnet calorimeter, and the instrumented return yoke (KLM), which facilitates the detection and identication of muons and neutral hadrons, primariliy neutrons and K_L^0 mesons. The return yoke also consists of a barrel portion and end caps, with alternating layers of resistive place chambers and iron plates. This description is based on [67].

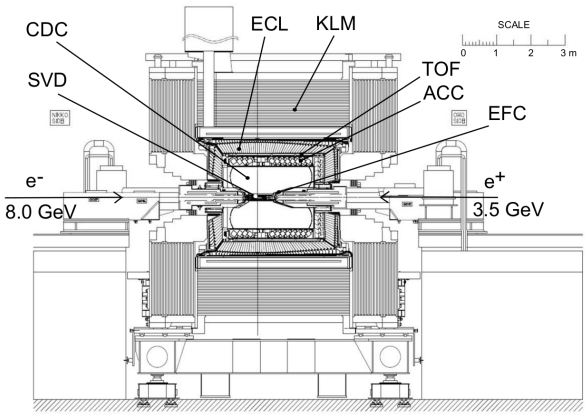

Figure 6: Schematic cross section view of the Belle detector. Figure taken from [67].

3.3.2 BaBar

Similarly to the Belle detector, the BaBar detector was designed to study the physics of b-hadrons. It was located at the PEP-II collider at the SLAC National Accelerator Laboratory at Stanford University. Data-taking occurred between October 1999 and April 2008, with a number of signal events recorded corresponding to an integrated luminosity of $L_{int} = 513\,\text{fb}^{-1}$. PEP-II accelerates electrons to energies of 9 GeV and positrons to 3.1 GeV, which results in collisions with a center-of-mass energy of $E_{\text{CMS}} = 10.58\,\text{GeV}$ inside the BaBar detector – the energy of the $\Upsilon(4S)$ resonance. The asymmetry of the electron and positron energies results in a Lorentz boost of the final state, which enhances the sensitivity to the lifetime of final state particles.

The detector design of the BaBar detector is very similar to the already described Belle detector, and a schematic view is shown in Figure 7. The detector is cylindrically symmetric around the beam line, with a magnet providing a 1.5 T magnetic field that allows for the momentum measurement of charged particles.

The innermost detector component is the silicon vertex tracker, which consists of five layers of double-sided silicon strips and is used for precise vertex determination and track momentum reconstruction. This component is followed by a drift chamber, which measures the energy loss $\frac{dE}{dx}$ and track momentum of traversing particles. The magnet is located outside these components.

To facilitate particle identification, BaBar uses the so-called *Detector of Internally Reflected Cherenkov light* (DIRC) in the barrel region. It allows for the separation of pions and kaons through their different emission angle of Cherenkov light from the passing of charged particles through quartz bars. The Cherenkov light is detected using photo multiplier tubes.

The pen-ultimate system is the electromagnetic calorimeter, which uses scintillating thallium-doped cesium iodide (CsI(Tl)) crystals, arranged in rings inside a barrel region and end caps.

The outermost system is dedicated to the detection of muons and the return of the magnetic field lines. To perform both functions, BaBar makes use of steel plates of increasing thickness, interspersed with glass-electrode-resitive plate chambers.

This description is based on [67].

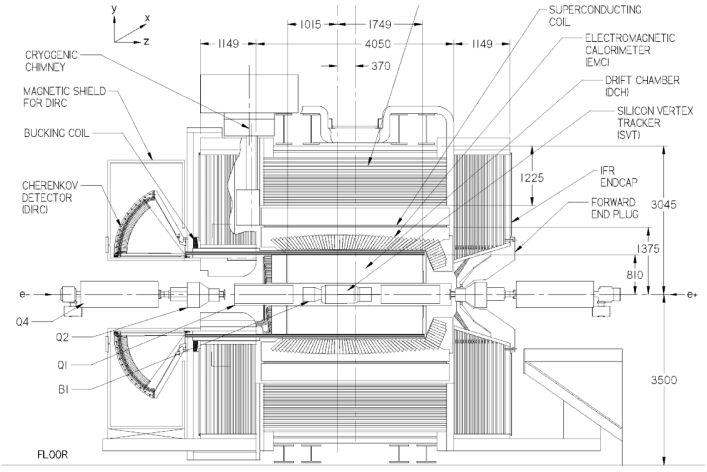

Figure 7: Schematic cross section view of the BaBar detector. Figure taken from [67].

3.3.3 LHCb

The LHCb experiment is an on-going experiment dedicated to the study of b-physics. It is located at the Large Hadron Collider at CERN (shortly introduced in Section 3.4), where data-taking started in 2011. It is an asymmetric, single-arm spectrometer covering the forward regions of proton-proton interactions at the LHC. This makes the design significantly different from both Belle and Babar, due to the fact that at the large energies of the LHC, the B-Hadrons are predominately produced in the forward regions. The luminosity at the LHCb experiment is tuned and leveled to below the maximum possible luminosity by changing the beam focus at the interaction point. This allows the operation at an optimal working point by weighing the number of events against the number of primary interactions per event and against the radiation tolerance of the LHCb detector. A schematic view of the LHCb detector is shown in Figure 8.

LHCb uses a di-pole magnet to generate the magnetic field for the bending of charged particle trajectories necessary to measure their momentum. The integrated magnetic field corresponds to 4 Tm.

The subsystem closest to the interaction region is the vertex locator (VELO) system. It is made up of many layers of silicon strip detectors and is used to precisely measure the primary and any secondary vertices. A set of silicon detector modules dedicated to pile-up rejection is located up-stream of the VELO detector.

Tracking is performed by two detectors, the track turicensis (TT) up-stream of the di-pole magnet, and the inner tracker, located in three stations, down-stream of the magnet. The TT and inner tracker use silicon microstrips to detect charged particles. The inner tracker is complimented by an outer tracker in each of the three stations. The outer tracker is made up of drift-tube chambers, arranged in individual modules.

LHCb contains Cherenkov detectors for the purpose of particle identification. To cover a larger range of momenta, two such detectors are used, RICH1 and RICH2, which are placed up-steam and down-stream of the magnet, respectively. They allow for the separation and identification of different particles, most importantly pions and kaons.

An electromagnetic calorimeter (ECAL) and a hadronic calorimeter (HCAL) are used to measure the energies of electrons, photons, and hadrons, and also assist in their identification. They are also used for event triggering purposes. Both the ECAL and the HCAL are sampling calorimeters, made up of layers of passive absorber and active scintillation elements, which are read out using wavelength-shifting fibers and photo-multiplier tubes. The passive elements of the ECAL and HCAL are lead and iron plates, respectively. To achieve a better background rejection, mainly of charged and neutral pions, a sre-shower (PS) detector and a scintillator pad detector (SPD) are located directly up-stream of the ECAL.

The final subsystem is the muon system, which consists of five stations M1 through M5. It is used to identify muons and trigger events based on their presence and momenta. It uses multi-wire proportional chambers to measure the muons, with the exception of the inner region of station M1, where triple-GEM detectors are used.

This detector description is based on [68]. The LHCb detector received an extensive upgrade during the shut-down period of the LHC between 2018 and 2022, however, as the measurements used in this work were all taken with the original design, this upgrade is not featured here. A description can be found on the LHCb website [69].

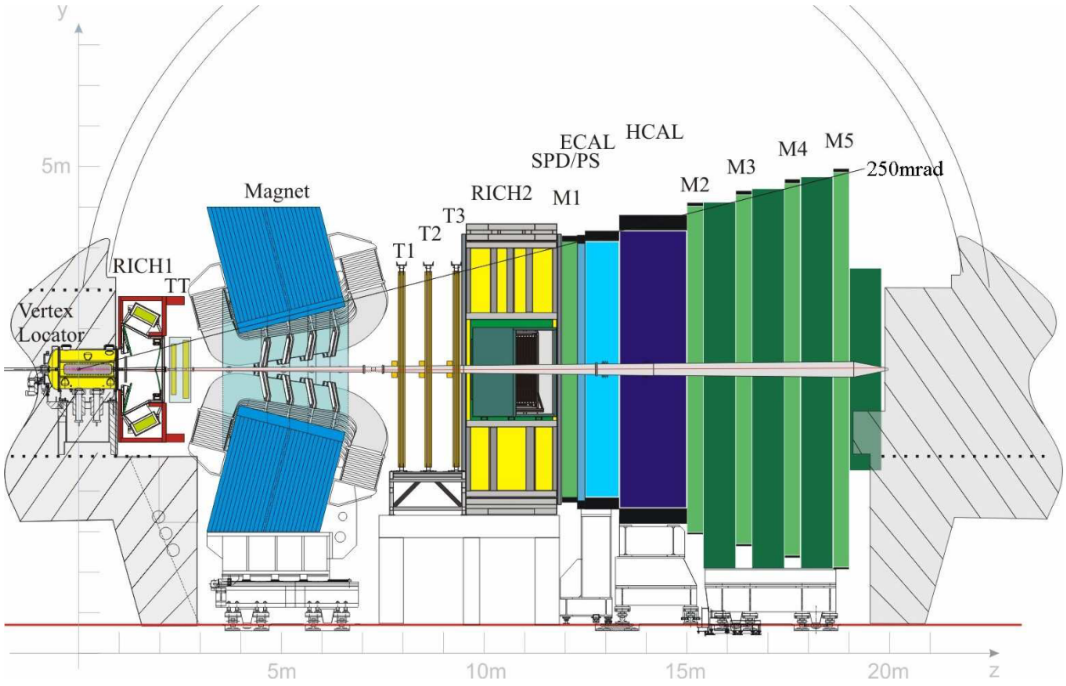

Figure 8: Schematic view of the LHCb detector. Figure taken from [68].

3.4 The Large Hadron Collider and its Detectors

The Large Hadron Collider (LHC) is a circular proton-proton collider located at Conseil Européen pour la Recherche Nucléaire (CERN) near Geneva. Its circumference is approximately 27 km and it is currently the most powerful particle collider in the world, achieving proton-proton collisions with a center-of-mass energy $\sqrt{s}$ of almost $\sqrt{s} = 14\,\text{TeV}$. It can be operated at large instantaneous luminosities, above $L \simeq 10^{34}\,\text{cm}^{-2}\text{s}^{-1}$. The collider complex, for which an overview is shown in Figure 9, houses four large particle detectors, the specialized detectors LHCb [68, 69, 70] and ALICE [71], designed to study b-physics and heavy-ion physics, and the two general-purpose detectors ATLAS [72] and CMS [73]. This work uses most data recorded by the ATLAS and CMS detectors, which are shortly described in this section, while the LHCb detector has already been introduced in Section 3.3 in the context of flavor physics.

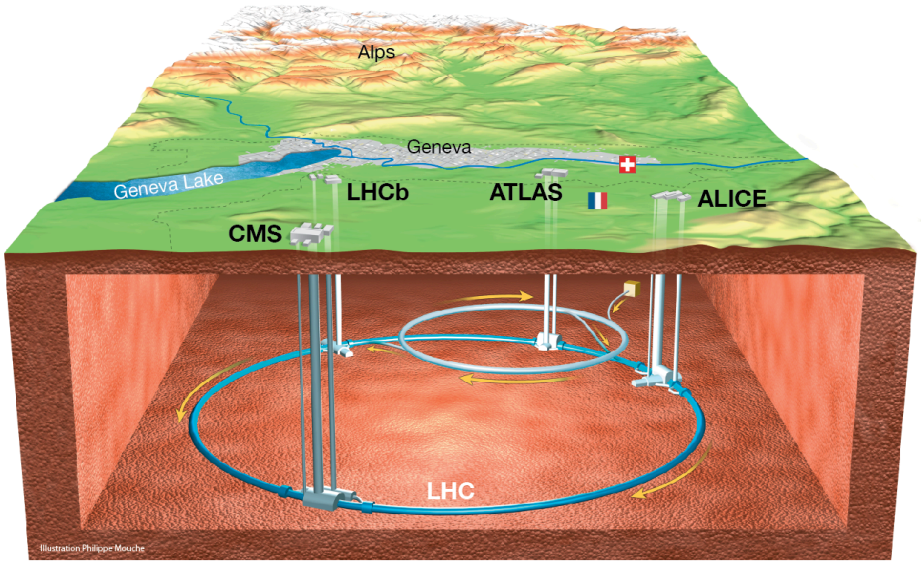

Figure 9: Overview of the Large Hadron Collider (LHC) complex near Geneva, including the four big particle colliders ALICE, ATLAS, CMS, and LHCb. Figure taken from [74].

3.4.1 The CMS detector

The CMS (Compact Muon Solenoid) detector is a general purpose detector, designed to reconstruct and study the final state of high-energy proton-proton collisions at the LHC. It is a full-coverage detector, meaning its acceptance is nearly 4π steradians, and its central feature is a large superconducting solenoid magnet with field strength $B = 3.8\,\text{T}$. With the exception of neutrinos, the CMS detector is capable of reconstructing all SM particles and thus gives an almost complete record of the events from the proton-proton collisions.

The detector is built in cylindrical layers around the beam pipe and beam crossing spot, with each layer consisting of different subsystems to help in reconstructing the collision events. An overview of the CMS detector is shown in Figure 10, a schematic for the layout of the different subsystems, as well as the expected signatures of commonly occurring Standard Model particles, are shown in Figure 11.

This section aims to give a short overview of the functionality of the CMS detector, and is based on [73].

The tracking system

The innermost layer is the tracking system, which makes use of silicon semiconductor detectors. Its purpose is the reconstruction of the trajectories of electrically charged particles. This type of detector works by the interaction of charged particles with the silicon material, in which electron-hole pairs are

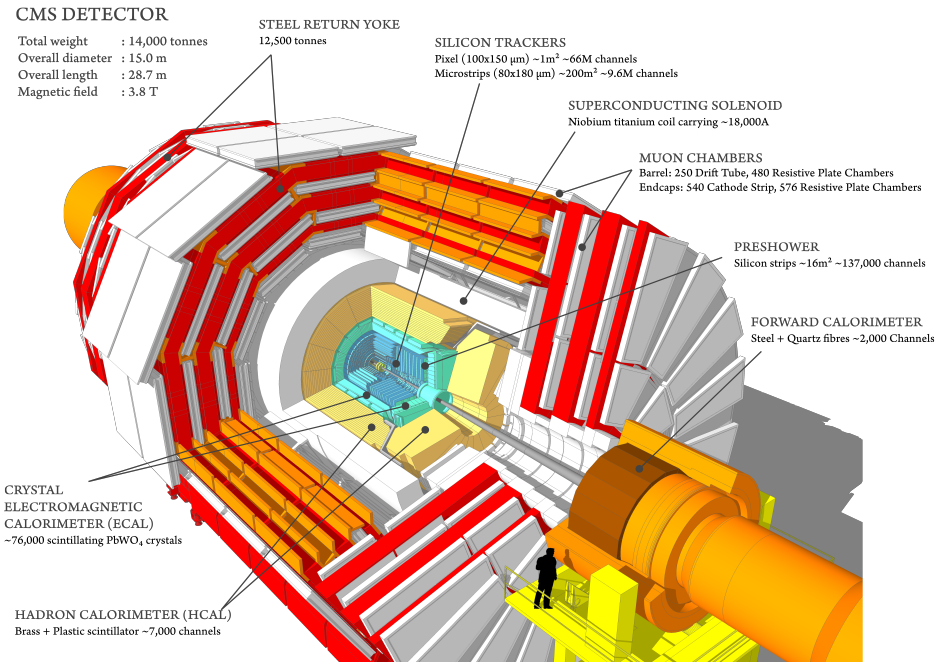

Figure 10: Schematic overview of the CMS detector. Figure taken from [75].

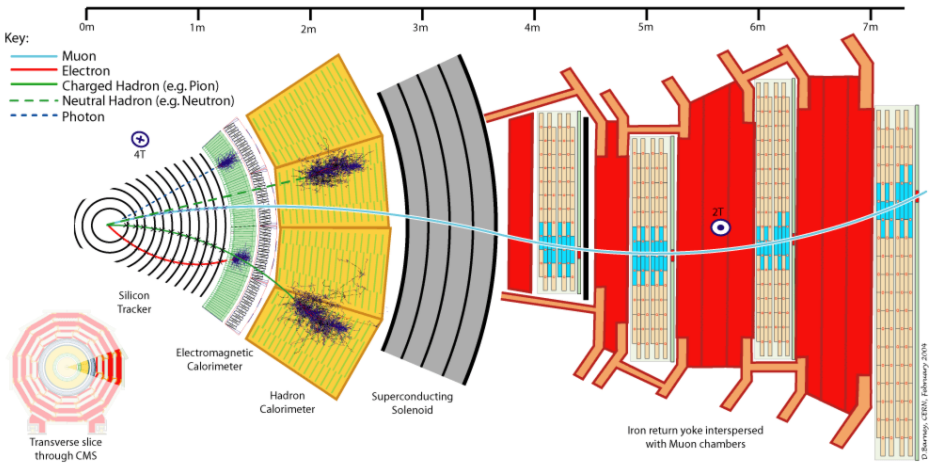

Figure 11: Structure of the CMS detector subsystems, and the expected signatures of commonly occurring Standard Model particles. Figure taken from [76].

created, with the number of electron hole pairs proportional to the deposited energy, which is usually a very small fraction of the particle energy. Time-integrated currents allow a determination of the energy lost by the traversing particle. This measurement is referred to as a hit. The tracker consists of a pixel detector close to the interaction spot, and 10 layers of silicon strip detectors farther out. The original pixel detector, referred to as the Phase 0 pixel detector, consisted of three layers covering the central detector region up to pseudorapidities of approximately $|\eta| = 1.5$, and two rows of pixel detector discs that extend the coverage to pseudorapidities of approximately $|\eta| = 2.5$. Similarly to the pixel detector, the coverage of the strip detector in the non-central part of the detector is given by 12 discs of silicon strip detector modules, which extend and match the pixel detector coverage to approximately $|\eta| = 2.5$. The pixel detector was upgraded to its Phase 1 design between data taking periods of 2016 and 2017 to include a fourth layer in the central region and a six-disk setup in the forward region [77].

An overview of the CMS tracking system can be found in Figure 12, an overview of the original and upgraded pixel detector can be found in Figure 13.

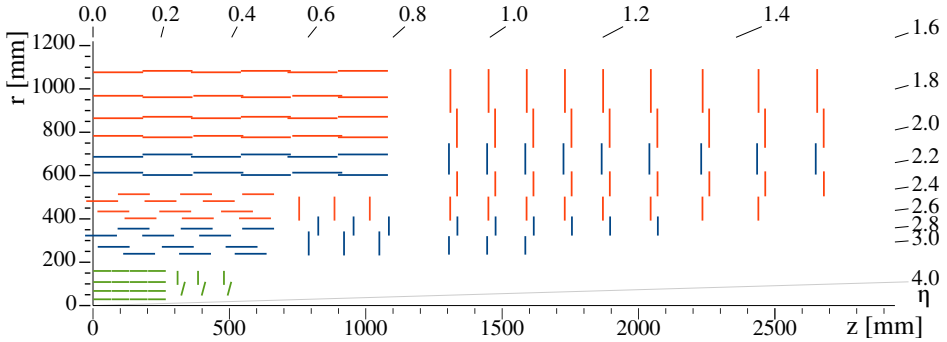

Figure 12: Overview of the CMS tracking system and its components. Green layers indicate the Phase-1 pixel detector, the blue and red layers indicate the strips detector. Figure taken from [78].

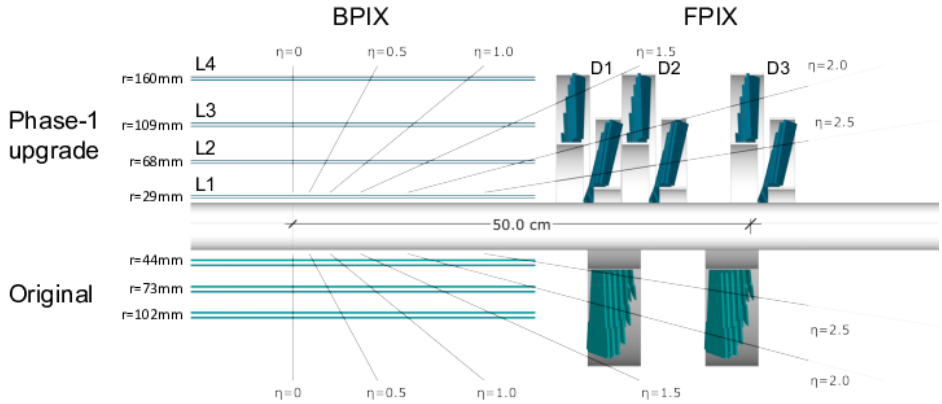

Figure 13: Schematic of the original (Phase 0) CMS pixel detector (bottom) and its Phase 1 upgrade (top). Figure taken from [77].

The electromagnetic calorimeter

The electromagnetic calorimeter (ECAL) is located outside the silicon tracker volume. It comprises lead tungstate ($PbWO_4$) crystals to absorb energy of incident charged particles, which produce scintillating light proportional to the deposited energy. The read-out of the scintillation signal occurs via avalanche photodiodes in the barrel region, covering psedorapidities up to $|\eta| \leq 1.479$, and vacuum phototriodes in the endcaps, extending the covered range to $|\eta| \leq 3$. The crystal lengths correspond to approximately 25.8 radiation lengths X_0 for the barrel and 24.7 X_0 in the endcaps. The calorimeter features a high granularity to be able to operate in the high-pile-up environment of the LHC, with 61200 individual crystals in the barrel and 7324 crystals in each endcap.

The hadronic calorimeter

The final subsystem inside the magnet is the hadronic calorimeter (HCAL). The techonology used is a sampling calorimeter, with alternating layers of passive brass absorber and active plastic scintillators. The readout occurs via wavelength shifting fibers connecting the scintilators to hybrid photodiodes. The calorimeter is segmented into the barrel region, covering pseudorapidities up to $|\eta| \lesssim 1.3$, endcaps that extend the range up to $|\eta| \lesssim 3$, and additional forward calorimeters that reach to $|\eta| \simeq 5$. Because the physical size of the magnet restricts the amount of absorber material that can be placed inside, especially in the barrel region, the absorber thickness perpendicular to the beam axis corresponds to only 5.82 interaction lengths λ_I. For this reason, the hadron calorimeter inside the barrel is complemented by additional layers of absorber and scintillators outside the CMS magnet to measure the tails of particularly long hadron showers.

The muon system

The outermost part of the CMS detector is the muon detection system. This system employs three different types of detectors due to different radiation conditions at different locations of the detector. Drift tubes are used in the barrel region for $|\eta| < 1.2$, where the lower radiation allows for their use. In the endcap region, covering pseudorapidities up to $|\eta| < 2.4$, cathode strip chambers are used. These systems are complemented by resistive plate chambers in the central region and up to $|\eta| < 2.1$. The muon system is interspersed with iron return yokes to enhance the magnet field outside the magnet.

A schematic layout of the CMS muon system, including the placement of the different types of muon detectors, is shown in Figure 14.

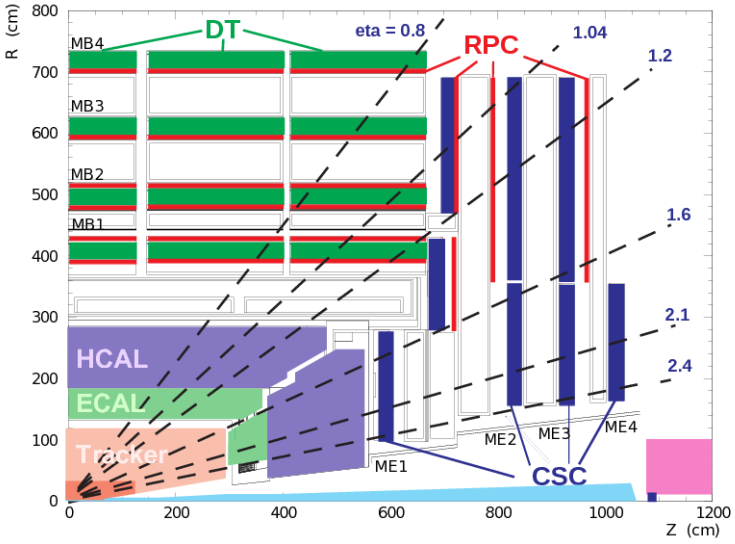

Figure 14: Schematic of one quadrant of the CMS detector, with a focus on the placement of the different types of muon detectors: the drift tubes (DT), the cathode strip chambers (CSC), and the resistive plate chambers (RPC). Figure taken from [79].

3.4.2 The ATLAS detector

The ATLAS detector is a general purpose detector, featuring a complex magnet setup, as well as powerful tracking and calorimetry. Like the CMS detector, ATLAS is a full-coverage detector that is capable of reconstructing the whole event content, with the exception of neutrinos and other potentially invisible particles. The design is forward-backward symmetric, and built around the magnet setup. In this section, we will shortly introduce the detector components, with a focus on the technologies employed. A schematic view of the ATLAS detector is given in Figure 15. This section is entirely based and closely follows [72].

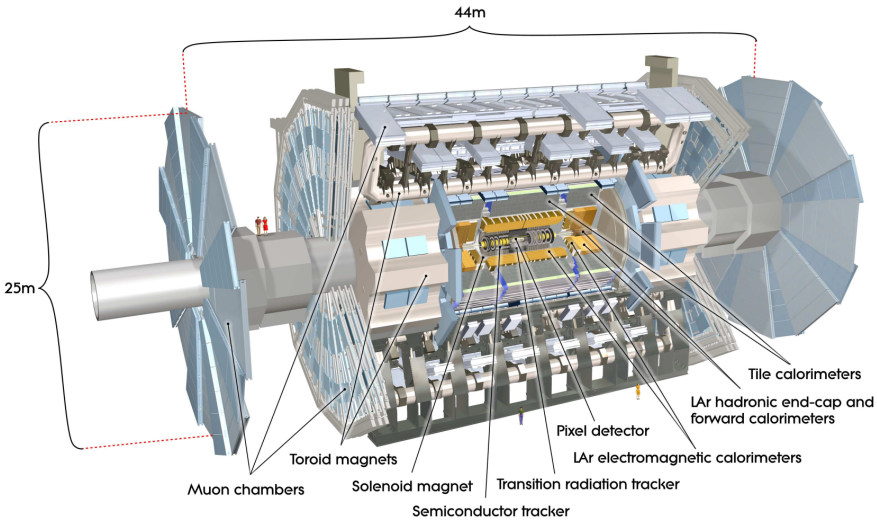

Figure 15: Schematic overview of the ATLAS detector and its subsystems. Figure taken from [72].

The magnet system

The magnet system consists of two different magnet configurations, with a thin superconducting solenoid surrounding the inner detector, and three superconducting toroids, one in the barrel region and one for each of the two endcaps. The toroid magnets are arranged with an eight-fold azimuthal symmetry. The solenoidal magnets immerse the inner detector in a 2 T magnetic field. The toroid magnets increase the bending power between the innermost and outermost muon chamber planes by creating a strong magnetic field orthogonal to the muon momentum direction. They achieve bending powers of $1.5 - 5.5\,\mathrm{Tm}$ at small pseudorapidities up to $|\eta| < 1.4$, and $1 - 7.5\,\mathrm{Tm}$ in the range of $1.6 < |\eta| < 2.7$. The overlap region between $1.4 < |\eta| < 1.6$ suffers from lower bending power.

The inner detector

The inner detector is specialized towards tracking, momentum and vertex measurements, and the identification of electrons. To this end, it makes use of three subsystems. Closest to the interaction point is a three-layered pixel detector, which is complemented by four layers of stereo pairs of silicon microstrips in the barrel region ($|\eta| < 1.4$), and additional layers of silicon microstrips in the endcaps to enlarge the pseudorapidity coverage to $|\eta| < 2.5$. These systems allow for precise momentum measurement and vertex reconstruction. Transition radiation trackers, made up of alternating gaseous straw tubes and transition radiation material, are placed outside the silicon microstrip layers. The straw tubes are placed in parallel to the beam pipe in the barrel region, and organized radially in wheels in the endcaps. They mainly facilitate the identification of electrons, by making use of their different radiation profile compared to hadrons. They also improve the momentum resolution by providing additional hits that can be used for track fitting. The inner detector covers the pseudorapidity range up to $|\eta| < 2.5$.

A diagram of the ATLAS inner detector is shown in Figure 16.

The calorimeters

The ATLAS calorimeter system surrounds the inner detector. The innermost component are lead-liquid argon sampling electromagnetic calorimeters, one in the barrel covering the region of $|\eta| < 1.475$,

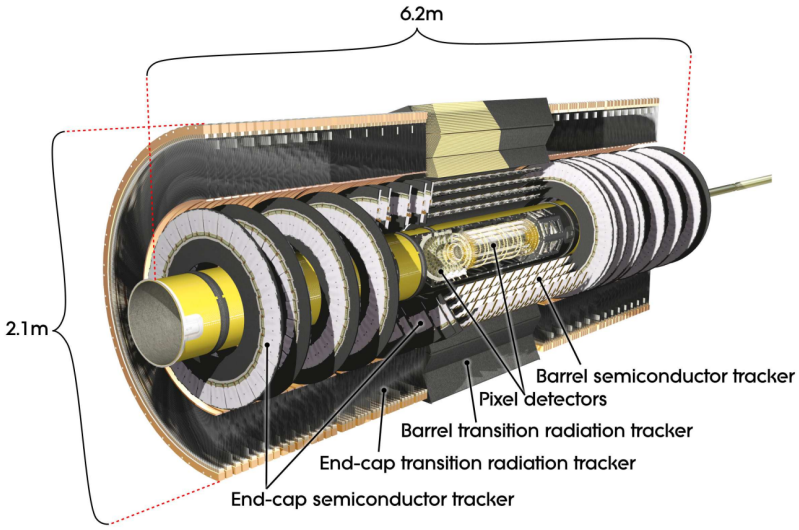

Figure 16: Schematic overview of the ATLAS inner detector and its components. Figure taken from [72].

and two endcaps that cover $1.375 < |\eta| < 3.2$. The passive elements of the sampling calorimeter comprise lead absorber plates. The electromagnetic calorimeter compliments the inner detector in the identification and measurement of photons and electrons.

The electromagnetic calorimeter is complemented by scintillation tile calorimeters, read out by wavelength shifting fibres and photomultiplier tubes. The tile calorimeter is segmented into a barrel region that covers $|\eta| < 1.0$, and two extended barrels in the region $1.0 < |\eta| < 1.7$. The tile calorimeter is radially segmented in three layers, resulting in a total effective thickness of the detector of 9.7 interaction lengths at $\eta = 0$ at the outer edge of the tile calorimeter.

The endcap region is complemented by a four-layered dedicated hadronic calorimeter using liquid argon as the active element, and copper plates as the passive element. This calorimeter overlaps with the tile and forward calorimeters to eliminate dead regions of the calorimetery coverage.

The final component is the forward calorimeter, which covers the region $3.1 < |\eta| < 4.9$. It consists of three layers of alternating active liquid argon and passive absorber, with the first passive layer made of copper, and the two other layers made of tungsten.

An overview of the ATLAS calorimetery system is shown in Figure 17.

The muon system

The muon system aims to identify and measure muons as they traverse and are bent by the magnetic field generated by the toroids. It is the outermost part of the ATLAS detector and employs four different types of detector. These are monitored drift tubes over most of the η-range, complemented by cathode strip chambers at large $|\eta|$ between $2 < |\eta| < 2.7$. The layout for these features three concentric cylindrical layers arranged in three layers perpendicular to the beam line. In addition to these two types of detectors whose primary function is the measurement of the muon momentum, resistive plate chambers and thin gap chambers are employed for triggering purposes. The resistive plate chambers are used in the barrel region up to $|\eta| < 1.05$, and thin gap chambers are used up to $1.05 < |\eta| < 2.7$.

A schematic of the ATLAS muon system is shown in Figure 18.

3.4.3 Trigger systems at ATLAS and CMS

Because of the very large interaction rate of approximately 40 MHz at the LHC, selection of potentially interesting events must occur at very early stages to reduce the data readout rate and size. For this reason, both ATLAS and CMS use event triggers, which select potentially interesting events and reject the rest, which is the vast majority of all events. CMS uses a two-level trigger system, consisting of hardware-based Level-1 (L1) triggers, and software-based High-Level triggers (HLT). The L1 triggers use coarse information from the calorimeters and the muon systems, while the HLT makes more

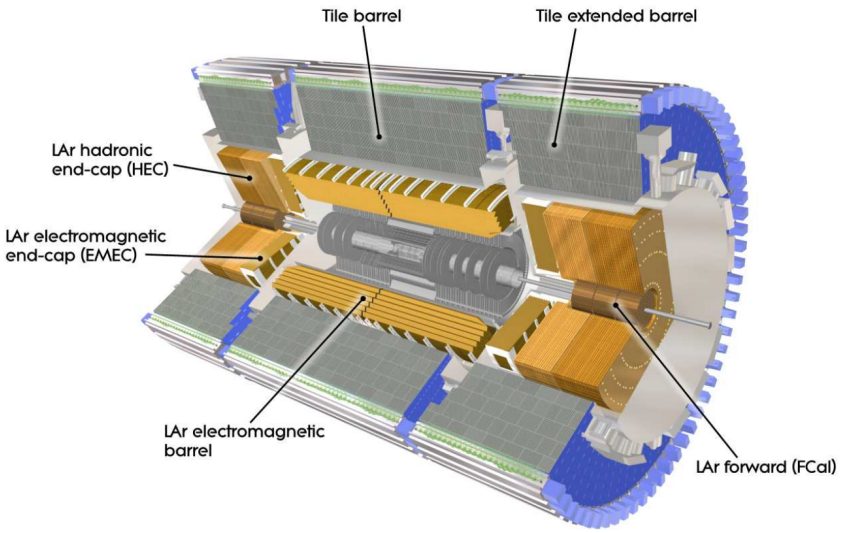

Figure 17: Schematic overview of the ATLAS calorimetry system and its components. Figure taken from [72].

sophisticated trigger decisions based on the full suite of detector subsystems. The L1 trigger reduces the event rate down to below 100 kHz, the HLT further reduces this to event rates in the order of a couple hundred Hertz for offline processing. ATLAS uses a three-level trigger system, where the first two levels run on hardware and the HLT is software-based and runs on computer farms.

Note that while the structure and purpose of the trigger systems are similar in ATLAS and CMS, there are differences between the two, most relevantly in terms of the software that defines the algorithms which form the basis of triggering decisions. Detailed information can be found for CMS in [80], and for ATLAS in [81].

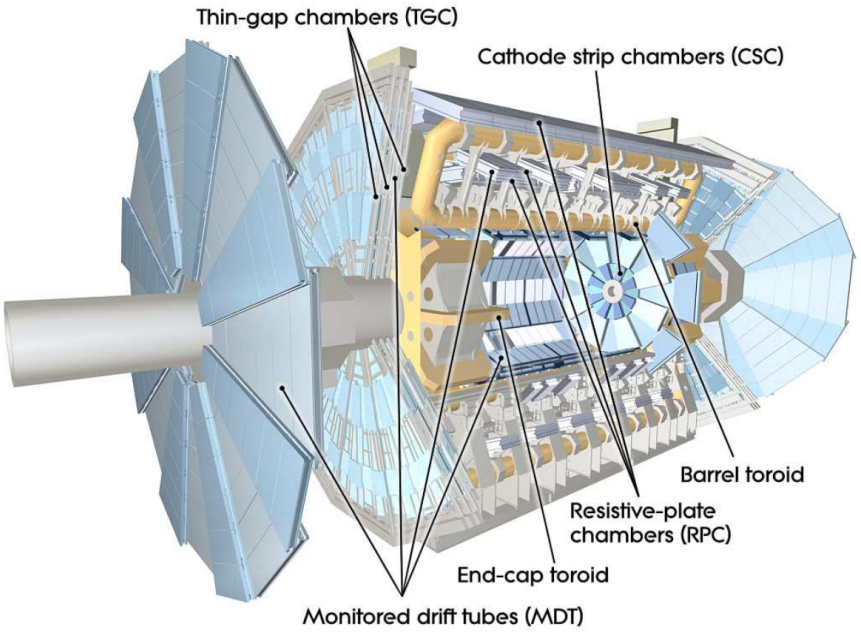

Figure 18: Schematic overview of the ATLAS muon system and its components. Figure taken from [72].

4 Scientific goals and methodology

This thesis aims to address a variety of open questions related to supersymmetry. These questions are shortly introduced, and the analysis strategy is discussed. The goals are to determine:

1. The impact of the LHC on the MSSM. The main theme of this study is to determine the impact of direct LHC searches on R-parity conserving supersymmetry. We take as prior the pMSSM after a variety of low-energy observables from the flavor sector and LEP constraints are applied, as well as constraints from the mass of the measured Higgs boson. We continue by simulating Monte Carlo proton-proton collision events for a large number of pMSSM models and confronting them with direct searches for supersymmetry designed by the CMS and ATLAS collaborations. The aim is to calculate a likelihood for each pMSSM model point, in order to construct a global posterior density with respect to the LHC. The LHC impact is then determined by analysis of the posterior density and its comparison with the prior, as well as the study of marginalized survival probabilities. We also survey the parameter space for theory space regions that fit the data better than the SM-only hypothesis.

2. The impact of dark matter constraints. The likely existence of dark matter is one of the two most conspicuous open questions left unaddressed by the SM. Accounting for it is one of the motivating features of the MSSM. Constraints on the MSSM from dark matter come in three forms: the measured dark matter density, searches for direct detection of dark matter, and searches for indirect detection of dark matter. The impact of all three types of constraints on the MSSM is studied individually, and in their combination. This is done by subjecting the LHC prior and posterior densities to these constraints on dark matter.

3. The viability of the low-fine tuning MSSM in light of all data. The hierarchy problem and the associated fine tuning in the Standard Model is one of the main discussed issues of the Standard Model. The elegant solution given by supersymmetric models to the hierarchy problem is one of the main motivations to search for supersymmetry. Because large parts of the MSSM are fine tuned as well, determining whether the low-fine tuning regions of the MSSM remain viable after the current constraints is an important task that is undertaken in this work.

4. The compatibility and complementarity of LHC and other constraints. Possible tensions of the LHC and other constraints are investigated. In case of null-results, the complementarity in constraining the MSSM of direct search experiments and at the LHC are determined. This is done by comparing the LHC posterior density with alternative posterior densities that include additional constraints from dark matter or fine tuning considerations.

5. The validity of simplified models in MSSM. Null results from direct searches for supersymmetry are usually interpreted in terms of upper limits on the production cross section in a variety of selected simplified models, which are introduced in Section 2.3.3. Because of the stringent assumptions made in these simplified models, conclusions drawn from them are not expected to apply generally in the context of complete models like the MSSM. The degree to which they do apply, as well as their validity in subspaces of the pMSSM that resemble the respective simplified models, is tested by comparing the published upper limits to the appropriate marginalized survival probabilities.

Methodology

The workflow of this analysis is sketched in Figure 19. Its base is that of iterative inference, where constraints from the flavor sector, Higgs sector, and previous colliders are implemented in the first step and are built in to the sampling of the pMSSM via Markov chain Monte Carlo. By iterative inference, the resulting posterior density is then taken to be the prior for all observables and constraints considered in the proceeding steps. These latter observations are not built directly into the sampling, but are incorporated into the posterior density via likelihood weights based on the observations. The direct searches for supersymmetry at the LHC are here implemented in a continuous form, which also includes Bayes factors indicating the relative compatibility of a pMSSM parameter point with the data compared to the SM-only hypothesis. The constraints from the dark matter sector, the anomalous magnetic moment of the muon, and fine tuning considerations are implemented using a binary exclusion of individual models, which result in a residual compatible space of the pMSSM that can be studied.

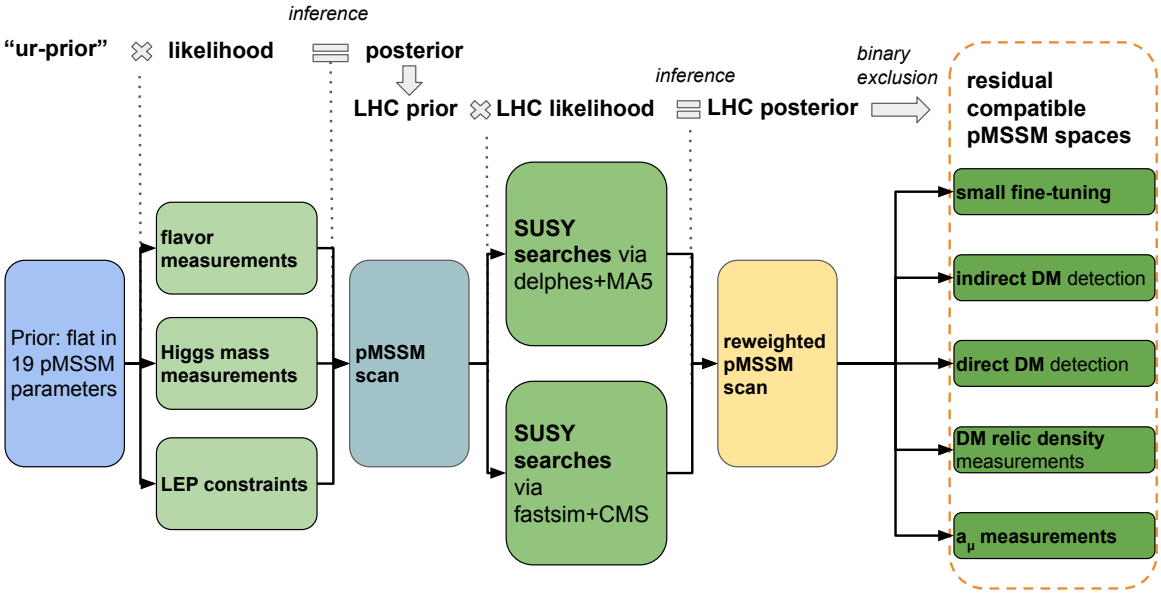

Figure 19: Sketch of the analysis strategy. Different measurements are included in three distinct steps, with iterative inference used to infer the posterior density with respect to a large set of observables.

Considered pMSSM parameter space The scanned pMSSM parameter space is chosen such as to allow for the full phenomenology of the pMSSM that is accessible at the LHC, while maintaining a high scan efficiency. To that end, a compromise is sought by the placement of the upper boundary of the scanned pMSSM parameters. On the one hand, the parameter borders need to be high enough to allow for parts of the pMSSM to be decoupled, so that we may study pure parts of the pMSSM, where, for example, only electroweak processes matter to the LHC sensitivity. On the other hand, the parameter border must be low enough so as to not waste valuable computation time in sampling the parts of the pMSSM that are not accessible at the LHC.

For the mass parameters relevant for strongly interacting particles, the squark mass parameters and the gluino mass parameter, a large range of up to 10 TeV is chosen, without any lower bound on the parameters. This is done for two reasons:

- if the upper edge of the parameter space is chosen too low, most points contain at least one low-mass strongly interacting particle, due to the large multiplicity of strongly interacting particles in the pMSSM. To emphasize more interesting regions, particularly regions with dominant electroweakino production, the upper edge is chosen significantly above the masses where colored production is relevant at the LHC;

- at around 10 TeV, colored particles are almost completely decoupled from the direct production of electroweakinos that can be directly produced at the LHC. In non-decoupled scenarios, the presence of colored particles usually interferes destructively and reduces the electroweak cross sections. Models with decoupled colored particles thus feature relatively high cross sections for electroweakino production, even for comparatively large masses of the electroweakinos.

For the electroweak mass parameters, a parameter range of up to 4 TeV for their absolute values is chosen. The following considerations were taken:

- if the upper edge of the allowed range for the electroweak masses is below the mass of a colored particle, then the colored particle will always have the decay channel into the electroweak particles open to it. Thus, the topology of decays of strongly interacting particles that cannot decay into an electroweak particle is only covered if the upper edge of the electroweak masses is above the mass of the colored particle. Since we expect direct production of colored particles with masses up to around 2.5 TeV to 3 TeV, the upper edge for the electroweak parameters needs to be significantly higher;

- in the electroweak sector, if the LSP is higgsino-like (wino-like), there is a near degeneracy in mass among the lightest electroweakino states, inversely related to the M_1 and M_2 (μ) parameters. For very large values of these parameters, the decay length of the next-to-lightest states is macroscopic on detector length scales. Allowing $|M_1|$ and $|M_2|$ to reach values of up to 4 TeV introduces a sector with long-lived charginos and neutralinos, which is phenomenologically distinct from the rest of the theory phase space.

The parameter range for the trilinear couplings A_t, A_b, and A_l is chosen to be in the range [−7 TeV,7 TeV]. For $\tan(\beta)$, the chosen range is 2 as a lower bound, and 60 as an upper bound. The lower bound of 2 is chosen to avoid non-perturbative behavior at the GUT scale [82].

To summarize, the constraints on the pMSSM parameter ranges are as follows:

- M_3, $M_{q,1}$, $M_{u,1}$, $M_{d,1}$, $M_{q,3}$, $M_{u,3}$, $M_{d,3} \in [0\,\text{TeV}, 10\,\text{TeV}]$;
- $M_{l,1}$, $M_{r,1}$, $M_{l,3}$, $M_{r,3}$, $m_A \in [0\,\text{TeV}, 4\,\text{TeV}]$;
- M_1, M_2, $\mu \in [-4\,\text{TeV}, 4\,\text{TeV}]$;
- A_t, A_b, $A_l \in [-7\,\text{TeV}, 7\,\text{TeV}]$;
- $\tan(\beta) \in [2, 60]$.

5 The pMSSM scan

As the first step of this thesis, an ensemble of model points in the pMSSM parameter space is generated, called the pMSSM scan. Basic constraints on model consistency, as well as constraints from low-energy observables from the SM flavor sector, constraints from pre-LHC collider searches, and Higgs mass measurements are built into the sampling procedure. This section details the creation of the pMSSM scan, and the impact that the various constraints have on the scan. The scan quality and biases are discussed at the end of this section.

5.1 Construction of the LHC prior

To obtain the LHC prior, inference is made with respect to the *ur-prior*, given by uniform distributions in the parameter ranges given in Section 4, by accounting for data from b-physics, strange-physics, from Higgs mass measurements, as well as from LEP measurements. These constraints are implemented directly with the sampling of the prior, by use of Markov chain Monte Carlo (McMC). The impact of measurements of observables, encoded in the likelihood based on these data, will have a rather profound and non-trivial impact on the scan density. In addition, interesting correlations are identified between the different measurements, as well as between observables and various pMSSM parameter space regions. This section attempts to first give the details on the observables used in the McMC steering likelihood, and then to provide a picture of the various ways in which these observables impact the pMSSM scan. Two example measurements from b- and strange-physics are discussed below, and Appendix C is included with a more comprehensive set of details regarding the impact.

To generate the LHC prior from the uniform ur-prior, we use a McMC enacted with a version of the Metropolis-Hastings algorithm [83]. The algorithm samples candidates for the next point in the Markov chain based on the parameters of the last accepted point in the chain. A new candidate point is created by sampling a new value for each of the 19 parameters from a Gaussian distribution centered on the respective values of the parameter of the last accepted point. The width of the Gaussians used for sampling is set here at 5% of the width of the allowed parameter range. If a parameter of the candidate point is sampled outside the region allowed by the scan, it is re-sampled until a value inside the allowed range is pulled. Once a candidate point inside the allowed parameter space is found, a likelihood is calculated. The candidate point is accepted into the Markov chain with a probability of $P = \min(1, L_{candidate}/L_{previous})$, where $L_{previous}$ is the likelihood of the last point that was accepted into the Markov chain. This means that candidate points whose likelihood exceeds that of the previous point are always accepted into the Markov chain, while candidate points whose likelihood is below that of the previous accepted point have a residual probability to be accepted. This allows the Markov chain to escape local maxima in the likelihood, map the whole likelihood distribution, and converge on the posterior distribution in a Bayesian sense. This is knows as the Markov chain central limit theorem [84].

The following results are used to construct the likelihood for the McMC:

- the Higgs mass $m(\mathrm{h}^0)$ and uncertainty prediction for the pMSSM are calculated using `FeynHiggs`[85, 86, 87, 88, 89, 90, 91, 92, 93] version 2.16.1, and compared to measurements by CMS $m(\mathrm{h}^0) = (125.26 \pm 0.20 \pm 0.08)\,\mathrm{GeV}$. The experimental uncertainty is neglected due to the significantly larger theory uncertainty;
- LEP constraints on the chargino mass $m(\widetilde{\chi}_1^{\pm})$, evaluated using `MicrOMEGAs` 5.2.1 [94];
- LEP constraints on the width of Z→invisible, evaluated using `MicrOMEGAs` 5.2.1;
- one set of flavor observables, for which correlations are treated and a χ^2 is calculated using `SuperIso` 4.0:
  - $\mathrm{BR}(\mathrm{b} \to \mathrm{s}\gamma)$ (April 2019 version of [95])
  - $\mathrm{BR}(\mathrm{B_s} \to \mu\mu)$ [96, 97, 98]
  - BR(B → Xsee) [99, 100, 101]
  - $\mathrm{BR}(\mathrm{B} \to \mathrm{Xs}\mu\mu)$ [99, 100, 101]
  - $\mathrm{BR}(\mathrm{B_d} \to \mu\mu)$ [96, 97, 98]
  - $\mathrm{BR}(\mathrm{B}^0 \to \mathrm{K}^{*0}\gamma)$ [102]

  - $\Delta_{0+}(\mathrm{K}^*\gamma)$ (`SuperIso` internal combination of [103, 104, 105])

- and a smaller set of flavor observables, which are taken as uncorrelated:
  - $\mathrm{BR}(\mathrm{B} \to \tau\nu)$ [106];
  - $\mathrm{BR}(\mathrm{D_s} \to \tau\nu)$ [107];
  - $\mathrm{BR}(\mathrm{D_s} \to \mu\nu)$ [107];
- $\Delta\rho$ [107]: the deviation from the predicted relationship between the W and Z mass in the $\overline{\mathrm{MS}}$ renormalization scheme; $\mathrm{M_Z} = \frac{\mathrm{M_W}}{\sqrt{\hat{\rho}}\,\hat{c}}$ [107]. The pMSSM prediction is here taken from `SPheno` 4.0.4 [108, 109].

For the low-energy observables not included in the `SuperIso` χ^2 calculation and $\Delta(\rho)$, the partial likelihood is attained by constructing a Gaussian centered at the measured value, with a width corresponding to the measurement uncertainty. The partial likelihood then is the height of that Gaussian evaluated at the observable value as calculated by `SuperIso` for the pMSSM point. The observables included in the `SuperIso` χ^2 calculation are included by exponentiation of the χ^2 value.

For the partial likelihood from the Higgs mass, the procedure deviates due to a significantly larger theory uncertainty compared to the experimental uncertainty. The Gaussian is centered on the calculated Higgs mass, with the width equal to the uncertainty of the calculated mass. The partial likelihood is the height of the Gaussian evaluated at the experimentally measured value. The experimental uncertainty is neglected due to the larger theory uncertainty.

Constraints from LEP on the chargino mass and on the width of Z→invisible are applied as a binary term. In addition to this, model inherent constraints are also applied in a binary fashion, namely that the lightest supersymmetric particle (LSP) is the lightest neutralino $\widetilde{\chi}_1^0$, and that the particle spectrum does not contain tachyons ($\mathrm{m}^2 < 0$). For each candidate model, the value of the top mass $m(\mathrm{t})$, the strong coupling constant $\alpha_s(M_Z)$, and the bottom mass $m(\mathrm{b})$ are sampled according to their measurement and uncertainties, and are used as input to `SPheno`. The McMC is not steered by these measurements, as they are all sampled from the same distribution that does not move along with the McMC. To be exact:

- the top mass is sampled from a gaussian distribution centered on the measurement $m(\mathrm{t}) = 173.1 \pm 0.9\,\mathrm{GeV}$ [107], where the width of the distribution is equal to the measurement uncertainty;
- the bottom mass is sampled from a two-sided gaussian centered on the measurement $m(\mathrm{b}) = 4.18^{+0.04}_{-0.03}\,\mathrm{GeV}$ [107], where the width of the gaussians on each side are equal to the respective measurement uncertainties;
- the strong coupling constant $\alpha_s(M_Z)$ is sampled from a gaussian centered on the measurement $\alpha_s(M_Z) = 0.1181 \pm 0.0011$ [107], where the width of the gaussian distribution is equal to the measurement uncertainty.

The sampling via Markov chain Monte Carlo is sketched schematically in Figure 20.

The full pMSSM scan, also labeled the **LEO posterior** in this section (and *prior* from Section 7 onward), consists of 597 Markov chains containing an average of 39,931 pMSSM points, coming out to a total of 23,839,249 pMSSM points. Each point is described in the `SLHA` [110] format. The starting point for each chain is sampled from uniform distributions in the 19 pMSSM parameters.

The effect of each individual contribution to the likelihood employed for the McMC is studied in different Markov chains that include only a subset of the observables of the primary (inclusive) Markov chain. By comparing projections onto relevant pMSSM quantities to reference chains, regions that are (dis)favored by different observables can be identified. In this section, we study the change in distributions going from the ur-prior that is flat in the 19 pMSSM parameters to the posterior density, highlighting:

- influences from the sampling algorithm;
- influences from theoretical constraints on the model, such as the requirement that there be no tachyon in the particle spectrum;
- influences and limitation of the spectrum generator;

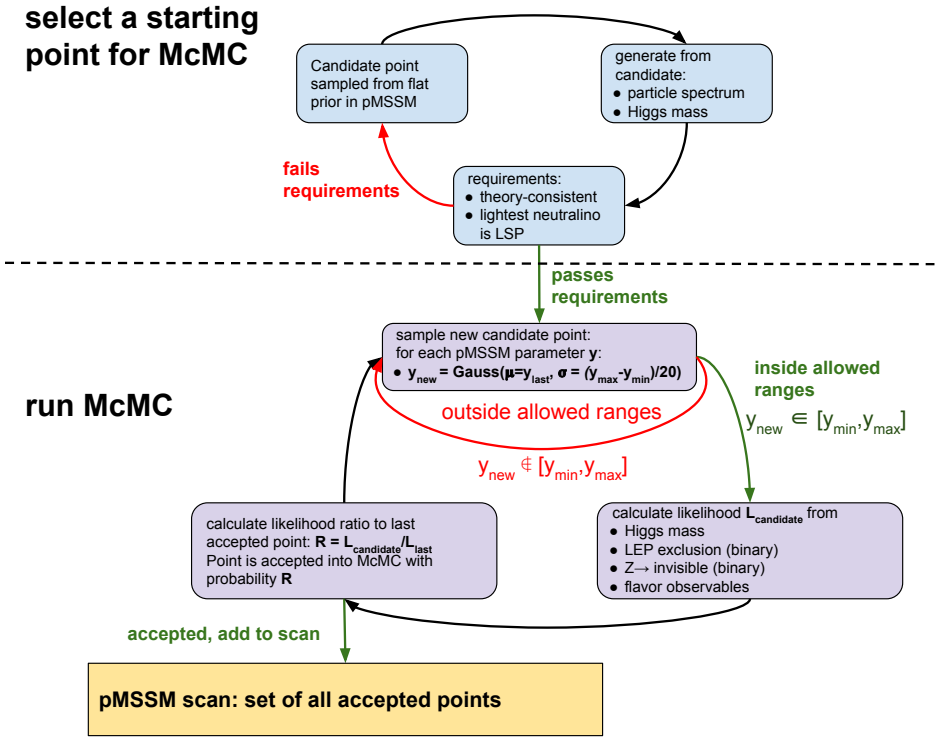

Figure 20: Schematic of the McMC algorithm used for sampling the pMSSM scan.

- the requirement that the LSP be the lightest neutralino;
- measurements of the Higgs mass;
- LEP constraints on the chargino mass and the width of Z→ invisible;
- the individual low-energy observables named above.

These influences are discussed in this section in the order of the list above.

Notable not included observables

Some notable observables were not included in the likelihood of the McMC. These include the dark matter relic density Ωh^2, the anomalous magnetic moment of the muon a_μ, dark matter direct and indirect detection measurements, as well as the ratios of branching ratios R(K) [111], R(K*) [112], R(D) and R(D*) [113]. At the time of creation of the pMSSM scan, these observables were either in significant tension with the SM in the case of a_μ[114, 115, 116, 66, 66] and the R observables, or require strong assumptions on the cosmological model of the early universe. Because the pMSSM scan is fundamentally limited in terms of its resolution in areas of small likelihoods, care must be taken to steer the McMC into regions that remain of interest. Including controversial measurements that deviate significantly from the SM, or are subject to strong model assumptions, can steer the McMC into a region that may later turn out to be less interesting if the deviations from the SM disappear due to new measurements or improved theory calculations. This has historically often happened. As a result, the resolution in these controversial regions would be good at the cost of worse resolution everywhere else.

These resolution issues can be somewhat mitigated by variable sampling in the further steps of the analysis, but there is a fundamental limit to how much can be achieved with this that is set by the original McMC sampling density. To avoid such a situation, the observables named above are not used to steer the McMC, but are instead over-sampled in a future analysis step. As of the writing of this thesis, the tension between the SM and R(K) [106], R(K*) [106], R(D) [106] and R(D*) [106] has decreased considerably, while the measurement of a_μ has been confirmed by additional measurements [66].

5.1.1 McMC Algorithm Impact

Because the parameter values of new candidate pMSSM points are re-sampled from the previous accepted value in the Markov chain until they are within the allowed parameter range, there is an asymmetry built into the algorithm that causes the Markov chain to prefer moving away from the edges of the allowed parameter space. This asymmetry in the probability of the step direction and step size is given, for each point, by integrating each side of the Gaussian from which a new parameter value is sampled to the edges of the allowed parameter space. Normalizing each individual side to the integral of the Gaussian over the whole allowed range gives the respective probabilities to step in each direction. While the impact on any individual parameter is independent of the dimensionality of the sampling, this effect compounds exponentially for requiring a model point to have multiple parameters near their respective sampling borders. This makes it virtually impossible to sample the parameter space where **all** of the parameters are near their respective parameter borders in 19 dimensions. Possible solutions to mitigate this effect are discussed in Appendix A, but were not implemented in this work.

5.1.2 Model-inherent constraints

We move on from the algorithmic effects to theoretical, model-inherent, constraints on the pMSSM itself. The spectrum generator `SPheno` is of particular importance here, as it calculates a physical particle spectrum from the pMSSM parameters, on which constraints can be imposed. The model inherent constraints are made up of two requirements on the pMSSM points:

- the particle spectrum generation is successful, which means that it is non-tachyonic and `SPheno` does not encounter other types of errors;
- the lightest neutralino $\widetilde{\chi}_1^0$ is the lightest supersymmetric particle (LSP).

We study the model-inherent constraints using two slightly different methods. In this section, we directly compare Markov chains that implement the model-inherent constraints (but without a steering likelihood) to Markov chains that do not. This allows the study of model-inherent constraints in the full context of McMC sampling. To complement this, we also show a (more thorough) study on the occurrence of tachyons (and other errors that occur during the spectrum generation) in Appendix B.

As a general consequence of the constraint that $\widetilde{\chi}_1^0$ be the LSP, the small-mass region of all pMSSM parameters directly related to the mass of particles are suppressed. This is because for a given particle mass $m(\mathrm{X})$, only the part of the pMSSM where $m(\mathrm{X}) > m(\widetilde{\chi}_1^0)$ is sampled.

The model-inherent constraints strongly shape the gluino mass parameter distribution, shown in Figure 21. Small mass values below 1 TeV are severely disfavored, in addition to also being suppressed by the McMC algorithm. Very large values of M_3 are also disfavored to a lesser degree, largely due to the increased occurrence of tachyons at large M_3 in combination with small $\mathrm{Q}_{\mathrm{SUSY}}$. A more detailed study on this dependence can be found in Appendix B.

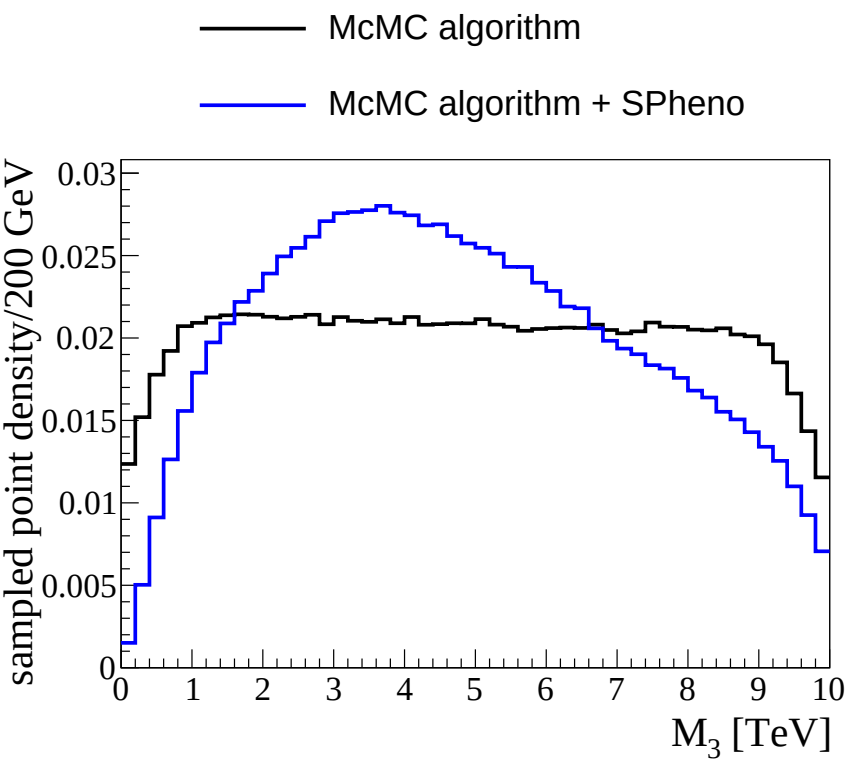

Figure 21: Comparison of distributions of the gluino mass parameter M_3 in McMC runs with and without constraints from model consistency and limitations of `SPheno`. The requirement that $\widetilde{\chi}_1^0$ is the LSP is enforced within the `SPheno` constraints.

Figures 22 and 23 show the impact of the model-inherent constraints in the squark sector and slepton sector, respectively. The small-mass region is suppressed in all sfermion mass parameters due to the presence of tachyonic models, the McMC algorithm effect, and the constraint that the LSP

is the lightest neutralino. The slepton, stop and sbottom mass parameters are particularly strongly affected by the occurrence of tachyons at small masses. The suppression of small values of $M_{q,3}$ and $M_{u,3}$ is tied to their use in the definition of the SUSY scale $Q_{SUSY} = \sqrt{M_{q,3} \times M_{u,3}}$. As shown in Appendix B, small values of Q_{SUSY} are extremely suppressed by the lack of valid particle spectra. At large masses, the drop in point density for all sfermions is mainly due to the McMC algorithm effect.

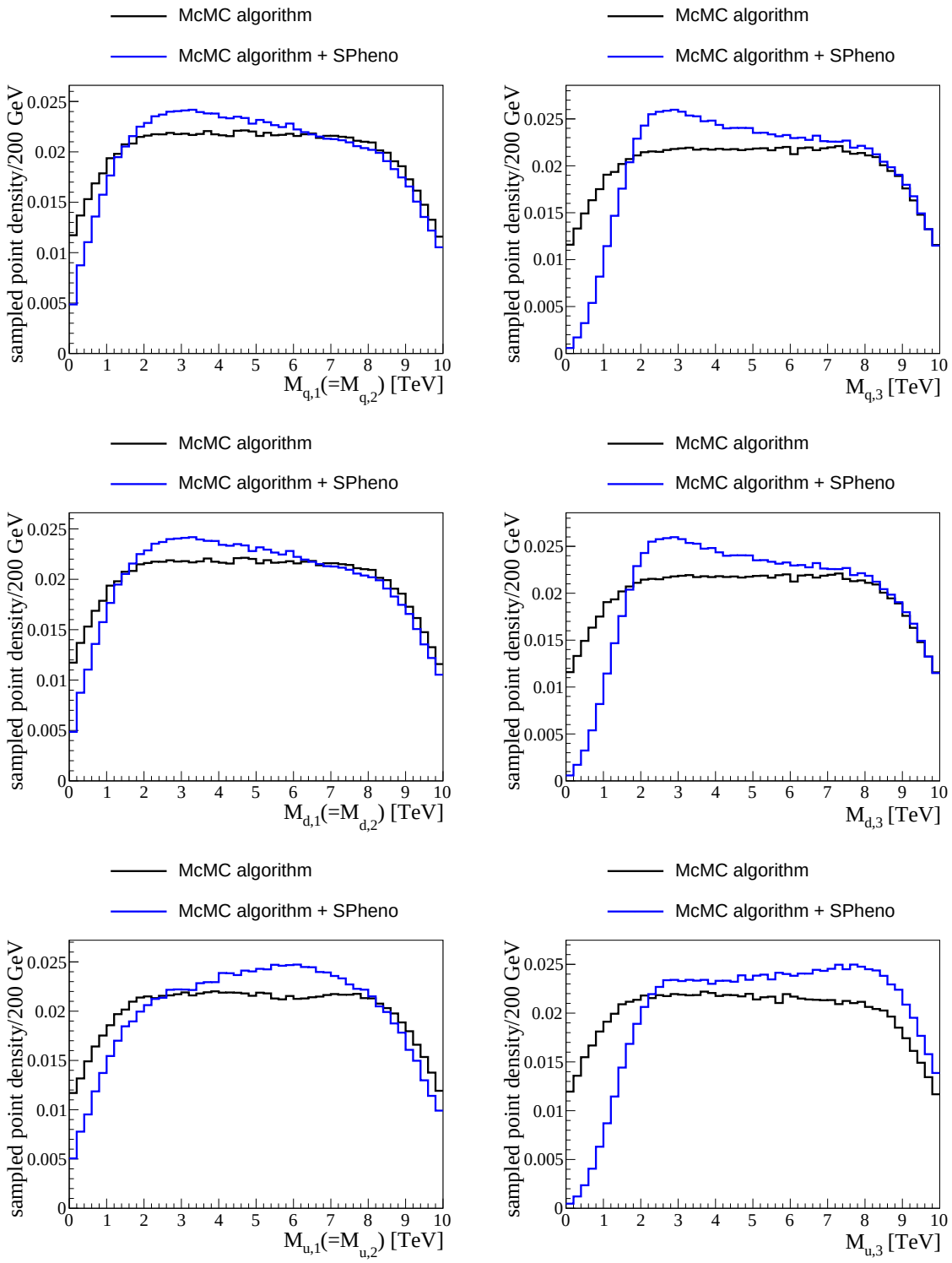

Figure 22: Comparison of distributions of the squark mass parameters in McMC run with and without the constraints coming from model consistency and approximations of `SPheno`. Shown are the first generation (left column) and third generation (right column) squark mass parameters, for the left-chiral (top row), the down-type right-chiral (center row), and the up-type right-chiral squarks (bottom row). The requirement that $\widetilde{\chi}_1^0$ is the LSP is enforced within the `SPheno` constraints.

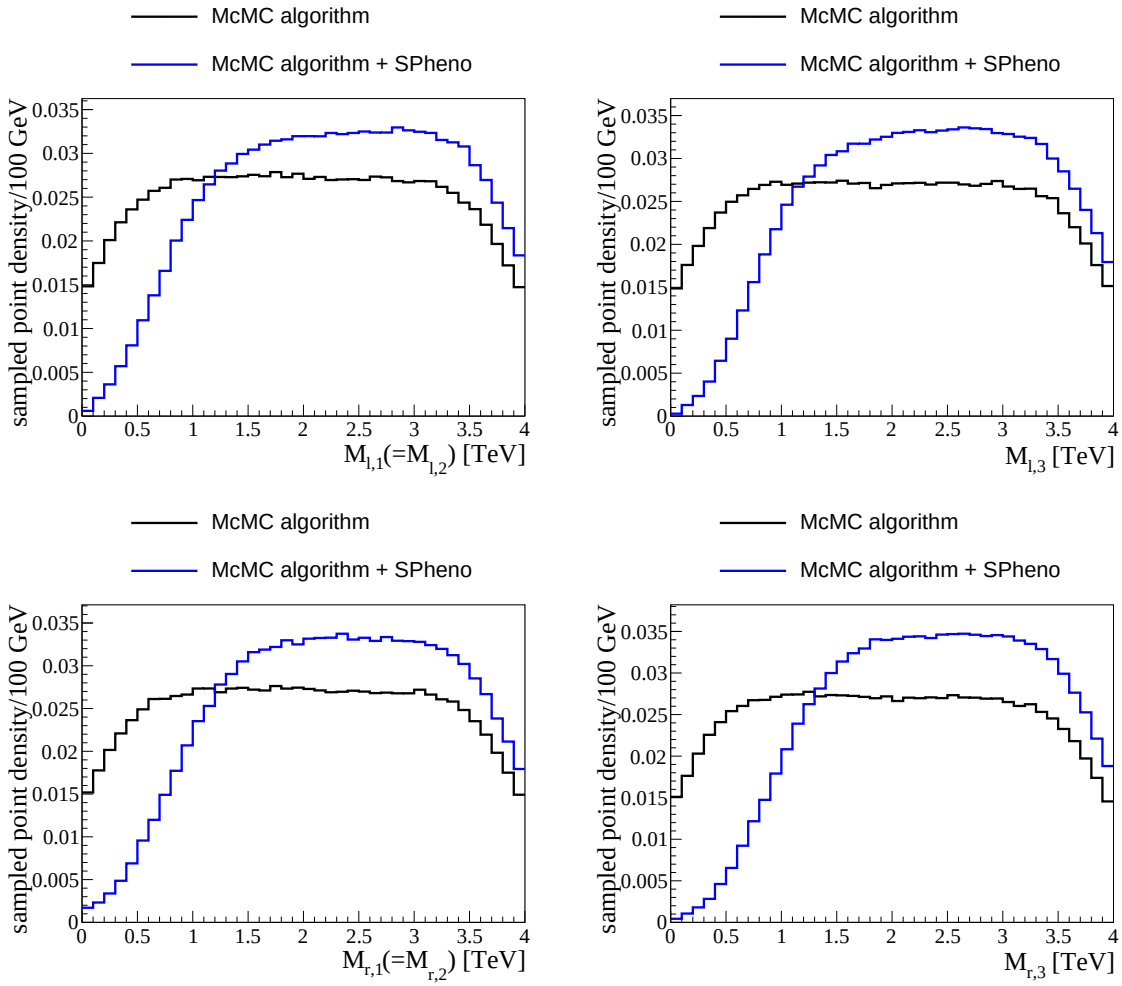

Figure 23: Comparison of distributions of the slepton sector in McMC run with and without the constraints coming from model consistency and approximations of `SPheno`. Shown are the left-chiral (top row) and right-chiral (bottom row) first-generation (left column) and third-generation (right column) slepton mass parameters $M_{l,1}$, $M_{r,1}$, $M_{l,3}$, and $M_{r,3}$. The requirement that $\widetilde{\chi}_1^0$ is the LSP is enforced within the `SPheno` constraints.

The effect of the model-inherent constraints on the electroweakino parameters is shown in Figure 24. Small $|\mu|$, where $|\mu| \lesssim 1\,\text{TeV}$, are heavily disfavored by the model-inherent constraints, due to the occurrence of tachyons, especially in combination with large Q_{SUSY}. The asymmetry of the distribution of μ, which favors positive μ, is the result of non-tachyon related errors encountered during the running of `SPheno` (more detail can be found in Appendix B). The peaks in the distributions of the bino-mass parameter M_1 and the wino-mass parameter M_2 are a consequence of the requirement that the LSP be a neutralino. Because of this requirement, in most of the pMSSM, the smallest mass parameter has to be either μ, M_1, or M_2. This peak is not seen in μ because the same region is so heavily suppressed by the model-inherent constraints.

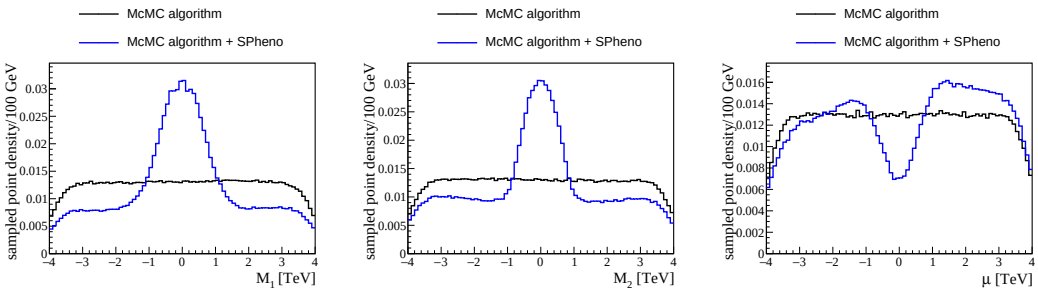

Figure 24: Comparison of distributions of the electroweakino sector in McMC run with and without the constraints coming from model consistency and acceptance of `SPheno`. Shown are the bino-mass parameter M_1 (left), the wino-mass parameter M_2 (center), and the higgsino-mass parameter μ (right). The requirement that $\widetilde{\chi}_1^0$ is the LSP is enforced within the `SPheno` constraints.

Finally, Figure 25 shows the the mass parameter for the heavy Higgs bosons m_A and the ratio of the Higgs doublet vacuum expectation values, $\tan(\beta)$. Again, small values of m_A are disfavored due to the presence of tachyons. There is an additional suppression of small m_A due to the requirement that the LSP is lighter than the heavy Higgs bosons A^0, H^0, and $H^\pm$. This requirement was an originally unintended choice in the scan settings, which results in on-average heavier heavy Higgs bosons in the pMSSM scan that persists in all the Markov chains shown throughout this analysis. The impact of this error is strongly mitigated by the fact that many of the included observables also strongly suppress small m_A, as is shown in Section 5.1.5 and Appendix C.

It can also be seen that large values of $\tan(\beta) \gtrsim 20$ are more and more disfavored by the model-inherent constraints, due to the increased presence of models with tachyonic states in that region of the parameter space.

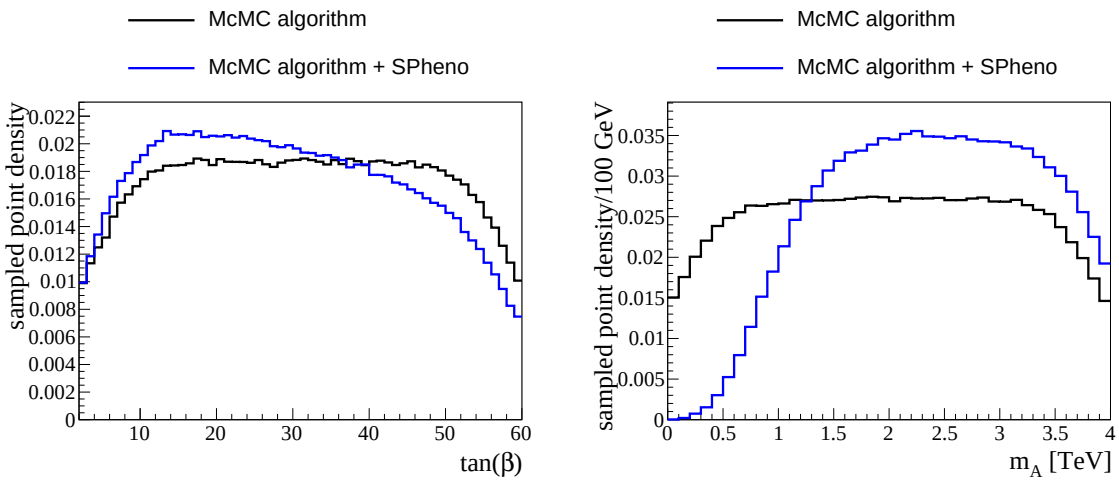

Figure 25: Distributions of the ratio of Higgs vacuum expectation values $\tan(\beta)$ (left), and the mass of the pseudoscalar Higgs boson m_A (right), in McMC run with and without the constraints coming from model consistency and limitations of `SPheno`. The requirement that $\widetilde{\chi}_1^0$ is the LSP is enforced within the `SPheno` constraints and applies (erroneously) to all the physical heavy Higgs bosons.

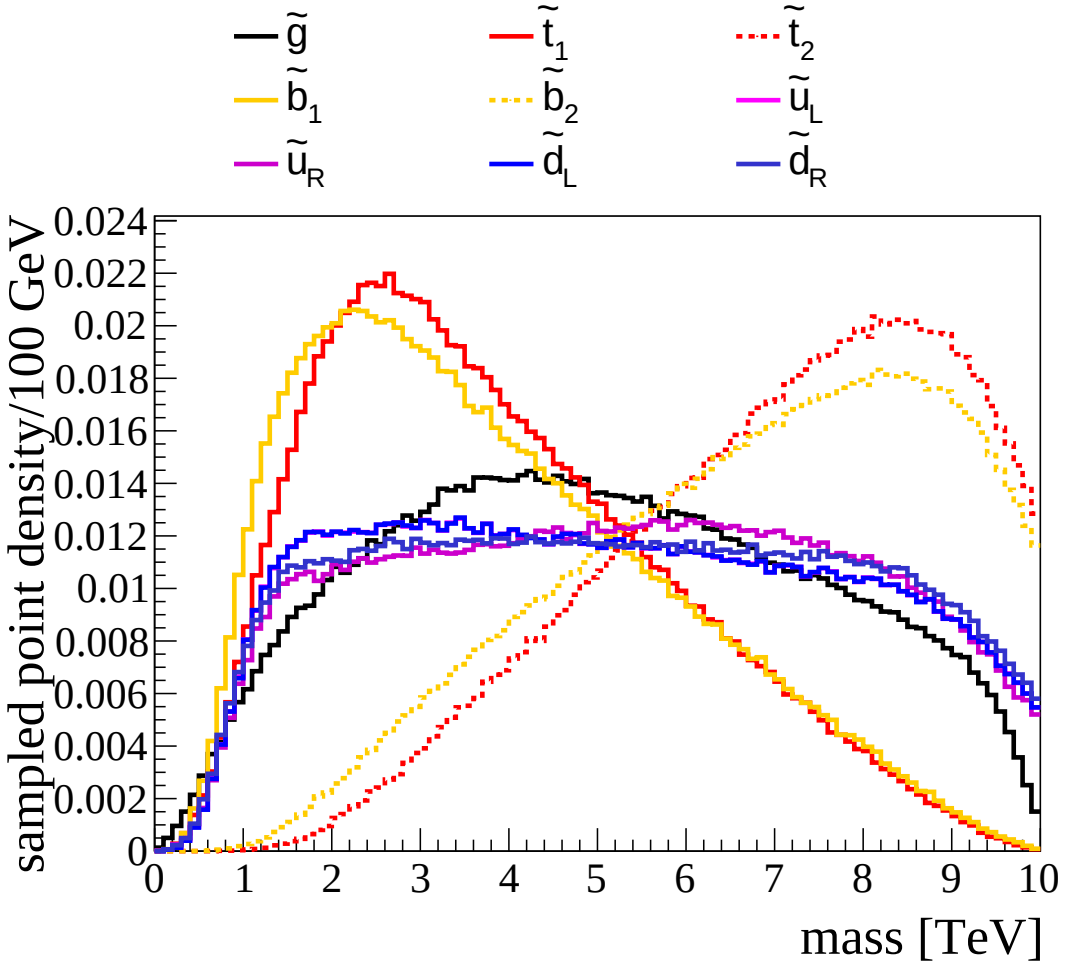

Figure 26: Summary distributions of the strongly interacting sparticle masses for McMC without likelihood steering. The only shaping occurs due to the sampling algorithm, and by imposing model-inherent constraints, such as the LSP requirement and the absence of tachyons.

From the pMSSM parameters, `SPheno` also generates the physical particle mass spectrum, which are the relevant quantities for constraints from collider and other experiments. In order to study the impact of these experiments, it thus makes sense to look at these derived particles masses, instead of at the pMSSM mass parameters. Summary distributions of the strongly interacting sparticle masses, slepton masses, electroweakino masses, as well as the heavy and light Higgs mass distributions can be found in Figures 26, 27, 28, and 29, respectively. The distributions of the physical squark, gluino, and slepton masses show the same features as their respective mass parameters, strongly disfavoring small masses and, to a lesser degree, disfavoring very large masses. An exception to this are the distributions for the third-generation sfermions, which differ significantly from the other sfermion mass distributions and their respective pMSSM parameters. This is almost entirely due to fact that they are mass-ordered mass eigenstates mixed together from their left- and right-chiral flavor eigenstates. This results in a peaking distribution at small masses for the $\widetilde{t}_1$, $\widetilde{b}_1$, and $\widetilde{\tau}_1$ distributions, and a peaking distribution at large masses for the $\widetilde{t}_2$, $\widetilde{b}_2$, and $\widetilde{\tau}_2$ masses. The masses of $\widetilde{u}_L$ and $\widetilde{d}_L$ are almost degenerate in the pMSSM.

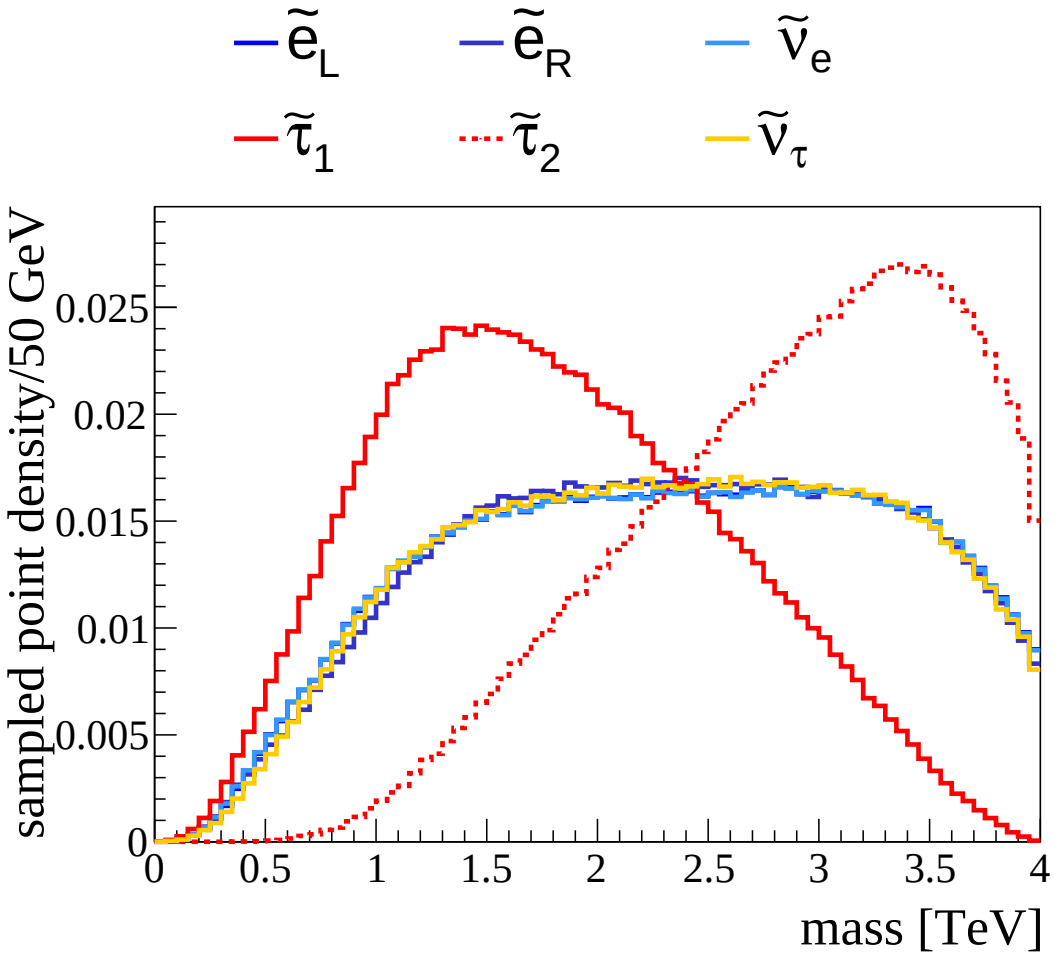

Figure 27: Summary distributions of the slepton masses for McMC without likelihood steering. The only shaping occurs due to the sampling algorithm, and by imposing model-inherent constraints, such as the LSP requirement and the absence of tachyons.

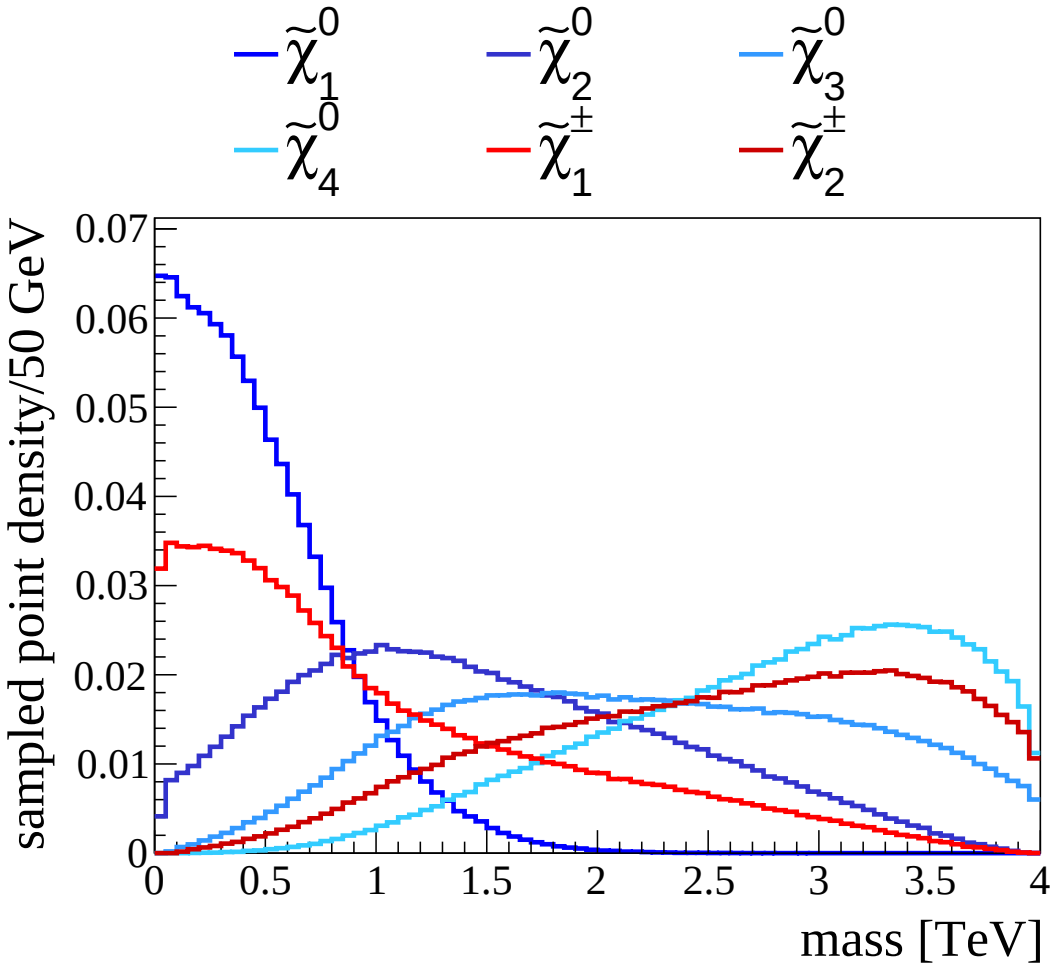

Figure 28: Summary distributions of the electroweakino masses for McMC without likelihood steering. The only shaping occurs due to the sampling algorithm, and by imposing model-inherent constraints, such as the LSP requirement and the absence of tachyons.

The distributions of the physical electroweakino masses are very different from their respective pMSSM parameters. Three effects contribute to this: firstly, as with the stops, sbottoms, and staus, the electroweakinos are mass eigenstates ordered by increasing mass, which pushes the distributions of the mass ordered particles away from each other and results in the four peaking distributions visible in Figure 28. Secondly, the particle masses are positive by definition, while the pMSSM parameters are not. This means that there is no lowered scan density at small electroweakino masses due to the McMC algorithm, as the pMSSM parameters do not have an edge to their allowed range at zero. Thirdly, the lightest neutralino is required to be the LSP, which further pushes the distribution of $\widetilde{\chi}_1^0$, $\widetilde{\chi}_1^\pm$ (in the case of wino-like and higgsino-like LSP), and, to a lesser degree, $\widetilde{\chi}_2^0$ (in the case of higgsino-like LSP) towards lower masses. This is because for each model point, these particles have the smallest mass of **all** SUSY particles, not just the electroweakinos, which enhances the effect of mass-ordering compared to what is seen for the stau, and the stop and sbottom quarks.

The distributions of the Higgs boson masses are shown in Figure 29. We see that the distribution of the light Higgs boson mass has a width that far exceeds both theoretical and experimental uncertainties of the measured Higgs boson, but is centered slightly below the measured value of $m(h^0) \simeq 125\,\text{GeV}$, even without being actively steered there by the McMC. The distributions of the heavy Higgs bosons are almost indistinguishable from that of the pMSSM parameter m_A. This is because in most models, H^0, A^0, and $H^\pm$ are almost mass degenerate, with significance differences between the masses only occurring rarely at large m_A.

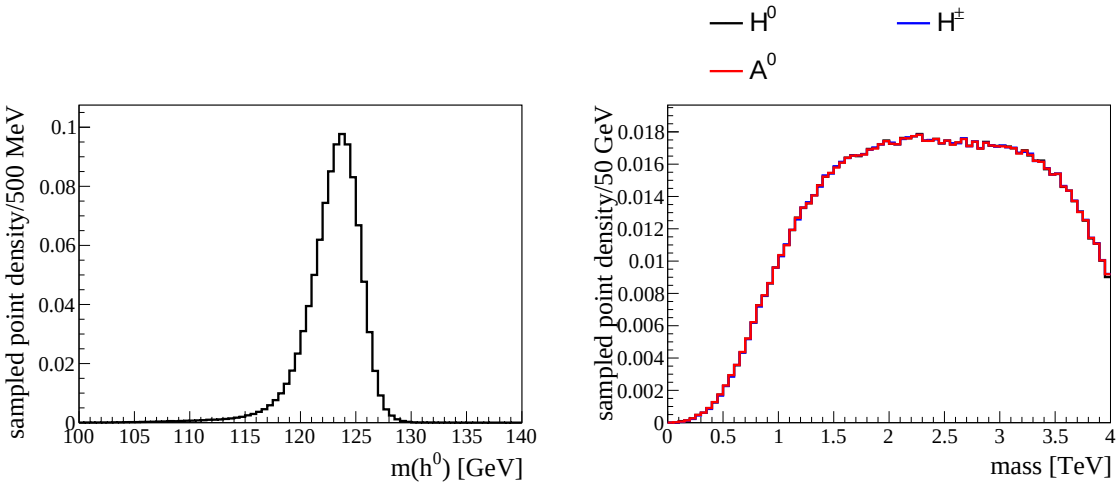

Figure 29: Distributions of the light (left) and heavy (right) Higgs boson masses for McMC without likelihood steering. The only shaping occurs due to the sampling algorithm, and by imposing model-inherent constraints, such as the LSP requirement and the absence of tachyons. The requirement that $\widetilde{\chi}_1^0$ is the LSP is enforced within the `SPheno` constraints and applies (erroneously) to the heavy Higgs bosons.

5.1.3 Impact of the Higgs mass constraint

The next constraint that is studied is the inclusion of the Higgs mass constraint to the Markov chain likelihood. The most striking impact is seen in the distribution of the light Higgs mass itself, shown in Figure 30. We see that the distribution collapses into a sharp peak around the measured Higgs mass value, which shows the desired shaping by the McMC.

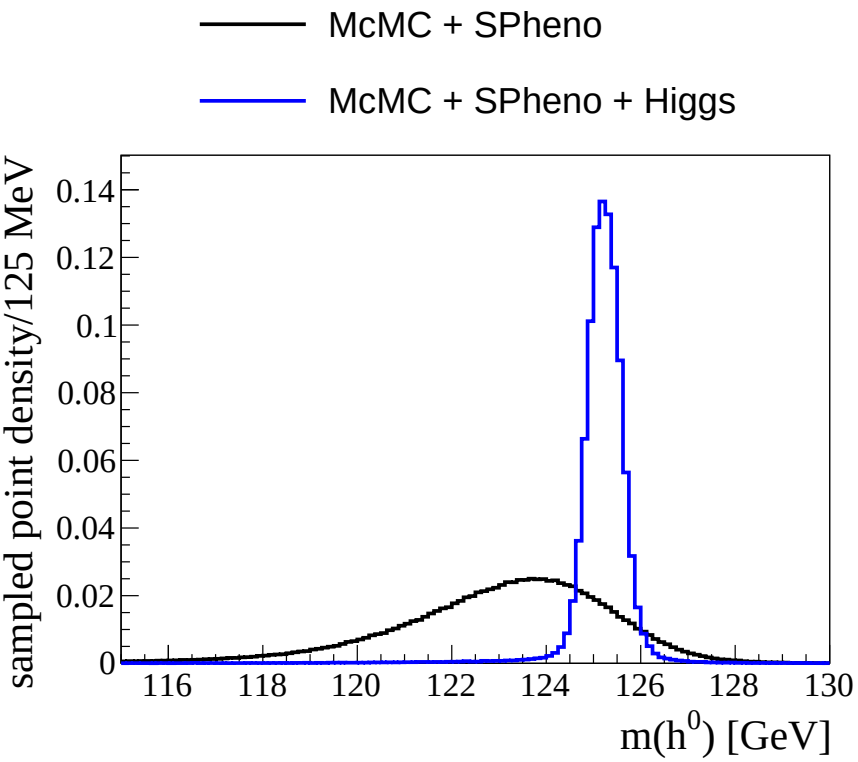

Figure 30: Comparison of the light Higgs boson mass in Markov chains shaped by McMC algorithm effects and model-inherent constraints implemented through `SPheno`, and McMC that also include the Higgs mass measurement as explained in Section 5.1.

Aside from the expected impact on the light Higgs mass, the constraint severely impacts the distributions of $\tan(\beta)$ and A_t, shown in Figure 31. Whereas the McMC without the Higgs mass constraint (see Section 5.1) favors large $\tan(\beta)$, the inclusion of the Higgs mass results in the strong suppression of small values of $\tan(\beta)$. Similarly, small values of $|A_t|$ are severely disfavored by the Higgs mass constraint and the need of large radiative corrections to the light Higgs mass in the pMSSM. The fact that the A_t distribution keeps rising towards larger $|A_t|$ (until the algorithm effect causes of drop in the point density for $|A_t| > 6\,\text{TeV}$) points to a flaw in the construction of the pMSSM scan – the edges of the samples parameter space are overconstrained to small $|A_t|$, since the McMC acceptance would be higher for $|A_t| > 7\,\text{TeV}$.

Also affected are the stop mass parameters $M_{q,3}$ and $M_{u,3}$, as well as the physical top squark and bottom squark masses, shown in Figure 32. The distributions for the stop masses and mass parameters are significantly shifted towards larger masses by the need for large radiative contributions to the Higgs mass. The distribution for the lighter stop mass $m(\tilde{t}_1)$ is now almost flat for intermediate stop masses. The sbottom masses are less affected, but are also shifted towards larger masses. The shift is likely not due to direct contributions of the sbottom to the Higgs mass, but rather because $M_{q,3}$, which is shifted by the need for heavier stops, also determines the mass of the left-chiral component of the sbottom mass state.

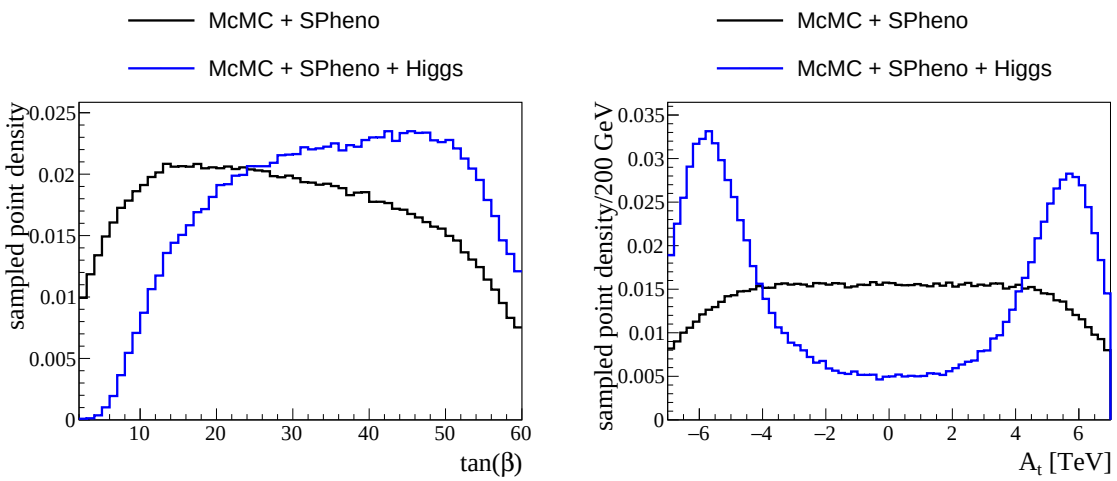

Figure 31: Comparison of the ratio of Higgs vacuum expectation values $\tan(\beta)$ (left) and the trilinear Higgs-stop coupling A_t (right), in Markov chains shaped by McMC algorithm effects and model-inherent constraints implemented through `SPheno`, and Markov chains that include the Higgs mass constraints (explained in Section 5.1) in addition.

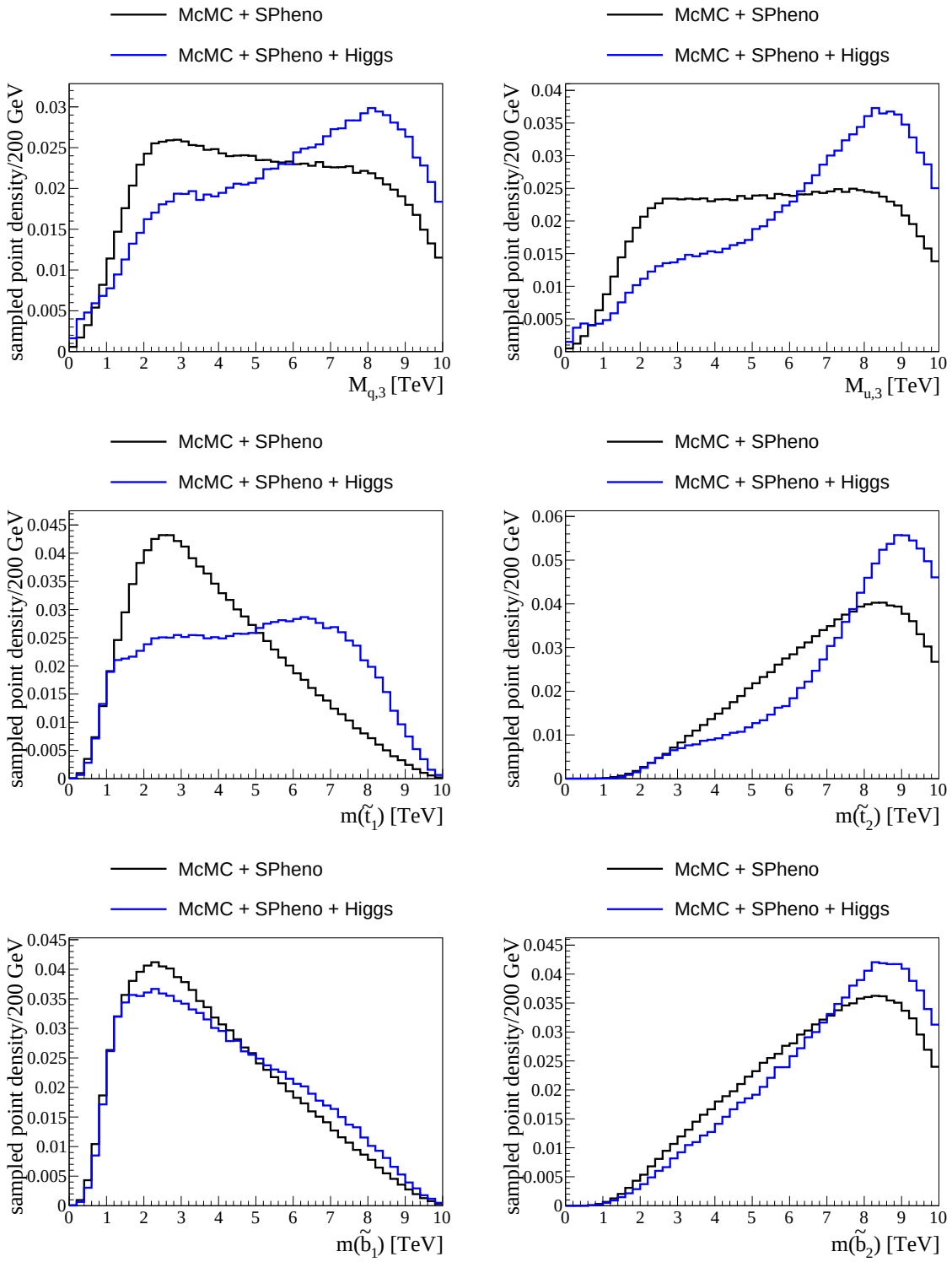

Figure 32: Comparison of the left-chiral (top left) and right-chiral (top right) third generation mass parameters $M_{q,3}$ and $M_{u,3}$, the lighter (center left) and heavier (center right) stop masses, $m(\tilde{t}_1)$ and $m(\tilde{t}_2)$, and the lighter (bottom left) and heavier (bottom right) sbottom masses, $m(\tilde{b}_1)$ and $m(\tilde{b}_2)$, in Markov chains shaped by McMC algorithm effects and model-inherent constraints implemented through `SPheno`, and Markov chains that include the Higgs mass constraint, explained in Section 5.1, in addition.

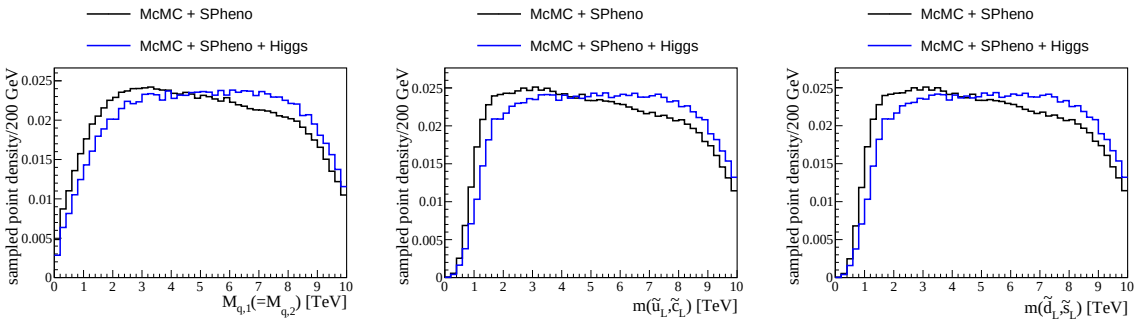

Figure 33: Comparison of the left-chiral first generation squark parameter $M_{q,1}$ (left) and the masses of the left-chiral sup $m(\widetilde{u}_L, \widetilde{c}_L)$ (center) and sdown $m(\widetilde{d}_L, \widetilde{s}_L)$ (right), in Markov chains shaped by McMC algorithm effects and model-inherent constraints implemented through `SPheno` and Markov chains that include the Higgs mass in addition. Note that the first two generations of sfermions are mass degenerate in the pMSSM, as well as the left-chiral up- and down-type squarks in the first two generations.

A small effect can be observed in the first and second generation of left-handed squarks, shown in Figure 33. Their distributions show a slight shift towards larger masses, which is likely due to correlations to the stop sector (and the SUSY scale Q_{SUSY}, which can have large impacts due to its connection to tachyons in `SPheno`), rather than direct contributions to the Higgs mass.

Lastly, a moderate change can be observed in the electroweak sector for the higgsino mass parameter μ and the wino mass parameter M_2. Their distributions are shown in Figure 34. Including the Higgs mass constraint in the McMC further favors small wino masses at the expense of small higgsino masses. It also unexpectedly reverses the asymmetry in the μ distribution. This is likely a result of non-convergence of the McMC used for these studies, which are performed with comparatively few parallel Markov chains with comparatively small number of pMSSM points each. Because of the small likelihood at small values of $|\mu|$, individual Markov chains are unlikely to cross the small-likelihood region, which leads to slower convergence. Given that the number of pMSSM points in each chain is comparatively small, non-converge can not be sufficiently ruled out here. This effect is made worse by the inclusion of the constraints from LEP and constraints on the Z→invisible branching fraction, as implemented using `MicrOMEGAs`, which is discussed next.

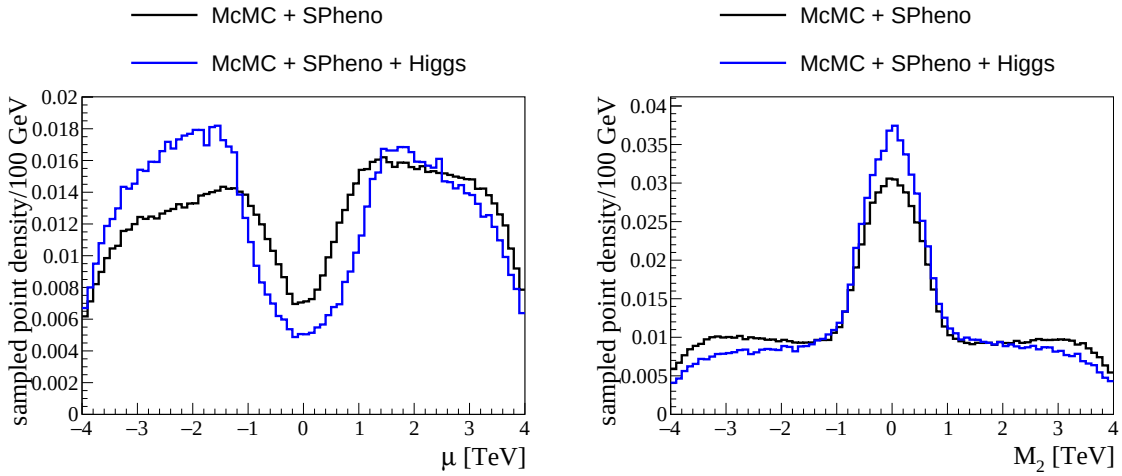

Figure 34: Comparison of the higgsino mass parameter μ (left) and the wino mass parameter M_2 (right) in Markov chains shaped by McMC algorithm effects and model-inherent constraints implemented through `SPheno` , and Markov chains that include the Higgs mass in addition.

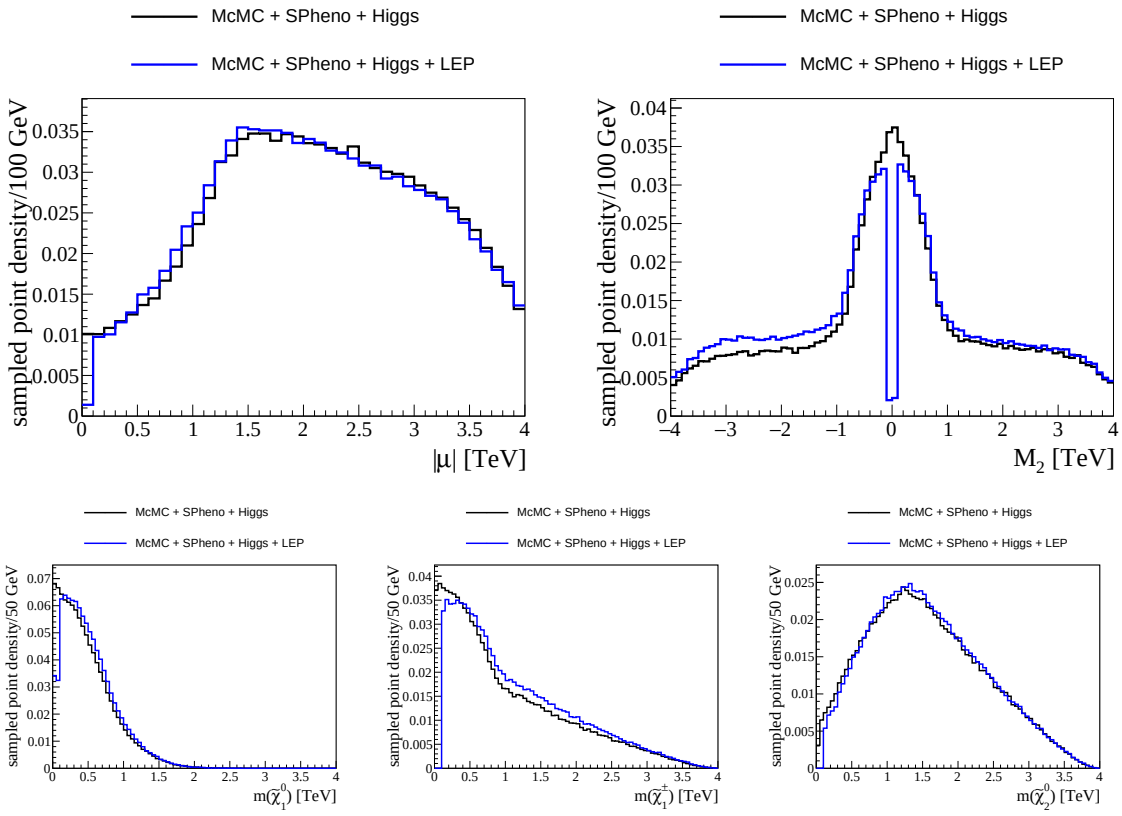

Figure 35: Comparison of the absolute value of the higgsino mass parameter $|\mu|$ (top left), the wino mass parameter M_2 (top right), as well as the masses of the lightest neutralino $m(\widetilde{\chi}_1^0)$ (bottom left), the lighter chargino $m(\widetilde{\chi}_1^\pm)$ (bottom middle), and the second lightest neutralino $m(\widetilde{\chi}_2^0)$ (bottom right). Markov chains shaped by McMC algorithm effects, model-inherent constraints implemented through `SPheno`, and the Higgs mass constraint, and Markov chains that include the LEP mass constraints and constraints on the branching ratio of Z→ invisible in addition, are shown.

5.1.4 Impact of the LEP chargino and Z to invisible constraints

The effect of the addition of the LEP constraints on charginos and Z to invisible constraints on the McMC is studied here. This constraint is applied in a binary fashion, and almost exclusively affects the electroweakino sector, shown in Figure 35. Almost all charginos below 100 GeV are excluded by LEP, which cuts out all pMSSM models with a wino-like or higgsino-like LSP below approximately 100 GeV. This does not affect pMSSM models with a bino-like LSP in a similar way, because the LSP mass and the mass of the lightest chargino are independent in pMSSM models with a bino-like LSP. This leads to approximately half the nominal point density remaining for $m(\widetilde{\chi}_1^0) < 100\,\text{GeV}$, with all remaining models in this region featuring a bino-like LSP. The distributions of $m(\widetilde{\chi}_1^\pm)$ and $m(\widetilde{\chi}_2^0)$, as well as M_2, are unchanged except for the drop to zero for masses m $\lesssim 100\,\text{GeV}$. The rest of the distributions do not deviate significantly from the previous step.

5.1.4.1 Non-convergence in μ in small Markov chains

The further drop in likelihood around zero for the higgsino mass parameter makes it very unlikely that any individual Markov chain will cross this threshold. As a consequence, these Markov chains used in this particular study of the impacts on individual contributions are unlikely to converge quickly enough on the distribution of μ, given that their length is comparatively small. The absolute value $|\mu|$ is found to be much less affected, allowing its use in studying the various impacts from individual McMC contributions in this section. The problem is limited to the McMC using an incomplete set of observables, which are exclusively used in this section. Convergence studies in Section 5.3 on the full McMC (=**LEO posterior** in Section 5.1.5), which includes the full set of observables and is significantly larger, show compatibility with convergence in μ. This allows for the study of the LHC impact on the sign of μ.

Faster convergence could have been attained by choosing a larger step size of the McMC for this particular study. Since the LEP constraints are implemented in all McMC shown from this point in the thesis, we do not comment on whether asymmetries in the distribution of μ are caused by flavor observables and use its absolute value $|\mu|$ instead.

This McMC now defines the pre-low energy observables (pre-LEO) prior that can be used to gauge the impact of the individual b-physics measurements, and can be compared to the "full" McMC setup that uses all of them.

5.1.5 Impact of included flavor observables

Judging the impact of the various included observables on the pMSSM comes with some additional difficulty. In the previous sections, we compared Markov chains with or without consecutively incorporated constraints to determine how the added observables affect the pMSSM space. However, we mostly neglected that the order in which the constraints are applied may change the outcome of this impact study. As an extreme example, imagine two observables that put almost identical constraints on the pMSSM space and perform the study we have done above. Since the first constraint would already remove the part of the pMSSM that both constraints eliminate, the conclusion would be that the second constraint has no impact. If the order in which the constraints are applied was reversed, the conclusion would be that the other constraint has little-to-no impact. For the constraints that we have already covered here, this problem is mostly nonexistent for three types of reasons. In the case of tachyonic models, we do not get a physical particle spectrum from `SPheno` that can be used to calculate the flavor observables – we always need to perform this step with its constraints before anything else. The Higgs mass measurement is a more centrally important constraint on the pMSSM than the various flavor observables. Finally, for the LEP constraints, we know that they are very localized in pMSSM space but very severe (by their binary nature), which means that the order of the constraints does not matter.

However, for the remaining flavor observables, the order can matter in terms of what impact is ascertained for them. At the same time, studying all permutations is not feasible.

Instead, for each of the flavor observables, we look at distributions for four Markov chains:

1. a **l**ow-**e**nergy **o**bservable prior **(LEO prior)**, constructed using all the constraints from the previous sections, namely use of McMC steered only by the Higgs mass constraint, as well as the LEP constraints, and constraints on the branching ratio of Z→invisible;

2. the observable in question applied in addition to the constraints in the LEO prior **(LEO prior+X)**;

3. the **l**ow-**e**nergy **o**bservable posterior **(LEO posterior)**, constructed using the complete final set of constraints and observables;

4. and the LEO posterior without the observable in question **(LEO posterior-X)**

By comparing distributions 1 and 2, we can infer the favored and disfavored regions for the observable on a comparatively unconstrained pMSSM. The McMC sampling the LEO prior+X has almost maximal freedom to scan the part of the pMSSM that is best compatible with the observable in question X. On the other hand, comparing distributions 3 and 4, we can see the impact the observation has on the maximally constrained pMSSM, which has to be compatible with a multitude of observations. We can interpret this impact as the observable in question X shaping the residual space given by the other observables. The difference between the LEO prior+X and the LEO posterior-X shows the, sometimes competing, favored and disfavored regions between the observable X and the remaining observables.
We will discuss the impact of two observables, BR($b \to s\gamma$) and BR($B_s \to \mu\mu$) in this section, with the remaining observables covered in Appendix C.

5.1.6 BR(b → sγ)

The decay of a bottom quark into a strange quark is a rare process in the SM, with the lowest-order process, shown in Figure 36, involving an up-type quark - W loop. Because of the significant hierarchy of the CKM matrix entries, the top quark contributes the most to this loop. To conserve four-momentum, the final state of a b→s transition must contain at least one other particle, such as a photon or leptons, which can be radiation from the virtual quark or W boson. The MSSM can contribute to that transition in multiple ways, for example via a squark-chargino loop.

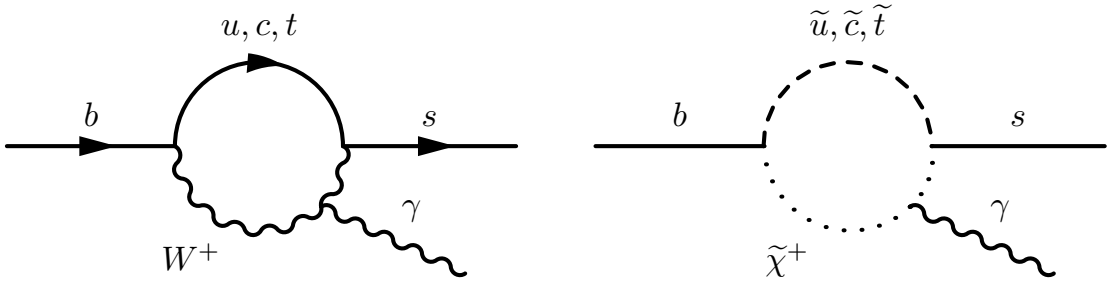

Figure 36: Leading-order Feynman diagrams for the b→sγ transition in the Standard Model (left) and the MSSM (right).

Given that the SM model prediction of the branching ratio $\mathrm{BR}(\mathrm{b} \to \mathrm{s}\gamma)_{\mathrm{SM}} = (3.15 \pm 0.23) \times 10^{-4}$ [117, 118] agrees well with the measurements of the branching ratio $\mathrm{BR}(\mathrm{b} \to \mathrm{s}\gamma) = (3.43 \pm 0.21 \pm 0.07) \times 10^{-4}$ [95], contributions from the MSSM can significantly impact the pMSSM both in the electroweak and the strong sector. Figure 37 shows the impact of BR(b → sγ) on the electroweak sector. Inclusion of BR(b → sγ) significantly shifts the distribution of the higgsino mass parameter $|\mu|$ to larger masses. This shift to larger masses is seen both on the LEO prior and on the LEO posterior-BR(b → sγ). The wino mass parameter is also strongly affected by BR(b → sγ), as small M_2 is significantly disfavored in prior+BR(b → sγ) compared to the prior. A smaller drop of the probability density is also present in comparing the LEO posterior-BR(b → sγ) to the full LEO posterior. The observable BR(b → sγ) competes with the other observables in terms of the wino mass parameter, which is seen in the fact that both the LEO posterior-BR(b → sγ) and the LEO posterior show a significantly larger probability density at small M_2 than the LEO prior+BR(b → sγ).

The impact on the electroweak sector can also be seen in terms of the masses of the physical particles, the neutralinos and charginos, also shown in Figure 37. As seen in the electroweakino mass parameters, small masses of the lighter neutralinos $\widetilde{\chi}_1^0$ and $\widetilde{\chi}_2^0$, and small masses of the ligher chargino $\widetilde{\chi}_1^\pm$ are disfavored by BR(b → sγ). The impacts are particularly noticeable in the distribution of $m(\widetilde{\chi}_1^\pm)$, since it does not include a contribution from the unaffected bino. In addition to the suppression of small $m(\widetilde{\chi}_1^\pm)$, reflected in the suppression of both small $|\mu|$ and small M_2, there is a rise of the distribution of $m(\widetilde{\chi}_1^\pm)$ between $m(\widetilde{\chi}_1^\pm) \simeq 1\,\mathrm{TeV}$ and $m(\widetilde{\chi}_1^\pm) \simeq 1.5\,\mathrm{TeV}$, when comparing the LEO prior to the LEO prior+BR(b → sγ), the LEO posterior-BR(b → sγ), and the full LEO posterior. The observable BR(b → sγ) is one of the causes of this feature of the $m(\widetilde{\chi}_1^\pm)$ distribution, which comes from an increased contribution of higgsinos compared to winos at this mass range, as is reflected in the distribution of $|\mu|$ in the same mass range. Because the LEO posterior-BR(b → sγ) shows the same feature, BR(b → sγ) can not be uniquely responsible for it. The related observable $\mathrm{BR}(\mathrm{B}^0 \to \mathrm{K}^{*0}\gamma)$ results in a very similar shift of the chargino mass distribution, as we discuss in Appendix C.3. The observable BR(b → sγ) can be seen to compete with the remaining observables on these physical masses as well.

The impact of BR(b → sγ) on the third generation squarks is shown in Figure 38. The distributions of $\mathrm{M}_{\mathrm{q},3}$ and $\mathrm{M}_{\mathrm{u},3}$ are noticeably shifted towards large masses, and BR(b → sγ) is seen to impact the distributions of both $\mathrm{M}_{\mathrm{q},3}$ and $\mathrm{M}_{\mathrm{u},3}$ with respect to both the LEO prior and the LEO posterior-BR(b → sγ). This effect is mirrored in the distribution of the lighter stop mass $m(\widetilde{\mathrm{t}}_1)$, where at $m(\widetilde{\mathrm{t}}_1) \lesssim 2\,\mathrm{TeV}$, the probability density of the LEO prior+BR(b → sγ) is approximately half that of the LEO prior, and the LEO posterior-BR(b → sγ) is approximately 30% larger than the full LEO posterior.

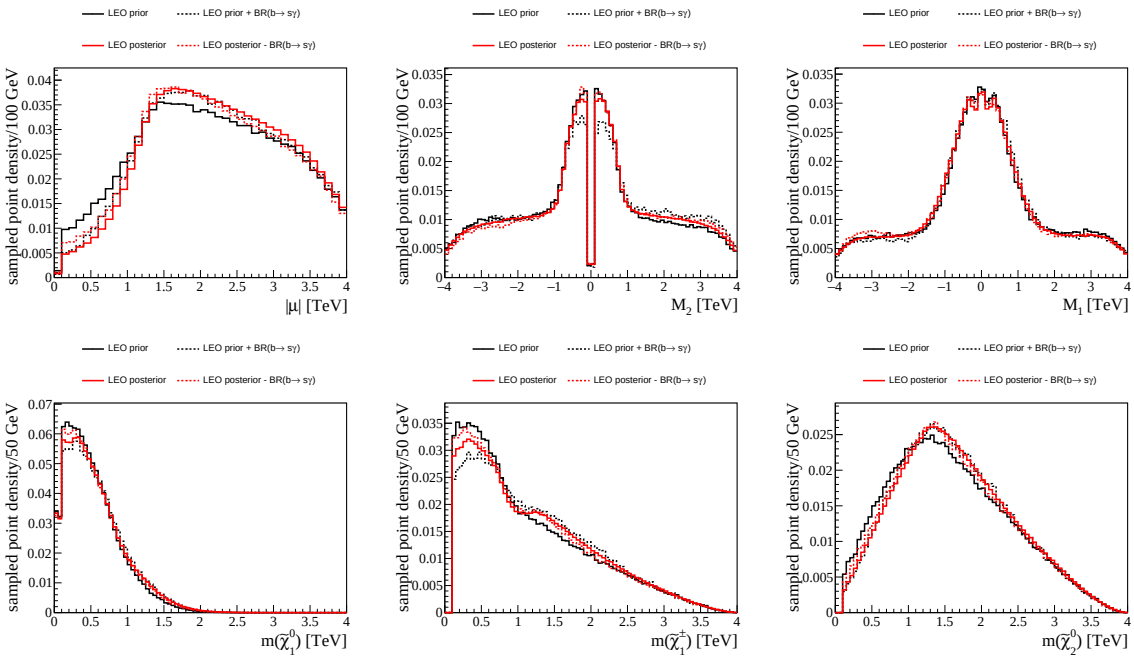

Figure 37: Distributions of the absolute value of the higgsino mass parameter $|\mu|$ (top left), the wino mass parameter M_2 (top center), and the bino mass parameter M_1 (top right), as well as the masses of the lightest neutralino $m(\widetilde{\chi}_1^0)$ (bottom left), the lighter chargino $m(\widetilde{\chi}_1^\pm)$ (bottom center), and the mass of the second lightest neutralino $m(\widetilde{\chi}_2^0)$ (bottom right). For each parameter, the distribution for the LEO prior (black), the LEO prior+BR(b $\to$ sγ) (dashed black), the LEO posterior (red), and the LEO posterior-BR(b $\to$ sγ) (dashed red), are shown.

These effects on $m(\widetilde{t}_1)$, as well as on $m(\widetilde{\chi}_1^\pm)$, can be directly understood from the lowest order SUSY contribution to the b$\to$s transition, which involves a $\widetilde{t}_1$-$\widetilde{\chi}_1^\pm$ loop. Small $m(\widetilde{t}_1)$ and $m(\widetilde{\chi}_1^\pm)$ can thus result in too large a contribution, which is disfavored by the measurements.

In contrast to the electroweakino sector, the observable BR(b $\to$ sγ) is seen to compliment and enhance the impact of the other observables, and does not visibly compete with them. It should be noted that because of the large tachyonic fraction at large Q_{SUSY} (which is completely correlated to $M_{q,3}$ and $M_{u,3}$) and small $|\mu|$, small values of the latter are correlated to lighter stops. This means that an observable that impacts either light stops or light higgsinos will also be seen to impact the other. Because of its still significant CKM matrix entry, a smaller impact of BR(b $\to$ sγ) can be seen on the right-chiral sbottom mass parameter $M_{d,3}$, with smaller masses favored over larger masses, with the inclusion of BR(b $\to$ sγ) contributing about half of the difference between the LEO prior and the LEO posterior. At larger masses, the LEO prior+BR(b $\to$ sγ) noticeably aligns with the full posterior, and the LEO posterior-BR(b $\to$ sγ) noticeably aligns with the LEO prior. This suggests that the observable BR(b $\to$ sγ) is the only included observable that significantly shapes the posterior density at large $M_{d,3}$, the combined impact of the other observables seems to be agnostic about the distribution of $M_{d,3}$ – at least in terms of the marginalized 1-dimensional distribution. In terms of the mass of the lighter sbottom $m(\widetilde{b}_1)$, we see an impact at small $m(\widetilde{b}_1)$ in the suppression of the LEO prior by the inclusion of BR(b $\to$ sγ). There is a much smaller impact of BR(b $\to$ sγ) on the LEO posterior-BR(b $\to$ sγ), which can be explained by the competing impacts on the two sbottom mass parameter $M_{q,3}$ and $M_{d,3}$. There is also a noticeable absence of an impact at large $m(\widetilde{b}_1)$, even though there is a strong impact at similar mass values in $M_{d,3}$. The conclusion is that at small masses, the left-chiral component of $\widetilde{b}_1$ is favored over the right-chiral component, while the opposite is true at large masses.

There is a somewhat striking impact on the left-chiral first (and second) generation squark mass parameter $M_{q,1}$ and the corresponding squark masses $m(\widetilde{u}_L, \widetilde{c}_L)$ and $m(\widetilde{d}_L, \widetilde{s}_L)$, shown in Figure 39. When included as the only observable, the probability density noticeably peaks around a mass of approximately 2.5 TeV. This region likely contributes to the b$\to$s transition in such a way that fits the measurement better than the SM does. In the full LEO posterior, this effect is no longer

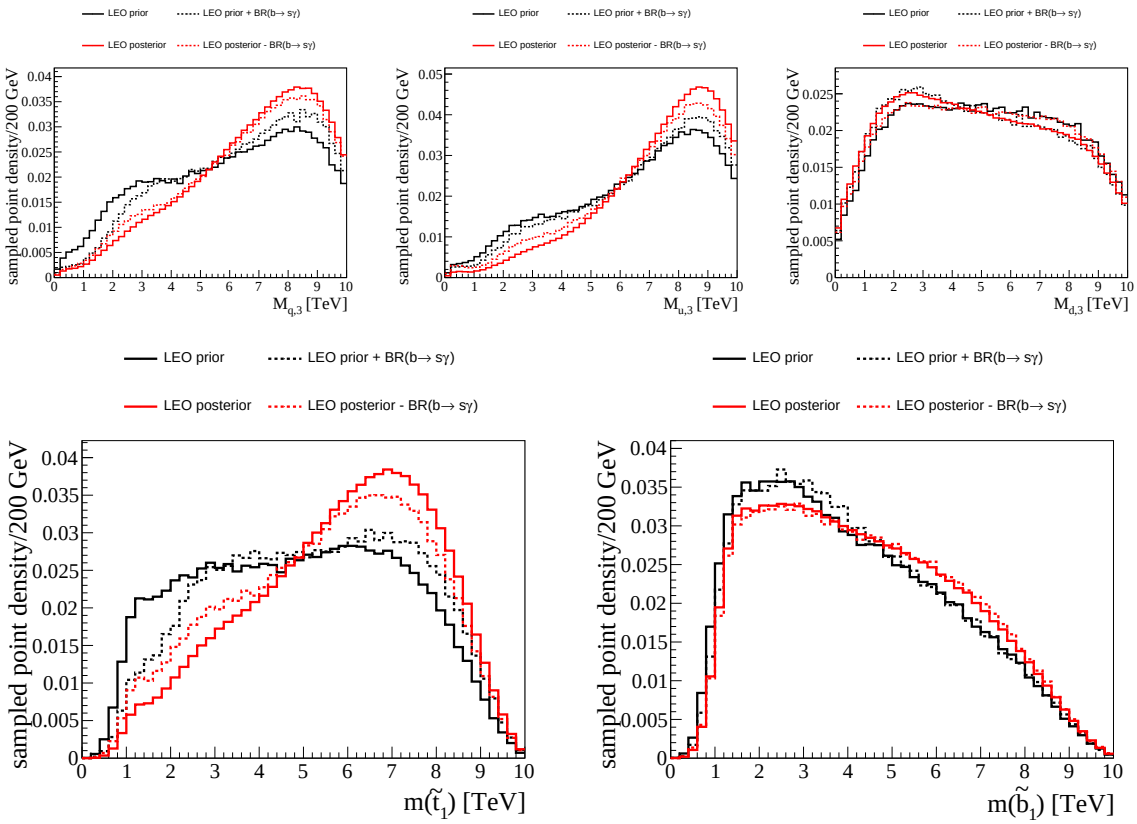

Figure 38: Distributions of the left-chiral third generation squark mass parameter $M_{q,3}$ (top left), the right-chiral top (top center) and bottom (top right) squark mass parameters $M_{u,3}$ and $M_{d,3}$, as well as the light stop mass $m(\tilde{t}_1)$ (bottom left) and light sbottom mass $m(\tilde{b}_1)$ (bottom right). The distributions are shown for the LEO prior (black), the LEO prior+BR(b $\rightarrow$ sγ) (dashed black), the LEO posterior (red), and the LEO posterior-BR(b $\rightarrow$ sγ) (dashed red).

present, likely due to the same region's incompatibility with other included observables. Inclusion of BR(b $\rightarrow$ sγ) with the other observables slightly shifts the left-chiral first generation squark masses towards larger masses.

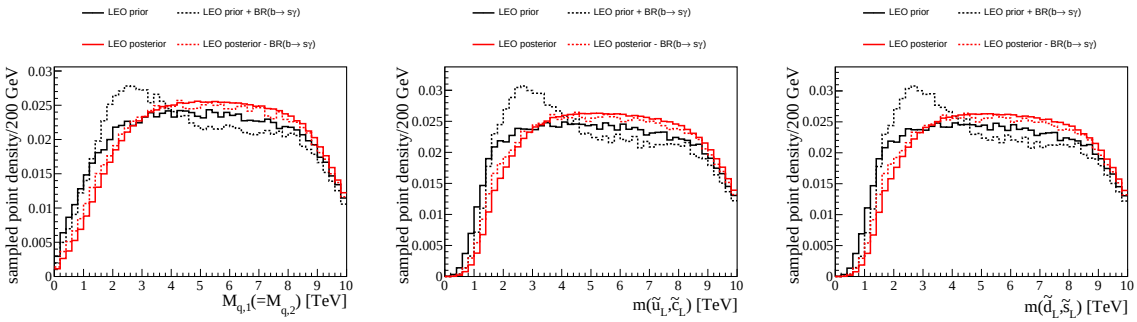

Figure 39: Distributions of the left-chiral first generation squark mass parameter $M_{q,1}$ (left), the left-chiral up squark mass $m(\widetilde{u}_L, \widetilde{c}_L)$ (center), and the left-chiral down squark mass $m(\widetilde{d}_L, \widetilde{s}_L)$ (right). The distributions are shown for the LEO prior (black), the LEO prior+BR(b $\rightarrow$ sγ) (dashed black) the LEO posterior (red), and the LEO posterior-BR(b $\rightarrow$ sγ) (dashed red). Note that the first two generations of sfermions are mass degenerate in the pMSSM, as well as the left-chiral up- and down-type squarks in the first two generations.

5.1.7 $\mathbf{BR(B_s \to \mu\mu)}$

Because flavor-changing neutral currents are forbidden at tree-level in the SM, the decay of neutral B-mesons into a di-muon final state can only occur in loops. This makes these decays very rare in the SM, and may make MSSM contributions significant in parts of the pMSSM. Example Feynman diagrams for the SM and the pMSSM are shown in Figure 40.

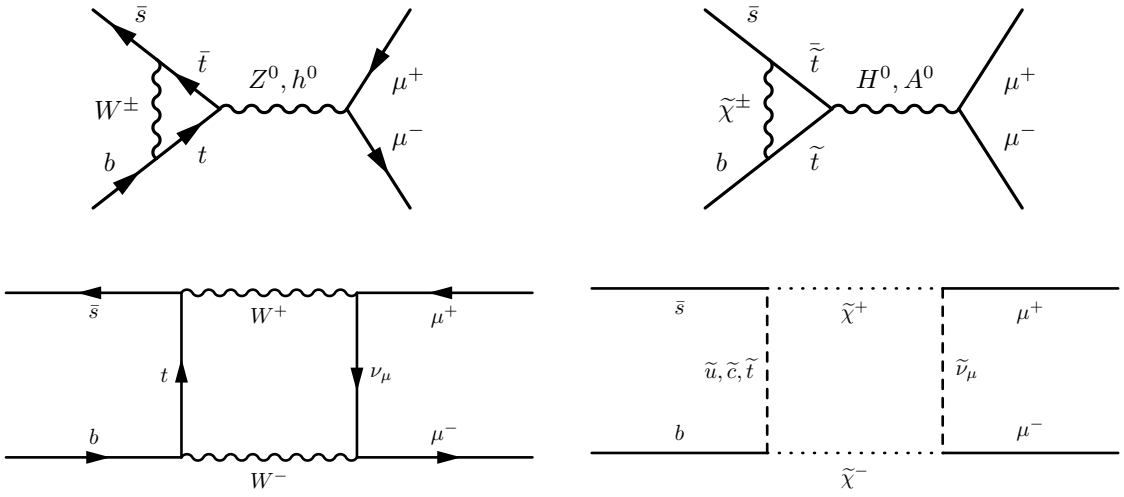

Figure 40: Examples of low-order Feynman diagrams for the di-leptonic B_s decay into muons in the Standard Model (left) and additional contributions from the MSSM (right).

The SM prediction is $BR(B_s \to \mu\mu)_{SM} = (3.66 \pm 0.14) \times 10^{-9}$ [119], which is in good agreement with the measurement $BR(B_s \to \mu\mu) = (2.9 \pm 0.7) \times 10^{-9}$ [96, 97, 98]. The constraint from this measurement significantly impacts the electroweak and colored sectors of the pMSSM. The impact on the electroweakino masses is shown in Figure 41, where there is a notable shift in the absolute value of $|\mu|$ towards intermediate values when $BR(B_s \to \mu\mu)$ is included on top of the constraints in the LEO posterior-$BR(B_s \to \mu\mu)$ and, to a milder degree, in the LEO prior. A similar suppression of large masses is also seen in terms of the wino mass parameter M_2, but only in the impact of $BR(B_s \to \mu\mu)$ on the LEO posterior-$BR(B_s \to \mu\mu)$. However, in the case of M_2, $BR(B_s \to \mu\mu)$ favors small M_2, not intermediate mass values. In terms of the mass of the lightest neutralino, at small $m(\widetilde{\chi}_1^0)$, $BR(B_s \to \mu\mu)$ competes and balances with the other LEO observables, such that the distribution of the LEO posterior resides in between the LEO prior+$BR(B_s \to \mu\mu)$ and the LEO posterior-$BR(B_s \to \mu\mu)$. A stronger impact is seen on the mass of $\widetilde{\chi}_1^\pm$, where the small-mass region is suppressed by the inclusion of $BR(B_s \to \mu\mu)$ to the LEO prior, and enhanced when included in the LEO posterior-$BR(B_s \to \mu\mu)$. The impact at small chargino masses is notably opposite to that of the observable $BR(b \to s\gamma)$, which suggests that these two observables compete in terms of the marginalized distribution of lighter chargino masses. When $BR(B_s \to \mu\mu)$ is not included in the LEO posterior, we see an enhanced tail at $m(\widetilde{\chi}_1^\pm) \gtrsim 2\,\text{TeV}$ that is caused by the enhanced probability of both large $|\mu|$ and large M_2.

Figure 42 shows the impact of the $BR(B_s \to \mu\mu)$ measurement on the third generation squarks. The impact here is very similar to that of $BR(b \to s\gamma)$ – a shift towards larger masses of the stop sector that synergizes with the impact of the other LEO observables, and a slight shift towards smaller masses of the sbottom sector. There is one visible difference in terms of the impact on the lighter sbottom mass $m(\widetilde{b}_1)$, where the LEO posterior-$BR(B_s \to \mu\mu)$ shows a more pronounced peak at $m(\widetilde{b}_1) \simeq 3\,\text{TeV}$ compared to the full posterior.

In addition to the third generation squarks, there is also an impact on the first generation squarks, shown in Figure 43. We can see that there is a noticeable shift towards larger $M_{q,1}$ and $m(\widetilde{u}_L, \widetilde{c}_L)$ when $BR(B_s \to \mu\mu)$ is included with the other LEO observables.

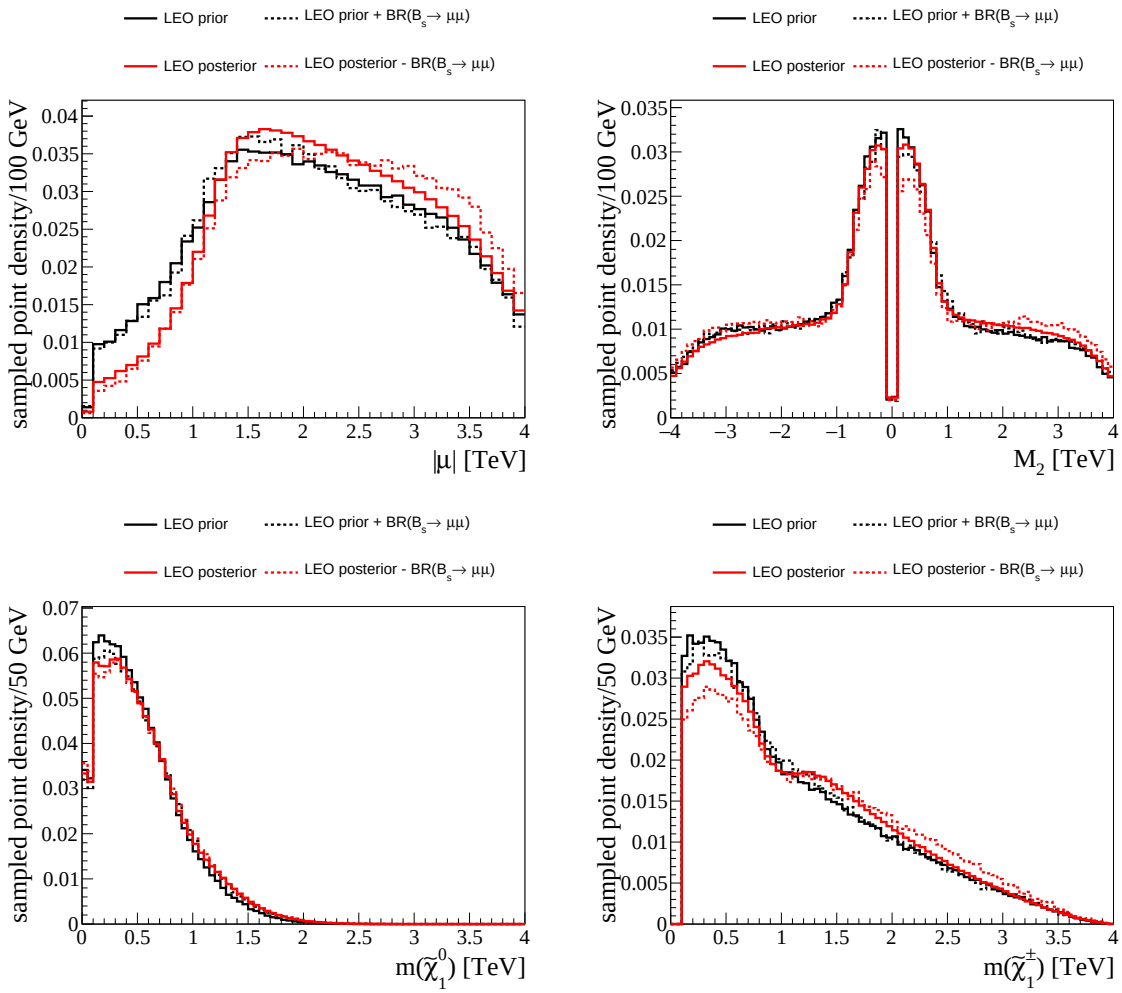

Figure 41: Distributions of the absolute value of the higgsino mass parameter $|\mu|$ (top left), the wino mass parameter M_2 (top right), as well as the masses of the lightest neutralino $m(\tilde{\chi}_1^0)$ (bottom left), and the lighter chargino $m(\tilde{\chi}_1^{\pm})$ (bottom right). The distributions are shown for the LEO prior (black), the LEO prior+BR($B_s \to \mu\mu$) (dashed black), the LEO posterior (red), and the LEO posterior-BR($B_s \to \mu\mu$) (dashed red).

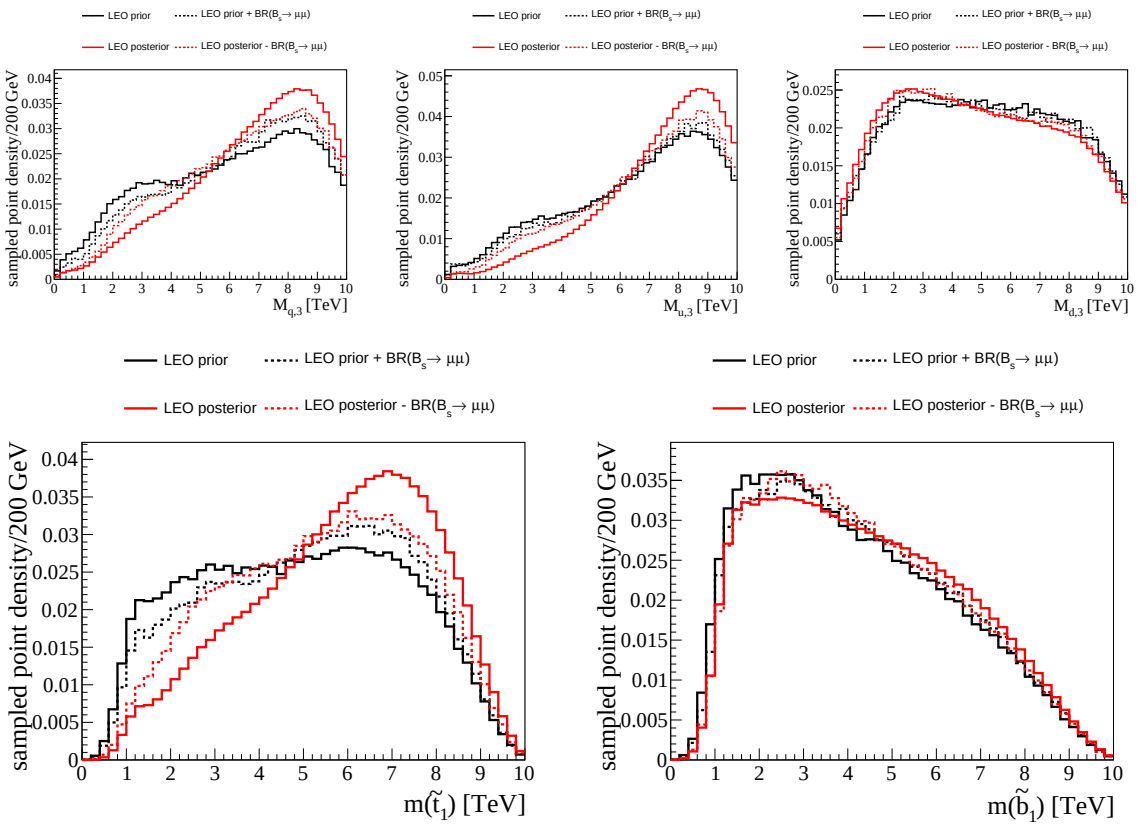

Figure 42: Distributions of the left-chiral third generation squark mass parameter $M_{q,3}$ (top left), the right-chiral stop mass parameter $M_{u,3}$ (top center), the right-chiral sbottom mass parameter $M_{d,3}$ (top right), as well as the mass of the lighter stop $m(\tilde{t}_1)$ (bottom left), and the mass of the lighter sbottom $m(\tilde{b}_1)$ (bottom right). The distributions are shown for the LEO prior (black), the LEO prior+BR($B_s \to \mu\mu$) (dashed black), the LEO posterior (red), and the LEO posterior-BR($B_s \to \mu\mu$) (dashed red).

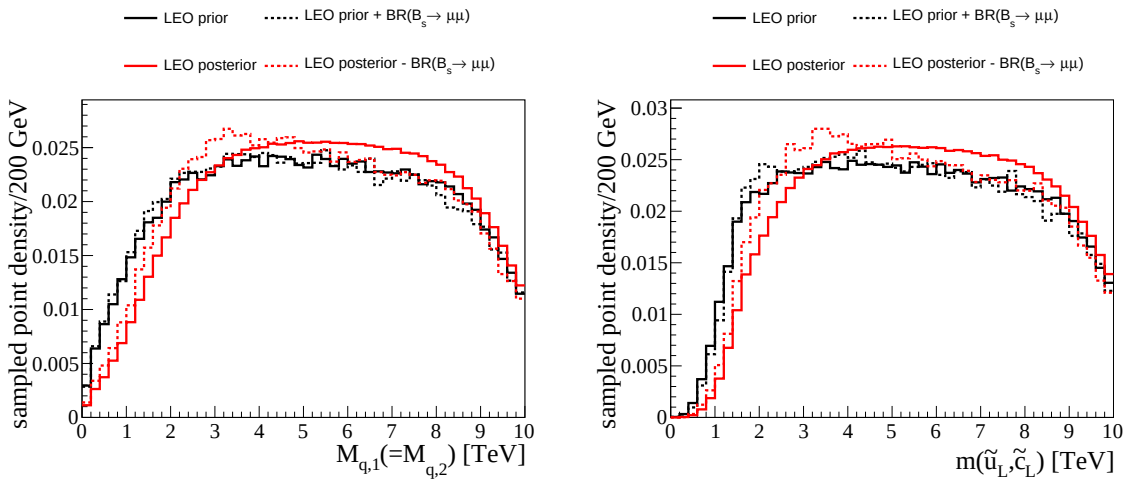

Figure 43: Distributions of the left-chiral first generation squark mass parameter $M_{q,1}$ (left) and the mass of the left-chiral sup $m(\tilde{u}_L, \tilde{c}_L)$ (right). The distributions are shown for the LEO prior (black), the LEO prior+BR($B_s \to \mu\mu$) (dashed black), the LEO posterior (red), and the LEO posterior-BR($B_s \to \mu\mu$) (dashed red). Note that the first two generations of sfermions are mass degenerate in the pMSSM, as well as the left-chiral up- and down-type squarks in the first two generations.

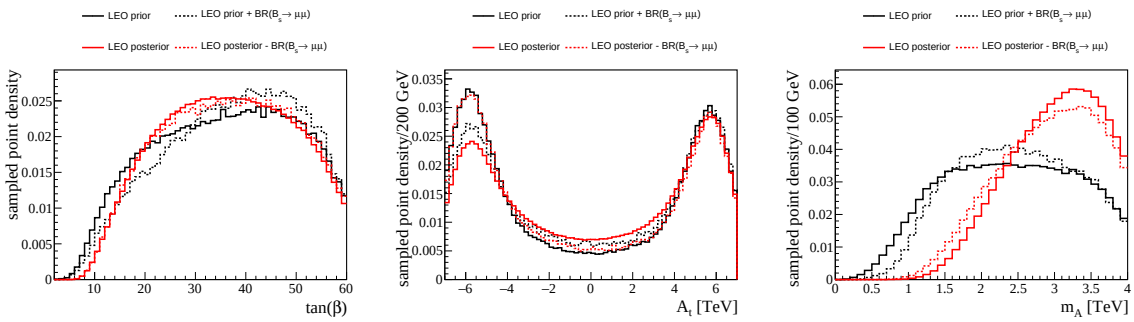

Figure 44: Distributions of the ratio of Higgs field vacuum expectation values $\tan(\beta)$ (left), the trilinear Higgs-stop coupling A_t (center), and the mass of the heavy Higgs bosons m_A (right). The distributions are shown for the LEO prior (black), the LEO prior+BR($B_s \to \mu\mu$) (dashed black), the LEO posterior (red), and the LEO posterior-BR($B_s \to \mu\mu$) (dashed red).

Lastly, the impact of BR($B_s \to \mu\mu$) on the Higgs sector is shown in Figure 44. The distribution of A_t is shifted towards smaller values, with large negative A_t more severely disfavored than large positive A_t. The fact that at large negative A_t, the distributions of LEO prior and LEO posterior-BR($B_s \to \mu\mu$) are almost identical suggests that BR($B_s \to \mu\mu$) is the dominant cause for the suppression of large negative A_t in the LEO posterior. The other contribution likely comes from the observable BR($B \to \tau\nu$), where we see a similar but weaker impact at large negative A_t (see Appendix C). In addition to the impact on A_t, the distribution of $\tan(\beta)$ is strongly shifted towards larger values in the LEO prior+BR($B_s \to \mu\mu$), compared to the LEO prior. However, there is almost no impact on the residual space of the LEO posterior-BR($B_s \to \mu\mu$). This comes from the fact that $\tan(\beta)$ is significantly shaped by multiple other observables, so that the additional impact of BR($B_s \to \mu\mu$) does not influence $\tan(\beta)$ significantly. Small masses of the heavy Higgs bosons m_A are somewhat suppressed by BR($B_s \to \mu\mu$), although the main contributions to its suppression in the LEO posterior come from other observables, as shown in Appendix C.

5.1.7.1 Remaining low-energy observables

A detailed study on the impact of the remaining LEO observables in the style of the two given examples for BR(b $\to$ sγ) and BR($B_s \to \mu\mu$) can be found in Appendix C. The most important impacts on the LEO posterior density are highlighted here.

Noticeably impacts occur in the electroweakino sector on the pMSSM parameters μ and M_2, which also results in shifts of the distributions of the masses of the neutralinos and charginos. Most importantly, small $m(\widetilde{\chi}_1^0)$, $m(\widetilde{\chi}_1^\pm)$, and $m(\widetilde{\chi}_2^0)$ are somewhat suppressed, with some observables contributing to a rise of the LEO posterior density at $|\mu| \simeq 1.5\,\text{TeV}$ and $m(\widetilde{\chi}_1^\pm) \simeq 1.5\,\text{TeV}$.

Noticeable impacts can also be seen in the squark mass parameters and squark masses, with small $m(\widetilde{t}_1)$ experiencing the most significant suppression, and the first generation and sbottom mass parameters and particle masses seeing only a slight suppression at small masses.

Finally, the Higgs related parameter $\tan(\beta)$ is shifted towards central values, with small $\tan(\beta)$ significantly disfavored in the LEO posterior. Large values of $|A_t|$ are disfavored, with large negative values disproportionally affected, resulting in a slightly asymmetric distribution favoring positive A_t in the posterior density. Small values of m_A are severely suppressed, with almost no posterior density remaining with $m_A \lesssim 1\,\text{TeV}$.

5.2 Summary and presentation of the low-energy posterior

To summarize the impact of the low-energy observables on the density of the considered pMSSM subspace, we examine marginalized 1D distributions for each pMSSM parameter and particle mass. The full LEO posterior is taken as the basis for the discussion of CMS and ALTAS searches and further phenomenological studies in the following sections, where, using iterative inference, it is considered the prior.

The extent of the low-energy observable impact on the marginalized 1-dimensional distributions varies, and can be identified in 3 categories:

1. Minimal impact, which includes:
   - the slepton mass parameters and the slepton masses, including the sneutrinos;
   - the bino- and wino- mass parameters M_1 and M_2;
   - the Higgs-sbottom and Higgs-stau trilinear couplings A_b and A_l.
2. Moderate impact, which includes:
   - the gluino mass parameter M_3 and the corresponding particle mass $m(\widetilde{g})$;
   - the right-chiral first generation squark mass parameters $M_{u,1}$ and $M_{d,1}$, and the corresponding right-chiral squark masses $m(\widetilde{u}_R, \widetilde{c}_R)$ and $m(\widetilde{d}_R, \widetilde{s}_R)$;
   - the right-chiral sbottom mass parameter $M_{d,3}$;
   - the neutralino masses $m(\widetilde{\chi}_1^0)$, $m(\widetilde{\chi}_2^0)$, $m(\widetilde{\chi}_3^0)$, and $m(\widetilde{\chi}_4^0)$;
   - the chargino masses $m(\widetilde{\chi}_1^\pm)$ and $m(\widetilde{\chi}_2^\pm)$;
   - the light scalar Higgs mass $m(h^0)$.
3. Strong impact on:
   - the first generation left-chiral squark mass parameter $M_{q,1}$and the corresponding physical masses $m(\widetilde{u}_L, \widetilde{c}_L)$ and $m(\widetilde{d}_L, \widetilde{s}_L)$;
   - the third generation squark mass parameters $M_{q,3}$, $M_{u,3}$, and $M_{d,3}$, as well as the stop masses $m(\widetilde{t}_1)$ and $m(\widetilde{t}_2)$, and the sbottom masses $m(\widetilde{b}_1)$ and $m(\widetilde{b}_2)$;
   - the ratio of the Higgs vacuum expectation values $\tan(\beta)$;
   - The pseudoscalar Higgs mass parameter m_A, and the corresponding heavy Higgs boson masses $m(H^0)$, $m(A^0)$, and $m(H^\pm)$;
   - the stop-Higgs trilinear coupling A_t;
   - the higgsino mass parameter μ and its absolute value $|\mu|$.

In the following, the impact is given in detail by particle class, beginning with the electroweak parameters, and proceeding with the colored sector.

5.2.0.1 Electroweakinos

The summary of the electroweakino sector is shown in Figure 45, which features the distributions of the electroweakino parameters for the LEO prior and posterior densities, as well as the distributions for the subspaces of the pMSSM that feature a pure LSP type. Pure in this context means that the square of the respective $\widetilde{\chi}_1^0$ mixing matrix entry exceeds 0.95. We can see that the LEO prior already features a severely suppressed distribution of $|\mu|$ at small masses. This is mostly due to the occurrence of tachyons at small $|\mu|$, as discussed in detail in Section 5.1.2 and Appendix B. The small $|\mu|$ region is further suppressed by the inclusion of the LEO observables, and enhanced at $|\mu| \simeq 2\,\text{TeV}$. As a consequence, the fraction of models with a higgsino-like LSP is very small in the LEO posterior, compared to models with a bino-like or wino-like LSP.

The distributions of M_1 and M_2 show a strong peak at small values, which is a consequence of the requirement that the lightest neutralino is the LSP. This requirement necessitates that at least one of $|\mu|$, $|M_1|$, or $|M_2|$ is small. An upward shift of the probability density is not seen for $|\mu|$ due to the suppression of small values caused by a frequent occurrence of tachyons.

In terms of the physical masses, the general distributions peak at very small masses near the lower bound of $m = 0\,\text{TeV}$ for $m(\widetilde{\chi}_1^0)$ and $m(\widetilde{\chi}_1^\pm)$, distributions peaking at very large masses near the upper bound of $m = 4\,\text{TeV}$ for $m(\widetilde{\chi}_4^0)$ and $m(\widetilde{\chi}_2^\pm)$, and peaking distributions close to the middle of the allowed mass range for $m(\widetilde{\chi}_2^0)$ and $m(\widetilde{\chi}_3^0)$. These general shapes are the consequence of the mass ordering of the particle states and are not driven by the experimental likelihoods. The region of $m(\widetilde{\chi}_1^0) \lesssim 100\,\text{GeV}$ has a significantly lowered probability density due to the constraints from LEP, which exclude charginos with $m(\widetilde{\chi}_1^\pm) \lesssim 100\,\text{GeV}$. As a consequence, only models with a bino-like LSP populate that part of the density. The sudden doubling of the probability density is the result of the sudden viability of models with a higgsino-like or wino-like LSP above the LEP exclusion threshold. The impact of the LEO observables results in a flat region between $m(\widetilde{\chi}_1^0) \gtrsim 100\,\text{GeV}$ and $m(\widetilde{\chi}_1^0) \lesssim 500\,\text{GeV}$, due to the suppression of small-mass higgsino-like models precipitated by the suppression of small $|\mu|$. The suppression of small $m(\widetilde{\chi}_1^0)$ results in a slightly enhanced tail at larger $m(\widetilde{\chi}_1^0)$ due to the normalization of the posterior density to one.

The suppression of small $|\mu|$ has the same effect on the distribution of the lighter chargino mass $m(\widetilde{\chi}_1^\pm)$. The shifting of the $|\mu|$ distribution to peak at $|\mu| \simeq 1.5\,\text{TeV}$ in the LEO posterior results in a bump in $m(\widetilde{\chi}_1^\pm)$ in the same mass range. These models predominately feature a bino-like LSP. The other electroweakino mass distributions experience a general suppression of small masses due to the suppression of models with a higgsino-like LSP, which shifts the distribution towards larger masses. The effects diminish for the heavier of the mass states, with almost no effect visible for the distribution of $m(\widetilde{\chi}_4^0)$. Their general shape is not significantly impacted in the LEO posterior.

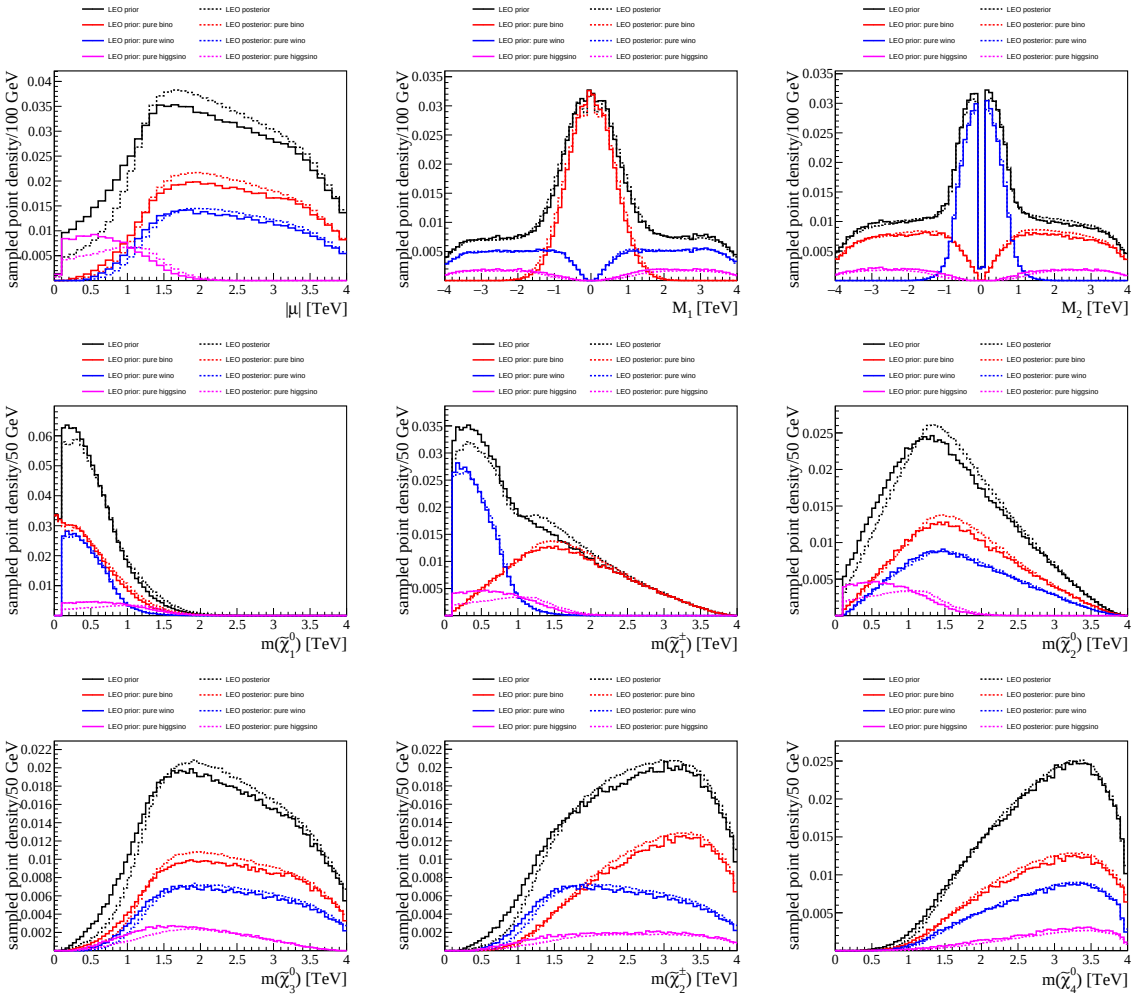

Figure 45: Summary of the LEO prior and posterior for the electroweakino sector, consisting of the absolute value of the higgsino mass parameter $|\mu|$ (top row, left column), the bino mass parameter M_1 (top row, center column), the wino mass parameter M_2 (top row, right column), as well as the masses of the lightest neutralino $m(\widetilde{\chi}_1^0)$ (center row, left column) and lighter chargino $m(\widetilde{\chi}_1^\pm)$ (center row, center column), the masses of the second lightest neutralino $m(\widetilde{\chi}_2^0)$ (center row, right column) and third lightest neutralino $m(\widetilde{\chi}_3^0)$ (bottom row, left column), and the masses of the heavier chargino $m(\widetilde{\chi}_2^\pm)$ (bottom row, center column) and the heaviest neutralino $m(\widetilde{\chi}_4^0)$ (bottom row, right column). The inclusive distributions are shown, as well as the distributions for the subset of models with pure LSP types. Pure in this context means that the square of the respective $\widetilde{\chi}_1^0$ mixing matrix entry exceeds 0.95.

Figure 46 shows the distribution of $m(\widetilde{\chi}_1^0)$ for the lightest neutralino for the subset of the LEO prior and posterior where the LSP is of mixed type. Mixed here refers to models where none of the $\widetilde{\chi}_1^0$ mixing matrix entries exceeds 0.95. Notice first that mixed LSP states are rare in the pMSSM. This is because significant admixture of more than one type requires that the mass hierarchy between the respective pMSSM parameters μ, M_1, and M_2 is small. Because these parameters are independently sampled, and there are no strong constraints from any of the included observables that prefer a mixed LSP type, the probability density is small in the part of the pMSSM where at least two of μ, M_1, and M_2 are close in mass. In terms of the impact of the low-energy observables, all models with a mixed LSP type are suppressed at small masses.

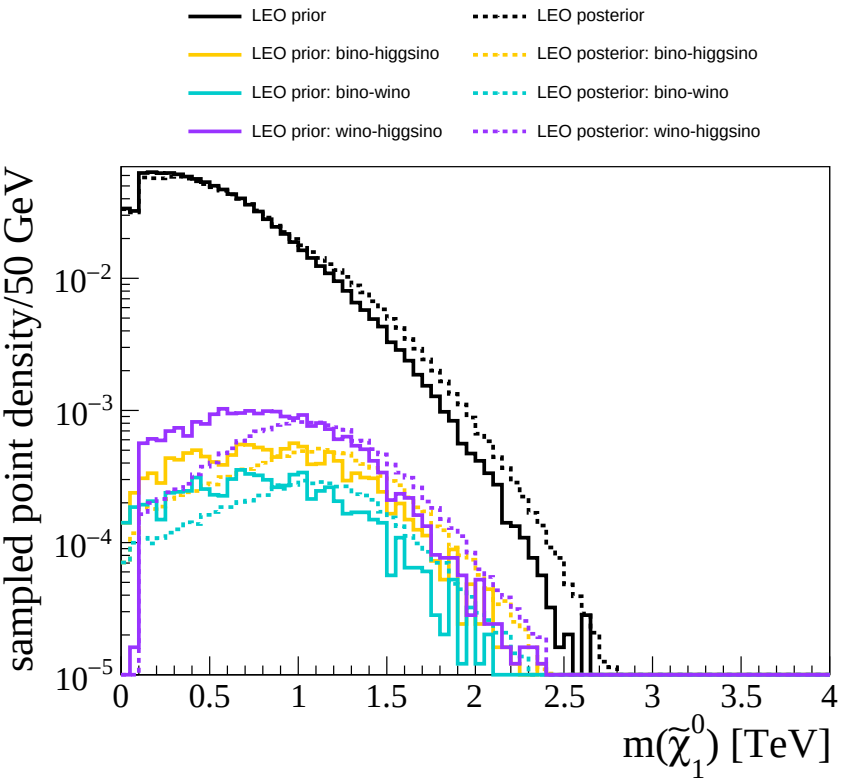

Figure 46: Summary of the LEO prior and posterior for the mass of the lightest neutralino $m(\widetilde{\chi}_1^0)$, for the inclusive pMSSM, and the subset of models with a mixed LSP type. The mixed states require that no square of the $\widetilde{\chi}_1^0$ mixing matrix entries exceeds 0.95, and the squares of the named LSP types are the two largest contributors.

5.2.0.2 Sleptons

The slepton sector, shown in Figure 47, is the least impacted sector of the pMSSM. All the slepton mass parameters and slepton masses are suppressed at small masses, due to effects of algorithm shaping, model-inherent constraints, and the requirement that $\widetilde{\chi}_1^0$ be the LSP. The suppression at large masses is caused almost exclusively by the McMC algorithm suppression near the upper boundary on the parameter. None of the low-energy observables, individually or in their combination, significantly constrain or shape the slepton sector.

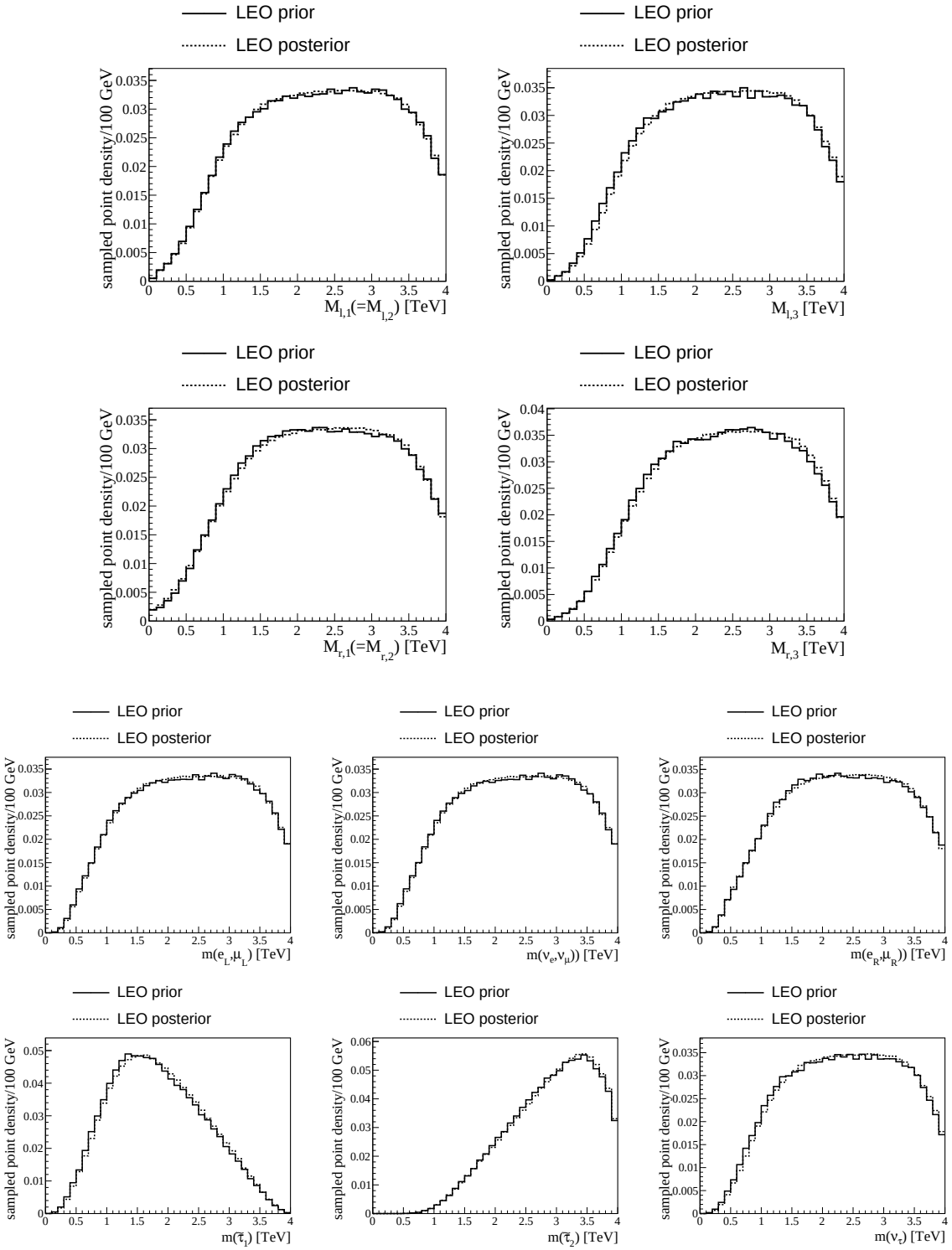

Figure 47: Summary of the LEO prior and posterior for the slepton sector, consisting of the left-chiral first (top row, left column) and third (top row, right column) generation slepton mass parameters $M_{l,1}$ and $M_{l,3}$, the right-chiral first (second row from top, left column) and third (second row from top, right column) generation slepton mass parameters $M_{r,1}$ and $M_{r,3}$, as well as the physical masses of the left-chiral selectron (smuon) $\widetilde{e}_L(\widetilde{\mu}_L)$ (second row from bottom, left column), the electron (smuon) sneutrino $\widetilde{\nu}_e(\widetilde{\nu}_\mu)$ (second row from bottom, center column), the right-chiral selectron (muon) $\widetilde{e}_R(\widetilde{\mu}_R)$ (second row from bottom, right column), the lighter stau $\widetilde{\tau}_1$ (bottom row, left column), the heavier stau $\widetilde{\tau}_2$ (bottom row, center column), and the tau sneutrino $\widetilde{\nu}_\tau$ (bottom row, right column).

5.2.0.3 Colored sector

Figure 48 shows the gluino mass $m(\widetilde{g})$ and mass parameter M_3. The LEO prior is heavily shaped by model-inherent constraints, which disfavor small and large gluino masses. These constraints also correlate the medium mass M_3 region to small values of $|\mu|$. For this reason, the marginalized LEO prior peaks at approximately $m(\widetilde{g}) \simeq 4\,\text{TeV}$. The impact of the LEO observables suppresses that peak due to its correlation to small $|\mu|$. The impact on the first generation squarks is summarized in

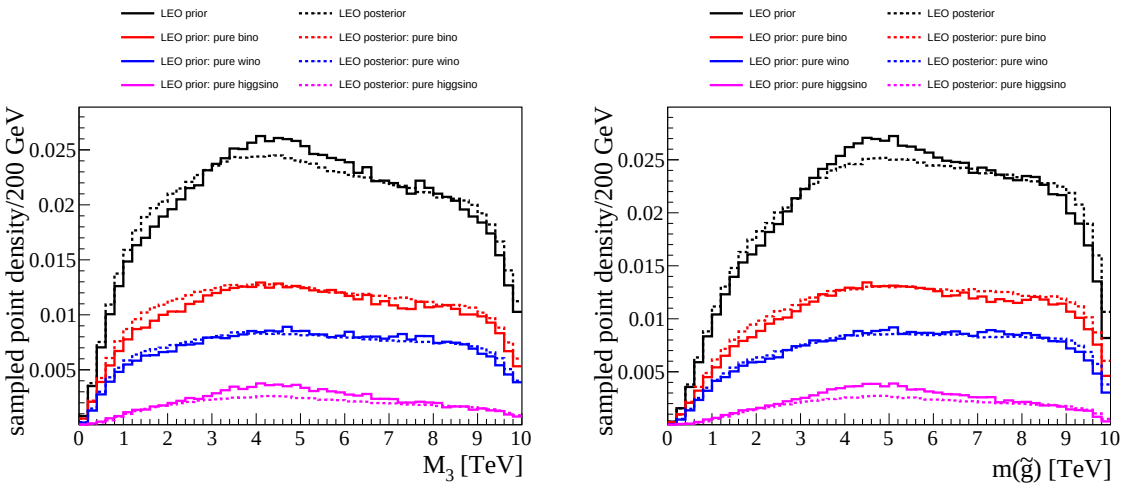

Figure 48: Summary of the LEO prior and posterior for the gluino sector, consisting of the gluino mass parameter M_3 (left), and the gluino mass $m(\widetilde{g})$ (right). The distributions are shown for the models with pure LSP types, as well as the inclusive distribution. Pure in this context means that the square of the respective $\widetilde{\chi}_1^0$ mixing matrix entry exceeds 0.95.

Figure 49. In general, the small-mass region is severely disfavored due to model-inherent constraints, with smaller contributions to the suppression due to the requirement that the LSP is the lightest neutralino $\widetilde{\chi}_1^0$, and the McMC algorithmic shaping. For large masses, near the edge of the allowed parameter range, the McMC algorithm is responsible for the drop in probability density.

The LEO observables have little effect on either the right-chiral mass parameters $M_{u,1}$ and $M_{d,1}$, or the particle masses $m(\widetilde{u}_R, \widetilde{c}_R)$ and $m(\widetilde{d}_R, \widetilde{s}_R)$, aside from a small increase of the posterior density at masses below approximately $m \lesssim 1.5\,\text{TeV}$. The impact on the left-chiral mass parameter $M_{q,1}$ is significantly larger, with the small $M_{q,1}$ region significantly suppressed. These features are also visible, to the same degree, in the distributions of the particle masses.

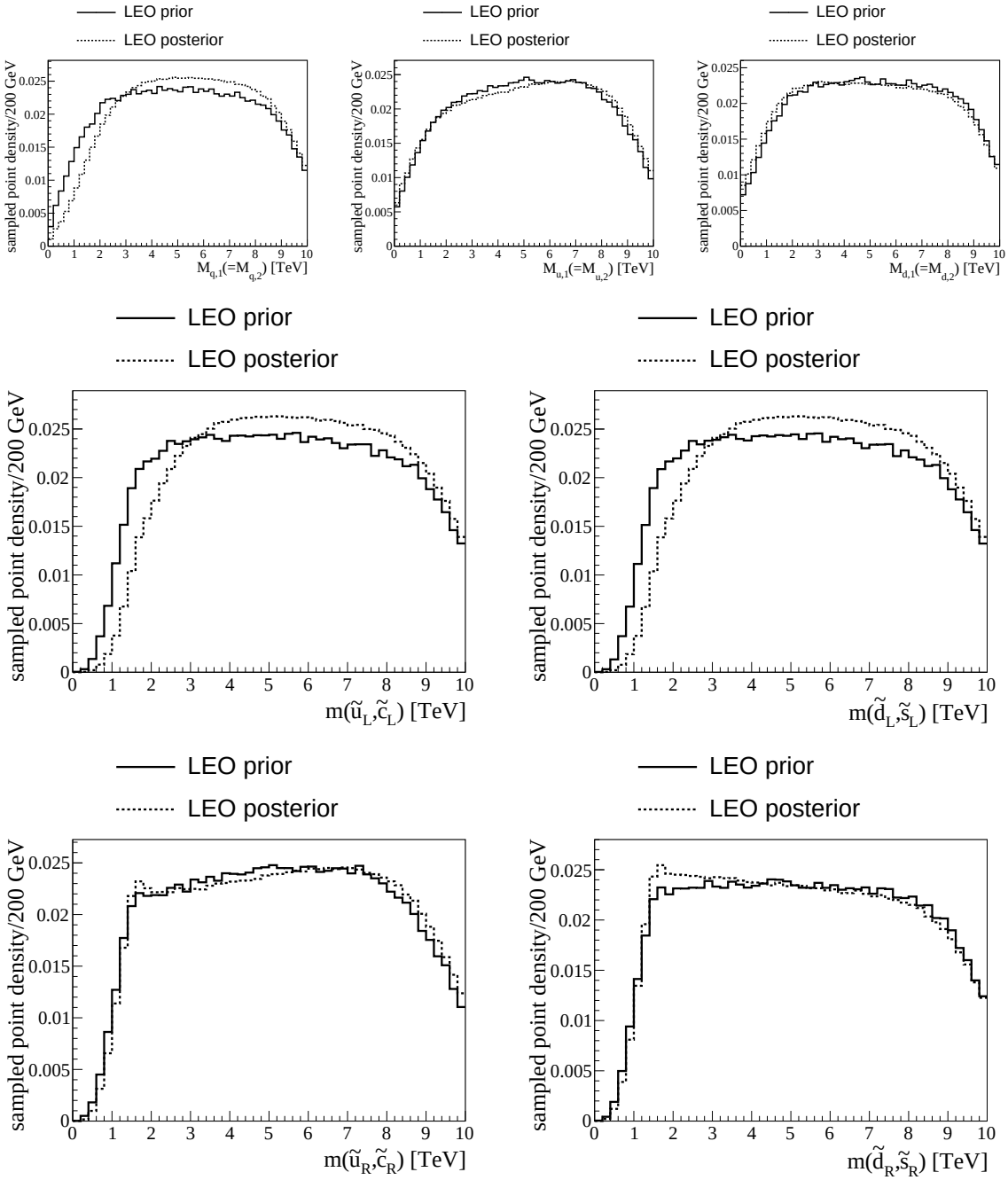

Figure 49: Summary of the LEO prior and posterior for the first generation squark sector, consisting of the left-chiral first generation squark mass parameters $M_{q,1}$ (top row, left column), the right-chiral sup mass parameter $M_{u,1}$ (top row, center column), the right-chiral sdown mass parameter $M_{d,1}$ (top row, right column), as well as the masses of the left-chiral sup $m(\tilde{u}_L, \tilde{c}_L)$ (center row, left column), the left-chiral sdown $m(\tilde{d}_L, \tilde{s}_L)$ (center row, right column), and the masses of the right-chiral sup $m(\tilde{u}_R, \tilde{c}_R)$ (bottom row, left column), and the right-chiral sdown $m(\tilde{d}_R, \tilde{s}_R)$ (bottom row, right column).

Figure 50 summarizes the impact on the third-generation squark sector. Small masses for the left-chiral mass parameter $M_{q,3}$ and the right-chiral stop mass parameter $M_{u,3}$ are already severely disfavored in the LEO prior. This is largely due to model-inherent constraints connected to Q_{SUSY}, which is correlated to these two parameters via its definition as their geometric mean. The LSP requirement and effects from the McMC algorithm only play a minor role in the suppression of small $M_{q,3}$ and $M_{u,3}$. As already seen for the gluino, there are correlations to the type of LSP present in the LEO prior. This correlation is generated by the significant suppression of the region of small $|\mu|$ and large Q_{SUSY} due to the occurrence of tachyons, discussed in Section 5.1.2 and Appendix B. As a consequence, small values of $M_{q,3}$ and $M_{u,3}$ are correlated to small values of $|\mu|$. The sbottom mass parameter is impacted to a much smaller degree by model-inherent constraints. The suppression at small $M_{d,3}$ is here generated in approximately equal measure by model-inherent constraints, the LSP requirement, and the McMC algorithm. The suppression at large $M_{d,3}$ is mostly caused by the McMC algorithm. In terms of the physical masses, the distributions of the lighter stop and sbottom masses show a much sharper drop in the probability density compared to their respective pMSSM parameters.

The LEO posterior is strongly suppressed at small masses for $M_{q,3}$, $M_{u,3}$, and the stop masses $m(\widetilde{t}_1)$ and $m(\widetilde{t}_2)$, compared to the LEO prior. This suppression is largely independent of the LSP type for the stop sector and affects small stop masses in approximately equal proportion for the different LSP types. This is different from what is seen for the sbottom masses. First, the small-mass region of $M_{d,3}$ is enhanced in the LEO posterior, compared to the LEO prior. The small-mass region for the physical sbottom masses is suppressed, as the suppression of $M_{q,3}$ overwhelms the enhancement given by $M_{d,3}$. However, we see a dependence on the type of LSP in this suppression. Whereas the distributions, between the LEO posterior and the LEO prior, for pure binos and pure winos are largely the same at small $m(\widetilde{b}_1)$, the LEO posterior for higgsino-like LSPs is strongly suppressed. The enhancement seen in $M_{d,3}$ is thus likely a consequence of the suppression of small $|\mu|$.

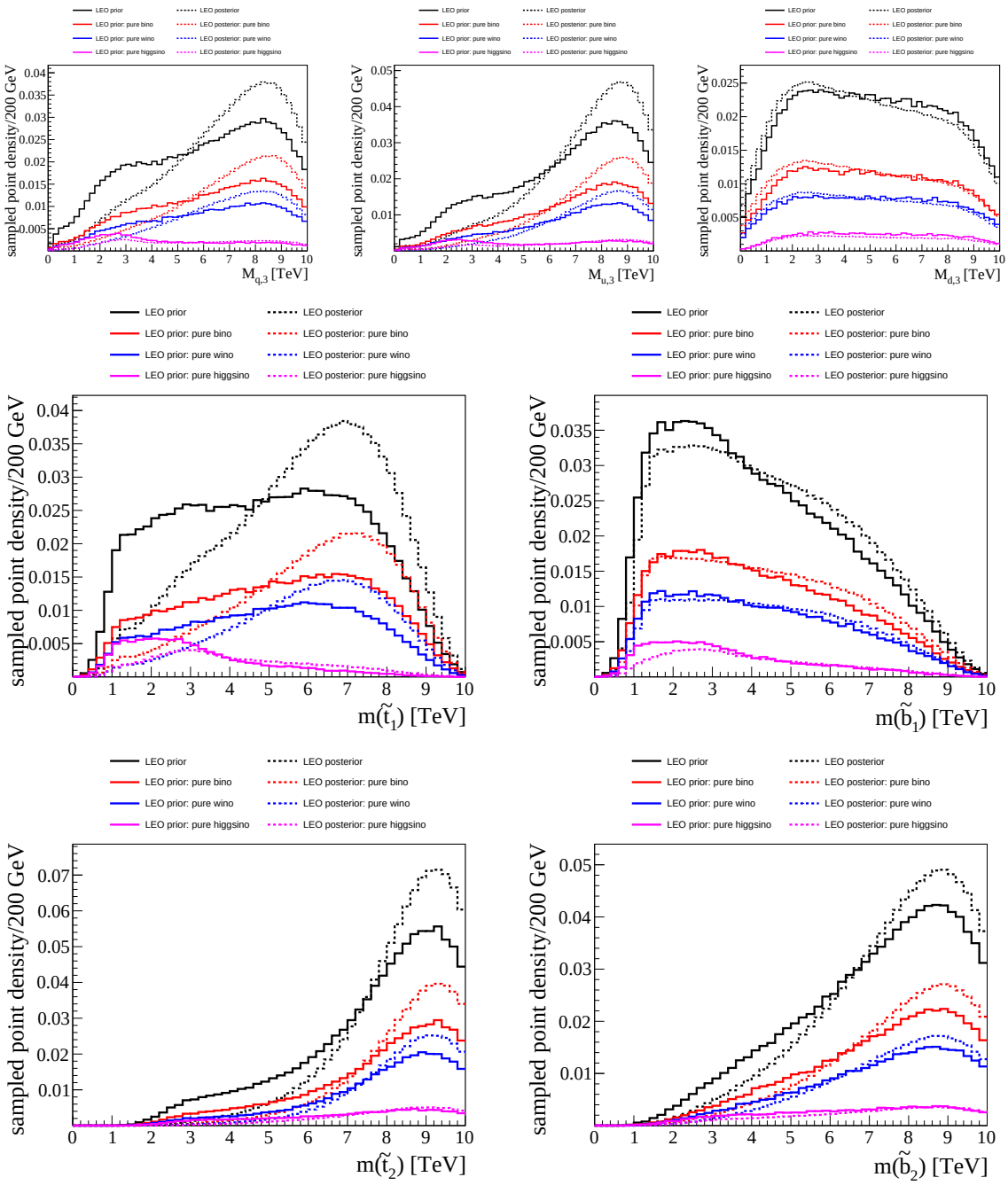

Figure 50: Summary of the LEO prior and posterior for the third generation squark sector, consisting of the left-chiral third generation squark mass parameters $M_{q,3}$ (top row, left column), the right-chiral stop mass parameter $M_{u,3}$ (top row, center column), the right-chiral sbottom mass parameter $M_{d,3}$ (top row, right column), as well as the masses of the lighter stop $m(\tilde{t}_1)$ (center row, left column), the lighter sbottom $m(\tilde{b}_1)$ (center row, right column), and the masses of the heavier stop $m(\tilde{t}_2)$ (bottom row, left column), and the heavier sbottom $m(\tilde{b}_2)$ (bottom row, right column).

5.2.0.4 Higgs sector

Finally, we summarize the Higgs sector, which consists of the third generation trilinear Higgs-sfermion couplings A_t, A_b, and A_l, the ratio of the Higgs field vacuum expectation values $\tan(\beta)$, and the pseudoscalar Higgs mass parameter m_A, as well as the physical heavy Higgs masses A^0,H^0, and $H^\pm$.

Figure 51 summarizes the impact of the LEO observables on the trilinear couplings. First, we can see that the trilinear Higgs-stau coupling A_l follows a simple distribution that only deviates from the flat prior towards the edges of the parameter space, due to shaping by the McMC algorithm. This implies that the data used for the prior do not constraint A_l. For A_b, the model-inherent constraints slightly reduce the probability density at small $|A_b|$, in addition to the algorithmic suppression at large $|A_b|$. In contrast, the distribution of A_t severely differs from the flat ur-prior. Due to radiative corrections, small $|A_t|$ are severely suppressed by the requirement of the light Higgs boson mass to be compatible with the measured mass at $m(h^0) \simeq 125\,\text{GeV}$. The probability density of the LEO prior and posterior drop towards the edges of the allowed range due to suppression by the McMC algorithm.

The LEO observables do not impact A_b and A_l, but do significantly shape A_t. Large positive and negative A_t are disfavored to the benefit of small $|A_t|$, with the negative A_t region more strongly suppressed. As a result, the A_t distribution is asymmetric in the LEO posterior, with positive A_t favored over negative A_t.

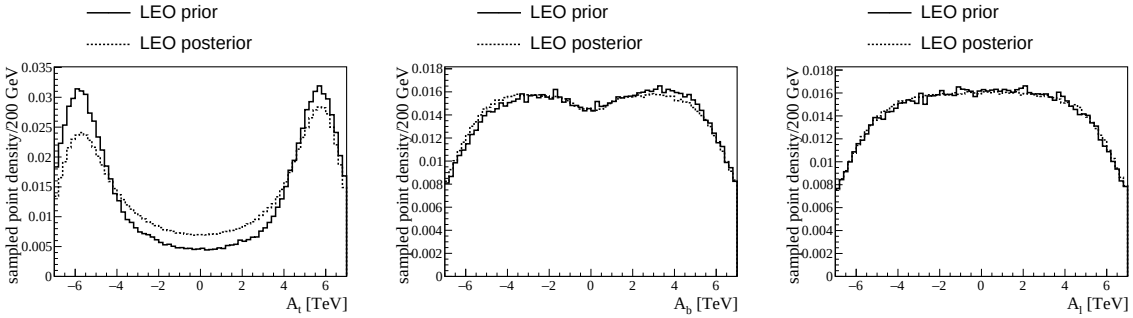

Figure 51: Summary of the LEO prior and posterior for the trilinear Higgs-sfermion couplings, consisting of the trilinear Higgs-stop coupling A_t (left), the trilinear Higgs-sbottom coupling A_b (center), and the trilinear Higgs-stau coupling A_l (right).

Figure 52 shows the marginalized distribution in $\tan(\beta)$ for the LEO prior and posterior. The LEO prior already strongly deviates from the flat ur-prior in that it is highly suppressed at small $\tan(\beta)$, and also somewhat suppressed at large $\tan(\beta)$. The suppression at small $\tan(\beta)$ is almost entirely due to the Higgs mass constraint, which requires large radiative contributions that favor large $\tan(\beta)$. The suppression at large $\tan(\beta)$ is due to model-inherent constraints and the McMC algorithm shaping.

The LEO observables further disfavor small values of $\tan(\beta)$, and somewhat disfavor large $\tan(\beta)$, which results in a softly peaking distribution around $\tan(\beta) \simeq 35$. The last remaining parameters are the mass parameter for the pseudoscalar Higgs boson m_A, and the heavy Higgs boson masses, which are shown in Figure 53. It is first noted that the distributions are indistinguishable, which is the reason why they are used interchangeably throughout this thesis. The LEO prior is already suppressed at small m_A, mostly due to model-inherent constraints and the LSP requirement (which is mistakenly applied to m_A). The prior density falls off towards large m_A due to the McMC algorithm suppression.

The LEO observables further strongly suppress the small m_A region, which results in almost no probability density of the LEO posterior at $m_A \lesssim 1\,\text{TeV}$. Because of this strong suppression, the requirement that $m(\tilde{\chi}_1^0) < m_A$ is of very little consequence for the LEO posterior.

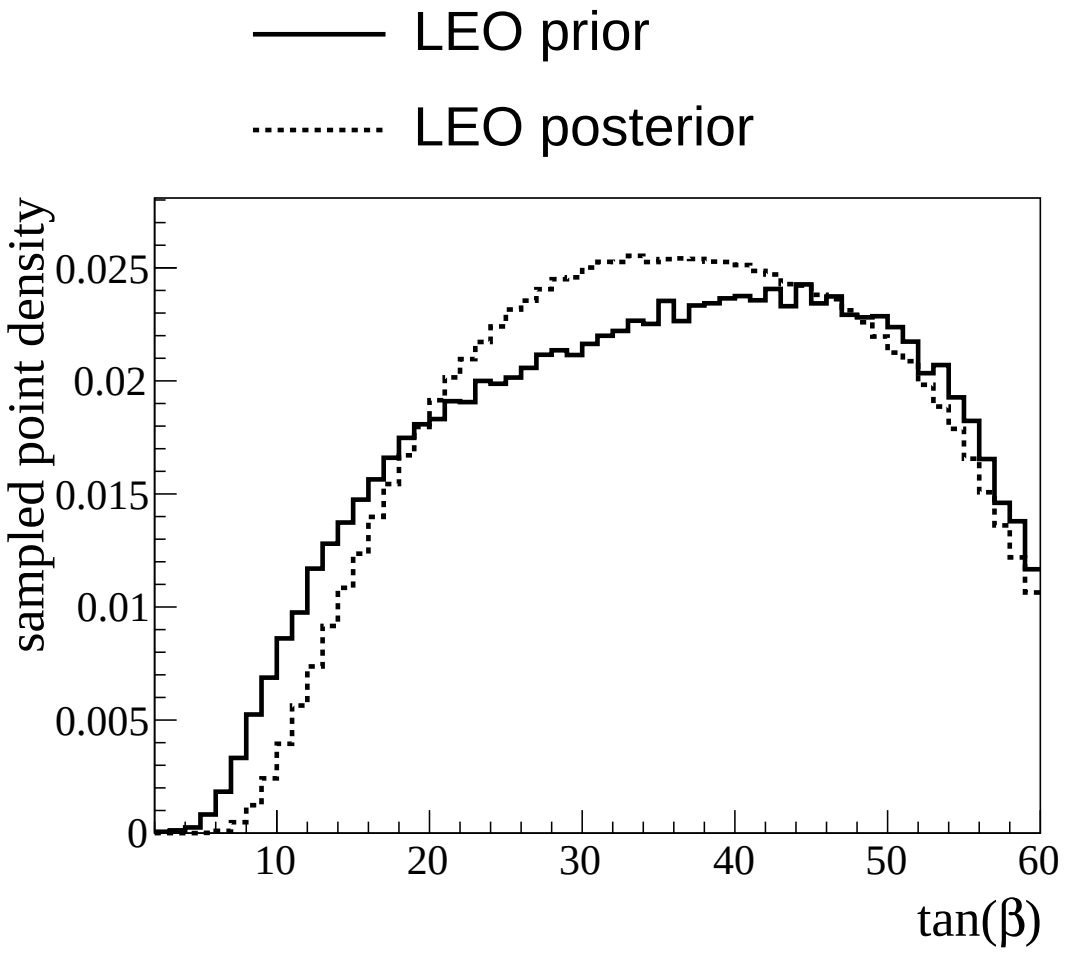

Figure 52: Summary of the LEO prior and posterior for the ratio of the Higgs field vacuum expectation values $\tan(\beta)$.

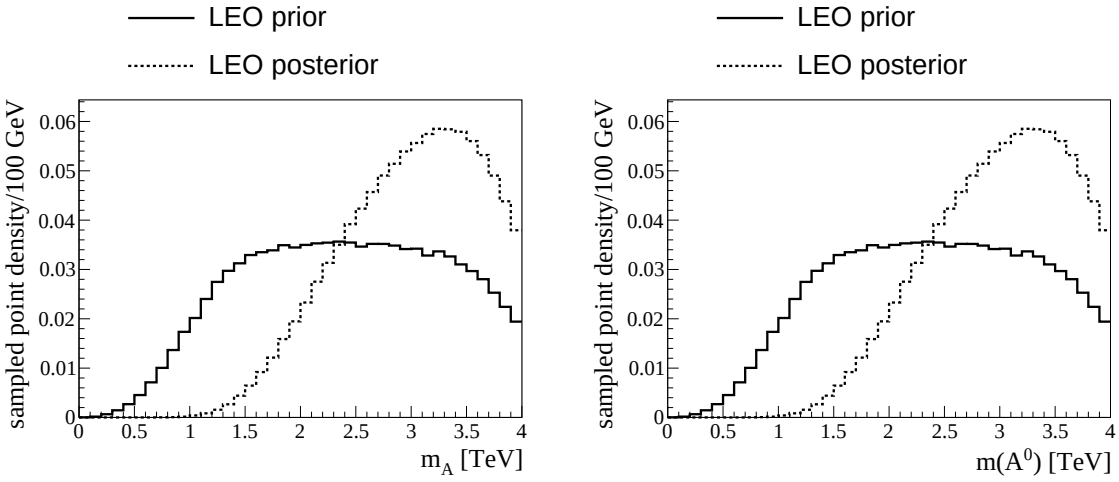

Figure 53: Summary of the LEO prior and posterior for the mass parameter of the pseudoscalar Higgs boson m_A (left), and the mass of the physical heavy Higgs bosons, represented here by $m(A^0)$ (right). The distributions for $m(H^0)$ and $m(H^\pm)$ are indistinguishable from that of $m(A^0)$.

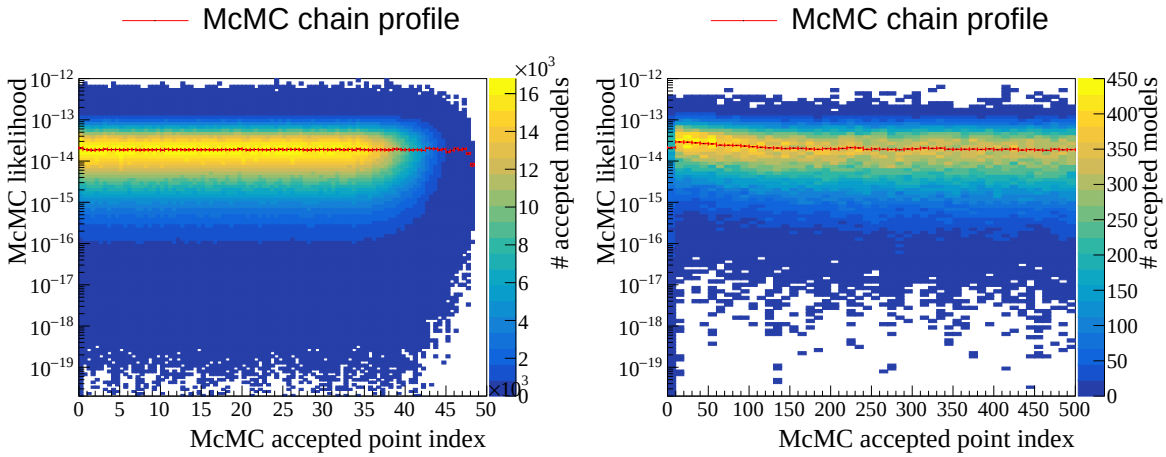

Figure 54: Time series of the McMC likelihood value of all 597 Markov chains, and their profile, which shows the binned mean and standard deviation for the different chains. The time series is binned in terms of the number of accepted Markov chain elements, with the z-axis giving the same number for a given bin. The left plot shows the full time series, the right plot is zoomed in to the first 500 accepted points.

5.3 McMC convergence

In order to consider the density of points in the pMSSM scan to be an unbiased discrete representation of the posterior density, the McMC has to have converged. However, convergence of an McMC is not a binary matter – a non-converged McMC is still an approximation of the posterior density, but one that is biased towards the prior. The approximation becomes better the closer the McMC is to convergence.

5.3.1 Burn-in

Because the initial points in each Markov chain are sampled from the ur-prior instead of the LEO posterior, the initial distribution of points will be strongly biased towards the ur-prior. In order to minimize this bias, the first couple of hundred or thousand accepted points in each Markov chain should be discarded. To determine a number to remove, we study Figure 54, which shows the time series of the McMC likelihood for all 597 Markov chains, as well as their mean and standard deviation, we can see that the likelihood normalizes after a couple of hundred iterations. After this period, we consider the Markov chains burned in. To allow a safe margin for error, we remove the first 1,000 points from each individual Markov chain.

5.3.2 Rubin-Gelman heuristic

The Rubin-Gelman heuristic is a measure of the potential scale reduction of an ensemble of independent Markov chains. In such an ensemble, it compares the variance of the in-chain means of the Markov chains against the mean of the in-chain variances of the Markov chains. In a converged Markov chain Monte Carlo, the measure, defined as [120]

$$\hat{R} = \sqrt{\frac{\hat{\sigma}^2}{s^2}}, \tag{15}$$

converges to one. In the above equation, s^2 is the ensemble mean of the m in-chain variances, and $\hat{\sigma}^2 = \frac{n-1}{n} * s^2 + \frac{B}{n}$, with the number of considered Markov chain entries per chain n, and the variance of the Markov chain means, B. In this study, we compute time series of the Rubin-Gelman heuristic for cumulative slices i of $i * 1000$ consecutive accepted points per chain for each of the 19 pMSSM parameters, and each of the physical particle masses. Figure 55 shows summary distributions including all the above-mentioned parameters, grouped in terms of the nature of the

parameters. In all of the studied time series, $\hat{R}$ quickly drops towards one, with the higgsino mass parameter μ converging the slowest, reaching the critical value of $\hat{R} < 1.1$ after approximately 5,000 accepted points. The reason for this slower convergence is the bi-modal posterior density in μ, with an extended region of small likelihood in a wide region around $\mu = 0$. Since both the likelihood and RG-heuristic time series show the expected behavior, we cautiously conclude that the McMC has converged.

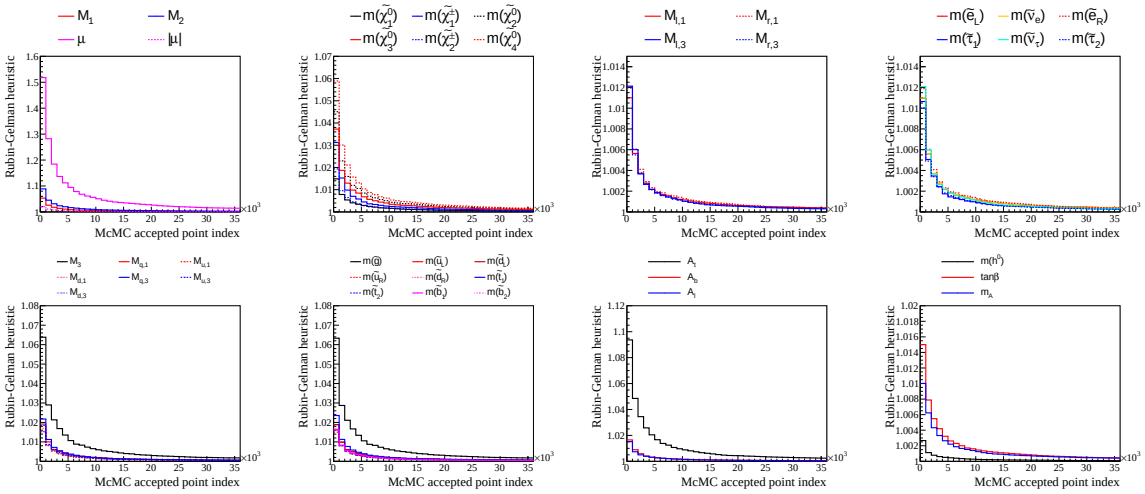

Figure 55: Summary time series of the Rubin-Gelman heuristic $\hat{R}$ for the electroweakino mass parameters (top row, left column), the physical electroweakino masses (top row, second from left column), the slepton mass parameters (top row, second from right column) and physical masses (top row, right column), as well as the colored mass parameters (bottom row, left column) and physical masses (bottom row, second from left column), and the trilinear Higgs couplings (bottom row, second from right column) and remaining Higgs parameters (bottom row, right column).

5.4 Known biases of the prior

Let us briefly summarize the biases of the pMSSM scan that have been identified, which will result in deviations from what we might consider the true posterior density.

Reduced posterior density of small-mA parameter space
Because of an error in the McMC setup, the parameter space where the heavy Higgs bosons are lighter than the LSP has not been sampled. This potentially shifts the mass of the heavy Higgs bosons towards larger values. The bias from this mistake is likely very small in the posterior density, as both the model-inherent constraints and the LEO observables included in the McMC disfavor light heavy Higgs bosons to an extreme degree. Thus, the pMSSM model space where the heavy Higgs bosons are lighter than the lightest neutralino would have been heavily suppressed by the McMC likelihood anyway, whether the ur-prior was flat in m_A or biased by this error.

Wino/Higgsino chargino-neutralino mass differences
The mass differences of pure winos and Higgsinos are in some cases not correctly calculated in `SPheno` 4.0.4 (and, as far as the author is aware, in any spectrum generator as of the time of writing of this work). This frequently leads to overly compressed mass spectra, with mass splittings of $\Delta m(\widetilde{\chi}_1^{\pm}, \widetilde{\chi}_1^0)$ below the pion mass, which drastically increases their lifetime to meters (or even kilometers). This means that those points need to be interpreted with care when discussing absolute point densities. Analyses can be sensitive to long-lived charginos either directly in the form of searches for disappearing tracks or heavy stable charged particles (HSCP), or indirectly, for example by vetoes on events containing muons, because detector-stable charginos are reconstructed as muons. The best way to interpret results to avoid a bias is to include $c\tau(\widetilde{\chi}_1^{\pm})$ or $\Delta m(\widetilde{\chi}_1^{\pm}, \widetilde{\chi}_1^0)$ as one of the axis variables, such that the bias is completely contained to a region of the plot.

Parameter edge suppression by McMC algorithm
Because the parameter values of new candidate pMSSM points are re-sampled from the last accepted value in the Markov chain until they are within the allowed parameter range, there is an asymmetry built into the algorithm that causes the Markov chain to prefer moving away from the edges of the allowed parameter space. This asymmetry in the probability of the step direction is given, for each point, by integrating each side of the Gaussian from which a new parameter value is sampled to the edges of the allowed parameter space. Normalizing each individual side to the integral of the Gaussian over the whole allowed range gives the respective probabilities to step in each direction. Some attempts to find an analytical weight for each value that corrects for the effects have been tried unsuccessfully. It may be possible to fit a function to the non-flat distribution of points in a 19 dimensional toy model, and use it on the pMSSM to correct for this effect. An alternative to the fit could be to train a neural network to model the weights.

It is possible to avoid this feature of the algorithm by modifying the McMC algorithm behavior at the edges. An example of this is discussed in Appendix A.

No solution has been applied to the final scan, which means that the posterior density is biased from this effect that results in a reduced density at the edges of the allowed parameter range.

Restricted coverage of A_t
The LEO posterior distribution of A_t peaks towards large values of $|A_t|$, and only falls in density towards the edges of the allowed parameter range due to the McMC algorithm effect. This behavior suggests that the McMC would sample more efficiently for $|A_t| > 7\,\text{TeV}$, and that this region of the pMSSM with $|A_t| > 7\,\text{TeV}$ is phenomenologically relevant to the LEO observables. The large $|A_t|$ region and the implications of its absence in this scan should be covered in future studies.

6 Including the LHC data

This sections concern various extra steps that are performed before the LHC data can be evaluated. These steps include the creation of a smaller, representative, sub-sample of the pMSSM scan present at the end of Section 5. This section also details the signal event simulation and their subsequent evaluation by the included analyses through one of two pipes. The first pipe makes use of the re-casting tool `MadAnalysis5` [121, 122, 123, 124] to model the detector response and get signal region counts for three of the included analyses. The second pipe makes use of a CMS-internal workflow, where the detector response is simulated using the CMS fast simulation package, and respective analysis groups process the signal events to the necessary inputs for the creation of the LHC likelihood. This section concludes with a short description of the included LHC analyses.

6.1 Variable sampling of subset for LHC results

Before incorporating the LHC results on the pMSSM, a subset of points is sampled from the pMSSM scan. This is mainly done because there is not enough computing power available to create Monte Carlo events for all 27 million pMSSM points sampled in the previous step. It is thus necessary to focus on a much smaller set of models that is then taken to represent the entire scan. To counteract the inevitable smaller resolution in particularly interesting regions of the pMSSM, the sampling rate for this subset is varied according to certain particularly interesting phenomenological characteristics of the models. This results in an enhanced scan resolution in regions where the sampling rate is increased (or over-sampled), at the cost of a reduced resolution in non-over-sampled regions, and in particular in regions where the sampling rate is explicitly decreased (under-sampled). The method to create this subset is probabilistic in nature – each model in the untouched pMSSM scan is iterated over, and is picked into the smaller subset with a base pick probability. The over-sampling and under-sampling is then implemented by multiplying two factors with the base pick probability b, such that

$$p = \max(k_{oversampling}) \cdot \min(k_{undersampling}) \cdot b, \tag{16}$$

where p is the actual pick probability, and $\max(k_{oversampling})$ and $\min(k_{undersampling})$ are the maximum and minimum of the respective over- and under-sampling factors that apply, respectively. The base pick probability is tuned such that the resulting smaller pMSSM scan, after the variable sampling is applied, contains approximately 500,000 models. For the smaller pMSSM scan to represent the entire pMSSM scan, each member of the sampled subset is weighted by the inverse of the members pick-probability. The reweighted distributions are then approximately equal in the smaller and the original pMSSM scans. Some tests for this are shown in Section 6.1.3.
An added benefit of this necessary step is that by sampling a sparse subset of the original McMC, we drastically reduce the auto-correlation of the pMSSM models in the created subset.

6.1.1 Over-sampled regions

The region with light stops is over-sampled for two reasons. First, the light-stop sector is interesting because of the little hierarchy problem. Secondly, the prior density is very small at small stop masses, where the LHC is likely to have an impact. We also over-sample, on their own merits, the region of comparatively small fine-tuning, according to the fine-tuning measure ΔEW (calculated in this work with the tool `SOFTSUSY` 4.1.6 [125]), the region where the predicted dark matter relic density saturates the measured relic density, and the region of the pMSSM that is compatible with the measurement of the anomalous magnetic moment of the muon, a_μ. The exact region definitions and over-sampling factors are:

- $m(\widetilde{t}_1) \leq 1\,\text{TeV}$, which is over-sampled with a factor of 10;
- $m(\widetilde{t}_1) \leq 1.5\,\text{TeV}$, which is over-sampled with a factor of 5;
- $\Delta\text{EW} \leq 100$, which is over-sampled with a factor of 3;
- $\Omega h^2 = 0.1199 \pm 2 \cdot 0.0022$ where the LSP is higgsino-like (which is defined here as the higgsino making up the biggest contribution to the LSP mixing), which is over-sampled with a factor of 5;

- $\Omega h^2 = 0.1199 \pm 2 \cdot 0.0022$ where the LSP is **not** higgsino-like, which is over-sampled with a factor of 20;
- $\Delta a_\mu^{SUSY} \geq (268 - 80) \cdot 10^{-11}$, where Δa_μ^{SUSY} is the SUSY contribution to a_μ, which is over-sampled with a factor of 10.

For the purpose of generating the over-sampling factor used in Equation 16, we take the maximum of the factors stated above that applies to the respective model.

6.1.2 Under-sampled regions

The region of the pMSSM that over-saturates the measured relic density is under-sampled, to give more emphasis to the region that is not explicitly excluded by this constraint. We also under-sample the region of the pMSSM that could already be excluded by the LHC using analyses on the basis of $\sqrt{s} = 7\,\text{TeV}$ and $\sqrt{s} = 8\,\text{TeV}$ data, according to the tool `SModelS` 1.2.2 [126, 127, 128, 129, 130, 131, 132, 133, 134, 135, 136, 137, 138, 139, 140]. `SModelS` is a tool that maps all the production modes within a model, including pMSSM models, onto a complete set of simplified model topologies, by following the decay paths of all production modes and aggregating them by their final state topology. Each topology is assigned a weighted fiducial cross section by the aggregate production cross section times the branching ratio into the decay paths that belong to the topology. This fiducial cross section is compared against published upper limits or efficiency maps from a large collection of LHC analyses, to determine whether the model in question is excluded. The SModelS method is conservative in its estimation in most cases.

Note that the variable sampling does not bias the impact of LHC analyses at $\sqrt{s} = 13\,\text{TeV}$, as the shape of the prior is not affected by the variable sampling. The variable sampling merely affects the scan resolution. The exact region definitions and under-sampling factors are:

- $\Omega h^2 \geq 0.1199 + 2 \cdot 0.0022$ is under-sampled by a factor of 0.5;
- models excluded according to `SModelS`, using only LHC analyses with $\sqrt{s} = 7\,\text{TeV}$ and $\sqrt{s} = 8\,\text{TeV}$, is under-sampled by a factor of 0.5.

The under-sampling factor of 0.5 is applied in Equation 16 if either of the two conditions above applies to the respective model.

6.1.3 Reweighting validation

To validate the re-weighting procedure, we compare the marginalized distributions from the untouched pMSSM to those of the re-weighted pMSSM sub-scan and estimate their difference. This is done for all particle masses and pMSSM parameters along one dimension. The re-weighting procedure works very well, with the binned difference between the re-weighted and untouched chain generally well below 5% in 1-dimensional marginalized distributions, assuming typical bin widths used throughout this thesis. The variations here do not exhibit signs of systematic bias. A set of typical examples are shown in Figure 56. Exceptionally large, but still moderate, variations are seen in the distributions of the LSP mass in models with a bino-wino or bino-higgsino mixed LSP, shown in Figure. This is mostly due to the small number of models with mixed LSP types.

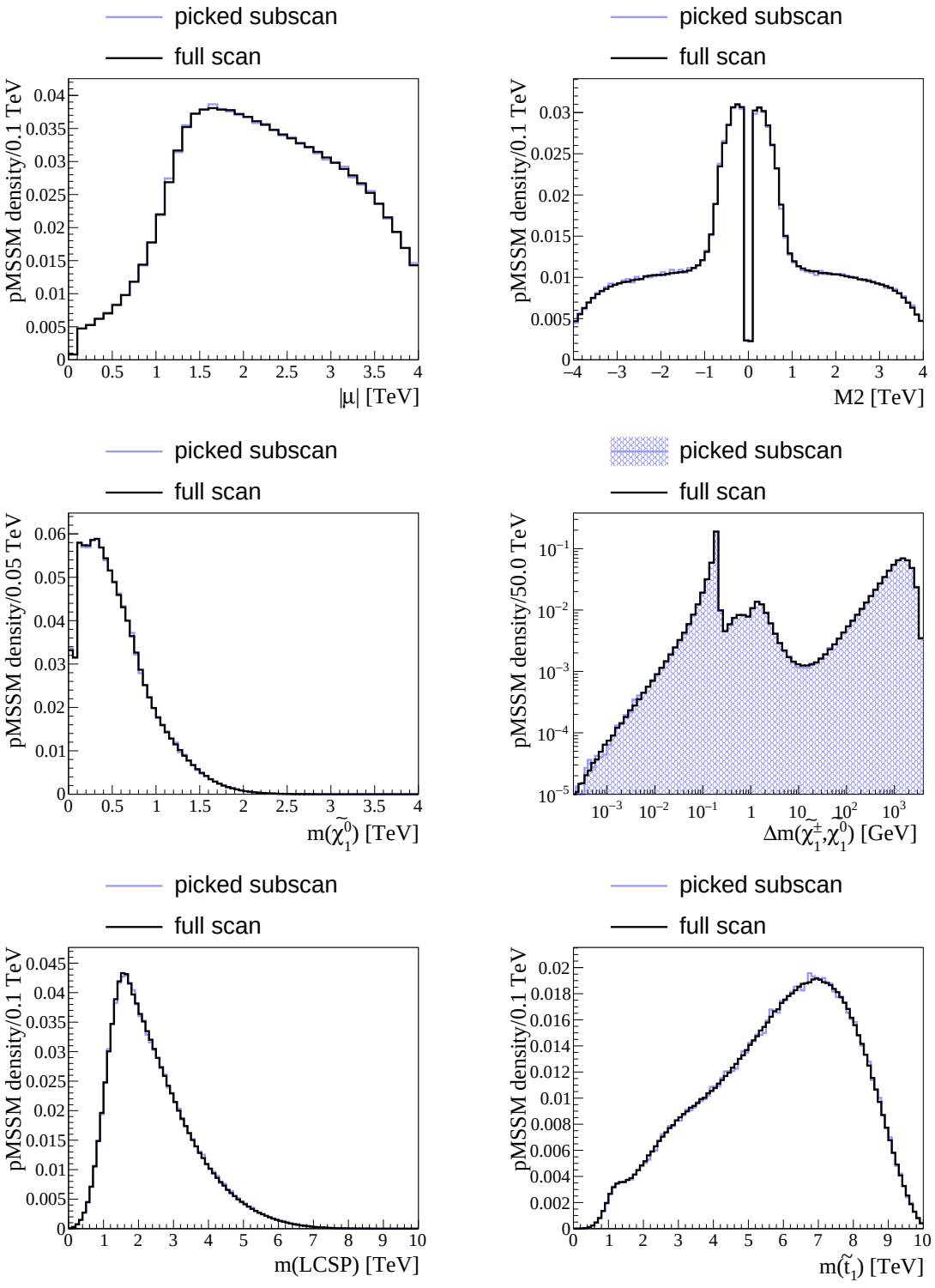

Figure 56: Validation of the re-weighting procedure to compensate for variable sampling. The displayed distributions and their variance are typical examples of 1-dimensional marginalizations of the pMSSM scan.

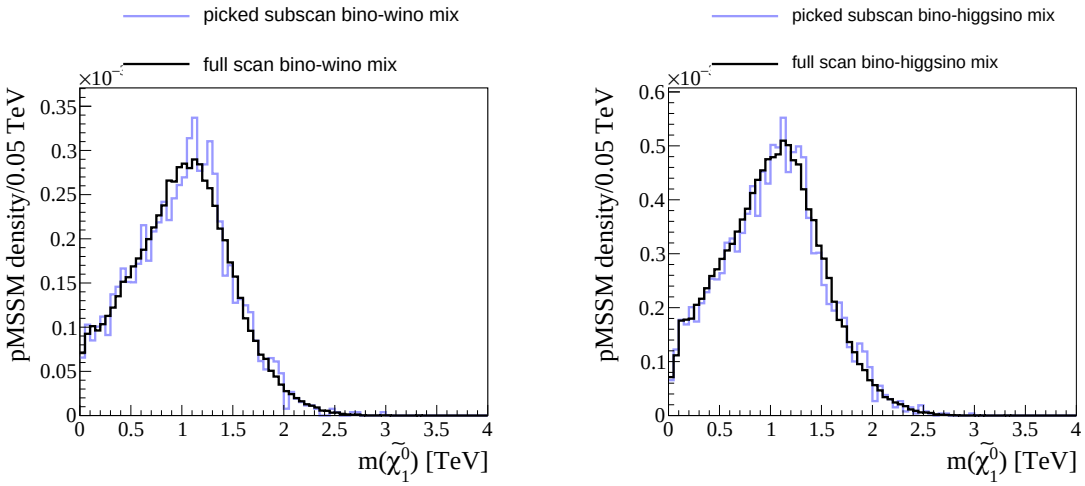

Figure 57: Validation of the re-weighting procedure to compensate for variable sampling. The variance is larger than elsewhere in the pMSSM, due to the small number of pMSSM points with a mixed LSP type.

6.2 Signal simulation

The signal simulation for the LHC analyses are performed for two separate workflows, one involving a CMS-internal simulation path, and another one involving the public recasting tool `MadAnalysis5` [121, 122, 123, 124]. In both workflows, the signal event simulation is performed using `Pythia8` [129, 130]. The number of simulated events varies on a point-by-point basis and scales with the total leading order production cross sections, estimated with `Pythia8`. The target number of events N is chosen to be 5 times the total production cross section $\sigma^{\text{total}}_{\text{Pythia8@LO}}$, multiplied by the approximate Run 2 luminosity of the LHC, $L = 138\text{fb}^{-1}$. Thresholds on the total number of events per point are applied, with a minimum and maximum number of simulated events of 1,000 and 60,000, respectively. This can be expressed as

$$N = \max\left(1000, \min\left(60000, \sigma^{\text{total}}_{\text{Pythia8@LO}} \cdot L\right)\right). \tag{17}$$

Compressed stops
Note at this point that the decay tables generated by `SPheno` do not include decays via virtual W-bosons for $\widetilde{\text{t}}_1$, if $m(\widetilde{\text{t}}_1) - m(\widetilde{\chi}^0_1) < m(\text{W})$. Significant differences in terms of sensitivity may occur for analyses that rely on such decays in their signal events.

6.2.1 `MadAnalysis5` workflow

Approximately 30 billion signal events were simulated across the pMSSM scan for the `MadAnalysis5` pipe, with 10 billion independent events for each of the three analyses that were used in this simulation path (see Section 6.3). This path uses a parameterized detector simulation implemented with `Delphes` [141]. No difference is made in these events concerning the different LHC and detector conditions in different data taking periods. The events, which now include the detector response, are then analyzed via the three implemented analyses in this path, which implement the object and signal region definitions. The final output are the number of signal events in each of the signal regions of each analysis.

6.2.2 CMS workflow

A further 6 billion signal events were produced for the CMS-internal path. The events are split into samples conforming to the 2017 and 2018 LHC and CMS detector conditions, with the sample sizes approximately conforming to the respective luminosities recorded by the CMS detector. The detector response is modeled with the CMS fast simulation software. Due to stochastic nature of assigning the number of events to generate inherent in this CMS-internal path, the target number of events is not always reached. In some instances, pMSSM points with small cross sections may not have been simulated at all. The effect of this on the final results is likely to be minimal, since the LHC is not sensitive to such small-cross section models. In addition, the events corresponding to the 2016 LHC and detector conditions have not been simulated as of the time of writing of this thesis. For each model, the total number of events corresponding to 2017 and 2018 conditions is thus reweighted to cover the missing events with 2016 conditions. The ratio of the weighted total number of events for 2017 and 2018 is kept to the ratio of their respective luminosities in this procedure.

truth-level event filter
To conserve valuable computation time, a Monte Carlo truth-level event filter is applied after the generation step performed in `Pythia8`. The filter is designed to only reject events that will not be triggered by of any included analysis. Events pass the filter if at least one of the following conditions is true:

- the event has a large hadronic momentum sum, $H_T > 140\,\text{GeV}$, where H_T is the sum over the transverse momenta of all anti-kt(R=4) gen-jets with $\text{p}_\text{T}{}^{jet} > 30\,\text{GeV}$ and $|\eta^{jet}| < 5$;
- or the event contains at least one muon or electron with $p_T^{\mu,e} > 15\,\text{GeV}$ and $|\eta| < 2.5$, where $|\eta|$ is the pseudorapidity;
- or the event contains a single photon with $\text{p}_\text{T}{}^{\gamma} > 70\,\text{GeV}$ and $|\eta| < 2.5$;
- or the event contains at least one tau lepton with $\text{p}_\text{T} > 30\,\text{GeV}$ and $|\eta| < 2.5$;

- or the event contains at least one long-lived chargino that reaches the muon system;
- or the event contains any combination with at least two of the following objects: electron with $p_T > 5\,\text{GeV}, |\eta| < 2.5$, muon with $p_T > 2.5\,\text{GeV}$, $|\eta| < 2.5$, or photon with $p_T < 30\,GeV, |\eta| < 2.5$;
- or the event contains at least two photons, of which one is required to have $p_T > 18\,\text{GeV}, |\eta| < 2.5$, and the other photon is required to have $p_T > 30\,\text{GeV}$ and $|\eta| < 2.5$.

The targeted number of events in Equation 17 is modified by the filter efficiency for this simulation path, such that

$$N = \max\left(1000, \min\left(60000, \frac{\sigma^{\text{total}}_{\text{Pythia8@LO}} \cdot L}{\epsilon_g}\right)\right), \tag{18}$$

where ϵ_g is the filter efficiency $\epsilon_g = \frac{N_{\text{passed}}}{N_{\text{total}}}$. The minimum and maximum threshold on the number of events are applied after the filter efficiency correction, so they apply to the fiducial number of events. The gen-filter takes on values ranging from $\epsilon_g \simeq 10^{-2}$ to $\epsilon_g = 1$.

6.3 Included LHC analyses

6.3.1 ATLAS_SUSY_2018_06 (*multi-lepton*)

This analysis [5, 142] targets electroweak supersymmetry using jigsaw [143, 144] variables. Signal events are required to contain at least three leptons with p_T exceeding at least 20 GeV, with thresholds tightening depending on the event category. Among the three leptons, there must be a same-flavor-opposite-sign lepton pair. The final event selection results in two signal regions, in which the largest excess observed corresponds to a significance of 1.21 standard deviations. The analysis publication includes an interpretation in terms of a simplified model in which only $\widetilde{\chi}_1^{\pm}\widetilde{\chi}_2^0$ production occurs, which subsequently decay to the LSP via on-shell W and Z bosons, respectively.

The analysis is incorporated with the simplified likelihood, described in Section 7.1.

6.3.2 ATLAS_SUSY_2018_32 (*di-lepton*)

The second analysis [3, 145] from ATLAS that is used also targets electroweak supersymmetry, in this case by targeting a di-lepton final state in combination with missing transverse momentum. The final event selection requires at least two leptons with $p_T > 25$ GeV, with their invariant mass exceeding 100 GeV. The analysis considers 36 search regions, based on the flavor combination of the leptons and the number of non-b-tagged jets, and are binned in the m_{T2} variable. The most significant excess in data corresponds to a local significance of approximately 2 standard deviations. The published analysis includes an interpretation of the results in terms of three simplified models. In the first, only $\widetilde{\chi}_1^{\pm}\widetilde{\chi}_1^{\pm}$ production occurs, with subsequent decays to the LSP via on-shell W bosons. A second simplified model also only considers $\widetilde{\chi}_1^{\pm}\widetilde{\chi}_1^{\pm}$ production, but decays via an intermediate slepton into the LSP. The third simplified model considers di-slepton production, with decays to the LSP via leptons.

The analysis is incorporated with the simplified likelihood, described in Section 7.1.

6.3.3 CMS_SUS_18_004 (*di-lepton SOS*)

This analysis [4] targets compressed electroweak supersymmetry by targeting final states with two or three leptons with low transverse momentum. The analysis selects leptons with $p_T > 5$ GeV for electrons and $p_T > 3$ GeV for muons. An upper threshold of $p_T < 30$ GeV is applied on the leptons. The analysis defines 61 search regions, based on the p_T^{miss} of the event and the minimum invariant mass of same-flavor-opposite-sign leptons pairs, $M_{SFOS}^{min}(ll)$. The most significant local excess in data corresponds to 2.4 standard deviations. This search has been interpreted in the TChiWZ ($\widetilde{\chi}_1^{\pm}\widetilde{\chi}_2^0 \to WZ\widetilde{\chi}_1^0\widetilde{\chi}_1^0$), TChiZ ($\widetilde{\chi}_2^0\widetilde{\chi}_1^0 \to Z\widetilde{\chi}_1^0\widetilde{\chi}_1^0$), T2Bff ($\widetilde{t}_1\widetilde{t}_1 \to bbffff\widetilde{\chi}_1^0\widetilde{\chi}_1^0$), and in the T2BW ($\widetilde{t}_1\widetilde{t}_1 \to bb\widetilde{\chi}_1^{\pm}\widetilde{\chi}_1^{\pm} \to WW\widetilde{\chi}_1^0\widetilde{\chi}_1^0$) simplified models.

The analysis is incorporated with the full likelihood, described in Section 7.1.

6.3.4 CMS_SUS_19_006 (p_T^{miss}+*jets*)

This search [1, 2] targets strongly interacting supersymmetry by looking at final states containing significant hadronic missing transverse momentum exceeding 300 GeV, in the 0-lepton final state. The analysis defines 174 signal regions based on the jet and b-tagged jet multiplicities, and the hadronic missing transverse momentum.

The analysis is incorporated with the simplified likelihood, described in Section 7.1.

6.3.5 CMS_SUS_21_006 (*disappearing tracks*)

This search [6, 7] targets very compressed electroweakinos by looking at final states with disappearing tracks, which can occur when the proper decay length of supersymmetric particles is in the order of the CMS detector. The analysis defines 49 signal regions based on the track length (short and long), the track $\frac{dE}{dx}$ (high and low), jet multiplicity, b-tagged jet multiplicity, and lepton multiplicity. Charginos with proper decay lengths between $c\tau(\widetilde{\chi}_1^{\pm}) = 1$ cm and $c\tau(\widetilde{\chi}_1^{\pm}) = 1000$ m are targeted.

The analysis is incorporated with the full likelihood, described in Section 7.1.

6.3.6 Summary of covered final states

This set of searches represents a mostly non-overlapping set of signal regions spanning a comprehensive range of final states. In terms of the lepton multiplicity, the final state coverage is as follows:

- 0-lepton: The 0-lepton final state is covered by cms_sus_19_006. This search covers strongly interacting supersymmetry in addition to providing some sensitivity to pure dark matter production.
- 1-lepton: This final state is not covered by any search. This is not too problematic, since the pair production of supersymmetric particles usually leads models that come with events containing a single lepton to also have events with two or more leptons.
- 2-lepton: This final state is covered by multiple searches in different regions of the di-lepton mass.
- multi-lepton: covered by atlas_susy_2018_06, in addition to these models always featuring events in the di-lepton final state as well.
- long-lived: parts of the pMSSM contain models with long-lived particles. Sensitivity to these topologies is given by cms_sus_21_006, which targets events with disappearing tracks.

7 Statistical methods and displays

The impact of the LHC on the pMSSM is evaluated first by calculating a likelihood for each of the analyses in Section 7.2 and a combined likelihood for all the included analyses. Each model of the prior is then reweighted by the respective likelihood, in order to, according to Bayes theorem, result in a posterior density with respect to the included analyses. The posterior density is then promoted to a proper posterior, by re-weighting it such that it integrates to unity.

This section discusses the construction of the analysis likelihood, and introduces a significance measure based on a Bayesian probability framework – the Z significance. Furthermore, three statistics have been developed to illustrate how the pMSSM model space is constrained and impacted by the considered analyses. The quantities included in the displays are meant to complement each other, and tend to accentuate either more or less the Bayesian aspects if the statistical analysis. Each display can correspond to either a 1-d or 2-d projection onto selected pMSSM parameters or variables derived from the pMSSM. The following contains a brief description of each type of display with an example, in addition to the construction of the LHC likelihood.

7.1 LHC likelihoods

The analysis likelihoods are calculated for each of the analyses included in Section 6.3. Two forms of the likelihood are computed. Where possible, a *full* likelihood is computed by extracting profile likelihoods that take background correlations into account. Where this is not possible, a simplified likelihood is employed that uses observed counts and the background estimates and uncertainties. Signal uncertainties are estimated by computing variations of the likelihood where the signal cross section is multiplied by a signal strength modifier μ. Combinations of analyses are performed by multiplying the individual analyses likelihoods. The analyses are thus treated as orthogonal, given that they cover different phase space regions. In order to provide a conservative estimate of the signal uncertainties, two large signal strength modifiers of $\mu = 0.5$ and $\mu = 1.5$ are chosen in addition to the nominal version of the results with $\mu = 1$. The likelihoods that are used here strongly resemble and are based on the respective definitions in the Run 1 CMS pMSSM paper [146].

7.1.1 Full likelihood

The profile likelihood

$$L(D^{\mathrm{LHC}}|\mu, \theta, \hat{\nu}(\mu, \theta)) \tag{19}$$

for a model θ is computed by the Higgs combine tool, where D^{LHC} is the observed data, μ is the signal strength modifier, and $\hat{\nu}(\mu, \theta)$ are the conditional maximum likelihood estimates for the nuisance parameters $\nu(\mu\theta)$. The profile likelihood is then directly taken as the full likelihood,

$$L_{\mathrm{full}}(D^{\mathrm{LHC}}|\theta) = L(D^{\mathrm{LHC}}|\mu, \theta, \hat{\nu}(\mu, \theta)). \tag{20}$$

The full likelihood is used for the di-lepton SOS analysis and the disappearing tracks analysis.

7.1.2 Simplified likelihood

Where it is not possible to compute the full likelihood, a simplified likelihood is used instead. This simplified likelihood is defined analogously to how it was used in the Run 1 CMS pMSSM paper [146]. For a single signal region i, the likelihood is given by

$$L_i(D^{\mathrm{LHC}}|\theta) = \int \mathrm{Poisson}(N|s(\theta) + b)\, p(b|B, \delta B)\mathrm{d}b\,, \tag{21}$$

with the observed counts N, the expected signal and background counts $s(\theta)$ and b, respectively, and the estimated background counts and uncertainty B and δB, and the prior density for the background, $p(b|B, \delta B)$. The prior density is estimated as a gamma density, $\mathrm{gamma}(x; \alpha, \beta) = \beta \exp(-\beta x) \frac{(\beta x)^{\alpha-1}}{\Gamma(\alpha)}$. The parameters α and β are chosen such that the mode and variance of gamma are B and $(\delta B)^2$, respectively. The simplified likelihood for a given model is then given by the product over the single signal region likelihoods in Equation 21:

$$L_{\mathrm{simplified}}(D^{\mathrm{LHC}}|\theta) = \Pi_i L_i(D^{\mathrm{LHC}}|\theta). \tag{22}$$

7.1.3 Bayes factor and Z significance

In general, a Z significance (or Z score) is a standardized score of a statistical model, which is usually employed in frequentist statistics. It gives the number of standard deviations that a sample of a distribution differs from its mean. The signed Z significance used here is based on the Bayes factor B. From a Bayesian point of view, the probability for a model hypothesis θ is

$$P(\theta|D) = \frac{P(D|\theta)\, P(\theta)}{P(D)}, \tag{23}$$

where D is the data, p is the prior for θ, and

$$P(D|\theta) = \int P(D|\Theta_\theta, \theta)\, P(\Theta_\theta|\theta)\, d\Theta_\theta \tag{24}$$

is the likelihood, Θ_θ is the parameter space for the hypothesis θ, and $P(\Theta_\theta)$ is a proper prior density over the parameterspace of θ, that integrates to one. Because the priors of the model hypotheses integrate to one, any differences in the dimensionality or degrees of freedom of the models are accounted for by the integration. We can now move on to consider θ a model in the pMSSM parameter space. The ratio of probabilities for any model θ and the SM is then

$$\frac{P(\theta)}{P(\mathrm{SM})} = \frac{P(D|\theta)}{P(D|SM)} \cdot \frac{P(\theta)}{P(\mathrm{SM})}, \tag{25}$$

which is proportional to the Bayes factor

$$B(D|\theta) = \frac{P(D|\theta')}{P(D|\mathrm{SM})}. \tag{26}$$

The notation $B_{\mu 0}$ is used for a signal strength modifier μ, as the likelihood for the standard model $P(\mathrm{SM})$ is identical to the likelihood for any pMSSM model where $\mu = 0$. B_{10} is thus the Bayes factor for a pMSSM model θ assuming the nominal signal strength of $\mu = 1$. A Bayesian analog of a Z significance can then be defined as [146]

$$Z = \mathrm{sign}(\ln(B_{10})) \cdot \sqrt{2 \cdot |\ln(B_{10})|}. \tag{27}$$

Because B_{10} is analogous to a likelihood ratio, $2 \cdot \ln(B_{10})$ is asymptotically χ^2 distributed [147] if the standard model hypothesis is true, and qualifies as a Z significance. The sign $\ln(B_{10}))$ is used to split the Z significance into two regions that can be interpreted independently:

- $\mathrm{sign}(\ln(B_{10})) > 0$ favors the pMSSM hypothesis, where a two-sided interval on the Z significance is used to judge whether the SM hypothesis should be rejected. This means that a Z significance of $Z = n$ corresponds to evidence at n standard deviations for the pMSSM hypothesis.
- In the negative regime, where $\mathrm{sign}(\ln(B_{10})) < 0$, a one-sided interval on the Z significance is used to determine whether to reject the pMSSM model in question. The (negative) Z significance corresponding to the 95% confidence level for exclusion that is usually used in particle physics is $Z = -1.64$, which means at $Z \leq -1.64$, the pMSSM model is rejected at $\geq 95\%$ confidence level. Note that the SM only hypothesis and the pMSSM hypothesis are interpreted equivalently in this Z significance, since the absolute value of the Z significance is invariant under the change $B_{10} \to B_{01}$. Differences between the model hypotheses are only made in the interpretation of the Z significance.

7.2 Impact plots

This type of plot shows the prior and posterior densities corresponding to the implemented LHC results. These quantities and their interpretation are intrinsically Bayesian in nature. The prior and posterior are projected onto different parameters, e.g., the gluino mass, as shown in Figure 58, resulting in the marginalized prior and posterior densities. The prior density here corresponds to the point density in the Markov chains from Section 5 and is shaped by the included observable-based likelihoods. Also shown are the posterior densities one obtained by varying the signal cross section up and down by 50% in the calculation of the LHC likelihood. This very large variation of the

signal cross section is intended to conservatively cover bin-to-bin correlated uncertainties not directly accounted for in the simplified likelihood. Unless otherwise stated, all distributions shown make use of the nominal signal cross section given by `Pythia8`.

Key questions can be addressed from the impact plots:

- Locations of preferred regions of the marginalized prior and posterior densities. These peaks may arise because of specific (positive) physics results that produce these peaks, or they could be residual peaks produced by negative physics results in nearby regions.
- Does the posterior peak in a region of low prior density? This would indicate little sensitivity of LHC results, but could also be due to the finite statistics of pMSSM points. Because the prior is the sampled point density up to the sampling factor, the relative uncertainty on both prior and posterior grows inversely with the prior density.
- Is the posterior suppressed in a region of high prior density? This would indicate strong complementarity between the LHC results and those physics experiments considered in the prior.
- Is there a significant shape difference between the marginalized prior and posterior densities, or do they only differ by a shift along a given observable? The former might point to specific physics results, whereas the latter usually comes from a simple suppression of a whole region of the pMSSM, e.g. low gluino masses. If there is only an overall factor, how large is it?
- Are there regions of non-negligible prior density where the posterior is vanishingly small? This would imply the local suppression of certain types of models by the analyzed data, and indicates a meaningful impact on knowledge about SUSY due to the analyses.
- How large and varied is the effect of the cross section variations? Regions where the impact of cross section variations is large indicate that the LHC is directly sensitive to the observable in question in that region of the pMSSM.

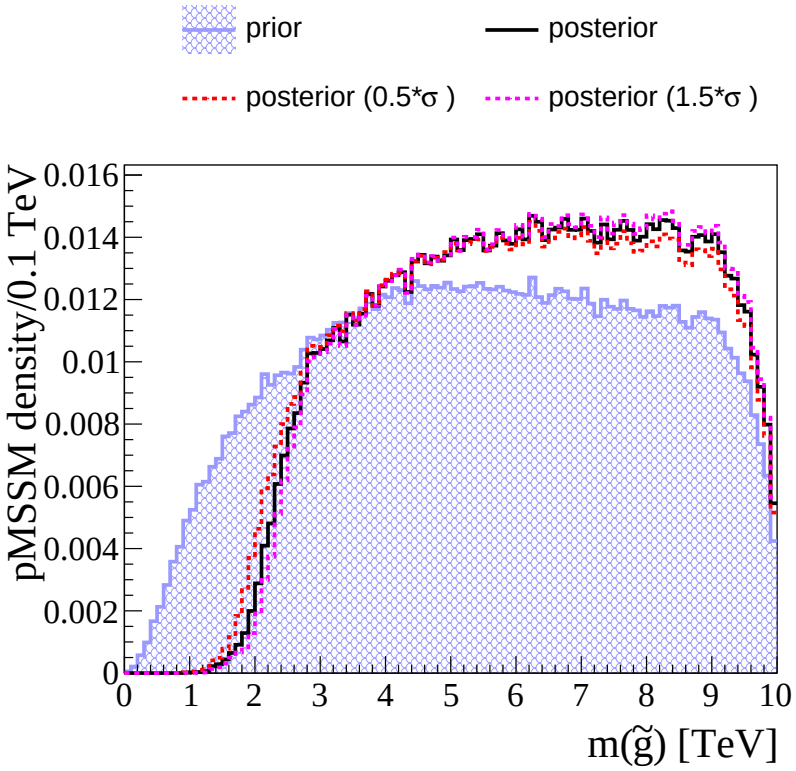

Figure 58: Example of an impact plot, showing the prior and posterior densities, as well as the posterior densities when assuming ±50 % signal cross section variations.

7.3 Survival probabilities

This measure can be made sense of in both a Bayesian and a frequentist framework and eliminates dependence on the prior to first order. It is defined as the fraction of models *surviving* LHC constraints out of all models. By *surviving*, it means that a given model is not excluded at the 95% CL by the analysis. To evaluate this criterion, we make use of the signed significance Z, defined in Section 7.1.3 and use it to designate a model as *surviving* if its Z significance is greater than $Z > -1.64$. Models where $Z \leq -1.64$ are excluded at 95% confidence level in a frequentist framework. Thus, the survival probability is defined as $\frac{N_{Z>-1.64}}{N_{total}}$. To first order, the prior density cancels in the numerator and denominator, and so the prior only determines the statistical accuracy of the survival probability, but not its shape. Figure 59 shows the bin-wise survival probability in the pMSSM, projected on the gluino mass in this example. The survival probability is useful to:

- identify regions that are mostly surviving or completely excluded at 95% confidence level. These regions can be compared to limits on simplified models to gauge the robustness of previous statements made about SUSY;
- find the edges of LHC sensitivity, for example, by looking at ranges in the distribution of the survival probability where the increase of the survival probability transitions into a plateau;

The survival probability is primarily sensitive to cases where the LHC data disfavors the pMSSM, but it also tends to highlight where data favor the pMSSM. ´

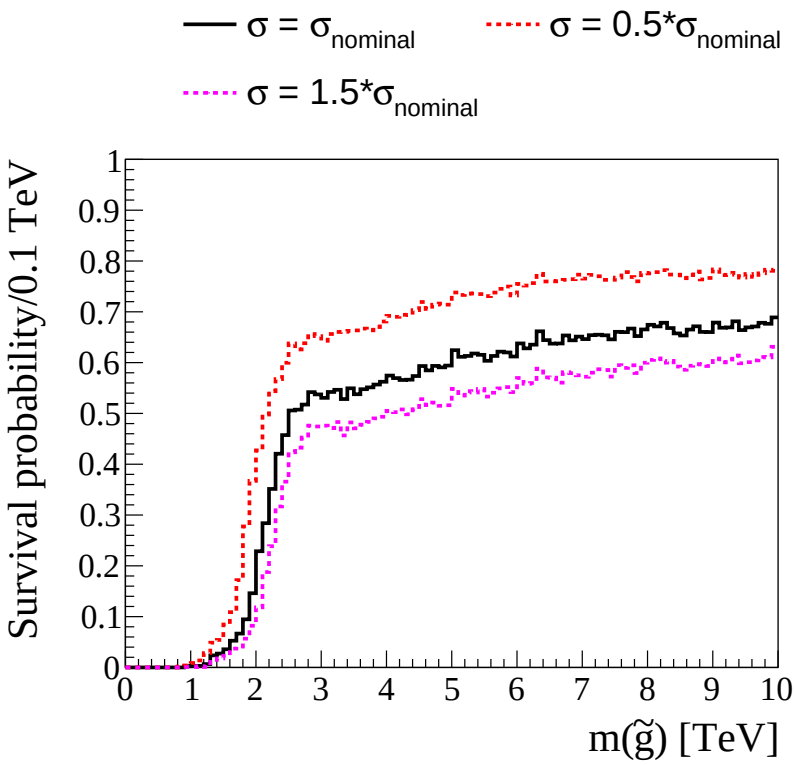

Figure 59: Example of a survival probability plot assuming the nominal signal cross sections, as well as the survival probability assuming ±50 % signal cross section variations.

7.4 Bayes factor quantiles

The median of the Bayes factor and various quantiles are compared for ensembles defined as the set of pMSSM points within a given bin. This type of plot, an example of which is given in Figure 60, is useful to show both the behavior of a typical model in a given bin, as well as outliers towards large Bayes factors, indicating the presence of models for which the data fit part of the pMSSM better than the SM. Plotting this quantity has the advantage over an alternative approach of plotting the

maximum likelihood value per bin in that the former does not scale with statistical precision, whereas the latter does. Among the information that can be extracted from the Bayes factor quantiles are:

- The edges of sensitivity of LHC searches, which can be inferred from the behavior of the median and 75th percentiles. A transition from low median Bayes factor to larger ones in the order of one represent an edge in sensitivity, as LHC becomes less and less sensitive to an increasing number of models.
- Wholly disfavored regions can be found in regions where the extreme quantiles have Bayes factors below one. That is because they by construction provide a lower bound on the fraction of models that have a Bayes factor larger than the value of the quantile.
- The extreme quantiles (95th+) will show a peak in the Bayes factor in regions where the data fit the pMSSM better than the SM. The height of the peak informs about the significance of the excess in data and its fit to the pMSSM, while the difference in the Bayes factors of the different quantiles informs us about the size of the region where data fit the pMSSM better. For example, if a peak is seen in the 99th percentile but not in the 90th percentile, then the favored region encompasses at least 1% of the model space in that region, but no more than 10%.

A feature that is often seen in distributions involving particle masses where the extreme quantiles show a peak in the Bayes factor, is that the median starts to move towards a Bayes factor of one in that same region. This can be explained by the correlation of the particle masses to the production cross section. In regions where the median Bayes factor is extremely small, the production cross section is often so large that any signal would be too strong to be compatible with data, given that no statistically significant excesses have been found in data. Both the gradual loss of exclusion power for null-results and the potential fit of models to small excesses in data tend to happen at similar cross sections, and with that, particle masses. Lastly, there is an interesting feature that connects

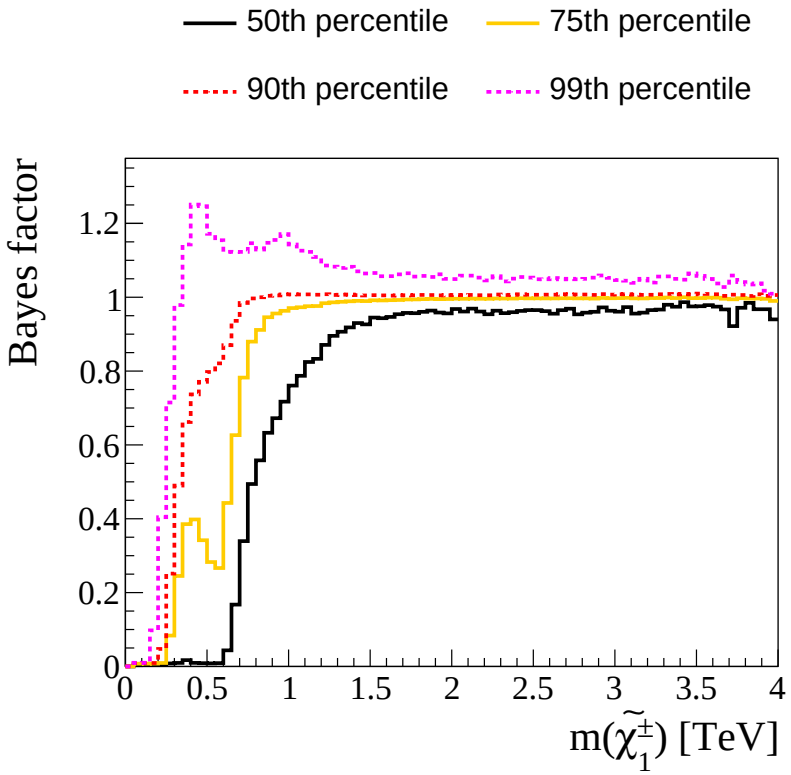

Figure 60: Example of a Bayes factor quantiles plot, showing the median Bayes factor, as well as the 75th, 90th, and 99th quantile.

the median Bayes factor and the posterior density. The posterior density is reduced in regions where the median (more precisely, the mean) Bayes factor is very small. Because the posterior is afterwards

re-weighted to integrate to one, a relative reduction in one region results in the relative enhancement in every other region. The posterior density is *pushed away* from regions of small median Bayes factors and can also be *pulled towards* regions of large Bayes factors. This often results in a posterior density that is larger in a given bin than the prior density, even though the LHC is not sensitive to the models in that bin.

Because of the relation of the Bayes factor and the likelihood ratio of the pMSSM and SM, these plots can be made sense of in both a Bayesian and a frequentist sense.

7.5 Credibility intervals

A set of useful statistics characterizing the prior and posterior densities are their credibility intervals. In a Bayesian framework, they can be interpreted as the probability of finding nature inside the interval (this of course assumes the prior is correct). While there is no unique way to construct the credibility interval given the freedom to shift the bounds of the interval up and down while preserving the integral of the interval, a couple´ of reasonable choices suffice to specify a unique set of credibility intervals. Their construction in this work is shown for an example in Figure 61. The credibility interval X here is defined as the smallest region in the observable space (given by the plot axes) that contains $X\%$ of the prior or posterior. This can be understood, in Figure 61, as lowering a horizontal threshold from high prior (or posterior) densities towards small densities. Histogram bins that are intersected by this threshold are added to the interval, until the $X\%$ credibility interval integrates to $X\%$ of the prior (posterior). The credibility intervals carry the shape information of the underlying probability density that can then be overlaid on otherwise informationally dense plots. This results in the global maximum of the marginalized density being contained in all credibility intervals, and that the probability density is equal along the boundary of any given credibility interval, within the resolution of the underlying histogram. A 2-dimensional example of the credibility intervals is shown

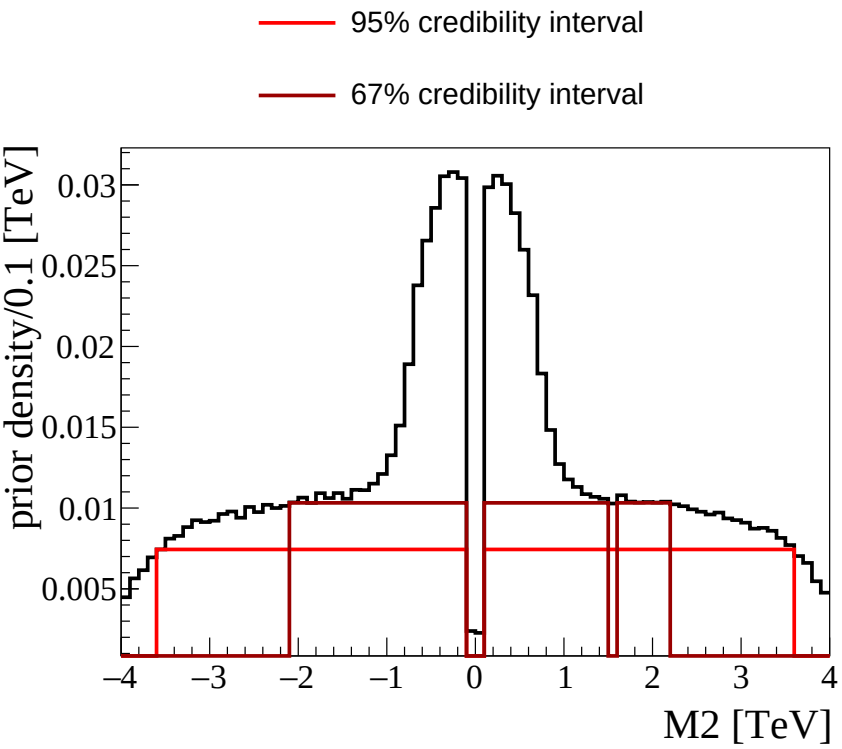

Figure 61: Showcase of credibility interval construction, here defined as the smallest set of histogram bins that contain the respective fraction of the probability density.

in Figure 62. The credibility intervals here show where the prior density peaks and encode high-level information about the general shape of the distribution, without taking up too much visual space. For this reason, they are here frequently used to make determinations about the relative probability

of Nature, similarly to the kind made in the impact plots in Section 7.2, but within 2-dimensional histograms. The way the credibility intervals are defined means they are explicitly dependent on the

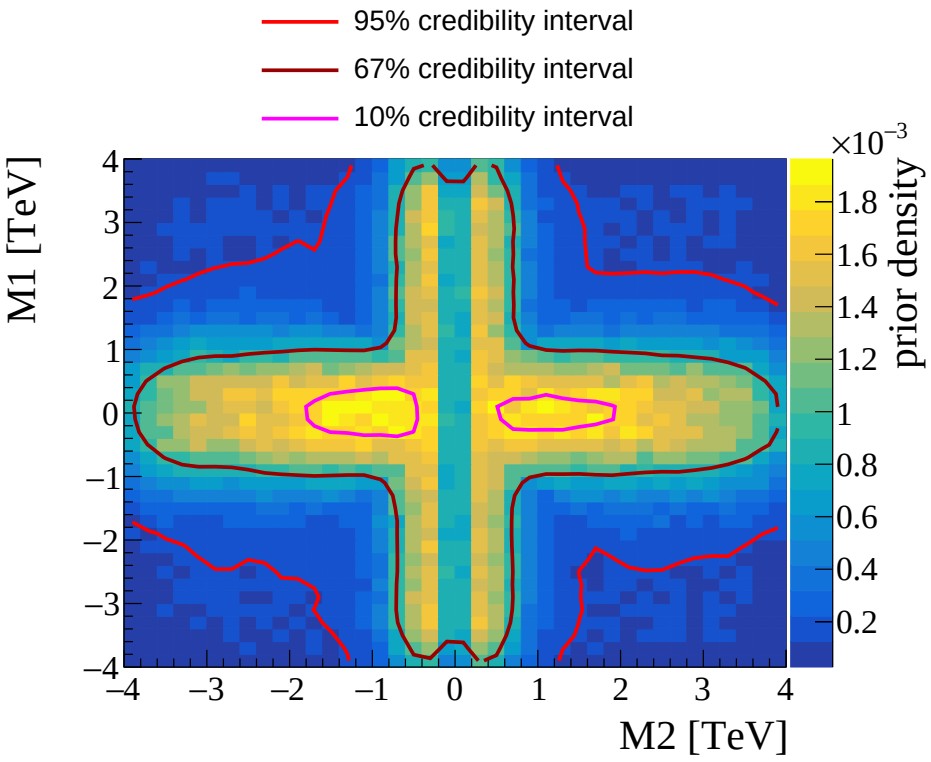

Figure 62: Depiction of the construction of credibility interval contours in two dimensions. The contours indicate regions of large probability density.

histogram binning. While the impact of the binning is generally small on intervals for linear and even binning, large differences arise for logarithmic binning.

7.6 Most significant models

The last piece of information featureed in the plots are the locations of the pMSSM models with the highest Z significance in any 2-dimension plane of observables. These models may be of particular interest on their own, since they represent our "best-fit" model to the data. Besides that, their position in conjunction with other aspects can be interesting, for example, in answering the following questions:

- Are these models clustered in a particular observable plane? This may indicate a region particularly well suited to fit the data.
- What is the local survival probability around the models? Are they in a region that is mostly excluded?
- Is there an excess in the extreme quantiles of the Bayes factor in their vicinity? If not, their occurrence may be a natural consequence of a large tail of the Bayes factor distribution in a well populated bin.

These models with the largest significance are our potentially most sensitive indicator for new physics in the pMSSM.

7.7 2D panels

The most ambitious but likewise most informationally dense display used in this thesis combines the previously described displays into one. Its background layer is either a Bayes factor quantile or the

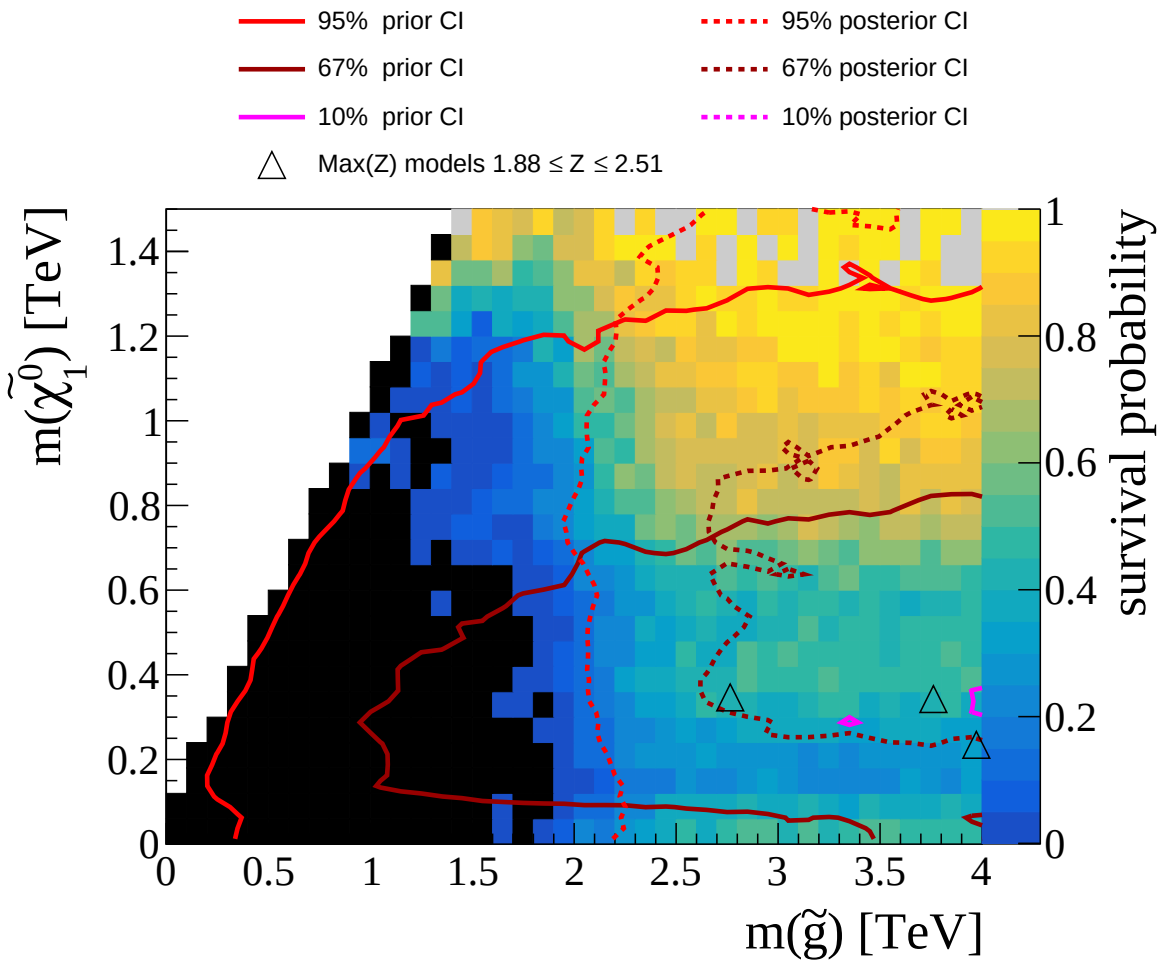

Figure 63: Example of a 2D summary plot. The colorscale shows the survival probability, with black bins denoting exactly zero and grey bins denoting exactly 1. White bins denote bins with zero prior density. The full (dotted) contours show the respective credibility intervals found in the plot legend of the prior (posterior). The black triangles show the (at most) 10 pMSSM models with the largest Z-significance. Some of the 10 highest Z-significance models may lie outside the displayed axis ranges and are thus not visible.

survival probability, with its value represented by a color code and corresponding z-axis value. The 95% and, where applicable, the 67% and 10% credibility intervals are drawn on top. Lastly, the locations of the 10 models with the largest Bayes factor (or equivalently, Z significance) are marked by black triangles. An example is shown in Figure 63. Such figures summarize nearly all of these statistical quantities in a single graphic, and allows for the interpretation of their interconnection. Beware of the z-axis differences. This can make it difficult to compare levels of variance and noise in between displays, even if they show similar projections of pMSSM parameters.

8 Results

We first look at a low-resolution summary of the LHC constraints on the prior, as well as at the complementarity of the implemented searches. There are two ways to interpret the impact of the LHC searches on the pMSSM after the Run 2 of the LHC. We can examine projections directly onto the pMSSM parameters, or onto any number of physical properties of the constituent particles, such as the mass or lifetime of a considered particle. The emphasis here is on the latter, because they are most directly correlated to the LHC data. The results are thus discussed first on the physical "observables" like particle masses, before the implications for the space of the pMSSM parameters are presented. We continue by examining the impact of direct and indirect dark matter detection, and dark matter relic density constraints on the pMSSM, and their complementarity to the direct SUSY searches performed using LHC data. We also examine the impact of the measurement of a_μ, and the implications of requiring small-fine tuning within the pMSSM. Finally, the viability of limits on the simplified model space are tested in terms of the pMSSM. We employ the suite of interpretative displays described in the previous Section 7.

8.1 Summary table on search complementarity

The overall sensitivity of the individual searches, as well as their combination, to the pMSSM, are summarized in Figure 64 in terms of exclusion and Figure 65 in terms of models preferred by the data over the SM-only prediction. For the preferred models, a threshold on the Z significance of $Z > 1$ selects models that are far out on the tail of the Z significance distribution for all of the included searches. In Figure 64, bins at the intersection of two red axis labels show exclusion by both searches, bins with two blue axis labels show the fraction of the prior that is excluded by neither of the searches on the axes. For different color intersections, the quantity shown is the fraction the prior excluded by the search with the red axis label, and not excluded by the search with the blue axis label. The same principle applies in Figure 65, with the difference that green axis labels refer to the fraction of the prior with $Z > 1$.

The combination of searches excludes approximately 53% of the prior. The biggest contributor to this is the search targeting p_T^{miss}+jets at approximately 43% exclusion of the prior (26% uniquely excluded by this analysis), followed by the search for disappearing tracks, which excludes approximately 17% of the prior. There is significant overlap in the set of excluded models among these two searches, where approximately 10.6% of the prior is excluded by both searches individually.
Small fractions of the prior are excluded by the multi-lepton, di-lepton, and di-lepton SOS searches, which is mostly due to the fact that the targeted decay topologies are rare.

It is additionally examined how much each analysis provides unique sensitivity to part of the prior, which can be inferred from Figure 64. The fraction of uniquely excluded points can be found in the bins showing the fraction of models that are excluded by one analysis and **not** excluded by the respective combined-X. The search for p_T^{miss}+jets uniquely excludes the largest fraction of the prior by a large margin, followed by the search for disappearing tracks, and the di-lepton and di-lepton SOS searches. The only search that does not uniquely exclude any part of the prior is the multi-lepton search. Part of the reason for that may lie in the fact that in one of the only two signal regions in that search, a small excess in data is observed. This means that the observed exclusion potential is less than expected and allows for models with larger cross sections to survive the constraints. On the other hand, this results in the comparatively large fraction of the pMSSM with positive Bayes factors seen in Figure 65.

Related to this, the bins at the intersection of non-exclusion by any individual analysis X and non-exclusion by the combination-X show the fraction of the prior that is neither excluded by the analysis alone, nor the combination of the other searches. The difference of this value to the value of the bin at the intersection of non-exclusion of the same analysis and non-exclusion by the whole combinations shows the net decrease of non-excluded models. They represent the part of the uniquely excluded models that require constraints from multiple analyses to exclude. The largest set of these shared-exclusion models can be found for the jets+p_T^{miss} search at approximately 1.5%, followed by the search for disappearing tracks, the di-lepton search, and the di-lepton SOS search at approximately 0.6%, 0.5%, and 0.3%, respectively. Note that this value is a net effect that also includes the opposite behavior, that models that are excluded by the combined-X searches are no longer excluded after the inclusion of X. For the multi-lepton search it shows a net decrease in excluded models. The models that are no longer excluded after the incorporation of the multi-lepton search were previously

excluded by the p_T^{miss}+jets search. This can be seen from the fact that it is the only analysis where a non-zero fraction of the prior is excluded by the analysis, but not by the combination. The fact that this only happens in for the p_T^{miss}+jets search is likely because it is the only included search that has large overlapping sensitivity with the other searches.

The search for disappearing tracks shows the largest fraction of the prior with a positive Z significance exceeding $Z > 1$, followed by the multi-lepton search and the di-lepton SOS search. The p_T^{miss}+jets search and the di-lepton search show negligible parts of the prior with $Z > 1$. There are rare occurrence of shared models with $Z > 1$ in more than one search for the di-lepton SOS search, the multi-lepton search, and the search for disappearing tracks. These models with a shared large Z significance each make up less than 0.01% of the prior. The rare occurrence of shared excess Z significance and shared exclusion indicates that the included searches are well targeted to specific signatures found in models in the pMSSM, such that signals tend to not be distributed across different analyses.

A large fraction of the models where $Z > 1$ in the di-lepton SOS search, the multi-lepton search, or the search for disappearing tracks, are excluded by the p_T^{miss}+jets search. A very small fraction of the prior that shows $Z > 1$ in the p_T^{miss}+jets search is excluded by the di-lepton SOS search or the disappearing tracks search.
There are some few models that are excluded by the p_T^{miss}+jets search that show a significantly positive Z significance in the combination, which indicates some tension between the p_T^{miss}+jets search and the other included searches.

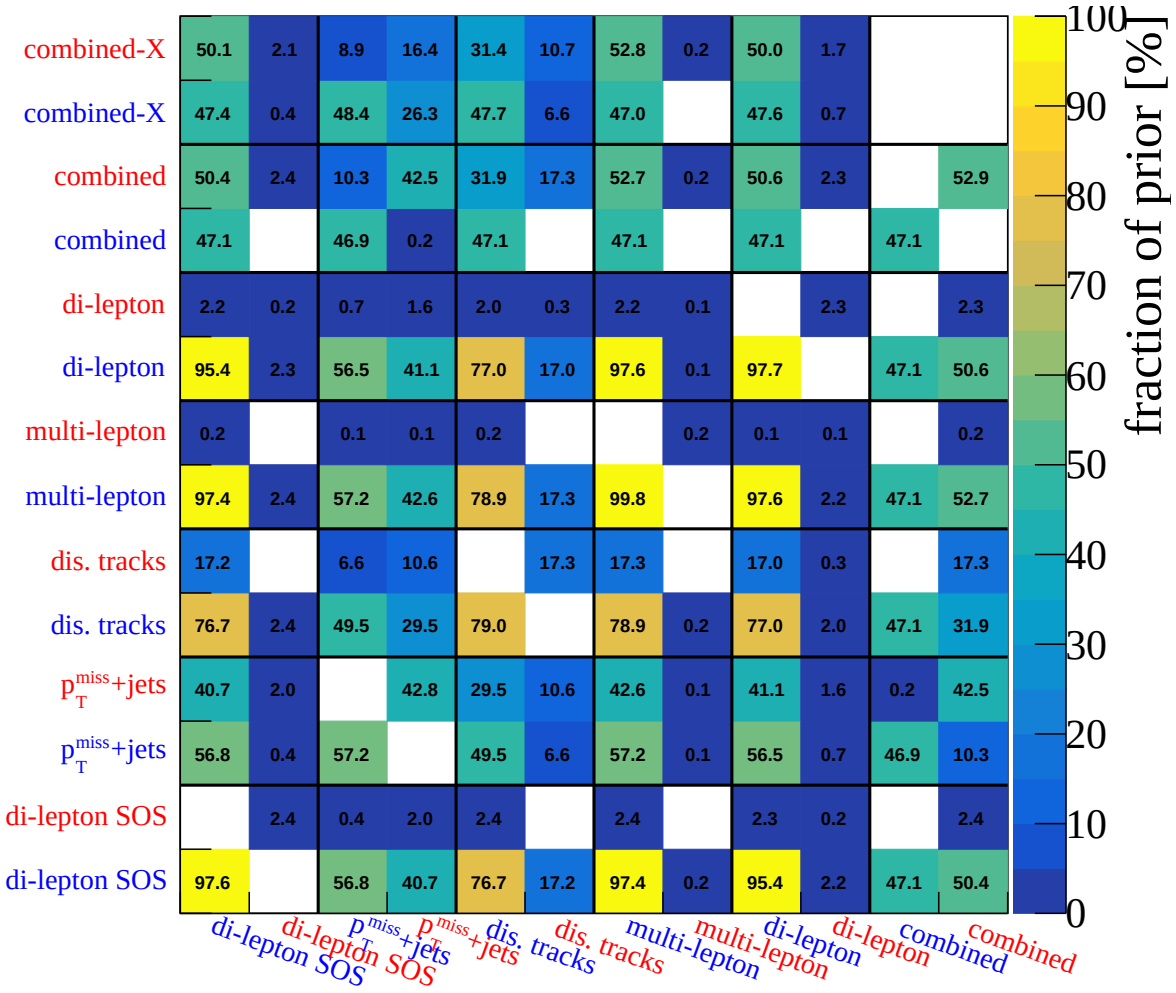

Figure 64: Complementarity among the included LHC searches in terms of exclusion power. Bins with a red axis label denote exclusion by the respective search at $Z < -1.64$, bins with a blue axis label denote non-exclusion by the respective search, $Z \geq -1.64$. The search descriptions can be matched to the respective search labels by referring to Section 6.3. Combined refers to the combination of all the individual analyses, combined-X refers to the combination of every analysis except the corresponding analysis on the x-axis. Bins with z-axis values of exactly zero are colored white.

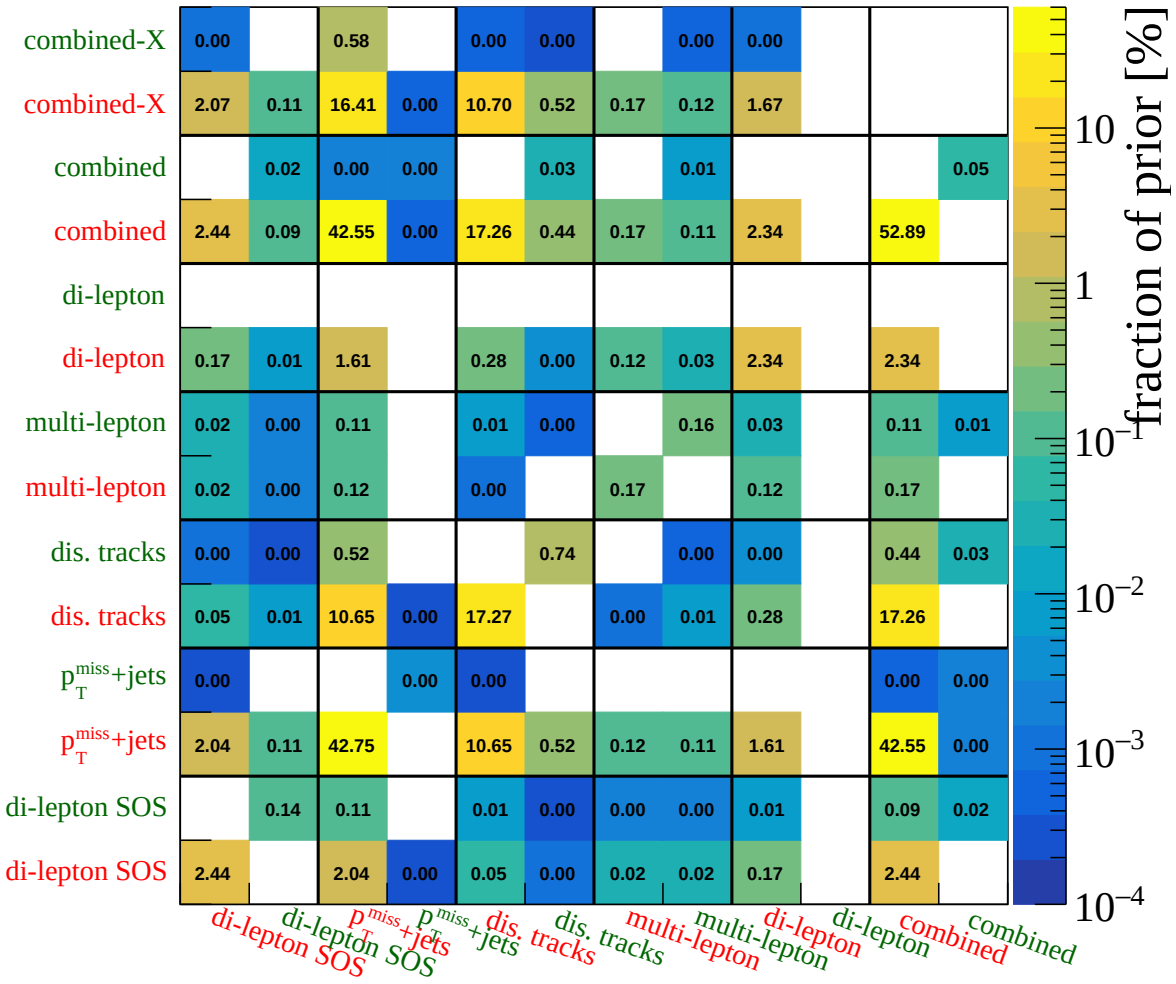

Figure 65: Complementarity among the included LHC searches in terms of competing searches. Bins with a green axis label denote positive Z significance by the respective search exceeding $Z > 1$, bins with a red axis label denote exclusion by the respective search at $Z < -1.64$. The search descriptions can be matched to the respective search labels by referring to Section 6.3. Combined refers to the combination of all the individual analyses, combined-X refers to the combination of every analysis except the corresponding analysis on the x-axis.

8.2 Impact on particle properties

We start the investigation into the particle properties in the electroweak sector, before continuing with the colored sector, and ending with the Higgs sector. This is because the electroweak sector nominally includes the LSP, which, given its unique importance in the pMSSM, provides an overview and informs the results in all the other sectors.

8.2.1 Electroweak SUSY

A key metric for sensitivity to the pMSSM, in particular in the absence of deviations from the SM, are constraints on the mass of the LSP. If an LSP mass below some value can be excluded, all other supersymmetric particles below that mass are excluded as well. For this reason, it also represents a hint of summary of the status of the pMSSM after the Run 2 of the LHC. We investigate electroweak supersymmetry further by looking at the role of the chargino.
To start, the LHC data disfavors LSP masses below $m(\widetilde{\chi}_1^0) \lesssim 500\,\text{GeV}$. This can be seen in the significant shift of the marginalized posterior density away from the prior towards larger values of $m(\widetilde{\chi}_1^0)$ in Figure 66, as well as the strong suppression of the median and 75th percentile of the Bayes factor at small $m(\widetilde{\chi}_1^0)$. In terms of exclusion, below 50% of models with $m(\widetilde{\chi}_1^0) \lesssim 500\,\text{GeV}$ survive the LHC data, with smaller survival probabilities for smaller $m(\widetilde{\chi}_1^0)$. The survival probability never reaches zero for any LSP mass however, which means that a large part of the pMSSM with a low-mass LSP is still viable. Additionally, this shows that in terms of the mass of the LSP, there is

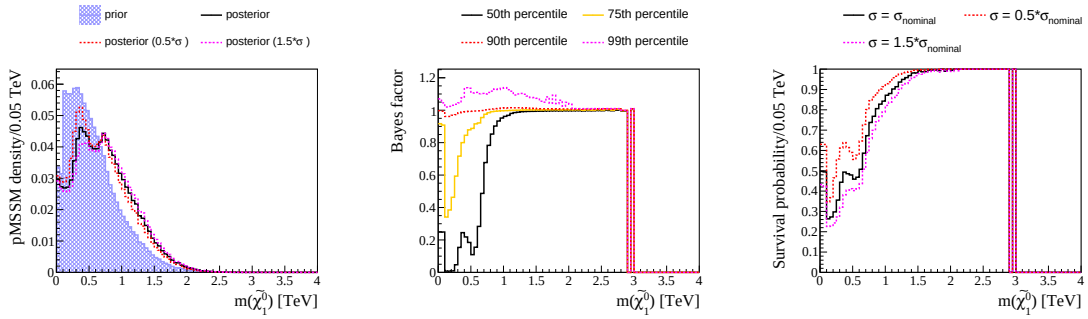

Figure 66: Impact of the considered LHC searches on the LSP mass $m(\widetilde{\chi}_1^0)$, in terms of the prior and posterior densities (left), Bayes factor quantiles (center), and the survival probability (right). A detailed description of the plot elements is given in Section 7.

good complementarity between LHC searches and the low-energy observables included in the prior, because there is a significant shape difference between the marginalized prior and posterior densities. The peak region of the prior, which is the region favored by the included low-energy observables, is severely suppressed in the posterior density.
Inclusion of the LHC data slightly favors points with an LSP mass of approximately $m(\widetilde{\chi}_1^0) \simeq 750\,\text{GeV}$, as seen in the 99th percentile of the Bayes factor. Incidentally, this region is also the same where one the posterior density peaks is located. While a peak in the marginalized posterior density can indicate a preferred region of the model, the fact that the LSP mass is a mass-ordered quantity merits more care than usual. Defining a quantity as the minimum of four masses practically guarantees a peak at small masses. However, the peak in the posterior density is particularly interesting because of the (small) excess in the 99th percentile of the Bayes factor in the same region. This is not at all guaranteed and arises due to a small excess in the data above the background-only hypothesis, consistent with a positive signal characteristic of supersymmetric models in the respective region. The excess is too small, however, to cause the peak in the posterior density, and the effect is washed out in the bulk of the pMSSM phase space. To see this, consider that a change in the Bayes factor of one model from 0.5 to 1 has the same effect on the posterior density as a change in the Bayes factor from 1 to 2. Because the peak in the 99th percentile of the Bayes factor also coincides with the loss of sensitivity to the majority of the pMSSM points, indicated by the median Bayes factor and survival probability rapidly increasing at the same LSP mass, both of these effects increase the posterior density in the same region. The effect of the suppression of the median, corresponding to 50% of models, is much stronger in shaping the marginalized posterior density than the small positive signal seen in the 99th percentile of the Bayes factor. Thus we conclude that the posterior density

peak is almost entirely a result of the loss in sensitivity of the LHC, which results in a steep rise of the median Bayes factor. However, in 2-dimensional projections of the posterior density, the effect of the excesses becomes more clear, as discussed below.
The description above is an overview of the LSP as a whole, but insight can be gained by examining the impact on the LHC to the different LSP types. We can further differentiate the LSP states by their purity. A pure LSP state is here defined as the case when the corresponding square of the mixing matrix entry is greater than 0.95. Mixed LSP states are here defined as the complement to pure states, with the largest contribution to the LSP state being explicitly named. For example, mixed bino LSP refers to non-pure LSP states where the largest square of any mixing matrix entry is the bino component. Variations in sensitivity to different types can be seen in the first bin of the survival probability in Figure 66, which shows a sudden increase compared to the adjacent bin. This increase comes from the fact that the LEP constraints exclude chargino masses below approximately $m(\widetilde{\chi}_1^{\pm}) \lesssim 100\,\text{GeV}$. Because of the approximate degeneracy of the chargino and neutralino masses for wino-like and higgsino-like LSP, this constraint also applies to $m(\widetilde{\chi}_1^0)$ for these types of LSP. This means that the first bin in Figure 66 only contains models with a bino-like LSP, to which the LHC is less sensitive. This is due to two factors: firstly, the electroweak production cross section depends on the type of LSP. The production cross section for winos is approximately twice as large as for higgsinos with a similar mass. Due to the Majorana nature of the neutralinos, which cancels tree-level $\widetilde{\chi}_1^0\widetilde{\chi}_1^0$ production, the cross section for binos is negligible unless there is significant admixture from either the wino or higgsino present. As a consequence, the LHC is more sensitive to winos than higgsinos for a fixed mass, and is much more sensitive to either of them compared to binos for similar masses. Secondly, there are differences in phenomenology of models with a pure bino, pure wino, pure higgsino or mixed bino LSP, which result in different sensitivity. Signal event kinematics and final state objects are greatly influenced by the mass difference between the lightest chargino and the LSP, $\Delta m(\widetilde{\chi}_1^{\pm}, \widetilde{\chi}_1^0)$, and the value of this mass difference is broadly dictated by the type of LSP. The distribution of mass differences is shown for various types of LSP in Figure 67. For model points with a pure bino LSP, $\Delta m(\widetilde{\chi}_1^{\pm}, \widetilde{\chi}_1^0)$ tends to be in the order of hundreds of GeV, whereas for models with a pure higgsino or pure wino LSP, the values of $\Delta m(\widetilde{\chi}_1^{\pm}, \widetilde{\chi}_1^0)$ are much smaller, in the order of a single GeV and hundreds of MeV, respectively. The region between $\Delta m(\widetilde{\chi}_1^{\pm}, \widetilde{\chi}_1^0) \simeq 10\,\text{GeV}$ and $\Delta m(\widetilde{\chi}_1^{\pm}, \widetilde{\chi}_1^0) \simeq 150\,\text{GeV}$ is strongly populated by models with a mixed bino LSP. The mass difference influences the branching fractions to the decay modes and the momentum distribution of particles in the final state, which all influence how large the acceptance of LHC searches is to a signal model. For pure bino models, decays usually occur via on-shell W bosons, with enough phase space in the final state to produce W boson decay products with considerable momentum. At the upper edge of the intermediate $\Delta m(\widetilde{\chi}_1^{\pm}, \widetilde{\chi}_1^0)$ range, where mixed bino states dominate, decays occur close to the W and Z resonances and are challenging to detect above the standard model background. In cases where $\Delta m(\widetilde{\chi}_1^{\pm}, \widetilde{\chi}_1^0)$ is smaller than the W boson mass, decays occur via off-shell W bosons. The difficulty in this region lies in the restricted phase space available to the final state particles, which leads to considerably smaller momentum, which can decrease the analysis acceptance. In the region where pure higgsinos dominate the prior density, leptons from off-shell gauge boson decays can usually no longer be identified as leptons by standard reconstruction algorithms, which presents a different phenomenology to the searches. In this region of $\Delta m(\widetilde{\chi}_1^{\pm}, \widetilde{\chi}_1^0)$, the phase space starts to be so limited that the lifetime of the chargino reaches observable values that can lead to unique signatures like displaced vertices. As $\Delta m(\widetilde{\chi}_1^{\pm}, \widetilde{\chi}_1^0)$ approaches the pion mass, the chargino lifetime and associated decay length $c\tau(\widetilde{\chi}_1^{\pm})$ becomes large enough to result in a new kind of powerful signature, a disappearing track, targeted by the analysis described in Section 6.3.5. For $\Delta m(\widetilde{\chi}_1^{\pm}, \widetilde{\chi}_1^0) < \mathrm{m}_{\pi}$, the only remaining decay modes for the W boson are the muon and electron, which drastically increases the chargino lifetime and decay length to values in the order of meters or even kilometers. Note that the pMSSM should not contain values of $\Delta m(\widetilde{\chi}_1^{\pm}, \widetilde{\chi}_1^0)$ below the pion mass. The fact that they are contained in this scan is due to a limitation in `SPheno` that can generate particle spectra where $\Delta m(\widetilde{\chi}_1^{\pm}, \widetilde{\chi}_1^0)$ is smaller than it should be, as is the case for most of our wino-like LSPs. This is discussed in more detail in Section 5.4.

The cross section and phenomenological differences discussed above cause varying impact on the mass of the LSP. Virtually all surviving models with an LSP mass below $m(\widetilde{\chi}_1^0) \lesssim 200\,\text{GeV}$ have a pure bino or mixed bino LSP. This can be directly seen from the survival probabilities for the subset of models with the respective pure LSP types in Figures 68 and mixed LSP types in Figure 69. Due to the negligible production cross section of binos, the LHC is not directly sensitive to the production of binos, but only to other SUSY particles that are in kinematic reach in terms of their mass, and in

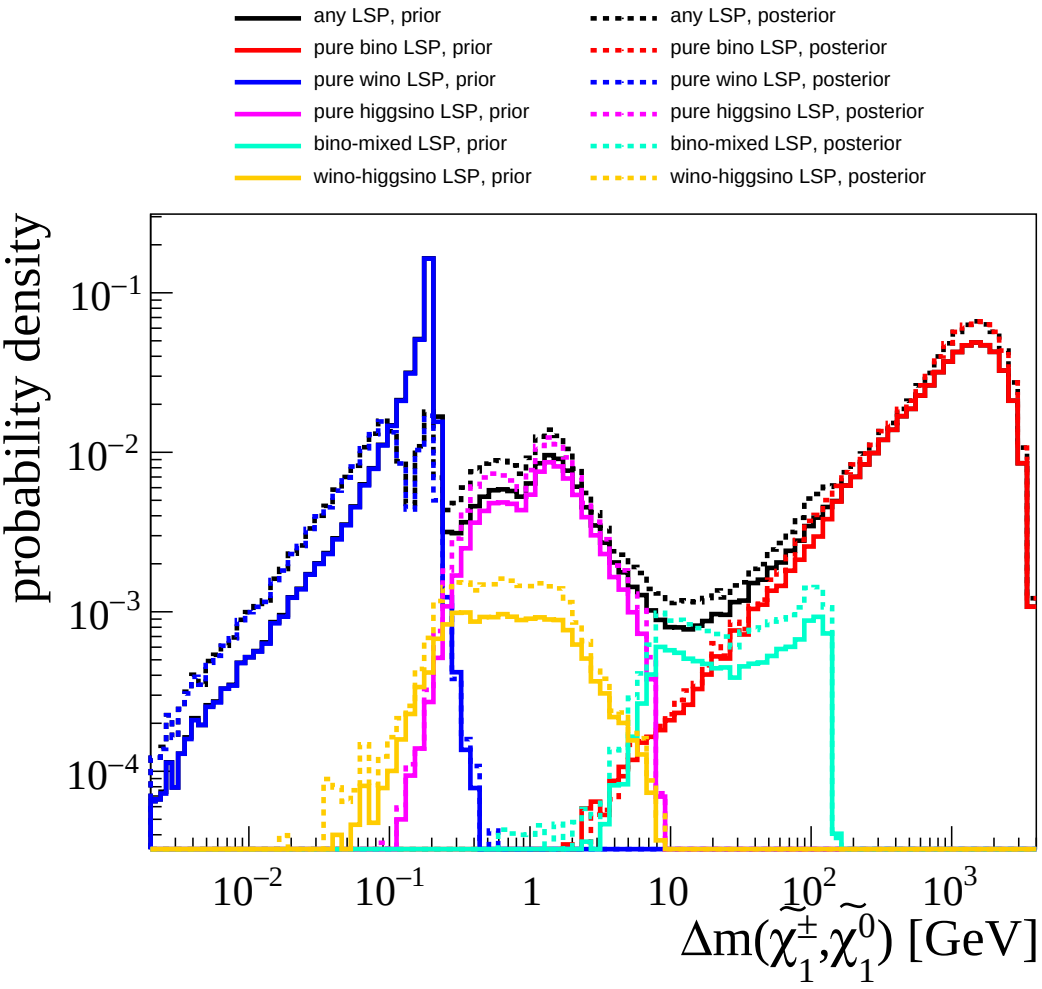

Figure 67: Prior and posterior densities in $\Delta m(\tilde{\chi}_1^{\pm}, \tilde{\chi}_1^0)$ for the different LSP types. Pure states are defined as LSP types where the respective square of the mixing matrix entry is greater than 0.95. Bino-mixed LSP is a non-pure state where the square of the bino component of the mixing matrix is the largest, wino-higgsino LSP are non-pure state where the square of either the wino or the higgsino components are largest.

terms of their production cross section. There remains a region of the pMSSM where the bino is light, but no other SUSY particles are produced in sufficient numbers to be detectable by the LHC. These models then survive the LHC constraints and result in a lower bound on the survival probability. For the same reason, part of the posterior will extend into the small $m(\tilde{\chi}_1^0)$ regime.

The LHC is not sensitive to direct bino production, but the survival probability decreases for models with a pure bino-like LSP towards smaller LSP masses. This occurs for two reasons. First, in the construction of the prior, the LSP mass bounds the allowed parameter space for the other masses from below. This means that the LSP mass and the mass of the other particles are positively correlated – a light LSP on average comes with smaller masses of the other supersymmetric particles. Secondly, a lower-mass bino-like LSP (which is not directly produced) on average has a much larger mass difference to heavier particles that are produced. All other things being equal, a larger mass difference leads to more momentum in the final state, which usually increases the signal acceptance and thus the LHC sensitivity to the model. This affects all types of LSPs, but is more evident in the case of bino-like LSPs, as the LHC is not directly sensitive to their production.

The sensitivity to models with the other types of LSP is larger than to the models with a pure bino LSP. Figure 68 shows the impact the pMSSM space with the different pure LSP states. Here we see that light winos with $m(\tilde{\chi}_1^0) \lesssim 250\,\text{GeV}$ and light higgsinos with $m(\tilde{\chi}_1^0) \lesssim 150\,\text{GeV}$ can be completely excluded by the LHC data if the nominal cross sections are assumed. The downward variation of

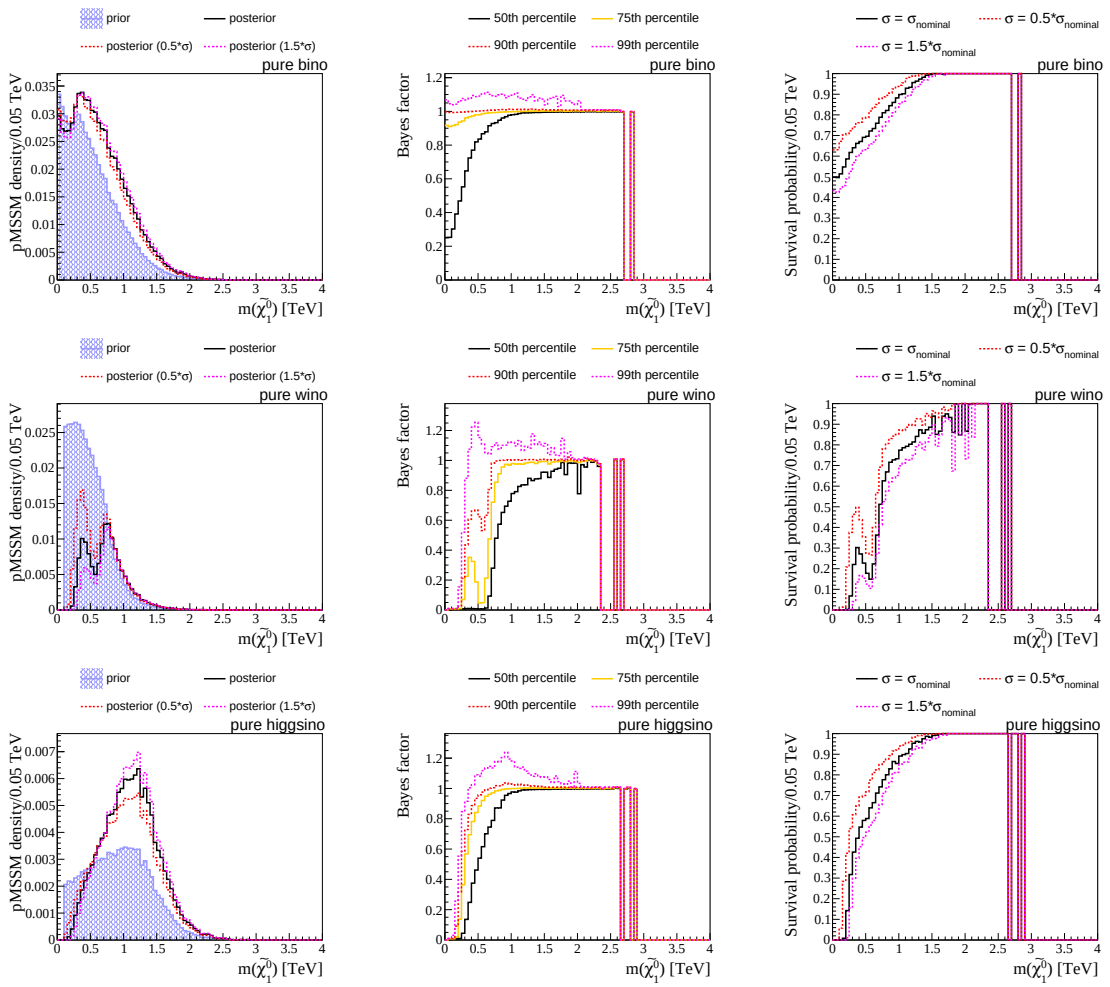

Figure 68: Impact of the considered LHC searches on the LSP mass $m(\tilde{\chi}_1^0)$, in terms of the prior and posterior densities (left column), Bayes factor quantiles (center column), and the survival probability (right column). The rows of plots correspond to the subset of models with pure bino (top row), pure wino (center row), and pure higgsino (bottom row) LSP type. The prior and posterior densities are normalized to the respective fraction of the inclusive prior or posterior density. A detailed description of the plot elements is given in Section 7.

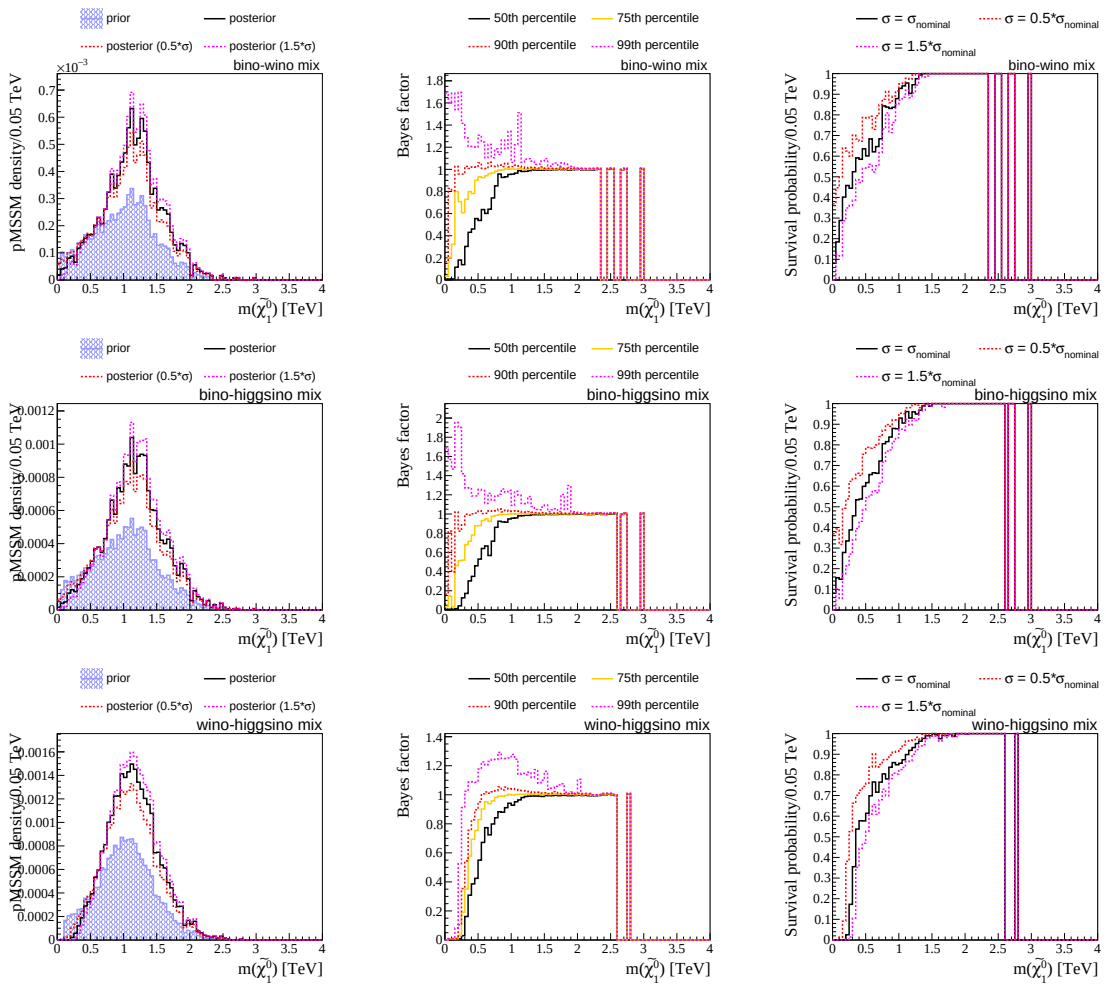

Figure 69: Impact of the considered LHC searches on the LSP mass $m(\tilde{\chi}_1^0)$, in terms of the prior and posterior densities (left column), Bayes factor quantiles (center column), and the survival probability (right column). The rows of plots correspond to the subset of models with mixed bino-wino (top row), mixed bino-higgsino (center row), and mixed wino-higgsino (bottom row) LSP type. The prior and posterior densities are normalized to the respective fraction of the inclusive prior or posterior density. A detailed description of the plot elements is given in Section 7.

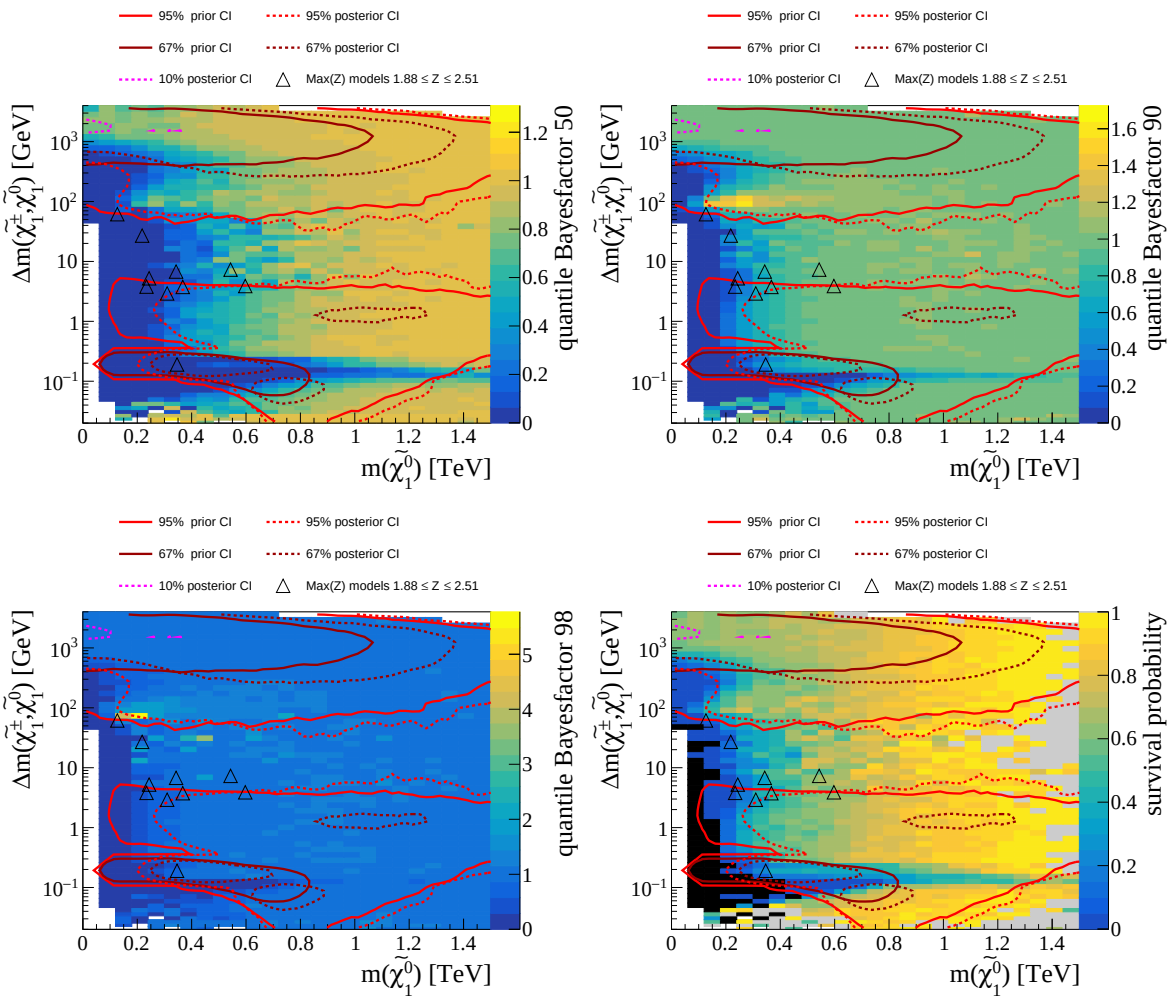

Figure 70: Impact of the considered LHC searches in the plane of $\Delta m(\widetilde{\chi}_1^\pm, \widetilde{\chi}_1^0)$ and $m(\widetilde{\chi}_1^0)$, in terms of the median (top left), 90th (top right), and 98th (bottom left) quantiles of the Bayes factor, as well as the survival probability (bottom right). Grey-colored bins have a survival probability of exactly one, black-colored bins have a survival probability of exactly zero, white bins are empty. A detailed description of the plot elements is given in Section 7.

the cross section still allows for winos with $m(\widetilde{\chi}_1^0) \geq 150\,\text{GeV}$ and higgsinos with $m(\widetilde{\chi}_1^0) \geq 100\,\text{GeV}$. The latter does not represent a strong improvement over the LEP constraints. The sensitivity to all models with winos or higgsinos in these respective mass ranges comes from the $\text{p}_\text{T}^\text{miss}$+jets search. Due to the small $\Delta m(\widetilde{\chi}_1^\pm, \widetilde{\chi}_1^0)$ of pure winos and higgsinos compared to the pure bino LSP case, as seen in Figure 67, the hadronic or leptonic components of the $\widetilde{\chi}_1^\pm$ or $\widetilde{\chi}_2^0$ decays from these models have too small p_T to be reconstructed. In events in which the initial state radiation has a sufficiently large p_T, the non-reconstructed and thus invisible $\widetilde{\chi}_1^\pm$ or $\widetilde{\chi}_2^0$ decay products recoil off this initial state radiation, which results in a $\text{p}_\text{T}^\text{miss}$+jet signature from signal events to which the search is sensitive. This gives the baseline sensitivity to all pMSSM models with sufficient production cross section that results in the complete exclusion of the small masses for winos and higgsinos. In Figure 66, there is a local maximum in the distributions of the posterior, the median Bayes factor and the survival probability in the range $m(\widetilde{\chi}_1^0) \in (400, 600)\,\text{GeV}$. This local maximum is the result of a smaller sensitivity to promptly decaying winos than to long-lived winos. To see this, first note that Figure 68 shows that the higher survival probability and median Bayes factor originates in models with a pure wino-like LSP. We can learn more about these winos by looking at the credibility intervals for the prior and posterior density in Figure 70. There is a large portion of the 67% prior credibility interval at very small $\Delta m(\widetilde{\chi}_1^\pm, \widetilde{\chi}_1^0)$, corresponding to models with a wino-like LSP (compare Figure 67). The results from LHC data disfavor small $m(\widetilde{\chi}_1^0)$, especially at small $\Delta m(\widetilde{\chi}_1^\pm, \widetilde{\chi}_1^0)$, which pushes the probability

density to larger $m(\widetilde{\chi}_1^0)$ and result in the posterior density. The part of the credibility interval with $\Delta m(\widetilde{\chi}_1^\pm, \widetilde{\chi}_1^0) > m_\pi$, where $\widetilde{\chi}_1^\pm$ decays promptly, extends to lower $m(\widetilde{\chi}_1^0)$ – LHC is less sensitive. The part of the interval with $\Delta m(\widetilde{\chi}_1^\pm, \widetilde{\chi}_1^0) < m_\pi$, where the chargino is long-lived, is pushed to larger $m(\widetilde{\chi}_1^0)$ – LHC is more sensitive. This is because $\Delta m(\widetilde{\chi}_1^\pm, \widetilde{\chi}_1^0) \simeq m_\pi$ and below leads to measurable chargino lifetimes to which the search for disappearing tracks is directly sensitive. The sensitivity to prompt charginos comes from the jets+$\mathrm{p_T^{miss}}$search and is weaker. The sensitivity to winos decreases again at extremely small mass differences, $\Delta m(\widetilde{\chi}_1^\pm, \widetilde{\chi}_1^0) \ll \mathrm{m}_\pi$. This is because the lifetime of the charginos extends into the hundreds of kilometers there, which makes the charginos stable on the length scale of the detector. This results in the loss of signal acceptance in the search for disappearing tracks, because the tracks no longer disappear. It also results in the loss of sensitivity of the $\mathrm{p_T^{miss}}$+jets search, because the stable charginos are reconstructed as muons, which in this analysis are vetoed. The peaks of the distributions of $\Delta m(\widetilde{\chi}_1^\pm, \widetilde{\chi}_1^0)$ for the different types of LSP in Figure 67 show up as distinct credibility intervals in Figure 70. The credibility intervals at large $\Delta m(\widetilde{\chi}_1^\pm, \widetilde{\chi}_1^0)$ are populated by models with a bino-like LSP. Higgsino-like LSP populate the credibility interval at $\Delta m(\widetilde{\chi}_1^\pm, \widetilde{\chi}_1^0)$ $\simeq 2\,\mathrm{GeV}$ and wino-like LSP at $\Delta m(\widetilde{\chi}_1^\pm, \widetilde{\chi}_1^0) \simeq 200\,\mathrm{MeV}$. Because the LHC data so far has been largely consistent with the SM, the posterior is mostly shaped due to suppression of regions of the pMSSM that would produce strong signals in the data. If the LHC data was less consistent with the SM, there could be more regions in the pMSSM where the posterior density is heightened as a consequence of large Bayes factors in the pMSSM.

Relatively small variations in $\Delta m(\widetilde{\chi}_1^\pm, \widetilde{\chi}_1^0)$ bring about significant changes in analysis sensitivity. This is both the result of the rapidly changing final state particle lifetime and transverse momentum distributions as a function of $\Delta m(\widetilde{\chi}_1^\pm, \widetilde{\chi}_1^0)$, the former of which can be seen in Figure 71. Sharp transitions in the LSP type as a function of $\Delta m(\widetilde{\chi}_1^\pm, \widetilde{\chi}_1^0)$, as seen in Figure 67, particularly at small $\Delta m(\widetilde{\chi}_1^\pm, \widetilde{\chi}_1^0)$, also play a role. These effects lead to discrete jumps in the sensitivity both in terms of the LSP mass, shown for the $\mathrm{p_T^{miss}}$+jets analysis in Figure 72, and in terms of the total production cross section as shown for the $\mathrm{p_T^{miss}}$+jets analysis in Figure 73. The effect of the changing LSP type leads to a sudden increase in the sensitivity of the $\mathrm{p_T^{miss}}$+jets search at $\Delta m(\widetilde{\chi}_1^\pm, \widetilde{\chi}_1^0) \simeq 200\,\mathrm{MeV}$, as the dominant LSP type changes from mostly higgsino-like LSPs in the models with larger $\Delta m(\widetilde{\chi}_1^\pm, \widetilde{\chi}_1^0)$ to models with almost exclusively wino-like LSP. The increase in sensitivity here is a result of the larger production cross section of wino-like LSPs compared to higgsino-like LSPs, which allows the $\mathrm{p_T^{miss}}$+jets search to constrain models with larger $m(\widetilde{\chi}_1^0)$. There is an additional, more subtle, difference to the sensitivity of the $\mathrm{p_T^{miss}}$+jets search to wino-like LSP and higgsino-like LSP, which explains the apparently increased sensitivity to wino-like LSP even in cases where the cross section is similar, which is visible in Figure 73 as a narrow region of small survival probability at $\Delta m(\widetilde{\chi}_1^\pm, \widetilde{\chi}_1^0) \simeq 200\,\mathrm{MeV}$. This feature can be explained by the fact that at similar production cross sections, wino-like LSP are heavier than higgsino-like LSP, which leads to a harder $\mathrm{p_T^{miss}}$ distribution. This in turn increases the signal acceptance of the $\mathrm{p_T^{miss}}$+jets search. The sudden drop in sensitivity as $\Delta m(\widetilde{\chi}_1^\pm, \widetilde{\chi}_1^0)$ becomes even smaller results from the lifetime increase of the chargino as $\Delta m(\widetilde{\chi}_1^\pm, \widetilde{\chi}_1^0)$ approaches, and finally crosses, the pion mass. As previously discussed, this leads to detector-stable charginos with lifetimes in the order of meters to kilometers, which consistently trigger the muon veto of the $\mathrm{p_T^{miss}}$+jets analysis, resulting in the loss of sensitivity of the $\mathrm{p_T^{miss}}$+jets analysis to these models. Because the search for disappearing tracks is sensitive to a large range of these long-lived charginos, the sensitivity of the LHC to this part of the pMSSM is maintained.

Overall, the LHC has the most impact on models with a pure wino. This can be seen by the fact that the integral of the posterior density for pure winos in Figure 68 (which is normalized to the fraction of pure winos to the inclusive posterior) shrinks considerably compared to the prior, while the integrals for pure binos and pure higgsinos, as well as for mixed LSP scenarios (Figure 69) increases. The reason for this is two-fold: first, a large part of the pMSSM where the LSP is a pure wino contains long-lived charginos, to which the LHC is very sensitive. Second, the cross section for direct production of winos is much larger than for higgsinos and binos, which means that a larger range of LSP masses can be constrained due to their generic ISR-jet+missing transverse momentum signature.

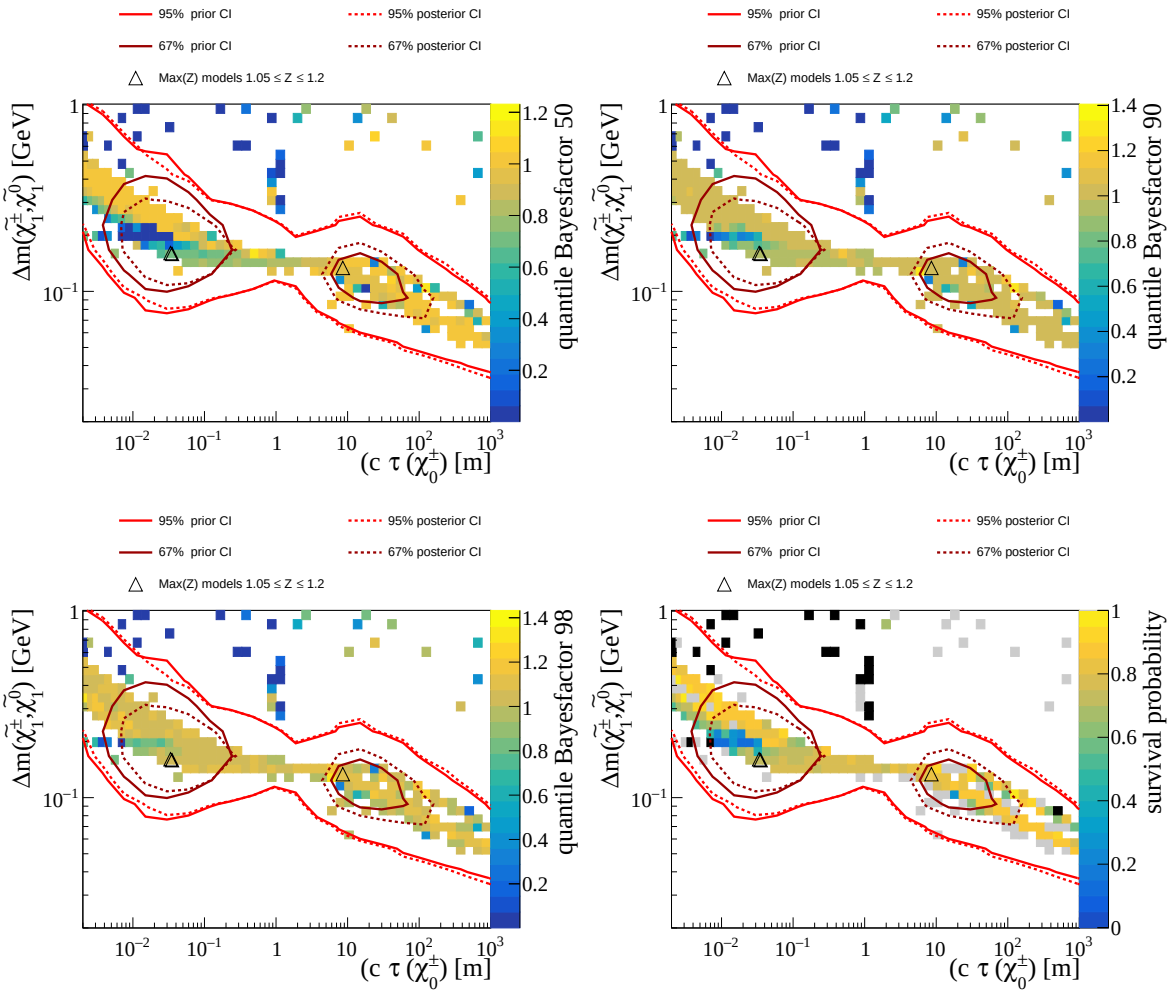

Figure 71: Impact from the p_T^{miss}+jets search on charginos with $c\tau(\widetilde{\chi}_1^{\pm})$ near the pion mass, in terms of the median (top left), 90th (top right), and 98th (bottom left) quantiles of the Bayes factor, as well as the survival probability (bottom right). Grey-colored bins have a survival probability of exactly one, black-colored bins have a survival probability of exactly zero, white bins are empty. A detailed description of the plot elements is given in Section 7. Because the chargino lifetime is almost entirely determined by $\Delta m(\widetilde{\chi}_1^{\pm}, \widetilde{\chi}_1^0)$, the pMSSM only exists in a narrow region in the plane of $\Delta m(\widetilde{\chi}_1^{\pm}, \widetilde{\chi}_1^0)$ and $c\tau(\widetilde{\chi}_1^{\pm})$.

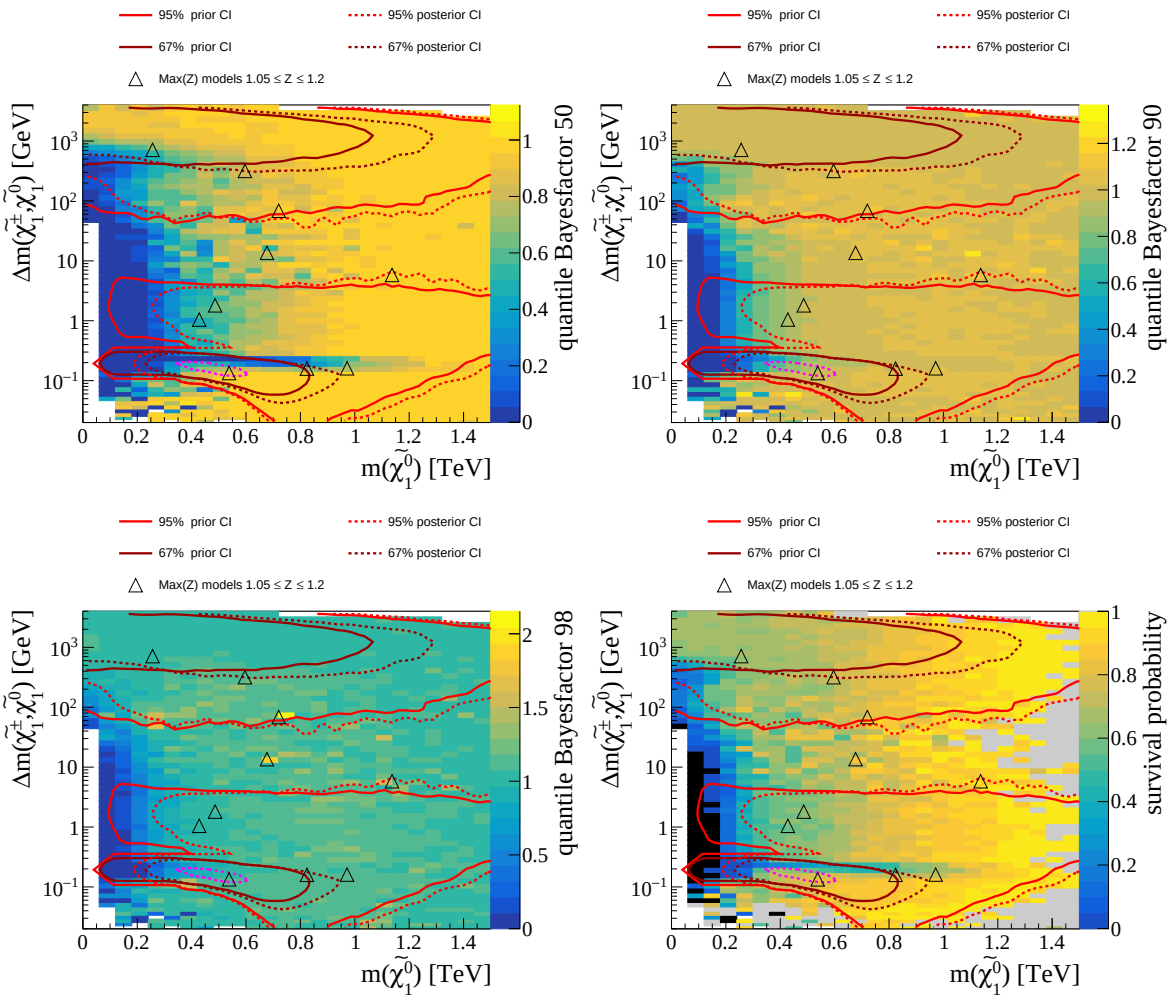

Figure 72: Impact from the search for p_T^{miss}+jets in the plane of $\Delta m(\tilde{\chi}_1^{\pm}, \tilde{\chi}_1^0)$ and $m(\tilde{\chi}_1^0)$, in terms of the median (top left), 90th (top right), and 98th (bottom left) quantiles of the Bayes factor, as well as the survival probability (bottom right). Grey-colored bins have a survival probability of exactly one, black-colored bins have a survival probability of exactly zero, white bins are empty. A detailed description of the plot elements is given in Section 7.

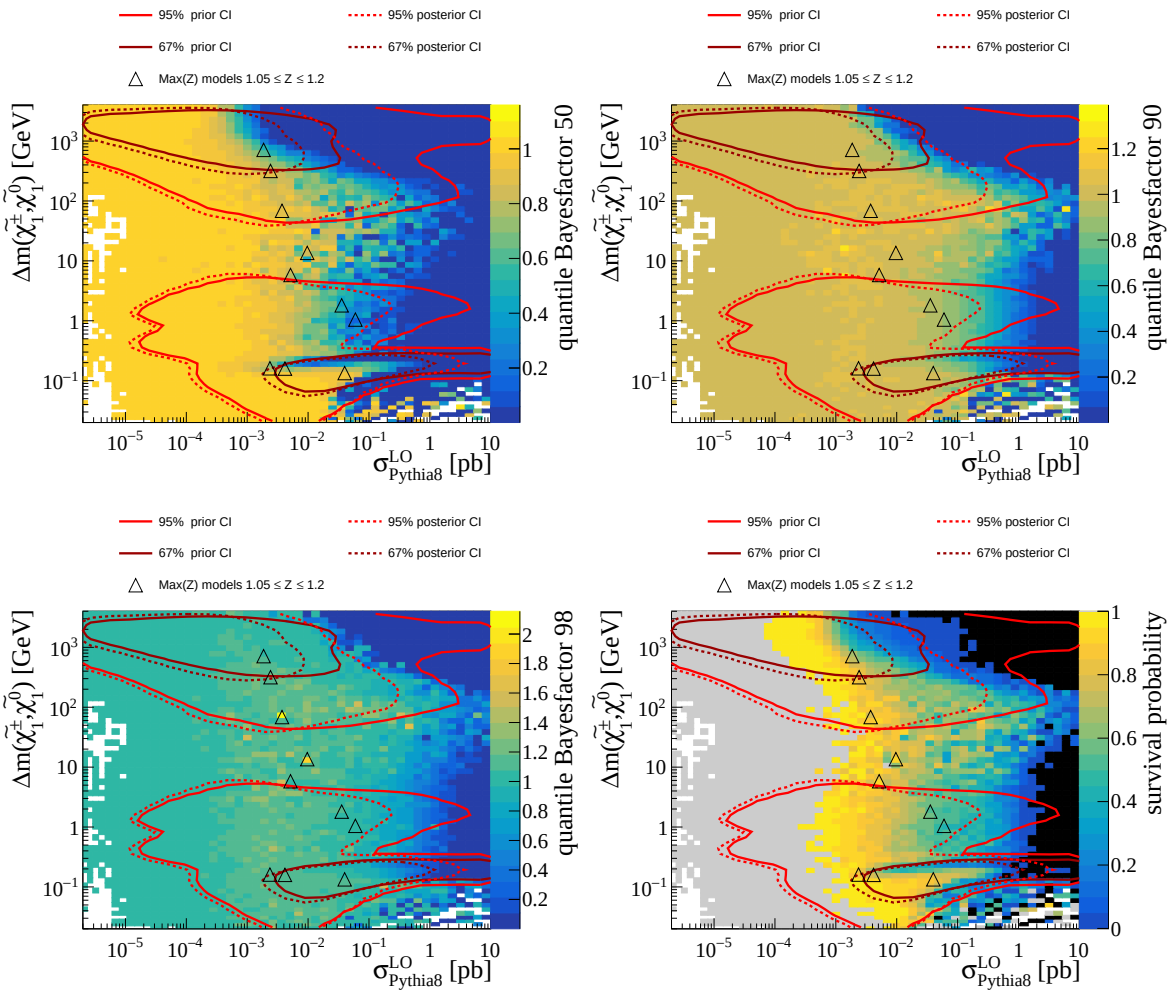

Figure 73: Impact of the p_T^{miss}+jets search in the plane of $\Delta m(\tilde{\chi}_1^\pm, \tilde{\chi}_1^0)$ and $\sigma^{total}_{Pythia8@LO}$, in terms of the median (top left), 90th (top right), and 98th (bottom left) quantiles of the Bayes factor, as well as the survival probability (bottom right). Grey-colored bins have a survival probability of exactly one, black-colored bins have a survival probability of exactly zero, white bins are empty. A detailed description of the plot elements is given in Section 7.

For models with a bino-mixed LSP, a population of models that increases with smaller LSP masses fit an excess in the data, as seen in the extreme quantiles of the Bayes factor in Figure 69. This can be traced to an excess in the data in the multi-lepton search. The important feature to fit the excess here is the difference in chargino and LSP mass. The relevant signature for these models is that of a low-mass LSP with $\Delta m(\widetilde{\chi}_1^{\pm}, \widetilde{\chi}_1^0) \simeq 100\,\text{GeV}$. This is because the leptonic decay mode of the produced charginos then fit the required kinematics to be accepted into the signal regions at the rate that fits the excess. The steadily rising Bayes factor towards lower LSP masses is the result of an increased cross section for the same $\Delta m(\widetilde{\chi}_1^{\pm}, \widetilde{\chi}_1^0)$. This hypothesis is supported by Figures 70, 75, and 74, which show that the Bayes factor is consistently above one for both the median and higher quantiles in a region at approximately $\Delta m(\widetilde{\chi}_1^{\pm}, \widetilde{\chi}_1^0) \simeq 100\,\text{GeV}$. Notice that in Figure 74, which shows only the impact of the multi-lepton search for $\Delta m(\widetilde{\chi}_1^{\pm}, \widetilde{\chi}_1^0) \simeq 100\,\text{GeV}$, there are many bins that show even median Bayes factors above one, and in which no model is excluded by this search (colored grey in the survival probability). The attentive reader may have noticed that Figure 67 shows that at large $\Delta m(\widetilde{\chi}_1^{\pm}, \widetilde{\chi}_1^0)$, the LSP type is mostly labeled pure bino, with only a small fraction of models labeled bino-mixed. Note that the labeling of whether a state is pure or mixed is distinction somewhat arbitrary for edge cases where the square of the corresponding mixing matrix entry is close to the threshold. Because the chargino mass is independent of the bino mass, $\Delta m(\widetilde{\chi}_1^{\pm}, \widetilde{\chi}_1^0)$ itself can be used as a measure of the LSP mixing if the LSP is mostly bino-like and not mostly wino-like. The lower $\Delta m(\widetilde{\chi}_1^{\pm}, \widetilde{\chi}_1^0)$, the larger the admixture of wino or higgsino into the LSP tends to be. Finally, by comparing the distributions for wino-higgsino scenarios in Figure 69 with those of pure winos and higgsinos in Figure 68, we find that the mixed scenario is very similar to the pure higgsino case. However, because the prior for all mixed-LSP scenarios strongly falls towards small LSP masses, the direct effect on the posterior distribution is very limited for mixed LSP scenarios.

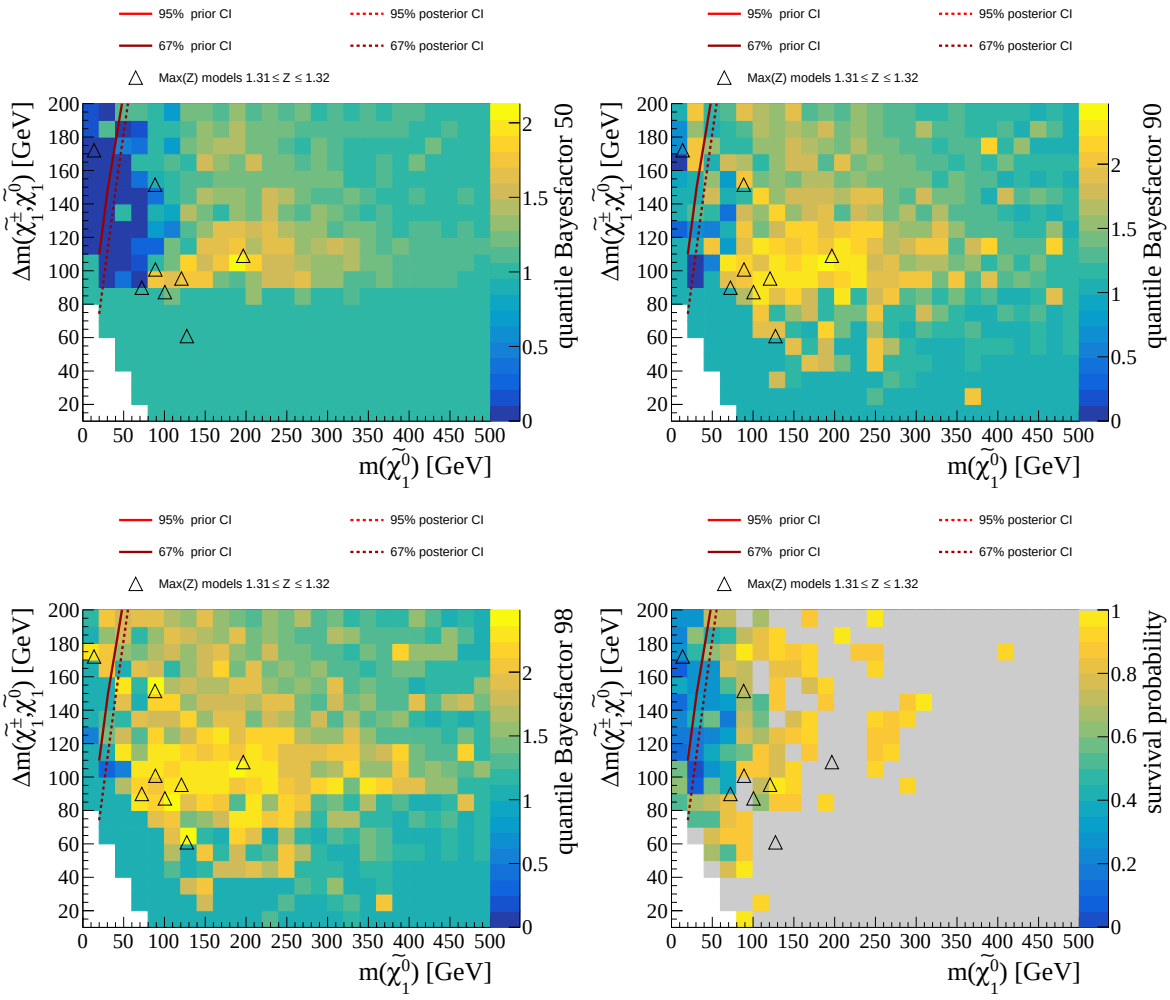

Figure 74: Impact of the multi-lepton search in the plane of $\Delta m(\widetilde{\chi}_1^{\pm}, \widetilde{\chi}_1^0)$ and $m(\widetilde{\chi}_1^0)$ in a region that fits a small excess in the multi-lepton search, in terms of the median (top left), 90th (top right), and 98th (bottom left) quantiles of the Bayes factor, as well as the survival probability (bottom right). Grey-colored bins have a survival probability of exactly one, black-colored bins have a survival probability of exactly zero, white bins are empty. A detailed description of the plot elements is given in Section 7.

One of the most powerful set of predictors for the sensitivity of LHC are $\Delta m(\widetilde{\chi}_1^\pm, \widetilde{\chi}_1^0)$ and the total production cross section of the models, which includes all possible production modes. This plane is shown in Figure 75. There are three peaks in the posterior density, indicated by the 67% posterior

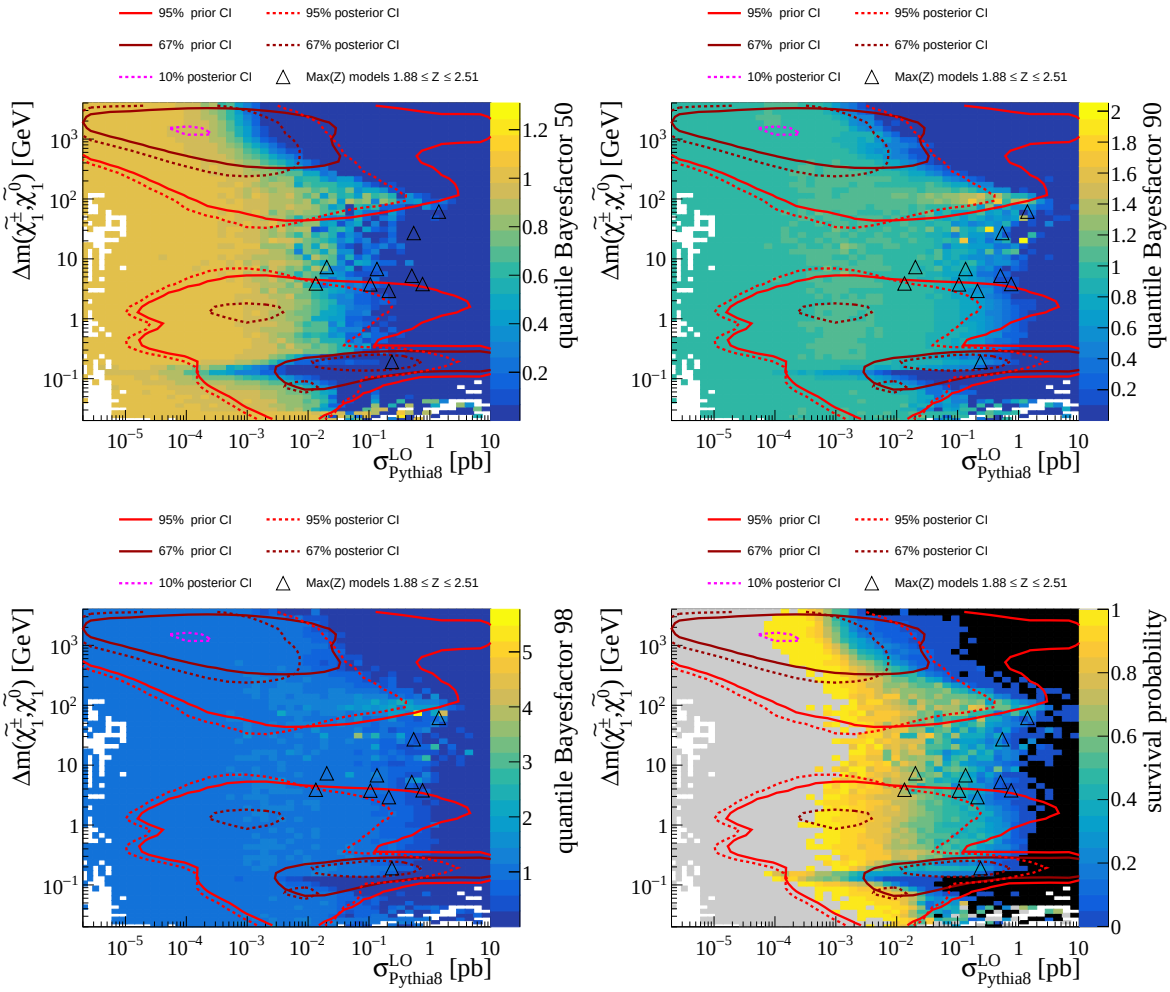

Figure 75: Impact of the considered LHC searches in the plane of $\Delta m(\widetilde{\chi}_1^\pm, \widetilde{\chi}_1^0)$ and $\sigma^{\text{total}}_{\text{Pythia8@LO}}$, in terms of the median (top left), 90th (top right), and 98th (bottom left) quantiles of the Bayes factor, as well as the survival probability (bottom right). A detailed description of the plot elements is given in Section 7.

credibility intervals, and corresponding to models with different respective pure LSP states. These peaks can be seen in credibility intervals in both Figure 70 and 75. This means that all types of LSP remain viable after the LHC data, to approximately the same degree. It is noticeable that the furthest extend, in terms of large total production cross sections, of the credibility intervals of bino-like LSP at large $\Delta m(\widetilde{\chi}_1^\pm, \widetilde{\chi}_1^0)$ and higgsinos are very similar, indicating a common kinematic feature. This might mean that the direct production of charginos is not the most important factor that affects the shift of the posterior w.r.t. the prior, but rather that the strong sector most determines the posterior for both types of LSP. This is different in the case of models with a pure wino-like LSP, where the credibility intervals of the posterior reach to far larger cross sections. One reason for this is the prior, which also extends towards larger cross sections compared to the other types of LSP.
The pMSSM in this plane can be split into five regions in terms of their most important phenomenology and searches that target them:

- At large $\Delta m(\widetilde{\chi}_1^\pm, \widetilde{\chi}_1^0) \gg 500\,\text{GeV}$, colored SUSY dominates in terms of importance. This is because the mass of the chargino is inversely correlated to its production cross section. At some mass of the chargino, the cross section for the direct production of charginos becomes

negligible compared to any colored sparticles that might exit in that model. This happens at different masses for higgsino-like charginos and wino-like charginos, which have smaller and larger production cross sections, respectively. The region of large $\Delta m(\widetilde{\chi}_1^{\pm}, \widetilde{\chi}_1^0)$ and cross section is thus populated by models where at least part of the colored particle spectrum is light enough to generate the cross section. In this region, searches for colored particles provide the most sensitivity, most notably inclusive searches for p_T^{miss}+jets. The sensitivity of the LHC is greater in regions where only colored particles are produced than in regions where both colored particles and charginos are light. This can be seen in Figure 75 from the fact that the regions of small median Bayes factors and survival probabilities reaches to smaller cross sections the larger the mass difference $\Delta m(\widetilde{\chi}_1^{\pm}, \widetilde{\chi}_1^0)$. Because of the inverse relationship of mass and production cross section, a larger chargino mass $m(\widetilde{\chi}_1^{\pm})$ (and with that, $\Delta m(\widetilde{\chi}_1^{\pm}, \widetilde{\chi}_1^0)$) means a smaller fraction of the total cross section. The sensitivity is lower for smaller $\Delta m(\widetilde{\chi}_1^{\pm}, \widetilde{\chi}_1^0)$ because the presence of charginos, either directly produced or in the decay chains of gluinos and squarks, leads to an increased occurrence of leptons in the signal events. These leptons are vetoed in the generic search for p_T^{miss}+jets that is most sensitive in most of the pMSSM. At the same time, the production cross section for colored particles, to which the LHC is very sensitive, is smaller for the same total cross section, because it makes up a smaller fraction of the total. In this region at large $\Delta m(\widetilde{\chi}_1^{\pm}, \widetilde{\chi}_1^0)$, the LHC can exclude models down to production cross sections of $\sigma^{\text{total}}_{\text{Pythia8@LO}} \simeq 10^{-4}\,\text{pb}$ and almost completely excludes the model space with $\sigma^{\text{total}}_{\text{Pythia8@LO}} \gtrsim 10^{-1}\,\text{pb}$.

- The second region is located around $\Delta m(\widetilde{\chi}_1^{\pm}, \widetilde{\chi}_1^0) \simeq 100\,\text{GeV}$. The part of this region with large total cross sections is characterized by the presence of both models with a large cross section of colored particles, and models with a large cross section of electroweakinos. The occurrence of models with a light colored sector and thus significant production cross section of squarks or gluinos is, to first order, independent of $\Delta m(\widetilde{\chi}_1^{\pm}, \widetilde{\chi}_1^0)$ and almost constant in this plane. However, the occurrence of models with significant production cross section of electroweakinos increases with smaller $\Delta m(\widetilde{\chi}_1^{\pm}, \widetilde{\chi}_1^0)$, which results in a larger fraction of models with electroweakino production for smaller $\Delta m(\widetilde{\chi}_1^{\pm}, \widetilde{\chi}_1^0)$. The fact that the models in this region are more heterogeneous also leads to the much larger extend, in terms of the production cross section, of the region with varied survival probability. The sensitivity to the colored production modes is, statistically speaking, smaller here than in the first region. This can be explained by the fact that the mass of the chargino is almost always in between the LCSP and the LSP at small $\Delta m(\widetilde{\chi}_1^{\pm}, \widetilde{\chi}_1^0)$, and the p_T^{miss}+jets search is less sensitive to the cascade decay through the chargino due to the increased occurrence of leptons in the decay chains. Comparatively large $\Delta m(\widetilde{\chi}_1^{\pm}, \widetilde{\chi}_1^0)$ in the order of $\sim 100\,\text{GeV}$ allow for the on-shell decay of the chargino, which comes with a large enough final state phase space to accommodate high-p_T leptons that lead to a veto of the event. This also explains that the smallest cross section where individual models are still excluded is significantly larger than for large $\Delta m(\widetilde{\chi}_1^{\pm}, \widetilde{\chi}_1^0)$. Searches that include one or more leptons in their signal regions are especially sensitive in this region, because of the presence of leptons in decay chains that contain charginos or neutralinos. The mass splitting of $\Delta m(\widetilde{\chi}_1^{\pm}, \widetilde{\chi}_1^0) > m(\text{Z}^0)$ allows for the on-shell decays of the respective gauge bosons, which provides sufficiently hard p_T of the final state leptons to be identified as such. As a result, the multi-lepton searches achieve their highest sensitivity in this region. As was previously discussed in this section, there is a class of models with $\Delta m(\widetilde{\chi}_1^{\pm}, \widetilde{\chi}_1^0) \simeq 100\,\text{GeV}$ that fits a small excess of data in the multi-lepton search. In this region at $\Delta m(\widetilde{\chi}_1^{\pm}, \widetilde{\chi}_1^0) \simeq 100\,\text{GeV}$, the LHC can exclude models down to production cross sections of $\sigma^{\text{total}}_{\text{Pythia8@LO}} \simeq 10^{-3}\,\text{pb}$ and almost completely excludes the model space with $\sigma^{\text{total}}_{\text{Pythia8@LO}} \gtrsim 1\,\text{pb}$.

- The third region is in the vicinity of the masses of the electroweak gauge bosons, spanning approximately from $\Delta m(\widetilde{\chi}_1^{\pm}, \widetilde{\chi}_1^0) \gtrsim 70\,\text{GeV}$ to $\Delta m(\widetilde{\chi}_1^{\pm}, \widetilde{\chi}_1^0) \simeq 100\,\text{GeV}$. While the signal final state does not substantially differ from that at larger $\Delta m(\widetilde{\chi}_1^{\pm}, \widetilde{\chi}_1^0)$, the SM background composition contains many more events from production of W and Z bosons. This means that dedicated signal regions or searches are required to be sensitive to these models, however, no such search is included in this study. For this reason, the sensitivity is lowest here in terms of $\Delta m(\widetilde{\chi}_1^{\pm}, \widetilde{\chi}_1^0)$, with individual models surviving at cross sections in the order of $\sigma^{\text{total}}_{\text{Pythia8@LO}} \simeq 10\,\text{pb}$.

- The fourth region roughly spans $\Delta m(\widetilde{\chi}_1^{\pm}, \widetilde{\chi}_1^0)$ ranging from 10 GeV to 70 GeV. It is sparsely populated, as these $\Delta m(\widetilde{\chi}_1^{\pm}, \widetilde{\chi}_1^0)$ values are above the natural values for winos and higgsinos,

and the space where both the bino mass and either the higgsino or wino mass are small is only sparsely sampled in this scan. This region is covered by the di-lepton SOS search, as well as the generic search for p_T^{miss}+jets, which leads to a slight recovery of sensitivity compared to the third region.

- In the fifths region, at $\Delta m(\widetilde{\chi}_1^{\pm}, \widetilde{\chi}_1^0) \lesssim 10\,\text{GeV}$, the sensitivity of the p_T^{miss}+jets search increases again. This is because the p_T spectrum of the final state leptons decreases with lower $\Delta m(\widetilde{\chi}_1^{\pm}, \widetilde{\chi}_1^0)$, until at some point the p_T of the leptons is so small that they are no longer reconstructed as leptons, and thus the signal events are no longer vetoed on that basis. The phenomenology drastically changes again as $\Delta m(\widetilde{\chi}_1^{\pm}, \widetilde{\chi}_1^0)$ approaches the pion mass, and as it crosses that threshold. In this region with $\Delta m(\widetilde{\chi}_1^{\pm}, \widetilde{\chi}_1^0) \lesssim 300\,\text{MeV}$, the lifetime of the charginos starts to increase noticeably and becomes detectable (see Figure 76), as a displaced vertex signature above the pion mass, mostly as disappearing tracks at and slightly below the pion mass, and as heavy stable charged particles (HSCP) well below the pion mass. In this final region, the LHC can exclude models down to production cross sections of $\sigma^{\text{total}}_{\text{Pythia8@LO}} \simeq 10^{-4}\,\text{pb}$ and almost completely excludes the model space with $\sigma^{\text{total}}_{\text{Pythia8@LO}} \gtrsim 2\,\text{pb}$ at $\Delta m(\widetilde{\chi}_1^{\pm}, \widetilde{\chi}_1^0) \gtrsim m_\pi$, and down to $\sigma^{\text{total}}_{\text{Pythia8@LO}} \simeq 10^{-1}\,\text{pb}$ for $\Delta m(\widetilde{\chi}_1^{\pm}, \widetilde{\chi}_1^0) \lesssim m_\pi$. Figure 76 shows that while the sampled phase space below the pion mass is very tiny in terms of $\Delta m(\widetilde{\chi}_1^{\pm}, \widetilde{\chi}_1^0)$, only covering tens to a hundred MeV, it corresponds to a very large region in terms of the chargino lifetime that stretches from approximately $c\tau(\chi_1^{\pm}) < 1\,\text{cm}$ to $c\tau(\chi_1^{\pm}) \gg 1\,\text{km}$. Figure 75 shows that the LHC is highly sensitive to these distinct features and is able to exclude models down to very small production cross sections. This includes well over 80% of models with $c\tau(\widetilde{\chi}_1^{\pm})$ between 1 cm and 10 m, as can be seen in Figure 77.

It should be noted here that the pMSSM should not contain chargino lifetimes that far exceed $c\tau(\widetilde{\chi}_1^{\pm}) \gtrsim 10\,\text{cm}$. The fact that these models exist in this scan is due to a limitation of the spectrum generators that result in too-low $\Delta m(\widetilde{\chi}_1^{\pm}, \widetilde{\chi}_1^0)$, even to values below the pion mass. Radiative corrections should always keep $\Delta m(\widetilde{\chi}_1^{\pm}, \widetilde{\chi}_1^0)$ above the pion mass, which prohibits these extremely long live times. This is not to say that the LHC is not sensitive to the *observable* $c\tau(\widetilde{\chi}_1^{\pm})$, but rather that there exists no map of $c\tau(\widetilde{\chi}_1^{\pm}) \gg 10\,\text{cm}$ onto the pMSSM parameter space.

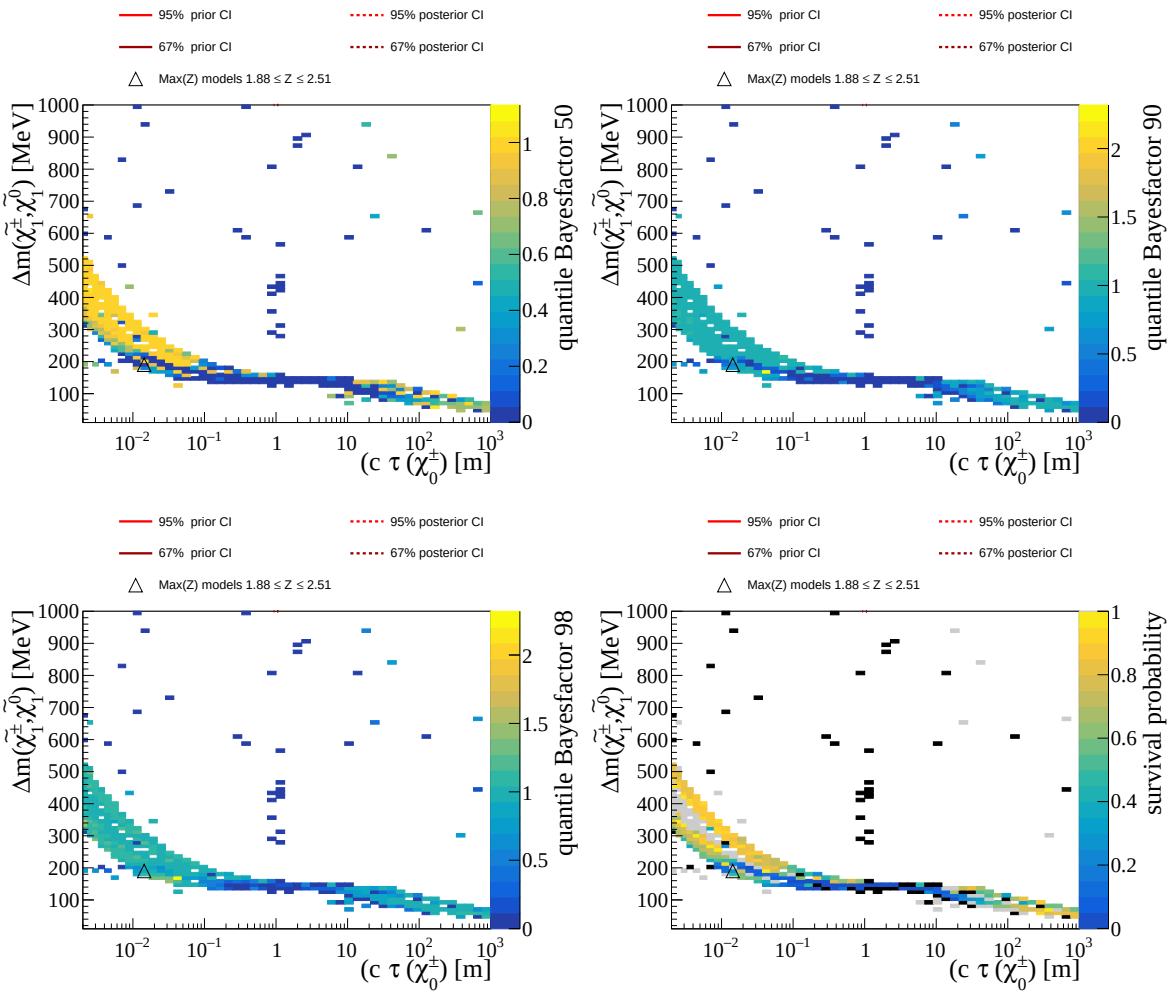

Figure 76: Impact of the LHC in the plane of $\Delta m(\widetilde{\chi}_1^{\pm}, \widetilde{\chi}_1^0)$ and $c\tau(\widetilde{\chi}_1^{\pm})$ close to the pion mass, in terms of the median (top left), 90th (top right), and 98th (bottom left) quantiles of the Bayes factor, as well as the survival probability (bottom right). Grey-colored bins have a survival probability of exactly one, black-colored bins have a survival probability of exactly zero, white bins are empty. A detailed description of the plot elements is given in Section 7.

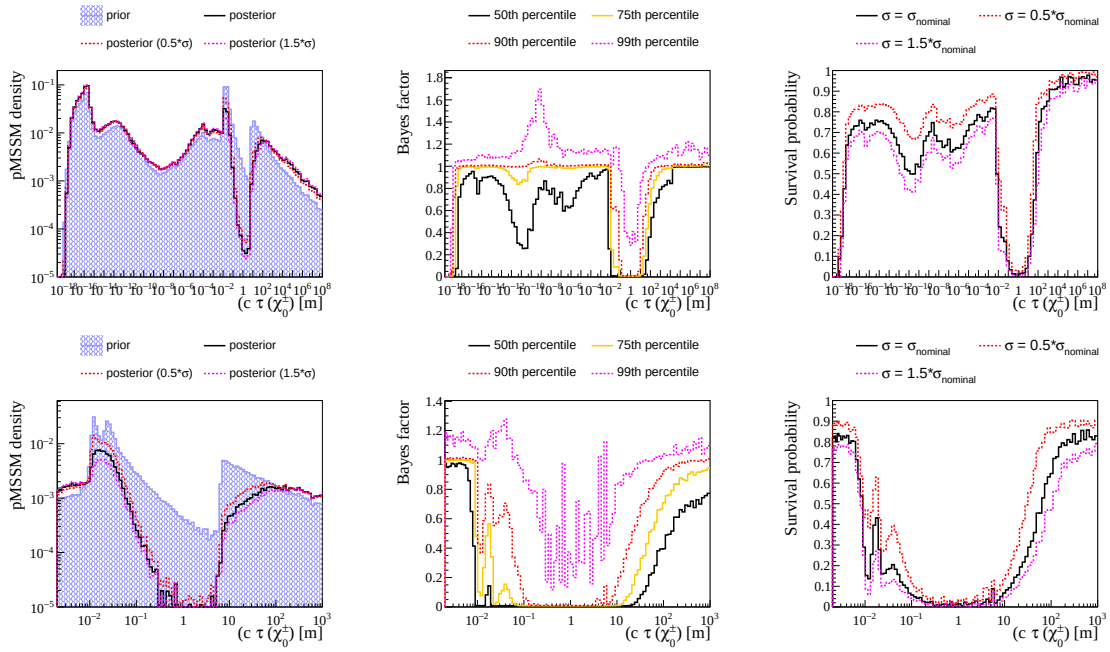

Figure 77: Impact of the LHC on the lighter chargino lifetime $c\tau(\widetilde{\chi}_1^\pm)$, in terms of the prior and posterior densities (left column), Bayes factor quantiles (center column), and the survival probability (right column). The upper row shows a very large $c\tau(\widetilde{\chi}_1^\pm)$ region, the bottom row of histograms are zoomed in to the directly observable $c\tau(\widetilde{\chi}_1^\pm)$ region. A detailed description of the plot elements is given in Section 7.

8.2.2 Sleptons

As a reminder, the masses of the respective left-chiral and right-chiral selectron and smuon are degenerate in the pMSSM. This means that any results shown for the selectron mass applies equally to the smuon mass. In the following, whenever a result is shown for the selectron, it should be read as applying to the corresponding smuon as well, unless otherwise stated. The LHC is sensitive to selectron masses of up to $m(\widetilde{\mathrm{e}}_\mathrm{L}, \widetilde{\mu}_\mathrm{L}) \simeq 500\,\mathrm{GeV}$. This can be seen in Figure 78 for left-chiral selectron $\widetilde{\mathrm{e}}_\mathrm{L}$ and Figure 79 for right-chiral selectron $\widetilde{\mathrm{e}}_\mathrm{R}$. The sensitivity to $\widetilde{\mathrm{e}}_\mathrm{L}$ is stronger, especially in the compressed region, where sensitivity is lost for $\widetilde{\mathrm{e}}_\mathrm{R}$. The search that is most sensitive here is di-lepton search. Even though the LHC is somewhat sensitive to low-mass selectrons and smuons, the effect of the considered LHC searches on the posterior mass in terms of the slepton masses is limited, mostly because the prior is already small where the LHC is sensitive. Thus, the small Bayes factors and survival probability seen in Figure 80 at small selectron masses do not shift the probability density much. Some of the impact on the marginalized slepton mass distributions comes from constraints on the LSP mass, which serves as a lower boundary for all the other sparticle masses. This contribution can be seen in Figure 80 in the distributions for the lighter stau. Even though there is little to no direct sensitivity to the stau in the searches included in this study, there is a slight decrease of the survival probability towards small stau masses and a slight shift of the posterior with respect to the prior.

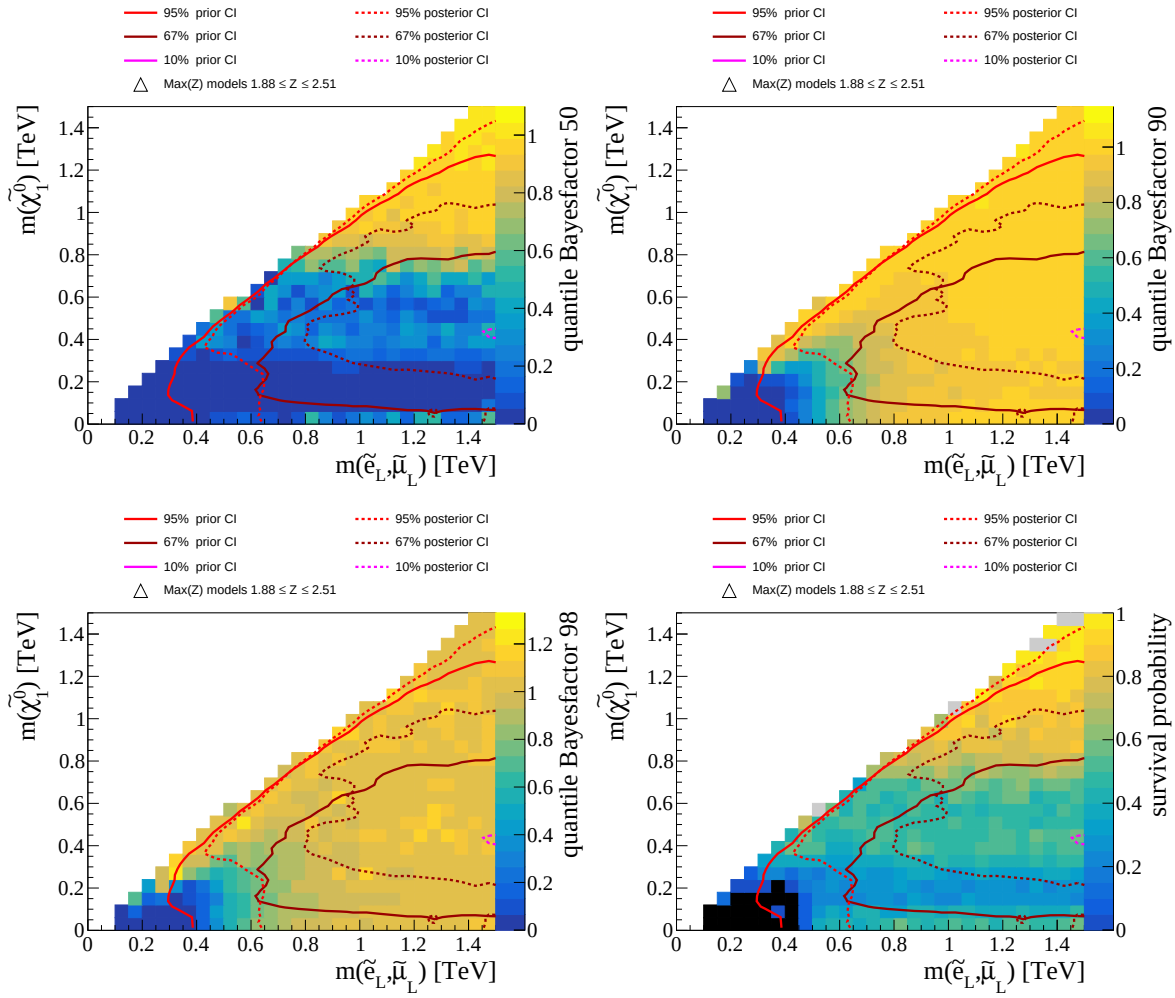

Figure 78: Impact of the LHC in the plane of the left-handed selectron (=smuon) mass $m(\widetilde{\mathrm{e}}_\mathrm{L}, \widetilde{\mu}_\mathrm{L})$ and $m(\widetilde{\chi}_1^0)$, in terms of the median (top left), 90th (top right), and 98th (bottom left) quantiles of the Bayes factor, as well as the survival probability (bottom right). Grey-colored bins have a survival probability of exactly one, black-colored bins have a survival probability of exactly zero, white bins are empty. A detailed description of the plot elements is given in Section 7.

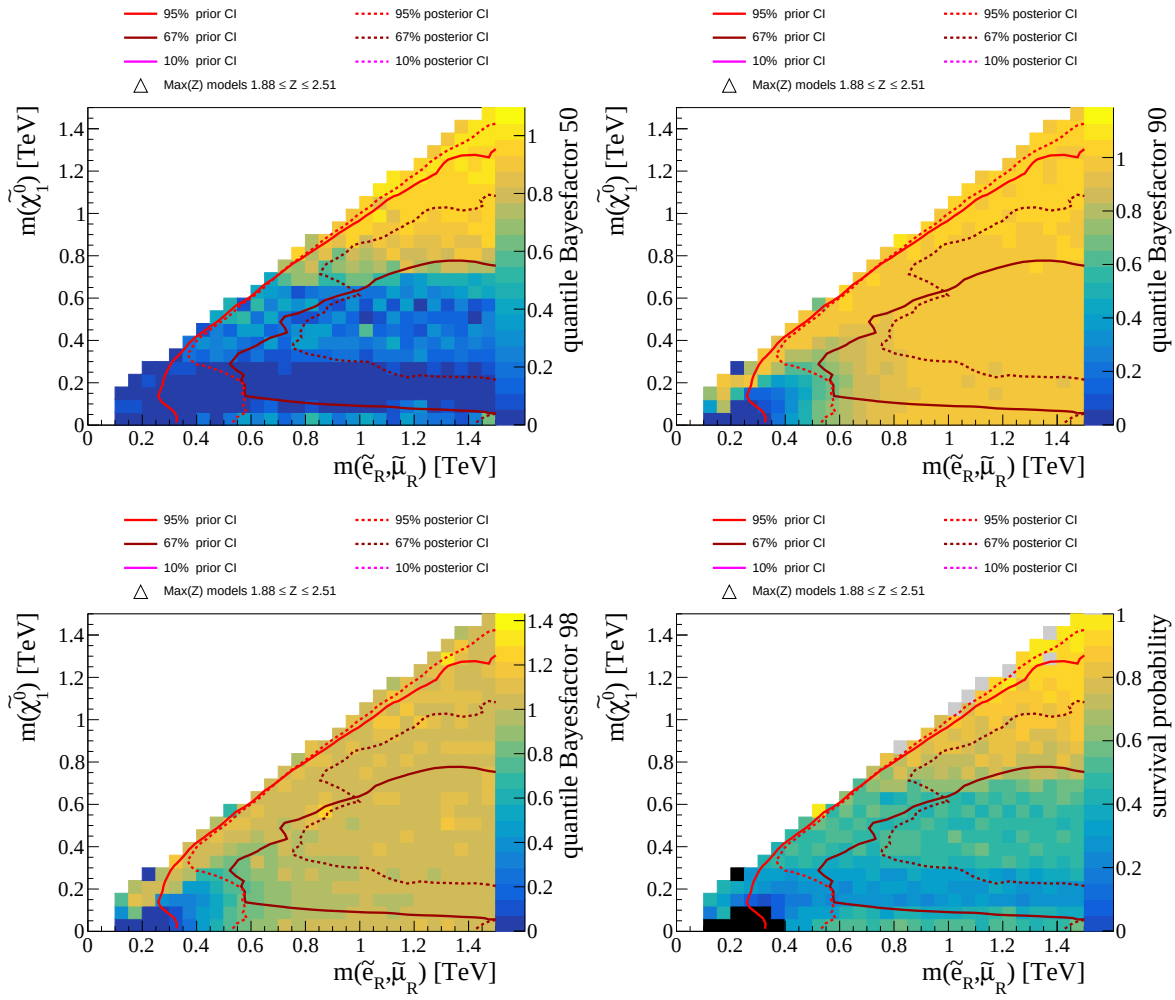

Figure 79: Impact of the LHC in the plane of the right-handed selectron (=smuon) mass $m(\widetilde{\mathrm{e}}_\mathrm{R}, \widetilde{\mu}_\mathrm{R})$ and $m(\widetilde{\chi}_1^0)$, in terms of the median (top left), 90th (top right), and 98th (bottom left) quantiles of the Bayes factor, as well as the survival probability (bottom right). Grey-colored bins have a survival probability of exactly one, black-colored bins have a survival probability of exactly zero, white bins are empty. A detailed description of the plot elements is given in Section 7.

Because the LHC is not directly sensitive to sneutrinos, any effects seen on their distributions come from correlation to other sectors of the pMSSM, which is why this results section does not feature them.

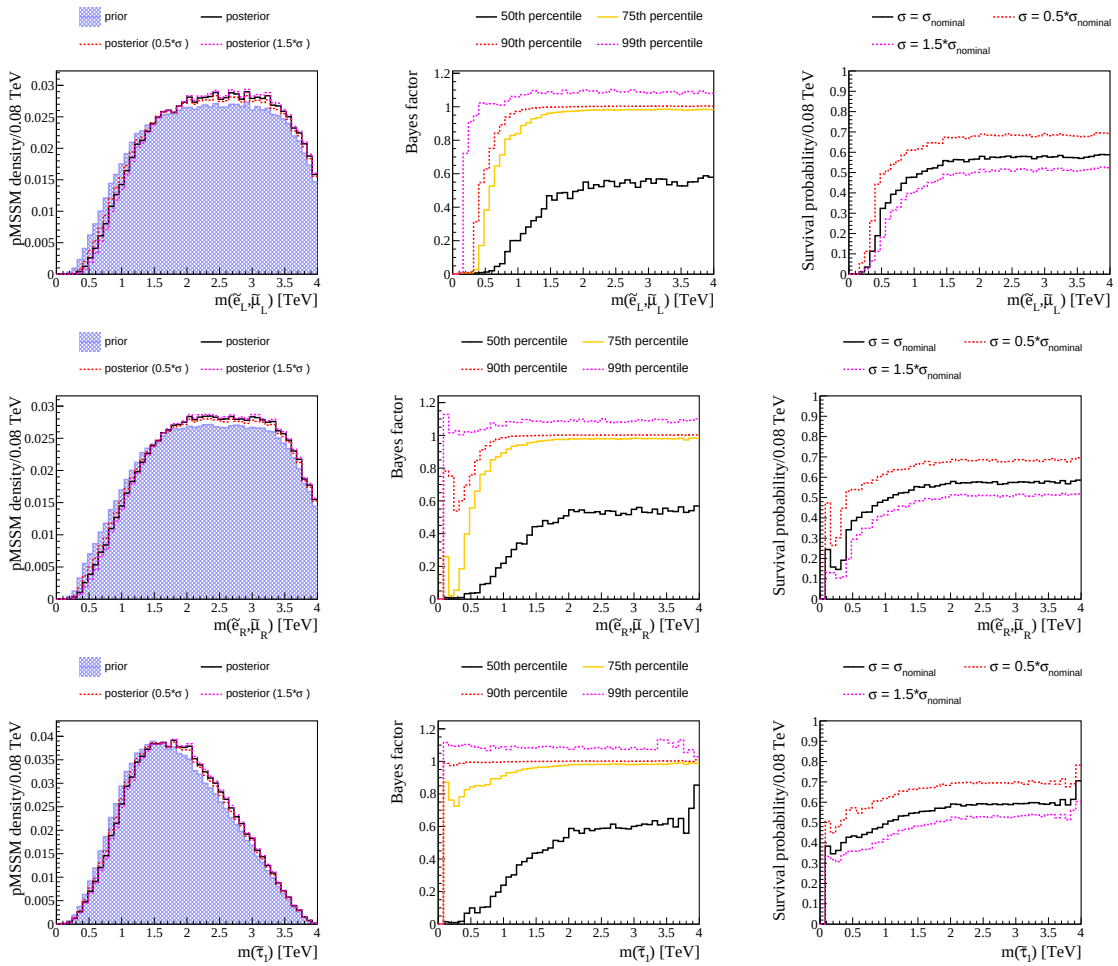

Figure 80: Impact of the considered LHC searches on the left-chiral selectron (=smuon) mass $m(\widetilde{\mathrm{e}}_\mathrm{L}, \widetilde{\mu}_\mathrm{L})$ (top row), the right-chiral selectron (=smuon) mass $m(\widetilde{\mathrm{e}}_\mathrm{R}, \widetilde{\mu}_\mathrm{R})$ (center row), and the lighter stau mass $m(\widetilde{\tau}_1)$ (bottom row), in terms of the prior and posterior densities (left column), Bayes factor quantiles (center column), and the survival probability (right column). A detailed description of the plot elements is given in Section 7.

8.2.3 Colored SUSY

At the LHC, colored production modes for supersymmetric particles have the largest production cross sections. Coupled with detectors that are well suited to the reconstruction of the associated final states, the LHC is also very sensitive to the colored sector in terms of the mass ranges that can be probed.

8.2.3.1 LCSP

To get an overview of the colored sector, it makes sense to start this section with the lightest colored supersymmetric particle (LCSP), whose mass is one of the strongest predictors of LHC sensitivity to a model (the other one is the mass of the lightest chargino). This is because all colored particles have a large production cross section at the LHC. The cross section is also highly mass dependent, with a significant decrease towards larger particle masses. Additionally, most of the colored sparticles are either sampled independently in this scan, which tends to produce significant mass differences, or completely correlated, resulting in almost degenerate masses. The strong correlation of mass and cross section, together with the fact of either degenerate or significantly different masses makes the LCSP either the dominant source of the total production cross section, or strongly correlated to a large cross section.

Figure 81 shows the results of the LHC constraints on $m(\text{LCSP})$. Similarly to the case for the neutralino and chargino masses, a peak of the posterior density for the LCSP at a small mass should not be interpreted as a particularly likely mass to be realized in Nature. The reason is that ordering multiple particles by their mass strongly favors distributions with a pronounced peak for each particle mass, with the minimum mass of the particles peaking at small values. That does not mean that everything about the posterior density is meaningless – the shift of the posterior with respect to the prior shows that the region below $m(\text{LCSP}) \lesssim 1.5\,\text{TeV}$ is strongly disfavored. The LHC is directly sensitive to LCSP masses up to $m(\text{LCSP}) \simeq 3\,\text{TeV}$, which is where the survival probability distribution (Figure 81) levels off into a plateau region that extends all the way to the edge of the maximum of the sampled LCSP masses at around $m(\text{LCSP}) \simeq 8.5\,\text{TeV}$. There are several features visible in the slope of the survival probability distribution that are caused by the different types of particle the LCSP can be. The change in slope at $m(\text{LCSP}) \simeq 1.3\,\text{TeV}$ is caused by the loss of sensitivity to models where the LCSP is the lightest stop or sbottom. The final turn-off at $m(\text{LCSP}) \simeq 3\,\text{TeV}$ is caused by the loss of sensitivity where the LCSP is the gluino, and at least one squark has a very small mass difference to the gluino. The resulting gluino-squark production has the largest production cross section at the LHC, and its turn-off marks the edge of LHC sensitivity to the colored sector. The sensitivity of the LHC to colored particles, and the LCSP in particular, strongly depends on their cross section. Because of this strong dependence, the peak position of $m(\text{LCSP})$ is highly dependent on the cross section variations, with a shift of approximately 200 GeV towards lower masses for a downward variation of 50% on the cross section. The strong correlation can also be directly seen in Figure 82, where it is evident in both the shape of the credibility intervals and in the lower-left edge of sampled models.

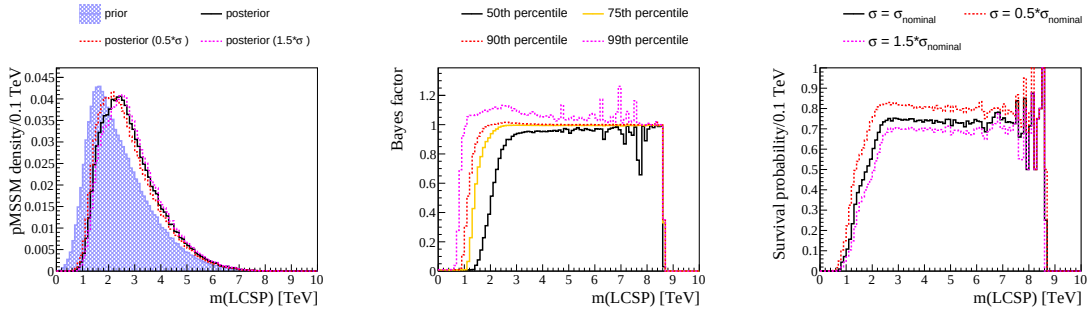

Figure 81: Impact of the considered LHC searches on the mass of the lightest colored supersymmetric particle $m(\text{LCSP})$, in terms of the prior and posterior densities (left), Bayes factor quantiles (center), and the survival probability (right). A detailed description of the plot elements is given in Section 7.

A good overview of the impact of the considered LHC searches on most of the pMSSM can be gleaned in the plane of $m(\widetilde{\chi}_1^0)$ and $m(\text{LCSP})$. In this plane, shown in Figure 83, we see both

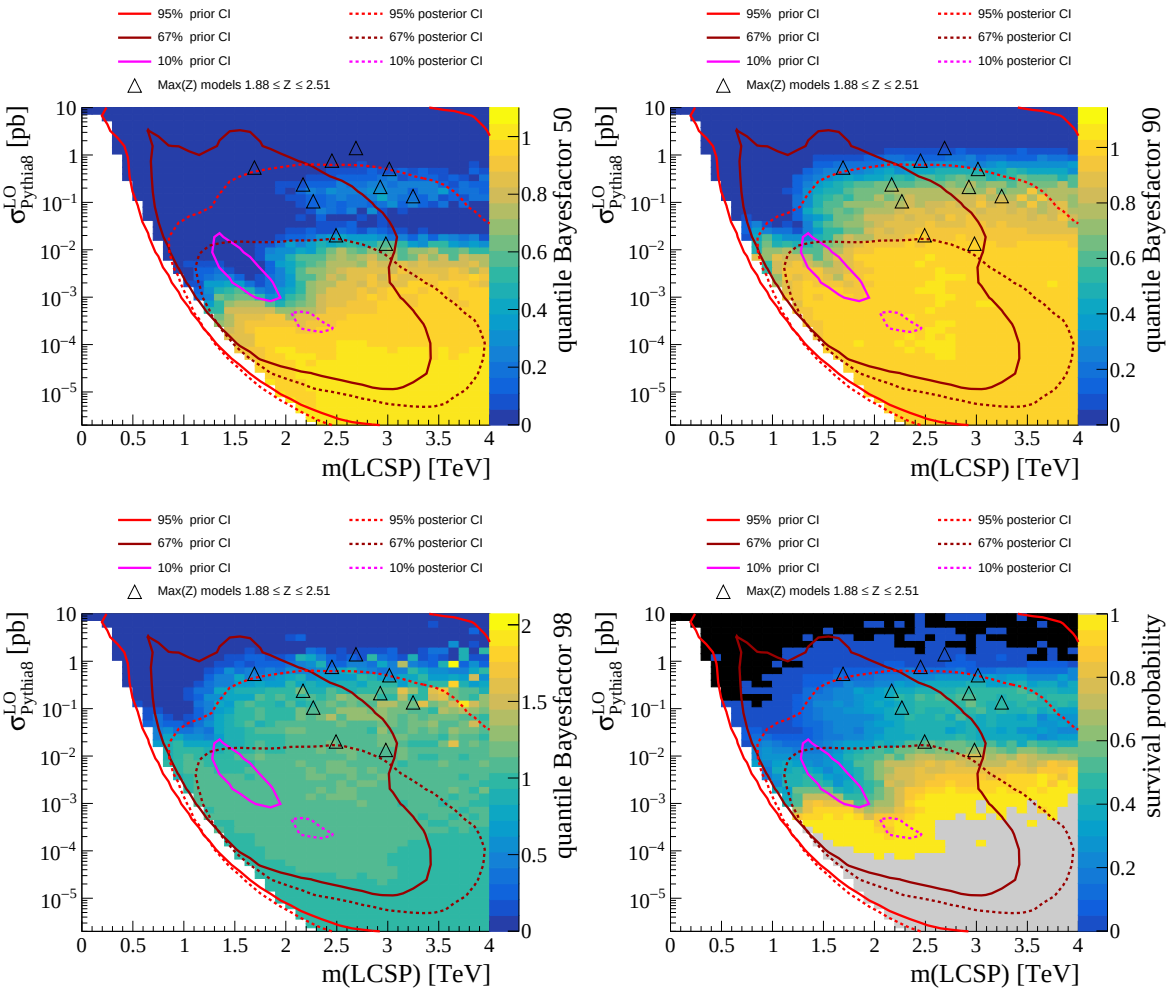

Figure 82: Impact of the considered LHC searches in the plane of $\sigma^{\text{total}}_{\text{Pythia8@LO}}$ and $m(\text{LCSP})$, in terms of the median (top left), 90th (top right), and 98th (bottom left) quantiles of the Bayes factor, as well as the survival probability (bottom right). Grey-colored bins have a survival probability of exactly one, black-colored bins have a survival probability of exactly zero, white bins are empty. A detailed description of the plot elements is given in Section 7.

vertical features, mostly corresponding to the influence of the LCSP, and horizontal features mostly corresponding to the influence of the LSP. Starting with the influence of the LCSP, we see extremely high sensitivity the larger the mass splitting between the LSP and LCSP. This sensitivity is lessened for LSP masses above $m(\widetilde{\chi}^0_1) \simeq 500\,\text{GeV}$, and becomes even less the larger $m(\widetilde{\chi}^0_1)$ is, due to the decreased available phase space for the final state. This leads to a softer p_T and p_T^{miss} spectrum, which is detrimental to the acceptance of the p_T^{miss}+jets search. As for the direct influence of the LSP, we see a fast transition at $m(\widetilde{\chi}^0_1) \simeq 100\,\text{GeV}$, where the region with smaller masses in much less constrained than the region above. This is because the region with $m(\widetilde{\chi}^0_1) \lesssim 100\,\text{GeV}$ contains no models with a higgsino-like or wino-like LSP due to constraints on the chargino mass from LEP. Consequently, the LHC is only sensitive to these models at small LCSP masses, or in the case of a low-mass wino, higgsino, or slepton with a mass slightly above the LSP mass. In the region immediately above $m(\widetilde{\chi}^0_1) \simeq 100\,\text{GeV}$, the LSP type is, with similar abundance, a pure wino or a pure bino, with a lot fewer pure higgsinos (see the prior distributions in Figure 68). The sensitivity to these models then decreases the larger $m(\widetilde{\chi}^0_1)$, and is mostly lost for $m(\widetilde{\chi}^0_1) \gtrsim 600\,\text{GeV}$.
Because the LHC is not directly sensitive to bino production, and because both pure higgsinos and pure winos come with a chargino that is nearly degenerate in mass to the LSP, the plane of $m(\widetilde{\chi}^\pm_1)$ and $m(\text{LCSP})$ in Figure 84 offers an even clearer picture into the sensitivity of the LHC. The top-right corner of the survival probability shows the region where both the chargino and the LCSP are

decoupled from direct production at the LHC. The survival probability starts to drop below one for $m(\text{LCSP}) \lesssim 2.5\,\text{TeV}$ or $m(\widetilde{\chi}_1^{\pm}) \lesssim 1\,\text{TeV}$ – the limits of LHC sensitivity to colored production and charginos, respectively. Further interesting features are visible in the median Bayes factor, where we see that a majority of the pMSSM is excluded if either $m(\text{LCSP}) \lesssim 1.5\,\text{TeV}$ or $m(\widetilde{\chi}_1^{\pm}) \lesssim 600\,\text{GeV}$. Not unexpectedly, the LHC is especially sensitive to models where both electroweak and colored particles are produced, since the cross sections for these processes add up and do not destructively interfere. This behavior can be most clearly seen in the median Bayes factor in the plane of $m(\widetilde{\chi}_1^{\pm})$ and $m(\text{LCSP})$, where the Bayes factor quantiles and survival probability is lower close to the diagonal.

We also see an island of larger survival probability at $m(\widetilde{\chi}_1^{\pm}) \simeq 400\,\text{GeV}$ and $m(\text{LCSP}) \gtrsim 2\,\text{TeV}$ (where the LHC has lost most of its sensitivity to strong production). This perceived lessened sensitivity is actually actually an abnormally high sensitivity to slightly larger chargino masses that results from an increased fraction of long-lived to prompt charginos at these masses. This can be seen from the shape of the 67% prior credibility interval in Figure 70, which is shaped towards smaller $\Delta m(\widetilde{\chi}_1^{\pm}, \widetilde{\chi}_1^0)$ for $m(\widetilde{\chi}_1^0) \gtrsim 400\,\text{GeV}$.

Finally, we see a lot of bins with large Bayes factors in the 98th quantile in the same region of $m(\widetilde{\chi}_1^{\pm}) \simeq 400\,\text{GeV}$ and $m(\text{LCSP}) \gg 2\,\text{TeV}$, as well as many of the models with the highest Z significance. These models with larger Bayes factors have a suitable chargino production cross section and favorable kinematics to fit the excess region at $\Delta m(\widetilde{\chi}_1^{\pm}, \widetilde{\chi}_1^0) \simeq 100$ GeV that was discussed before (Figure 70), while not containing strong production.

We also see in this plane that no chargino mass is completely excluded in the pMSSM. Note that complete exclusion of small $m(\text{LCSP})$ is only given for $m(\text{LCSP}) < 600\,\text{GeV}$ (we graciously allow for the single surviving model with $m(\text{LCSP}) \simeq 450\,\text{GeV}$ to not spoil this general statement), which is well below what is traditionally seen in interpretations in terms of simplified models. A comparison to simplified model limits is presented in more detail in Section 8.7.

The LHC is especially well suited to constraining the colored sector of the pMSSM and is complementary to the measurements that shape the prior. We can see in Figure 82 that the sensitivity extends to significantly lower cross sections for two diagonal regions at lower $m(\text{LCSP})$, each corresponding to different types of LCSP. Incidentally, one of the channels of high sensitivity aligns with the peak of the prior, which results in a significant shift of the probability density after confrontation with the LHC data. Since the observables and assumptions shape the prior, the fact that the prior density is high where the LHC is particularly sensitive shows complementarity between the results.

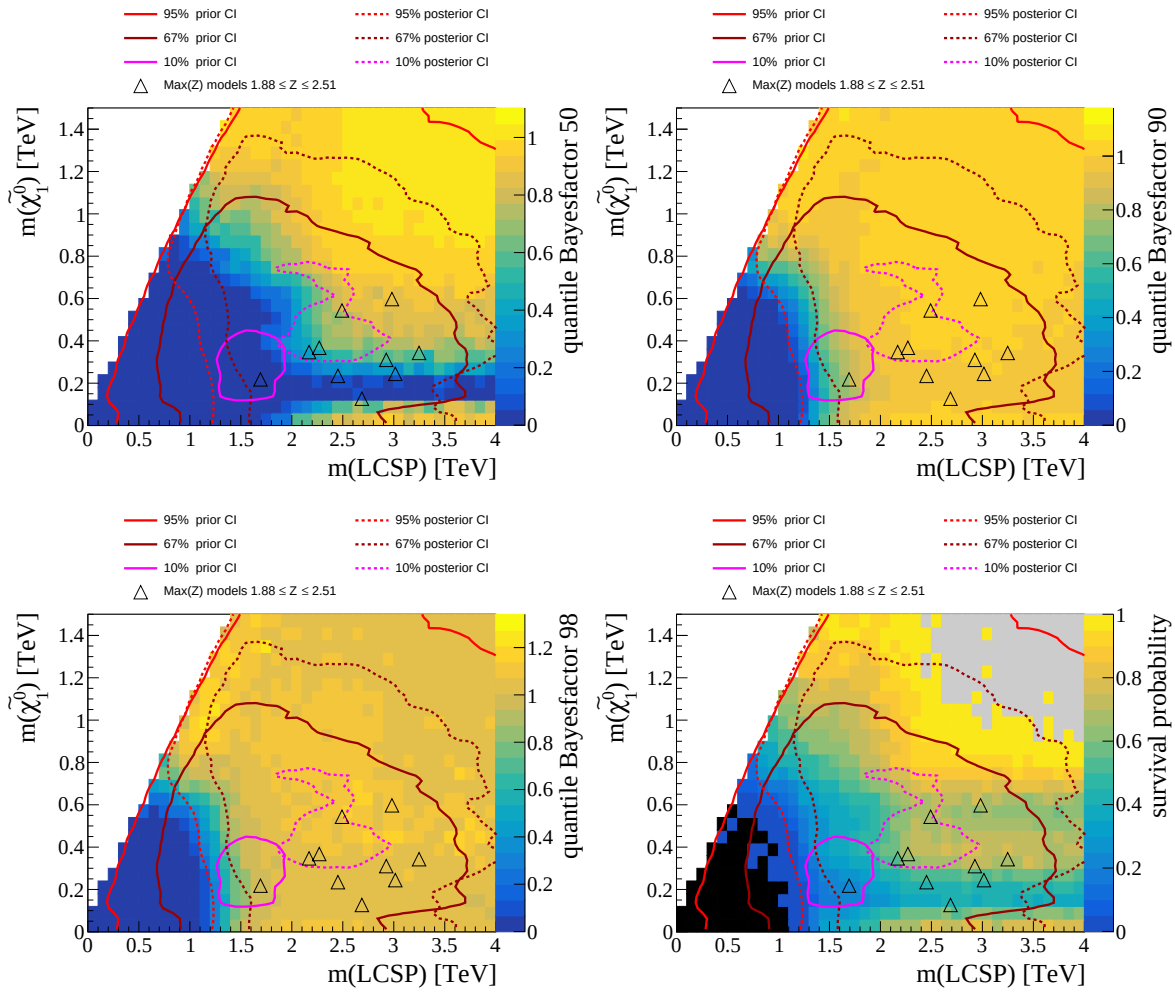

Figure 83: Impact of the considered LHC searches in the plane of $m(\tilde{\chi}_1^0)$ and m(LCSP), in terms of the median (top left), 90th (top right), and 98th (bottom left) quantiles of the Bayes factor, as well as the survival probability (bottom right). Grey-colored bins have a survival probability of exactly one, black-colored bins have a survival probability of exactly zero, white bins are empty. A detailed description of the plot elements is given in Section 7.

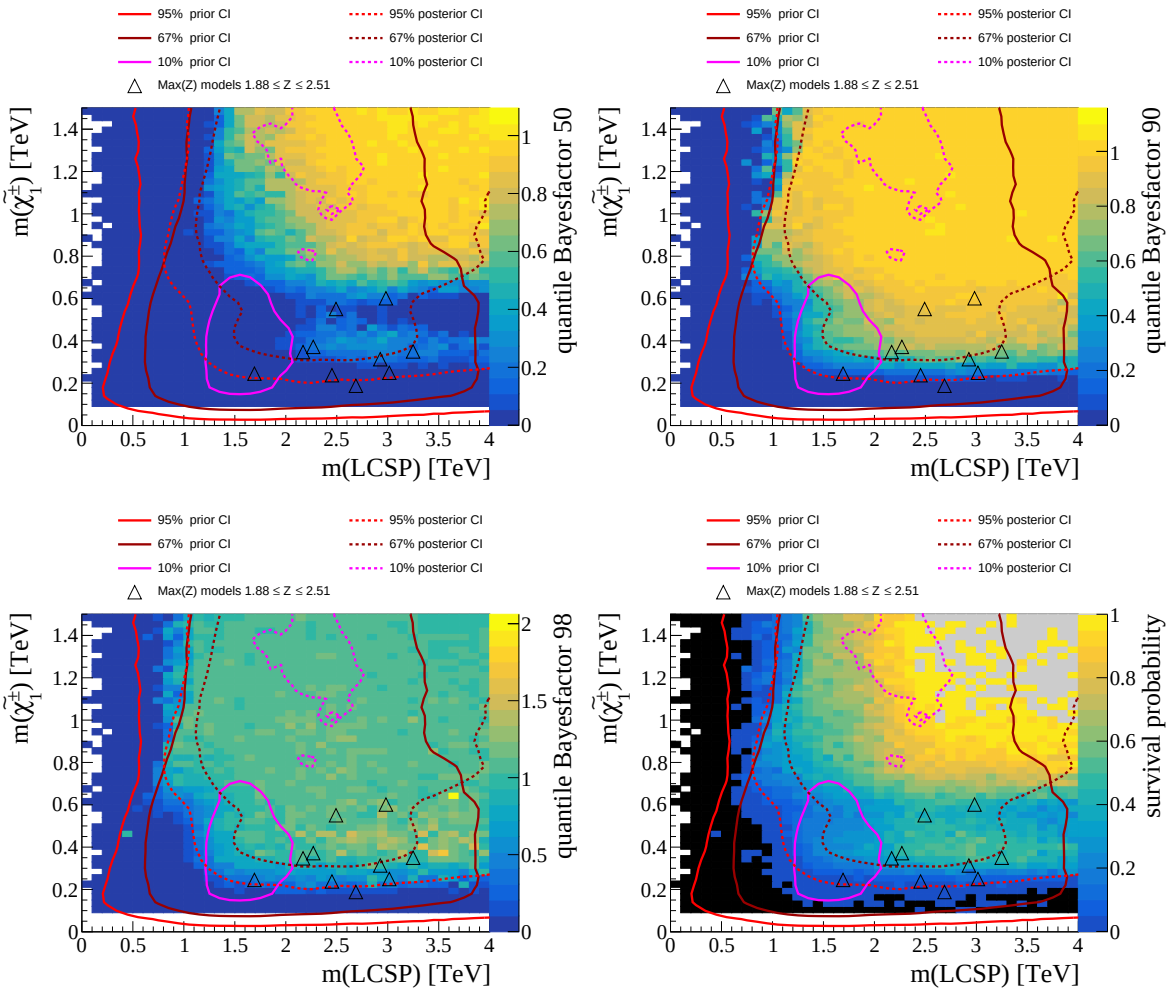

Figure 84: Impact of the considered LHC searches in the plane of $m(\widetilde{\chi}_1^{\pm})$ and m(LCSP), in terms of the median (top left), 90th (top right), and 98th (bottom left) quantiles of the Bayes factor, as well as the survival probability (bottom right). Grey-colored bins have a survival probability of exactly one, black-colored bins have a survival probability of exactly zero, white bins are empty. A detailed description of the plot elements is given in Section 7.

After the overview of the colored sector given by studying the LCSP, it is worthwhile to discuss the different colored sparticles individually.

8.2.3.2 Gluino

Of the different types of colored sparticles, light gluinos are particularly disfavored by the LHC. As visible in Figure 85, the posterior density is extremely suppressed for $m(\widetilde{g}) \lesssim 2\,\text{TeV}$, and the median of the Bayes factor is close to zero for $m(\widetilde{g}) < 2\,\text{TeV}$. Well over 90% of models in that mass range are excluded at 95%CL, and only 10% of models with $m(\widetilde{g}) \simeq 2\,\text{TeV}$ survive the LHC constraints. The extra sensitivity to the gluino compared to the other colored sparticles is due to the presence of extra jets, associated with the lowest-order decay chain into a neutralino via an intermediate squark. If there is no squark with a mass between $m(\widetilde{g})$ and $m(\widetilde{\chi}_1^0)$, this decay is usually written as a four-point interaction $\widetilde{g} \to q\bar{q}\widetilde{\chi}_1^0$, with an unresolved virtual squark. As shown in Figure 86, the surviving models with $m(\widetilde{g}) \lesssim 2\,\text{TeV}$ almost all feature a somewhat compressed model space in the gluino mass and the LSP mass. This is because the smaller mass difference leads to a smaller available phase space for the final state, which results in a softer p_T and p_T^{miss} spectrum. This in turn lowers the acceptance of the generic p_T^{miss}+jets analysis to the model.

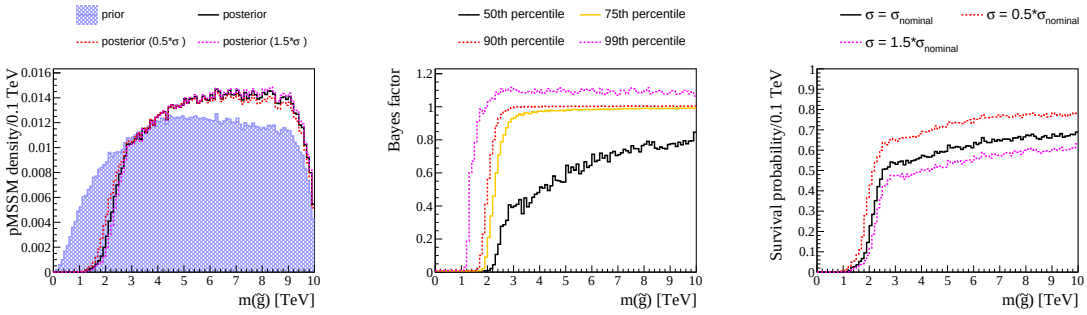

Figure 85: Impact of the considered LHC searches on the gluino mass $m(\widetilde{g})$, in terms of the prior and posterior densities (left), Bayes factor quantiles (center), and the survival probability (right). A detailed description of the plot elements is given in Section 7.

8.2.3.3 Stop & sbottom

A particle of particular interest, due to its connection in stabilizing the Higgs mass, is the top squark. The impact of the considered LHC searches on the lighter states of the stop and sbottom is shown in Figure 87. Note that the p_T^{miss}+jets search includes categories with b-tagged jets and thus is sensitive to $\widetilde{t}_1$ and $\widetilde{b}_1$ decays. As can be seen there, the LHC only has a large impact at small $m(\widetilde{t}_1)$, but not so much at large $m(\widetilde{t}_1)$. The survival probability distribution shows that well over 90% of models with a stop mass below 1 TeV are excluded. The prior already heavily disfavors low-mass stops, which means that the inclusion of LHC results does not result in a strong shift of the probability density. The reason for the low prior at small stop masses, and the strong difference compared to the sbottom mass, is primarily due to the requirement on the Higgs boson mass, which is further exacerbated by results from flavor physics. This has already been established in Section 5. The LHC is sensitive to the direct production of stops up to $m(\widetilde{t}_1) \simeq 1.5\,\text{TeV}$. This threshold can be deduced from the kink in the survival probability distribution in Figure 87, where the rise of the survival probability transitions into a plateau towards larger masses of the stop. The fact that this transition occurs very quickly in terms of the stop mass indicates the absence of other factors that influence the LHC sensitivity in this region. If the transition happened more gradually, this would indicate that other observables beside the stop mass also significantly affect the LHC sensitivity. The sensitivity to the sbottom is slightly lower than to the stop mass, but terminates at approximately the same mass. This is directly evident in the distribution of the survival probabilities. It is also interesting that the median Bayes factor is significantly larger for comparable sbottom masses, further supporting that sensitivity is lowered compare to the stop. The similarity at least partially comes from the fact that in low-mixing scenarios where the light stop is left-chiral, it is almost degenerate in mass to the light sbottom. There is one more peculiar feature visible: the median Bayes factor and the survival probability rises significantly towards very large stop masses. This feature comes from a correlation of large stop masses to large LSP masses, which is caused by the tachyon issue discussed in detail in Appendix B. Because the

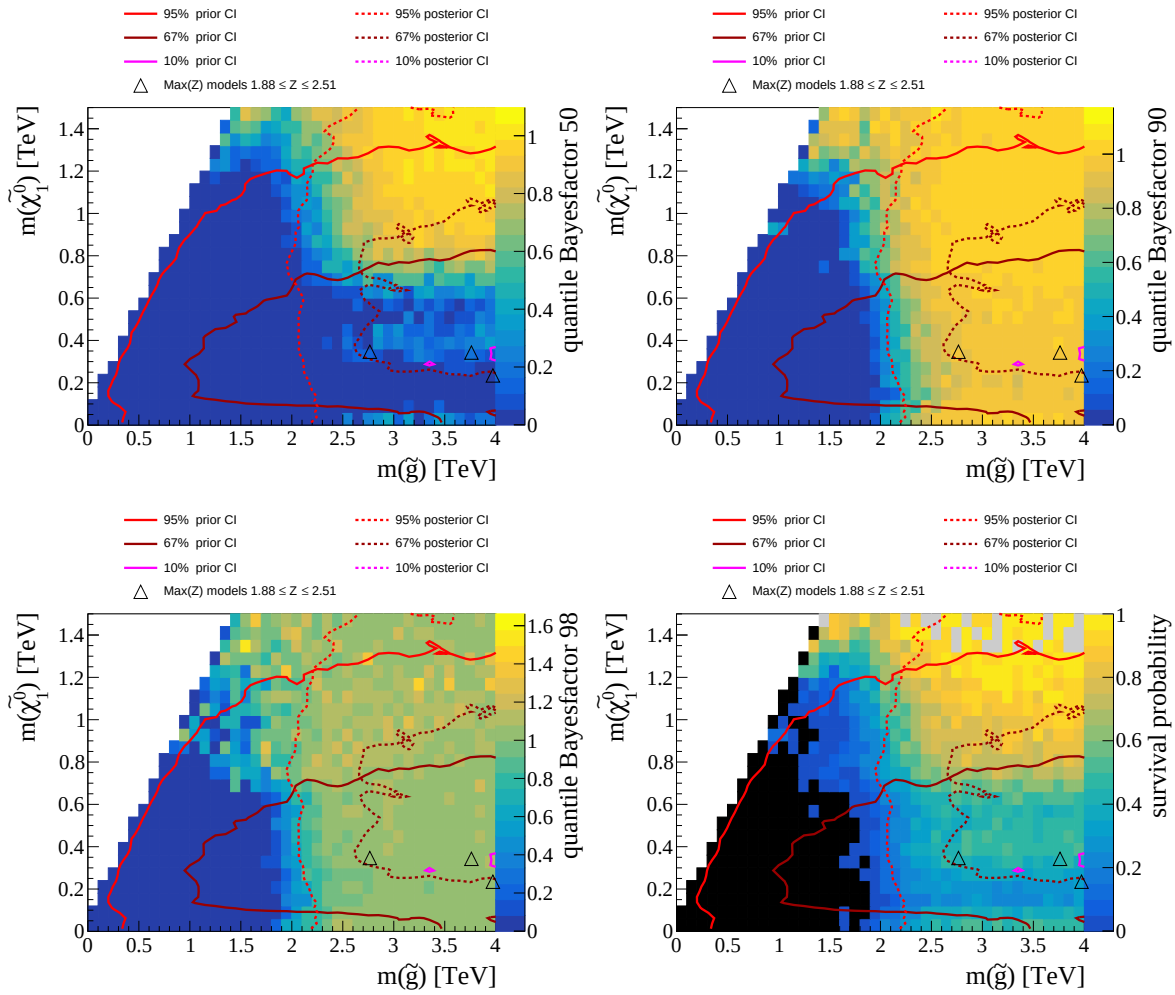

Figure 86: Impact of the LHC in the plane of m($\tilde{g}$) and $m(\tilde{\chi}_1^0)$, in terms of the median (top left), 90th (top right), and 98th (bottom left) quantiles of the Bayes factor, as well as the survival probability (bottom right). Grey-colored bins have a survival probability of exactly one, black-colored bins have a survival probability of exactly zero, white bins are empty. A detailed description of the plot elements is given in Section 7.

small $|\mu|$ - large Q_{SUSY} region is completely tachyonic, the large Q_{SUSY} region is overpopulated with large LSP masses. On average, this results in less sensitivity to the region and is thus visible in both the survival probabilities and medians of quantities that are positively correlated to Q_{SUSY}. The most affected are thus the stop mass parameters $M_{q,3}$ and $M_{u,3}$, since they are directly used to define Q_{SUSY}. The sbottom is also visibly affected because $M_{q,3}$ determines the mass of the left-chiral sbottom mass. As is the case with the gluino, LHC is less sensitive to the stop mass in the compressed region, where the mass difference between $m(\tilde{t}_1)$ and $m(\tilde{\chi}_1^0)$ becomes small. We can see this in the larger survival probabilities, as well as Bayes factor quantiles for large $m(\tilde{\chi}_1^0)$ for similar $m(\tilde{t}_1)$.

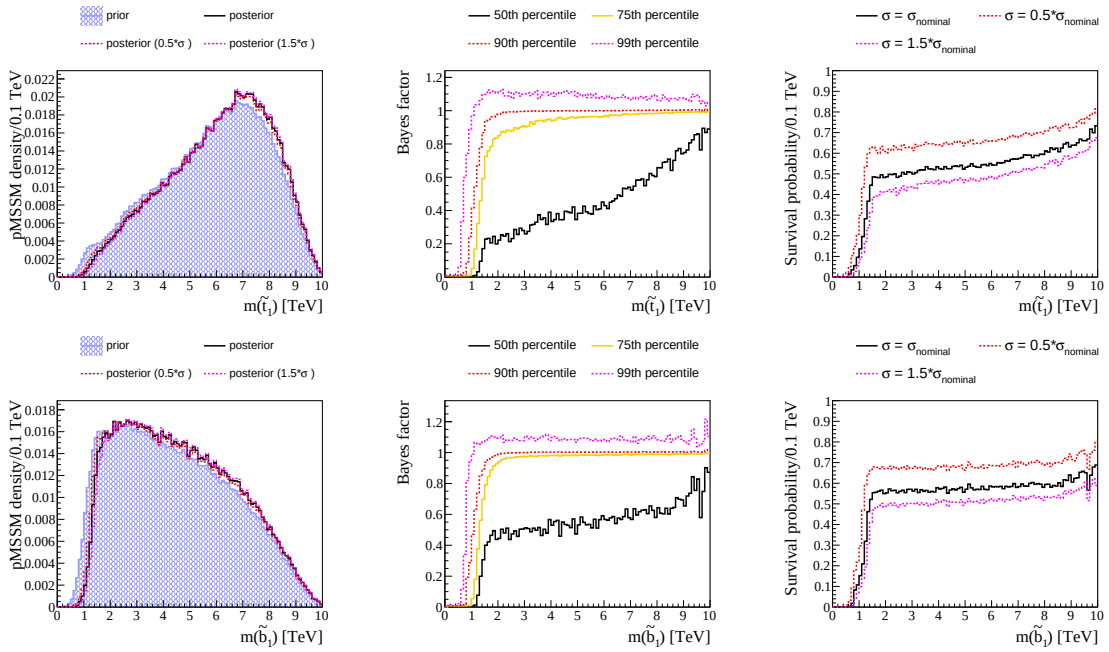

Figure 87: Impact of the considered LHC searches on the mass of the lighter states of the stop $m(\widetilde{\mathrm{t}}_1)$ (upper row) and the sbottom $m(\widetilde{\mathrm{b}}_1)$ (lower row), in terms of the prior and posterior densities (left column), Bayes factor quantiles (center column), and the survival probability (right column). A detailed description of the plot elements is given in Section 7.

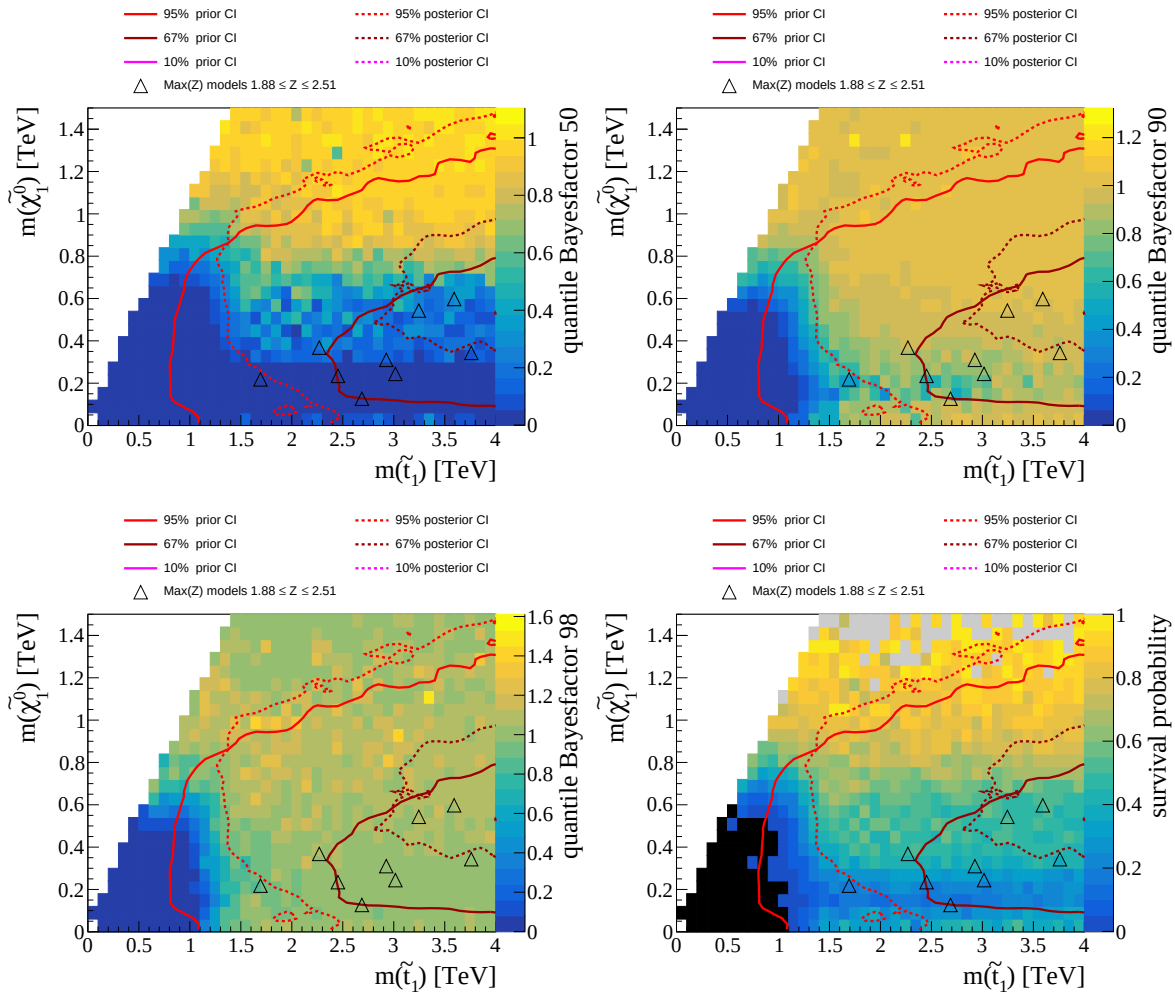

Figure 88: Impact of the considered LHC searches in the plane of the mass of the lighter stop state $m(\tilde{t}_1)$ and the LSP mass $m(\tilde{\chi}_1^0)$, in terms of the median (top left), 90th (top right), and 98th (bottom left) quantiles of the Bayes factor, as well as the survival probability (bottom right). Grey-colored bins have a survival probability of exactly one, black-colored bins have a survival probability of exactly zero, white bins are empty. A detailed description of the plot elements is given in Section 7.

8.2.3.4 Sup and sdown

To start, remember that the first and second generation squarks are mass degenerate in the pMSSM, which means that any conclusions drawn towards the first generation squarks only apply in the context of this model constraint. Whenever statements are made about the first generation squarks, they also apply to their respective second generation partner, unless stated otherwise. As with all the colored particles, Figure 89 shows that the small mass region for first generation squarks, particularly below $m(\widetilde{q}) \simeq 1\,\text{TeV}$ is severely disfavored by the LHC. Above that mass, differences are noticeable for the different types of first generation squarks.

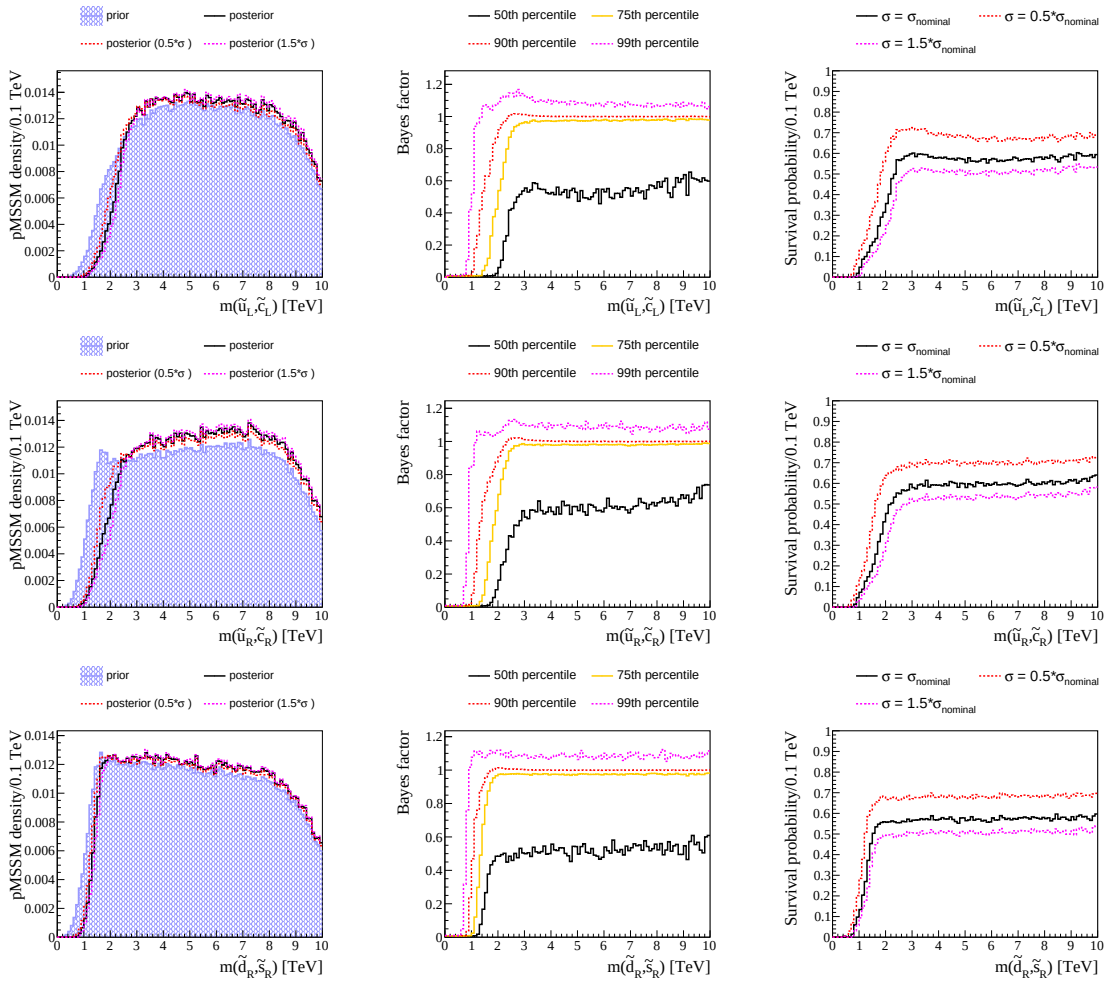

Figure 89: Impact of the considered LHC searches on the masses of the left-chiral sup $m(\widetilde{\mathrm{u}}_\mathrm{L}, \widetilde{\mathrm{c}}_\mathrm{L})$ (top row), the right-chiral sup $m(\widetilde{\mathrm{u}}_\mathrm{R}, \widetilde{\mathrm{c}}_\mathrm{R})$ (center row), and the right-chiral sdown $m(\widetilde{\mathrm{d}}_\mathrm{R}, \widetilde{\mathrm{s}}_\mathrm{R})$ (bottom row), in terms of the prior and posterior densities (left column), Bayes factor quantiles (center column), and the survival probability (right column). Note that the distributions for $m(\widetilde{\mathrm{d}}_\mathrm{L}, \widetilde{\mathrm{s}}_\mathrm{L})$ are not shown because of the near mass degeneracy to $m(\widetilde{\mathrm{u}}_\mathrm{L}, \widetilde{\mathrm{c}}_\mathrm{L})$ in the pMSSM. A detailed description of the plot elements is given in Section 7.

For instance, the sensitivity to up-type squarks is larger than to down-type squarks. This is evident from the survival probability and Bayes factor quantiles. The survival probability and median Bayes factor is slightly smaller for up-type squarks compared to $\widetilde{\mathrm{d}}_\mathrm{R}$ for similar masses, and the plateau of the distributions is also only reached at much larger masses. There are at least two different contributing factors to this. Figure 90 shows that a significant fraction of the models with light $m(\widetilde{\mathrm{d}}_\mathrm{R}, \widetilde{\mathrm{s}}_\mathrm{R}) < 2\,\text{TeV}$ has much smaller cross sections than models with up-type squarks in the same mass region. One reason for this is that the production cross section for the $\widetilde{\mathrm{d}}_\mathrm{R}$ is significantly smaller the for same mass, at least in part due to the larger parton density of up-quarks in protons, which lead to larger cross sections at proton collisions at the LHC.
In the same figure, the survival probabilities for the different light squark regions are significantly

different between the squarks, with a significantly larger survival probability of the light $\widetilde{\mathrm{d}}_\mathrm{R}$ region at similar total production cross sections. This likely does not indicate that the LHC is less sensitive to events with $\widetilde{\mathrm{d}}_\mathrm{R}$ production compared to similar events with $\widetilde{\mathrm{u}}_\mathrm{R}$ production, since no included LHC analysis can differentiate between the final states associated with different light squark production modes. A more likely explanation is that the pMSSM models in the light $\widetilde{\mathrm{d}}_\mathrm{R}$ region are substantially different than in the light $\widetilde{\mathrm{u}}_\mathrm{R}$ region in ways not directly related to $\widetilde{\mathrm{d}}_\mathrm{R}$ and $\widetilde{\mathrm{u}}_\mathrm{R}$. Figure 91 shows the profiles of the lighter chargino mass $m(\widetilde{\chi}_1^\pm)$ and the LCSP mass $m(\mathrm{LCSP})$ in bins of the total production cross section $\sigma^{\mathrm{total}}_{\mathrm{Pythia8@LO}}$, for the region of the pMSSM where $m(\widetilde{\mathrm{u}}_\mathrm{R}, \widetilde{\mathrm{c}}_\mathrm{R}) < 2\,\mathrm{TeV}$, and where $m(\widetilde{\mathrm{u}}_\mathrm{R}, \widetilde{\mathrm{c}}_\mathrm{R}) < 2\,\mathrm{TeV}$. Each entry here corresponds to the mean of the respective mass for a given bin of the production cross section $\sigma^{\mathrm{total}}_{\mathrm{Pythia8@LO}}$. We can see that for similar but small production cross sections $\sigma^{\mathrm{total}}_{\mathrm{Pythia8@LO}} \lesssim 0.01\,\mathrm{pb}$, the mean mass of the LCSP is significantly larger in the light $\widetilde{\mathrm{u}}_\mathrm{R}$ region than in the light $\widetilde{\mathrm{d}}_\mathrm{R}$ region. This means that the available phase space for the decay $\widetilde{q} \rightarrow \mathrm{q}\widetilde{\chi}_1^0$ tends to be larger in the light $\widetilde{\mathrm{u}}_\mathrm{R}$ region, which leads to increased jet-$\mathrm{p_T}$ in the final state. Additionally, the fraction of pMSSM models where there are sparticles with masses lighter than $m(\mathrm{LCSP})$ is larger, on average, for larger $m(\mathrm{LCSP})$. This leads to a difference in the occurrence of long decay chains that can result in more jets or a larger frequency of leptons in the final state, both of which can alter the signal acceptance in the included searches. This difference in mass hierarchies becomes more important for larger production cross sections, which is hinted at by the fact that the mean chargino mass decreases much more quickly than the LCSP mass towards larger cross sections. It is also visible in the branching fraction of decays into the LSP, shown in Figure 92. We can see that the branching fraction $\mathrm{BR}(\widetilde{\mathrm{u}}_\mathrm{R} \rightarrow \widetilde{\chi}_1^0)$ remains mostly constant for different total production cross sections in the light $\widetilde{\mathrm{u}}_\mathrm{R}$ region, while $\mathrm{BR}(\widetilde{\mathrm{d}}_\mathrm{R} \rightarrow \widetilde{\chi}_1^0)$ goes down significantly towards larger $\sigma^{\mathrm{total}}_{\mathrm{Pythia8@LO}}$. These differences in the pMSSM prior affect the signal acceptance and result in a much reduced sensitivity to $\widetilde{\mathrm{d}}_\mathrm{R}$.
There are several other interesting features in the profiles of $m(\widetilde{\chi}_1^\pm)$ and $m(\mathrm{LCSP})$ in Figure 91. We can see that the mean of $m(\mathrm{LCSP})$ remains constant for $\sigma^{\mathrm{total}}_{\mathrm{Pythia8@LO}} \gtrsim 0.03\,\mathrm{pb}$ and the difference of the mean $m(\mathrm{LCSP})$ between the light $\widetilde{\mathrm{u}}_\mathrm{R}$ and light $\widetilde{\mathrm{d}}_\mathrm{R}$ disappears at these large production cross sections. This is because the LCSP production is no longer the dominant contributor to the total production cross section in that part of the pMSSM, with the chargino becoming more important. This can also be seen from the distribution of the mean chargino mass for the same region of $\sigma^{\mathrm{total}}_{\mathrm{Pythia8@LO}}$, which continues to drop towards smaller masses. The difference of the mean chargino mass in the light $\widetilde{\mathrm{u}}_\mathrm{R}$ and light $\widetilde{\mathrm{d}}_\mathrm{R}$ also disappear for $\sigma^{\mathrm{total}}_{\mathrm{Pythia8@LO}} \gtrsim 0.5\,\mathrm{pb}$.

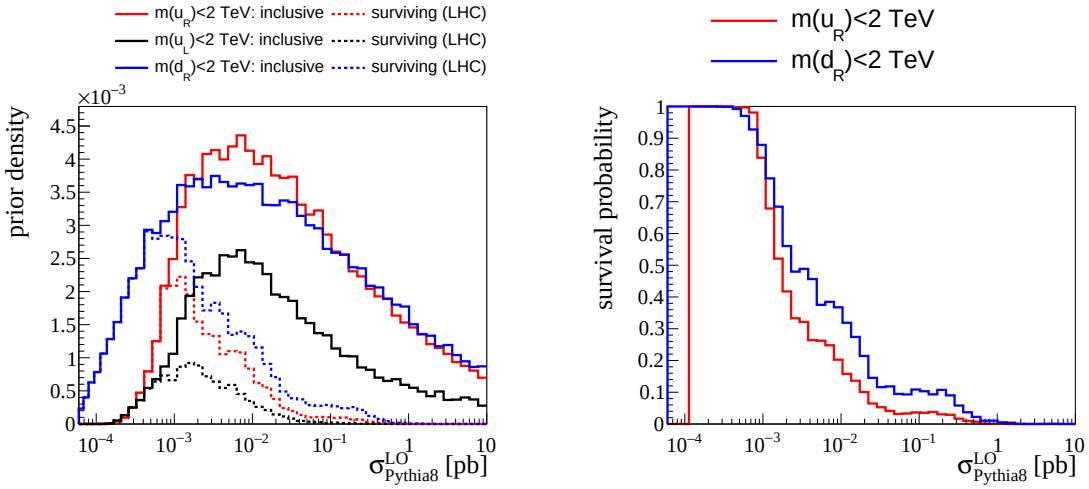

Figure 90: Comparison between squark types for typical total production cross sections $\sigma^{\mathrm{total}}_{\mathrm{Pythia8@LO}}$ and survival probabilities for models in light squark regions for the respective squarks.

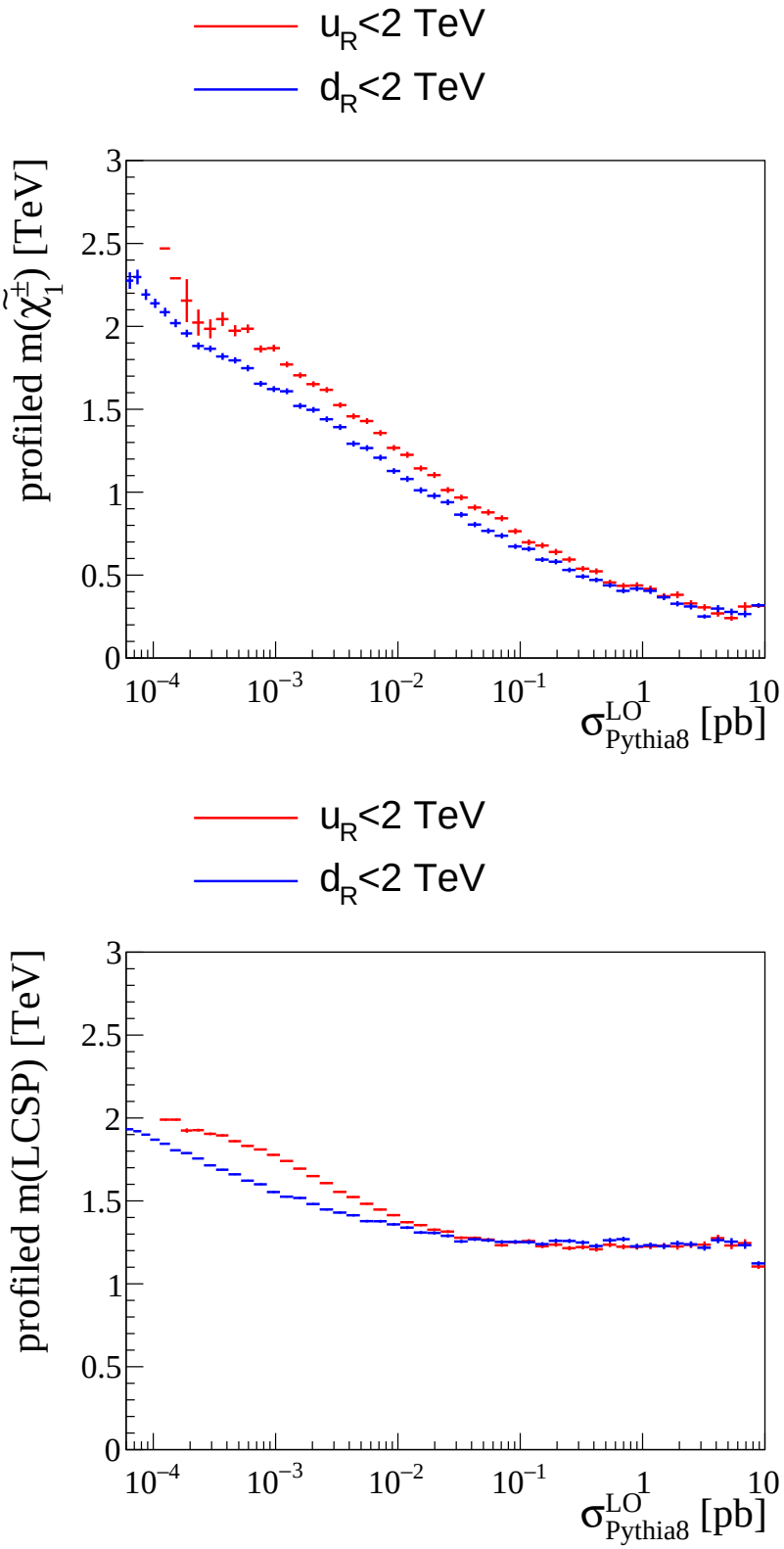

Figure 91: Profiled distributions of $m(\widetilde{\chi}_1^{\pm})$ (top) and m(LCSP) (bottom) in bins of the total production cross section $\sigma^{\text{total}}_{\text{Pythia8@LO}}$ in the subspaces of the pMSSM where $m(\widetilde{\text{d}}_{\text{R}}, \widetilde{\text{s}}_{\text{R}}) < 2\,\text{TeV}$ or $m(\widetilde{\text{u}}_{\text{R}}, \widetilde{\text{c}}_{\text{R}}) < 2\,\text{TeV}$.

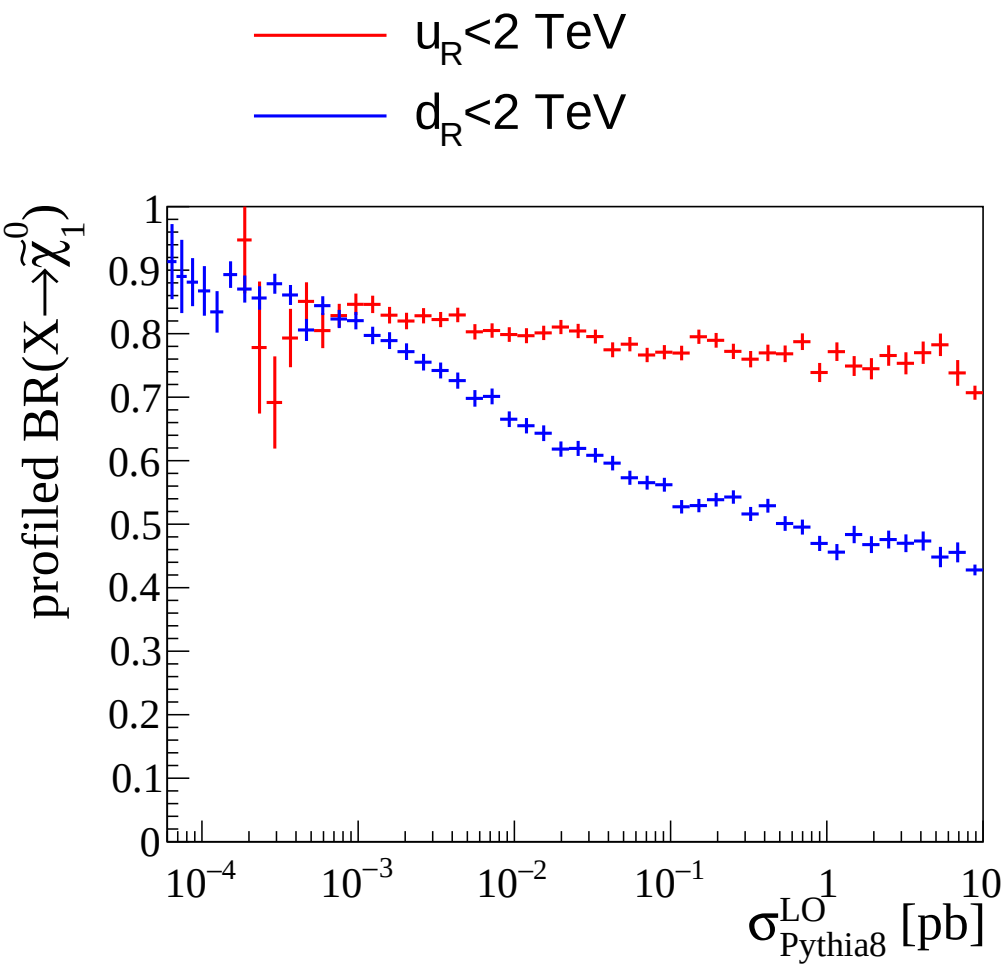

Figure 92: Profiled distributions the branching ratio of X into the LSP in bins of $\sigma^{\text{total}}_{\text{Pythia8@LO}}$ in the subspaces of the pMSSM where $m(\widetilde{\text{d}}_\text{R}, \widetilde{\text{s}}_\text{R}) < 2\,\text{TeV}$ or $m(\widetilde{\text{u}}_\text{R}, \widetilde{\text{c}}_\text{R}) < 2\,\text{TeV}$, where X is the $\widetilde{\text{d}}_\text{R}$ and $\widetilde{\text{u}}_\text{R}$ in the respective region.

8.3 Impact on the pMSSM parameters

The relationship between the pMSSM parameters and the particle masses used in Section 8.2 are not trivial, where usually more than one pMSSM parameter influences the mass of any particular particle. Differences between associated pMSSM parameters and particle masses may also occur due to the running of the renormalization group equations.

8.3.1 Colored SUSY

As seen in Figure 93, no region for the third generation pMSSM squark mass parameters can be excluded. This is true even at very low masses, where the corresponding particle masses are completely excluded. Figure 94 shows that while the LHC excludes most models where either $M_{q,3}$ or $M_{u,3}$ is small, some models at small $M_{q,3}$ survive exclusion if $M_{u,3}$ is large, and vice versa. Otherwise, there is almost no structure visible in this plane. The survival probability distributions for the stop mass parameters levels off at around 2 TeV, which marks the end of direct sensitivity of the LHC. Because the prior density is already small for $M_{q,3} \lesssim 2\,\text{TeV}$ and $M_{u,3} \lesssim 2\,\text{TeV}$, there is limited scope for the posterior density to grow in the absence of large Bayes factors. The sensitivity to the right-chiral sbottom mass parameter $M_{d,3}$ is lower than for the stop equivalent $M_{u,3}$. Both the Bayes factor quantiles and the survival probabilities are always larger for comparable $M_{u,3}$, and the edge of the LHC sensitivity is reached at $M_{d,3} \simeq 1.5\,\text{TeV}$, which is significantly smaller than for $M_{u,3}$. However, the impact of the considered LHC searches on $M_{d,3}$ is actually larger, because the prior at small $M_{d,3}$ is an order of magnitude larger than for small $M_{q,3}$ and $M_{u,3}$. This is mostly due to the Higgs mass constraint, which is discussed in Section 5.1.3.

The picture is similar to the sbottom parameters for the first-generation squark mass parameters $M_{q,1}$, $M_{u,1}$, and $M_{d,1}$, shown in Figure 95: we see a significant fraction of the posterior remaining at small masses, and no mass region where all models are excluded.

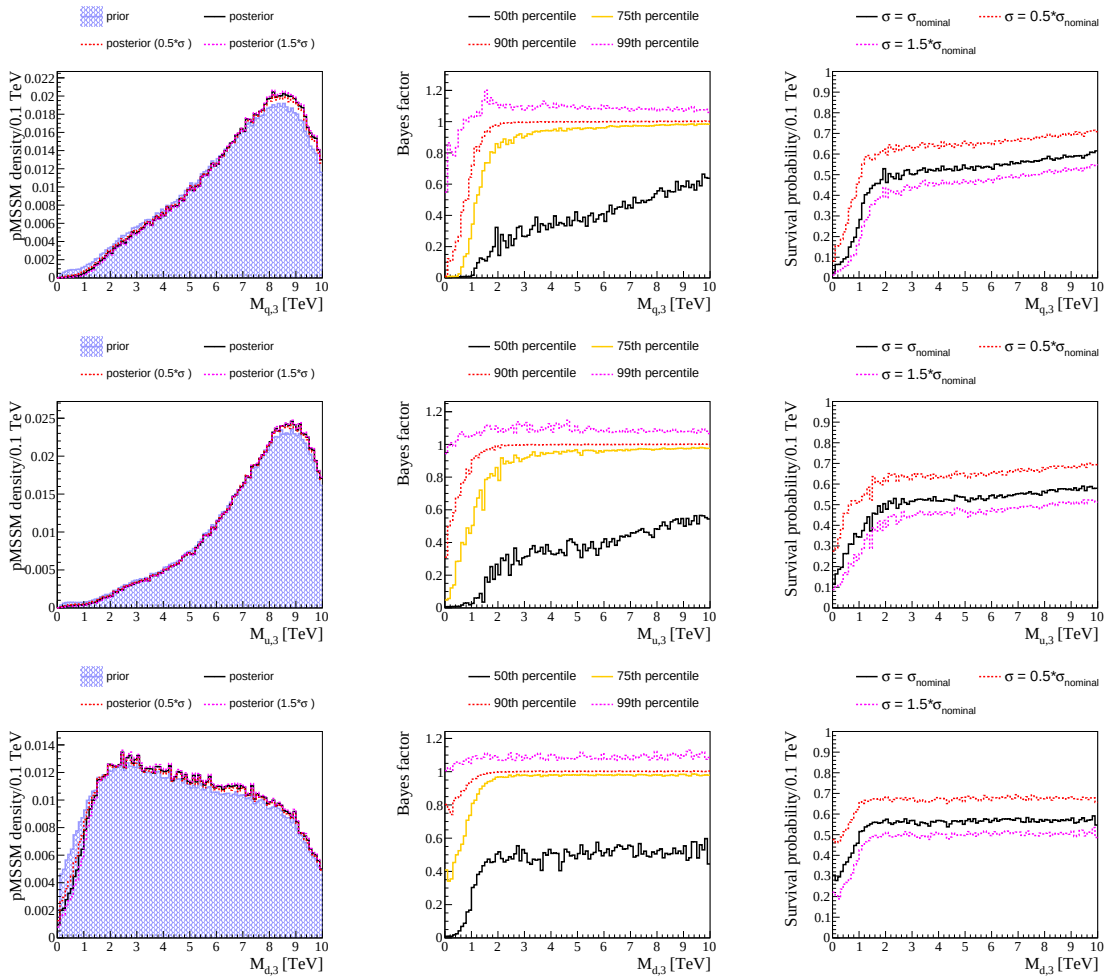

Figure 93: Impact of the considered LHC searches on the third-generation squark mass parameters $M_{q,3}$ (top row), $M_{u,3}$ (center row), and $M_{d,3}$ (bottom row), in terms of the prior and posterior densities (left column), Bayes factor quantiles (center column), and the survival probability (right column). A detailed description of the plot elements is given in Section 7.

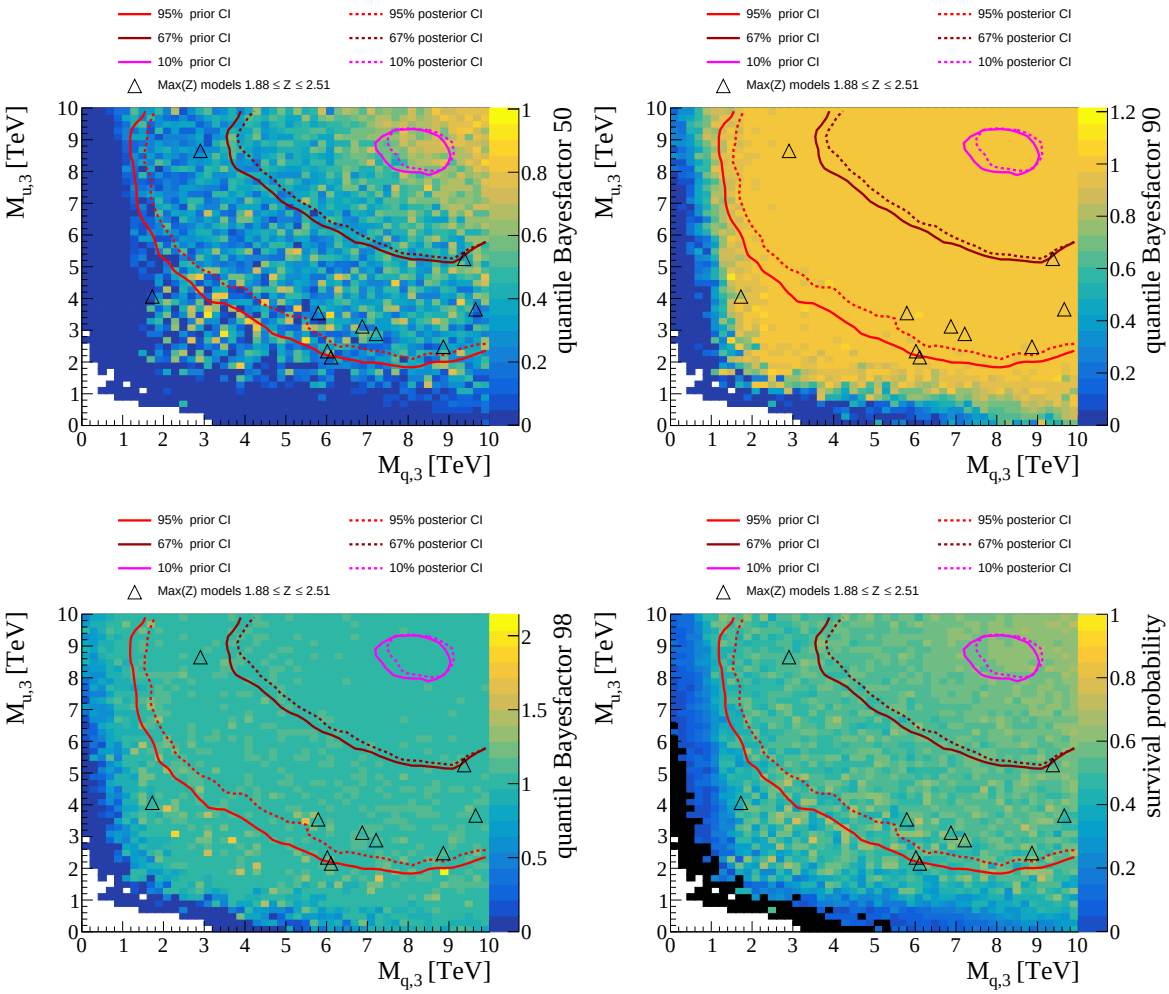

Figure 94: Impact of the considered LHC searches in the plane of the stop mass parameters $M_{q,3}$ and $M_{u,3}$, in terms of the median (top left), 90th (top right), and 98th (bottom left) quantiles of the Bayes factor, as well as the survival probability (bottom right). Grey-colored bins have a survival probability of exactly one, black-colored bins have a survival probability of exactly zero, white bins are empty. A detailed description of the plot elements is given in Section 7.

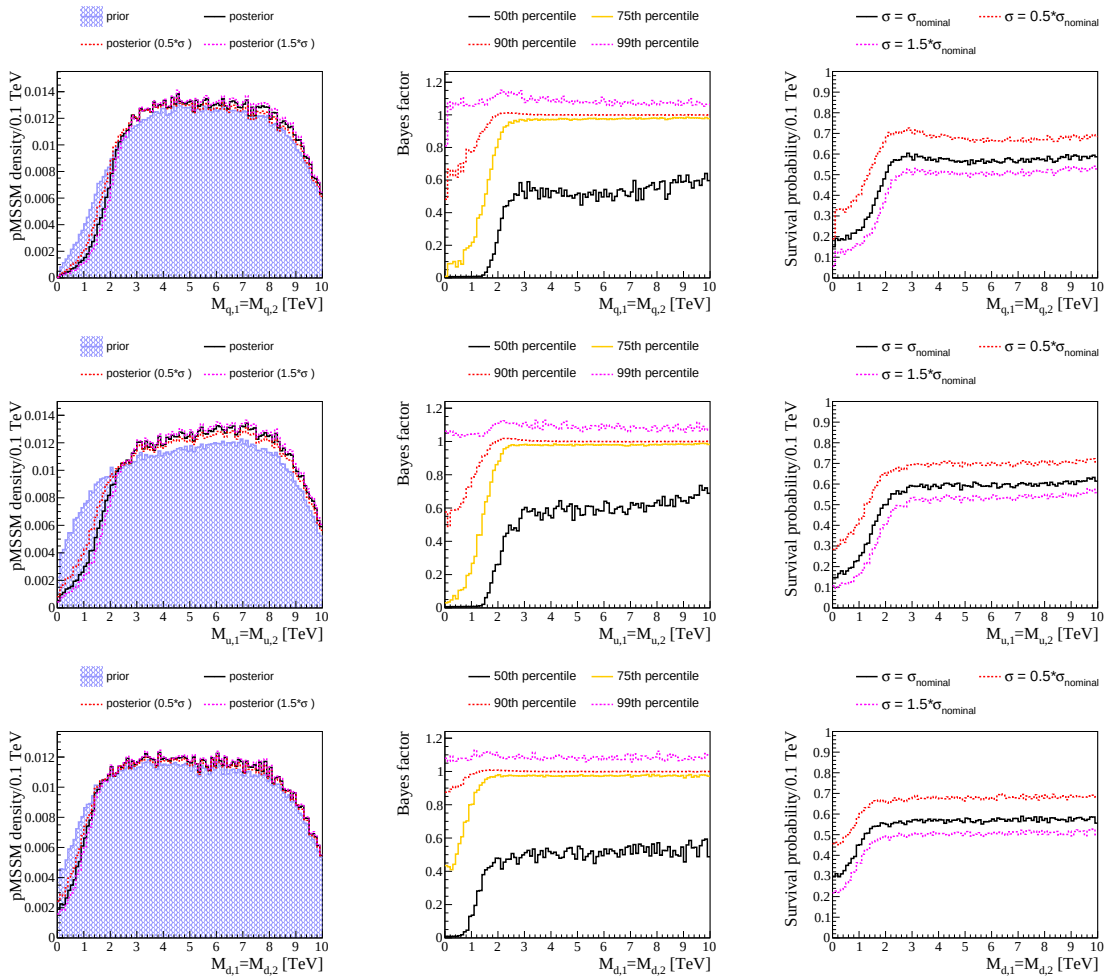

Figure 95: Impact of the considered LHC searches on the first-generation squark mass parameters $M_{q,1}$ (top row), $M_{u,1}$ (center row), and $M_{d,1}$ (bottom row), in terms of the prior and posterior densities (left column), Bayes factor quantiles (center column), and the survival probability (right column). A detailed description of the plot elements is given in Section 7.

In contrast to the squark mass parameters, the distributions for the gluino mass parameter M_3 (Figure 96) looks almost identical to those of the gluino mass $m(\widetilde{g})$. This is because the gluino mass is almost completely determined by the gluino mass parameter, with a trend of $\frac{M_3}{m(\widetilde{g})} \to \frac{1}{2}$ towards small gluino masses. The features visible in the distributions are thus shifted towards smaller masses in M_3, compared to $m(\widetilde{g})$.

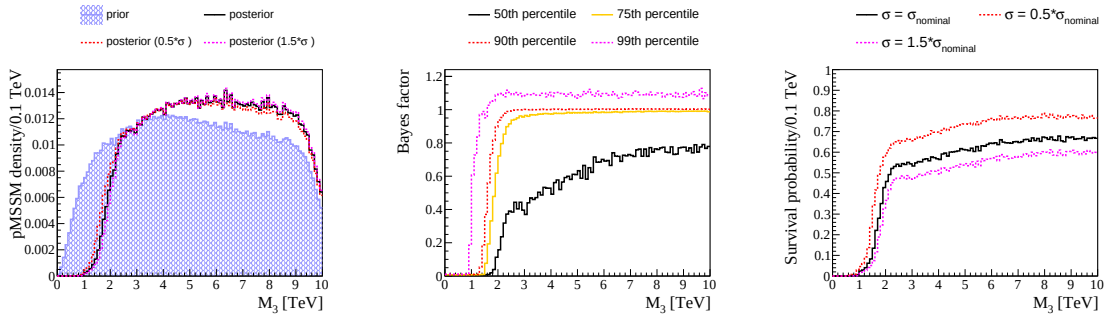

Figure 96: Impact of the considered LHC searches on the gluino mass parameter M_3, in terms of the prior and posterior densities (left), Bayes factor quantiles (center), and the survival probability (right). A detailed description of the plot elements is given in Section 7.

8.3.2 Electroweak SUSY

As discussed in detail in Section 5.4, limitations in the spectrum generators, which lead to chargino lifetimes in the order of meters and kilometers, make statements on the wino-mass parameter M_2 unreliable in the no-mixing limit of the gauge eigenstates, especially in models where the LSP is a pure wino. Similarly, the small $|\mu|$ - large Q_{SUSY} limit is not accessed due to the (likely) artificial occurrence of tachyons in the particle spectra of these models. To start, Figure 97 shows the impact of the considered LHC searches on the the higgsino mass parameter μ. The LHC impact is largely symmetric with respect to the sign of μ, at least for the marginalized 1-D distributions. The posterior density is suppressed at small $|\mu|$ due to direct sensitivity of the LHC to higgsino-like LSP and a lack of significant excess consistent with such models. However, the peak position of the posterior is shifted towards smaller $|\mu|$. This shift is also seen in the distribution of survival probabilities, which shows a peak at $|\mu| \simeq 1\,\text{TeV}$ and a subsequent drop towards larger $|\mu|$.

This peak has two likely contributions. The less important contribution comes from the fact that the cross section is positively correlated to $|\mu|$ for $|\mu| \gtrsim 1\,\text{TeV}$, which can be seen from the prior credibility intervals in Figure 100. This correlation is likely caused by the tachyon issue discussed in Appendix B. For $|\mu| < 1\,\text{TeV}$, parts of the large-Q_{SUSY} region is not sampled. This large-Q_{SUSY} region is correlated to larger cross sections, which can be seen from the prior credibility intervals in Figure 99. The facts that larger Q_{SUSY} is correlated to larger cross sections $\sigma^{\text{total}}_{\text{Pythia8@LO}}$ and large $|\mu|$ is correlated to large Q_{SUSY}, transitively means that $|\mu|$ is positively correlated to $\sigma^{\text{total}}_{\text{Pythia8@LO}}$ for $|\mu| \gtrsim 1\,\text{TeV}$ (compare prior credibility intervals in Figure 100). However, this effect is minor compared to the fact that $|\mu| \gtrsim 1\,\text{TeV}$ allows for models with more pure winos, which requires that $M_2 \ll \mu$ and $M_2 \ll M_1$. Because $\Delta m(\widetilde{\chi}_1^{\pm}, \widetilde{\chi}_1^0)$ is inversely correlated to its purity in the case of winos, the charginos in pure wino models tend to have a longer lifetime. This increases the signal acceptance in the search for disappearing tracks. Figure 98 shows the survival probabilities for two scenarios, one where only the search for disappearing tracks is considered, and one where every search except for the search for disappearing tracks is considered. We can see that the drop in survival probability for large $|\mu| \gtrsim 1\,\text{TeV}$ is almost exclusively due to the search for disappearing tracks. Additionally the survival probability distribution that considers all searches except for the search for disappearing tracks can be used to estimate the effect from the correlation of large $|\mu|$ to smaller cross sections, which comes out as a drop in the survival probability of approximately 5%. The fact that the purity of the winos is the correct explanation is established by Figure 101, which shows that the search for disappearing tracks loses sensitivity to small M_2 as $|\mu|$ or M_1 become small.

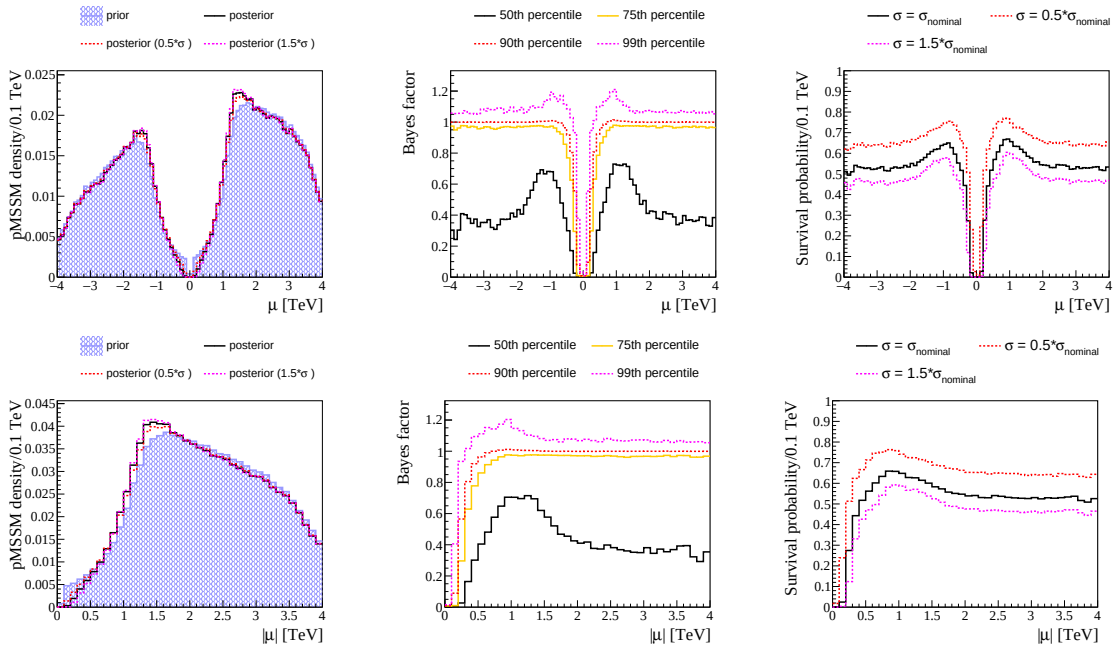

Figure 97: Impact of the considered LHC searches on the higgsino mass parameter μ (top row) and its absolute value $|\mu|$ (bottom row), in terms of the prior and posterior densities (left column), Bayes factor quantiles (center column), and the survival probability (right column). A detailed description of the plot elements is given in Section 7.

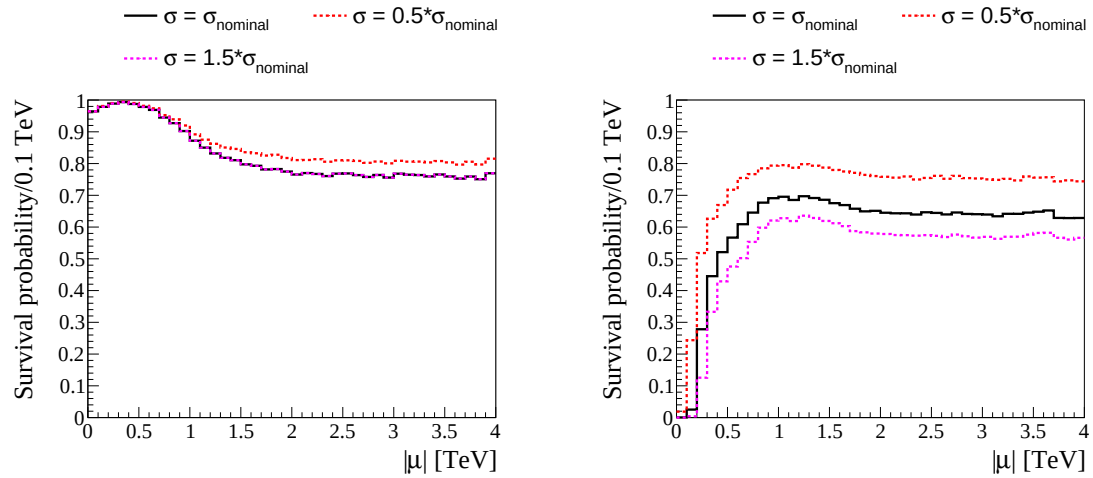

Figure 98: Survival probabilities in the space of $|\mu|$, considering only the search for disappearing tracks (left) and all searches except that for disappearing tracks (right).

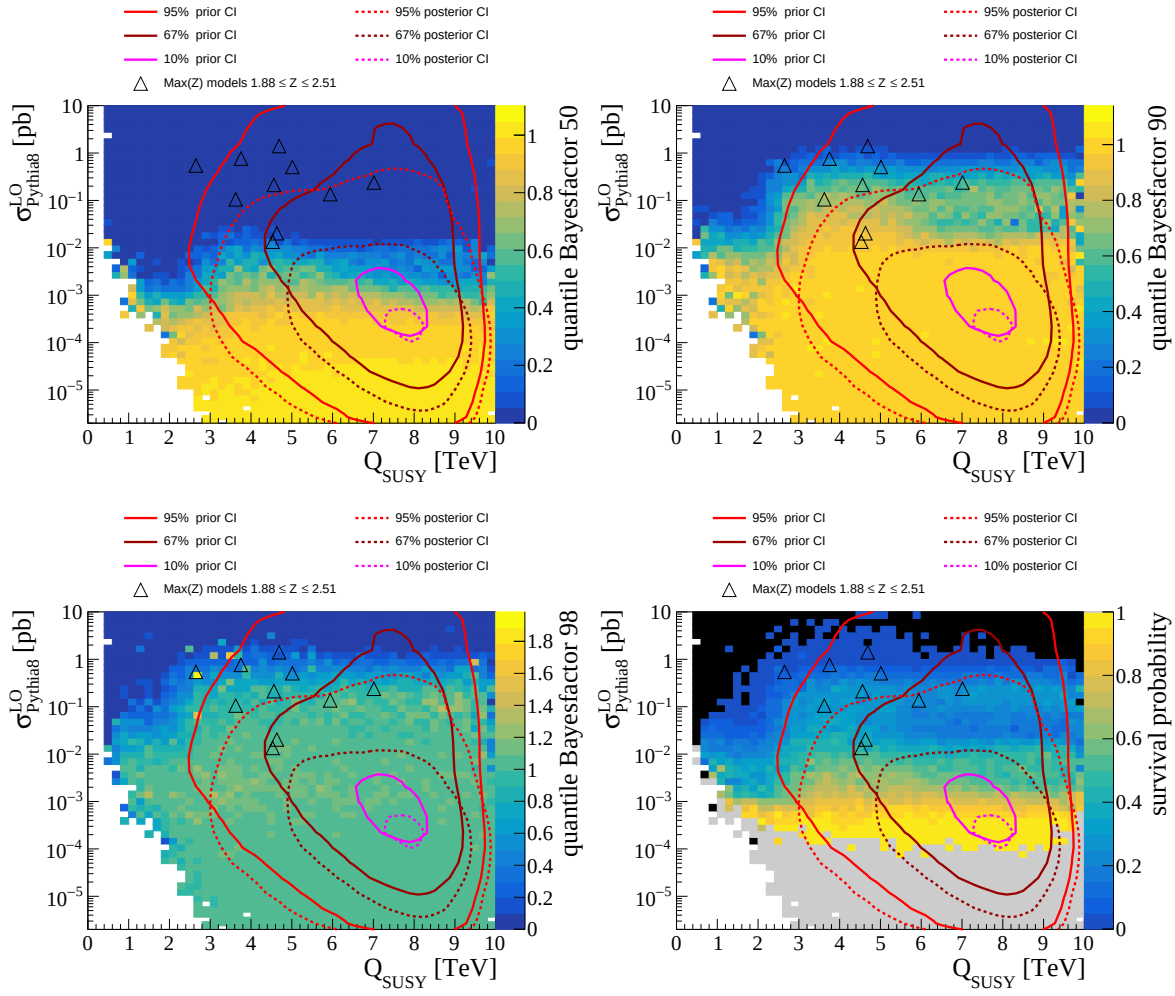

Figure 99: Impact of the considered LHC searches in the plane of the SUSY scale Q_{SUSY} and the total production cross section $\sigma^{total}_{Pythia8@LO}$, in terms of the median (top left), 90th (top right), and 98th (bottom left) quantiles of the Bayes factor, as well as the survival probability (bottom right). Grey-colored bins have a survival probability of exactly one, black-colored bins have a survival probability of exactly zero, white bins are empty. A detailed description of the plot elements is given in Section 7.

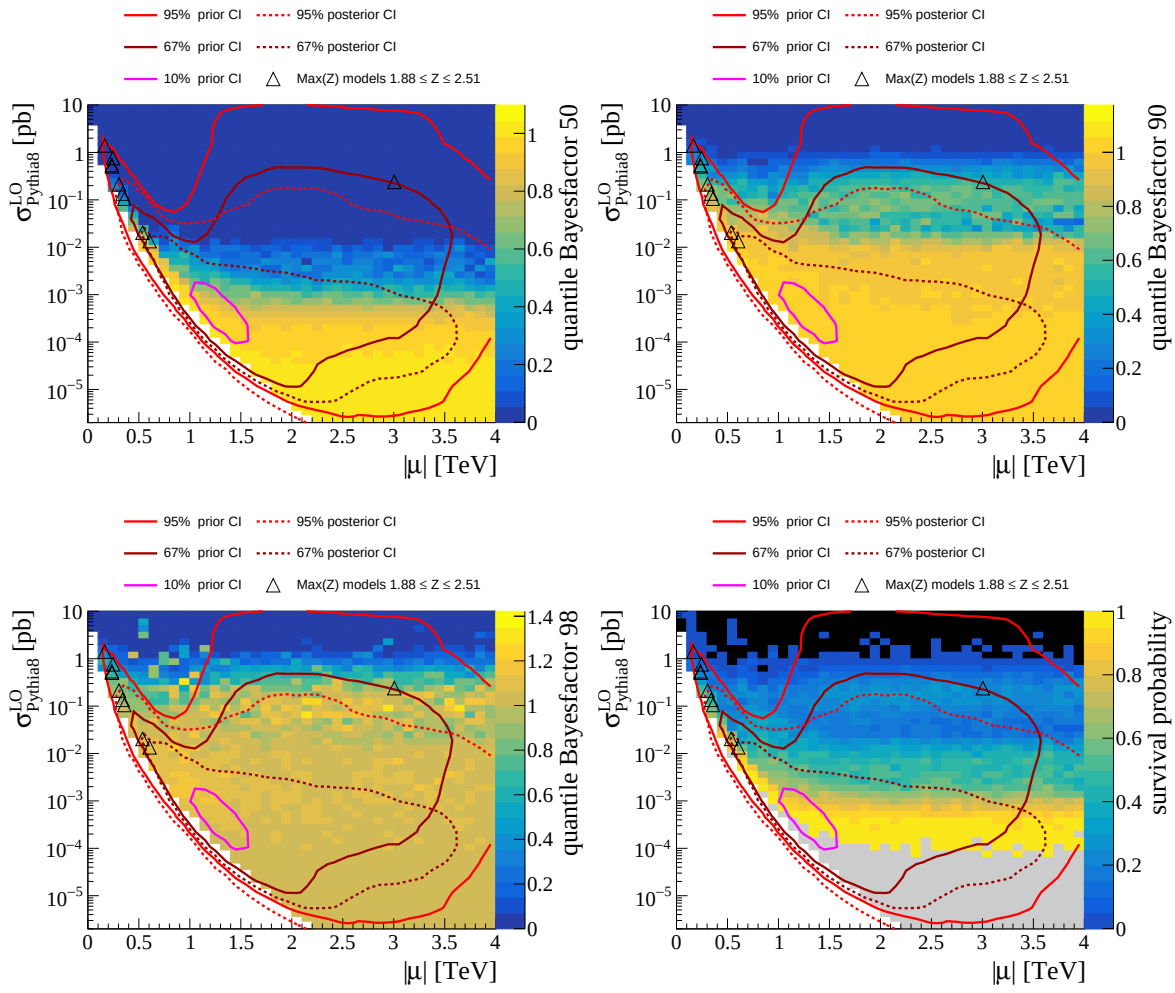

Figure 100: Impact of the considered LHC searches in the plane of the absolute value of the higgsino mass parameter $|\mu|$ and the total production cross section $\sigma^{\text{total}}_{\text{Pythia8@LO}}$, in terms of the median (top left), 90th (top right), and 98th (bottom left) quantiles of the Bayes factor, as well as the survival probability (bottom right). Grey-colored bins have a survival probability of exactly one, black-colored bins have a survival probability of exactly zero, white bins are empty. A detailed description of the plot elements is given in Section 7.

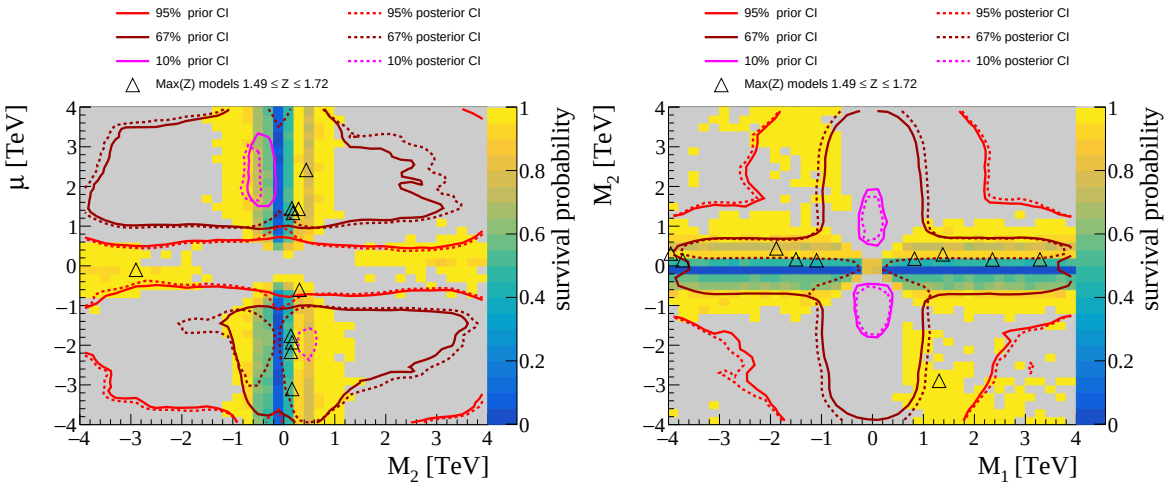

Figure 101: Survival probability, considering only the search for disappearing tracks, in the plane of μ and M_2. Grey-colored bins have a survival probability of exactly one, black-colored bins have a survival probability of exactly zero, white bins are empty. A detailed description of the plot elements is given in Section 7.

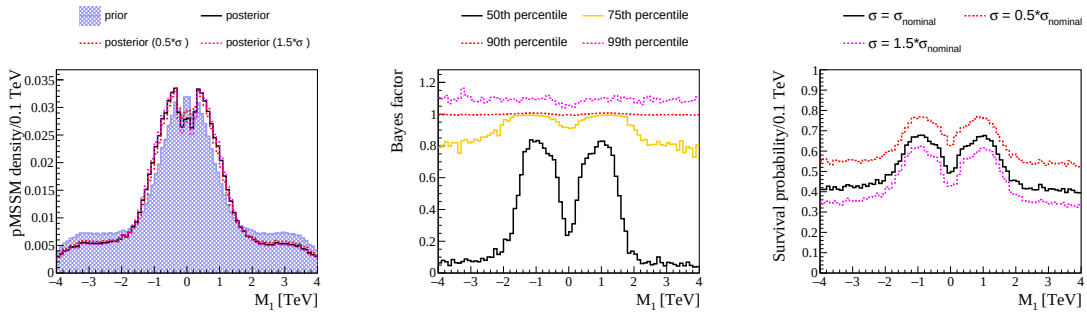

Figure 102: Impact of the considered LHC searches on the bino-mass parameter M_1, in terms of the prior and posterior densities (left), Bayes factor quantiles (center), and the survival probability (right). A detailed description of the plot elements is given in Section 7.

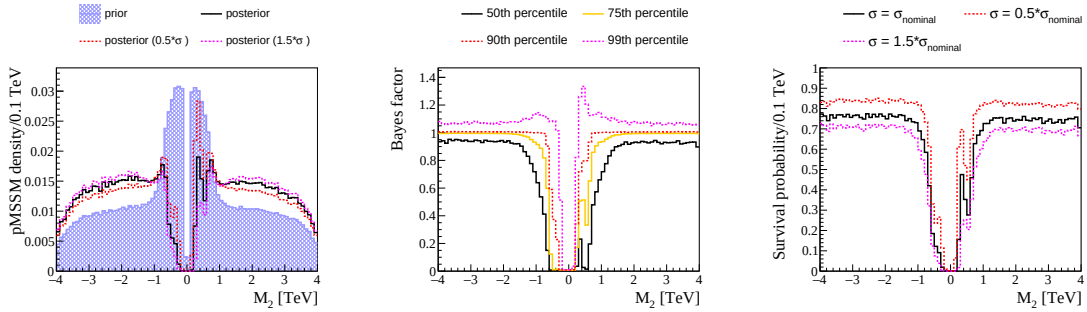

Figure 103: Impact of the considered LHC searches on the bino-mass parameter M_2, in terms of the prior and posterior densities (left), Bayes factor quantiles (center), and the survival probability (right). A detailed description of the plot elements is given in Section 7.

Consequently, the same feature can be seen to affect the bino-mass parameter M_1, as shown in Figure 102. The impact on the bino-mass parameter is otherwise largely symmetric with regards to its sign. An exception to this can be seen in Figure 101, where there is a slight increase in sensitivity at large M_1 and M_2, but only where $M_1 \times M_2 < 0$.

Contrary to this, there is a significant dependence of the LHC impact on the sign of M_2 for small $|M_2|$, a region populated by models with a wino-like LSP. The one-dimensional marginalized impact distributions are shown in Figure 103, where we see that there is a local maximum in the survival probability and posterior density at $M_2 \simeq 400\,\text{GeV}$, which is not present at $M_2 \simeq -400\,\text{GeV}$. This is caused by differences in the chargino lifetime for models positive and negative M_2, where a larger part of this region with a negative M_2 comes with a larger chargino lifetime. This enhances the acceptance of the search for disappearing tracks in the relevant mass range to negative M_2 and serves to suppress the survival probability. This is clearly established in Figure 104, which shows the $c\tau(\widetilde{\chi}_1^\pm)$ in the region relevant to disappearing tracks against the value of M_2. We can see that the region of $c\tau(\widetilde{\chi}_1^\pm) \simeq 1\,\text{m}$ that the search for disappearing tracks is most sensitive to is much more populated for negative M_2 than for positive M_2. However, while making general statements about connections between the sign of M_2 to the life time may be safe, to infer the exact impact on M_2 is unreliable here, as the mapping of M_2 to the chargino lifetime $c\tau(\widetilde{\chi}_1^\pm)$ is questionable due to limitations of the spectrum generator in generating correct chargino-neutralino mass splittings – as discussed in Section 5.4.

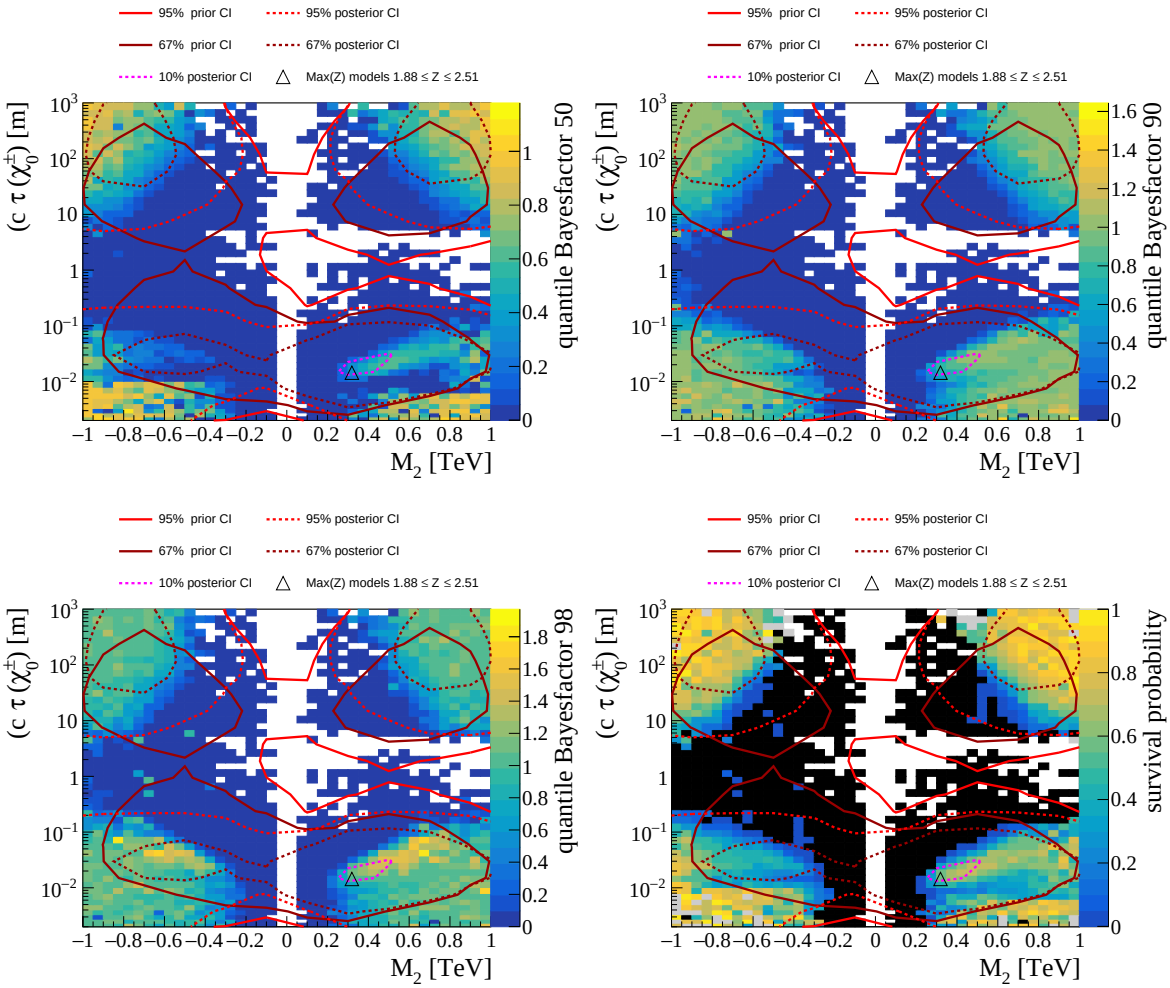

Figure 104: Impact of the considered LHC searches in the plane of the wino-mass parameter M_2 and the lifetime of the lighter chargino $c\tau(\widetilde{\chi}_1^{\pm})$, in terms of the median (top left), 90th (top right), and 98th (bottom left) quantiles of the Bayes factor, as well as the survival probability (bottom right). A detailed description of the plot elements is given in Section 7.

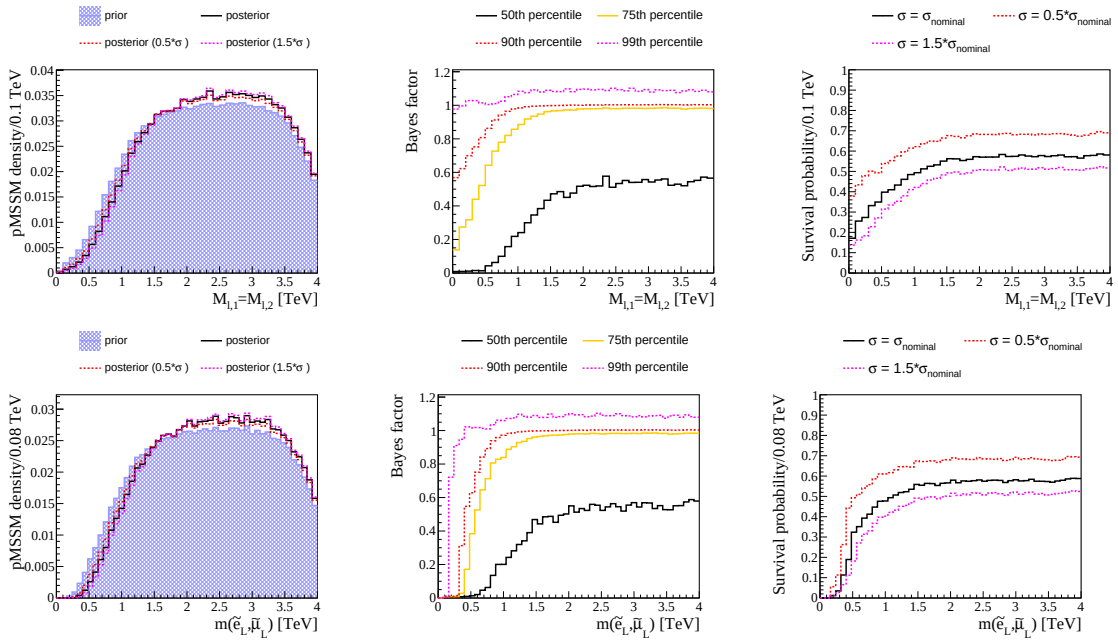

Figure 105: Comparison of the impact of the considered LHC searches on the slepton mass parameter $M_{l,1}$ (top row) and the left-chiral selectron (smuon) mass $\widetilde{e}_L$ ($\widetilde{\mu}_L$) (bottom row), in terms of the prior and posterior densities (left column), Bayes factor quantiles (center column), and the survival probability (right column). A detailed description of the plot elements is given in Section 7.

8.3.3 Slepton sector

The distributions for the slepton mass parameters $M_{l,1}$, $M_{l,3}$, $M_{r,1}$, and $M_{r,3}$ are almost identical to their respective slepton masses, except that the posterior density is somewhat larger for small masses (compare Figure 105 as an example). This is because, at small mass values, there exist models where the slepton is significantly heavier than the respective pMSSM parameter due to mixing and running of the renormalization group equations. Because the LHC constrains the physical observable and not the pMSSM parameter directly, the model space where the pMSSM parameter is very small and the slepton is heavy enough to evade constraints remains well populated in the posterior.

8.3.4 Higgs sector

There seems to be direct sensitivity in the considered searches to the heavy Higgs bosons, which can be seen as a steep drop in the survival probability in Figure 106, although no direct searches for heavy Higgs bosons are included. This apparent sensitivity comes from a positive correlation of the heavy Higgs mass to other light sparticles, mostly the LCSP mass. The correlation to the LCSP mass can be seen in Figure 107, where most of the models with a low m_A also contain a light m(LCSP). Most of the remaining excluded models either feature a long-lived chargino, or a very light slepton, on which basis the models are excluded. However, the survival probability seems to be slightly smaller if $m_A < m$(LCSP), which may be related to an increases sensitivity if the decay mode to a heavy Higgs boson is open to the LCSP. The low Bayes factors at small m_A have very little impact of the posterior density however, since the prior at small m_A is already extremely suppressed. The LHC is

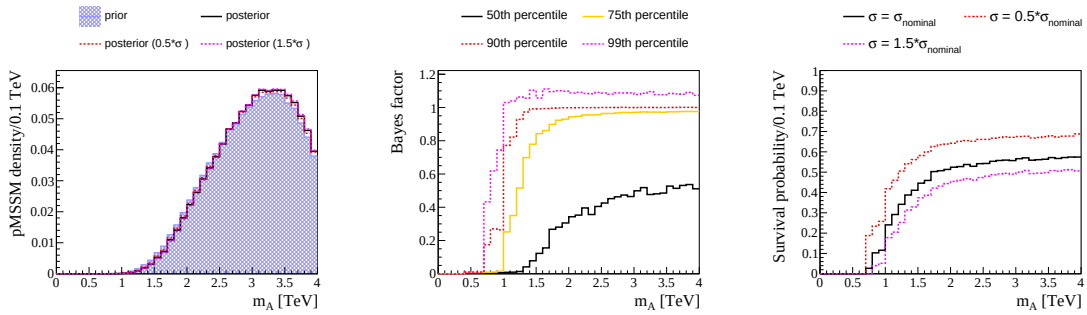

Figure 106: Impact of the considered LHC searches on the heavy Higgs boson mass m_A, in terms of the prior and posterior densities (left), Bayes factor quantiles (center), and the survival probability (right). A detailed description of the plot elements is given in Section 7.

slightly more sensitive to small tan(β), as seen in Figure 108.

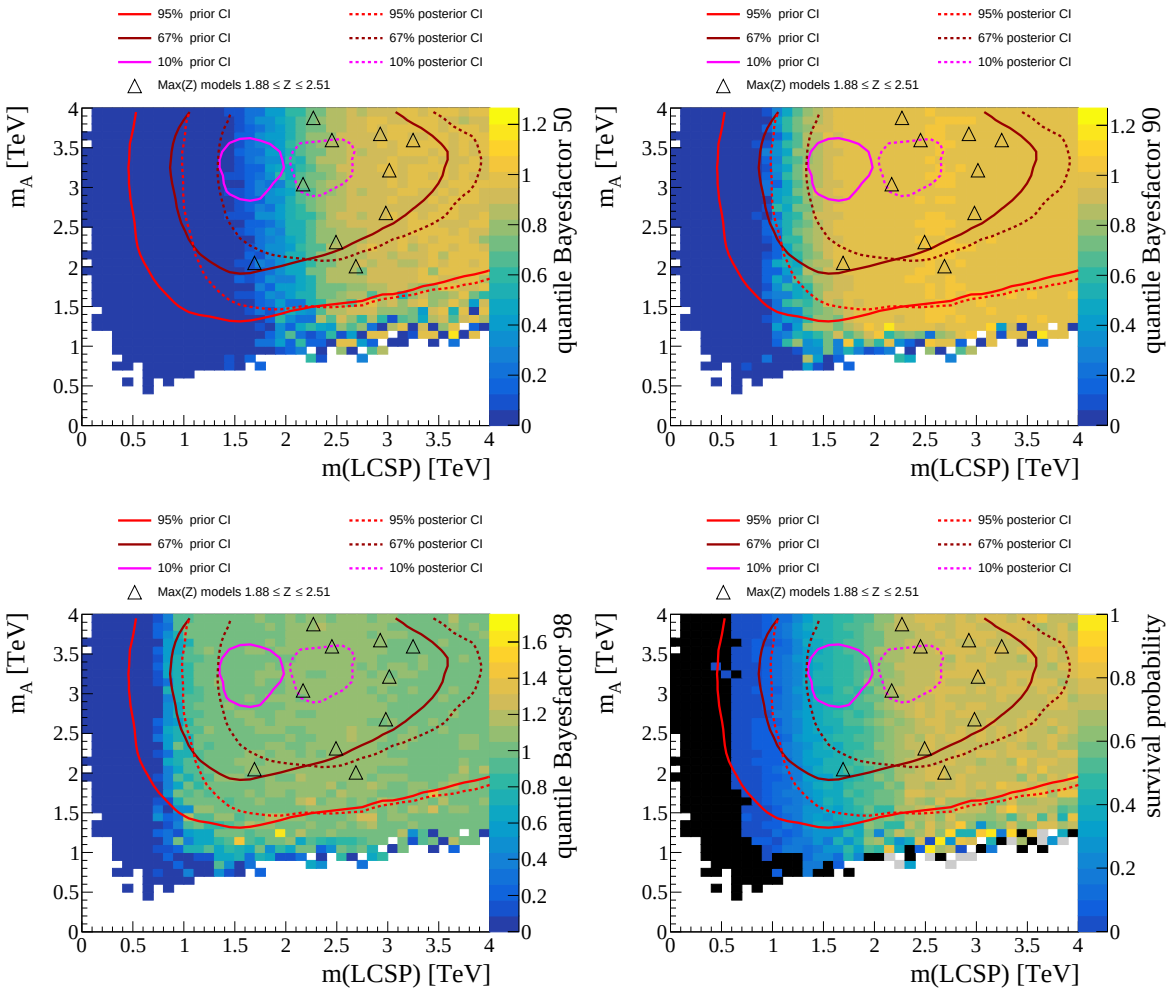

Figure 107: Impact of the considered LHC searches in the plane of heavy Higgs boson mass m_A and the LCSP mass m(LCSP), in terms of the median (top left), 90th (top right), and 98th (bottom left) quantiles of the Bayes factor, as well as the survival probability (bottom right). Grey-colored bins have a survival probability of exactly one, black-colored bins have a survival probability of exactly zero, white bins are empty. A detailed description of the plot elements is given in Section 7.

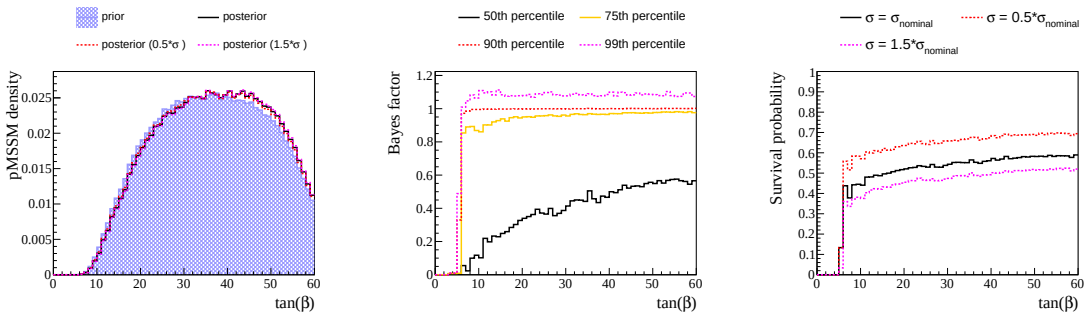

Figure 108: Impact of the considered LHC searches on the ratio of the Higgs vacuum expectation values $\tan(\beta)$, in terms of the prior and posterior densities (left), Bayes factor quantiles (center), and the survival probability (right). Note that the scan resolution is very limited at small $\tan(\beta)$ due to the very small prior density. A detailed description of the plot elements is given in Section 7.

8.4 Dark matter

There are three ways in which dark matter is considered in this thesis, firstly in form of constraints by direct detection experiments on the $\widetilde{\chi}_1^0$-nucleon interaction cross sections. Secondly in form of the compatibility of the dark matter relic density predicted for each pMSSM model with its measurement by the Planck satellite observatory [8]. Thirdly, limits on the indirect dark matter annihilation cross section are included. These observables were not included in the initial sampling of the pMSSM, but rather are implemented here in terms of binary exclusion, which allows for the study of the residual pMSSM spaces.

8.4.1 Direct detection

The direct detection cross sections and corresponding p-value are calculated for each pMSSM point using `MicrOMEGAs` 5.2.1 [94]. This p-value considers results from the `XENON1T` [148], `CRESST-III` [57], `DarkSide-50` [149], and `PICO-60` [59] experiments. More recent results with larger sensitivity, in particular from the LUX-ZEPLIN experiment [60], could not be considered in this work due to time constraints. Based on the published upper limits on the spin-independent LSP-nucleon cross section in [60], an increase in sensitivity to this cross section by approximately a factor 3 should be expected for its inclusion.

These p-values, and in general the sensitivity of direct detection experiments in the pMSSM, are almost exclusively driven by the LSP-nucleon interaction cross sections. There are four interactions to consider: the spin-dependent and spin-independent interactions between the LSP and protons, and the LSP and neutrons. Here, the spin refers to the spin of the nucleon, where the interaction comes from a coupling of the LSP spin to the spin of the nucleon. The distributions of the four interaction cross sections are shown in Figure 109 for the LHC prior and posterior densities, along with the survival probability with regards to the direct detection constraints. Models are here considered excluded if the p-value from `MicrOMEGAs` is $p < 0.05$, which corresponds to exclusion at 95%CL. We can see that the spin-dependent cross sections tend to be significantly larger than the spin-independent cross sections. The much steeper survival probability distribution for the spin-independent cross sections indicates that they are much more important in terms of exclusion: for most pMSSM models, a large spin-independent cross section leads to an exclusion by direct detection experiments. The same is not true for spin-dependent cross sections. This is also directly confirmed in Figure 110, which shows that the prior density far more extends into the region of excluded spin-independent cross sections than into the region of excluded spin-dependent cross sections.

The LSP-nucleon cross sections are strongly dependent on the type of LSP, as shown in Figures 109 to 113. We can see that models with a higgsino-like LSP have the largest interaction cross sections, followed by models with a wino-like LSP. This is because the interaction is mediated by Higgs or Z exchange. As a consequence, bino-like do not couple directly at all, which results in very small cross sections, and differences arise for wino-like and higgsino-like LSP due to their different couplings. It turns out that the interaction cross section is suppressed at tree level by $\sigma^{\mathrm{SI}} \sim \mathrm{M}_2^2 \times \mu^{-4}$ for pure wino-like LSP, and by $\sigma^{\mathrm{SI}} \sim \mathrm{M}_2^{-2}$ for pure higgsino-like LSP [150]. In conjunction with the shape of the low-energy prior, which favors large values of $|\mu|$ (shown for example in Figure 45), the interaction cross sections for winos is suppressed for a large fraction of models that feature large $|\mu|$. The opposite is true for models with higgsino-like LSP, as both M_1 and M_2 are predominately small in the low-energy prior. As a result, the interaction cross section tends to be larger for pure higgsinos than for pure winos. Note also that the suppression is smaller for more mixed states, with smaller differences in at least two of the mass parameters, which will become important later.

The different suppression of the interaction cross section for wino-like and higgsino-like LSP also shows in different sensitivity of the direct detection experiments to the LSP mass, seen in Figure 111. We can see directly that direct detection experiments are not sensitive to models with a bino-like LSP, because they do not interact sufficiently with nucleons. For models with a higgsino-like LSP, the survival probability is low at small $m(\widetilde{\chi}_1^0)$ and increases towards larger $m(\widetilde{\chi}_1^0)$. This behavior is due to the generally decreasing interaction cross section with large LSP masses. Winos show the opposite behavior, with a decreasing survival probability towards larger $m(\widetilde{\chi}_1^0)$. For them, the spin-dependent cross section seems to be mostly uncorrelated with the LSP mass, while the spin-independent cross sections decrease towards smaller masses for the bulk of the models with a wino-like LSP. These effects can be seen in Figure 112. The decrease of the spin-independent cross section in the bulk of the pMSSM is due to the suppression discussed in the previous paragraph.

Another question that can be addressed from this plot is that of the complementarity between

direct LHC searches and direct dark matter detection experiments. The direct detection experiments are sensitive to the regions not covered by the LHC at large wino or higgsino masses. This is a region where the production cross sections at the LHC have fallen so much that it is no longer sensitive to their direct production, but the interaction cross section with nucleons is large enough to exclude a multitude of models. Figure 113 most clearly shows this in the plane of the LHC production cross section and the LSP-nucleon cross sections. Likewise, the LHC is sensitive to regions where the direct detection cross sections are too small to be constrained by direct detection experiments.

To gauge the impact that the inclusion of the direct-detection experiments has on the pMSSM, we compare the survival probabilities and credibility intervals in two observable planes, which focus on the colored sector of the pMSSM and the electroweak sector of the pMSSM. First, in Figure 114 we can see that some sensitivity is gained in the region at large $m(\widetilde{\chi}_1^0)$ and large $m(\text{LCSP})$ that is not constrained by the LHC. This results in a shift of the probability density towards smaller $m(\widetilde{\chi}_1^0)$ and larger $m(\text{LCSP})$. The shift to smaller $m(\widetilde{\chi}_1^0)$ is here entirely complementary to constraints from the LHC, which tend to shift the posterior of particles masses to larger values, in the absence of a positive signal of new physics.

A notable exception to this is found in the search for disappearing tracks, where the correlation of chargino lifetime to the purity of the wino-like LSP softly constrains the bino- and higgsino-mass parameters from above. This is visible, for example, in Figure 115. We first notice that there is a strong increase in sensitivity if the direct detection searches are included, indicated by the drop of the survival probability in the range of intermediate $\Delta m(\widetilde{\chi}_1^\pm, \widetilde{\chi}_1^0)$ from 300 MeV to 200 GeV. This increased sensitivity and lowered survival probability extends towards very large $m(\widetilde{\chi}_1^0)$. The effect is especially pronounced in this region because the fraction of models with a bino-like LSP is very small, and the direct detection constraints most strongly affect higgsinos and winos. In terms of the posterior shape, we see a shift away from the intermediate $\Delta m(\widetilde{\chi}_1^\pm, \widetilde{\chi}_1^0)$ region and a suppression of the posterior peak associated with higgsino-like LSPs.

There is no apparent impact of the direct detection constraints on either the colored or the slepton sector of the pMSSM.

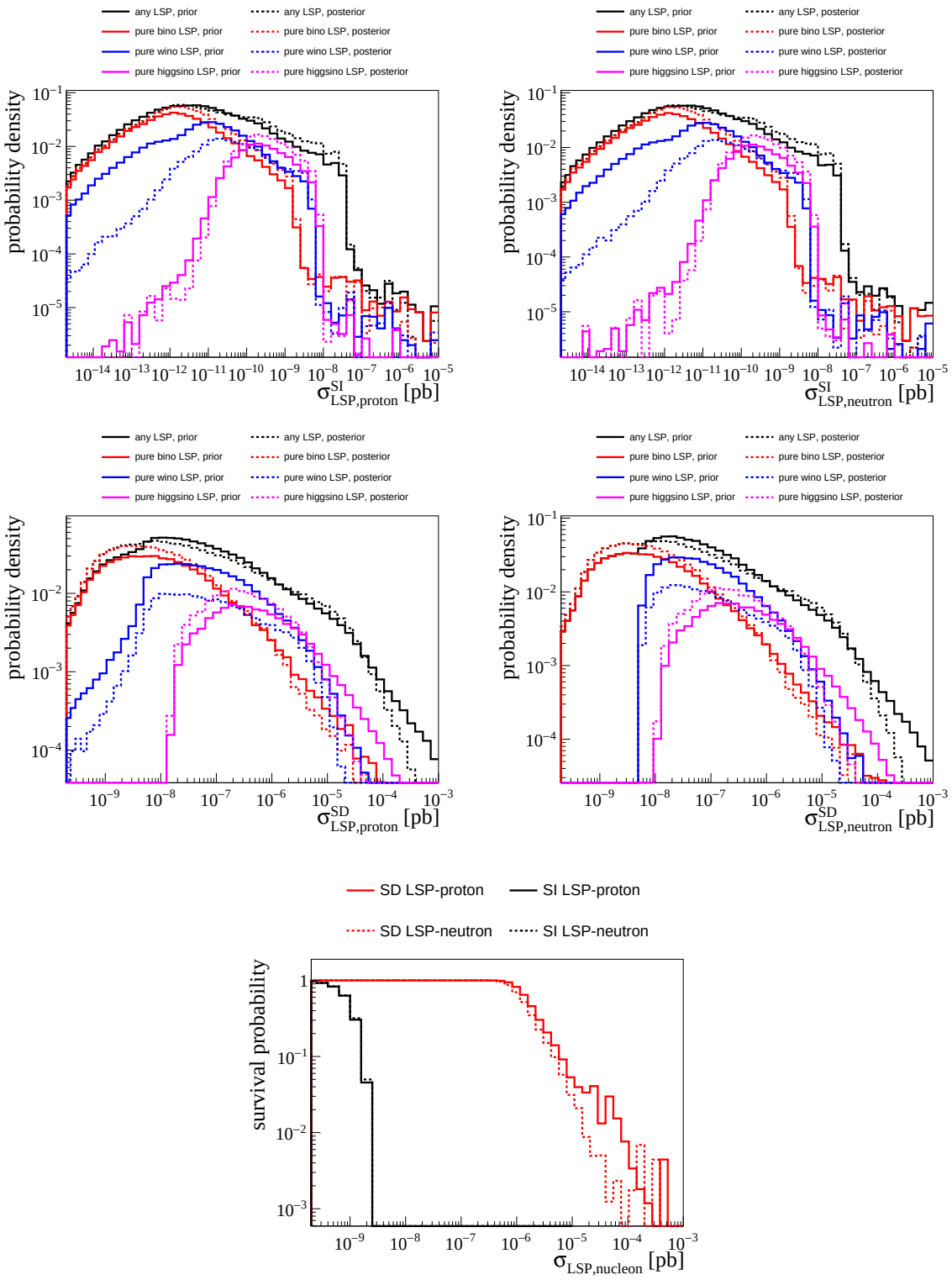

Figure 109: Distribution of pMSSM points as a function of the spin-independent (top) and spin-dependent (center) LSP-proton (left) and LSP-neutron (right) cross sections. The bottom plot shows the survival probability, with respect to only direct detection constraints, for the four interaction cross sections. The x-axis quantity is here the spin-dependent LSP-nucleon interaction cross section for the black histograms, and the spin-independent cross section for the red histograms.

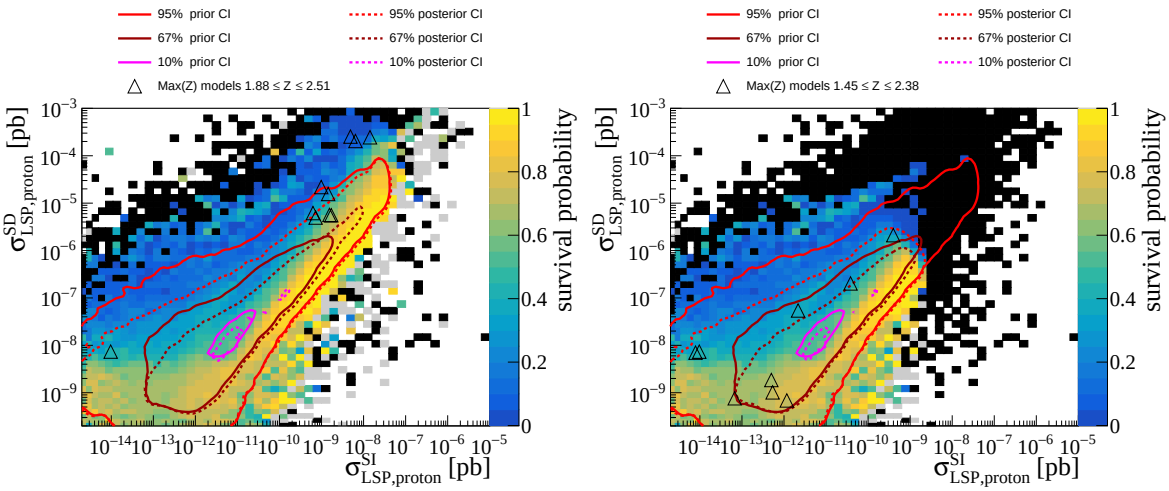

Figure 110: Survival probability with respect to the **LHC constraints** (left) and the **LHC constraints + direct detection constraints** (right) in the plane of the spin-independent and spin-dependent LSP-proton cross sections. Black color denotes bins with zero survival probability, grey denotes bins with a survival probability of exactly 1, white bins are empty. A detailed description of the plot elements is given in Section 7.

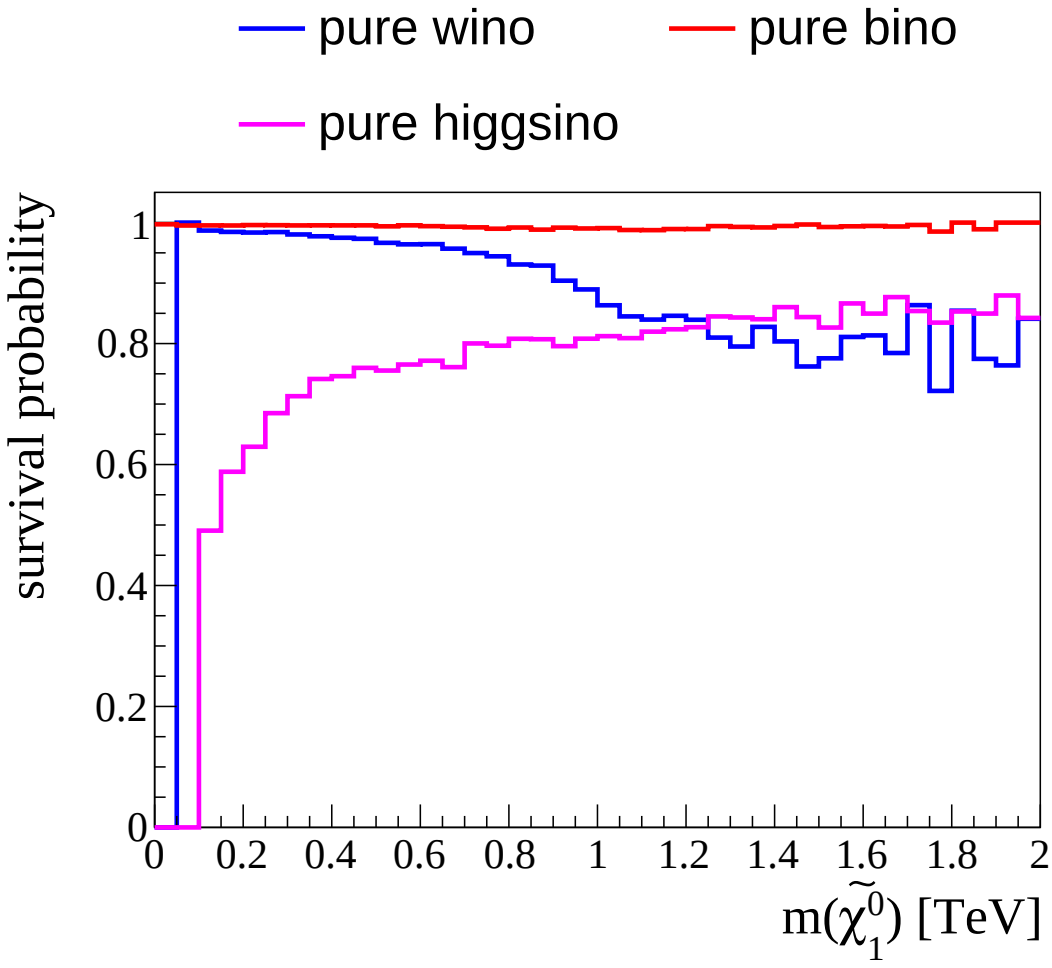

Figure 111: Survival probabilities with respect to constraints from direct detection experiments for the different types of LSP.

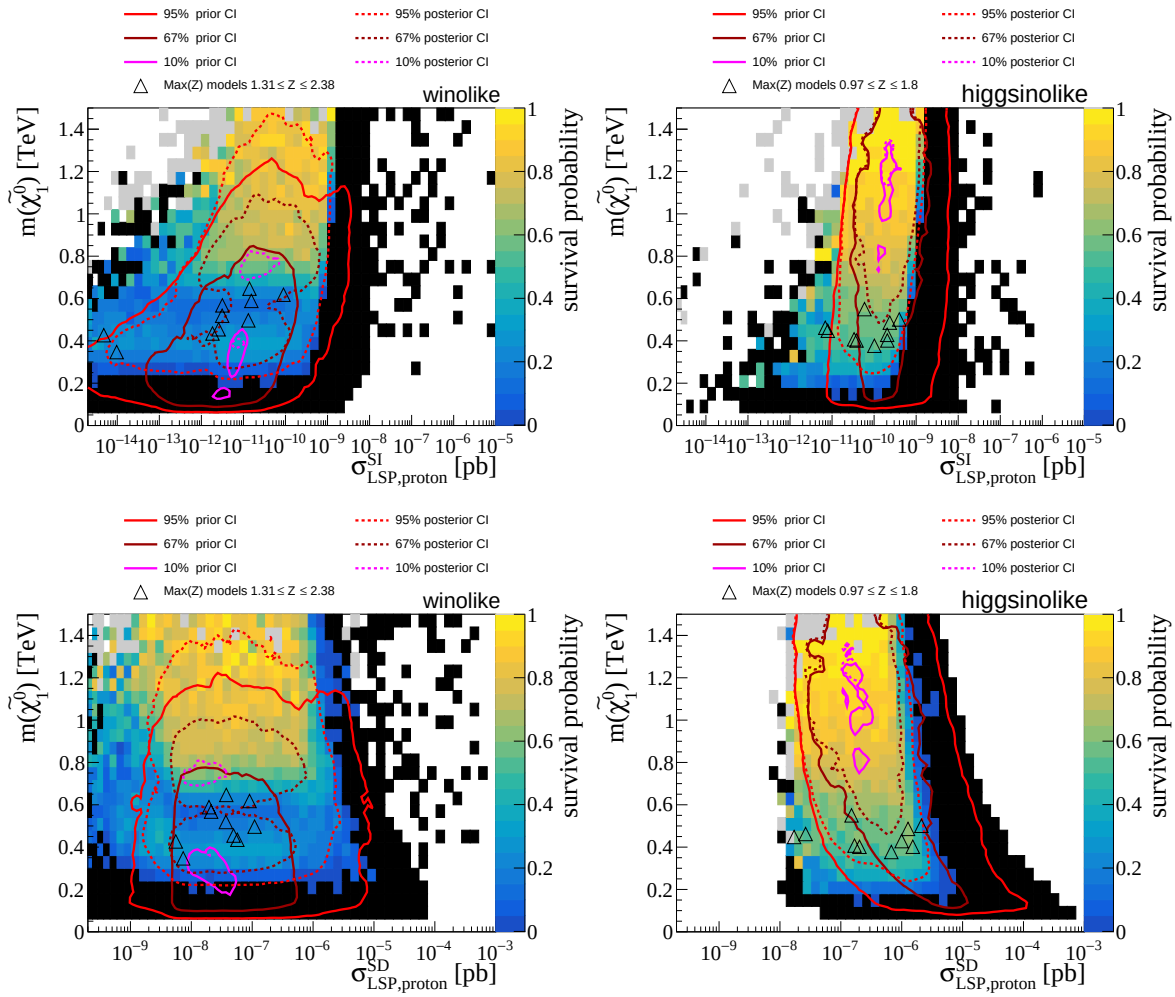

Figure 112: Survival probabilities for direct detection experiments and the LHC for wino-like (left column) and higgsino-like (right column) LSP, in the plane of $m(\widetilde{\chi}_1^0)$ and the spin-independent (top row) and spin-dependent (bottom row) $\widetilde{\chi}_1^0$-proton cross sections. Black color denotes bins with zero survival probability, grey denotes bins with a survival probability of exactly 1, white bins are empty. A detailed description of the plot elements is given in Section 7.

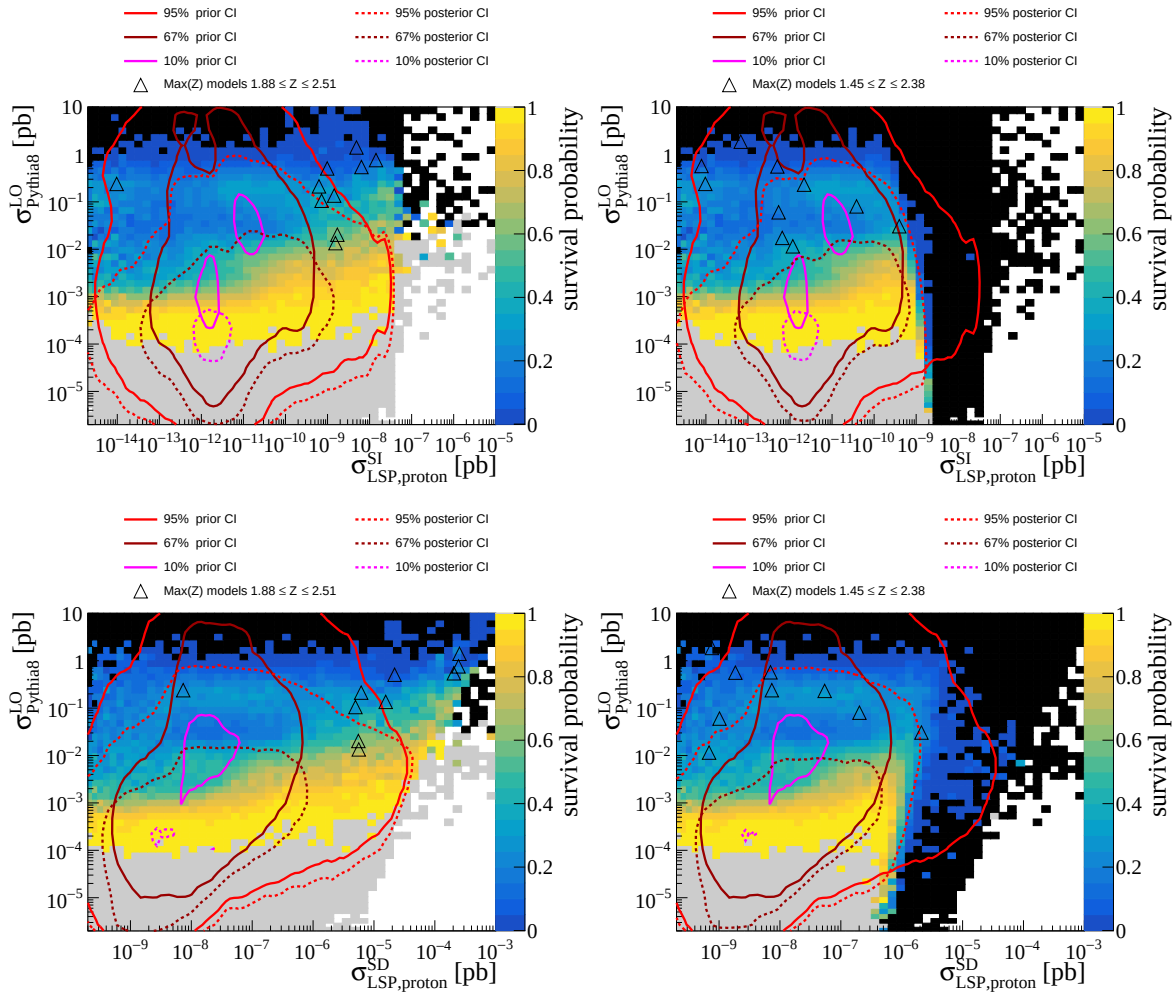

Figure 113: Survival probabilities considering the **LHC constraints** (left column) and the **LHC constraints + direct detection constraints** (right column) in the plane of the LHC production cross section $\sigma^{\text{total}}_{\text{Pythia8@LO}}$ and the spin-independent (top row) and spin-dependent (bottom row) $\widetilde{\chi}^0_1$-nucleon interaction cross sections. Black color denotes bins with zero survival probability, grey denotes bins with a survival probability of exactly 1, white bins are empty. A detailed description of the plot elements is given in Section 7.

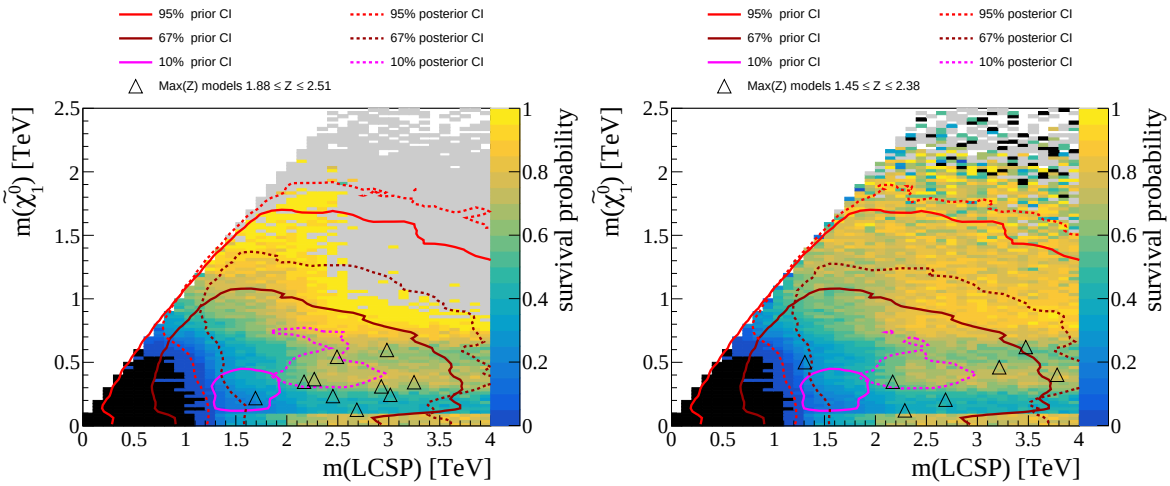

Figure 114: Survival probabilities considering the **LHC constraints** (left) and the **LHC constraints + direct detection constraints** (right), in the plane of $m(\tilde{\chi}_1^0)$ and m(LCSP). Black color denotes bins with zero survival probability, grey denotes bins with a survival probability of exactly 1, white bins are empty. A detailed description of the plot elements is given in Section 7.

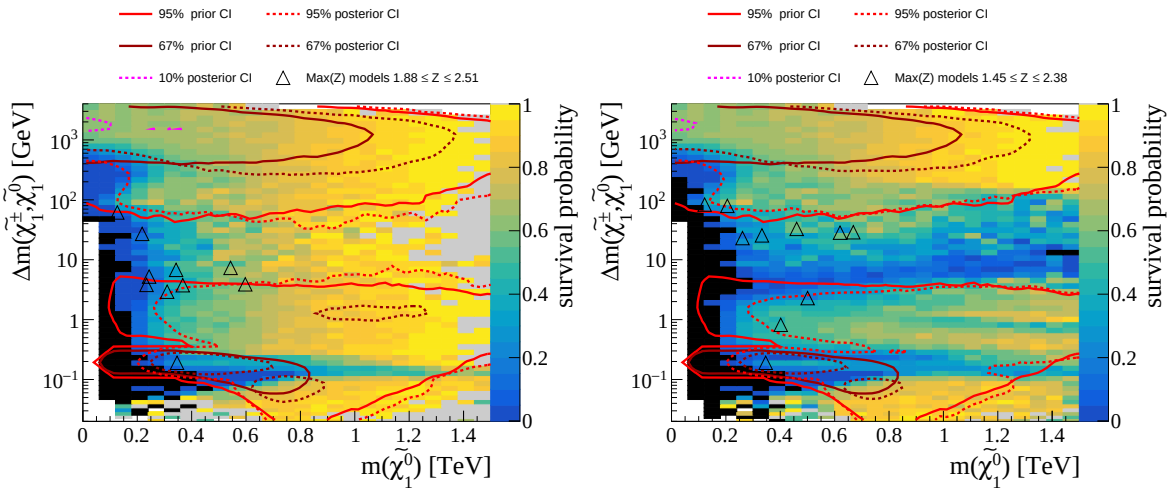

Figure 115: Survival probabilities in the the plane of $m(\tilde{\chi}_1^0)$ and $\Delta m(\tilde{\chi}_1^\pm, \tilde{\chi}_1^0)$, considering the **LHC constraints** (left), and the **LHC constraints + direct detection constraints** (right). Black color denotes bins with zero survival probability, grey denotes bins with a survival probability of exactly 1, white bins are empty. A detailed description of the plot elements is given in Section 7.

8.4.2 Relic density

There are various interesting ways in which the dark matter relic density Ωh^2 constrains the pMSSM. Because calculating the relic density for the pMSSM requires assumptions to be made about the cosmological model, we do not include the dark matter relic density in the likelihood that steers McMC generating the prior. The distribution of models in this scan thus covers a very wide range of Ωh^2 values. However, we examine the impact of the relic density constraint on the pMSSM after the fact in terms of residual compatible pMSSM subspaces.

8.4.2.1 LHC impact on relic density

The distribution of pMSSM model points as a function of the relic density is shown in Figure 116. On a logarithmic scale, we can see three peaks in the distribution. We find models with a wino-like LSP at very small relic densities $\Omega h^2 \lesssim 0.01$, models with a higgsino-like LSP at intermediate relic densities of $\Omega h^2 \simeq 0.1$, which encloses the measured value of the relic density, and models with a bino-like LSP which tend to have very large relic densities that usually exceed the measured value by multiple orders of magnitude. For the bino case, there is notably a tail that extends to small Ωh^2. For models with a bino-mixed LSP, the prior density peaks at $\Omega h^2 \simeq 0.2$ near the measure value, while for wino-higgsino mixed LSP the prior density peaks lower at $\Omega h^2 \simeq 0.05$. The LHC strongly

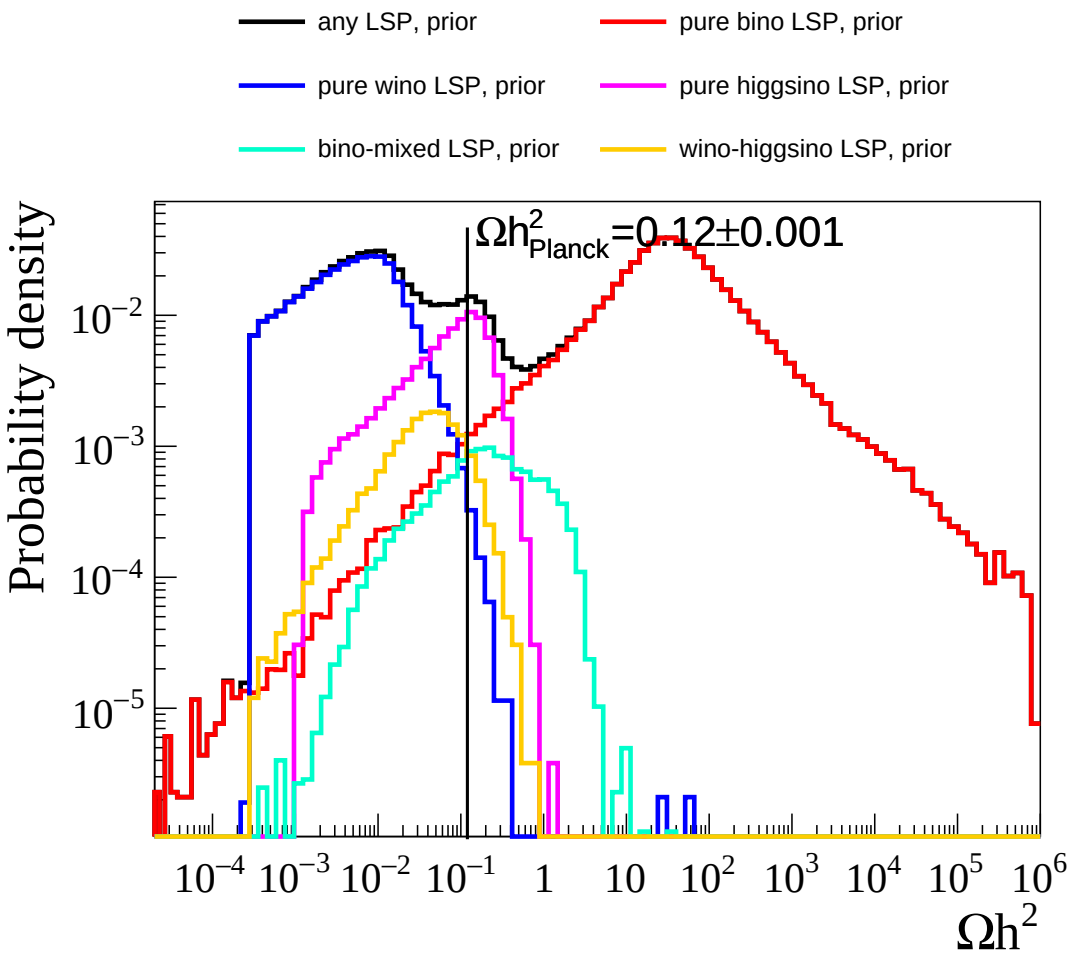

Figure 116: Distributions of the dark matter relic density Ωh^2 for the different types of LSP. Pure states here refer to LSP states with the square of the respective mixing matrix entry exceeding 0.95, bino-mixed LSP refers to non-pure states where the bino component is the largest, and wino-higgsino LSP refer to non-pure states where the bino component is smallest. The measured value of the relic density is indicated by the vertical black line at $\Omega h^2_{\text{Planck}} = 0.12 \pm 0.001$ [8].

constrains the small-relic density region of the pMSSM, and, to a somewhat lesser degree, the large relic density region. This can be seen in Figure 117. For small Ωh^2, the impact stems from the LHC sensitivity to long-lived charginos, which in the pMSSM most often occur in pure-wino models. Note again that in this scan, due to limitations of the spectrum generators, there is an abundance of models with extremely long-lived charginos that do not map onto the pMSSM (further details in Section 5.4). If this issue with the spectrum generator is resolved, the small relic density region would likely be shifted towards larger values more compatible with the measured value than what is shown here. Starting from small Ωh^2, the sensitivity of the LHC decreases as Ωh^2 increases. The reason can be found in Figure 118, where the prior credibility intervals show that at small Ωh^2, a region populated by models with a wino-like LSP or a higgsino-like LSP, the relic density is positively correlated to $m(\widetilde{\chi}_1^0)$. Thus, as the relic density increases, $m(\widetilde{\chi}_1^0)$ becomes larger and the LHC loses sensitivity.

Continuing to focus on Figure 118, the 95% prior credibility interval at small Ωh^2 features two overlapping modes, of which the one at smaller Ωh^2 contains the 67% prior credibility interval, and the other one is parallel to the first one at slightly larger Ωh^2. The mode at smaller relic density results from models with a pure wino-like LSP, while the mode at slightly larger relic densities results from models with a pure higgsino-like LSP. This credibility interval intersects the measured relic density of $\Omega h^2_{\text{Planck}} = 0.12 \pm 0.001$ [8] at approximately $m(\widetilde{\chi}_1^0) \simeq 650\,\text{GeV}$ – above this mass we can expect to start finding models with higgsino-like LSP that are compatible with $\Omega h^2_{\text{Planck}}$. However, the bulk of the higgsino-like models compatible with $\Omega h^2_{\text{Planck}}$ is found at larger $m(\widetilde{\chi}_1^0) \simeq 1.1\,\text{TeV}$. Extrapolating the smaller-Ωh^2 mode of the same credibility interval we can expect to find wino-like models that are compatible with data above approximately $m(\widetilde{\chi}_1^0) \gtrsim 1.5\,\text{TeV}$. Because of these comparatively large LSP masses, the LHC is not yet sensitive enough to constrain the bulk of pMSSM models that are compatible with the measurement at $\Omega h^2_{\text{Planck}}$. Figure 117 shows that the survival probability drastically increases towards and reaches 80% at the measured relic density. A larger luminosity might allow the LHC to probe into this most interesting region. Because the pMSSM model space where $\Omega h^2 \simeq \Omega h^2_{\text{Planck}}$ is less constrained than everywhere else, the posterior is lifted above the prior density in the region compatible with $\Omega h^2_{\text{Planck}}$. Figure 118 further shows that a significant part of the 67% credibility interval of the posterior density now covers the region of $\Omega h^2 \simeq \Omega h^2_{\text{Planck}}$, corresponding to LSP masses of $m(\widetilde{\chi}_1^0) \simeq 1.1\,\text{TeV}$. However, due to the comparatively small prior at $\Omega h^2 \simeq \Omega h^2_{\text{Planck}}$, the posterior density is still larger in the regions that under- and over-saturate the relic density.

The mass dependence of the relic density is opposite in the case of modes with a bino-like LSP, where the relic density is negatively correlated to the LSP mass, as seen in Figure 118 at large Ωh^2. This can be explained by the fact that the relic density for models with a bino-like LSP strongly depends on co-annihilation processes of the LSP – much more so than on the LSP mass itself. The cross sections for co-annihilation processes increase as the mass difference between the LSP and its prospective co-annihilation partner decreases. Due to the upper limit imposed on the pMSSM parameters, and therefore particle masses, in this scan, the tail of large mass differences to prospective co-annihilation partners increases as $m(\widetilde{\chi}_1^0)$ becomes lighter, which results in the extreme values of Ωh^2 seen in Figure 118.

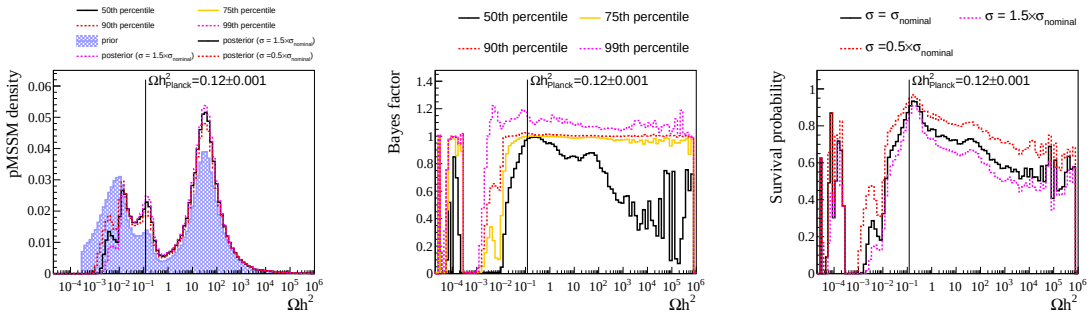

Figure 117: Impact of the considered LHC searches on the relic density Ωh^2, in terms of the prior and posterior densities (left), Bayes factor quantiles (center), and the survival probability (right). A detailed description of the plot elements is given in Section 7. The measured value of the relic density is indicated by the vertical black line at $\Omega h^2_{\text{Planck}} = 0.12 \pm 0.001$ [8].

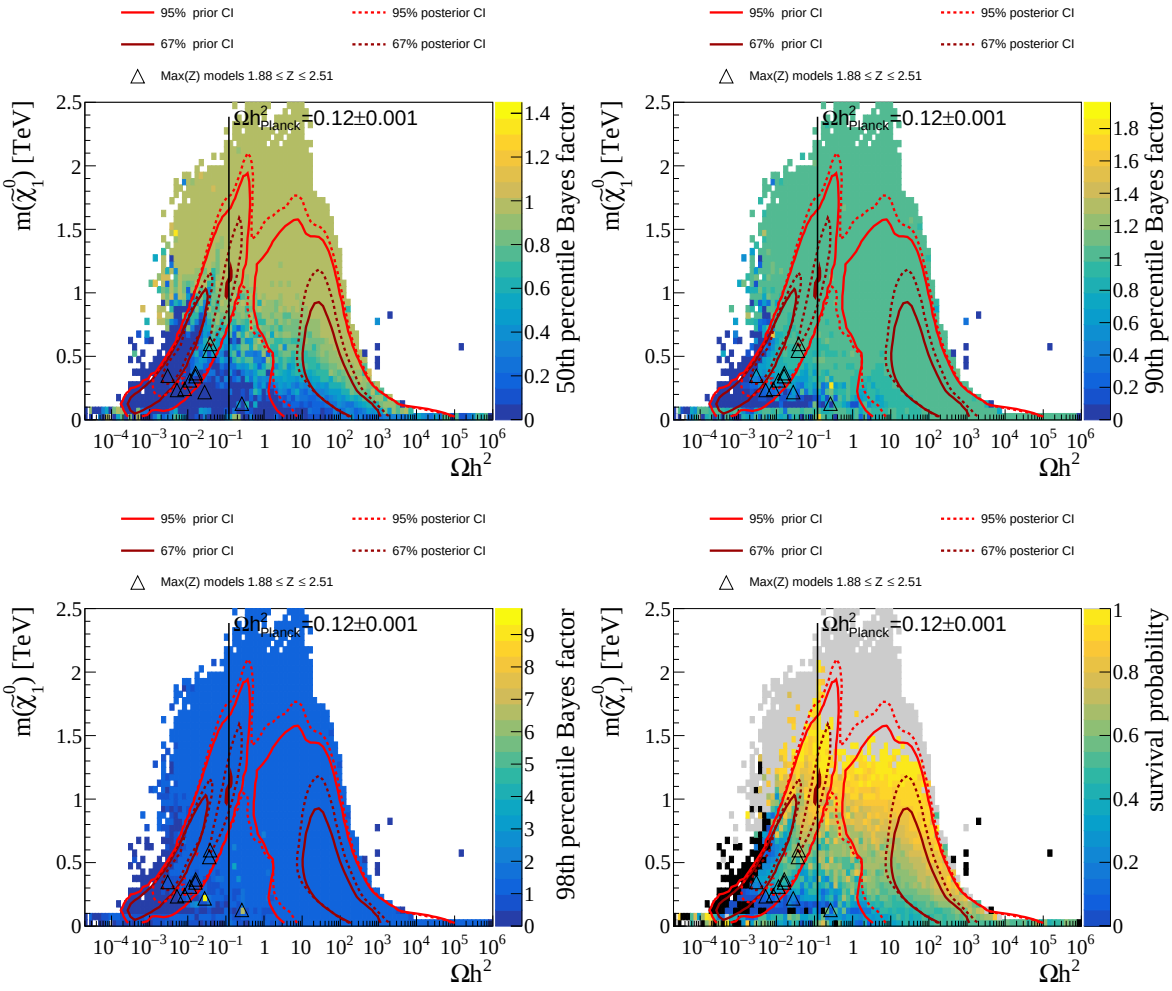

Figure 118: Impact of the considered LHC searches in the plane of the relic density Ωh^2 and the LSP mass $m(\tilde{\chi}^0_1)$, in terms of the median (top left), 90th (top right), and 98th (bottom left) quantiles of the Bayes factor, as well as the survival probability (bottom right). Black color denotes bins with zero survival probability, grey denotes bins with a survival probability of exactly 1, white bins are empty. A detailed description of the plot elements is given in Section 7. The measured value of the relic density is indicated by the vertical black line at $\Omega h^2_{\text{Planck}} = 0.12 \pm 0.001$ [8].

8.4.2.2 Relic density impact on pMSSM

Three versions of relic density constraints are studied.

- In the first, **tight**, version, we consider the residual pMSSM space that is left after constraining the scan to be compatible with the current best measurement of $\Omega h^2_{\text{Planck}} = 0.12 \pm 0.001$ [8] within 10% of that measurement. The 10% window is given by $\Omega h^2 \in [0.108, 0.132]$ and is considered for two reasons:
  - The theory uncertainty in the calculated relic density is expected to be much larger than the experimental uncertainty, reaching up to 300% in a study performed by comparing the outcomes of different calculation pipelines for a variety of benchmark models [151].
  - Despite the over-sampling around $\Omega h^2_{\text{Planck}}$ (see Section 6.1), which increases the resolution in the pMSSM model space, the scan density is still quite small for a multi-dimensional analysis of the residual space. Moreover, if only models within the experimental uncertainty were considered in this window, the statistical precision would be even smaller. At the same time, there is not much change in the phenomenology of the models accessible at the LHC in the models within the experimental uncertainty compared to the models in the wider 10% acceptance window. Thus, for practical reasons, it makes sense to allow a wider range of model to retain an acceptable resolution of the model space.
- The second version of the constraint, **loose**, is defined by the requirement that model points predict at least 10% of the measured relic density, and do not produce more than 110% of $\Omega h^2_{\text{Planck}}$, which accounts for a 10% theory uncertainty. This allows for a look at scenarios in which dark matter is only partially explained in the pMSSM, with room left for other beyond-standard model particles, e.g., the axion, to make up the remaining relic density. This requirement corresponds to to $\Omega h^2 \in [0.012, 0.132]$.
- The third version of the constraint, **upper bound**, is to only require that the relic density is not over-saturated, that is $\Omega h^2 \leq 0.132$ (which is less than 110% of $\Omega h^2_{\text{Planck}}$). This constraint is to treat the measurement of the relic density as any other constraint, and to drop from the interpretation the implicit desire to explain the dark matter relic density within the pMSSM.

Tight constraint on Ωh^2

If we restrict the pMSSM scan to the **tight** region, we eliminate all models with a light wino-like LSP, and almost all models with a bino-like LSP. Figure 119 shows the impact of the LHC and the tight relic density constraint on the LSP mass, with significant variation based on the type of LSP. This **tight** constraint on the relic density excludes most of the pMSSM. Almost all models with a mass of $m(\widetilde{\chi}^0_1) \lesssim 1\,\text{TeV}$ are excluded, with only a small population of models surviving in that region. In the inclusive distribution (top row), there is a sharp peak in the posterior density at a mass slightly above 1 TeV, where the survival probability peaks to approximately 15%. There is also a tail of surviving models with significantly larger LSP masses. As the surviving models are all at large $m(\widetilde{\chi}^0_1)$, where the prior density is small, the impact of this **tight** version of the relic density is dramatic in the shift from prior to posterior.

The distributions for the individual LSP types in the same figure indicate that the sharp peak at $m(\widetilde{\chi}^0_1) \simeq 1.1\,\text{TeV}$ is populated almost exclusively by models with a higgsino-like LSP, while the extended tail towards larger LSP masses mostly contains models with a pure wino-like LSP. The small population of models with $m(\widetilde{\chi}^0_1) < 1\,\text{TeV}$ contains models with (mostly bino-) mixed LSP types. As already mentioned, the relic density is highly sensitive to the difference in mass between the LSP and the second lightest state. For higgsino and wino-like LSPs, this co-annihilation partner is most often a chargino.

Three different phenomenologies associated with different LSP types are compatible with the **LHC constraints + tight Ωh^2 constraint**. These show up in Figure 120 as regions of higher survival probability, and in the shape of the posterior credibility intervals. The horizontal arm of the 95% posterior credibility interval at $\Delta m(\widetilde{\chi}^\pm_1, \widetilde{\chi}^0_1) \simeq 20\,\text{GeV}$ is populated by models with bino-mixed LSP, where either the wino or higgsino is close in mass to the bino. This arm transitions into a vertical feature of heightened survival probability and posterior density at around $m(\widetilde{\chi}^0_1) \simeq 1.1\,\text{TeV}$, which contains models with a pure higgsino-like LSP. The region of higher survival probability at $m(\widetilde{\chi}^0_1) \simeq 1.8\,\text{TeV}$ and $\Delta m(\widetilde{\chi}^\pm_1, \widetilde{\chi}^0_1) \simeq 0.1\,\text{GeV}$ is populated by models with a wino-like LSP. The credibility interval here also shows the interplay between $m(\widetilde{\chi}^0_1)$ and $\Delta m(\widetilde{\chi}^\pm_1, \widetilde{\chi}^0_1)$, where for the same LSP type,

a larger LSP mass requires a lower $\Delta m(\widetilde{\chi}_1^{\pm}, \widetilde{\chi}_1^0)$ to remain compatible with the Planck measurement.

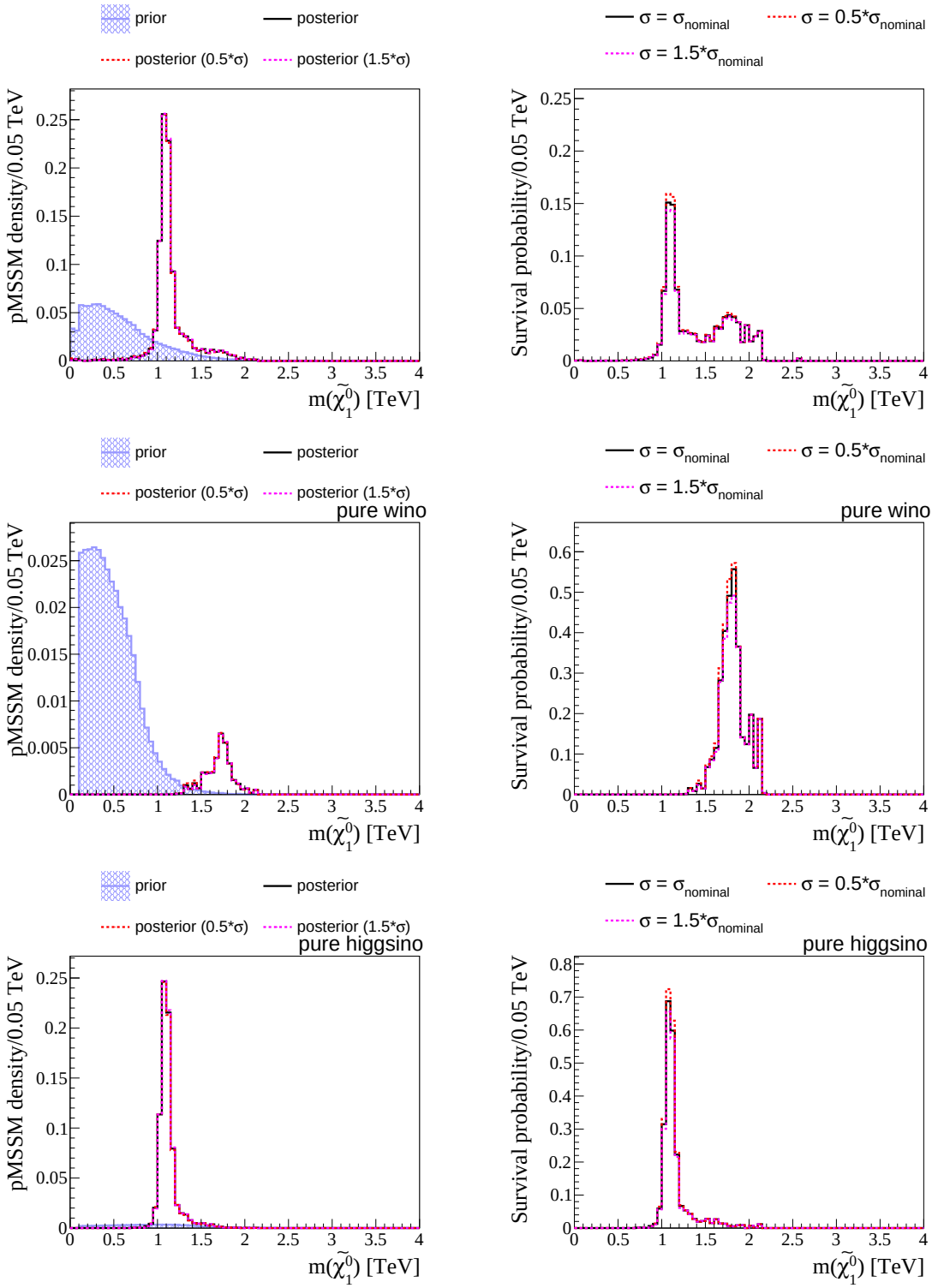

Figure 119: Impact of the **LHC constraints + tight Ωh^2 constraint** on the LSP mass $m(\widetilde{\chi}_1^0)$ (top row), and on the pMSSM sub-space with a wino-like LSP (center row), and a higgsino-like LSP (bottom row), in terms of the prior and posterior densities (left column), and the survival probability (right column). The survival probabilities for the individual LSP types use models with the respective LSP type in the denominator, not the inclusive totality of models. A detailed description of the plot elements is given in Section 7.

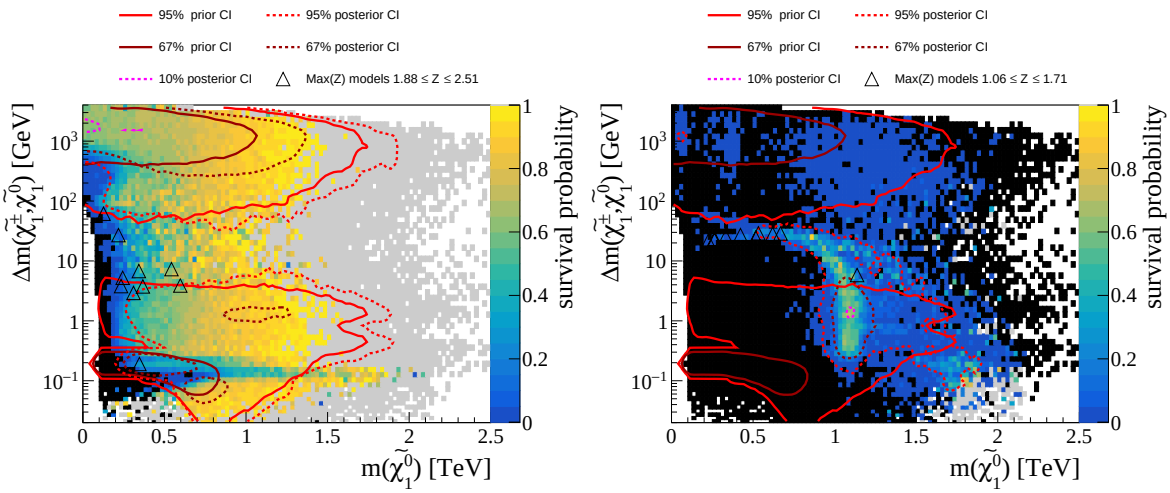

Figure 120: Survival probabilities in the plane of $\Delta m(\widetilde{\chi}_1^{\pm}, \widetilde{\chi}_1^0)$ and $m(\widetilde{\chi}_1^0)$, considering the **LHC constraints** (left) and the **LHC constraints + tight Ωh^2 constraint** (right). Black color denotes bins with zero survival probability, grey denotes bins with a survival probability of exactly 1, white bins are empty. A detailed description of the plot elements is given in Section 7.

The LHC impact and relic density constraints are also evaluated on an interesting subset of models in which a bino-like LSP can undergo pair annihilation via the so-called A-funnel, where the annihilation cross section of dark matter via an s-channel H^0 or A^0 increases due to resonance effects. This population of models is visible as a diagonal tendril of the 95% posterior credibility interval in Figure 121, which shows the plane of m_A and $m(\tilde{\chi}_1^0)$. The tendril is located at $m_A \simeq 2\, m(\tilde{\chi}_1^0)$ and coincides with a slightly increased survival probability. This increased annihilation cross section allows for some bino-models with a small enough relic density to be compatible with the measurements. Figure 122 shows that most of the models with large $\Delta m(\tilde{\chi}_1^\pm, \tilde{\chi}_1^0)$ that are nonetheless compatible with the tight constraint on $\Omega h^2_{\text{Planck}}$ feature a $m_A \simeq 2\, m(\tilde{\chi}_1^0)$. This can be seen by the fact that part of the 95% credibility interval of the posterior density extends to that region.

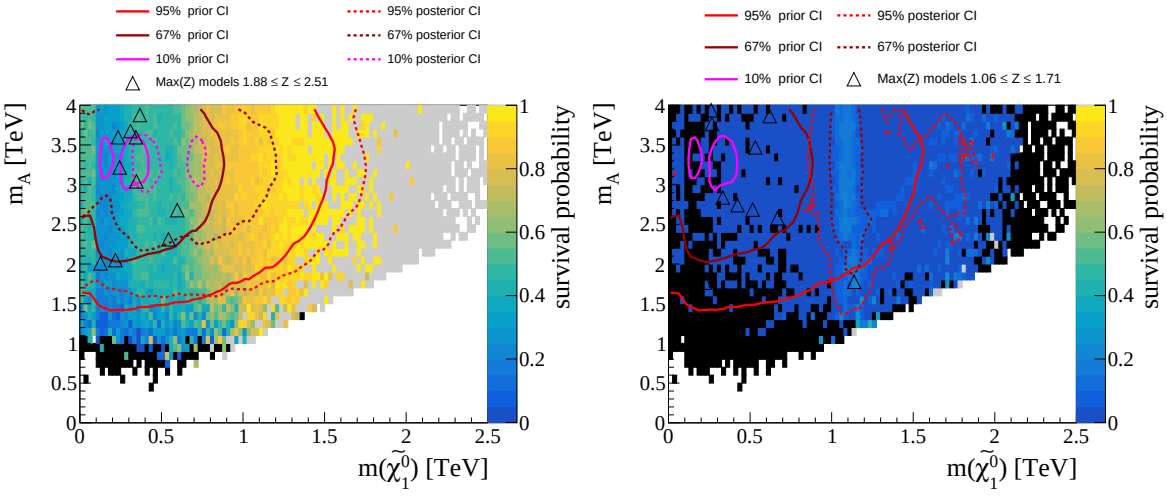

Figure 121: Survival probability in the plane of m_A and the LSP mass $m(\tilde{\chi}_1^0)$, considering the **LHC constraints** (left), and the **LHC constraints + tight Ωh^2 constraint** (right). Black color denotes bins with zero survival probability, grey denotes bins with a survival probability of exactly 1, white bins are empty. A detailed description of the plot elements is given in Section 7.

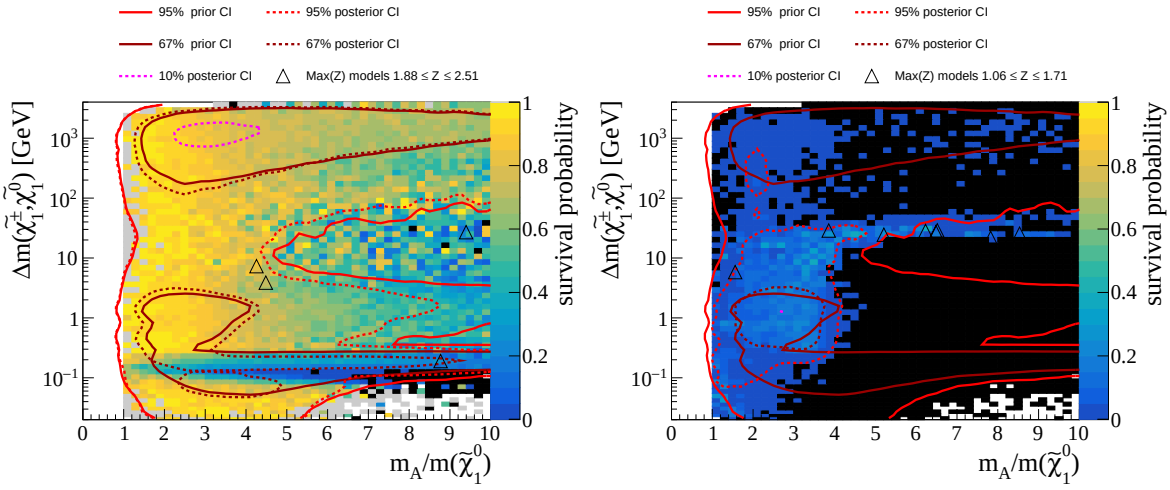

Figure 122: Survival probabilities in the plane of $\Delta m(\widetilde{\chi}_1^{\pm}, \widetilde{\chi}_1^0)$ and the ratio of the pseudoscalar Higgs boson mass m_A to the LSP mass $m(\widetilde{\chi}_1^0)$, considering the **LHC constraints** (left), and the **LHC constraints + tight Ωh^2 constraint** (right). Black color denotes bins with zero survival probability, grey denotes bins with a survival probability of exactly 1, white bins are empty. A detailed description of the plot elements is given in Section 7.

Loose constraint on Ωh^2

Loosening the constraint on the relic density to have the pMSSM account for at least 10% of dark matter, but not exceeding 110% of the measured relic density, allows for a much wider variety of models. In terms of the allowed LSP masses and types, we can see from Figure 123 that the peak of the posterior density to this constraint shifts towards lower masses. This shift is induced because the **loose Ωh^2 constraint** allows for models with a much lighter, but still somewhat heavy wino-like LSP. Because wino-like LSPs make up a larger fraction of the prior compared to higgsino-like LSP, the posterior density corresponding to the **loose Ωh^2 constraint** is dominated by winos with $m(\widetilde{\chi}_1^0) \in [0.7, 1]$ TeV. Due to the positive correlation between the dark matter mass and relic density for models with a wino-like LSP, few models with a wino-like LSP with $m(\widetilde{\chi}_1^0) \lesssim 700$ GeV survive the **loose** constraint on the relic density, as these small wino masses lead to relic densities below 10% of the measured value. The tail of the LSP mass at $m(\widetilde{\chi}_1^0) \lesssim 700$ is mostly populated by models with a higgsino-like LSP.

Comparing the survival probability as a function of $m(\widetilde{\chi}_1^0)$ for wino-like LSP for the combined **LHC + loose Ωh^2** constraint in Figure 123 to the version that only contains the LHC constraints in Figure 68, we see that the LHC by itself progressively loses sensitivity for increasing LSP mass, particularly above $m(\widetilde{\chi}_1^0) \simeq 700$ GeV. This means that, because of the strong positive correlation of mass and Ωh^2 for wino-like LSP, the LHC is starting to probe and constrain the lower end of the **loose** window on Ωh^2. The furthest extent of the LHC sensitivity to pure winos comes from the search for disappearing tracks. Figure 124 shows that the posterior density now significantly extends to the wino-rich region at small $\Delta m(\widetilde{\chi}_1^\pm, \widetilde{\chi}_1^0) \lesssim 0.2$ GeV. It also shows that the region of lowered survival probability caused by the search for disappearing tracks extends to approximately $m(\widetilde{\chi}_1^0) \simeq 1.5$ TeV, well into the region of models with a wino-like LSP and $\Omega h^2 > 0.1\,\Omega h^2_{\text{Planck}}$.

As with the **tight Ωh^2 constraint**, the region with large $\Delta m(\widetilde{\chi}_1^\pm, \widetilde{\chi}_1^0)$ that is compatible with $\Omega h^2 \in [0.1, 1.1]\,\Omega h^2_{\text{Planck}}$ is almost entirely made up of models in the A-funnel regime, where $m_A \simeq 2m(\widetilde{\chi}_1^0)$. This is shown in Figure 125, where the A-funnel region clearly exhibits a heightened survival probability and disproportionate fraction of the posterior density, visible as a vertical feature in that plot.

The **loose Ωh^2 constraint** disfavors very heavy stop masses. The lessened survival probability for $m(\widetilde{t}_1) \gtrsim 3$ TeV, which can be seen in Figure 126, is likely caused by the positive correlation of the stop masses to $|\mu|$, caused by the occurrence of tachyons at large $Q_{\text{SUSY}} = \sqrt{M_{q,3} \cdot M_{u,3}}$ (see Appendix B). For larger stop masses, the higgsino mass parameter is required to be large in order to avoid a tachyonic spectrum. Thus, the LSP is more likely to be a wino or bino at large $m(\widetilde{t}_1)$, both of which are strongly constrained by the loose requirement on Ωh^2. As a result, the posterior density is significantly shifted towards smaller stop masses, although the region that the LHC is sensitive to is not enhanced by the relic density constraint.

Aside from a shift of the posterior density towards smaller $m(\widetilde{t}_1)$, there is no significant impact of the relic density constraints on the colored and slepton sector of the pMSSM.

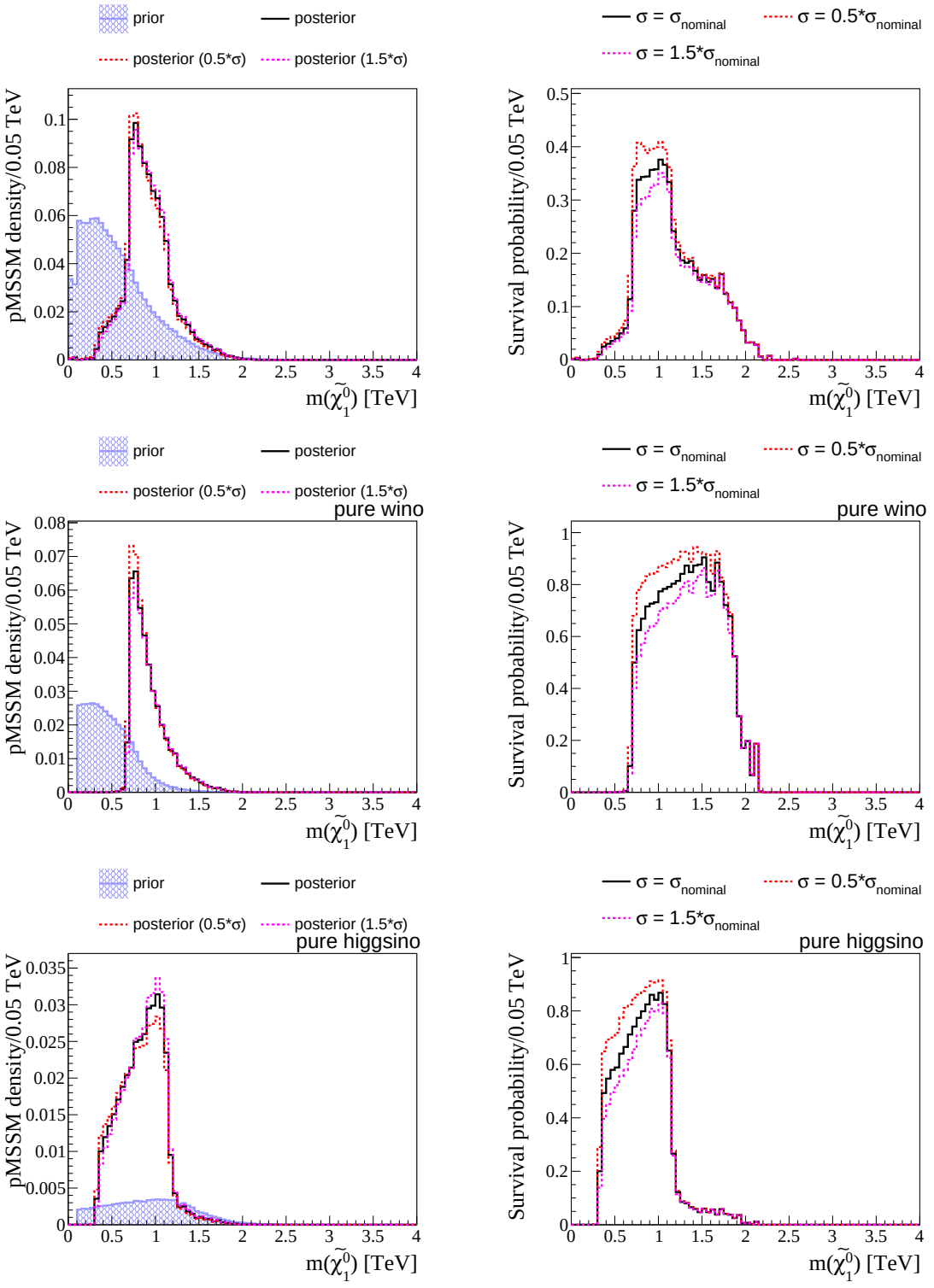

Figure 123: Impact of the **LHC + loose Ωh^2** constraint on the LSP mass $m(\tilde{\chi}_1^0)$ (top row), and on the pMSSM sub-space with a wino-like LSP (center row), and a higgsino-like LSP (bottom row), in terms of the prior and posterior densities (left column), and the survival probability (right column). The survival probabilities for the individual LSP types refer to the respective LSP type in the denominator, not to all LSP types. A detailed description of the plot elements is given in Section 7.

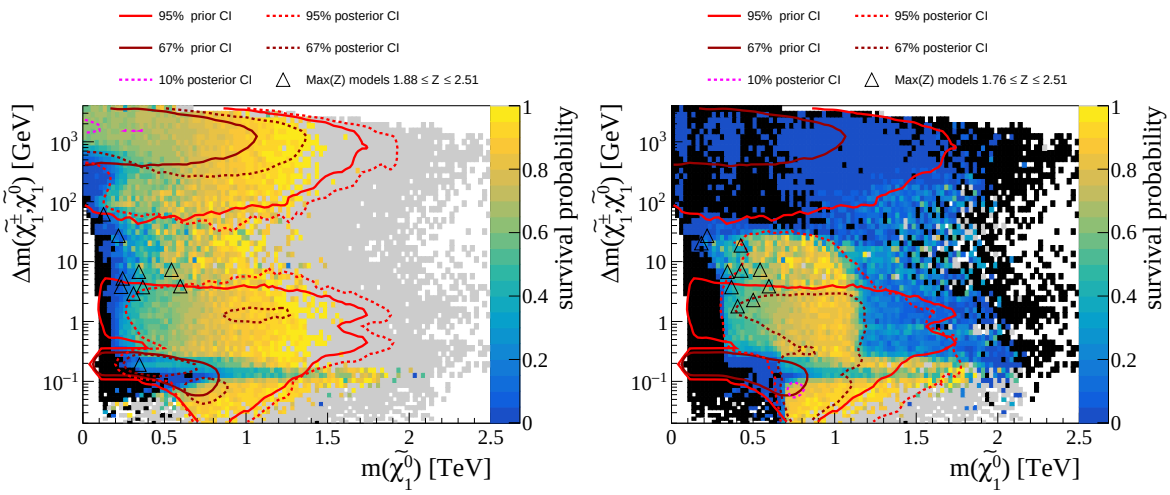

Figure 124: Survival probabilities in the plane of $\Delta m(\widetilde{\chi}_1^{\pm}, \widetilde{\chi}_1^0)$ and $m(\widetilde{\chi}_1^0)$, considering the **LHC constraints** (left) and the **LHC + loose constraint on Ωh^2** (right). Black color denotes bins with zero survival probability, grey denotes bins with a survival probability of exactly 1, white bins are empty. A detailed description of the plot elements is given in Section 7.

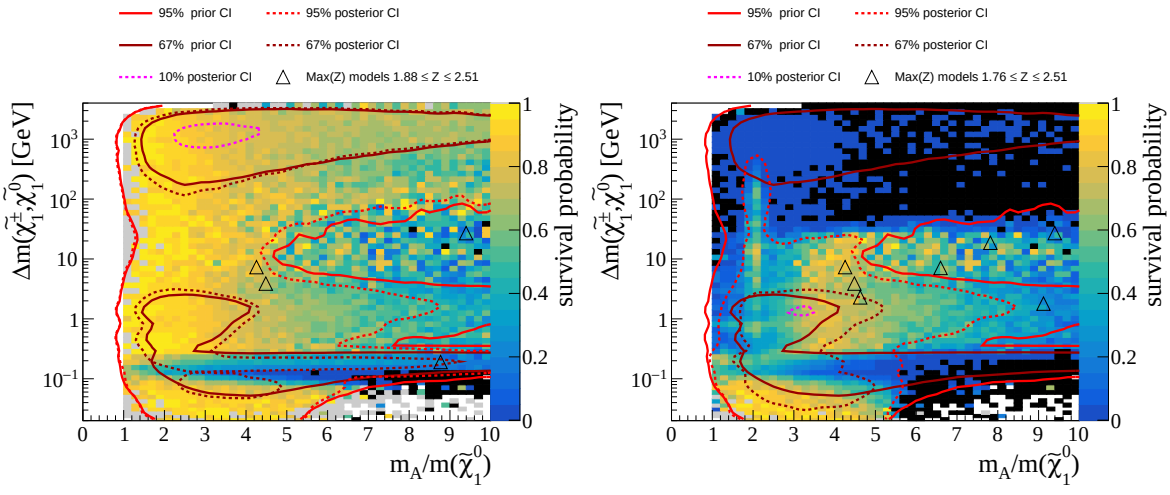

Figure 125: Survival probabilities in the plane of $\Delta m(\widetilde{\chi}_1^{\pm}, \widetilde{\chi}_1^0)$ and the ratio $\frac{m_A}{m(\widetilde{\chi}_1^0)}$, considering the **LHC constraints** (left), and the **LHC constraints + loose constraint on Ωh^2** (right). Models with A-funnel dark matter annihilation show up as a vertical feature at $m_A \simeq 2\, m(\widetilde{\chi}_1^0)$ when the **loose Ωh^2 constraint** is applied. A detailed description of the plot elements is given in Section 7.

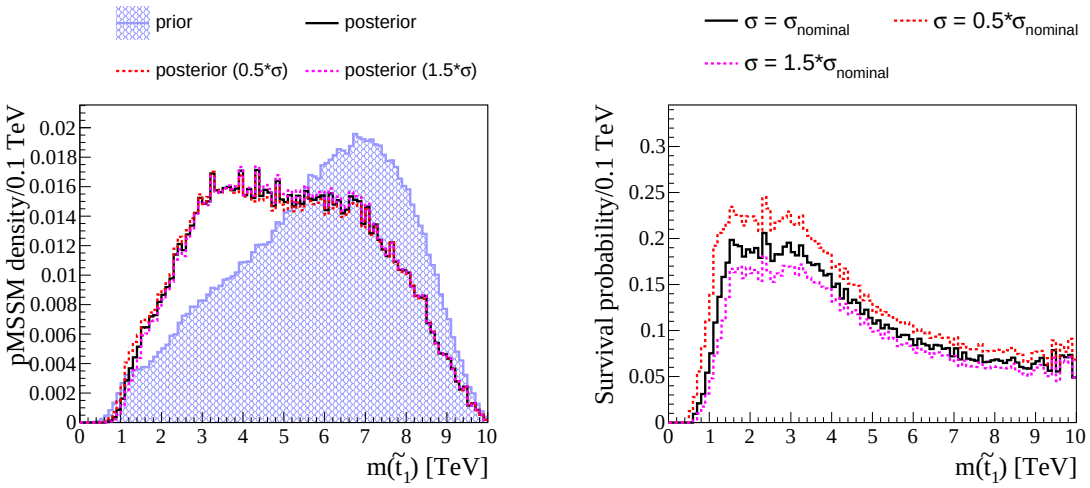

Figure 126: Impact of the **LHC + loose Ωh^2 constraint** on the lightest stop mass $m(\tilde{t}_1)$, shown in terms of the prior and posterior densities (left), and the survival probability (right). A detailed description of the plot elements is given in Section 7.

Upper bound on Ωh^2

Loosening the constraint on Ωh^2 even further by removing the lower bound on Ωh^2 allows models with almost no contribution to the relic density, but ensures that the supersymmetric contribution to the relic density does not exceed the measured value. These additional models compared to the loose and tight constraint on Ωh^2 feature LSPs that are predominately wino-like.

The impact of the **upper bound** for Ωh^2 on the mass of the LSP is shown in Figure 127. It affects the whole spectrum of $m(\widetilde{\chi}_1^0)$, but is especially noticeable at very small $m(\widetilde{\chi}_1^0)$ and at large $m(\widetilde{\chi}_1^0) \gtrsim 1\,\text{TeV}$. At small $m(\widetilde{\chi}_1^0)$, the exclusion of almost all models with a bino-like LSP results in the posterior density dropping to almost zero below $m(\widetilde{\chi}_1^0) \simeq 300\,\text{GeV}$. This is because the LHC is sensitive to and excludes models with very light winos or higgsinos, but is less sensitive to models with a pure bino. This deficiency in sensitivity to pure binos is compensated for by the **upper bound** on Ωh^2, since these models almost always result in too large Ωh^2, which are excluded by the **upper bound** on Ωh^2. The surviving models with a bino-like LSP at small $m(\widetilde{\chi}_1^0)$ necessarily either feature another SUSY particle, such that the co-annihilation process sufficiently reduces the relic density of the model, or are part of a funnel region that increases the direct annihilation cross section to escape the **upper bound** on Ωh^2. The survival probability for models with a bino-like LSP increases towards larger $m(\widetilde{\chi}_1^0)$ up until $m(\widetilde{\chi}_1^0) \simeq 1.5\,\text{TeV}$, above which it becomes exceedingly rare to find a pMSSM model with a bino-like LSP and a sufficiently small relic density.

At large $m(\widetilde{\chi}_1^0)$, the **upper bound** on Ωh^2 excludes models with a higgsino-like LSP and large $m(\widetilde{\chi}_1^0) \gtrsim 1\,\text{TeV}$, and models with a wino-like LSP and large $m(\widetilde{\chi}_1^0) \gtrsim 1.7\,\text{TeV}$. Thus, in this most conservative application of the Ωh^2 constraint, the LHC and relic density constraint are very complementary and constrain the pMSSM particle masses from below and above, respectively.

The A-funnel region plays an important role in the models with bino-like LSP that survive the **upper bound** on Ωh^2. This can be seen in Figure 128, which shows the survival probability for the LHC constraints and **upper bound** on Ωh^2 in the plane of $\Delta m(\widetilde{\chi}_1^\pm, \widetilde{\chi}_1^0)$ and $m_A \simeq 2\, m(\widetilde{\chi}_1^0)$. Most of the surviving models with a bino-like LSP, found predominately at large $\Delta m(\widetilde{\chi}_1^\pm, \widetilde{\chi}_1^0)$, are located in the A-funnel region at $m_A \simeq 2\, m(\widetilde{\chi}_1^0)$, which can easily be identified by a locally large survival probability that overlaps with the 95% posterior credibility interval at large $\Delta m(\widetilde{\chi}_1^\pm, \widetilde{\chi}_1^0)$.

The region of the pMSSM that is still viable after the **LHC constraints + upper bound on Ωh^2** is visible in the plane of $\Delta m(\widetilde{\chi}_1^\pm, \widetilde{\chi}_1^0)$ and $m(\widetilde{\chi}_1^0)$, shown in Figure 129. Here we can see that the posterior density is very sparse at large $\Delta m(\widetilde{\chi}_1^\pm, \widetilde{\chi}_1^0)$, with a slight preference for small $m(\widetilde{\chi}_1^0)$. This is due to the constraints on models with a bino-like LSP from the upper bound on Ωh^2. The posterior density mostly occupies the region of $\Delta m(\widetilde{\chi}_1^\pm, \widetilde{\chi}_1^0) \lesssim 20\,\text{GeV}$, with constraints on $m(\widetilde{\chi}_1^0)$ from below due to the LHC sensitivity to models with a higgsino-like or a wino-like LSP, and from above due to the elimination of over-saturated relic density that higgsino-like LSPs and wino-like LSP produce at large $m(\widetilde{\chi}_1^0)$.

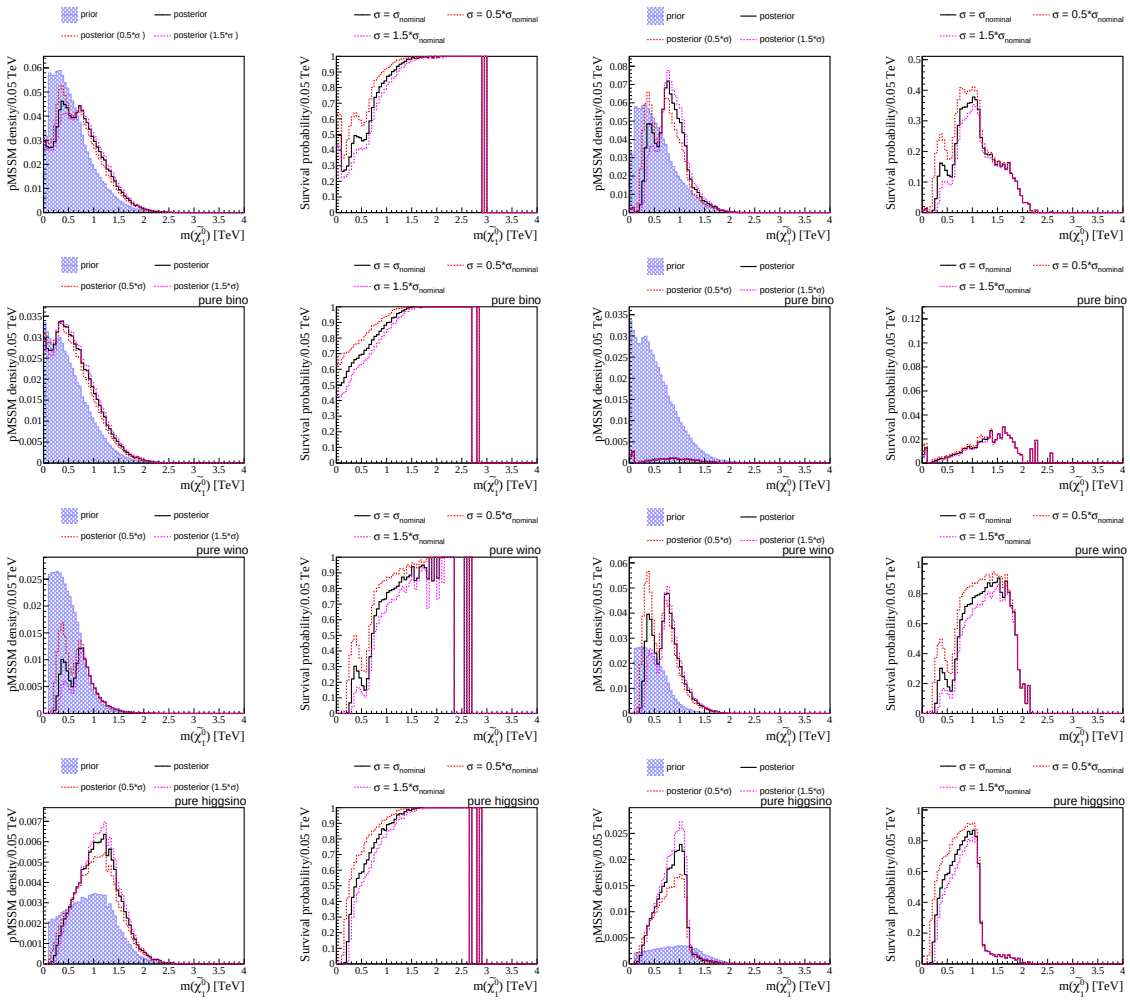

Figure 127: Impact on $m(\widetilde{\chi}_1^0)$ of the **LHC constraints**, in terms of the prior and posterior densities (left column) and the survival probability (second from left column), and the **LHC constraints + upper bound on Ωh^2**, also in terms of the prior and posterior densities (second from right column) and the survival probability (right column). The row of plots differ in terms of the LSP type, with inclusive LSP types (top row), bino-like LSPs (second row from top), wino-like LSPs (second row from bottom), and higgsino-like LSPs (bottom row). A detailed description of the plot elements is given in Section 7.

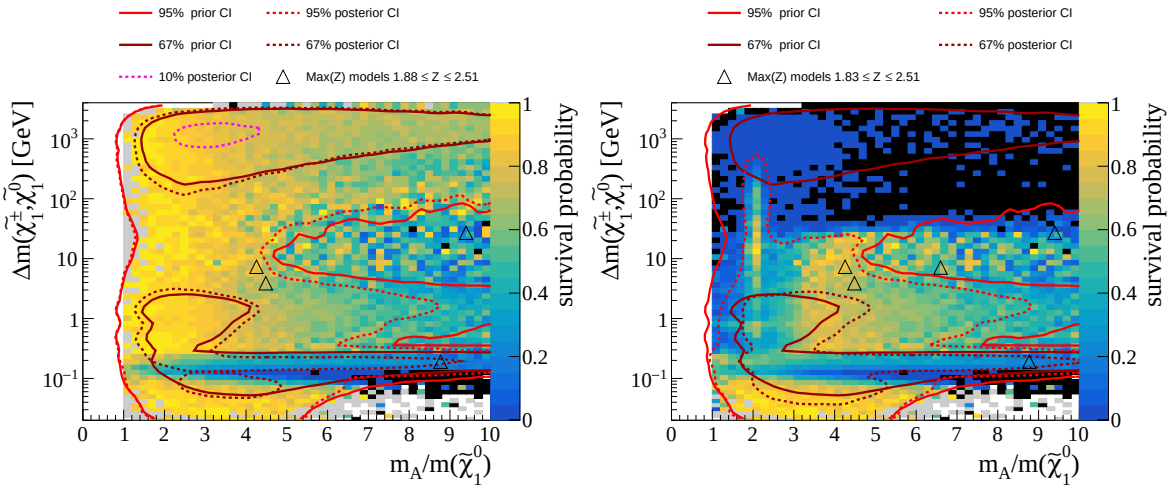

Figure 128: Survival probability in the plane of $\Delta m(\widetilde{\chi}_1^{\pm}, \widetilde{\chi}_1^0)$ and the ratio $\frac{\mathrm{m_A}}{m(\widetilde{\chi}_1^0)}$, considering the **LHC constraints** (left), and the **LHC constraints + upper bound on $\Omega\mathrm{h}^2$** (right). Models with A-funnel dark matter annihilation show up as a vertical feature at $\mathrm{m_A} \simeq 2\, m(\widetilde{\chi}_1^0)$ when the upper bound on $\Omega\mathrm{h}^2$ is applied. Black color denotes bins with zero survival probability, grey denotes bins with a survival probability of exactly 1, white bins are empty. A detailed description of the plot elements is given in Section 7.

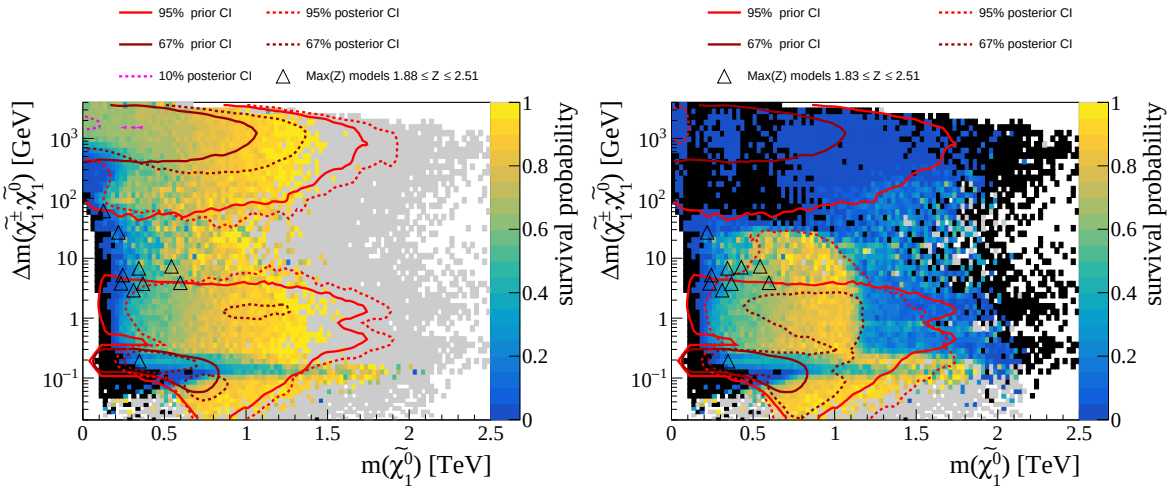

Figure 129: Survival probability in the plane of $\Delta m(\widetilde{\chi}_1^{\pm}, \widetilde{\chi}_1^0)$ and $m(\widetilde{\chi}_1^0)$, considering the **LHC constraints** (left), and the **LHC + upper bound on $\Omega\mathrm{h}^2$** (right). Black color denotes bins with zero survival probability, grey denotes bins with a survival probability of exactly 1, white bins are empty. A detailed description of the plot elements is given in Section 7.

8.4.3 Indirect Detection

In addition to constraints on the relic density and constraints from direct dark matter detection experiments, we also include constraints from experiments for indirect detection of dark matter. For this, we obtain the thermally averaged dark matter annihilation cross section and branching ratios into the four decay channels, $\widetilde{\chi}_1^0 \to W^+W^-$, $\widetilde{\chi}_1^0 \to b\bar{b}$, $\widetilde{\chi}_1^0 \to \mu^+\mu^-$, $\widetilde{\chi}_1^0 \to \tau^+\tau^-$, from `MicrOMEGAs`. We then incorporate the dark matter relic density of each model and calculate a fiducial annihilation cross section, here defined as

$$\sigma_i^{\text{fiducial}} := \sigma_{\text{total}}^{\text{annihilation}} \times \text{BR}(\widetilde{\chi}_1^0 \to i) \times \min\left(\frac{\Omega\text{h}^2}{\Omega\text{h}^2_{\text{Planck}}}, 1\right)^2, \tag{28}$$

where i is the respective decay channel. Note that neither the annihilation cross section, nor the relic density, considers higher order corrections or non-perturbative contributions to the annihilation cross section, such as the Sommerfeld enhancement [152, 153, 154].

We then compare the fiducial cross sections against upper limits from a combination of two experimental results [62] from gamma-ray searches, which uses data from the Fermi-LAT [64] and the MAGIC [63] experiments. The limits on the fiducial cross section are dependent on $m(\widetilde{\chi}_1^0)$ and range from $\text{UL}(\sigma^{\text{fiducial}}) \simeq 10^{-27}\ \frac{\text{cm}^3}{\text{s}}$ at small $m(\widetilde{\chi}_1^0)$ to $\text{UL}(\sigma^{\text{fiducial}}) \simeq 10^{-25}\ \frac{\text{cm}^3}{\text{s}}$ at large $m(\widetilde{\chi}_1^0)$.

Constraints from other indirect detection experiments, such as the AMS [155] experiment, are not considered in this work due to time constraints.

Figure 130 shows the distributions and impact of the LHC on the fiducial annihilation cross sections for the four indirect detection channels. We can see that the sampled pMSSM space does not reach annihilation cross sections that are constrained by the indirect detection constraints in any of the four channels. The largest fiducial annihilation cross sections are present in models with a wino-like LSP or a higgsino-like LSP, with larger cross sections towards larger $m(\widetilde{\chi}_1^0)$. The reason for this apparent insensitivity comes from the fact that models with a large annihilation cross section almost always have a very small relic density, which strongly suppresses the fiducial cross section. This picture may change significantly if higher-order corrections are applied on the annihilation cross section and the resulting different relic density, and which disproportionally affect the annihilation rate that dictates the sensitivity of indirect detection experiments compared to the relic density.

To provide a picture of how large an increase would be necessary to constrain the pMSSM, we also present the prior and posterior densities in terms of the fraction of the fiducial annihilation cross sections to the respective upper limit in Figure 131. Individual models are excluded at small $m(\widetilde{\chi}_1^0)$ by constraints from the WW-channel if the annihilation cross section is increased by a factor of at least 2, and at large $m(\widetilde{\chi}_1^0)$ by the $\text{b}\bar{\text{b}}$-channel at similar enhancement factors. A significant fraction of the pMSSM starts to be constrained a large $m(\widetilde{\chi}_1^0)$ if the enhancement factor exceeds 10, as this is where the edges of the prior and posterior credibility intervals are located.

Since the fiducial annihilation cross section increases towards larger $m(\widetilde{\chi}_1^0)$ for a significant population of the pMSSM, there is a significant potential for complementarity between constraints from the LHC and constraints from indirect detection experiments. This complementarity would be realized if either the limits on the annihilation cross section improve, or if it turns out that higher-order corrections significantly increase the annihilation cross section without a proportionate decrease of the relic density, especially at large $m(\widetilde{\chi}_1^0)$.

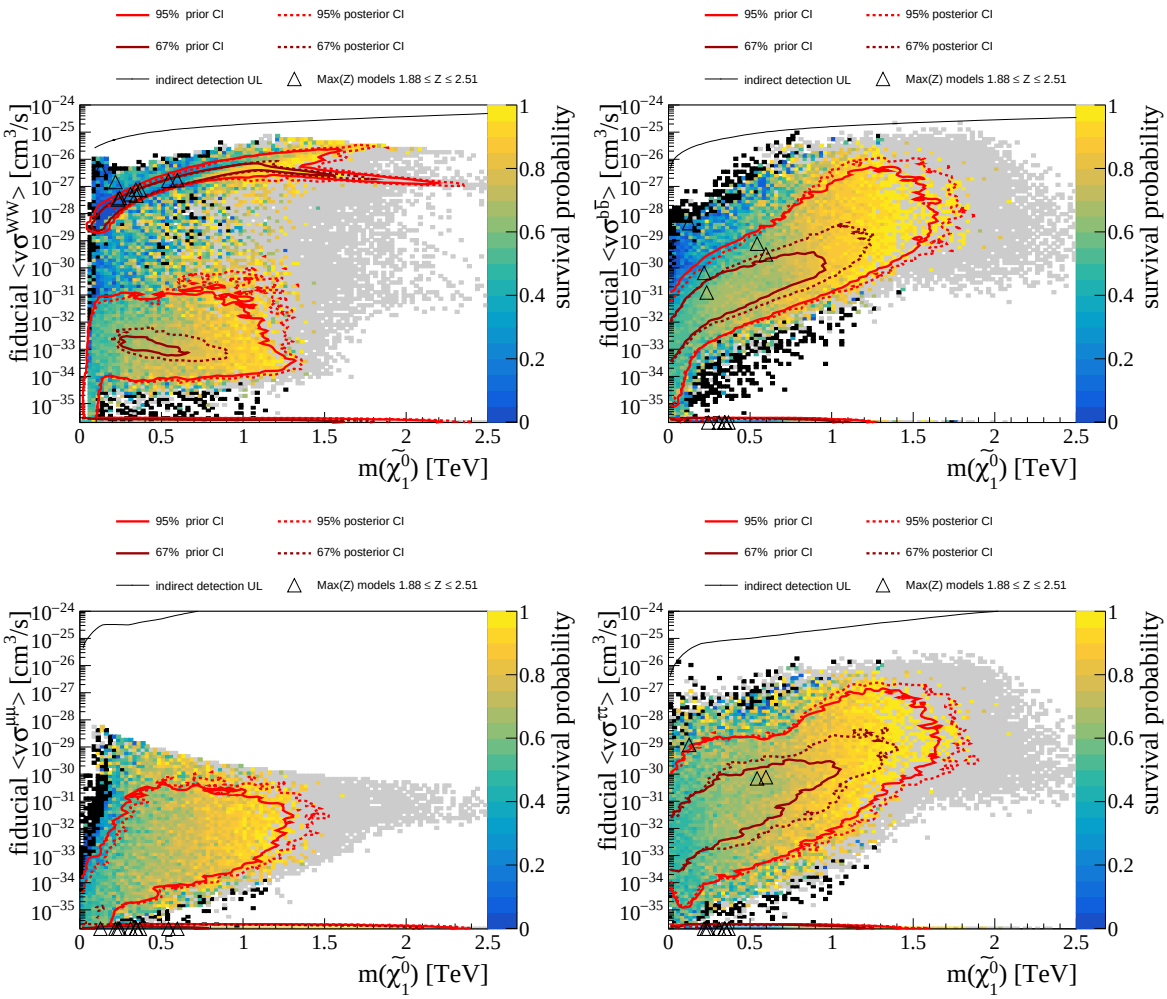

Figure 130: Survival probabilities considering the LHC constraints for the fiducial dark matter annihilation cross sections $\sigma^{\mathrm{WW}}_{\mathrm{fiducial}}$ (top left), $\sigma^{\mathrm{b\bar{b}}}_{\mathrm{fiducial}}$ (top right), $\sigma^{\mu\mu}_{\mathrm{fiducial}}$ (bottom left), and $\sigma^{\tau\tau}_{\mathrm{fiducial}}$ (bottom right). The upper limits, shown as black lines, are taken from [62]. Black color denotes bins with zero survival probability, grey denotes bins with a survival probability of exactly 1, white bins are empty. A detailed description of the plot elements is given in Section 7.

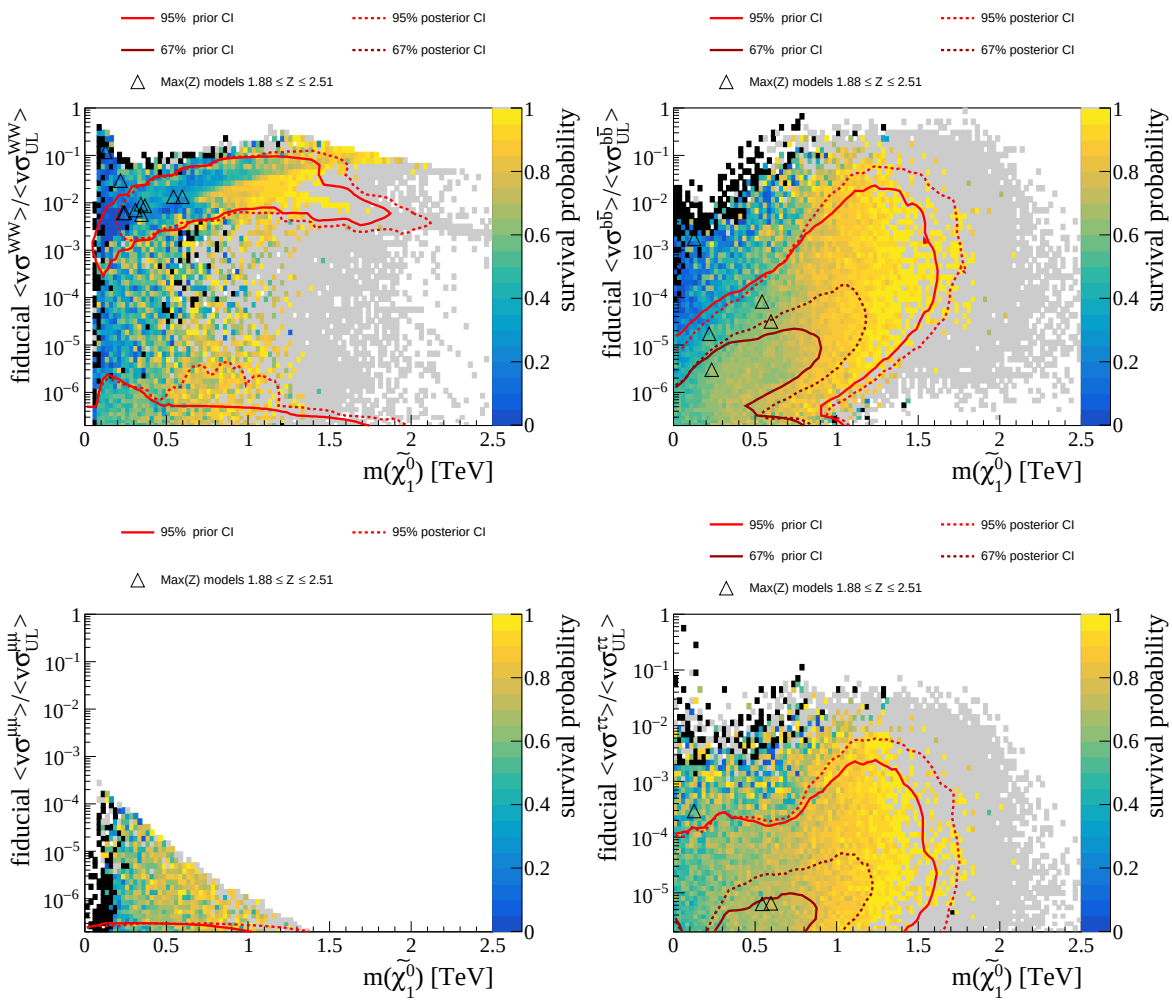

Figure 131: Survival probabilities considering the LHC constraints for the fraction of the fiducial dark matter annihilation cross sections to the respective upper limit, showing $\sigma^{\mathrm{WW}}_{\mathrm{fiducial}}$ (top left), $\sigma^{\mathrm{b\bar{b}}}_{\mathrm{fiducial}}$ (top right), $\sigma^{\mu\mu}_{\mathrm{fiducial}}$ (bottom left), and $\sigma^{\tau\tau}_{\mathrm{fiducial}}$ (bottom right). Black color denotes bins with zero survival probability, grey denotes bins with a survival probability of exactly 1, white bins are empty. A detailed description of the plot elements is given in Section 7.

8.4.4 Combined dark matter direct detection and relic density

Part of the posterior density for the **LHC constraints + tight Ωh^2 constraint** extends into a region of large LSP-nucleon interaction cross sections, as seen in Figure 132. The absence of a positive signal from direct detection experiments, primarily XENON1T, eliminate this region. In particular, these constraints strongly suppress the subset of models with a wino-higgsino mixed LSP that survive the relic density constraint. This can be seen in Figure 133, where the 95% posterior credibility interval becomes disjointed into three regions, corresponding to the pure LSP types. The space between these disjoint parts of the posterior density is populated by the respective mixed-LSP states, to which the direct detection experiments seem particularly sensitive.

Figure 134 shows the LSP-nucleon interaction cross sections and LSP masses for the **loose** Ωh^2 constraint. We can see that a much larger population of models remains at large LSP-nucleon interaction cross sections, which is then subsequently excluded by the direct detection experiments. Figure 135 shows the plane of $\Delta m(\widetilde{\chi}_1^{\pm}, \widetilde{\chi}_1^0)$ and $m(\widetilde{\chi}_1^0)$ for the **loose** Ωh^2 constraint and direct detection constraints. As with the **tight** Ωh^2 constraint, we see that the regions of large posterior density become disjoint, with the mixed-LSP models connecting the regions of pure LSP type excluded by the inclusion of direct detection experiments. The impact of the direct detection constraints on the mixed-LSP models thus does not qualitatively differ when considering the **loose** Ωh^2 constraint instead of the **tight** Ωh^2 constraint. Additionally, many of the models with the highest significance given the **LHC constraints + loose Ωh^2 constraints** show large interaction cross sections, and are excluded by the introduction of the direct detection constraints. The A-funnel region is not particularly affected by the additional constraints from the direct detection experiments.

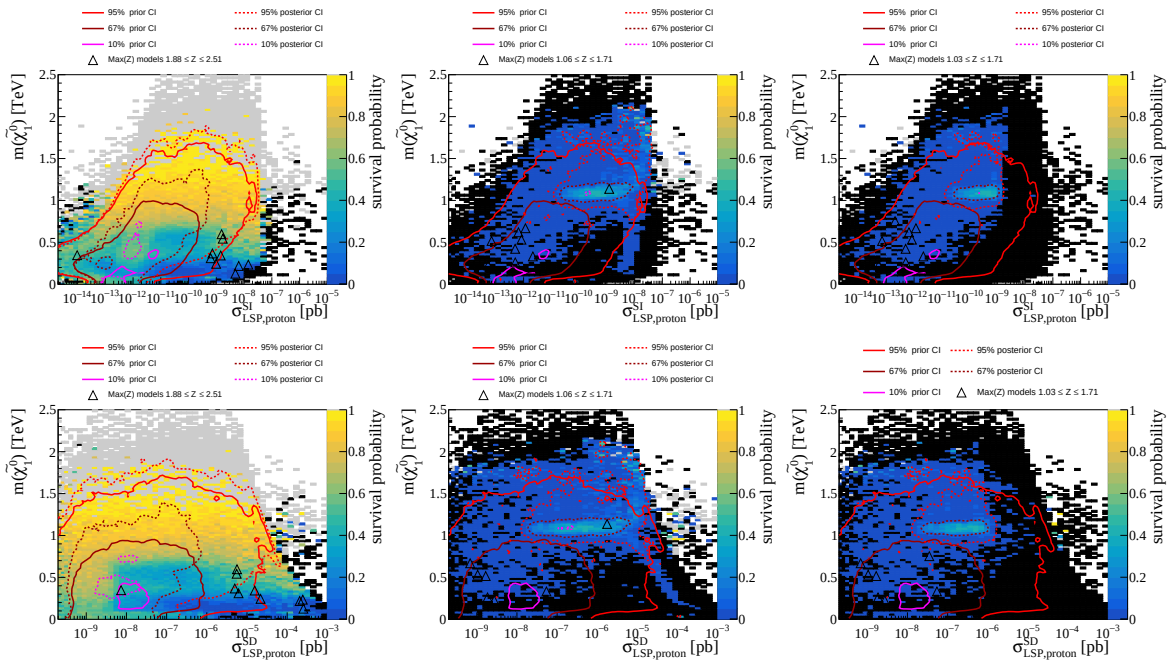

Figure 132: Survival probabilities in the plane of $m(\widetilde{\chi}_1^0)$ and spin independent (top row) and the spin-dependent (bottom row) LSP-proton interaction cross sections, considering the **LHC constraints** (left column), the **LHC constraints + tight Ωh^2 constraint** (center column), and the **LHC constraints + tight Ωh^2 constraint + direct detection constraints** (right column). Black color denotes bins with zero survival probability, grey denotes bins with a survival probability of exactly 1, white bins are empty. A detailed description of the plot elements is given in Section 7.

Finally, Figure 136 shows the LSP-nucleon interaction cross sections for the **upper bound** on Ωh^2. The additional surviving models, which almost exclusively feature a light wino-like LSP, can be found at small $m(\widetilde{\chi}_1^0)$ and small interaction cross sections. This can best be seen by comparing the shapes of the posterior density credibility intervals between Figures 134 and 136 at the lower left part of the plots. Because of their small LSP-nucleon interaction cross sections, these new models are not constrained by the direct detection experiments.

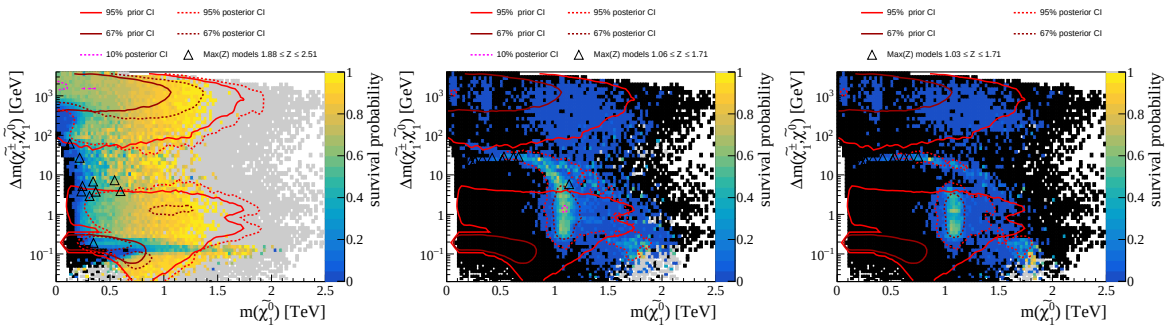

Figure 133: Survival probabilities in the plane of $\Delta m(\widetilde{\chi}_1^{\pm}, \widetilde{\chi}_1^0)$ and $m(\widetilde{\chi}_1^0)$, considering the **LHC constraints** (left), the **LHC constraints + tight Ωh^2 constraint** (center), and the **LHC constraints + tight Ωh^2 constraint + direct detection constraints** (right). Black color denotes bins with zero survival probability, grey denotes bins with a survival probability of exactly 1, white bins are empty. A detailed description of the plot elements is given in Section 7.

Nonetheless, if the upper bound is adopted as the constraint of choice for the relic density, an interesting complementarity emerges between the LHC constraints, the relic density constraints, and the direct detection constraints. This complementarity can be seen in Figure 137, which shows the plane of $\Delta m(\widetilde{\chi}_1^{\pm}, \widetilde{\chi}_1^0)$ and $m(\widetilde{\chi}_1^0)$ for the consecutive application of the three constraints. We can see that the LHC is most constraining at small $m(\widetilde{\chi}_1^0)$ and small $\Delta m(\widetilde{\chi}_1^{\pm}, \widetilde{\chi}_1^0)$, while the upper bound on Ωh^2 heavily constrains large $m(\widetilde{\chi}_1^0)$ because of the positive correlation of $m(\widetilde{\chi}_1^0)$ and Ωh^2, and large $\Delta m(\widetilde{\chi}_1^{\pm}, \widetilde{\chi}_1^0)$ because the pMSSM there is dominated by models with a bino-like LSP, which tend to over-saturate the relic density. The inclusion of the direct detection constraints severely impacts both models with a pure higgsino-like LSP, and models with a mixed LSP type at comparatively small $\Delta m(\widetilde{\chi}_1^{\pm}, \widetilde{\chi}_1^0)$, which excludes the connecting regions of large posterior density and survival probability between the posterior density peaks that correspond to the pure LSP types. This can be seen most clearly in Figure 137. These models are typically challenging for the LHC to constrain, which is why the inclusion of direct detection constraints has a visible impact in this plane of observables.

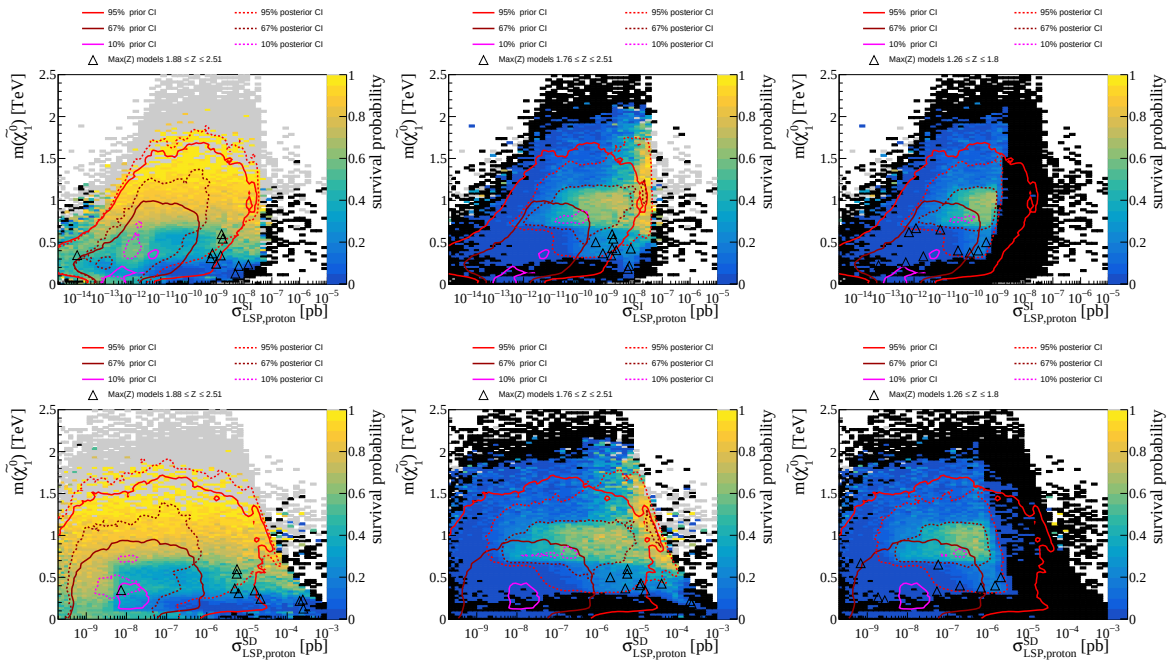

Figure 134: Survival probabilities in the plane of $m(\tilde{\chi}_1^0)$ and the spin independent (top row) and spin-dependent (bottom row) LSP-proton interaction cross sections, considering the **LHC constraints** (left column), the **LHC constraints + loose Ωh^2 constraint** (center column), and the **LHC constraints + loose Ωh^2 constraint + direct detection constraints** (right column). A detailed description of the plot elements is given in Section 7.

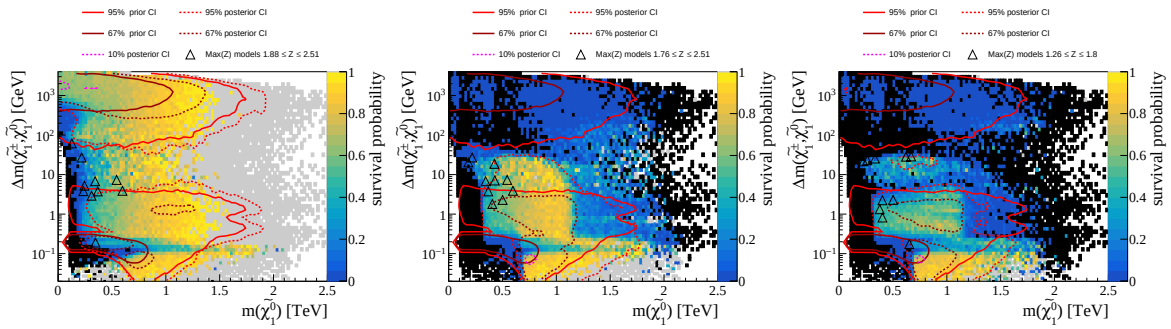

Figure 135: Survival probabilities in the plane of $\Delta m(\tilde{\chi}_1^\pm, \tilde{\chi}_1^0)$ and $m(\tilde{\chi}_1^0)$, considering the **LHC constraints** (left), the **LHC constraints + loose Ωh^2 constraint** (center), and the **LHC constraints + loose Ωh^2 constraint + direct detection constraints** (right). Black color denotes bins with zero survival probability, grey denotes bins with a survival probability of exactly 1, white bins are empty. A detailed description of the plot elements is given in Section 7.

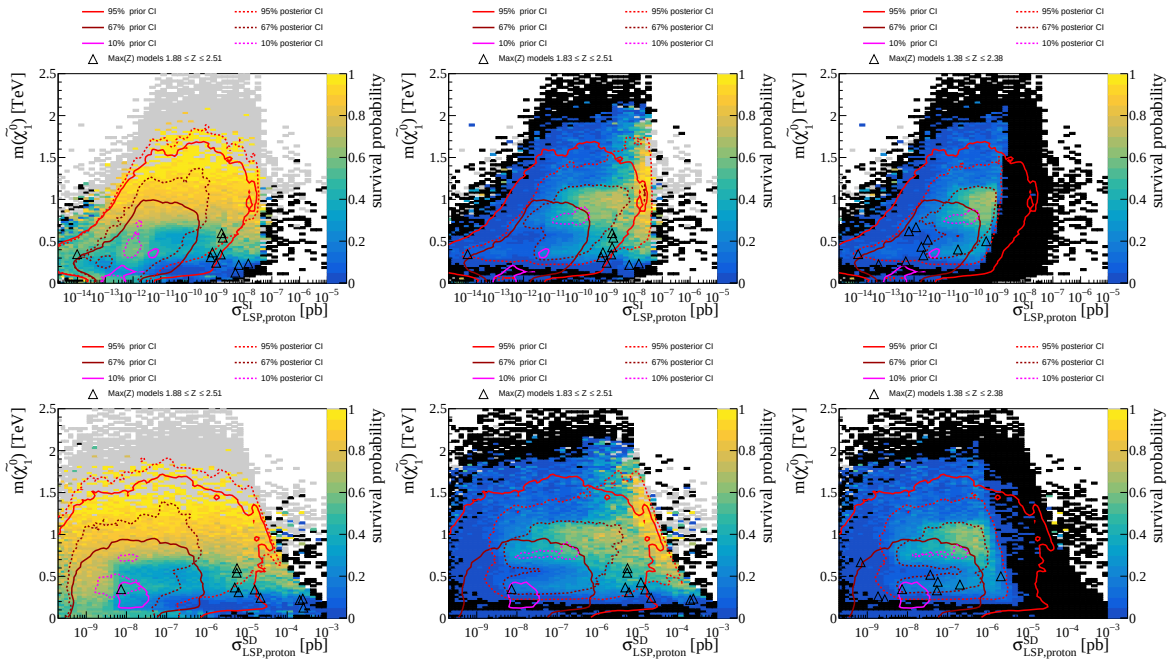

Figure 136: Survival probabilities in the plane of $m(\widetilde{\chi}_1^0)$ and spin independent (top row) and the spin-dependent (bottom row) LSP-proton interaction cross sections, considering the **LHC constraints** (left column), the **LHC + upper bound on Ωh^2** (center column), and the **LHC constraints + upper bound on Ωh^2 + direct detection constraints** (right column). Black color denotes bins with zero survival probability, grey denotes bins with a survival probability of exactly 1, white bins are empty. A detailed description of the plot elements is given in Section 7.

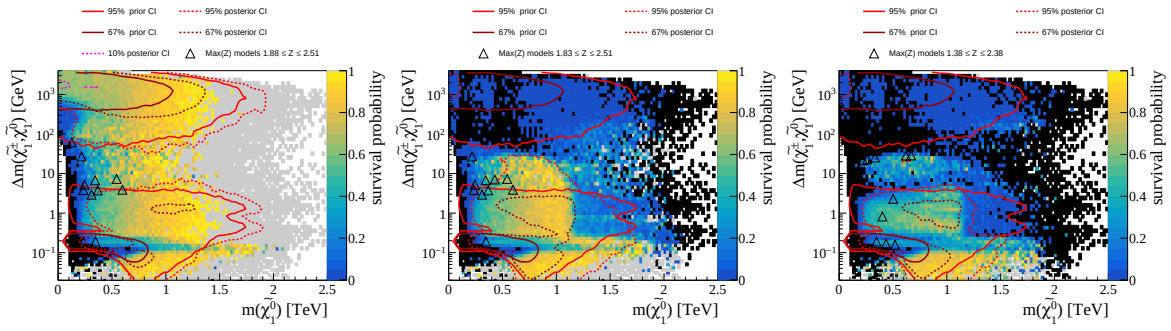

Figure 137: Survival probabilities in the plane of $\Delta m(\widetilde{\chi}_1^\pm, \widetilde{\chi}_1^0)$ and $m(\widetilde{\chi}_1^0)$, considering the **LHC constraints** (left), the **LHC constraints + upper bound on Ωh^2** (center), and the **LHC constraints + upper bound on Ωh^2 + direct detection constraints** (right). Black color denotes bins with zero survival probability, grey denotes bins with a survival probability of exactly 1, white bins are empty. A detailed description of the plot elements is given in Section 7.

8.5 Fine tuning

Figure 138 shows the impact of the considered LHC searches on the pMSSM in terms of the fine tuning measure ΔEW (defined and described in Section 2.3.2). We can see that in the prior, the distribution of ΔEW peaks at around a value of 500, with the small ΔEW region disfavored. The prior distribution of ΔEW and its peak are strongly correlated to, and bounded from below by, the square of the higgsino mass parameter μ, which follows directly from the definition of ΔEW in Equations 11 and 12. Thus, there is a peak at $|\mu| \simeq 1.5\,\text{TeV}$ that corresponds to the peak at $\Delta\text{EW} \simeq 500$. The correlation of ΔEW to $|\mu|$ can clearly be seen in the prior credibility intervals in Figure 139. We can also see here that even though there is a strong correlation of ΔEW and $|\mu|$, there are models with small $|\mu|$ and large ΔEW, where one of the non-μ terms in Equation 11 becomes large. The small ΔEW region is most strongly disfavored by the non-tachyon constraint, with smaller contributions from the Higgs mass constraint and several flavor observables (more details can be found in Section 5).

Because of the construction of the measure ΔEW, a lower bound on $|\mu|$, which is given by the LHC through constraints on $m(\widetilde{\chi}_1^0)$, results in a lower bound on ΔEW. As shown in Figure 140, the LHC disfavors very small $\Delta\text{EW} \lesssim 100$ on top of the already small prior density, mostly because it disfavors small $|\mu|$ due to constraints on higgsino-like LSP. The sensitivity here comes from the $\text{p}_\text{T}^\text{miss}$+jets search, which provides the strongest constraints on small higgsino-like $m(\widetilde{\chi}_1^0)$ of the LHC analyses included in this thesis. At small $m(\widetilde{\chi}_1^0)$ and larger ΔEW, including the prior density peak region at $\Delta\text{EW} \in (400, 650)$, the prior is made up of wino-like LSP and bino-like LSP. The LHC constraints suppress the posterior here, such that no corresponding 10% credibility interval in the posterior density is identified. Larger ΔEW are also somewhat disfavored by the LHC, since it is very sensitive to the pMSSM where the LSP is a pure wino due to the increased prevalence of long-lived charginos, which requires $\text{M}_2 \ll |\mu|$. Larger ΔEW are thus correlated to more pure winos, which leads to a slight decrease of the median Bayes factor and survival probability. The small fine tuning region is not completely excluded after the LHC, as there are still models with levels of fine tuning as small as $\Delta\text{EW} \simeq 4$ that survive the LHC exclusion.

Finally, most data-compatible models, namely models with the highest positive Z significance, have small ΔEW, owing to the fact that they feature a light higgsino-like LSP with a small value of $|\mu|$, and are absent other features that strongly contribute to a large ΔEW.

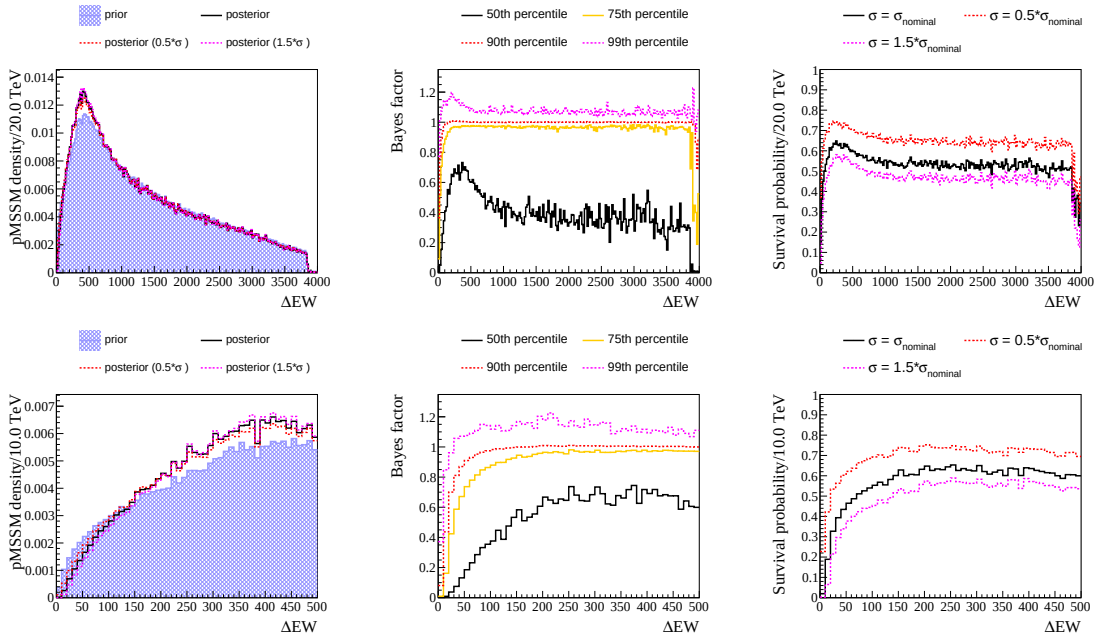

Figure 138: Impact of the considered LHC searches on the fine-tuning measure ΔEW, in terms of the prior and posterior densities (left column), Bayes factor quantiles (center column), and the survival probability (right column). The top row shows the whole distribution, the bottom row is zoomed in to the small-ΔEW region. Black color denotes bins with zero survival probability, grey denotes bins with a survival probability of exactly 1, white bins are empty. A detailed description of the plot elements is given in Section 7.

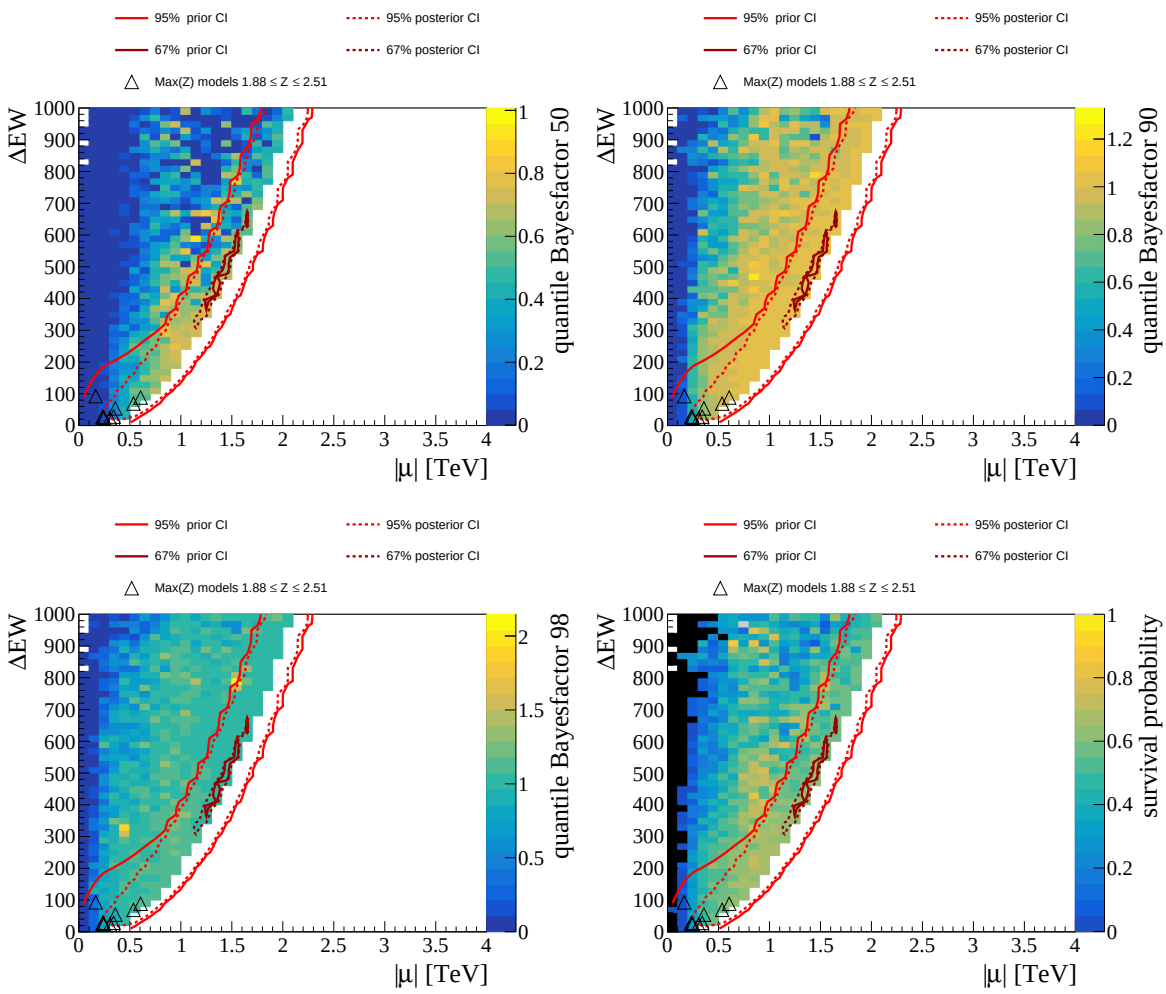

Figure 139: Impact of the LHC in the plane of the absolute value of the higgsino mass parameter $|\mu|$ and the fine tuning measure ΔEW, in terms of the median (top left), 90th (top right), and 98th (bottom left) quantiles of the Bayes factor, as well as the survival probability (bottom right). Black color denotes bins with zero survival probability, grey denotes bins with a survival probability of exactly 1, white bins are empty. A detailed description of the plot elements is given in Section 7.

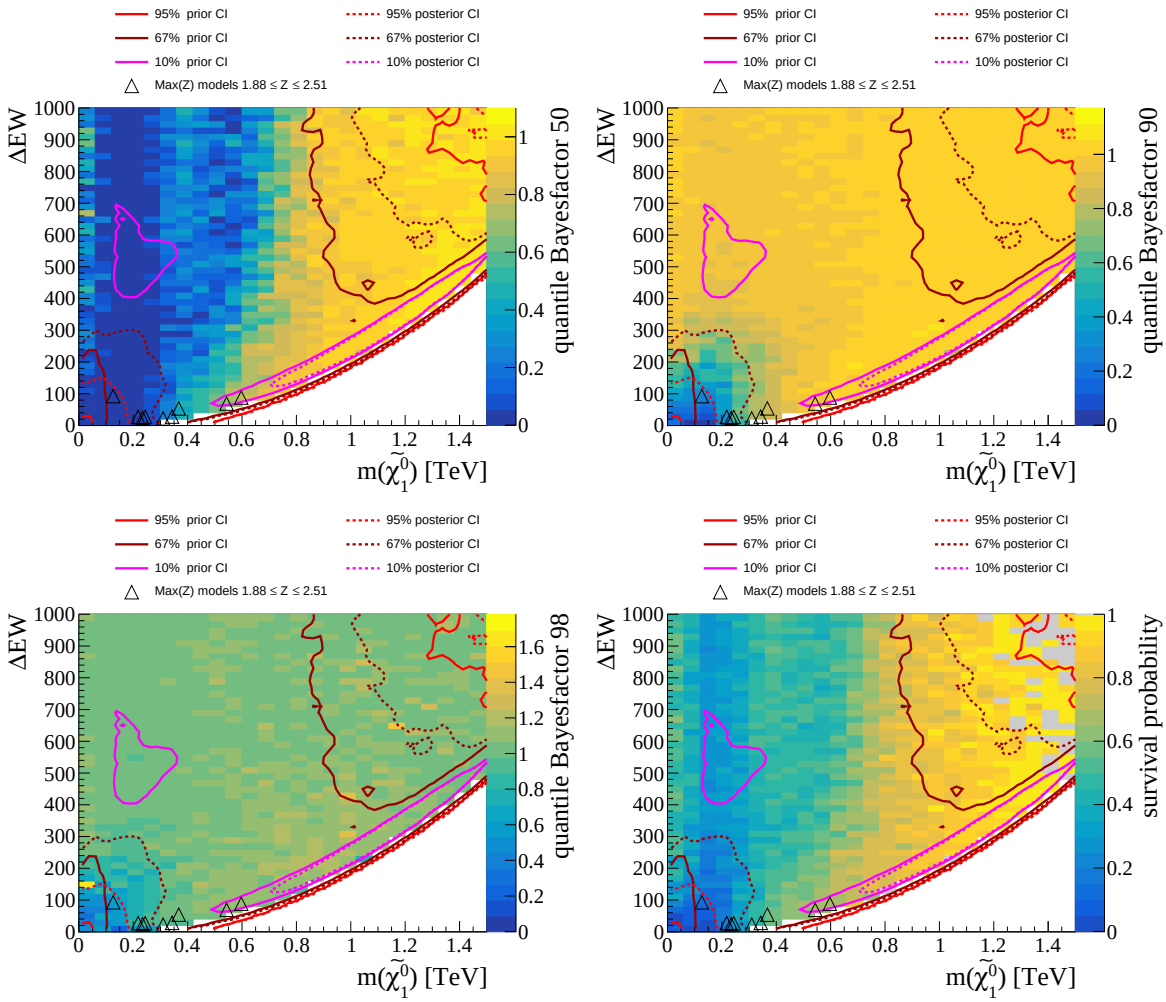

Figure 140: Impact of the LHC in the plane of the LSP mass $m(\tilde{\chi}_1^0)$ and the fine-tuning measure ΔEW, in terms of the median (top left), 90th (top right), and 98th (bottom left) quantiles of the Bayes factor, as well as the survival probability (bottom right). Black color denotes bins with zero survival probability, grey denotes bins with a survival probability of exactly 1, white bins are empty. A detailed description of the plot elements is given in Section 7.

8.5.1 Small fine tuning regions

As a next step, we study how the pMSSM looks in regions of small fine tuning, by looking at the subspaces of the pMSSM that are compatible with a **loose** ΔEW ≤ 100 constraint, and a **tight** ΔEW ≤ 30 constraint.

Loose ΔEW region

In the **loose** region, the main effect is that $|\mu|$ is bounded from above, seen in the vanishing survival probability for $|\mu| > 650\,\text{GeV}$ in Figure 141. This directly follows from the $-\mu^2$ term in Equation 12. The posterior density shows a strong peak at $|\mu| \simeq 500\,\text{GeV}$ that is a result of the LHC suppressing smaller $|\mu|$, and the upper bound on $|\mu|$ from the ΔEW constraint. As a consequence of small $|\mu|$,

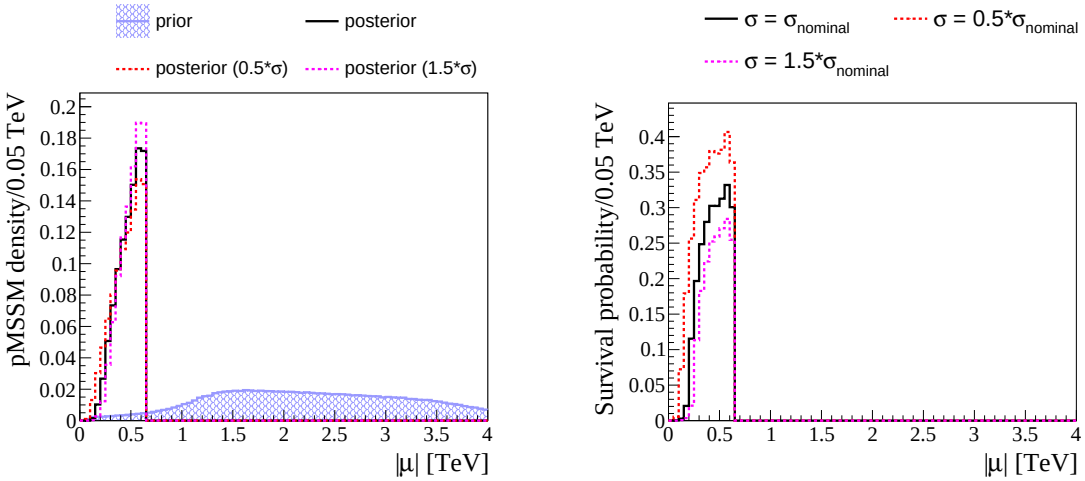

Figure 141: Impact of the **LHC constraints + loose ΔEW constraint** on the absolute value of the higgsino mass parameters, $|\mu|$, in terms of the prior and posterior densities (left) and the survival probability (right). A detailed description of the plot elements is given in Section 7.

there is always a multitude of electroweakino states with masses m $< 650\,\text{GeV}$ in the **loose** ΔEW region, which also bounds the LSP mass $m(\tilde{\chi}_1^0)$ from above. This can be seen in Figure 142, which shows the impact of the combined **LHC constraint + loose ΔEW constraints** on the LSP mass. Note that while most of the surviving models feature pure higgsino-like LSP, there are also surviving models with pure binos, pure winos, or mixed LSP states, in which the lightest higgsino state is not the LSP.

The inclusion of the **loose ΔEW constraint** also reveals a striking correlation of small ΔEW to a boomerang-shaped region in the plane of the stop mass parameters $M_{q,3}$ and $M_{u,3}$, seen in Figure 143. Here we see that the region of large $M_{q,3}$ and large $M_{u,3}$ is excluded by the **loose ΔEW constraint**. This is because the small $|\mu|$ region where $Q_{SUSY} = \sqrt{M_{q,3} \times M_{u,3}}$ is large is entirely tachyonic, as described in Section 5 and Appendix B. Because small ΔEW requires $|\mu|$ to be small, this region does not survive the constraint. We can also see by the shape of the credibility intervals of the posterior density that the loose ΔEW favors larger, but not maximal, differences among $M_{q,3}$ and $M_{u,3}$. They further inform us that the posterior density is comparatively small when $M_{q,3} \simeq M_{u,3}$, since the 67% credibility intervals do not extend into that region. Furthermore the tilt of these intervals in the plane of $M_{q,3}$ and $M_{u,3}$ show that the maximal difference between these two parameters is slightly disfavored in the posterior density. The boomerang shape in the plane of the stop mass parameters leads to a sharply peaking distribution of the lighter stop mass, centered at $m(\tilde{t}_1) \simeq 3\,\text{TeV}$, as can be seen in Figure 144.

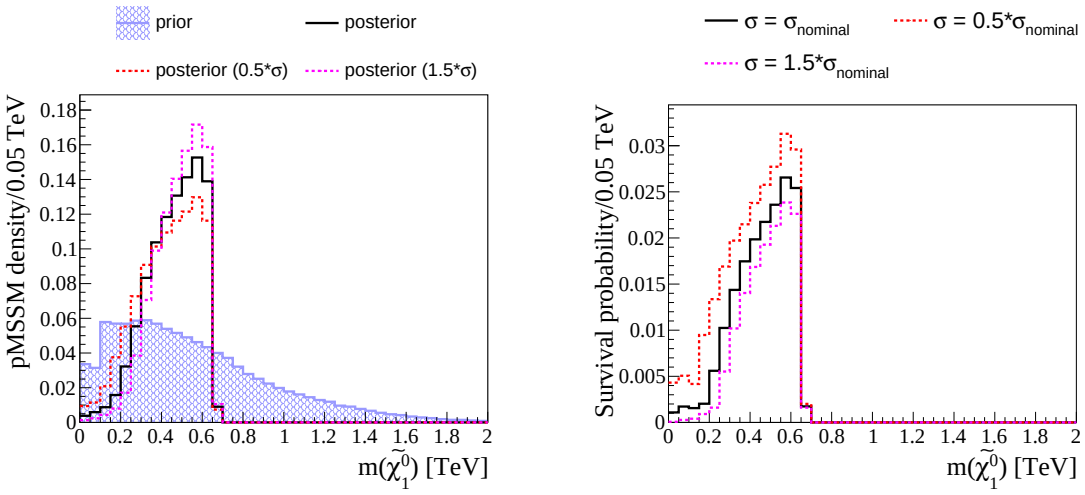

Figure 142: Impact of the **LHC constraints + loose ΔEW constraint** on the mass of the lightest neutralino, $m(\tilde{\chi}_1^0)$, in terms of the prior and posterior densities (left) and the survival probability (right). A detailed description of the plot elements is given in Section 7.

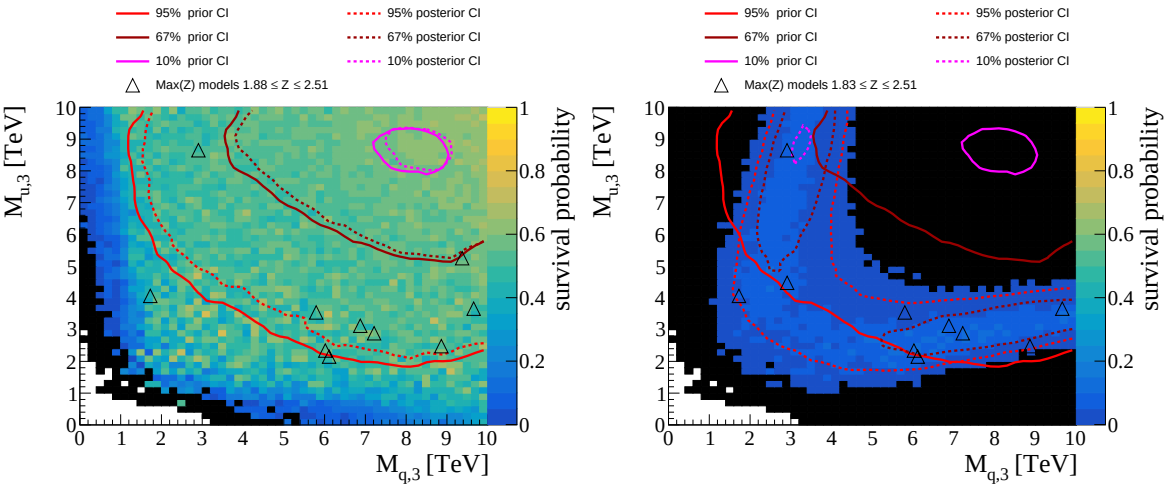

Figure 143: Survival probabilities, considering the **LHC constraints** (left) and the **LHC constraints + loose ΔEW constraint** (right), in the plane of the left-chiral third generation squark mass parameter $M_{q,3}$ and the right-chiral stop mass parameter $M_{u,3}$. Black color denotes bins with zero survival probability, grey denotes bins with a survival probability of exactly 1, white bins are empty. A detailed description of the plot elements is given in Section 7.

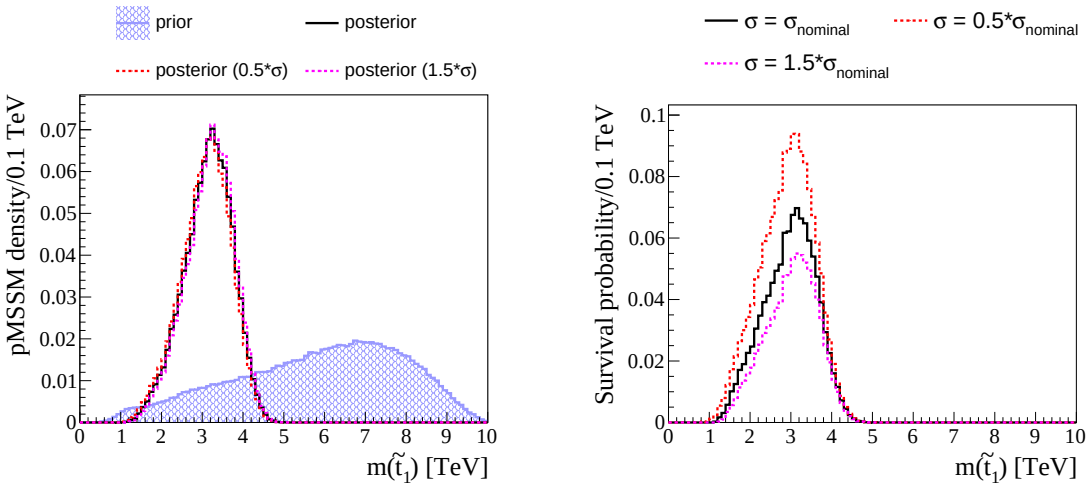

Figure 144: Impact of the **LHC constraints + loose ΔEW constraint** on the mass of the lighter stop $m(\tilde{t}_1)$, in terms of the prior and posterior densities (left), and the survival probability (right). A detailed description of the plot elements is given in Section 7.

8.5.1.1 Tight ΔEW region

There are no substantial differences between the **tight** and **loose** ΔEW regions in terms of the phenomenology in the pMSSM. The upper threshold on $|\mu|$ decreases, as shown in Figure 145. This similarly affects the LSP mass, shown in Figure 146. The LSP types are dominated by pure higgsinos, with a small fraction of models with a pure wino, pure bino, or mixed LSP type, surviving. In the plane of the stop mass parameters, shown in Figure 147, the shape for the allowed models is almost identical for the **loose** and **tight** ΔEW regions. One difference with little phenomenological consequence is that the allowed region is approximately half as large in the **tight** ΔEW region compared to the **loose** ΔEW region. The stop mass distribution, shown in Figure 148, is not significantly changed in the **tight** region compared to the **loose** ΔEW region.

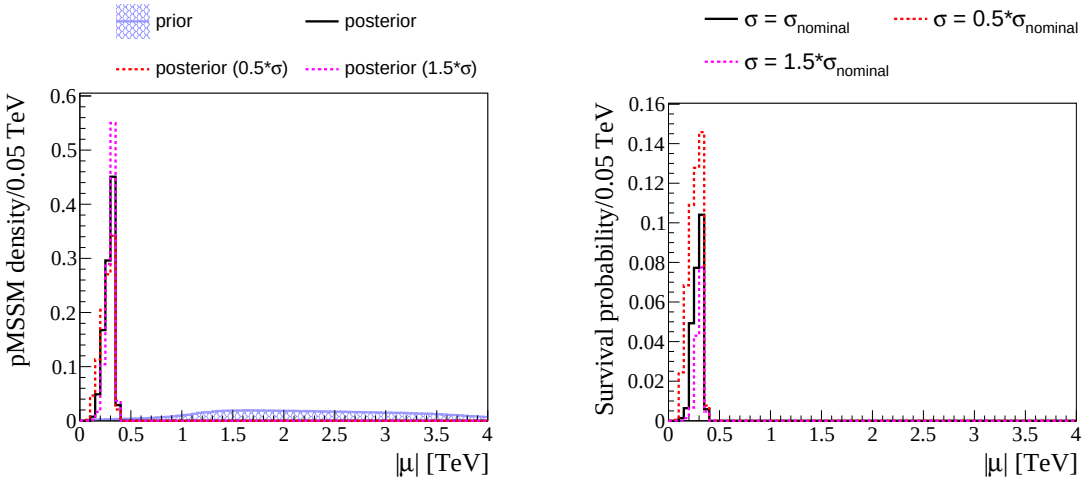

Figure 145: Impact of the **LHC constraints + tight ΔEW constraint** on the absolute value of the higgsino mass parameters $|\mu|$, in terms of the prior and posterior densities (left), and the survival probability (right). A detailed description of the plot elements is given in Section 7.

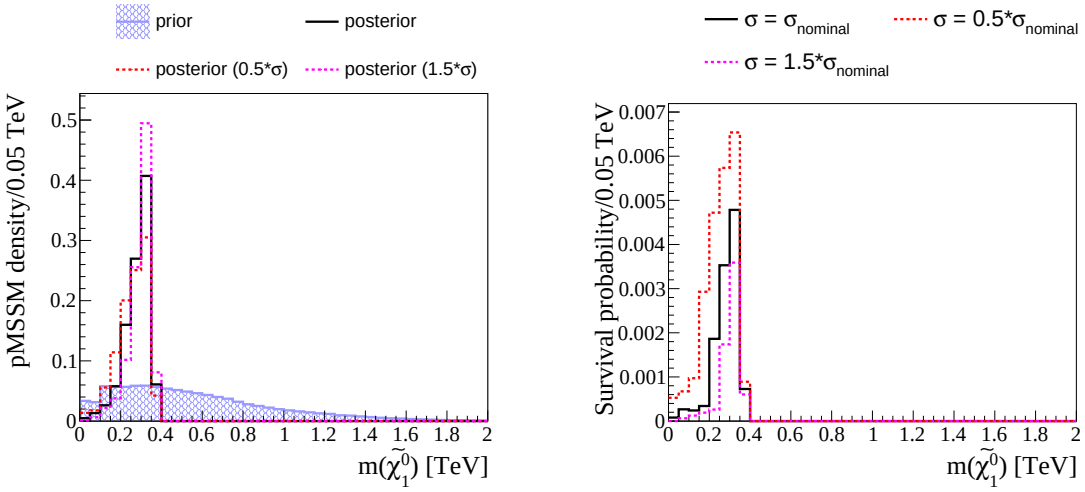

Figure 146: Impact of the **LHC constraints + tight ΔEW constraint** on the mass of the LSP $m(\widetilde{\chi}_1^0)$, in terms of the prior and posterior densities (left), and the survival probability (right). A detailed description of the plot elements is given in Section 7.

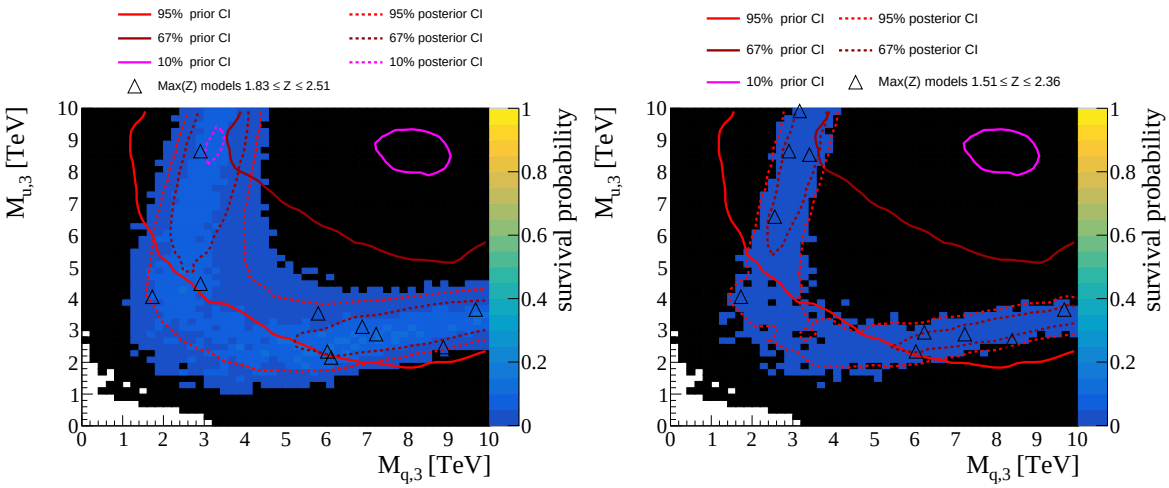

Figure 147: Survival probabilities, considering the **LHC constraints** (left) and the **LHC constraints + tight ΔEW constraint** (right), in the plane left-chiral third generation squark mass parameter $M_{q,3}$ and the right-chiral stop mass parameter $M_{u,3}$. Black color denotes bins with zero survival probability, grey denotes bins with a survival probability of exactly 1, white bins are empty. A detailed description of the plot elements is given in Section 7.

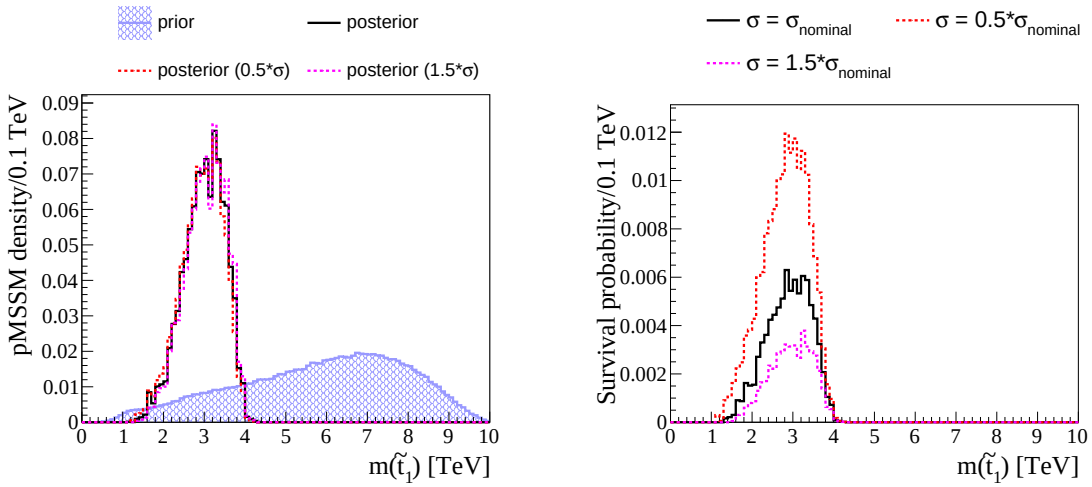

Figure 148: Impact of the **LHC constraints + tight ΔEW constraint** on the mass of the lighter stop, $m(\tilde{t}_1)$, in terms of the prior and posterior densities (left), and the survival probability (right). A detailed description of the plot elements is given in Section 7.

8.5.2 Combined fine tuning and dark matter constraints

Constraints on the fine tuning measure ΔEW are complementary to constraints on dark matter. To see this, first consider Figure 149, which shows the impact the combined **LHC constraint + loose ΔEW constraint** on the observables most relevant to the dark matter constraints. We can see that the peak of the posterior density after the **LHC constraints + loose ΔEW constraint** corresponds to a relic density that is compatible with the **loose** constraint of the relic density, where $\Omega h^2 \in [0.1, 1.1]\ \Omega h^2_{\text{Planck}}$ is required. These models are predominately light higgsino-like LSP, as per the ΔEW constraint. It is also in this region that the largest fraction of the prior survives the **LHC constraints + loose ΔEW constraint**.

The posterior density is much smaller, but non-zero, in the region of the **tight** Ωh^2 constraint, which requires $\Omega h^2 \in [0.9, 1.1]\ \Omega h^2_{\text{Planck}}$. Such comparatively large relic densities, combined with the constraints on the LSP mass from ΔEW that require $m(\widetilde{\chi}^0_1) \lesssim 650\,\text{GeV}$, can only be realized in the pMSSM if the LSP is partly bino-like. There then needs to be a small mass gap between the LSP and the next-to-lightest SUSY particle (NLSP) to sufficiently enhance the co-annihilation cross section to achieve $\Omega h^2 \simeq \Omega h^2_{\text{Planck}}$.

Towards much smaller relic densities, there is a sharp drop in the survival probability and posterior density after the **loose** ΔEW constraint is applied. If the **upper bound** on Ωh^2 is adopted as the constraint for the relic density, then these models would survive both the relic density and the **loose** ΔEW constraint. They almost exclusively feature a very light higgsino-like LSP.

Concerning the impact of the direct detection constraints, we see that the **LHC constraints + loose ΔEW constraint** mostly eliminate the part of the prior with small LSP-nucleon interaction cross sections. This makes the direct detection data well suited to constrain the small ΔEW region. The reason for this synergy is that the considered direct detection experiments are most sensitive to models with a higgsino-like LSP.

The complementarity of the dark matter and fine tuning constraints can be summarized by looking at the plane of the relic density and the p-value for the direct detection experiments, shown in Figure 150, after applying the two versions of the constraints on ΔEW. Here we can see that the posterior density, which considers the LHC and respective ΔEW constraints, still populates the regions compatible with the **loose** constraint on Ωh^2 that are not excluded by the direct detection experiments ($p > 0.05$). Adopting the **upper bound** on Ωh^2 as the constraint of choice for the relic density does not significantly alter the results in combination with the **loose** ΔEW constraint, as most of the models with $\Omega h^2 < 0.1\,\Omega h^2_{\text{Planck}}$ are excluded by the direct detection constraints. These few models with $\Omega h^2 < 0.1\,\Omega h^2_{\text{Planck}}$ that are not excluded by the direct detection constraints can be significant if the **tight** ΔEW constraint is applied however, as they make up a significant fraction of the models surviving the **tight** ΔEW and direct detection constraints. The region compatible with the **tight** Ωh^2 constraint and compatible with the direct detection constraints is very sparsely populated for the **loose** ΔEW constraint, and empty for the **tight** ΔEW constraint.

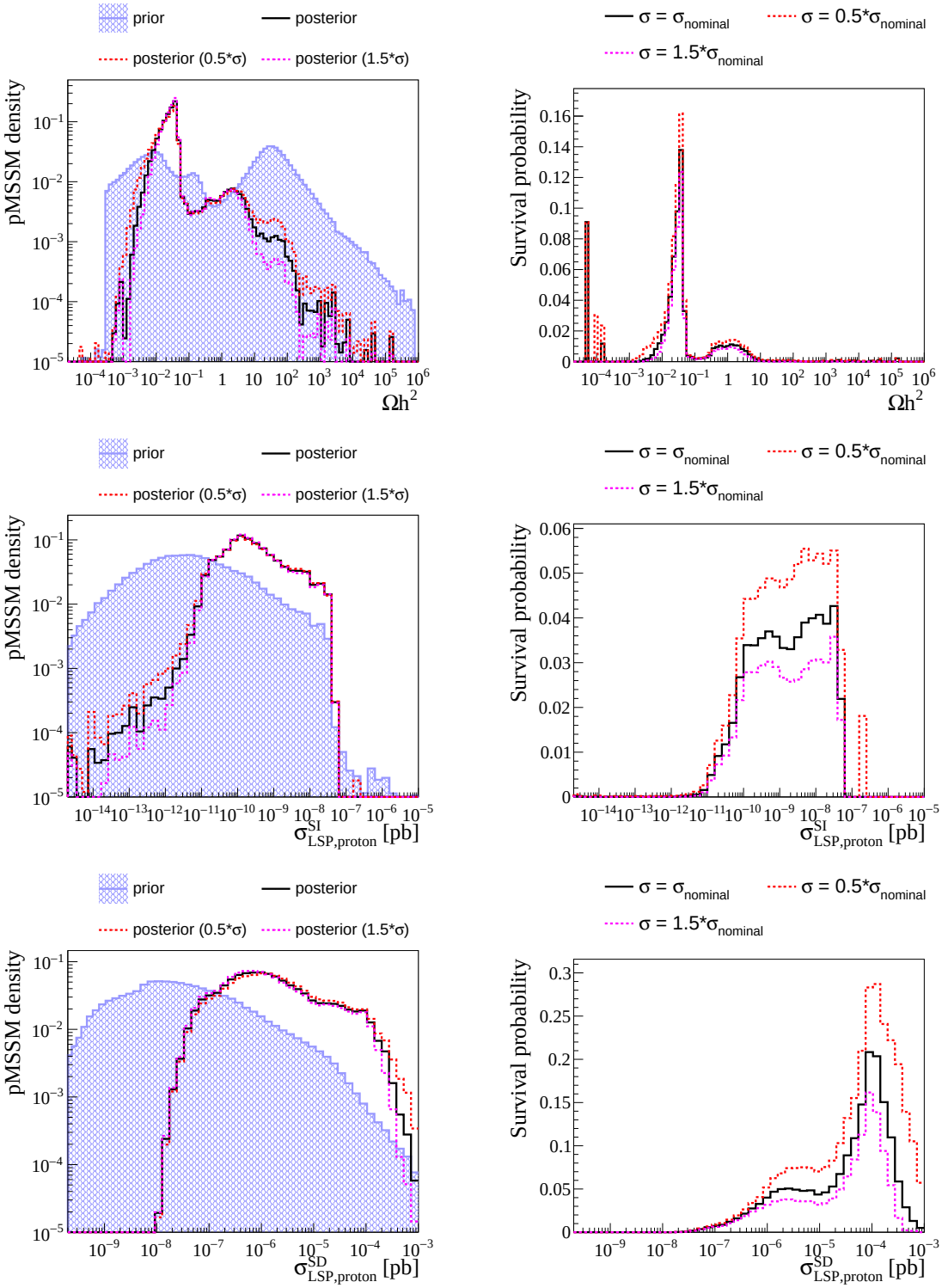

Figure 149: Impact of the **LHC constraints + loose ΔEW constraint** on the relic density Ωh^2 (top row), the spin-independent (center row) and spin-dependent (bottom row) LSP-proton interaction cross sections, in terms of the prior and posterior densities (left column) and the survival probability (right column). A detailed description of the plot elements is given in Section 7.

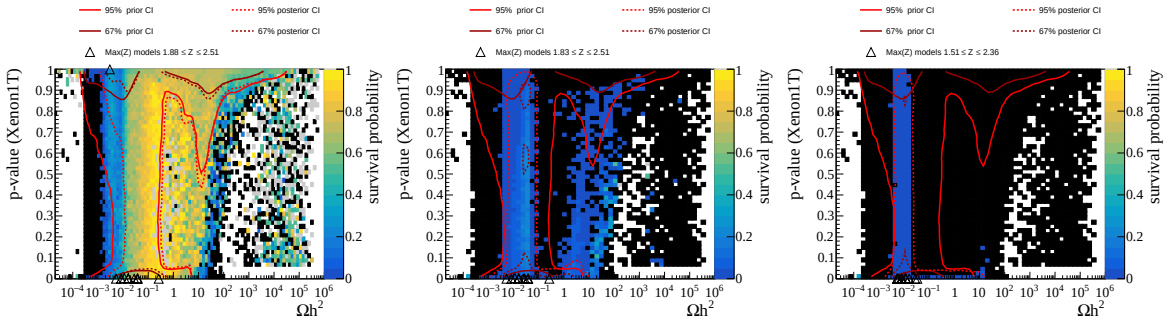

Figure 150: Survival probabilities in the plane of Ωh^2 and the p-value for compatibility with the direct detection constraints, considering the **LHC constraints** (left), the **LHC constraints + loose ΔEW constraint** (center), and the **LHC constraints + tight ΔEW constraint** (right). A p-value $p < 0.05$ means exclusion at 95%CL by the direct detection experiments. Black color denotes bins with zero survival probability, grey denotes bins with a survival probability of exactly 1, white bins are empty. A detailed description of the plot elements is given in Section 7.

Figure 151 shows the impact of the ΔEW and dark matter constraints on the absolute value of the higgsino mass parameter $|\mu|$. We can see that the constraints on ΔEW are far more restricting than the dark matter constraints. Additionally, the inclusion of the **upper bound** on the relic density has almost no impact on $|\mu|$, since requiring ΔEW to be small already removes all of the models with large Ωh^2 that feature a higgsino-like or wino-like LSP, and most of the models with a bino-like LSP that would be excluded by the constraint on Ωh^2. The remaining models with large Ωh^2 are then excluded by the direct detection constraints, so that only scenarios with small Ωh^2 survive the constraints. Introducing a lower bound on Ωh^2 translates to a lower bound on $|\mu|$, as models with a very light higgsino-like LSP also feature a relic density below the threshold of $\Omega h^2 < 0.1\,\Omega h^2_{\text{Planck}}$ imposed by the **loose** constraint on Ωh^2. In the **loose** ΔEW region, this combination restricts $|\mu|$ to an approximately 300 GeV wide region around $|\mu| \simeq 500$ GeV. In the **tight** ΔEW region, a very small region of the pMSSM remains viable with $|\mu| \simeq 300$ GeV. Because all of the remaining models are mostly higgsino-like, the distributions of $m(\widetilde{\chi}_1^0)$ are almost identical to those of $|\mu|$.

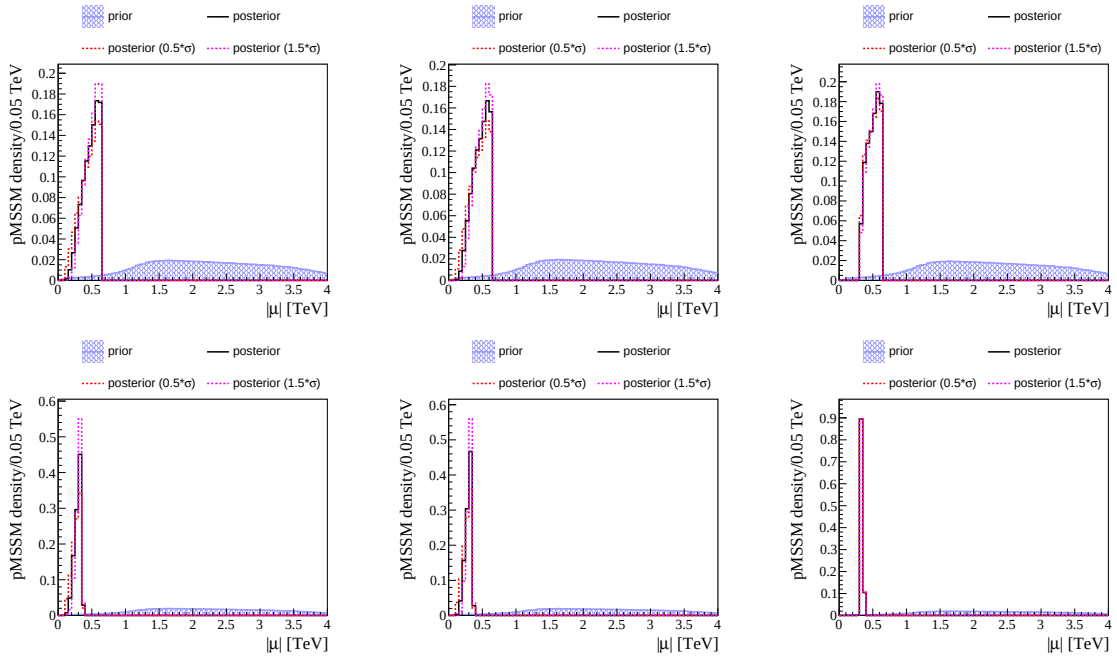

Figure 151: Impact of the dark matter and ΔEW constraints on $|\mu|$, in terms of the prior and posterior densities. The distributions are considering the **loose ΔEW constraint** (top row) and the **tight ΔEW constraint** (bottom row), in combination with the **LHC constraints** (left column), the **LHC constraints + upper bound on Ωh^2 + direct and indirect detection constraints** (center column), and the **LHC constraints + loose Ωh^2 + direct and indirect detection constraints** (right column). A detailed description of the plot elements is given in Section 7.

In contrast to the small effect seen in $|\mu|$, the effect of the dark matter constraints can be seen in the plane of $\Delta m(\widetilde{\chi}_1^{\pm}, \widetilde{\chi}_1^0)$ and $m(\widetilde{\chi}_1^0)$, shown in Figure 152. The top two plots show that the ΔEW constraints introduce an upper bound on $m(\widetilde{\chi}_1^0)$, while the LHC constrains $m(\widetilde{\chi}_1^0)$ from below. There is a significant population of the pMSSM towards larger $\Delta m(\widetilde{\chi}_1^{\pm}, \widetilde{\chi}_1^0)$ that remains compatible with both of these constraints. These models feature a bino-like LSP with an additional light higgsino triplet. Almost all of these models are excluded by the dark matter constraints, mostly due to the direct detection constraints, such that even if there is no lower bound on Ωh^2, the remaining models are clustered at $\Delta m(\widetilde{\chi}_1^{\pm}, \widetilde{\chi}_1^0) \simeq 1\,\text{GeV}$ and $m(\widetilde{\chi}_1^0) \simeq 350\,\text{GeV}$. If a lower bound on Ωh^2 is imposed, there is no significant change in $\Delta m(\widetilde{\chi}_1^{\pm}, \widetilde{\chi}_1^0)$ visible, but small $m(\widetilde{\chi}_1^0)$ are no longer viable. As previously mentioned, assuming the tightest set of constraints excludes all pMSSM models in the scan. A relaxation of the Ωh^2 constraint from **tight** to **loose**, featured in the bottom right of Figure 152, allows for a little over 0.1 % of the prior to survive, which corresponds to 629 pMSSM points.

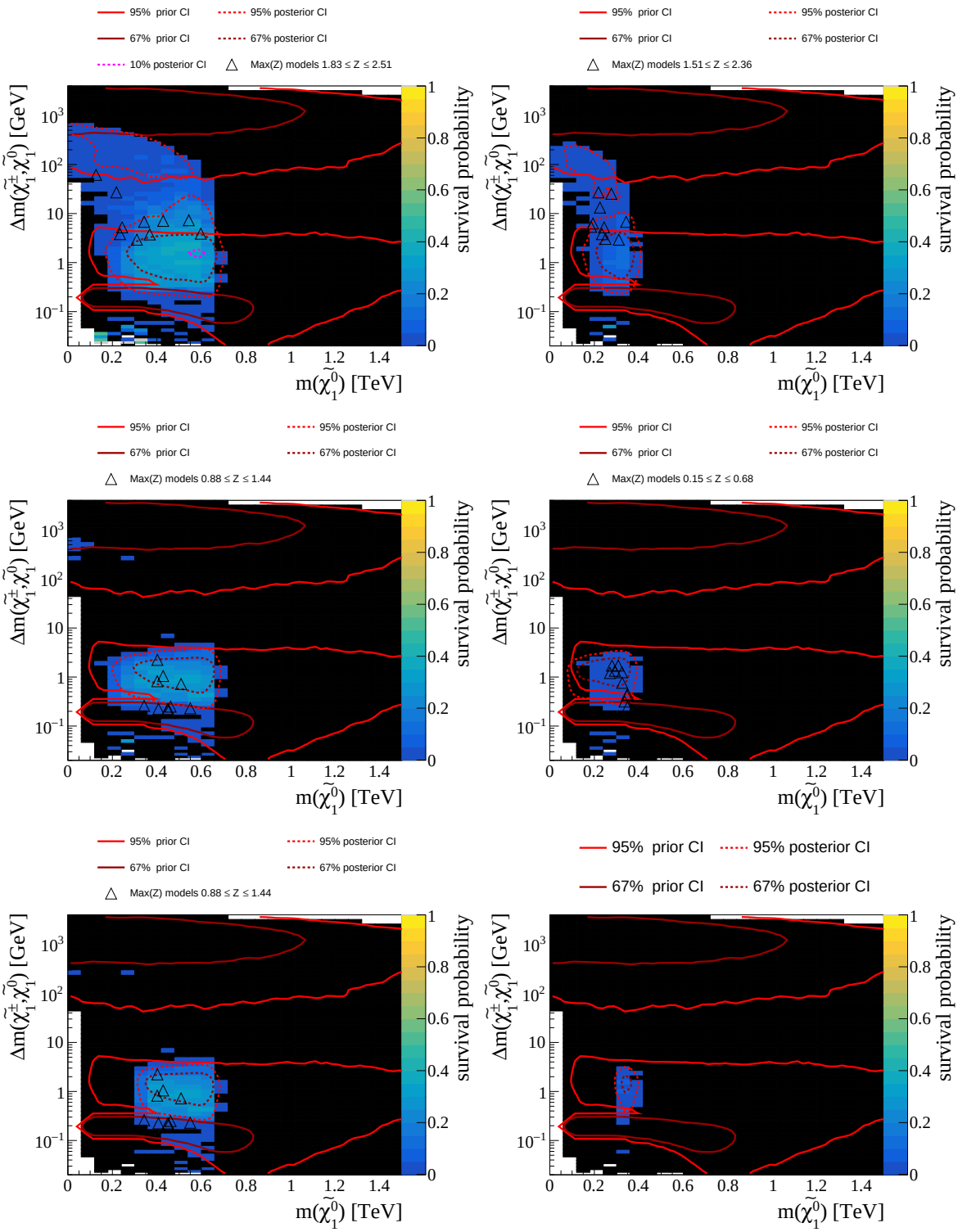

Figure 152: Survival probabilites in the plane of $\Delta m(\tilde{\chi}_1^{\pm}, \tilde{\chi}_1^0)$ and $m(\tilde{\chi}_1^0)$. Shown are the survival probability for the **loose ΔEW constraint** (left column) and the **tight ΔEW constraint** (right column), in combination with the **LHC constraints** (top row), the **LHC constraints + upper bound on Ωh^2 + direct and indirect detection constraints** (center row), and the **LHC constraints + loose Ωh^2 constraint+ direct and indirect detection constraints** (bottom row). Black color denotes bins with zero survival probability, grey denotes bins with a survival probability of exactly 1, white bins are empty. A detailed description of the plot elements is given in Section 7. Assuming the tightest constraints (bottom right), only $\sim 0.1\,\%$ of the prior survives, which corresponds to 629 pMSSM points.

8.6 Anomalous magnetic moment of the muon

Recent measurements of the anomalous magnetic moment of the muon at Fermilab [116, 66] have confirmed and increased the long-standing tension with the SM expectation, with the new world average $a_\mu^{observed} = (116592059 \pm 22) \times 10^{-11}$ [66] diverging from the SM prediction $a_\mu^{SM} = (116591810 \pm 43) \times 10^{-11}$ [157] at the level of approximately 5 standard deviations. If there is a resolution within the SM, it is now likely to show itself as a correction to the current theory predictions. Incidentally, a new prediction based on lattice calculations [158] is itself in tension with the currently accepted SM prediction. Until the two SM predictions are reconciled, it is premature to claim evidence for new physics. However, the very real possibility of new physics is sufficient motivation to consider the implications of a_μ on the MSSM.

Examples for 1-loop and 2-loop MSSM contributions to a_μ are shown in Figure 153 and include contributions from smuon-electroweakino loops, as well as contributions from sfermions and the MSSM Higgs sector. The MSSM contribution to a_μ thus decreases with increasing smuon and electroweakino masses. Note that the left-chiral charged sleptons and the sneutrinos are almost mass degenerate in the pMSSM, with mass differences not exceeding 10 GeV in the whole pMSSM scan. We take the

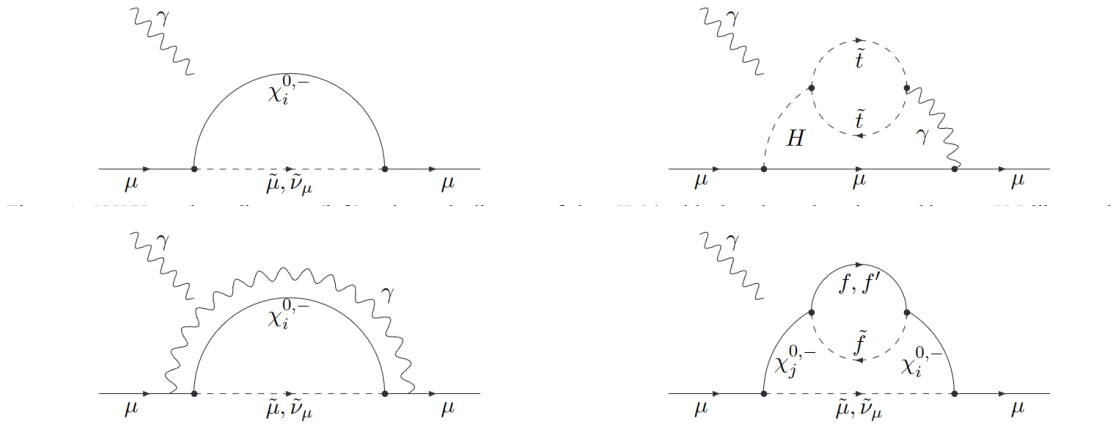

Figure 153: Example one- and two-loop MSSM contributions to a_μ. The external photon can couple to any charged particle in the diagram. Figure taken from [159] with original caption removed.

MSSM contribution to a_μ, together with its uncertainty, from `GM2Calc1.7.3` [159, 160] and compute a combined uncertainty by taking the square root of the sum of the squared SM [157] and MSSM [159, 160] theory uncertainties, and the uncertainty in the new world average [66].

The prior density and LHC impact on a_μ are shown in Figure 154. The vast majority of the pMSSM produces very small contributions to a_μ and in approximately half the scan, the contribution to a_μ is negative, which fits the data worse than the SM-only hypothesis. The sign of the MSSM contribution to a_μ is mostly determined by the sign of the product of M_2 and μ, with $M_2 \times \mu < 0$ predominately leading to negative contributions to a_μ, and $M_2 \times \mu > 0$ predominately leading to positive contributions to a_μ. A very small fraction of less than 0.2% of the pMSSM scan conforms to the measured world average within 2 standard deviations and approximately 90% of these models are excluded by the LHC. The small fraction of the prior with significant MSSM contributions to a_μ is explained by the fact that these contributions usually require the presence of light smuons, which are heavily suppressed in the prior (see also Section 5), and the presence of light charginos. The large LHC sensitivity to these models, visible as a low survival probability at large $\Delta a_\mu^{\text{SUSY}}$ in Figure 154, is largely due to the need for low-mass charginos to which the LHC is sensitive.

Despite oversampling the a_μ-compatible region, the remaining 135 models that survive the LHC data are an insufficient set to perform the usual way of analysis shown for the other constraints in this thesis. Instead, we characterize the surviving models and the interplay of the a_μ constraint with the LHC, dark matter, and fine tuning constraints in a parallel coordinates plot, shown in Figure 155. All models compatible with a_μ data, represented by the sum of all shown lines, feature a comparatively light $\widetilde{\chi}_1^0$ with $m(\widetilde{\chi}_1^0) < 750$ GeV, a large majority of these models have $m(\widetilde{\chi}_1^0) < 500\,GeV$. The LSP

type of most of these models is a wino or higgsino, resulting in a similarly massive $\widetilde{\chi}_1^\pm$. However, a not insignificant fraction of models have a bino-like LSP with a heavy $\widetilde{\chi}_1^\pm$. As expected from the nature of the MSSM contribution to a_μ, all a_μ-compatible models feature a light slepton with $m(\widetilde{e}_L, \widetilde{\mu}_L) < 1\,\text{TeV}$ or $m(\widetilde{e}_R, \widetilde{\mu}_R) < 1\,\text{TeV}$. A light $\widetilde{\mu}_L$ is far more common, likely due to the near mass degeneracy of $\widetilde{\mu}_L$ and $\widetilde{\nu}_\mu$ in the pMSSM, which also contributes to a_μ (see Figure 153). The colored sector is not particularly affected by the g-2 constraint.

The LHC data exclude all grey-colored lines in Figure 155. Very small $\widetilde{\chi}_1^0$ and $\widetilde{\chi}_1^\pm$ masses are excluded below $m(\widetilde{\chi}_1^0) \lesssim 100\,\text{GeV}$ and $m(\widetilde{\chi}_1^\pm) \lesssim 250\,\text{GeV}$, which can be explained by the LHC sensitivity to direct production of charginos. Most a_μ-compatible scenarios with large $m(\widetilde{\chi}_1^\pm)$are also excluded by the LHC. Light $\widetilde{\mu}_L$ with $m(\widetilde{e}_L, \widetilde{\mu}_L) \lesssim 250\,\text{GeV}$ are excluded by the combined a_μ and LHC data. This is caused both by direct sensitivity of the LHC to $\widetilde{\mu}_L$, and correlations of small $m(\widetilde{e}_L, \widetilde{\mu}_L)$ to small $m(\widetilde{\chi}_1^0)$ in the prior. The right-chiral sleptons are not noticeably impacted by the LHC data. The LHC also has a big impact on $m(\text{LCSP})$, where most models with $m(\text{LCSP}) \lesssim 2\,\text{TeV}$ are excluded by the LHC data.

The **upper bound** on Ωh^2 additionally excludes all models represented by green lines in Figure 155. Only two pMSSM models with $m(\widetilde{\chi}_1^\pm) \gtrsim 600\,\text{GeV}$ survive the addition of the upper Ωh^2 bound. This is because these models feature a bino-like LSP, which almost always results in an over-saturated Ωh^2. There is no noticeable impact on $m(\text{LCSP})$ and $m(\widetilde{e}_L, \widetilde{\mu}_L)$. However, almost all of the models excluded by the upper bound on Ωh^2 feature a light $\widetilde{\mu}_R$ in addition to a light $\widetilde{\mu}_L$. The reason for this is likely because large contributions to a_μ in models with a heavy $\widetilde{\chi}_1^\pm$ require especially light sleptons. However, the LHC data excludes very light sleptons, either through direct sensitivity or due to sensitivity to $\widetilde{\chi}_1^0$, whose mass bounds $m(\widetilde{e}_L, \widetilde{\mu}_L)$ from below. Thus, to achieve the size of a_μ-contribution necessary, both $\widetilde{\mu}_L$ and $\widetilde{\mu}_R$ need to be light.

The direct and indirect detection constraints exclude all pMSSM models represented by orange lines. These constraints eliminate most of the remaining surviving models with $m(\widetilde{\chi}_1^0)$ and $m(\widetilde{\chi}_1^\pm)$ too large to be excluded by the LHC data. The impact on $m(\widetilde{e}_L, \widetilde{\mu}_L)$, $m(\widetilde{e}_R, \widetilde{\mu}_R)$, and $m(\text{LCSP})$ is unremarkable.

Of the remaining 12 models, eight models are excluded by the **loose** fine tuning constraint, represented by the red lines. Among these are the last surviving models with a bino-like LSP and all remaining models with a wino-like LSP.

This leaves four models with comparatively low fine tuning that survive the a_μ and LHC data, the **upper bound** on Ωh^2, the direct and indirect detection constraints. These four models, colored in blue, teal, and magenta, are higgsino-like with $m(\widetilde{\chi}_1^0)$ and $m(\widetilde{\chi}_1^\pm) \simeq 250\,\text{GeV}$, right at the edge of LHC sensitivity, and all four feature a light $\widetilde{\mu}_L$ with $m(\widetilde{e}_L, \widetilde{\mu}_L) \lesssim 400\,\text{GeV}$. Two of the models, represented by the teal lines, have very small fine tuning of $\Delta\text{EW} < 30$. The one model represented by the magenta line conforms to the **loose** Ωh^2 constraint ($> 10\%$ Ωh^2 saturation), but is not quite as natural, with $30 < \Delta\text{EW} < 100$.

Finally, the LHC is at least somewhat sensitive to all models that survive the a_μ data, as the last axis in Figure 155 shows that all models have a non-zero Z-significance. If the tension between the SM prediction for a_μ and its observed value is upheld when the issue of the incompatible SM predictions is resolved, SUSY may be found within the pMSSM, or the pMSSM may be entirely excluded in the near future, when more LHC data becomes available.

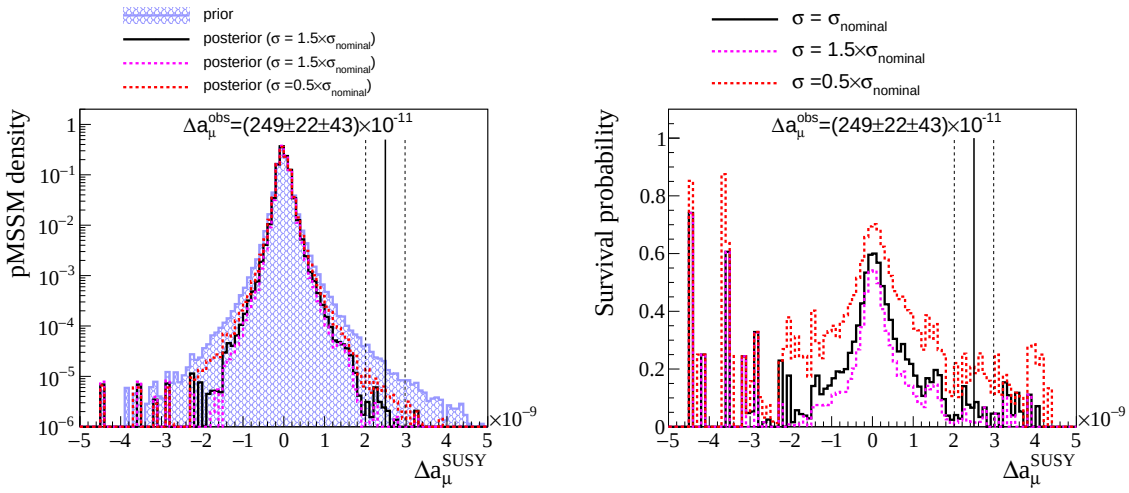

Figure 154: Impact of the considered LHC searches on the MSSM contribution to the anomalous magnetic moment of the muon a_μ, in terms of the prior and posterior densities (left) and the survival probability (right). The observed value and uncertainties of $\Delta a_\mu = 249 \pm 22 \times 10^{-11}$ [66] are indicated by black lines, assuming the 2020 SM theory prediction and uncertainties ${a_\mu}^{\mathrm{SM}} = 116591810(43) \times 10^{-11}$ [157]. Theory uncertainties for each pMSSM model are computed with `GM2Calc` [159, 160] and are of order 23×10^{-11} [159], but are not indicated in these plots. A detailed description of the plot elements is given in Section 7.

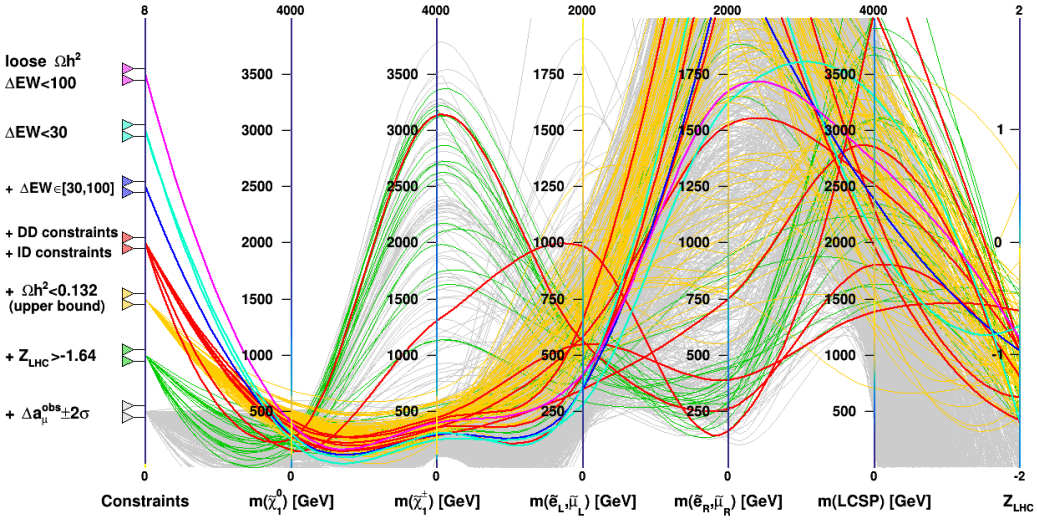

Figure 155: Parallel coordinates for various constraints applied on the pMSSM, showing the LSP mass $m(\widetilde{\chi}_1^0)$, the lighter chargino mass $m(\widetilde{\chi}_1^\pm)$, the left- and right-chiral selectron and smuon masses, the LCSP mass, and the LHC Z-significance. Each line represents a pMSSM model, whose intersections with the axes indicate the respective model value for the axis variable. The line color indicates the set of constraints that apply on the respective pMSSM model. The constraint categories are **exclusive** with respect to the pMSSM models contained therein – each pMSSM model is only shown once, in the tightest constraint category it conforms to. While the two constraint categories at the top of the axis are not orthogonal, there is no overlap in this set of pMSSM models. Constraints whose labels start with a **plus sign** are added with a logical **and** to the constraints below, constraints that are labeled **without a plus sign** replace the respective constraint below. The constraints are: compatibility with the a_μ data (grey) [66] (assuming the 2020 white paper theory prediction [157] for the SM), with a_μ+LHC data (green), with a_μ+LHC+**upper** $\Omega\mathbf{h}^2$ **bound** (orange), with a_μ+LHC+**upper** $\Omega\mathbf{h}^2$ **bound**+(in)direct detection (red), a_μ+LHC+**upper** $\Omega\mathbf{h}^2$ **bound**+(in)direct detection+loose ΔEW (blue), a_μ+LHC+**upper** $\Omega\mathbf{h}^2$ **bound**+(in)direct detection+**tight** ΔEW (teal), a_μ+LHC+**loose** Ωh^2+(in)direct detection+**loose** ΔEW(magenta).

8.7 Simplified model limit compatibility

In this final section, we study the usefulness of simplified model limits in developing an intuition about SUSY in general.

For each analysis used in this work, we compare the upper limits on simplified models in the plane of parameters as published by the respective analysis to the survival probability in the pMSSM. In a second step, we study their viability on subspaces of the pMSSM that mirror the assumptions made in the simplified models as closely as possible, while retaining sufficient statistical precision in the pMSSM model space.

8.7.1 Jets + $\mathbf{p_T^{miss}}$

The p_T^{miss}+jets search [1] (shortly introduced in Section 6.3) has published limits in simplified models featuring di-gluino production, which includes the T1 and T5 simplified model families. In particular, limits exist in the plane of m($\widetilde{g}$) and $m(\widetilde{\chi}_1^0)$ in the T1qqqq ($\widetilde{g}\widetilde{g} \to qqqq\widetilde{\chi}_1^0\widetilde{\chi}_1^0$), T1tttt ($\widetilde{g}\widetilde{g} \to tttt\widetilde{\chi}_1^0\widetilde{\chi}_1^0$), T1bbbb ($\widetilde{g}\widetilde{g} \to bbbb\widetilde{\chi}_1^0\widetilde{\chi}_1^0$), and T5qqqqVV ($\widetilde{g}\widetilde{g} \to qqqqVV\widetilde{\chi}_1^0\widetilde{\chi}_1^0$) simplified models, each assuming 100% branching fraction to their respective final states. Figure 156 shows the survival probability, with respect to the p_T^{miss}+jets search, for the inclusive pMSSM in the plane of m($\widetilde{g}$) and $m(\widetilde{\chi}_1^0)$. Overlaid are the limits of the p_T^{miss}+jets search on the same plane assuming the three different T1 simplified models. We can see that most, but not all pMSSM model points are excluded in the region excluded in the T1qqqq simplified model, and survival probabilities are well below 20% in that region. The limits on the T1tttt and T1bbbb simplified models are more stringent due to the presence of b-jets in the final state of signal events, to which the p_T^{miss}+jets search is especially sensitive. These more constraining limits do not translate well to the pMSSM, with a significant fraction of models in the excluded region surviving the claimed simplified model exclusion. On the other hand, there is a horizontal band of lower survival probability visible at $m(\widetilde{\chi}_1^0) \simeq 200\,\text{GeV}$ that extends far past the simplified model limits, but the simplified model limits do not show an enhanced sensitivity in that region of $m(\widetilde{\chi}_1^0)$. This band comes from sensitivity of the p_T^{miss}+jets search to direct production of electroweakinos, which is not considered in any of the simplified model limits published by the p_T^{miss}+jets search.

The picture changes considerably in regions of the pMSSM that more closely resemble the simplified models, shown in Figure 157. In the pMSSM subspace where BR($\widetilde{g}\widetilde{g} \to qqqq\widetilde{\chi}_1^0\widetilde{\chi}_1^0$) > 0.8, the almost completely excluded region of the pMSSM by the p_T^{miss}+jets search almost perfectly aligns with the observed limit on the T1qqqq simplified model, with only a sprinkling of models surviving close to the limit. The same can be seen, although with a significantly reduced scan resolution, in the subspaces that resemble the BR($\widetilde{g}\widetilde{g} \to bbbb\widetilde{\chi}_1^0\widetilde{\chi}_1^0$), BR($\widetilde{g}\widetilde{g} \to tttt\widetilde{\chi}_1^0\widetilde{\chi}_1^0$), and BR($\widetilde{g}\widetilde{g} \to qqqqVV\widetilde{\chi}_1^0\widetilde{\chi}_1^0$) simplified models, for their respective limits. The reduced scan resolution comes from the rarity of the subspaces compared to the inclusive pMSSM. While the T1qqqq and T1bbbb simplified models are comparatively well represented in the pMSSM at approximately 12.8% and 3.8% of the inclusive prior density, the subspaces resembling the T1tttt and T5qqqqVV simplified models each make up less than 1% of the inclusive prior density. In fact, for the T1tttt simplified model, the constraint on the resembling pMSSM subspace is loosened to BR($\widetilde{g}\widetilde{g} \to tttt\widetilde{\chi}_1^0\widetilde{\chi}_1^0$)> 0.6 due to vanishing model space statistics.

Since the simplified model limits apply well in their respective subspaces, the surviving pMSSM models visible in the inclusive pMSSM that lie inside the T1qqqq excluded region must have features not covered by the simplified model topologies, such as the presence of addition SUSY particles. These can alter the decay chain of the gluino in such a way to escape exclusion. One likely candidate for this is the presence of long-lived charginos in the decay chain, which are reconstructed as muons and the events are vetoed by the p_T^{miss}+jets search.

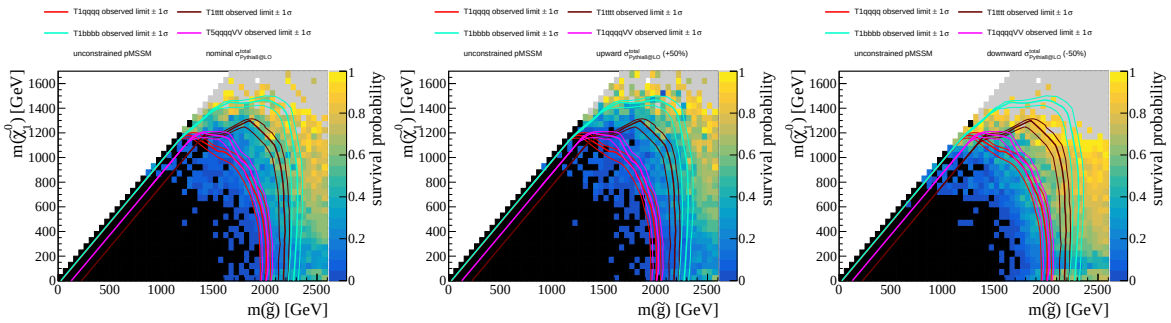

Figure 156: Comparison of the pMSSM survival probability relative to the prior and the published simplified model limits of the p_T^{miss}+jets search [1] in the plane of m($\tilde{g}$) and $m(\tilde{\chi}_1^0)$, for the simplified models T1qqqq, T1tttt, T1bbbb, and T5qqqqVV. The pMSSM survival probability is shown assuming the nominal signal cross section (left), assuming a 50% increased signal cross section (center), and a 50% decreased signal cross section (right). Black color denotes bins with zero survival probability, grey denotes bins with a survival probability of exactly 1, white bins are empty.

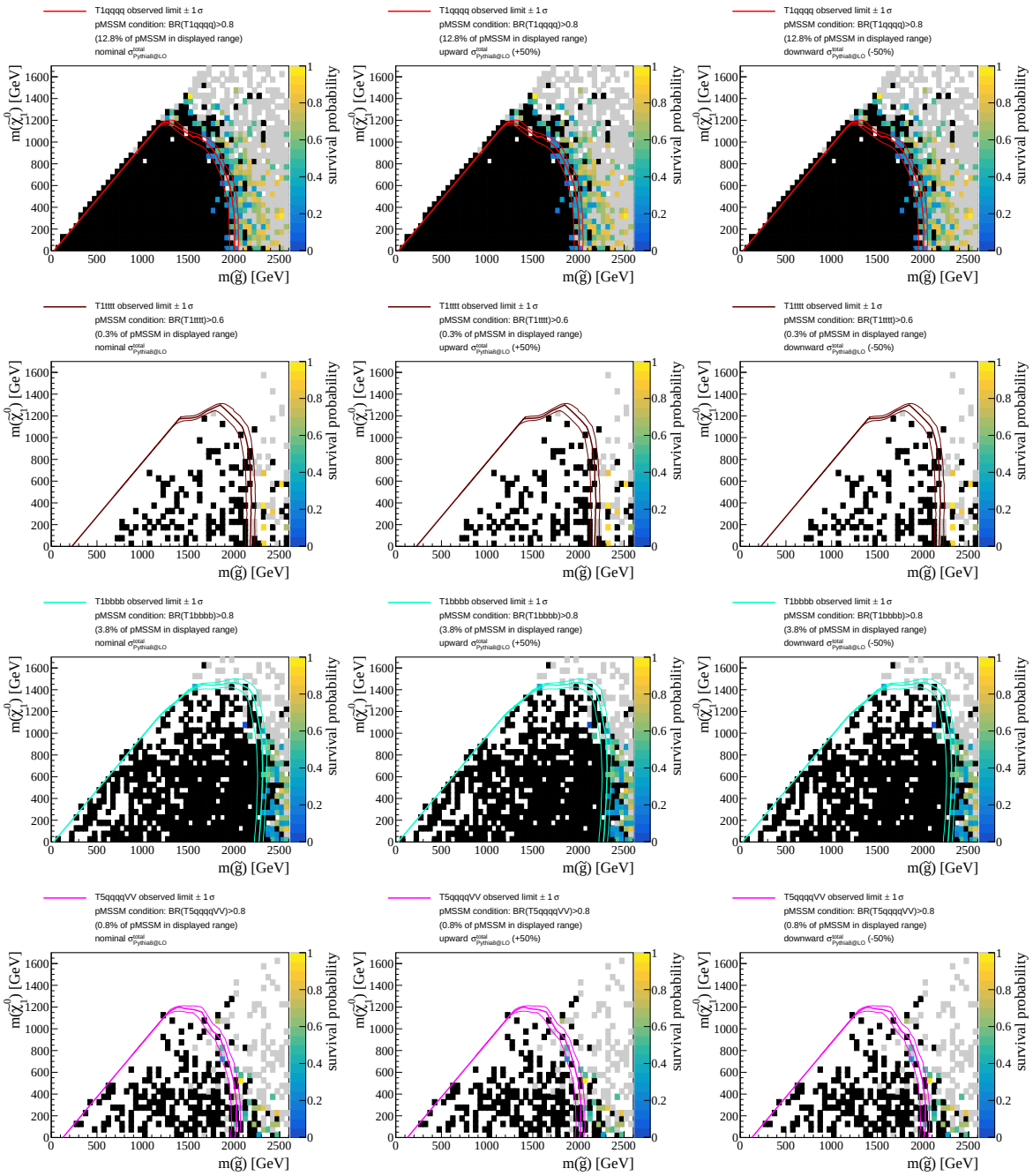

Figure 157: Comparison of the survival probability in pMSSM subspaces that resemble the respective simplified models (see plot legends) with the published limits of the p_T^{miss}+jets [1] search in the plane of m($\tilde{g}$) and $m(\tilde{\chi}_1^0)$, in terms of the simplified models T1qqqq, T1tttt, T1bbbb, and T5qqqqVV. The pMSSM survival probability is shown assuming the nominal signal cross section (left), assuming a 50% increased signal cross section (center), and a 50% decreased signal cross section (right). Black color denotes bins with zero survival probability, grey denotes bins with a survival probability of exactly 1, white bins are empty.

A similar picture emerges for the simplified models featuring squark production, the T2qq ($\widetilde{q}\widetilde{q} \to qq\widetilde{\chi}_1^0\widetilde{\chi}_1^0$), T2tt ($\widetilde{q}\widetilde{q} \to tt\widetilde{\chi}_1^0\widetilde{\chi}_1^0$), and T2bb ($\widetilde{q}\widetilde{q} \to bb\widetilde{\chi}_1^0\widetilde{\chi}_1^0$). The comparison for the T2qq simplified model is shown in Figure 158. Two limits [1] are published for this simplified model, one in which there is a single first generation squark, and one in which there is an eight-fold degeneracy of the left- and right-chiral $\widetilde{d}_L$, $\widetilde{d}_R$, $\widetilde{u}_L$, $\widetilde{u}_R$, $\widetilde{s}_L$, $\widetilde{s}_R$, $\widetilde{c}_L$, and $\widetilde{c}_R$. The pMSSM survival probability is shown in terms of the smallest light squark mass, which does not quite correspond to either of the simplified model limits. This is because there is always at least a two-fold degeneracy in the pMSSM in terms of the lightest squark mass, since the first- and second generation of sfermions are assumed to be degenerate. Because the left-chiral up- and down-type are also almost degenerate, a four-fold degeneracy is also quite common in the pMSSM. Considering the versions of the pMSSM survival probabilities that assume an upward or downward variation of the signal cross section can be expected to compensate for this effect somewhat. The limit assuming a single quark applies quite well in the equivalent pMSSM subspace, with only a small handful of models surviving inside the region excluded in the simplified model. The other limit, assuming an eight-fold degeneracy, massively overestimates the exclusion potential and does not apply in the inclusive pMSSM, even when assuming a 50% increased signal cross section.

The pMSSM subspace constructed to resemble the T2qq simplified models assumes $\mathrm{BR}(\widetilde{q}\widetilde{q} \to qq\widetilde{\chi}_1^0\widetilde{\chi}_1^0) > 0.8$, and is quite rare in the pMSSM at 3.8% of the prior density within the mass ranges displayed in Figure 158. In this subspace, the single-squark T2qq limit substantially underestimates the excluded regions, which can in part be explained by the squark degeneracy in the pMSSM. Instead, the degenerate-squark T2qq limit somewhat accurately delineates the excluded and non-excluded regions of the pMSSM, with only individual models surviving inside the regions excluded in the simplified model. The applicability of the degenerate squark limit is even better if we consider the upward cross section version of the pMSSM survival probability, which should somewhat compensate for the different levels of squark degeneracy between the simplified model and the pMSSM. The fact that the degenerate T2qq limit applies much better in the constrained pMSSM subspace, defined by requiring a substantial branching ratio into the simplified model topology, suggests the presence of alternative decay modes for the squarks in the unconstrained pMSSM, due to the presence of additional particles lighter than the lightest squark.

Next, we evaluate the applicability of the T2tt limit in the pMSSM, shown in Figure 159. In the inclusive pMSSM, the T2tt limits apply reasonably well in the non-compressed mass region, with only a small fraction of surviving models in the region excluded in the simplified model. These few surviving models tend to be close to the limit. In the very compressed mass region with $\Delta m\left(\widetilde{t}_1, \widetilde{\chi}_1^0\right) < 80\,\mathrm{GeV}$, no limits are given in the simplified model, however the survival probability in the pMSSM suggests that the p_T^{miss}+jets search is very sensitive here, with zero survival probability up to similar $m(\widetilde{\chi}_1^0)$ as seen in the less compressed pMSSM space. However, it is unclear how reliable the results in the pMSSM are in this region, as the compressed stop region is typically challenging to simulate, and no special care was given to this region in the context of this study. In fact, the decay tables generated by `SPheno` do not include decays via virtual W-bosons for $\widetilde{t}_1$. The subspace of the pMSSM that is similar to the T2tt simplified model, where $\mathrm{BR}(\widetilde{t}\widetilde{t} \to tt\widetilde{\chi}_1^0\widetilde{\chi}_1^0) > 0.8$, is well populated with approximately 26.6% of the prior density conforming to that constraint in the considered mass ranges. In addition to that, the T2tt limits apply particularly well to this subspace, with the transition of the completely excluded region to a region where some few models survive happening almost exactly at the T2tt limit. Note that the compressed $m(\widetilde{t}_1)$-$m(\widetilde{\chi}_1^0)$ region does not feature a large enough branching fraction into $\mathrm{BR}(\widetilde{t}\widetilde{t} \to tt\widetilde{\chi}_1^0\widetilde{\chi}_1^0)$, and as such is not part of the considered subspace. As with the previous comparisons, the surviving models in the inclusive pMSSM likely feature additional particles in the decay chain of the top squarks to which the p_T^{miss}+jets search is less sensitive.

Finally, Figure 160 compares the T2bb simplified model limits to the pMSSM survival probability in the plane of $m(\widetilde{b}_1)$ and $m(\widetilde{\chi}_1^0)$. The picture here is similar to what is seen in the case of T2tt, with the notable exception that the compressed region with $\Delta m\left(\widetilde{t}_1, \widetilde{\chi}_1^0\right) < 80\,\mathrm{GeV}$ is covered by the T2bb limit and is comparable to the pMSSM interpretation. The viability of the T2bb limit on the inclusive pMSSM is reasonably high, with a small fraction of the prior density surviving in the region excluded in the T2bb simplified model. The surviving models here are mostly close to the limit. As stated for previous simplified model comparisons, the reason for their survival inside the excluded region is likely due to the presence of additional particles in the $\widetilde{b}_1$ decay chains that make these models substantially different from the T2bb simplified model.

In the pMSSM scan, a considerable fraction of the prior density in the considered mass ranges conforms to the simplified model topology, with approximately 47% of models showing a significant

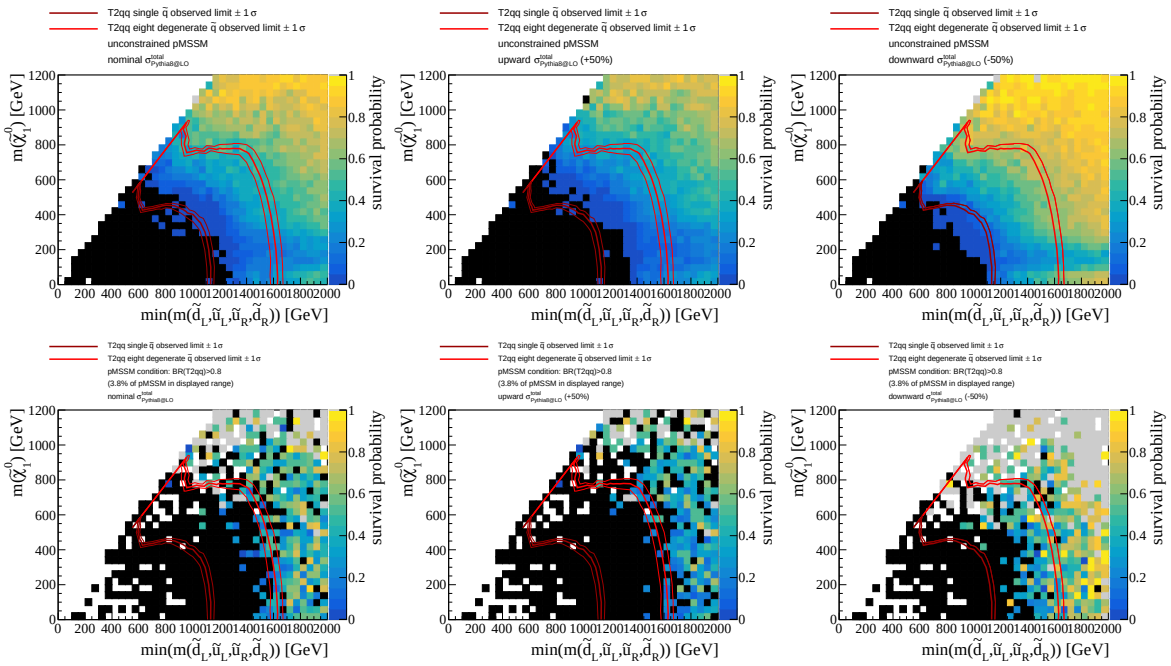

Figure 158: Comparison of the pMSSM survival probability and the published limits of the p_T^{miss}+jets search [1] in the plane of the smallest squark mass, $\min(m(\widetilde{d}_L, \widetilde{u}_L, \widetilde{u}_R, \widetilde{d}_R))$, and the mass of the lightest neutralino, $m(\widetilde{\chi}_1^0)$, in terms of the simplified model T2qq. Limits from two versions of the T2qq simplified model are shown, one assuming a single squark, and one assuming eight mass degenerate squarks. The pMSSM survival probability is shown assuming the nominal signal cross section (left), assuming a 50% increased signal cross section (center), and a 50% decreased signal cross section (right). The top rows of plots correspond to the inclusive pMSSM, the bottom row shows the subspace of the pMSSM that resembles the T2qq simplified model. Black color denotes bins with zero survival probability, grey denotes bins with a survival probability of exactly 1, white bins are empty.

branching fraction of $BR(\widetilde{b}\widetilde{b} \to b\bar{b}\widetilde{\chi}_1^0\widetilde{\chi}_1^0) > 0.8$. As with the T2tt limit, the transition from the completely excluded pMSSM to the first surviving models aligns almost perfectly with the T2bb limit.

There is a horizontal band of low survival probability for small $m(\widetilde{\chi}_1^0)$ present in all planes with a colored sparticle mass on the x-axis in the inclusive pMSSM. This region of the pMSSM that seems uncorrelated from the colored sector features direct electroweak production and is likely dominated by models with a higgsino-like or wino-like LSP. Its absence in the simplified model-like subspaces of the pMSSM indicates and in the simplified model limits indicates that the simplified model limits tend to apply better to the pMSSM model space that feature bino-like LSPs.

In summary, the simplified model limits for the p_T^{miss}+jets search apply reasonably well on the colored sector of the inclusive pMSSM, with a consistently very small survival probability inside the regions excluded by the simplified model limits. Differences of particularly larger than expected exclusion is observed, and is likely due to production mechanisms that are not considered in the simplified models. Because the simplified model limits are shown to apply very well to subspaces of the pMSSM that conform closely to the respective simplified model topologies, it is likely that the surviving models survive due to deviations from the simplified model decay topologies.

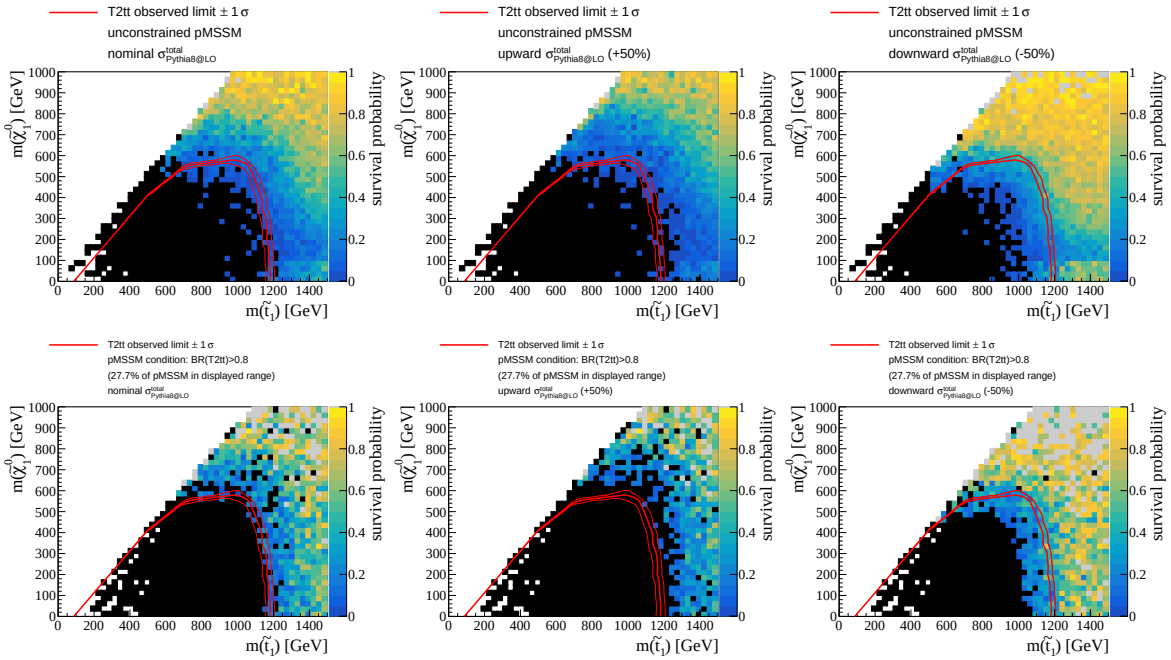

Figure 159: Comparison of the pMSSM survival probability and the published limits of the p_T^{miss}+jets search [1] in the plane of the lighter stop mass, $m(\tilde{t}_1)$, and the mass of the lightest neutralino, $m(\tilde{\chi}_1^0)$, in terms of the simplified model T2tt. The pMSSM survival probability is shown assuming the nominal signal cross section (left), assuming a 50% increased signal cross section (center), and a 50% decreased signal cross section (right). The top row of plots correspond to the inclusive pMSSM, the bottom row shows the subspace of the pMSSM that resembles the T2tt simplified model. Black color denotes bins with zero survival probability, grey denotes bins with a survival probability of exactly 1, white bins are empty.

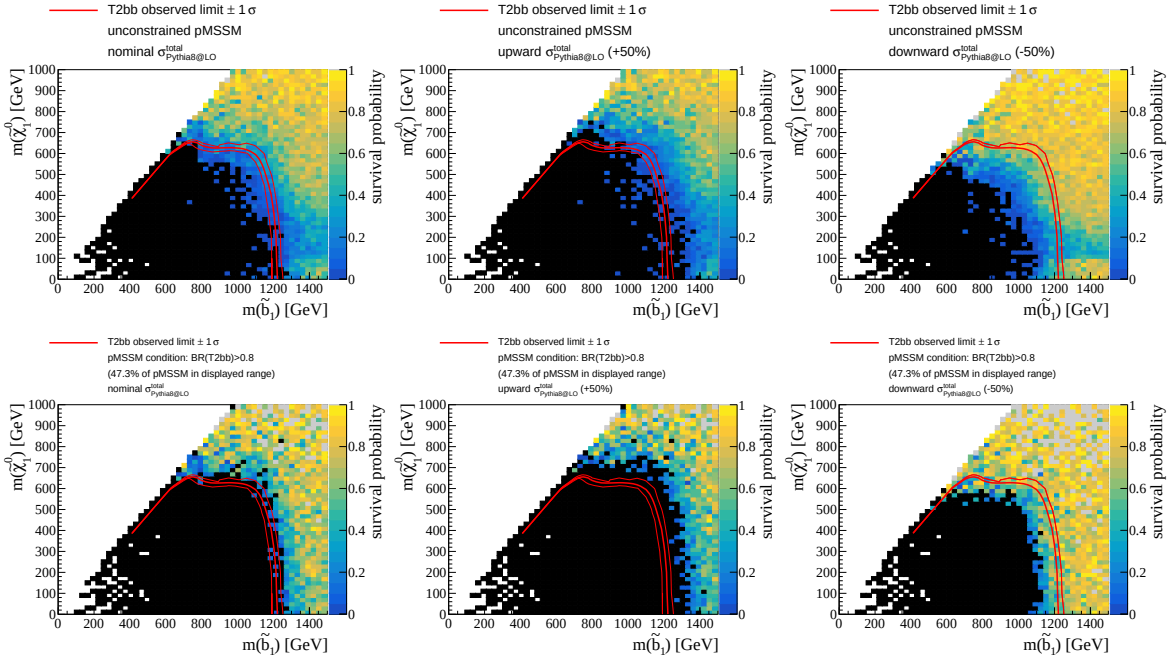

Figure 160: Comparison of the pMSSM survival probability and the published limits of the p_T^{miss}+jets search [1] in the plane of the lighter sbottom mass, $m(\tilde{b}_1)$and the mass of the lightest neutralino, $m(\tilde{\chi}_1^0)$, in terms of the simplified model T2bb. The pMSSM survival probability is shown assuming the nominal signal cross section (left), assuming a 50% increased signal cross section (center), and a 50% decreased signal cross section (right). The top rows of plots correspond to the inclusive pMSSM, the bottom row shows the subspace of the pMSSM that resembles the T2bb simplified model. Black color denotes bins with zero survival probability, grey denotes bins with a survival probability of exactly 1, white bins are empty.

8.7.2 Di-lepton

The di-lepton search [3] (shortly introduced in Section 6.3) has published limits in three simplified models, the TChiWW ($\widetilde{\chi}_1^{\pm}\widetilde{\chi}_1^{\mp} \rightarrow \mathrm{WW}\widetilde{\chi}_1^0\widetilde{\chi}_1^0$), the TChiSlep ($\widetilde{\chi}_1^{\pm}\widetilde{\chi}_1^{\mp} \rightarrow 2 * \mathrm{l}\widetilde{\nu}_l(\nu_l\widetilde{\mathrm{l}}) \rightarrow 2 * \nu_l(\mathrm{l})\widetilde{\chi}_1^0$), and the TSlep ($\widetilde{\mathrm{l}}\widetilde{\mathrm{l}} \rightarrow \mathrm{ll}\widetilde{\chi}_1^0\widetilde{\chi}_1^0$). The comparison of the pMSSM survival probability and the TChiWW and TChiSlep limits is shown in Figure 161. We can immediately see that the TChiSlep simplified model limit does not correspond to the inclusive pMSSM result, as most models within the region excluded by the TChiSlep limit survive in the pMSSM. This is because the large branching fraction to leptons in the final state assumed by the TChiSlep simplified model leads to the powerful limits on the simplified model space. However, this large branching fraction relies on the presence of a light slepton, which is very rare at approximately 1.4% of the prior conforming to the constraint $\mathrm{BR}(\widetilde{\chi}_1^{\pm}\widetilde{\chi}_1^{\mp} \rightarrow 2 * \mathrm{l}\widetilde{\nu}_l(\nu_l\widetilde{\mathrm{l}}) \rightarrow 2 * \nu_l(\mathrm{l})\widetilde{\chi}_1^0) > 0.8$. In the pMSSM subspace that more closely resembles the TChiSlep simplified model, we see relatively good agreement between the TChiSlep limit and the transition from small survival probabilities to larger ones. However, even in this pMSSM subspace, there are individual models that survive exclusion by the di-lepton search, even at masses well inside the region excluded by the TChiSlep limit. The surviving models feature sleptons that are either close in mass to $m(\widetilde{\chi}_1^0)$ or $m(\widetilde{\chi}_1^{\pm})$, and thus still differ significantly from the simplified model, which assumes $m(\widetilde{\mathrm{e}}_\mathrm{L}, \widetilde{\mu}_\mathrm{L}) = \left(\frac{m(\widetilde{\chi}_1^{\pm}) + m(\widetilde{\chi}_1^0)}{2}\right)$. This can have an impact on the sensitivity of the di-lepton search, as the mass difference at one of the vertices is small, restricting the available phase space for the final state standard model particles. Events in which it is the charged lepton with a restricted phase space then are likely to have lower-$\mathrm{p_T}$ charged leptons, which reduces the search sensitivity to these events.

The TChiWW limit aligns well with a region of very small survival probability, however this region is not completely excluded in the pMSSM. This also holds in a subspace of the pMSSM that is a little closer to the simplified model, where we require that the LSP is bino-like, and the lighter chargino is wino-like.

The comparison of the TSlep simplified model limits with the pMSSM survival probability is shown in Figure 162, for the plane of the mass of the lightest first-generation slepton and the LSP mass. Here we can see that the limits far exceed the region of sensitivity seen in the pMSSM, with only a comparatively small part at $m(\widetilde{\chi}_1^0) < 100\,\mathrm{GeV}$ completely excluded in the pMSSM. The hard transition from complete exclusion below $m(\widetilde{\chi}_1^0) < 100\,\mathrm{GeV}$ to above that threshold likely comes from the fact that there are no charginos at smaller masses, which means that the sleptons exclusively decay into the LSP. If charginos are present in the decay chains, the fraction of di-leptonic events is severely reduced, which removes the analysis acceptance. However, even in the subspace of the pMSSM where the branching ratio into the TSlep topology exceeds 0.8, the limits on the simplified model space are far stronger that what is seen in the pMSSM.

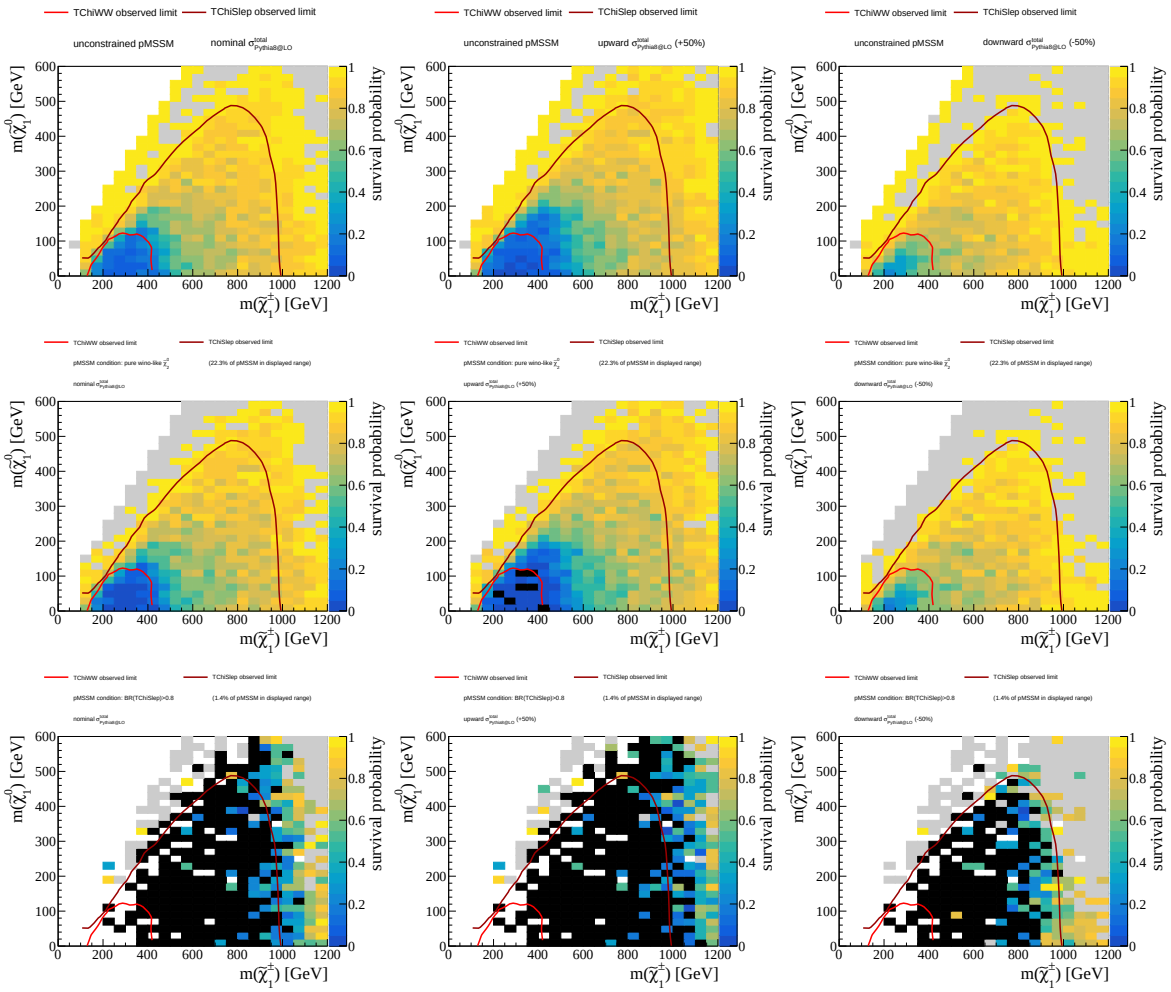

Figure 161: Comparison of the pMSSM survival probability and the published limits of the di-lepton analysis [3] in terms of the simplified models TChiWW and TChiSlep, in the plane of the lighter chargino mass $m(\widetilde{\chi}^\pm_1)$ and the mass of the lightest neutralino, $m(\widetilde{\chi}^0_1)$. The pMSSM survival probability is shown assuming the nominal signal cross section (left), assuming a 50% increased signal cross section (center), and a 50% decreased signal cross section (right). The top row of plots corresponds to the inclusive pMSSM, the center row shows the subspace of the pMSSM that resembles the TChiWW simplified model, and the bottom row shows the subspace that resembles the TChiSlep simplified model. The condition $m(\widetilde{\mathrm{l}}) < m(\widetilde{\chi}^\pm_1)$ considers $\widetilde{\mathrm{l}}$ to be a first or second generation slepton. The di-lepton analysis does not provide uncertainties on the limit. Black color denotes bins with zero survival probability, grey denotes bins with a survival probability of exactly 1, white bins are empty.

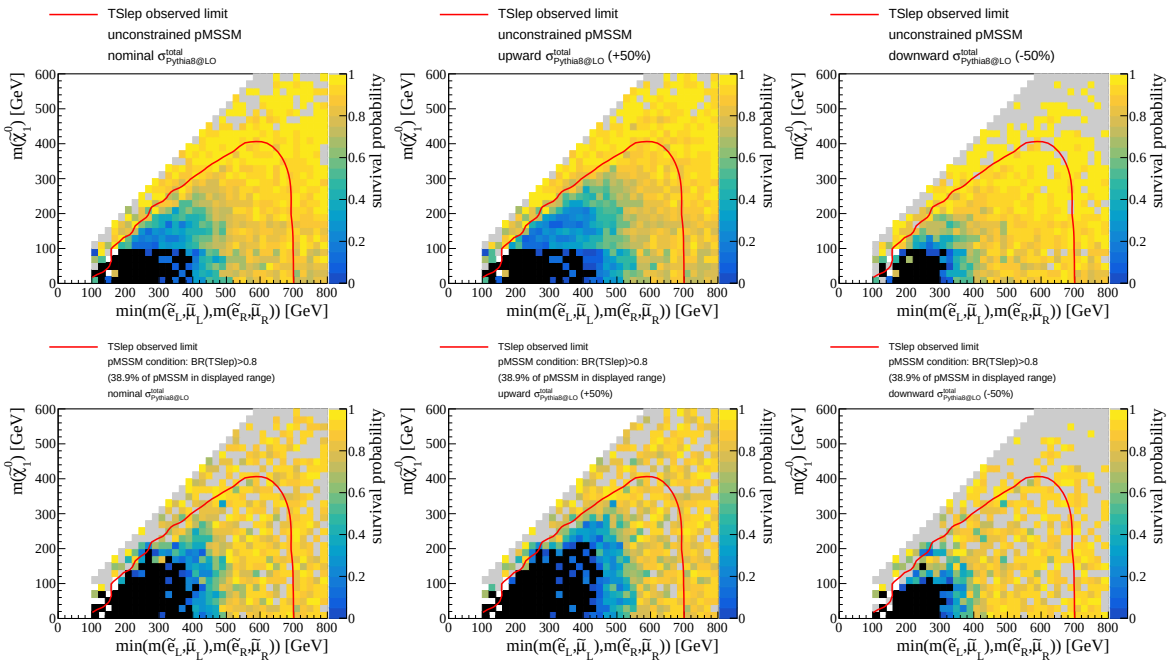

Figure 162: Comparison of the pMSSM survival probability and the published limits of the di-lepton analysis [3] in terms of the simplified model TSlep, in the plane of the lightest slepton mass $\min(m(\widetilde{\mathrm{e}}_\mathrm{R},\widetilde{\mu}_\mathrm{R}),m(\widetilde{\mathrm{e}}_\mathrm{L},\widetilde{\mu}_\mathrm{L}))$ and the mass of the lightest neutralino, $m(\widetilde{\chi}^0_1)$. The pMSSM survival probability is shown assuming the nominal signal cross section (left), assuming a 50% increased signal cross section (center), and a 50% decreased signal cross section (right). The top rows of plots correspond to the inclusive pMSSM, the bottom row shows the subspace of the pMSSM that resembles the TSlep simplified model. The di-lepton analysis does not provide uncertainties on the limit. Black color denotes bins with zero survival probability, grey denotes bins with a survival probability of exactly 1, white bins are empty.

8.7.3 Di-lepton soft-opposite sign

The di-lepton soft-opposite sign (SOS) search [4] (shortly described in Section 6.3) has published limits on a variety of simplified models that feature two or more low-p_T leptons. These include the TChiWZ simplified model ($\widetilde{\chi}_1^{\pm}\widetilde{\chi}_2^0 \to \mathrm{WZ}\widetilde{\chi}_1^0\widetilde{\chi}_1^0$) in the compressed electroweakino region, and the T2bff ($\widetilde{\mathrm{tt}} \to \mathrm{bff}\widetilde{\chi}_1^0\mathrm{bff}\widetilde{\chi}_1^0$) and T2bW ($\widetilde{\mathrm{tt}} \to \mathrm{bb}\widetilde{\chi}_1^{\pm}\widetilde{\chi}_1^{\pm} \to \mathrm{WW}\widetilde{\chi}_1^0\widetilde{\chi}_1^0$) simplified models. The T2bff simplified model is based on the T2tt simplified model, in the parameter region where on-shell decays via the top quark and W boson are kinematically forbidden by the compressed phase space. The T2bW simplified model assumes a decay chain via an intermediate chargino. The comparison for the TChiWZ simplified model is shown in Figure 163. While the region inside the excluded region has a noticeably smaller survival probability, there are still plenty of surviving models there. Almost all of the models in this range of $\Delta m(\widetilde{\chi}_2^0, \widetilde{\chi}_1^0)$ are higgsino-like models, which makes the combination of a wino-like $\widetilde{\chi}_2^0$ and a bino-like $\widetilde{\chi}_1^0$ rare with approximately 7% for each sign combinations of $\widetilde{\chi}_2^0 \times \widetilde{\chi}_1^0$. The simplified model limits apply significantly better, but nevertheless with large inconsistencies, in the subspaces that are close to the respective simplified model topology, with models surviving in the entire region excluded by the simplified model limit.

The other simplified models place limits in the plane of $m(\widetilde{\mathrm{t}}_1)$ and $\Delta m(\widetilde{\mathrm{t}}_1, \widetilde{\chi}_1^0)$, shown in Figure 164. Unfortunately, the spectrum generator used in this work to generate the decay tables does not generate decays with virtual W bosons for stop decays. As a consequence, the region of $\Delta m(\widetilde{\mathrm{t}}_1, \widetilde{\chi}_1^0) < m_W$ is not reliably simulated, and the comparison to the simplified model limits can not be performed.

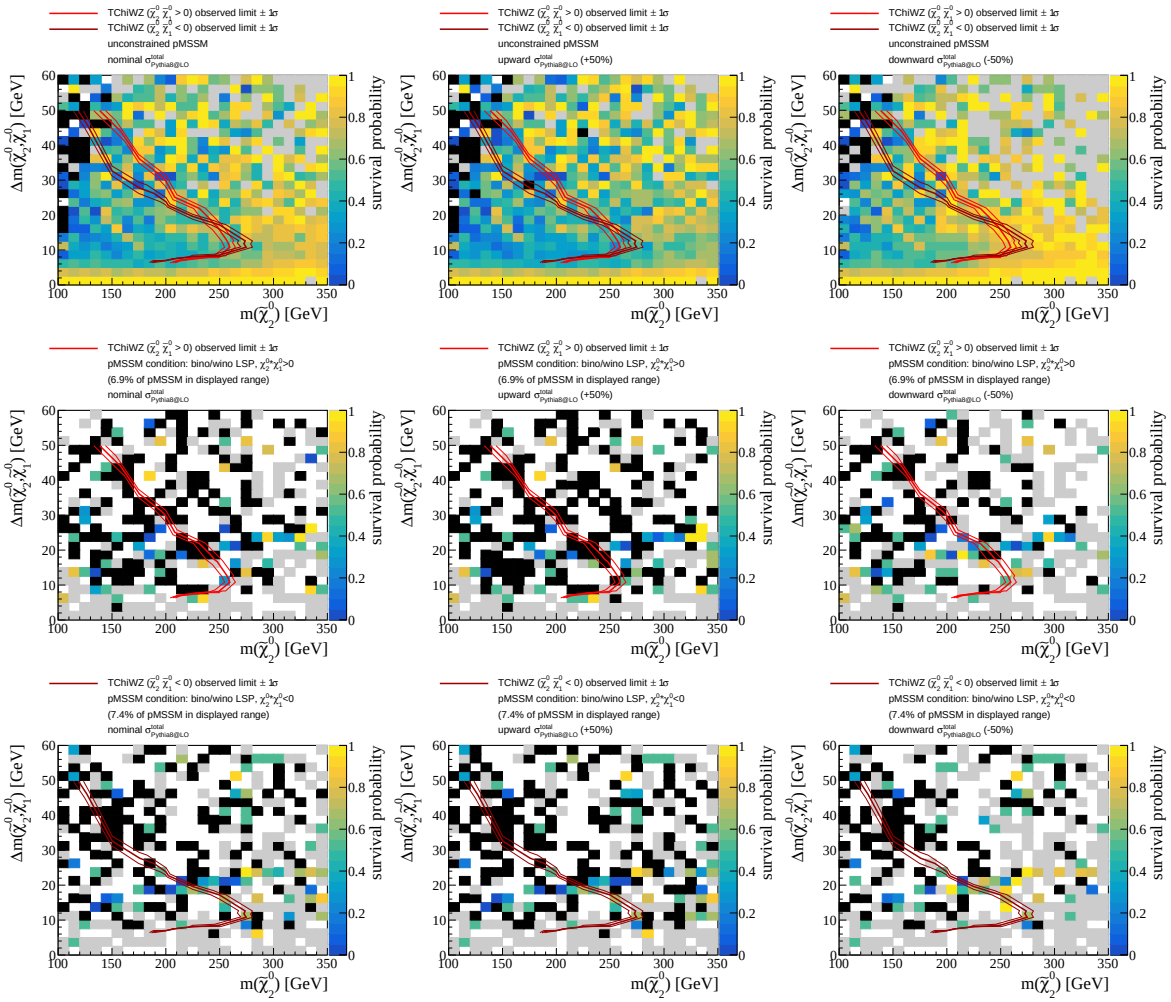

Figure 163: Comparison of the pMSSM survival probability and the published limits of the di-lepton SOS analysis [4] in the plane of $\Delta m(\widetilde{\chi}_2^0, \widetilde{\chi}_1^0)$ and $m(\widetilde{\chi}_1^0)$, in terms of the simplified model TChiWZ. The pMSSM survival probability is shown assuming the nominal signal cross section (left), assuming a 50% increased signal cross section (center), and a 50% decreased signal cross section (right). The top row of plots correspond to the inclusive pMSSM, the center and bottom rows show the subspace of the pMSSM that resembles the TChiWZ simplified model, by requiring the LSP to be bino-like, $\widetilde{\chi}_1^{\pm}$ and $\widetilde{\chi}_2^0$ to be wino-like, and with $\widetilde{\chi}_2^0 \times \widetilde{\chi}_1^0 > 0$ for the center row, and $\widetilde{\chi}_2^0 \times \widetilde{\chi}_1^0 < 0$ for the bottom row. Black color denotes bins with zero survival probability, grey denotes bins with a survival probability of exactly 1, white bins are empty.

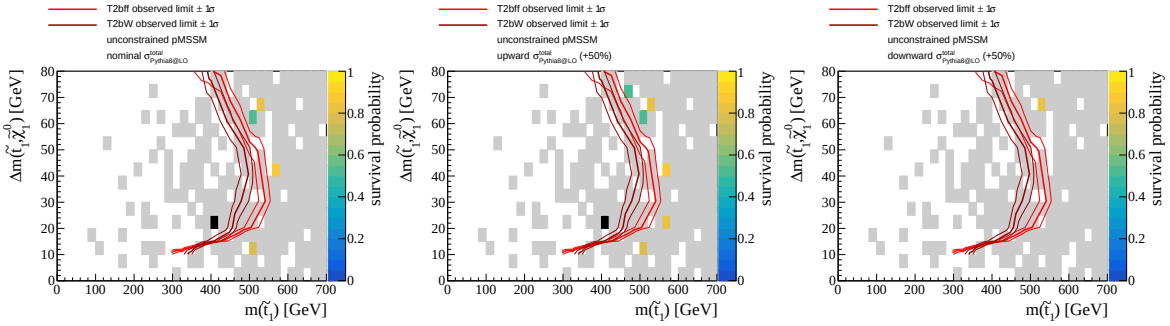

Figure 164: Comparison of the pMSSM survival probability and the published limits of the dilepton SOS analysis [4] in the plane of $\Delta m(\widetilde{\mathrm{t}}_1, \widetilde{\chi}_1^0)$ and $m(\widetilde{\mathrm{t}}_1)$, in the very compressed region of $m(\widetilde{\mathrm{t}}_1, \widetilde{\chi}_1^0) < m_W$, in terms of the simplified models T2bff and T2bW. The pMSSM survival probability is shown assuming the nominal signal cross section (left), assuming a 50% increased signal cross section (center), and a 50% decreased signal cross section (right). Black color denotes bins with zero survival probability, grey denotes bins with a survival probability of exactly 1, white bins are empty.

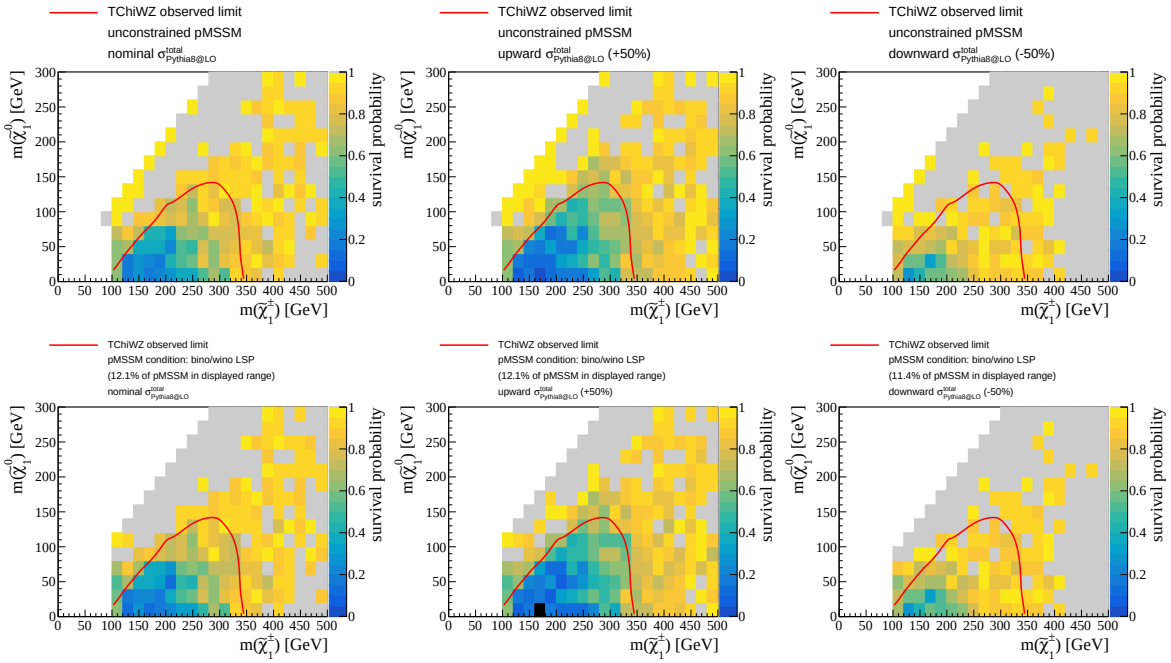

Figure 165: Comparison of the pMSSM survival probability and the published limits of the multi-lepton analysis [5] in the plane of $m(\widetilde{\chi}^{\pm}_1)$ and $m(\widetilde{\chi}^0_1)$, in terms of the simplified model TChiWZ. The pMSSM survival probability is shown assuming the nominal signal cross section (left), assuming a 50% increased signal cross section (center), and a 50% decreased signal cross section (right). The top row of plots corresponds to the inclusive pMSSM, the bottom row shows the subspace of the pMSSM that resembles the TChiWZ simplified model, by requiring the LSP to be bino-like, and $\widetilde{\chi}^{\pm}_1$ and $\widetilde{\chi}^0_2$ to be wino-like. Black color denotes bins with zero survival probability, grey denotes bins with a survival probability of exactly 1, white bins are empty.

8.7.4 Multi-lepton

Like the di-lepton SOS search, the multi-lepton search [5] (shorly described in Section 6.3) has been interpreted in the TChiWZ simplified model ($\widetilde{\chi}^{\pm}_1\widetilde{\chi}^0_2 \to \mathrm{WZ}\widetilde{\chi}^0_1\widetilde{\chi}^0_1$), but in a less compressed region of the simplified model space. Figure 165 shows the comparison of the TChiWZ limit and the pMSSM survival probability. We can see that the pMSSM survival probability is significantly smaller in the region excluded in the simplified model space, but non-zero everywhere. In the pMSSM subspace that resembles the TChiWZ simplified model by requiring a bino-like $\widetilde{\chi}^0_1$ and a wino-like $\widetilde{\chi}^{\pm}_1$, the pMSSM survival probability almost identical, with only minimal differences for $m(\widetilde{\chi}^0_1) \simeq m(\widetilde{\chi}^{\pm}_1)$. This suggests that there is no significant dependence on the type of chargino. Lastly, the flavor requirement on the LSP and lighter chargino are satisfied in approximately 12% of the pMSSM in the relevant range. However, most on the prior where this constraint is not fulfilled is made up of models with a pure wino-like or higgsino-like LSP, which can be found along the diagonal of the figures at $m(\widetilde{\chi}^0_1) \simeq m(\widetilde{\chi}^{\pm}_1)$ – well outside the region of expected sensitivity. If these models with a pure higgsino-like or wino-like LSP are excluded from the consideration, the TChiWZ-like pMSSM subspace makes up almost 90% of the pMSSM in the displayed plot range.

8.7.5 Disappearing tracks

The search for disappearing tracks [7] has previously been interpreted in the T6btLL ($\widetilde{\mathrm{tt}} \to \mathrm{b}\widetilde{\chi}_1^{\pm}/\mathrm{t}\widetilde{\chi}_1^0$), the T6tbLL ($\widetilde{\mathrm{bb}} \to \mathrm{t}\widetilde{\chi}_1^{\pm}/\mathrm{b}\widetilde{\chi}_1^0$), and the T5tbtbLL ($\widetilde{\mathrm{gg}} \to \mathrm{btbt}\widetilde{\chi}_1^{\pm}\widetilde{\chi}_1^{\pm} \to \mathrm{XX}\widetilde{\chi}_1^0\widetilde{\chi}_1^0$) simplified models. These simplified models differ from their common definitions by assuming a long lifetime of the chargino. In addition to these simplified models with strong production modes, there is also an interpretation in a pure higgsino simplified model available.

Figure 166 shows the comparison for the T6tbLL simplified model. We can see that the limits of the T6tb simplified model are much stronger than what is seen in terms of the pMSSM survival probability in the unconstrained pMSSM. This is mostly due to the rarity of the respective simplified model topologies in the pMSSM, with approximately 10% of models featuring long-lived charginos, and only 7% of models featuring similar decay topologies to the T6btLL simplified model in addition. This is seen in the subspaces corresponding to the two reference lifetimes of the simplified models, where we see good agreement for shorter lifetimes and reasonable agreement for the larger lifetimes. The simplified model limit for the longer lifetime aligns well with the furthest extent of sensitivity in the pMSSM at large $m(\widetilde{\mathrm{b}}_1)$ and $m(\widetilde{\chi}_1^0)$, indicated by the transition from bins with survival probabilities smaller than one to the region where all models survive. However, a significant fraction of the models still survive inside the simplified model limit with a larger assumed chargino lifetime. In addition, we see from comparing the second row of plots to the third and fourth row that the requirement on the sbottom decay chain does not significantly increase the sensitivity to the pMSSM, nor the matching of the simplified model limits and the pMSSM survival probability. An exception for this is the compressed region of $m(\widetilde{\mathrm{b}}_1)$-$m(\widetilde{\chi}_1^0) \leq m(\mathrm{t})$, where the additional requirement on the sbottom decay results in a better agreement between simplified model limit and pMSSM survival probability for $m(\widetilde{\mathrm{b}}_1) \lesssim 1\,\mathrm{TeV}$. This region is not present in the pMSSM subspaces that include the decay requirements of the T6tbLL models, because the spectrum generator used does not generate decays via a virtual top quark, and thus the branching ratio requirement for the simplified model topology is not fulfilled.

Similar conclusions to the T6tbLL simplified model can be drawn for the T6btLL simplified model, shown in Figure 167. Significant branching ratios into the simplified model topology, $\mathrm{BR}(\widetilde{\mathrm{tt}} \to \mathrm{b}\widetilde{\chi}_1^{\pm}/\mathrm{t}\widetilde{\chi}_1^0)$, is even rarer in the pMSSM, at approximately 5% of models that contain long-lived charginos at the same time. This rarity results in almost complete disagreement of the simplified model limits with the inclusive pMSSM survival probability, but applies reasonably well on the subspace of the pMSSM with a long-lived chargino, although individual bins feature large survival probabilities inside the region excluded in the simplified model space.

It is curious that no disagreement of the simplified model limits to the pMSSM can be traced back to the fact that a significant part of the pMSSM features a nearly mass degenerate $m(\widetilde{\mathrm{t}}_1)$ and $m(\widetilde{\mathrm{b}}_1)$. This should lead to an enhanced sensitivity to the pMSSM compared to simplified models where only one of the particles is in kinematic reach.

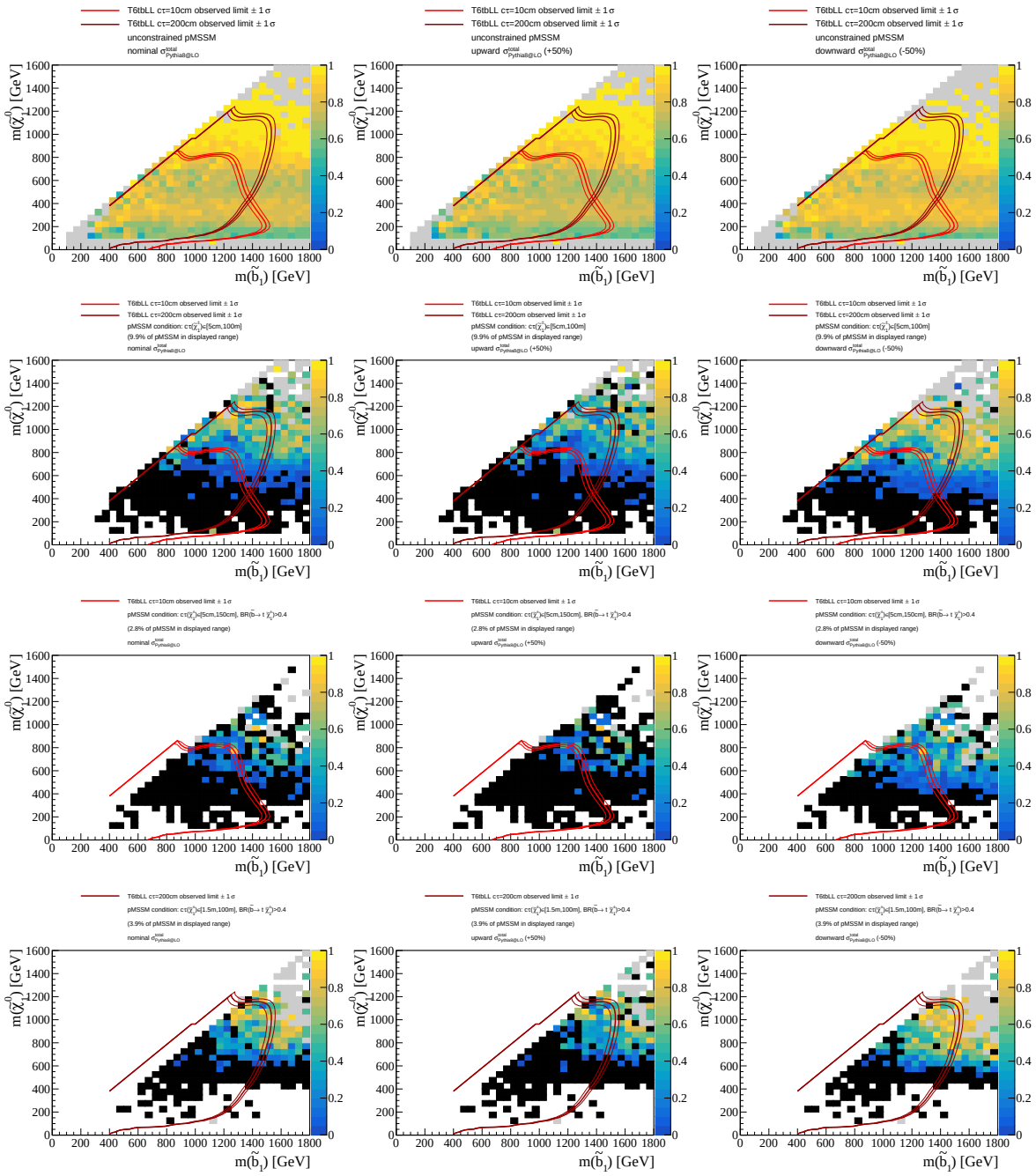

Figure 166: Comparison of the pMSSM survival probability and the published limits of the disappearing tracks analysis [7] in the plane of $m(\tilde{b}_1)$ and $m(\tilde{\chi}_1^0)$, in terms of the simplified model T6tbLL. The pMSSM survival probability is shown assuming the nominal signal cross section (left), assuming a 50% increased signal cross section (center), and a 50% decreased signal cross section (right). The top row of plots correspond to the inclusive pMSSM, the row second from top shows the pMSSM subspace with a long-lived chargino, the two bottom rows show the subspaces of the pMSSM that resembles the T6tbLL simplified model, by requiring the branching ratio of the sbottom into a chargino to exceed 0.4, and the proper chargino decay length to be inside $c\tau(\tilde{\chi}_1^{\pm}) \in [1\,\text{cm}, 150\,\text{cm}]$ (second from bottom) and $c\tau(\tilde{\chi}_1^{\pm}) \in [1.5\,\text{m}, 100\,\text{m}]$ (bottom), respectively. Black color denotes bins with zero survival probability, grey denotes bins with a survival probability of exactly 1, white bins are empty.

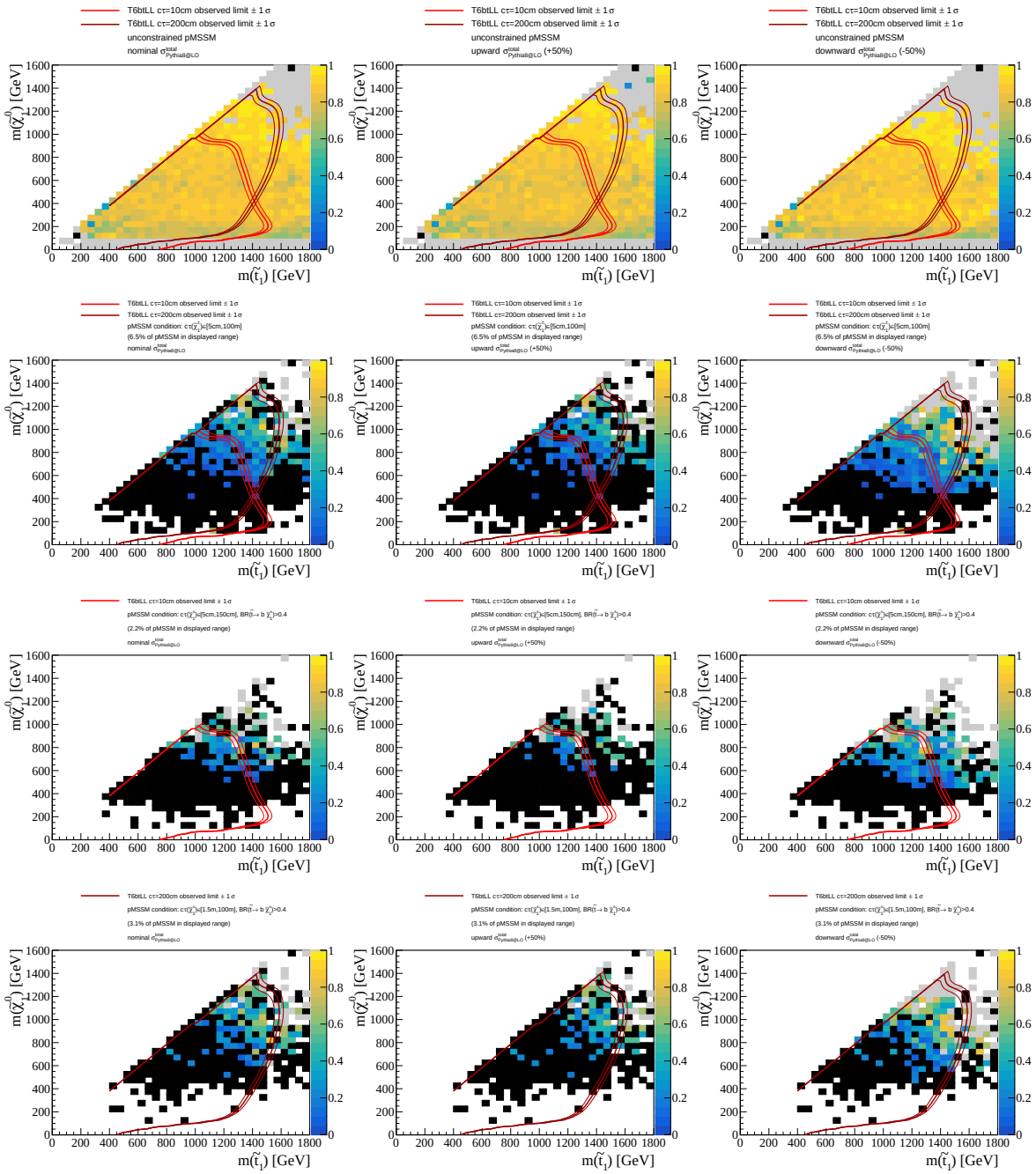

Figure 167: Comparison of the pMSSM survival probability and the published limits of the disappearing tracks analysis [7] in the plane of $m(\widetilde{\mathrm{t}}_1)$ and $m(\widetilde{\chi}_1^0)$, in terms of the simplified model T6btLL. The pMSSM survival probability is shown assuming the nominal signal cross section (left), assuming a 50% increased signal cross section (center), and a 50% decreased signal cross section (right). The top row of plots corresponds to the inclusive pMSSM, the row second from top shows the pMSSM subspace with a long-lived chargino, the two bottom rows show the subspaces of the pMSSM that resembles the T6btLL simplified model, by requiring the branching ratio of the stop into a chargino to exceed 0.4, and the proper chargino decay length to be inside $c\tau(\widetilde{\chi}_1^{\pm}) \in [1\,\mathrm{cm}, 150\,\mathrm{cm}]$ (second from bottom) and $c\tau(\widetilde{\chi}_1^{\pm}) \in [1.5\,\mathrm{m}, 100\,\mathrm{m}]$ (bottom), respectively. Black color denotes bins with zero survival probability, grey denotes bins with a survival probability of exactly 1, white bins are empty.

The comparison for the T5tbtb simplified model is shown in Figure 168. The simplified model limit again vastly overestimates the exclusion, also extending into a region of large LSP and gluino masses where no model could be excluded in the pMSSM. This region suffers from low scan resolution in general, which is made worse in the pMSSM subspace with a long-lived chargino. The T5btbt-like subspaces of the pMSSM which include constraints on the gluino decay reveal that the branching ratio into a top (bottom) final state are also rare in the pMSSM, with only approximate 1% (1.5%) of the pMSSM conforming to the full T5btbt requirement. This is because the branching ratio of the gluino into a top and bottom competes with decays into other particles, mostly quarks, and drops strongly towards larger $m(\widetilde{\chi}_1^0)$. As a result, models with a significant chargino lifetime and branching ratio into the T5btbt topology only populate the part of the pMSSM where
$500\,\text{GeV} \lesssim m(\widetilde{\chi}_1^0) \lesssim 1\,\text{TeV}$. In this region, however, the exclusion is almost total for $\text{m}(\widetilde{\text{g}}) < 2.5\,\text{TeV}$. It turns out that the presence of a top or bottom in the final state does not matter much to the sensitivity of the search for disappearing tracks in the final state. This can be seen from the pMSSM subspace with a long-lived chargino (second from top), where we can see that the simplified model limits apply well to the gluino production mode in the pMSSM, irrespective of its decay chain.

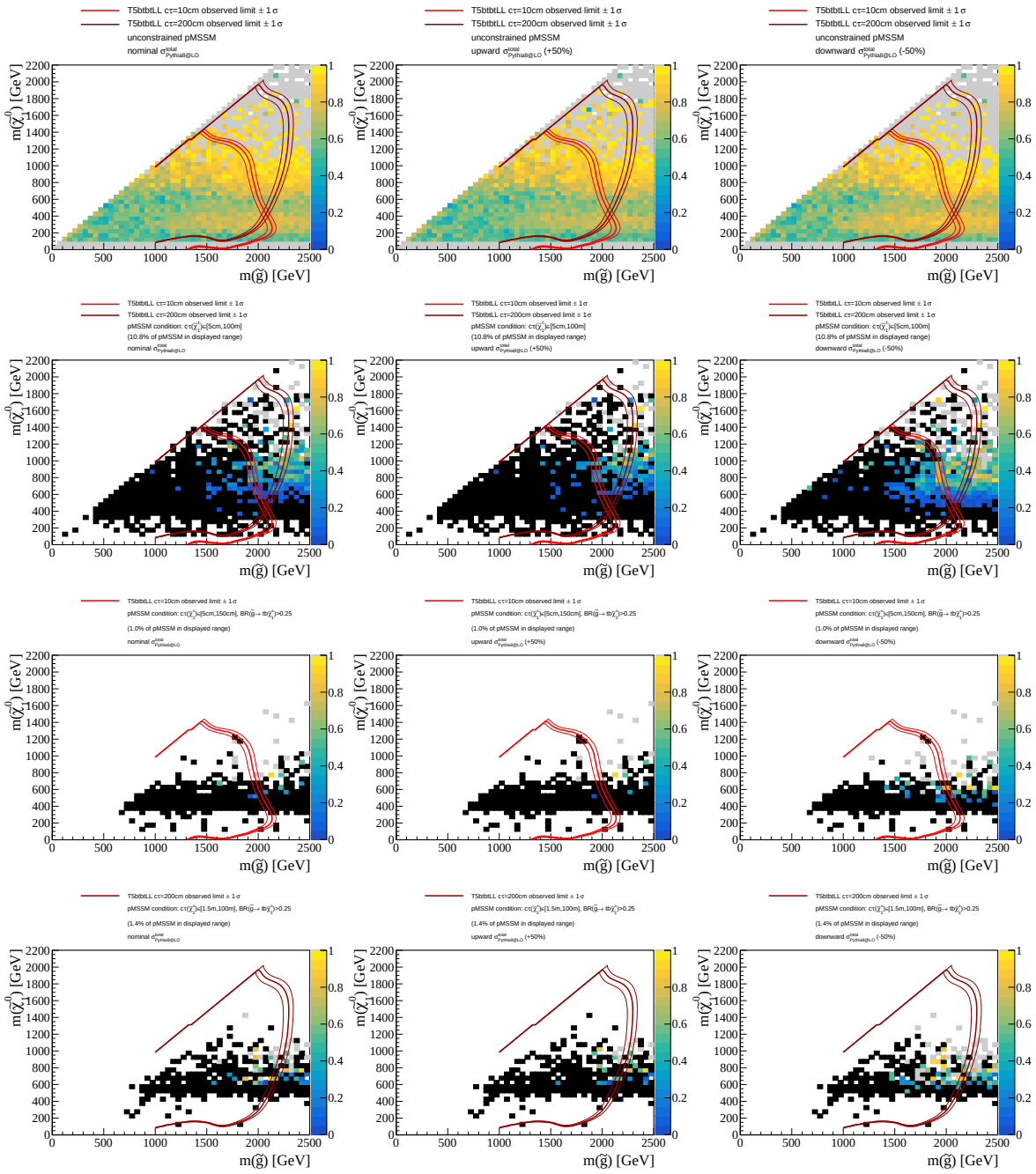

Figure 168: Comparison of the pMSSM survival probability and the published limits of the disappearing tracks analysis [7] in the plane of m($\widetilde{g}$) and $m(\widetilde{\chi}_1^0)$, in terms of the simplified model T5btbtLL. The pMSSM survival probability is shown assuming the nominal signal cross section (left), assuming a 50% increased signal cross section (center), and a 50% decreased signal cross section (right). The top row of plots correspond to the inclusive pMSSM, the row second from top shows the pMSSM subspace with a long-lived chargino, the two bottom rows show the subspaces of the pMSSM that resembles the T5btbtLL simplified model, by requiring BR($\widetilde{g} \to bt\widetilde{\chi}_1^{\pm}$)$> 0.25$, and the proper chargino decay length to be inside $c\tau(\widetilde{\chi}_1^{\pm}) \in [1\,\text{cm}, 150\,\text{cm}]$ (second from bottom) and $c\tau(\widetilde{\chi}_1^{\pm}) \in [1.5\,\text{m}, 100\,\text{m}]$ (bottom), respectively. Black color denotes bins with zero survival probability, grey denotes bins with a survival probability of exactly 1, white bins are empty.

Finally, the comparison for the pure higgsino simplified model and the pMSSM is shown in Figure 169. A large part of the pMSSM model space within the excluded region survives the constraints from the search for disappearing tracks. However, the transition from partial sensitivity to the region of no sensitivity, indicated by grey bins, maps very well onto the simplified model limit. The discrepancy between the simplified model limit and the pMSSM survival probability can be explained by the rarity of higgsino-like models in this part of the pMSSM, making up only approximately 2% of models in the displayed region. In the subspace of the pMSSM that features pure higgsinos, the simplified model limit maps well onto the pMSSM survival probability. In the complementary part of the pMSSM that does not contain pure higgsinos, but mostly pure winos, the sensitivity of the search for disappearing tracks vanishes well below the simplified model limit in terms of $\Delta m(\widetilde{\chi}_1^{\pm}, \widetilde{\chi}_1^0)$.

Another visible feature is that at very small values of $\Delta m(\widetilde{\chi}_1^{\pm}, \widetilde{\chi}_1^0) \lesssim 150\,\text{MeV}$, the region of zero survival probability in the pMSSM extends to far larger $m(\widetilde{\chi}_1^0)$ than indicated by the simplified model limit, even if it were to extend to larger $m(\widetilde{\chi}_1^0)$. This part of the parameter space was not considered in the simplified model, as radiative corrections to $\Delta m(\widetilde{\chi}_1^{\pm}, \widetilde{\chi}_1^0)$ should prevent these small $\Delta m(\widetilde{\chi}_1^{\pm}, \widetilde{\chi}_1^0)$. They are present in the pMSSM scan due to limitations of `SPheno` (Section 5.4), and their extremely small $\Delta m(\widetilde{\chi}_1^{\pm}, \widetilde{\chi}_1^0)$ leads to very large chargino lifetimes that are excluded by the search for disappearing tracks up to very large $m(\widetilde{\chi}_1^0)$.

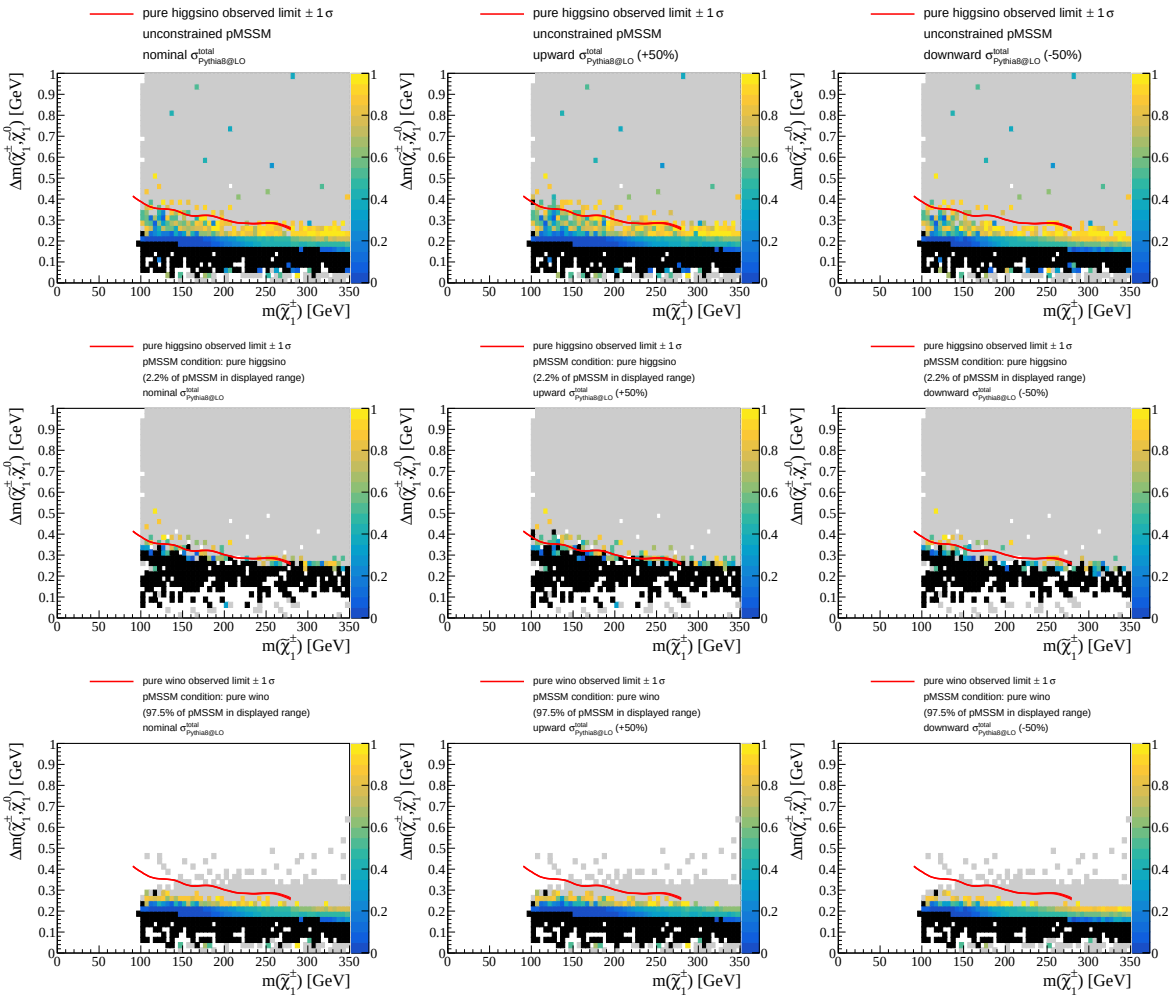

Figure 169: Comparison of the pMSSM survival probability and the published limits of the disappearing tracks analysis [7] in the plane of m($\tilde{g}$) and $m(\tilde{\chi}_1^0)$, in terms of a pure higgsino simplified model. The pMSSM survival probability is shown assuming the nominal signal cross section (left), assuming a 50% increased signal cross section (center), and a 50% decreased signal cross section (right). The top row of plots correspond to the inclusive pMSSM, the center row shows the subspace of the pMSSM that resembles the pure higgsino simplified model, by requiring the higgsino admixture to the LSP to exceed 95%. The bottom row shows the subspace of the pMSSM with a pure wino LSP. Black color denotes bins with zero survival probability, grey denotes bins with a survival probability of exactly 1, white bins are empty.

9 Summary

This thesis presents a study of the viability of the MSSM given a wide variety of experimental results. It makes use of the pMSSM-19 as a proxy model for the MSSM, to avoid the impracticability of fully covering a parameter space with over 100 free parameters. The analysis is set up in an iterative Bayesian inference framework, where the various experimental results are included at different stages of the process. The process starts with an ur-prior that is flat in the 19 parameters of the pMSSM. The pMSSM is then sampled by means of Markov chain Monte Carlo (McMC), in which measurements of the Higgs mass, constraints from LEP on the mass of the charginos, as well as on the branching ratio BR($Z \rightarrow$ invisible) are used to steer the McMC. Also included are a suite of measurements from the flavor sector. The resulting ensemble of pMSSM points, called the pMSSM scan, is a discrete representation of the posterior density with respect to the measurements included in the McMC, provided that the McMC has converged on its stationary distribution. It consists of approximately 27 million pMSSM models and is the most detailed and extensive study of this nature to date. A study on the McMC convergence has been performed, which shows compatibility with convergence.

A study on the impact of the different contributions to the pMSSM has been performed by comparing an unsteered McMC to the full McMC containing all the low energy observables, McMCs steered by one of the low-energy observables each, and McMCs using all but one observable for steering. The pMSSM scan is significantly shaped by the constraints and the McMC sampling, with a large impact of model-inherent constraints, such as the need for an absence of tachyons in the particle spectrum. The occurrence of tachyons is partially unphysical due to limitations of the spectrum generators. While the distributions of all of the pMSSM parameters and particle masses deviate from the flat "ur-prior", there are some parameters that are particularly strongly impacted. These are

- the higgsino mass parameter μ, where small values are significantly disfavored;
- the stop-Higgs trilinear coupling A_t, where small values of $|A_t|$ are strongly disfavored;
- the pseudoscalar Higgs mass parameter m_A, and the corresponding heavy Higgs masses A^0, H^0, and $H^\pm$, where small to medium masses are heavily disfavored;
- the ratio of vacuum expectation values $\tan(\beta)$, where small values are significantly disfavored, and, to a lesser degree, large values;
- the third generation squark mass parameters and masses, where small masses are strongly disfavored;
- and the left-chiral first (and second) generation squark mass parameters and masses, where small masses are somewhat strongly disfavored.

Additionally, it was found that the particle spectra of the electroweakinos can not be reliably computed by the current spectrum generators, which leads to an under-estimation of the mass difference between the lightest neutralino and lighter chargino for a significant part of the pMSSM, including most models with a wino-like LSP. This has implications due to the enlarged presence of models with long-lived charginos, to which the LHC is particularly sensitive. This is partially compensated for by interpreting the results in terms of the observables directly responsible for LHC sensitivity, which are the mass differences and resulting observables such as the chargino lifetime. Inferences from constraints on the physical observables to the pMSSM parameters remain dubious in the cases of high sensitivity to the chargino life time.

Using iterative inference, the posterior density represented by the pMSSM scan is taken to be the prior for constraints from the LHC, as well as constraints from the dark matter relic density, and constraints from direct and indirect searches for dark matter. To conserve precious computation time, a subset of approximately 500,000 pMSSM points is sampled from the full pMSSM scan. We make use of over-sampling interesting regions, such as the parts of the pMSSM with light stop masses, small fine-tuning, or a dark matter relic density compatible with the measured dark matter relic density or the measurement of a_μ, which is in significant tension with the SM. This is done to increase the scan resolution in these regions at the expense of the residual pMSSM. To the same purpose, we under-sample regions where a smaller scan resolution is sufficient, such as the part of the pMSSM that over-saturates the measured dark matter relic density, or is excluded by LHC analyses based

only on the 7 TeV or 8 TeV datasets. The effect of the variable sampling is corrected for by weighting each pMSSM point by the inverse of its sampling factor.

The LHC impact is evaluated on the basis of five direct SUSY searches, covering the 0-lepton p_T^{miss}+jets final state [1, 2], the di-lepton final state [3], the soft-di-lepton final state [4], the multi-lepton final state [5], and the final state featuring disappearing tracks [6, 7]. The single lepton final state is not covered by a dedicated analysis. Two paths for including the analyses are used. The first path, used for the soft-di-lepton search and the search for disappearing tracks, uses approximately 6 billion signal events, with event generation performed using `Pythia8`, for which the detector response is modeled via the CMS-internal fast simulation process. Valuable computation time is conserved in the signal event generation by using an event filter that quickly rejects events after the generation step, based on truth-level observables. The event filter is designed to only reject events that do not pass the triggers used in any of the used analyses. In this path, the analyses are run directly by the two analysis groups, with the likelihoods computed with Higgs combine tool, which takes background correlations into account. The second path, for the p_T^{miss}+jets search, the di-lepton search, and the soft-di-lepton search, another statistically independent set of approximately ten billion signal events, also generated using `Pythia8` [129, 130], are processed with the recasting tool `MadAnalysis5` [121, 122, 123, 124], which makes use of a parameterized detector simulation using `Delphes` ¸[141]. Using the resulting signal event counts in the signal regions, as well as the predicted background and measured data, a simplified likelihood is computed for each of these analyses. This simplified likelihood does not include any correlation model.

The individual analysis likelihoods for both paths are combined by multiplying their Bayes factors. The posterior density for the LHC is computed by weighting each point in the pMSSM scan by the combined likelihood, and then reweighting the pMSSM scan such that it integrates to one.

Overall, approximately 47% of the considered pMSSM model space is excluded by the LHC, with the largest contribution from the p_T^{miss}+jets search, followed by the search for disappearing tracks.

In the electroweak sector, the LHC is indirectly sensitive up to LSP masses of approximately $m(\widetilde{\chi}_1^0) \simeq 1.5\,\text{TeV}$, and directly sensitive up to $m(\widetilde{\chi}_1^0) \simeq 700\,\text{GeV}$. The region below $m(\widetilde{\chi}_1^0) \lesssim 500\,\text{GeV}$ is significantly disfavored, but all LSP masses remain viable in some parts of the pMSSM. Models with a wino-like LSP are particularly disfavored, owing to their larger production cross section, and their very small chargino-neutralino mass splitting $\Delta m(\widetilde{\chi}_1^\pm, \widetilde{\chi}_1^0)$, which leads to long-lived charginos in a large fraction of the models with a wino-like LSP. For this reason, the LHC sensitivity to the electroweak sector is strongest at these very small $\Delta m(\widetilde{\chi}_1^\pm, \widetilde{\chi}_1^0)$ and long live times, with models containing a chargino with $1\,\text{cm} \lesssim c\tau(\widetilde{\chi}_1^\pm) \lesssim 100\,\text{m}$ severely disfavored. A small excess in the data seen by the multi-lepton search is well fit by the pMSSM at $\Delta m(\widetilde{\chi}_1^\pm, \widetilde{\chi}_1^0) \simeq 100\,\text{GeV}$.

In the slepton sector, models with a left-chiral selectron and smuon with masses below 600 GeV are severely disfavored, with masses below 400 GeV almost entirely excluded. Sensitivity to right-chiral sleptons is significantly smaller, with surviving models featuring slepton masses as small as 100 GeV. Compressed slepton-LSP scenarios remain particularly viable even to very small slepton masses.

In the colored sector, colored sparticles with masses below 1 TeV are strongly disfavored, but not completely excluded. While large stop masses are strongly preferred in the pMSSM, a significant population of models with light stop survive in the compressed model space. The strongest impact is on the gluino mass, where the marginalized posterior density is strongly suppressed up to gluino masses of $m(\widetilde{g}) \simeq 2\,\text{TeV}$. The LHC excludes most models with a sbottom mass below $m(\widetilde{b}_1) \lesssim 1\,\text{TeV}$, but sbottom masses slightly above the direct LHC sensitivity remain viable. The LHC strongly disfavors left-chiral first (and second) generation squark masses below $m(\widetilde{u}_L, \widetilde{c}_L) \simeq m(\widetilde{d}_L, \widetilde{s}_L) \lesssim 1\,\text{TeV}$, and still significantly disfavors the pMSSM with $m(\widetilde{u}_L, \widetilde{c}_L) \simeq m(\widetilde{d}_L, \widetilde{s}_L) \lesssim 2\,\text{TeV}$. The same result is seen for the right-chiral $m(\widetilde{u}_R, \widetilde{c}_R)$. The impact on the right-chiral $m(\widetilde{d}_R, \widetilde{s}_R)$ is more limited but strongly disfavors $m(\widetilde{d}_R, \widetilde{s}_R) \lesssim 1\,\text{TeV}$.

The LHC impact has also been studied in terms of the pMSSM parameters instead of the particle masses. Small values of the higgsino mass parameter μ are further suppressed by the LHC results, resulting in a very small marginalized posterior density at small $|\mu|$. Similarly, small masses of the bino- and wino-mass parameters M_1 and M_2 are disfavored, with $|M_2| \lesssim 200\,\text{GeV}$ completely excluded due to direct sensitivity to wino production. In addition, large $|\mu|$ and $|M_1|$ are disfavored due to constraints on the long-lived charginos present in models with pure winos, for which $|M_2| \ll |\mu|, |M_1|$ is required. For the slepton and squark mass parameters, no part of the parameter space can be completely excluded. For the pseudoscalar Higgs boson mass parameter and masses, while small masses are disfavored, there is almost no impact on top of the already small prior density.

The impact of three types of dark matter constraints is studied, as well as their interplay with the

constraints from direct searches at the LHC. These are constraints from direct dark matter detection, indirect dark matter detection, and constraints on the dark matter relic density. For the direct dark matter detection constraints, a p-value is calculated by the tool `MicrOMEGAs`[94], which uses limits on spin-dependent and spin-independent $\widetilde{\chi}_1^0$-nucleon cross sections for protons and neutrons from four direct detection experiments. Direct detection constraints, predominately from the `XENON1T` [148] experiment, exclude approximately 15% of both the LHC prior and posterior densities. They are most constraining on models with a higgsino-like LSP or a wino-like LSP, especially mixed wino-higgsino scenarios. In contrast to constraints from the LHC, the direct detection results allow to exclude models in the whole range of scanned LSP masses, including large LSP masses that are currently out of reach for the LHC.

For indirect dark matter detection, we obtain the dark matter annihilation cross section for each model from `MicrOMEGAs`, as well as the contributions of the WW, $b\bar{b}$, $\mu\mu$, and $\tau\tau$ final states to the total annihilation cross section. Higher order effects, like the Sommerfeld enhancement [152, 153, 154], are not taken into account here. We then compute a fiducial annihilation cross section for each channel, which also considers the dark matter relic density of each model. The fiducial cross section is tested against upper limits from a combination of results from the Fermi-LAT and MAGIC experiments [62]. We find that no model in the pMSSM can be excluded by these indirect detection constraints that is not also excluded by the LHC. However, if it turns out that higher-order corrections lead to an increase in the fiducial annihilation cross section factor of at least ten, parts of the pMSSM, especially where the LSP is heavy, would be excluded.

Finally, the impact of constraints on the relic density Ωh^2, calculated with `MicrOMEGAs`, are studied in terms of three constraints:

- an upper bound at the measured relic density $\Omega h^2 \leq 1.1\ \Omega h^2_{\text{Planck}}$, where $\Omega h^2_{\text{Planck}} = 0.12 \pm 0.001$ [8]. This constraint excludes most models with a bino-like LSP, as well as models with a higgsino-like LSP above $m(\widetilde{\chi}_1^0) \gtrsim 1.2\,\text{TeV}$, and models with a wino-like LSP above $m(\widetilde{\chi}_1^0) \gtrsim 1.8\,\text{TeV}$. Surviving models with a bino-like LSP are often in the A-funnel region. An upper bound on Ωh^2 thus constrains $m(\widetilde{\chi}_1^0)$ from above for wino-like and higgsino-like LSPs.

- The same upper bound and a lower bound that requires models to saturate at least 10% of the measured relic density. The addition of the lower bound excludes almost all models with a wino-like LSP below $m(\widetilde{\chi}_1^0) \lesssim 600\,\text{GeV}$, and higgsino-like LSPs below $m(\widetilde{\chi}_1^0) \lesssim 300\,\text{GeV}$. Because of this, it excludes most of the pMSSM parameter space with electroweak production that is accessible by current LHC data.

- A tight constraint that requires the relic density to be compatible within 10% of $\Omega h^2_{\text{Planck}}$. Surviving models include pure higgsino-like LSPs at $m(\widetilde{\chi}_1^0) \simeq 1.1\,\text{TeV}$, pure wino-like LSPs at $m(\widetilde{\chi}_1^0) \simeq 1.7\,\text{TeV}$, and wino-higgsino mixed LSPs. Some models with a pure bino LSP survive inside the A-funnel region.

The importance of the direct detection constraints depends on the choice of constraint on the relic density. If only an upper bound is adopted on the relic density, direct detection constraints significantly suppress models with a pure higgsino-like LSP and models with higgsino-admixture. Since a lower bound on Ωh^2 also constrains light higgsino-like LSPs, the relative impact of the direct detection constraints on pure higgsinos lessens. However, its suppression of mixed LSPs remains relevant for all three constraints on Ωh^2.

The importance of the LHC and complementarity with the dark matter constraints again strongly depends on the choice of constraint on Ωh^2. If the tight constraint on Ωh^2 is adopted, the LHC constrains light bino-mix LSP scenarios, and light pure bino scenarios inside of funnel regions, either of which can result in the measured relic density and evade both direct and indirect detection constraints. If the lower bound on Ωh^2 is loosened, then the LHC becomes more important in constraining pure higgsino and pure wino LSP, with its impact becoming stronger the looser the lower bound on Ωh^2. If the lower bound on Ωh^2 is abandoned entirely, then the LHC and dark matter constrains are fully complementary, in that the dark matter results constrain the LSP mass from above at large masses, and the LHC constrains the LSP mass from below at small masses. In addition, the upper bound on Ωh^2 still excludes most of the pure bino LSPs, to which the LHC is less sensitive.

In addition to the dark matter sector, the low-fine tuning sector of the pMSSM (defined by the measure ΔEW [51]) is studied in relation to the LHC and dark matter constraints. Two regions are defined by setting an upper bound on ΔEW, with a loose region given by $\Delta\text{EW} < 100$, and a tight region given by $\Delta\text{EW} < 100$. The most important impact of these constraints is that they result

in an upper bound on the higgsino mass parameter of $|\mu| \lesssim 650\,\text{GeV}$ and $|\mu| \lesssim 350\,\text{GeV}$ for the loose and tight regions, respectively. This excludes most models with a pure bino-like LSP or a pure wino-like LSP, and introduces an upper bound on $m(\widetilde{\chi}_1^0) \simeq 650\,\text{GeV}$. Because of a correlation of small $|\mu|$ to small $m(\widetilde{t}_1)$ in the pMSSM, $m(\widetilde{t}_1)$ peaks somewhat sharply at $m(\widetilde{t}_1) \simeq 3\,\text{TeV}$ in both low-fine tuning regions. The LHC constrains ΔEW from below due to its sensitivity to light higgsino-like LSPs, excluding 50% of models in the loose ΔEW region and approximately 75% of models in the tight ΔEW region. Considering also the dark matter constraints, we find that no model survives in the region defined by the tight ΔEW constraint and the tight dark matter constraints. Adopting the upper bound on Ωh^2 instead of the tight constraint on Ωh^2, the dark matter constraints exclude almost all models with a mixed LSP type, leaving almost exclusively models with a pure higgsino-like LSP. A lower bound of 10% on Ωh^2 constrains $m(\widetilde{\chi}_1^0)$ from below, to a stronger degree than the current LHC data. In the loose ΔEW part of this small subspace of the pMSSM, a small set of models with $m(\widetilde{\chi}_1^0) \in [350\,\text{GeV}, 600\,\text{GeV}]$ and $\Delta m(\widetilde{\chi}_1^\pm, \widetilde{\chi}_1^0) \simeq 1\,\text{GeV}$ survive the combined LHC and dark matter constraints. In the tight ΔEW subspace, a small sliver of models with $m(\widetilde{\chi}_1^0) \simeq 350\,\text{GeV}$ and $\Delta m(\widetilde{\chi}_1^\pm, \widetilde{\chi}_1^0) \simeq 1\,\text{GeV}$ survive.

The impact of recent measurements of the anomalous magnetic moment of the muon [66] on the pMSSM is studied. This measurement powerfully constrains the pMSSM and excludes approximately 98.2% of the prior, due to the necessity of light sleptons that are heavily disfavored by the LHC prior. Confronting the remaining pMSSM models with LHC excludes a further 90% of models, with the LHC data limiting the slepton masses from below and a_μ data from above. Considering the dark matter constraints again reduces the number of surviving models by an order of magnitude, leaving only 12 models that survive the a_μ, LHC, and dark matter data. The surviving models usually feature low levels of fine-tuning, with 4 models below the threshold of $\Delta\text{EW} < 100$, of which two models have even smaller values of $\Delta\text{EW} < 30$. The LHC is at least somewhat sensitive to all pMSSM models that explain the a_μ measurement, which means that if a_μ turns out to be new physics caused by SUSY, the LHC will be sensitive with new data. However, if no signal is found in future LHC data, the pMSSM model space with large contributions to a_μ that are compatible with the measured discrepancy to the SM may be entirely excluded. In this case, an explanation to a_μ would have to be sought outside of minimal supersymmetry.

Finally, the viability of published simplified model limits in the context of the pMSSM is tested by comparing upper limits on the various simplified model spaces to survival probabilities in the pMSSM. A consistency check is also done by comparing the upper limits to subspaces of the pMSSM that resemble the simplified model topology as closely as possible, for example by restricting to models with corresponding large branching ratios. It is found that while limits on simplified models targeting strong production apply reasonably well in the pMSSM subspaces that resemble the respective models, their applicability to the inclusive pMSSM is very limited, mostly due to the rarity of the simplified model topologies in the pMSSM. In the inclusive pMSSM, models are found inside any simplified model limit that survive the analysis constraints, likely due to the presence of particles and decay modes not considered in the simplified models. Simplified model limits targeting electroweak supersymmetry apply considerably worse to the pMSSM, partly due to the rarity of their topology, and partly due to very restrictive constraints on the particle decays inside the simplified models. The simplified model limits on the part of the pMSSM with long-lived charginos apply reasonably well for the strong production modes, especially for the shorter chargino lifetimes. The impact of the strong production modes on models with large $m(\widetilde{\chi}_1^0)$ and longer lifetimes is somewhat overestimated in the simplified models, especially in the more compressed region of the strongly produced particle and the LSP mass. The simplified model limits on pure higgsinos apply well on the higgsino-like subspace of the pMSSM. A naive application of the limit on the pMSSM suffers from the rarity of pure higgsinos at $\Delta m(\widetilde{\chi}_1^\pm, \widetilde{\chi}_1^0) \lesssim 1\,\text{GeV}$, where most of the models feature a wino-like LSP, and overestimates the exclusion above $\Delta m(\widetilde{\chi}_1^\pm, \widetilde{\chi}_1^0) \gtrsim 200\,\text{MeV}$.

This thesis represents the most comprehensive study to date on supersymmetry based on Run 2 data from the CERN LHC, incorporating constraints from LEP, flavor physics, direct and indirect dark matter detection experiments, cosmological considerations, and recent measurements of a_μ. Nearly 500,000 pMSSM model points have been selected from an McMC scan, and each point has been subjected to a detailed process including Monte Carlo event simulation, detector simulation, and analysis application. If the tension between SM prediction and measurement of a_μ is upheld, future LHC data will potentially be able to find supersymmetry in the a_μ-compatible parameter space, or falsify the pMSSM model space with large contributions to a_μ entirely. If a_μ is left out of the analysis, between 0 and 28,000 pMSSM models survive all constraints, depending on the strictness of

the considered constraints. Most of the surviving models lie in a region of the pMSSM that is difficult to probe, and new experimental techniques and more collider data will be required to possibly falsify or discover SUSY.

A McMC algorithm shaping solutions

The version of the Metropolis-Hastings employed in this work results in a reduced scan density at the edges, due to an asymmetric step probability that disfavors steps towards the edges of the allowed parameter ranges. The reason is that candidate points are rejected and re-sampled from the same distribution if the sampled parameter value lies outside the allowed range.

It is possible to avoid this bias of the algorithm by modifying the McMC algorithm behavior at the edges, by allowing the algorithm to temporarily step outside the allowed range and then force it to the move back towards the allowed range. Points outside the allowed range are still rejected, but are taken as the origin for sampling the new candidate point. Once a model point inside the allowed range is sampled, that point is taken as the next candidate in the chain. These behaviors and solutions are shown graphically, for a 1-dimensional toy model, in Figure 170. Alternatively, a less efficient solution lies in sampling a larger region first, which is then truncated to remove the affected areas, and to achieve the desired scan boundaries.

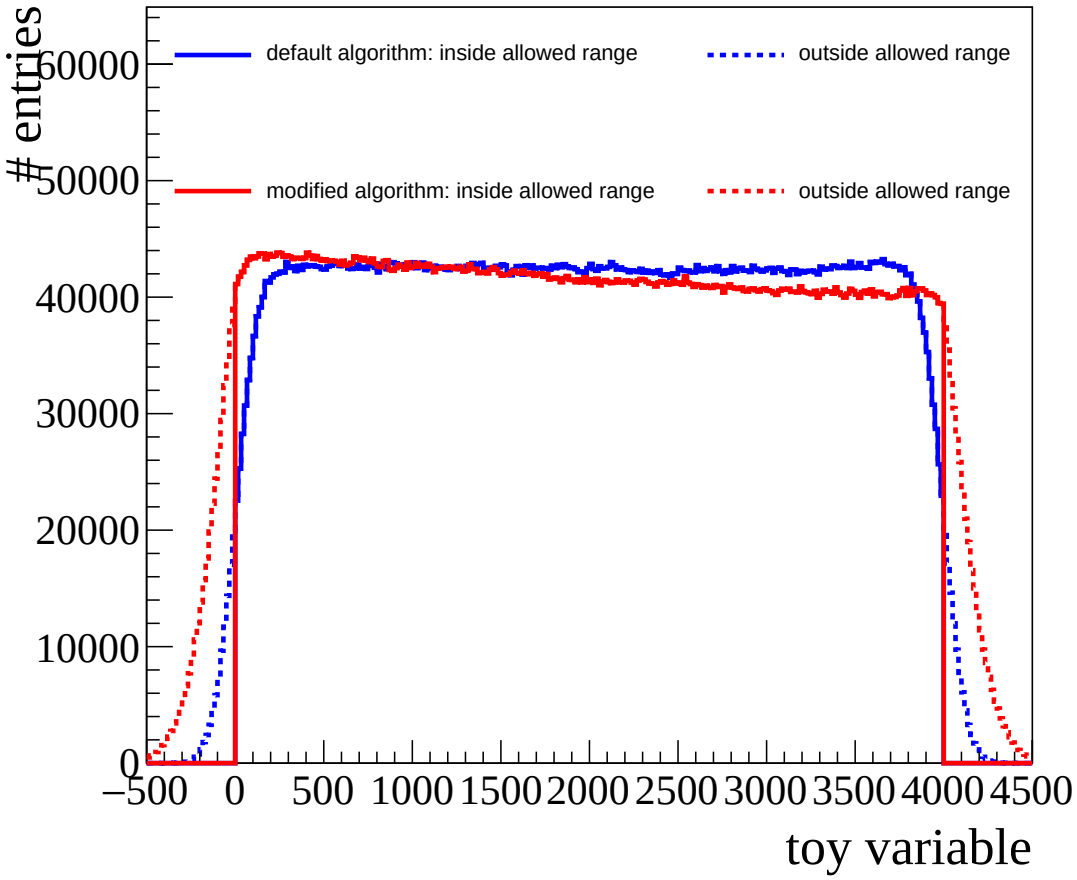

Figure 170: The distribution of 10 million values sampled with via Markov chain Monte Carlo. The blue distribution uses the default McMC algorithm, the red distribution results from a modified version of the algorithm that is allowed to step outside the allowed range temporarily.

B Tachyons and SPheno error codes

Here, we study the occurrence of tachyons in the pMSSM by sampling the space from uniform distributions in the 19 pMSSM parameters. We thus eliminate the influence that the McMC sampling may introduce.

The reasons for SPheno to reject a pMSSM point fall in two categories:

- there is a tachyon in the particle spectrum (about 60% of the flat ur-prior);
- another type of error occurs during spectrum generation (about 4% of the flat ur-prior).

The remaining 36% of the flat ur-prior contains valid particle spectra according to SPheno. The presence of tachyons can be considered a model-inherent constraint, while the other errors should be considered a limitation of SPheno itself, not a constraint of the pMSSM. However, even for the tachyons, it is questionable whether all tachyonic models should be considered invalid due to model-inherent constraints. Because SPheno does not calculate all perturbation orders in the generation of the physical particle spectrum, it is inevitable that some model points contain tachyons erroneously. Whether a given point is erroneously tachyonic or not can not be definitively determined here. Any increase in the tachyonic fraction that is strongly correlated to the SUSY scale directly, and much weaker with other pMSSM parameters, is likely to be an artifact of inaccuracies of the perturbative calculation of the masses, since a dependence on the SUSY scale indicates a dependence on the running with the renormalization group equations.

We take a closer look at the regions of the pMSSM that are disfavored because they contain an abundance of tachyonic states, by looking at 1D projections onto the pMSSM parameters, and at 2-dimensional planes that show localized variations in the fraction of tachyonic models. In this first step, it was chosen to not sample the pMSSM space via Markov chain Monte Carlo, to eliminate any influences that this way of sampling might have on the fraction of tachyonic models. Instead, the space is uniformly sampled from flat distributions in the 19 pMSSM parameters. In addition to this, an ensemble of points is created with the same settings, except that the SUSY scale is sampled from a uniform distribution between 0 and 10 TeV, instead of its usual definition as the geometric mean of the stop mass parameters. This is done to determine the direct influence of the SUSY scale and, with that, identify regions where large tachyonic fractions are not model-inherent but a result of limited perturbative calculation. The regions identified this way should not be considered genuinely excluded by the presence of a tachyon – the tachyons may be genuine, but we can not be certain enough of this.

We start by identifying regions in the 19 pMSSM parameters where a strong increase in the fraction of tachyonic models can be correlated to the SUSY scale. Figure 171 shows the fraction of valid models, tachyonic models, and models with other errors in SPheno, for different SUSY scales Q_{SUSY}, where Q_{SUSY} is sampled uniformly from 0 to 10 TeV. First note that the tachyonic fraction is quite dependent on Q_{SUSY} directly, with tachyonic fractions ranging from approximately 55% to almost 90%. Because Q_{SUSY} is sampled uniformly and indepedently of the pMSSM parameters in the left plot in Figure 171, the variance in tachyonic fraction is not related to the pMSSM, but purely to the choice of scale. The tachyonic fraction is smallest at $Q_{SUSY} \simeq 5$ TeV, exactly at the center of the allowed range of the colored sector. In other words, the occurrence of tachyonic models according to SPheno is tied to the difference between Q_{SUSY} and the pMSSM parameters. This suggests that the immediate cause of occurring tachyons is the running of the spectrum with the renormalization group equations, the impact of which increases with the difference of Q_{SUSY} and the respective particle masses. The large variation in the tachyonic fraction with Q_{SUSY} suggests that a significant fraction of the model space is labeled tachyonic due to limitations of the spectrum generator, not necessarily due to the actual occurrence of tachyons. However, the latter cannot be ruled out on this basis.

In the planes of the pMSSM parameters, two regions can be found where the tachyonic fraction of models is directly and very strongly correlated to the scale. These are shown in Figure 172. One set of regions with large tachyonic fractions are at large differences between the gluino mass parameter M_3 and Q_{SUSY}: small values of M_3 combined with large Q_{SUSY}, as well as large M_3 and small Q_{SUSY} lead to a strong enlargement in the fraction of tachyonic models. In the latter case, the tachyonic fraction reaches 90% for $Q_{SUSY} < 1.5$ TeV, $M_3 > 8$ TeV. The other region of extreme tachyonic fraction is found in the plane of Q_{SUSY} and the higgsino mass parameter μ, an extreme increase in the tachyonic fraction is observed for $|\mu| < 1$ TeV, $Q_{SUSY} > 5$ TeV. Virtually all points are tachyonic in this region, according to SPheno. Because of their strong dependence on Q_{SUSY}, these regions should not be

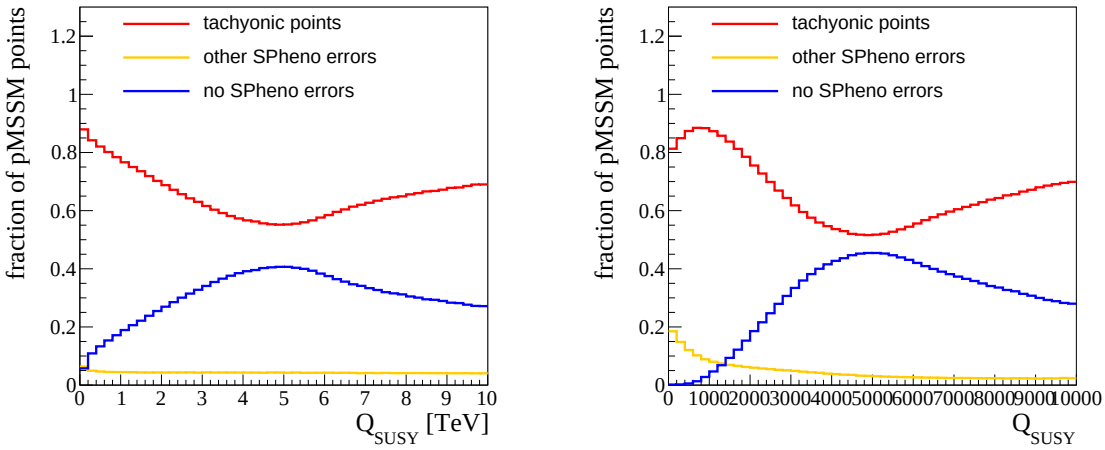

Figure 171: Fraction of tachyonic models, models with other `SPheno` errors, and valid models, projected on the SUSY scale Q_{SUSY}. The left plot shows the distribution where Q_{SUSY} is uniformly sampled from 0 to 10 TeV, the right plot shows the distributions for a scan where Q_{SUSY} is defined as the geometric mean of the stop mass parameters, $Q_{SUSY} = \sqrt{M_{q,3} \cdot M_{u,3}}$.

claimed to be excluded by model-inherent constraints, but will still be severely under-represented, or not at all, in the prior and posterior densities.

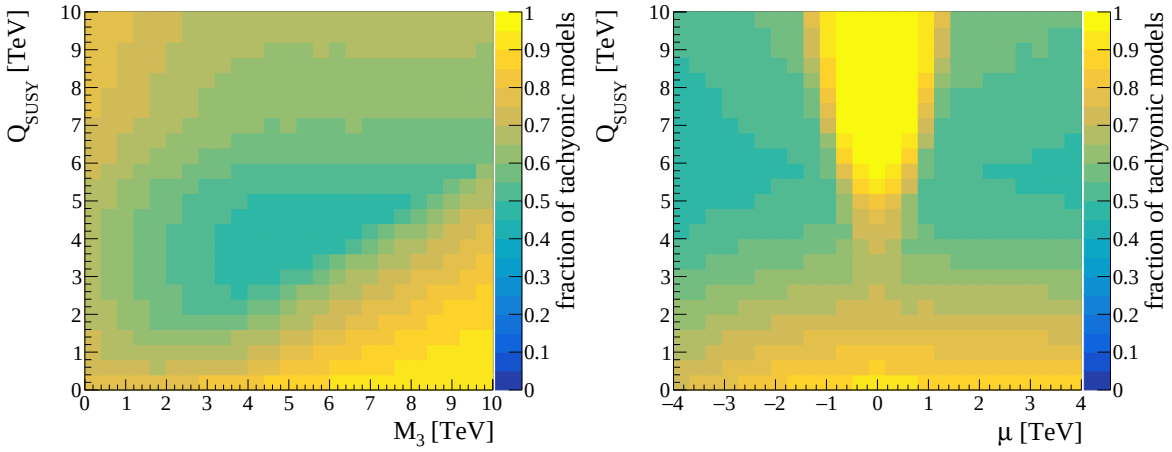

Figure 172: Fraction of tachyonic models, models with other `SPheno` errors, and valid models, projected in the planes of Q_{SUSY} and M_3, and Q_{SUSY} and μ. The scale Q_{SUSY} is uniformly sampled from 0 to 10 TeV.

We continue our study in the electroweak sector of the pMSSM, but switch to the SUSY scale definition as used in the McMC scan, namely $Q_{SUSY} = \sqrt{M_{q,3} \cdot M_{u,3}}$. As could already be seen in Figure 172, the tachyonic fraction shows strong features in the higgsino mass parameter μ. These features are also present when the scale is defined as the geometric mean of the stop mass parameters, as shown in Figure 173. The very large tachyonic fraction for $|\mu| < 1\,\text{TeV}$ is almost entirely located in the large Q_{SUSY} region, which is entirely tachyonic. Towards large $|\mu|$, we see an increase in the occurrence of other `SPheno` errors, with a much larger effect seen at negative μ. The large tachyonic fraction at small $|\mu|$ has severe consequences on the phenomenology at the LHC, because there will not be many, if any, models with a light higgsino and very heavy stops. Additionally, there will not be any models with a light higgsino where the stops are completely decoupled, which is expected to happen for stop masses of approximately 10 TeV.

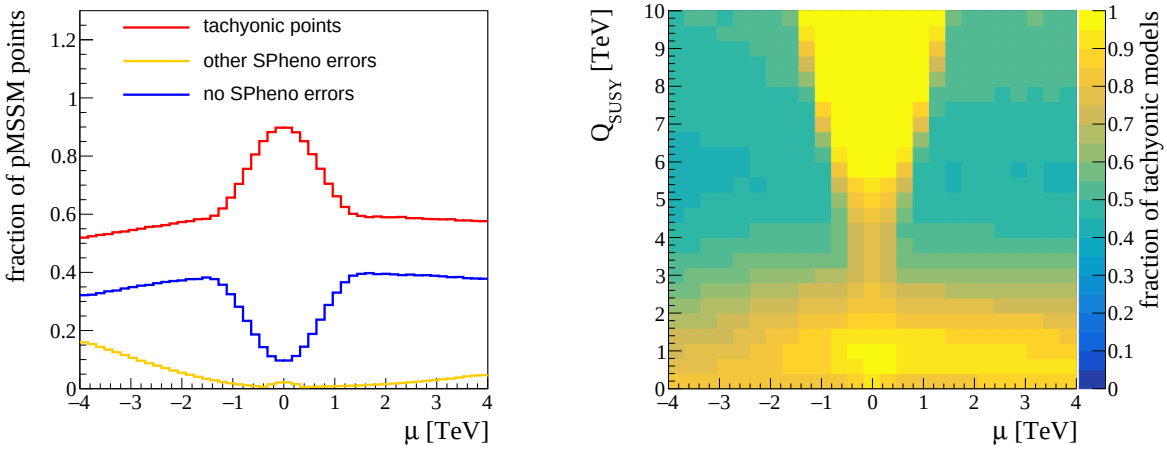

Figure 173: Fraction of tachyonic models projected on the higgsino mass parameter μ (left), and in the plane of μ and the SUSY scale Q_{SUSY} (right). The SUSY scale is defined here as $Q_{SUSY} = \sqrt{M_{q,3} \cdot M_{u,3}}$.

Figure 174 shows the tachyonic fraction for the bino-mass parameter M_1 and the wino-mass parameter M_2. We see a slight decrease of the fraction of tachyonic models as its absolute value becomes large. This is slightly more pronounced for M_2. We can also see a sudden but slight increase in other `SPheno` errors at $|M_1| < 400\,\text{GeV}$ and $|M_2| < 400\,\text{GeV}$, where the increase is more sudden and pronounced for M_1. Overall, there is little dependence and shaping in M_1 and M_2 due to model-inherent constraints.

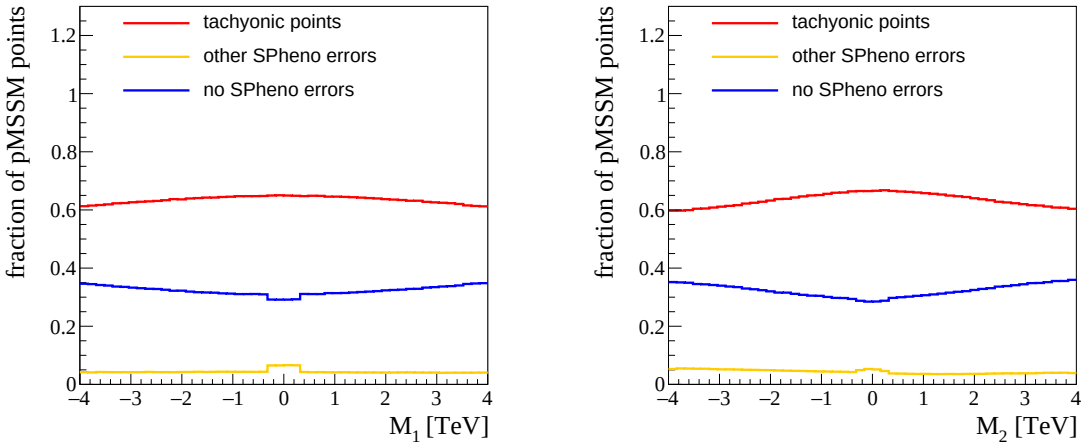

Figure 174: Fraction of tachyonic models, models with other `SPheno` errors, and valid models, projected on the bino- and wino-mass parameters M_1 (left) and M_2 (right). The SUSY scale is defined here as $Q_{SUSY} = \sqrt{M_{q,3} \cdot M_{u,3}}$.

Significant increases in the tachyonic fraction correlate to the stop mass parameters $M_{q,3}$ and $M_{u,3}$, and to the gluino mass parameter M_3. The corresponding distributions are shown in Figure 175. We can see that the tachyonic fraction in the gluino mass parameter has a minimum at around $M_3 \simeq 3.5\,\text{TeV}$, and increases towards both smaller and larger M_3. For both of the stop mass parameters, the tachyonic fraction sharply increases below masses of 3 TeV, reaching 90% in the lowest bin. We can also see that the tachyonic fractions compound in the regions where it is large in both M_3 and either one of the stop mass parameters. This results in an almost completely tachyonic region at large $M_3 \gtrsim> 6\,\text{TeV}$ and $M_{q,3} \lesssim 1\,\text{TeV}$ and $M_{u,3} \lesssim 1\,\text{TeV}$, respectively. The plane of $M_{q,3}$ and $M_{u,3}$ shows that the tachyonic fraction does not compound in the region where the 1-dimensional marginalizations show a larger tachyonic fraction for both of these parameters individually. On the contrary, the tachyonic fraction actually decreases in the region where both $M_{q,3}$ and $M_{u,3}$ are small, compared to larger hierarchies where only one of the two parameters is small. This reduction in the tachyonic fraction does not mean that a larger fraction of the pMSSM in this region is valid, rather there is a significant increase in other errors in `SPheno` in that region. This can be seen in the right side plot in Figure 171, which shows the fractions of tachyonic, non-tachyonic and other `SPheno` errors for the SUSY scale Q_{SUSY}, defined here as the geometric mean of the stop mass parameters. We can see that there is a steady increase of the fraction of models with "other" `SPheno` errors towards small Q_{SUSY}, and with that, small $M_{q,3}$ and $M_{u,3}$. Because of the large tachyonic fraction at small values of the stop mass parameters, the same region will be only sparsely populated in the prior sampled with the McMC, which will worsen the scan resolution in this region. The tachyonic fraction for the right-chiral sbottom mass parameter $M_{d,3}$ is shown in Figure 176. Similarly to the stop mass parameters, the tachyonic fraction rises steeply towards smaller masses and there is a steady increase of the other `SPheno` errors towards smaller masses. However, both of these features are not as strongly pronounced as for the stop mass parameters, and the tachyonic fraction in particular only starts to increase at smaller masses. In the plane of $M_{d,3}$ and M_3, there is an increase in the tachyonic fraction for very small $M_{d,3}$ and M_3, similar to what is seen for very small M_3 and $M_{q,3}$, and $M_{u,3}$, respectively. We also see an increase in the tachyonic fraction for larger mass hierarchies, even if it is less pronounced compared to the stop mass parameters.

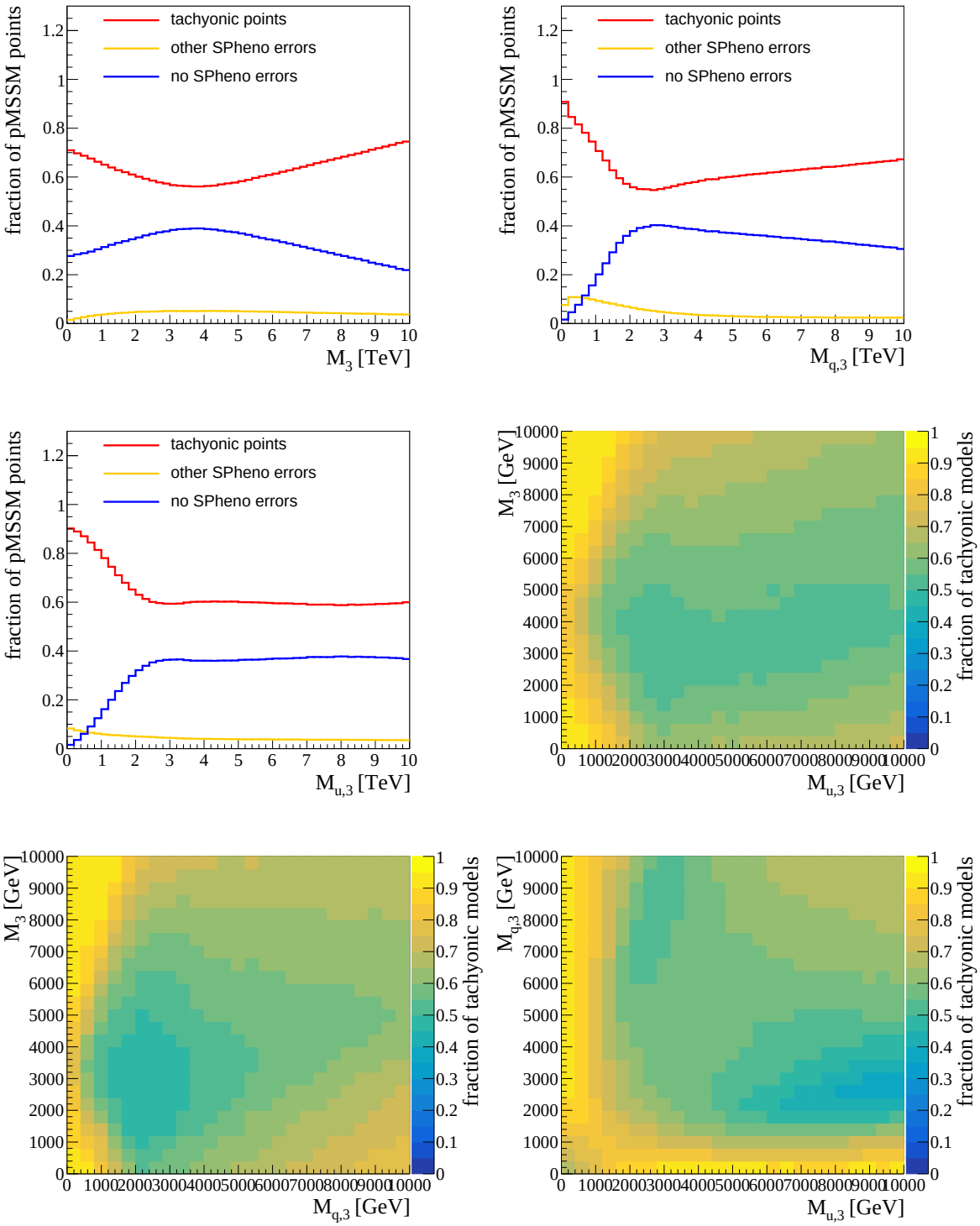

Figure 175: Fraction of tachyonic models, models with other SPheno errors, and valid models, projected on the gluino mass parameter M_3 (top left), the left-handed third generation squark mass parameter $M_{q,3}$ (top right), and the right handed up-type third generation squark mass parameter $M_{u,3}$ (middle left). Also shown is the fraction of tachyonic models in the plane of M_3 and $M_{u,3}$ (middle right), M_3 and $M_{q,3}$ (bottom left), and $M_{q,3}$ and $M_{u,3}$ (bottom right). The SUSY scale is defined here as $Q_{SUSY} = \sqrt{M_{q,3} \cdot M_{u,3}}$.

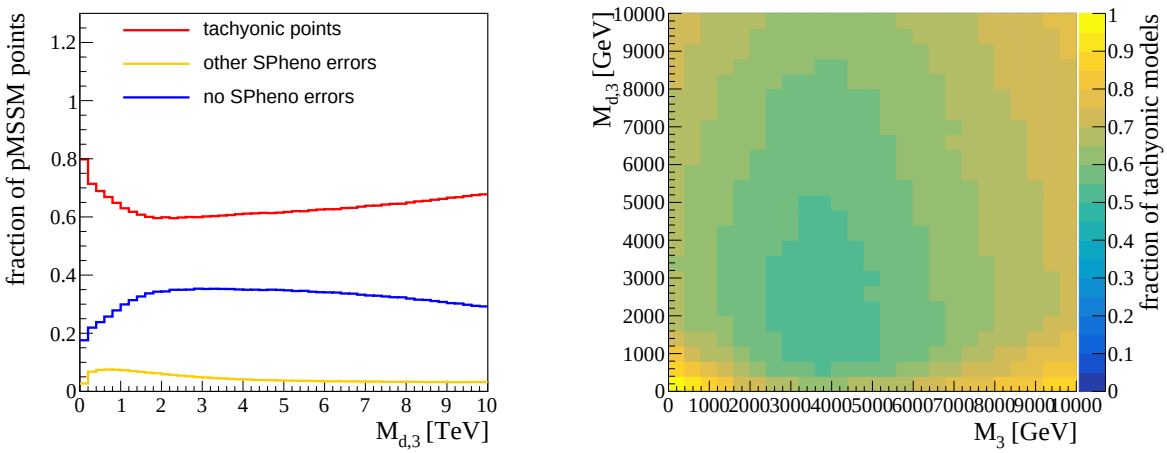

Figure 176: Fraction of tachyonic models, models with other `SPheno` errors, and valid models, projected on the right handed down-type third generation squark mass parameter $M_{d,3}$ (left), and in the plane of $M_{d,3}$ and M_3 (right). The SUSY scale is defined here as $Q_{SUSY} = \sqrt{M_{q,3} \cdot M_{u,3}}$.

Figure 177 shows the first generation squark mass parameters. Over most of the sampled range, the distributions for $M_{q,1}$ and $M_{d,1}$ are almost flat, with only a slight gradual increase in the the tachyonic fraction towards large values. $M_{q,1}$ shows a sharp increase in the tachyonic fraction in the lowest bin, which, due to its location at extremely small masses, is likely caused by genuine tachyons, rather than those caused by limitations of the spectrum generator. Peculiarly, the distributions for $M_{u,1}$ are substantially different from those of all other pMSSM parameters, with a soft minimum of the tachyonic fraction at $M_{u,1} \simeq 6.5\,\text{TeV}$. The distribution of the other `SPheno` errors in completely flat in $M_{u,1}$. The shape of the tachyonic fraction in the plane of $M_{u,1}$ and $M_{q,1}$, which shows diagonal features of equal tachyonic fraction, suggests that the increase of the tachyonic fraction is again correlated or caused by larger and larger mass hierarchies between $M_{u,1}$ and $M_{q,1}$. The opposite effect is seen in the plane of $M_{d,1}$ and $M_{q,1}$, with the edges of equal tachyonic fraction appearing in anti-diagonal features. The region of small $M_{d,1}$ and $M_{q,1}$ exhibits an exceptionally small tachyonic fraction.

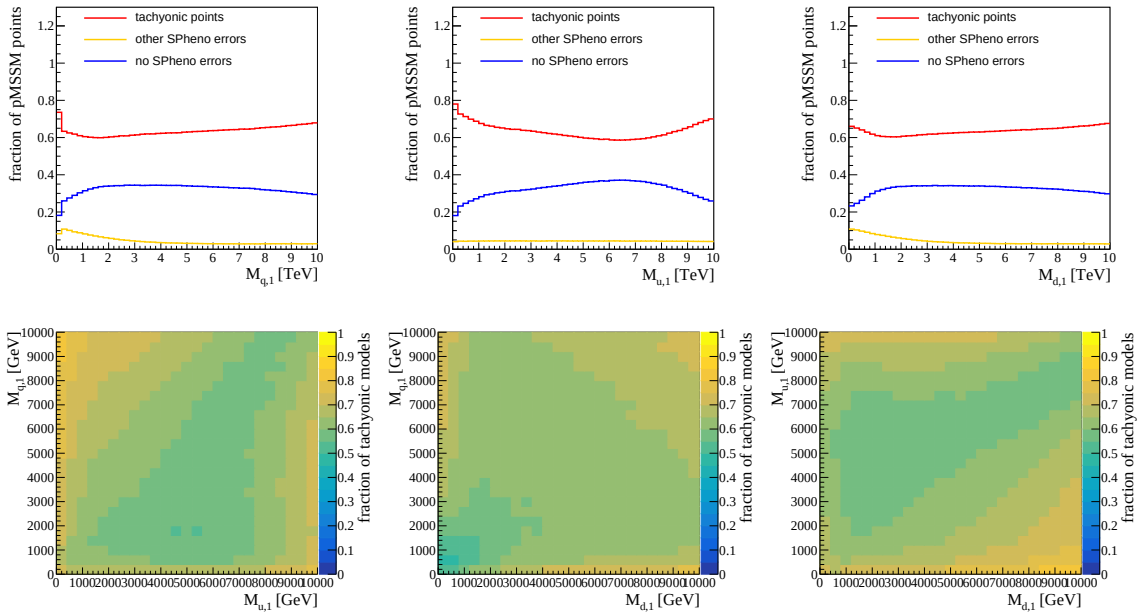

Figure 177: Fraction of tachyonic models, models with other `SPheno` errors, and valid models, projected on the left-chiral first generation squark mass parameter $M_{q,1}$ (top left) and the right-chiral first generation up- (top center) and down (top right) squark mass parameters. Also shown is the fraction of tachyonic models in the plane of $M_{q,1}$ and $M_{u,1}$ (bottom left), $M_{q,1}$ and $M_{u,1}$ (bottom center), and $M_{d,1}$ and $M_{u,1}$ (bottom right). The SUSY scale is defined here as $Q_{\text{SUSY}} = \sqrt{M_{q,3} \cdot M_{u,3}}$.

The distributions for the slepton mass parameters are shown in Figure 178. We see very similar behavior for all the slepton mass parameters, where the tachyonic fraction remains uniform for medium and large values of the slepton mass parameters, and a strong increase towards smaller values. The left-chiral slepton mass parameters $M_{l,1}$ and $M_{l,3}$ exhibit a jump in the tachyonic fraction in the lowest bin that is absent in their right-chiral counterparts, likely due to the additional presence of a sneutrino. The right-chiral slepton mass parameter $M_{r,1}$ shows a much softer increase of the tachyonic fraction, compared to the other parameters. The fact that the distributions are almost completely flat above slepton masses $\gtrsim 1.5\,\text{TeV}$ suggests that the slepton mass parameters are not correlated to tachyon appearing beyond that directly related to its small mass. It further suggests that the tachyons are genuine, as they appear more frequently at smaller and smaller masses, and are not visibly correlated to the SUSY scale. The part of the pMSSM where all slepton masses are heavy, indicated by large values of the minimal slepton mass, shows a flat and comparatively small tachyonic fraction of below 50% for masses above $\min_{\tilde{l}}(m_{\tilde{l}}) \gtrsim 1.4\,\text{TeV}$. On the other hand, the increased tachyonic fraction with smaller individual slepton mass parameter values compounds in the part of the pMSSM where multiple sleptons are light, which is indicated in the most extreme scenarios by the distributions for the maximum slepton mass parameter, $\max_{\tilde{l}}(m_{\tilde{l}})$. The part of the pMSSM where all slepton mass parameters are small is almost entirely tachyonic.

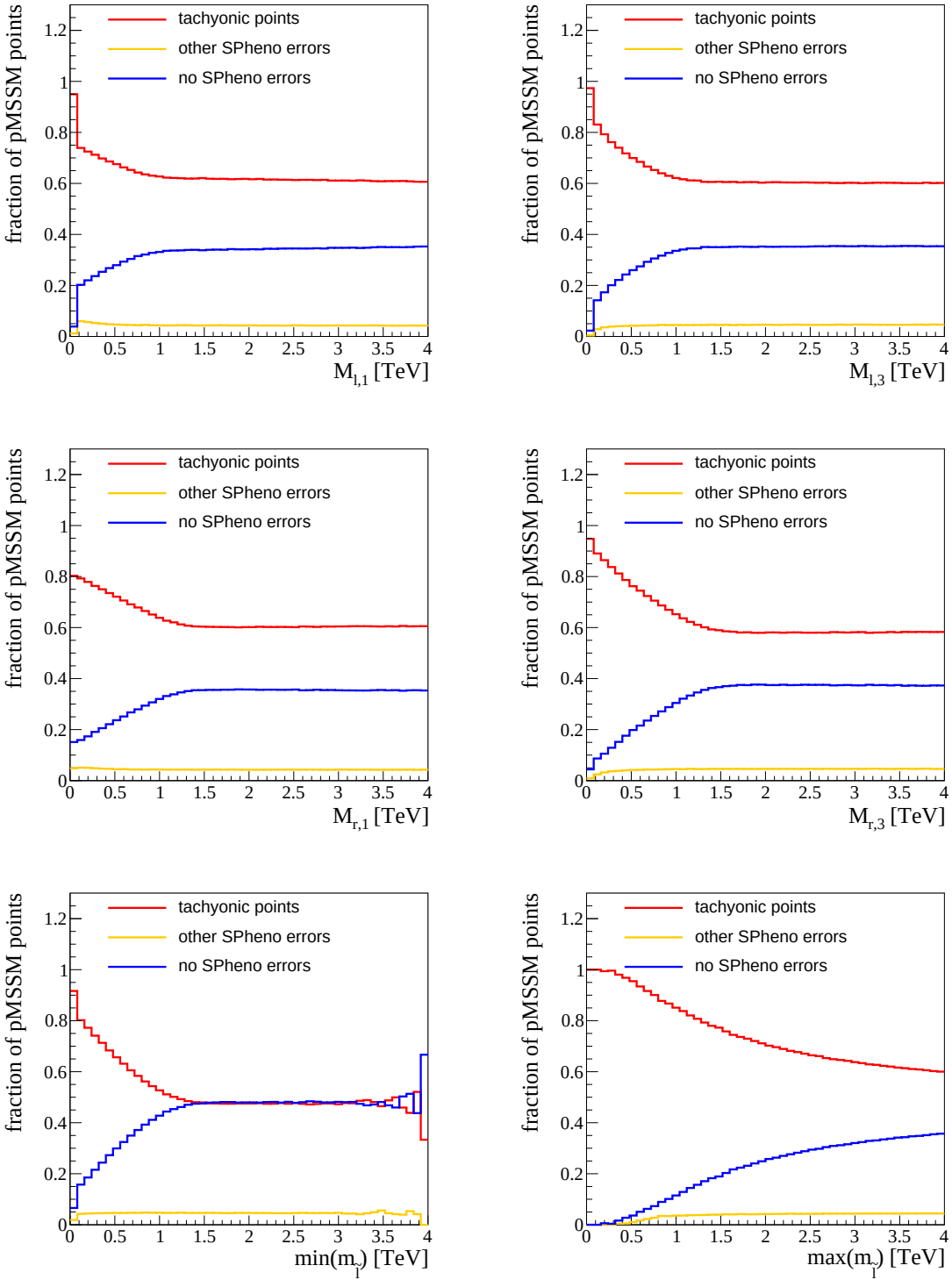

Figure 178: Fraction of tachyonic models, models with other `SPheno` errors, and valid models, projected on the left-handed first generation slepton mass parameter $M_{l,1}$ (top left) and third generation slepton mass parameter $M_{l,3}$ (top right), the right handed first generation (center left) and third generation (center right) slepton mass parameters. Also shown are the projections onto the smallest (bottom left) and largest (bottom right) slepton mass parameters in the pMSSM model, $\min(m_{\tilde{l}})$ and $\max(m_{\tilde{l}})$, respectively. The SUSY scale is defined here as $Q_{SUSY} = \sqrt{M_{q,3} \cdot M_{u,3}}$.

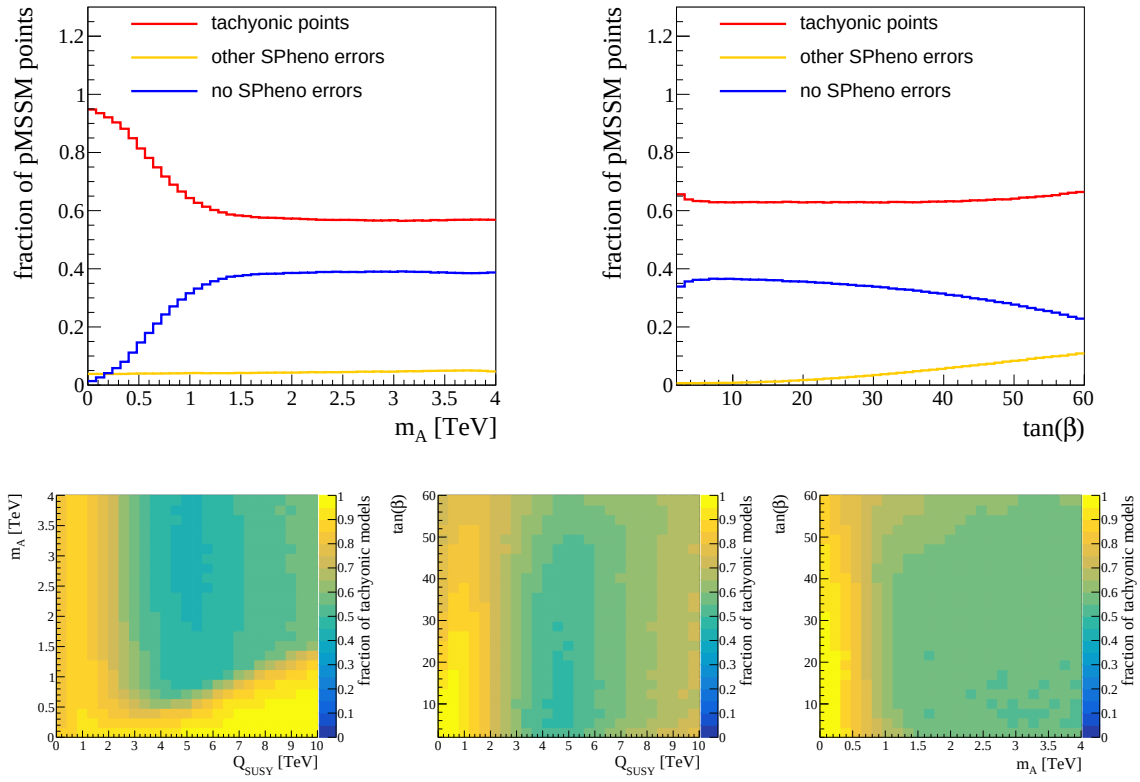

Figure 179: Fraction of tachyonic models, models with other `SPheno` errors, and valid models, projected on the mass of the pseudoscalar Higgs boson m_A (top left), and the ratio of the Higgs field vacuum expectation values $\tan(\beta)$ (top right). Also shown are the projections onto the plane of m_A and Q_{SUSY} (bottom left), the plane of $\tan(\beta)$ and Q_{SUSY} (bottom center), and the plane of $\tan(\beta)$ and m_A (bottom right). The SUSY scale is defined here as $Q_{SUSY} = \sqrt{M_{q,3} \cdot M_{u,3}}$.

We also investigate the pMSSM Higgs sector, which consists of the mass of the pseudoscalar Higgs boson m_A, and the ratio of Higgs field vacuum expectation values $\tan(\beta)$. Their distributions are shown in Figure 179. Similarly to the slepton mass parameters, the tachyonic fraction remains constant for $m_A \gtrsim 1.5\,\text{TeV}$, and increases towards smaller m_A. This suggests that there is no correlation of large m_A to a localized tachyonic region. The increasing fraction of tachyonic models is consistent with the behavior expected of genuine tachyons, which are expected to increase in regions where masses are small. However, there is a strong dependence of the tachyonic fraction on Q_{SUSY} in the region of small m_A. The increase here is similar to what is seen in Figure 173 for the higgsino mass parameter, where the region of small m_A and $Q_{SUSY} \gtrsim 6\,\text{TeV}$ is almost entirely tachyonic. This scale dependence suggests that a large fraction of the tachyonic models at small m_A are tachyonic due to the limitations of `SPheno` (and all other spectrum generators). For $\tan(\beta)$, the tachyonic fraction is mostly flat on average, but the fraction of models with other `SPheno` errors increases steadily towards larger $\tan(\beta)$. There are localized regions where the tachyonic fraction is noticeably large, namely at small $\tan(\beta)$ and small Q_{SUSY}, and small m_A, respectively.

As a final point, the trilinear couplings do not show significant correlation to tachyons in the pMSSM, or other errors given by `SPheno`.

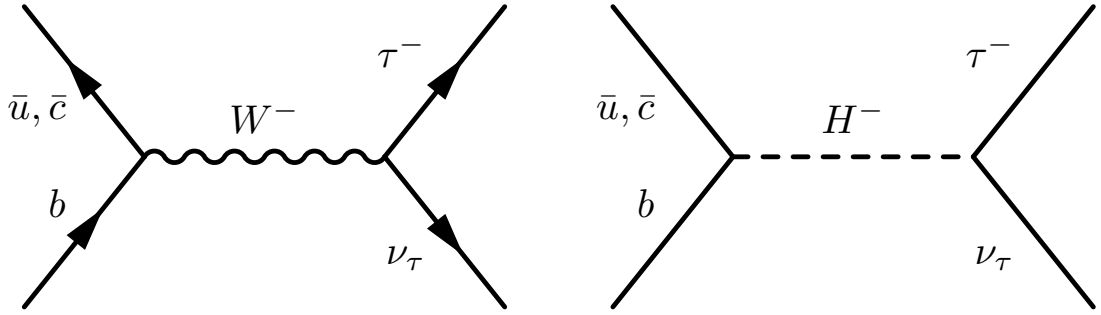

Figure 180: Feynman diagram for the leptonic decay of charged B-mesons into a tauon final state for the SM (left) and an example contribution in the MSSM (right).

C Low-energy observable impact

In this part of the appendix, we cover the impact of the remaining low-energy observables included in the McMC in detail.

C.1 BR(B $\to \tau\nu$)

The McMC includes measurements of the leptonic decay of B-mesons into a tauon final state. Example Feynman diagrams for the principle SM process and a MSSM contribution are shown in Figure 180. BR(B $\to \tau\nu$) has been measured to BR(B $\to \tau\nu$) $= (1.44 \pm 0.31) \times 10^{-4}$ [106], while the standard model prediction of BR(B $\to \tau\nu)_{SM} = (0.84 \pm 0.11) \times 10^{-4}$ [161] prefers a smaller value. Positive contributions to BR(B $\to \tau\nu$) are thus preferred by the measurement, while negative contributions are disfavored.

Figure 181 shows the impact of BR(B $\to \tau\nu$) on the electroweakino sector. For $|\mu|$, no significant deviation of the LEO prior from the LEO prior+BR(B $\to \tau\nu$) is seen. However, comparing the distribution of the full LEO posterior to the LEO posterior-BR(B $\to \tau\nu$), we see that inclusion of BR(B $\to \tau\nu$) disfavors small masses of $|\mu|$ in the residual pMSSM constrained by the other observables. There is also a small impact on the wino mass parameter M_2, where small M_2 are disfavored in favor of the large positive M_2 region.

This results in a small change in the distribution of the mass of the lightest neutralino, where masses between $m(\widetilde{\chi}_1^0) \simeq 100$ GeV and $m(\widetilde{\chi}_1^0) \simeq 500$ GeV are slightly disfavored in the LEO posterior. It is peculiar that both the prior+BR(B $\to \tau\nu$) and the posterior-BR(B $\to \tau\nu$) show very similar distributions, which means that they tend to favor and disfavor the same regions in $m(\widetilde{\chi}_1^0)$, but the full posterior significantly differs from all three other distributions. This suggests that there is a substantial difference between the LEO prior and the LEO posterior-BR(B $\to \tau\nu$) that does not show up in the marginalized 1-dimensional distributions, but which causes a shift of the same when BR(B $\to \tau\nu$) is included in the full LEO posterior. A similar effect can be seen on the distribution of the mass of the lighter chargino $m(\widetilde{\chi}_1^\pm)$. In addition to the suppression at small $m(\widetilde{\chi}_1^\pm)$, including BR(B $\to \tau\nu$) with the other LEO observables results in a slightly increased probability density at $m(\widetilde{\chi}_1^\pm) \simeq 1.5$ TeV, which is caused by a similar increase in the distribution of $|\mu|$ in the same mass range. Thus, the inclusion of BR(B $\to \tau\nu$) partially causes the difference between the LEO prior and the LEO posterior in this region. As is the case in terms of the distribution of $m(\widetilde{\chi}_1^0)$, BR(B $\to \tau\nu$) only seems to have an impact when combined with the other LEO observables.

Figure 182 shows the impact of BR(B $\to \tau\nu$) on the heavy Higgs boson masses m_A and the trilinear coupling A_t. The mass of the heavy Higgs bosons are significantly shifted towards larger masses, both when BR(B $\to \tau\nu$) impacts the prior and when it impacts the LEO posterior-BR(B $\to \tau\nu$). This means that in terms m_A, BR(B $\to \tau\nu$) and the other observables suppress the small-m_A region – the observables do not compete in their impacts. As a result, almost no models remain with $m_A \lesssim 1$ TeV. At the same time, the distribution of $\tan(\beta)$ is significantly shifted towards smaller values by the inclusion of BR(B $\to \tau\nu$) in both the LEO prior, and the LEO posterior-BR(B $\to \tau\nu$).

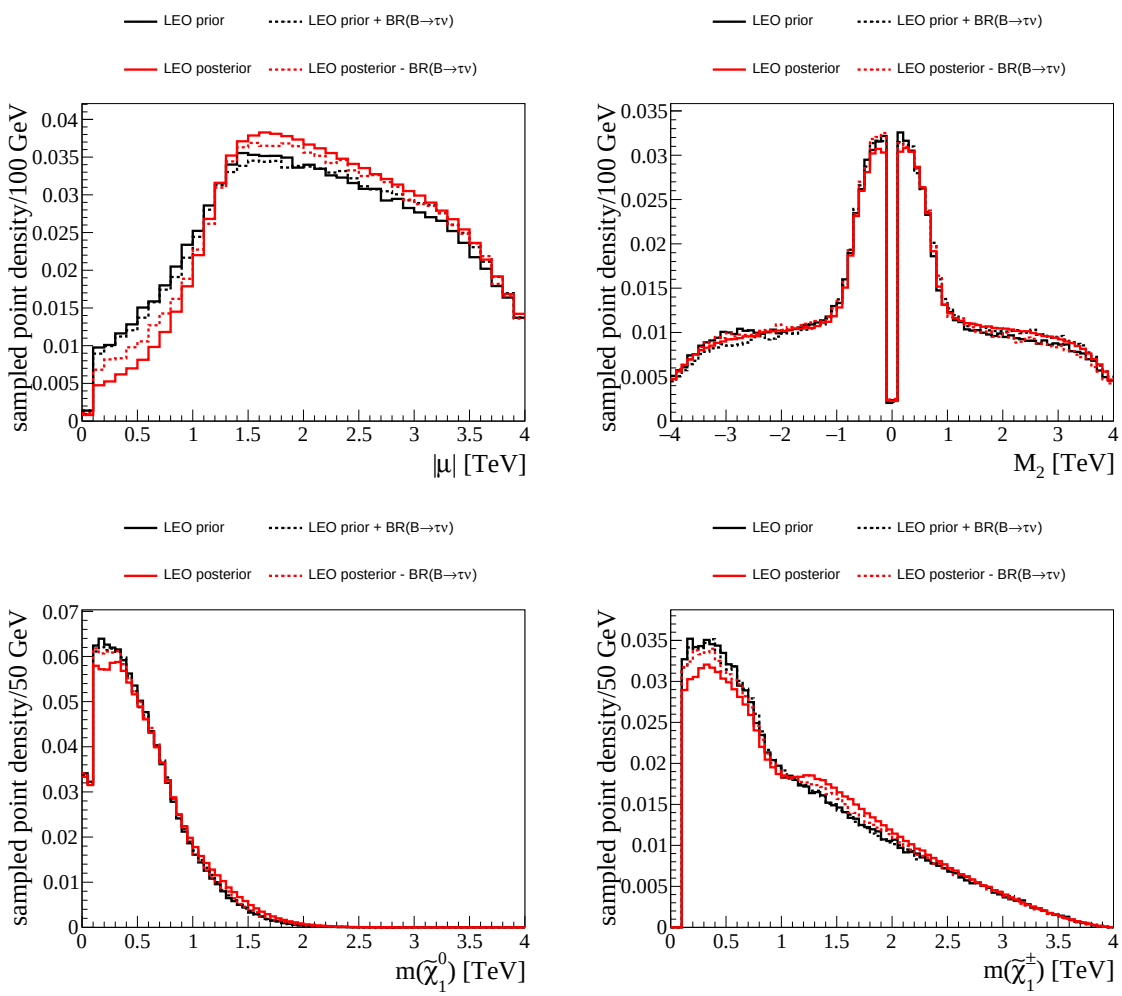

Figure 181: Distributions of the absolute value of the mass of the higgsino mass parameter $|\mu|$ (top left), the wino mass parameter M_2 (top right), and the masses of the lightest neutralino $\widetilde{\chi}_1^0$ (bottom left) and chargino $\widetilde{\chi}_1^\pm$ (bottom right). For each parameter, the distribution for the LEO prior (black), the LEO prior+BR(B $\to \tau\nu$) (dashed black), the LEO posterior (red), and the LEO posterior-BR(B $\to \tau\nu$) (dashed red), are shown.

These two effects can be understood in terms of the MSSM contribution to the B-meson decay shown in Figure 180, which interferes destructively with the SM decay via a W-boson. The MSSM contribution to BR(B $\to \tau\nu$) via charged Higgs bosons becomes larger for smaller m_A and larger $\tan(\beta)$ (compare also [161]).

The inclusion of BR(B $\to \tau\nu$) also has a small effect on the trilinear coupling A_t, where it favors larger and positive A_t. As with the distributions in $m(\widetilde{\chi}_1^0)$, there is no visible difference between the LEO prior and the LEO prior+BR(B $\to \tau\nu$) in the distribution of A_t. This again suggests that there are substantial differences between the LEO prior and the LEO posterior-BR(B $\to \tau\nu$) that are not visible in the marginalized 1-dimensional distributions.

Lastly, there is a significant effect on the distributions of the third generation squark mass parameters, shown in Figure 183. While the effect of BR(B $\to \tau\nu$) on the LEO prior is negligible, it significantly disfavors small stop masses in the residual space given by the LEO posterior-BR(B $\to \tau\nu$). The sbottom mass parameter $M_{d,3}$ is affected in the opposite way, where large values of $M_{d,3}$ are slightly disfavored by BR(B $\to \tau\nu$). Because both $M_{q,3}$ and $M_{d,3}$ contribute to the sbottom mass eigenstates, we observe only a slight shift in the distribution of $\widetilde{b}_1$ that disfavors both small and large $m(\widetilde{b}_1)$.

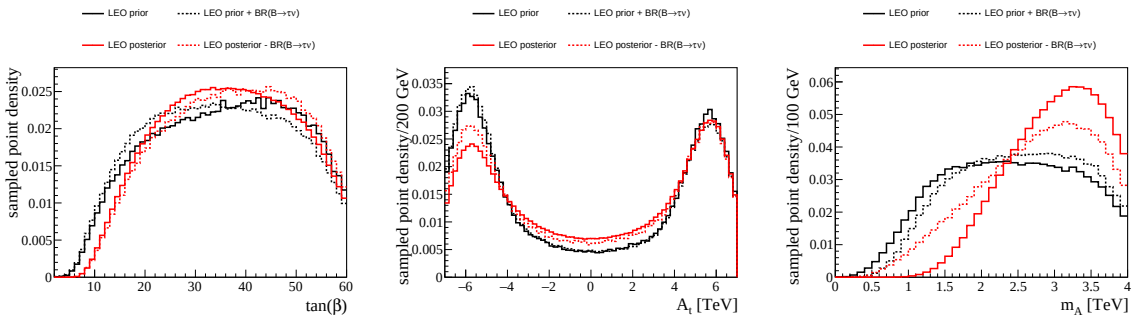

Figure 182: Distributions of the mass of the ratio of Higgs field vacuum expectation values tan(β) (left), the trilinear Higgs-stop coupling A_t (center), and the mass of the heavy Higgs bosons m_A (right). For each parameter, the distribution for the LEO prior (black), the LEO prior+BR(B $\to \tau\nu$) (dashed black), the LEO posterior (red), and the LEO posterior-BR(B $\to \tau\nu$) (dashed red), are shown.

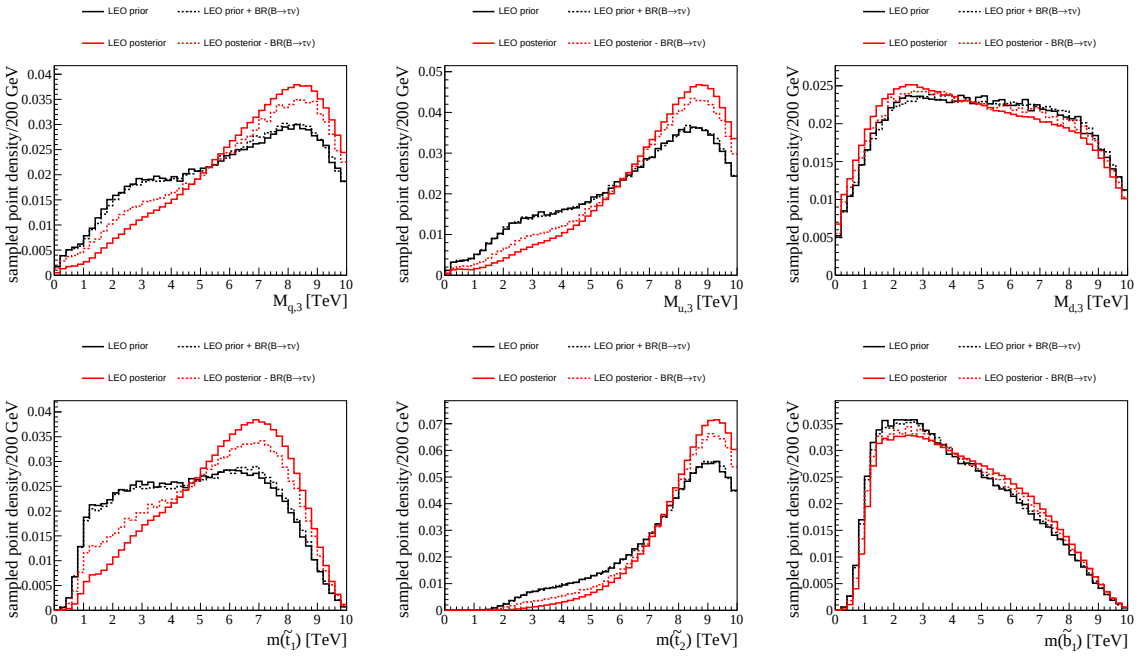

Figure 183: Distributions of the left-chiral third generation squark mass parameter $M_{q,3}$ (top left), the right-chiral stop mass parameter $M_{u,3}$ (top center) and sbottom mass parameters $M_{d,3}$ (top right), the lighter (bottom left) and heavier (bottom center) stop masses $\widetilde{t}_1$ and $\widetilde{t}_2$, as well as the lighter sbottom mass $\widetilde{b}_1$ (bottom right). For each parameter, the distribution for the LEO prior (black), the LEO prior+BR(B $\to \tau\nu$) (dashed black), the LEO posterior (red), and the LEO posterior-BR(B $\to \tau\nu$) (dashed red), are shown.

C.2 BR(B → Xsee) and BR(B → Xs$\mu\mu$)

The b→s transition has also been measured in the di-leptonic final state. Example Feynman diagrams for the SM and MSSM contributions are shown in Figure 184. These are understood to occur in the context of B-meson decays for this constraint.

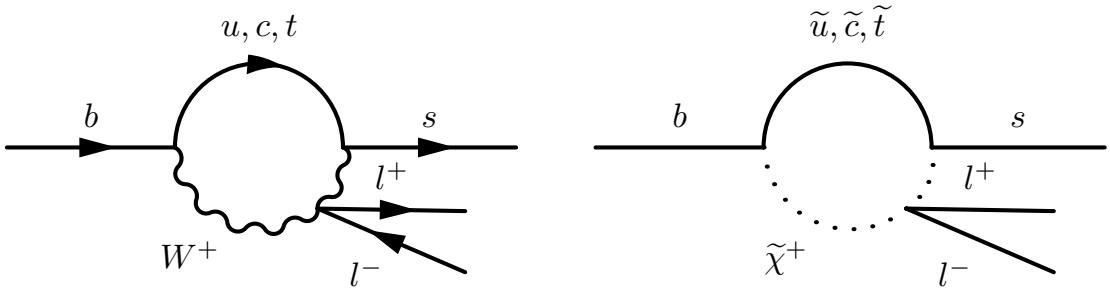

Figure 184: Example Feynman diagrams for the b→s transition with a di-leptonic final state in the SM (left), and a MSSM contribution (right).

Constraints from measurements of the branching ratios

$$\mathrm{BR(B \to Xsee)} = \begin{cases} (1.96 \pm 0.55) \times 10^{-6} & \text{small q} \\ (0.56 \pm 0.19) \times 10^{-6} & \text{large q} \end{cases} \text{[99, 100, 101]}$$

and

$$\mathrm{BR(B \to Xs\mu\mu)} = \begin{cases} (0.66 \pm 0.88) \times 10^{-6} & \text{small q} \\ (0.6 \pm 0.31) \times 10^{-6} & \text{large q} \end{cases} \text{[99, 100, 101]}$$

only noticeably impact the distribution of the mass of the heavy Higgs bosons, shown in Figure 185. Small masses are disfavored when both BR(B → Xsee) and BR(B → Xs$\mu\mu$) are included in the McMC, as seen in the difference of the distributions for the LEO posterior and the LEO posterior-BR(B → Xsee)and the LEO posterior-BR(B → Xs$\mu\mu$), respectively. A similar impact is not seen when only one of either BR(B → Xsee) or BR(B → Xs$\mu\mu$) is included on top of the LEO prior, which suggests that the other observables prefer a region of the pMSSM that is slightly disfavored by the combination of both BR(B → Xsee) and BR(B → Xs$\mu\mu$).

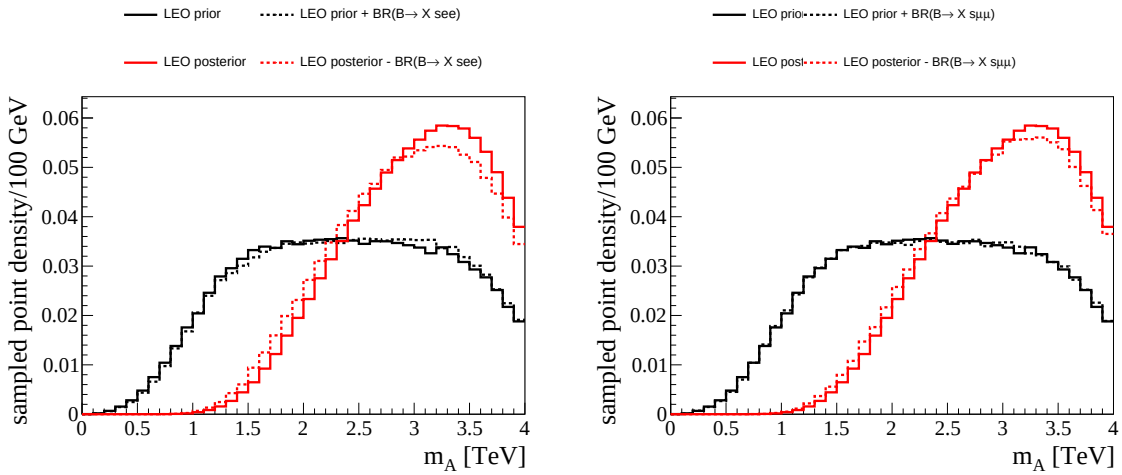

Figure 185: Distribution of the mass of the pseudoscalar Higgs boson m_A for constraints from BR(B → Xsee) (left) and BR(B → Xs$\mu\mu$) (right). The distribution for the LEO prior (black), the LEO prior+BR(B → Xsee) or BR(B → Xs$\mu\mu$) (dashed black), the LEO posterior (red), and the LEO posterior-BR(B → Xsee) or BR(B → Xs$\mu\mu$) (dashed red), are shown.

C.3 $\mathbf{BR(B^0 \to K^{*0}\gamma)}$

The observable $BR(B^0 \to K^{*0}\gamma)$ is an exclusive decay that is part of the inclusive $BR(b \to s\gamma)$ observable. Example Feynman diagrams of the processes in the SM and MSSM that underlie the measurement can be found in Figure 36.

The measurement $BR(B^0 \to K^{*0}\gamma) = (4.33 \pm 0.15) \times 10^{-5}$ [102] has a peculiar impact on many of the pMSSM parameters and particles masses, stretching across the colored, electroweak, and Higgs sector of the pMSSM. In most of the distributions, the LEO prior+$BR(B^0 \to K^{*0}\gamma)$, the LEO posterior-$BR(B^0 \to K^{*0}\gamma)$, and the LEO posterior are very similar. This means that the observable is quite impactful, since its lone inclusion induces most of the shift from LEO prior to LEO posterior. However, its removal from the full likelihood does not impact the probability density, as the distributions of the LEO posterior and the LEO posterior-$BR(B^0 \to K^{*0}\gamma)$ are almost identical. The reason for this is likely that $BR(B^0 \to K^{*0}\gamma)$ is very correlated, or even included in, the much more inclusive observable $BR(b \to s\gamma)$. Because the correlations are treated by `SuperIso`, removal of $BR(B^0 \to K^{*0}\gamma)$ does not result in large changes in many marginalized 1-dimensional distributions.

We start with the impact on the electroweak sector, which is shown in Figure 186. The impact at small $|\mu|$ shifts the probability density to the full posterior density, even when only $BR(B^0 \to K^{*0}\gamma)$ is included. At larger $|\mu|$, the LEO prior+$BR(B^0 \to K^{*0}\gamma)$ starts to deviate from the LEO posterior density, as $BR(B^0 \to K^{*0}\gamma)$ prefers larger values of $|\mu|$. In the distributions of the masses of the lightest two neutralinos and the lighter chargino, there is remarkable agreement between the distributions of the LEO prior+$BR(B^0 \to K^{*0}\gamma)$ and the LEO posterior. This suggests that $BR(B^0 \to K^{*0}\gamma)$ is a dominant observable in terms of impacting the electroweakino mass distributions. We see almost no difference between the LEO posterior-$BR(B^0 \to K^{*0}\gamma)$ and the full LEO posterior, likely because of the strong correlation between $BR(B^0 \to K^{*0}\gamma)$ and $BR(b \to s\gamma)$.

We see a similar impact on the third-generation squarks, shown in Figure 187. The distributions of the stop mass parameters $M_{q,3}$ and $M_{u,3}$, as well as the mass of the lighter stop $m(\widetilde{t}_1)$, are strongly shifted towards larger masses. The inclusion of $BR(B^0 \to K^{*0}\gamma)$ alone does not explain the whole difference between the LEO prior and LEO posterior however. This is different for the right-chiral sbottom mass parameter $M_{d,3}$ and the sbottom mass $m(\widetilde{b}_1)$, where the much less pronounced impact aligns the LEO prior+$BR(B^0 \to K^{*0}\gamma)$ with the full LEO posterior. As already seen for the electroweakino masses, the removal of $BR(B^0 \to K^{*0}\gamma)$ in the LEO posterior-$BR(B^0 \to K^{*0}\gamma)$ does not noticeably change the distribution, likely due to its correlation to $BR(b \to s\gamma)$.

An impact of $BR(B^0 \to K^{*0}\gamma)$ is also seen on the first (and second) generation squarks, shown in Figure 188. The left-chiral squarks are particularly strongly affected, with the small-mass region suppressed in both $M_{q,1}$ and $m(\widetilde{u}_L, \widetilde{c}_L)$. Note that in the pMSSM, the second generation mass parameters are degenerate with the first generation mass parameters, and the left-chiral down squarks are almost degenerate to the left-chiral up squarks. The impact more realistically comes from sensitivity to the scharm $\widetilde{c}_L$ and sstrange $\widetilde{s}_L$, rather than to $\widetilde{u}_L$ and $\widetilde{d}_L$. While the impact on the right-chiral squark mass parameters is much less, only including $BR(B^0 \to K^{*0}\gamma)$ in the likelihood does result in distributions that are very close to the full LEO posterior. As previously seen for other parameters, the marginalized 1-dimensional distributions of the LEO posterior-$BR(B^0 \to K^{*0}\gamma)$ are nearly identical to the LEO posterior.

Finally, there is an impact on the Higgs sector, shown in Figure 189. The inclusion of $BR(B^0 \to K^{*0}\gamma)$ on the prior suppresses large A_t particularly the negative regime. Small values of A_t are slightly favored. In contrast to most of the other parameters, there is a slight difference of the LEO posterior-$BR(B^0 \to K^{*0}\gamma)$ and the full LEO posterior, where the LEO posterior-$BR(B^0 \to K^{*0}\gamma)$ is slightly more asymmetric, favoring large positive A_t. There is a notable difference in terms of $\tan(\beta)$, which shows that $BR(B^0 \to K^{*0}\gamma)$ prefers smaller $\tan(\beta)$ than either the LEO prior, or the LEO posterior. Lastly, $BR(B^0 \to K^{*0}\gamma)$ strongly suppresses small m_A. In contrast to many of the other observables, the distributions of the LEO prior+$BR(B^0 \to K^{*0}\gamma)$ and the full posterior are noticeably different in m_A, which shows that other observables have a significant impact on the posterior density.

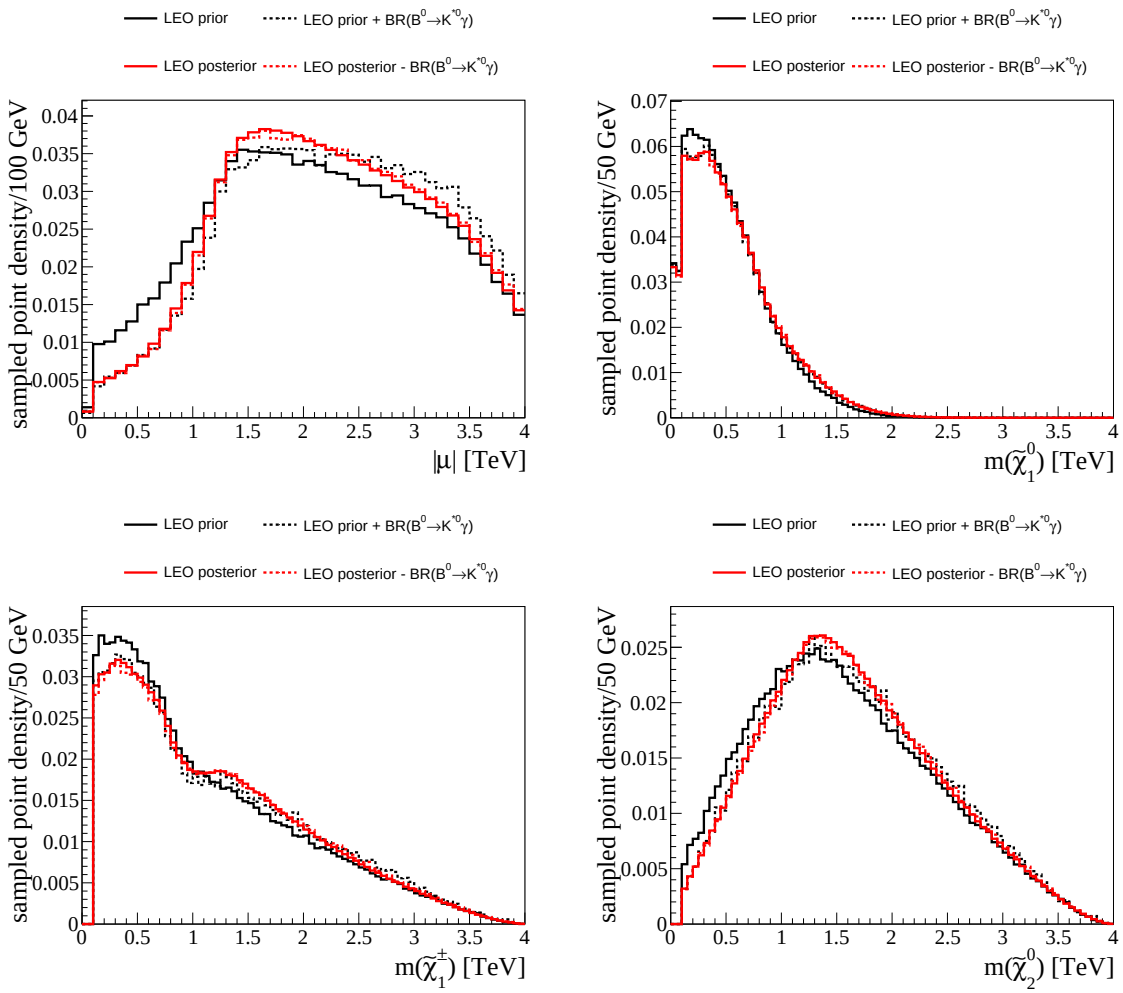

Figure 186: Distributions of the absolute value of the higgsino mass parameter $|\mu|$ (top left), the mass of the lightest neutralino $m(\tilde{\chi}_1^0)$ (top right), the mass of the lighter chargino $m(\tilde{\chi}_1^\pm)$ (bottom left), and the mass of the second lightest neutralino $m(\tilde{\chi}_2^0)$ (bottom right). The distributions are shown for the LEO prior (black), the LEO prior+BR($B^0 \to K^{*0}\gamma$) (dashed black), the LEO posterior (red), and the LEO posterior-BR($B^0 \to K^{*0}\gamma$) (dashed red).

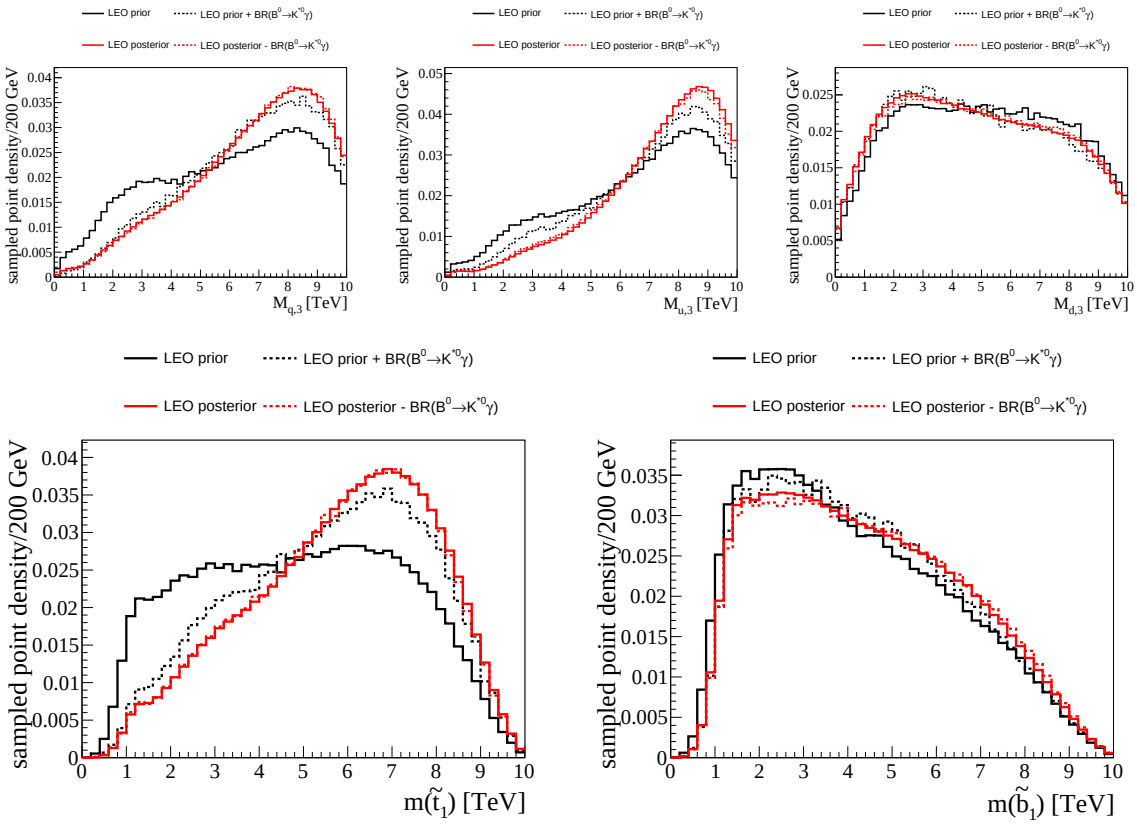

Figure 187: Distributions of the left-chiral third generation squark mass parameter $M_{q,3}$ (top left), the right-chiral stop mass parameter $M_{u,3}$ (top center), the right-chiral sbottom mass parameter $M_{d,3}$ (top right), as well as the mass of the lighter stop $m(\tilde{t}_1)$ (bottom left), and the mass of the lighter sbottom $m(\tilde{b}_1)$ (bottom right). The distributions are shown for the LEO prior (black), the LEO prior+BR($B^0 \to K^{*0}\gamma$) (dashed black), the LEO posterior (red), and the LEO posterior-BR($B^0 \to K^{*0}\gamma$) (dashed red).

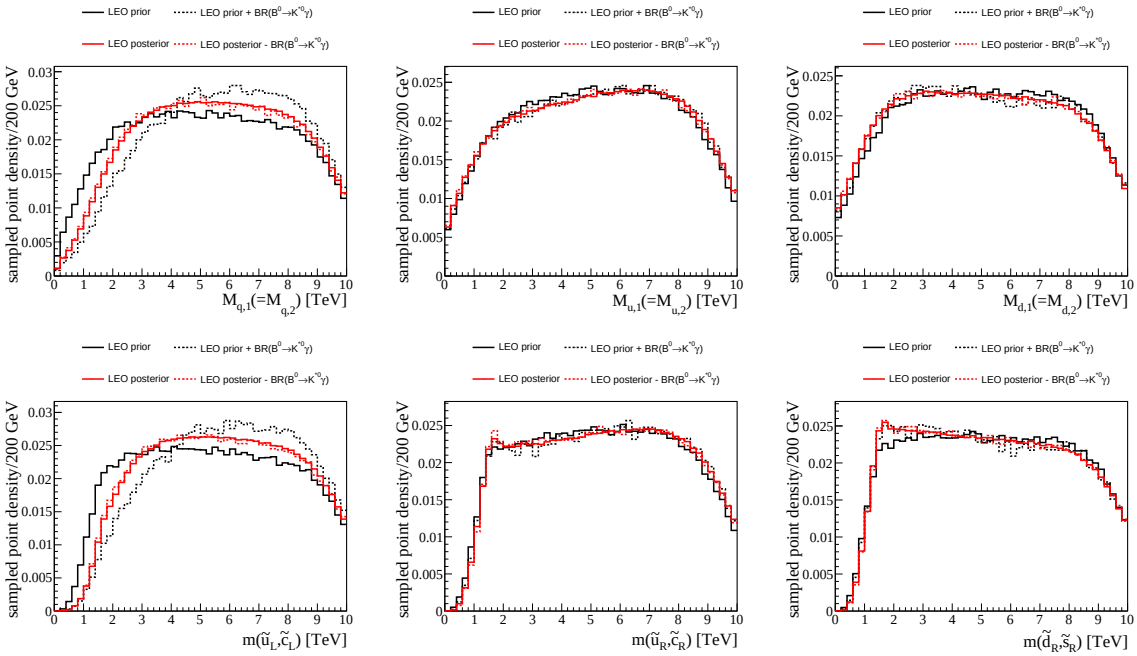

Figure 188: Distributions of the left-chiral first generation squark mass parameter $M_{q,1}$ (top left), the right-chiral sup mass parameter $M_{u,1}$ (top center), the right-chiral sdown mass parameter $M_{d,1}$ (top right), as well as the mass of the left-chiral sup $m(\tilde{u}_L, \tilde{c}_L)$ (bottom left), the mass of the right-chiral sup $m(\tilde{u}_R, \tilde{c}_R)$ (bottom center), and the mass of the right-chiral sdown $m(\tilde{d}_R, \tilde{s}_R)$ (bottom right). The distributions are shown for the LEO prior (black), the LEO prior+BR($B^0 \to K^{*0}\gamma$) (dashed black), the LEO posterior (red), and the LEO posterior-BR($B^0 \to K^{*0}\gamma$) (dashed red). Note that the first two generations of sfermions are mass degenerate in the pMSSM, as well as the left-chiral up- and down-type squarks in the first two generations.

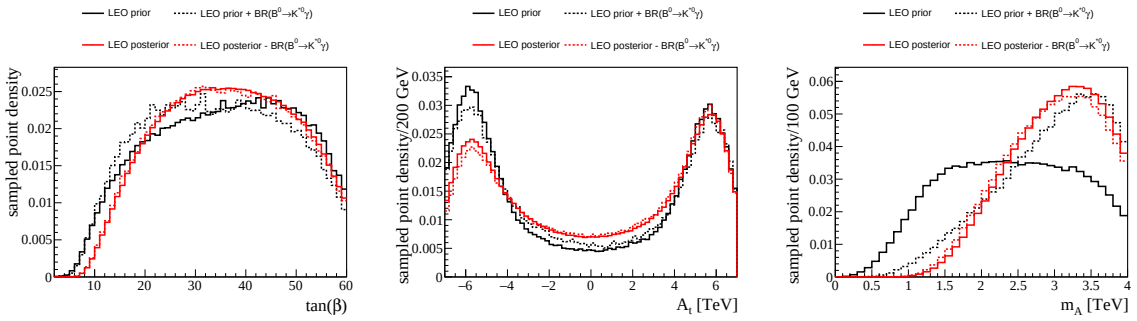

Figure 189: Distributions of the ratio of the Higgs field vacuum expectation values $\tan(\beta)$ (left), the stop trilinear coupling A_t (center), and the mass of the heavy Higgs bosons mA (right). The distributions are shown for the LEO prior (black), the LEO prior+BR($B^0 \to K^{*0}\gamma$) (dashed black), the LEO posterior (red), and the LEO posterior-BR($B^0 \to K^{*0}\gamma$) (dashed red).

C.4 $\Delta(\rho)$

In the SM, the masses of the W and Z boson are fixed by the Weinberg angle θ_W, such that

$$M_Z = \frac{M_W}{\cos(\theta_W)} [107]. \tag{29}$$

This equation can be parameterized in terms of the coefficient ρ:

$$\rho = \frac{M_W}{M_Z \cos(\theta_W)}. \tag{30}$$

Processes in the MSSM can modify that relation, which leads to a contribution $\Delta(\rho)$ that can be constrained by measurement. The measurement of $\Delta(\rho) = (3.9 \pm 1.9) \times 10^{-4}$ [107] impacts the electroweakino sector, the third and first generation squarks, as well as the Higgs sector. Figure 190 shows the impact on the higgsino mass parameter, and the lightest neutralino and chargino masses. Small values of the higgsino mass parameter are disfavored when $\Delta(\rho)$ is included on top of the LEO posterior-$\Delta(\rho)$, which also disfavors small masses of $m(\widetilde{\chi}_1^0)$ and $m(\widetilde{\chi}_1^\pm)$. The mode of the $m(\widetilde{\chi}_1^\pm)$ distribution at $m(\widetilde{\chi}_1^\pm) \gtrsim 1\,\text{TeV}$, which is a consequence of the increasing distribution of $|\mu|$ and contains more higgsino-like models, is slightly enhanced as well.

Figure 191 shows the impact of $\Delta(\rho)$ on the third generation squarks. As previously seen for other LEO observables, the inclusion of $\Delta(\rho)$ disfavors small stop masses. The effect is much larger when $\Delta(\rho)$ constrains the pMSSM in conjunction with the other LEO observables, as indicated by the difference between the LEO posterior-$\Delta(\rho)$ and the full LEO posterior. The effect on the left- and right-chiral stops, as well as the physical stop mass is here comparably strong. The inclusion of $\Delta(\rho)$ alongside the other LEO observables also somewhat disfavors large values of the sbottom mass parameter $\mathrm{M_{d,3}}$. The net effect on the physical sbottom mass from impacts on the left-chiral and right-chiral mass parameters is a suppression of small and intermediate sbottom masses, which is contrary to the impact on $\mathrm{M_{d,3}}$. This indicates that the right-chiral component of the lighter sbottom is made more important at small masses by the inclusion of $\Delta(\rho)$, but only when considered alongside the other LEO observables.

The impact on the first generation squarks is shown in Figure 192. Only the left-chiral parameters are affected, where the small-mass region of $\mathrm{M_{q,1}}$ and the left-chiral squarks are suppressed. As has already been found on a couple of other occasions, there only seems to be an effect when $\Delta(\rho)$ is included along with the other LEO observables, as the LEO prior and the LEO prior+$\Delta(\rho)$ do not substantially differ in these marginalized distributions.

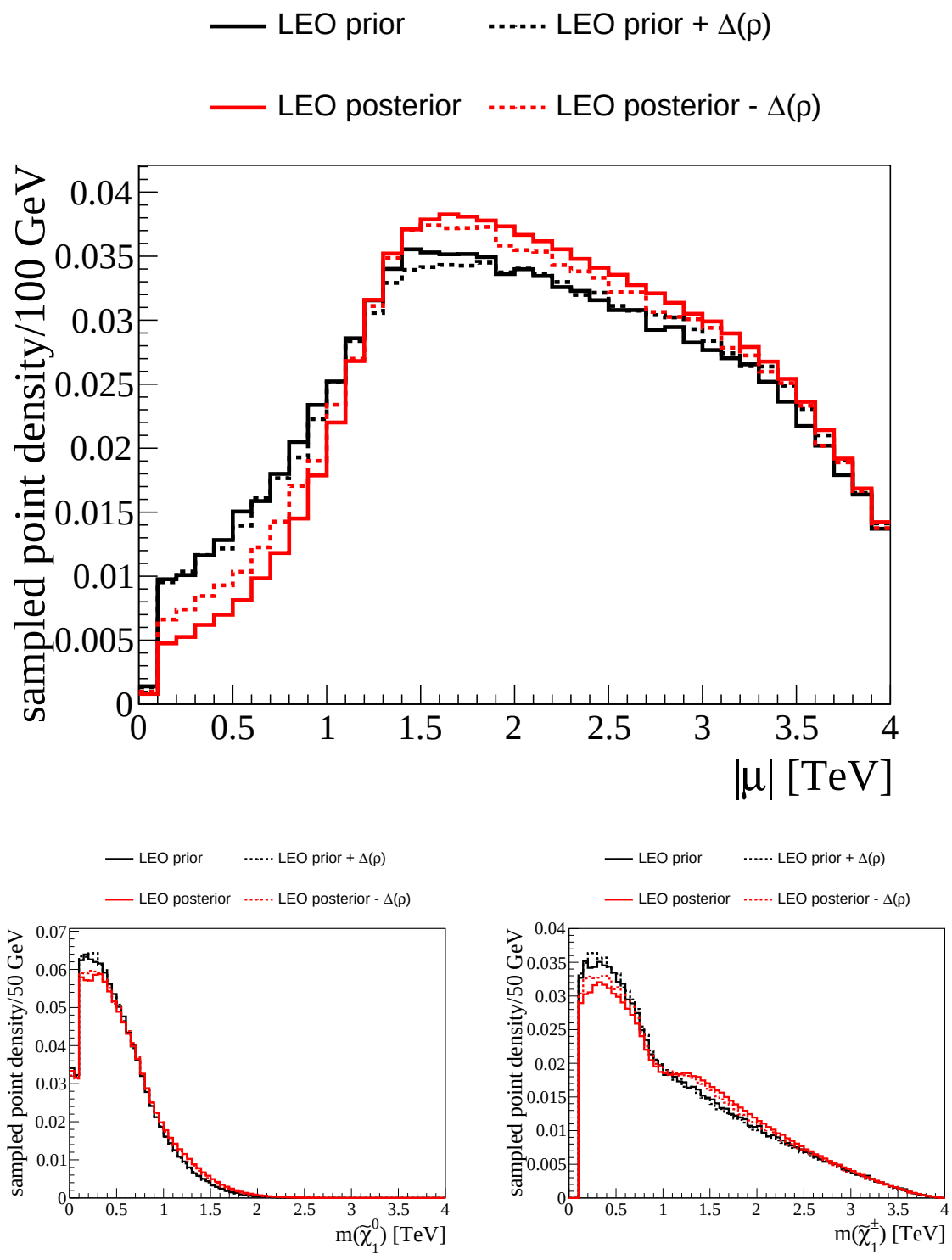

Figure 190: Distributions of the absolute mass of the higgsino mass parameter $|\mu|$ (top), and the masses of the lightest neutralino $m(\tilde{\chi}_1^0)$ (bottom left) and the lighter chargino $m(\tilde{\chi}_1^\pm)$ (bottom right). The distributions are shown for the LEO prior (black), the LEO prior+$\Delta(\rho)$ (dashed black), the LEO posterior (red), and the LEO posterior-$\Delta(\rho)$ (dashed red).

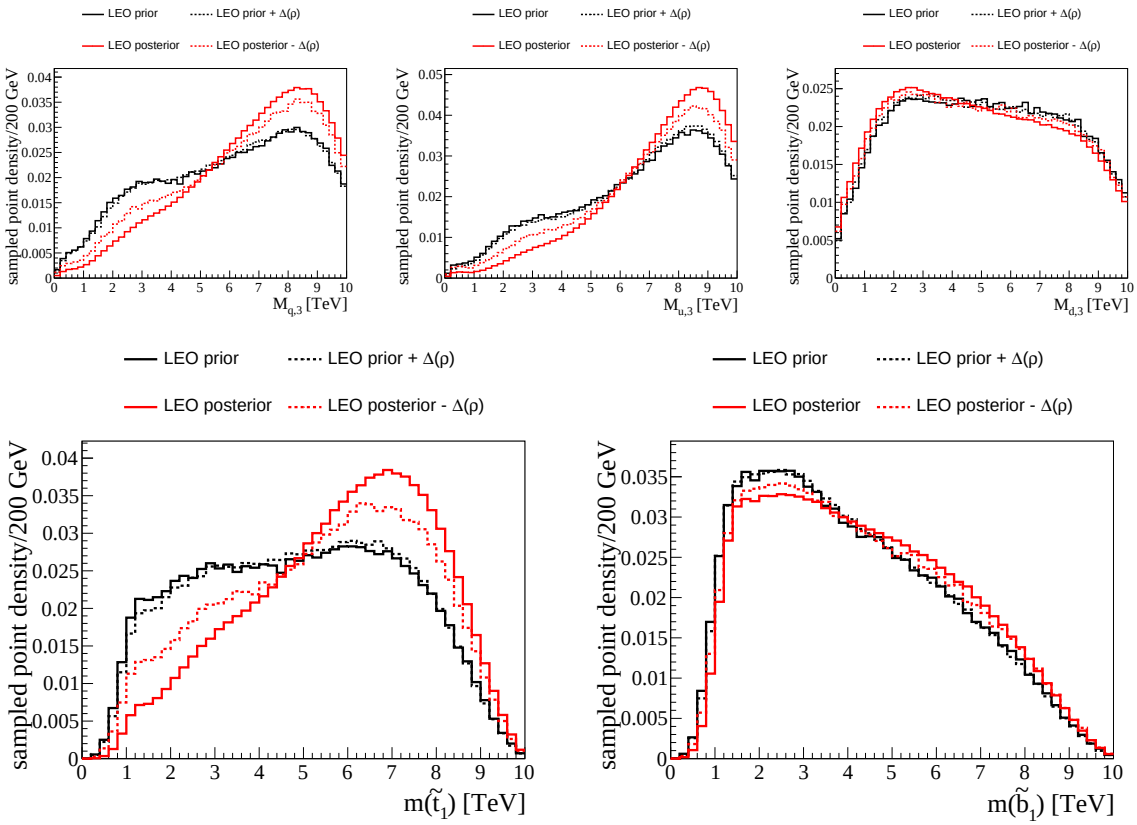

Figure 191: Distribution of the left-chiral third generation squark mass parameter $M_{q,3}$ (top left), the right-chiral stop mass parameter $M_{u,3}$ (top center), the right-chiral sbottom mass parameter $M_{d,3}$ (top right), as well as the resulting lighter stop mass $m(\tilde{t}_1)$ (bottom left) and sbottom mass $m(\tilde{b}_1)$ (bottom right). The distributions are shown for the LEO prior (black), the LEO prior+$\Delta(\rho)$ (dashed black), the LEO posterior (red), and the LEO posterior-$\Delta(\rho)$ (dashed red).

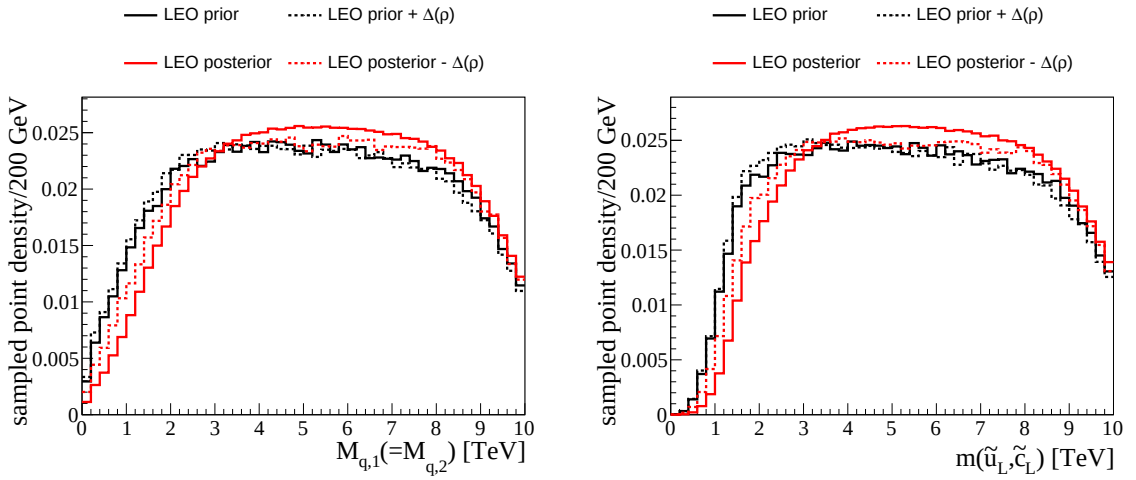

Figure 192: Distributions of the left-chiral first generation squark mass parameter $M_{q,1}$(left) and the left-chiral squark mass $m(\tilde{u}_L, \tilde{c}_L)$. The distributions are shown for the LEO prior (black), the LEO prior+$\Delta(\rho)$ (dashed black), the LEO posterior (red), and the LEO posterior-$\Delta(\rho)$ (dashed red). Note that the first two generations of sfermions are mass degenerate in the pMSSM, as well as the left-chiral up- and down-type squarks in the first two generations.

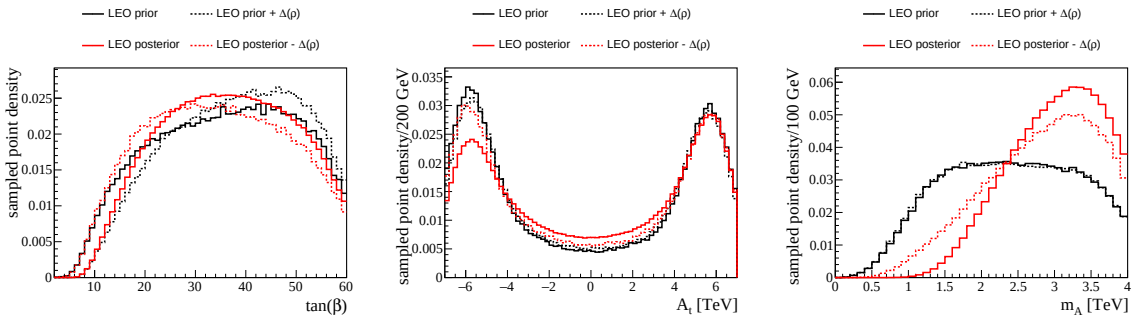

Figure 193: Distributions of the ratio of Higgs vacuum expectation values $\tan(\beta)$(left), the trilinear Higgs-stop coupling A_t (center), and the mass of the heavy Higgs bosons m_A (right). The distributions are shown for the LEO prior (black), the LEO prior+$\Delta(\rho)$ (dashed black), the LEO posterior (red), and the LEO posterior-$\Delta(\rho)$ (dashed red).

Finally, the impact on the Higgs sector is shown in Figure 193. Small values of $\tan(\beta)$ are significantly disfavored by $\Delta(\rho)$, so much so that the distribution in the LEO prior+$\Delta(\rho)$, where the McMC has a lot of freedom to conform to the $\Delta(\rho)$ constraint, prefers even larger values of $\tan(\beta)$ than in the full LEO posterior. Without the inclusion of $\Delta(\rho)$, the net impact of the other observables is to push the probability density towards smaller $\tan(\beta)$, as can be inferred from the distribution of the LEO posterior-$\Delta(\rho)$, which prefers smaller $\tan(\beta)$ compared to the LEO prior. Thus, the observable $\Delta(\rho)$ is the dominant contributor to the preference of large $\tan(\beta)$ in the full LEO posterior.

The observable $\Delta(\rho)$ is one of the main contributors to an asymmetric A_t distribution in the full posterior, which is seen directly in the symmetric distribution of the LEO posterior-$\Delta(\rho)$ in A_t. The asymmetry is generated by the suppression of the large negative A_t region, which results in a larger probability density at small $|A_t|$ in the full LEO posterior. The suppression of large negative A_t also happens when only $\Delta(\rho)$ is included, although it is not as strong, and can be seen when comparing the LEO prior to the LEO prior+$\Delta(\rho)$.

Lastly, the inclusion of $\Delta(\rho)$ along with the other LEO observables results in a strong suppression of the small m_A region, a feature not visible when only $\Delta(\rho)$ is used in the McMC likelihood.

C.5 $\mathbf{BR(D_s \to \tau\nu)}$

The McMC includes measurements of the leptonic decay of D_S-mesons into a tauon final state. Example Feynman diagrams for the principle SM process and a MSSM contribution are shown in Figure 194.

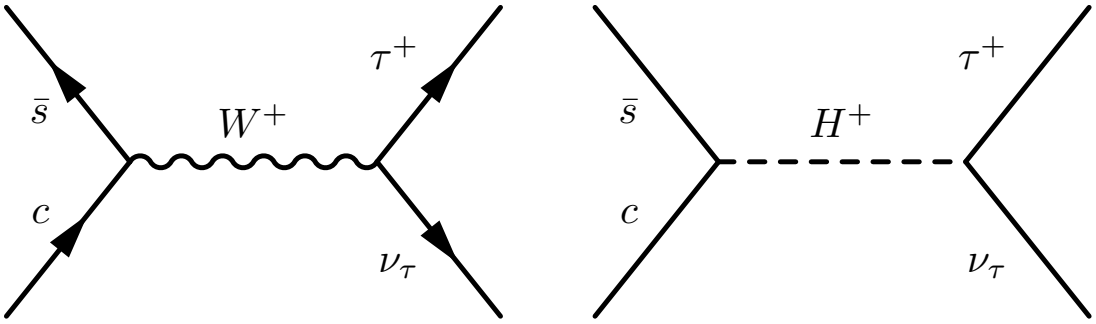

Figure 194: Feynman diagram for the leptonic decay of D_s-mesons into a tauon final state for the SM (left) and an example contribution in the MSSM (right).

The measurement $BR(D_s \to \tau\nu) = (5.48 \pm 0.23) \times 10^{-2}$ [107] has a small impact on the higgsino mass parameter and the first generation squarks, and strong effects on the third generation squarks and the Higgs sector. Its impact on the higgsino mass parameter is shown in Figure 195. We can see that including $BR(D_s \to \tau\nu)$ in the McMC alone does not noticeably impact $|\mu|$, but its inclusion alongside the other observables results in the additional suppression of small $|\mu|$. This impact makes itself visible in the mass of the lightest neutralino and lighter chargino by a small suppression at small $m(\widetilde{\chi}_1^0)$ and $m(\widetilde{\chi}_1^\pm)$, respectively, as well as contributing to an enhanced probability density at chargino masses around $m(\widetilde{\chi}_1^\pm) \simeq 1.5\,\text{TeV}$.

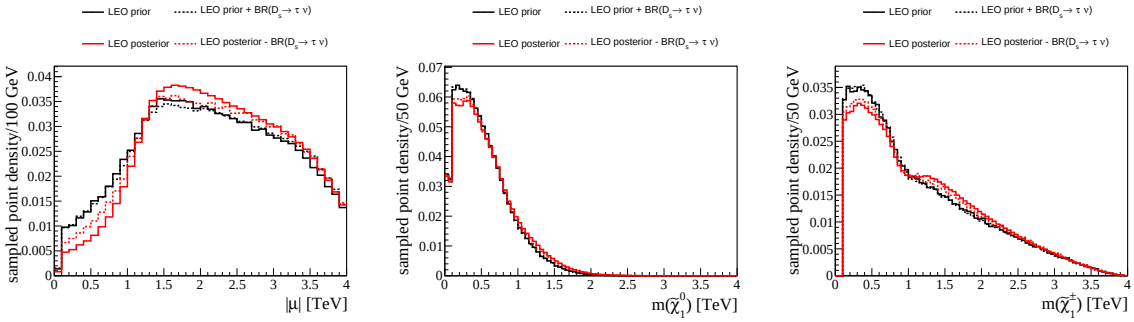

Figure 195: Distributions of the absolute value of the higgsino mass parameter $|\mu|$ (left), the mass of the lightest neutralino $m(\widetilde{\chi}_1^0)$ (center), and the mass of the lighter chargino $m(\widetilde{\chi}_1^\pm)$ (right). The distributions are shown for the LEO prior (black), the LEO prior+$BR(D_s \to \tau\nu)$ (dashed black), the LEO posterior (red), and the LEO posterior-$BR(D_s \to \tau\nu)$ (dashed red).

The impact of $BR(D_s \to \tau\nu)$ on the third generation squarks is shown in Figure 196. As observed previously for other LEO observables, small $M_{q,3}$, $M_{u,3}$, and $m(\widetilde{t}_1)$ are strongly suppressed by the combined impact of all the included LEO observables, seen in the difference between the LEO prior and posterior. The inclusion of $BR(D_s \to \tau\nu)$ contributes to this suppression comparatively strongly as already seen for other observables, but does not impact the LEO prior when included by itself. This behavior is also seen in the sbottom mass parameter $M_{d,3}$ and the lighter sbottom mass $m(\widetilde{b}_1)$, with the difference that small $M_{d,3}$ are favored by the inclusion of $BR(D_s \to \tau\nu)$. Because small sbottom masses experience a net suppression due to the suppression of small $M_{q,3}$, the inclusion of

$BR(D_s \to \tau\nu)$ increases the importance of the right-chiral component at small $m(\widetilde{b}_1)$ in the LEO posterior.

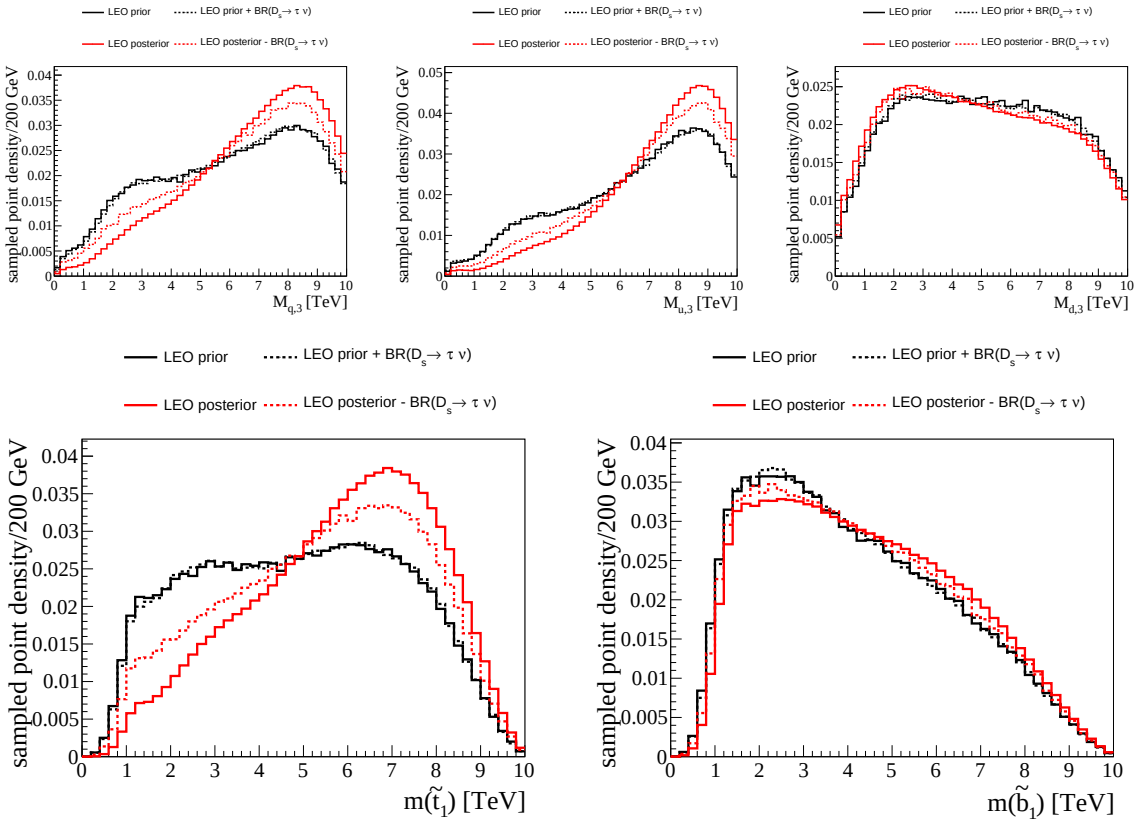

Figure 196: Distributions of the left-chiral third generation squark mass parameter $M_{q,3}$ (top left), the right-chiral stop mass parameter $M_{u,3}$ (top center), the right-chiral sbottom mass parameter $M_{d,3}$ (top right), and the resulting lighter stop mass $m(\widetilde{t}_1)$ (bottom left) and lighter sbottom mass $m(\widetilde{b}_1)$ (bottom right). The distributions are shown for the LEO prior (black), the LEO prior+$BR(D_s \to \tau\nu)$ (dashed black), the LEO posterior (red), and the LEO posterior-$BR(D_s \to \tau\nu)$ (dashed red).

The impact on the first and second generation squarks is shown in Figure 197. The only affected parameters are $M_{q,1}$ and the mass distribution of the left-chiral up-type squarks $m(\widetilde{u}_L, \widetilde{c}_L)$, in both of which the small mass region is somewhat suppressed.

Finally, the impact on the Higgs sector is shown in Figure 198. The impact on the trilinear Higgs-stop couplin A_t is somewhat peculiar. While the LEO prior+$BR(D_s \to \tau\nu)$ prefers large negative A_t at the expense of large positive A_t when compared to the LEO prior, the large negative A_t region is suppressed when comparing the LEO posterior-$BR(D_s \to \tau\nu)$ to the full LEO posterior. It is possible that the McMC for the LEO posterior+$BR(D_s \to \tau\nu)$ has not converged in A_t due to the comparatively short McMC that is used here. Because of the bi-modal character of the distributions in A_t, we can expect a longer convergence time for the McMC, as it is difficult for individual Markov chains to populate both the negative and positive peaks of the distribution. The impact on the mass of the heavy Higgs bosons is the now familiar suppression of small m_A when $BR(D_s \to \tau\nu)$ is included along with the other observables, visible in the suppression of the full LEO posterior with respect to the LEO posterior-$BR(D_s \to \tau\nu)$ at small m_A.

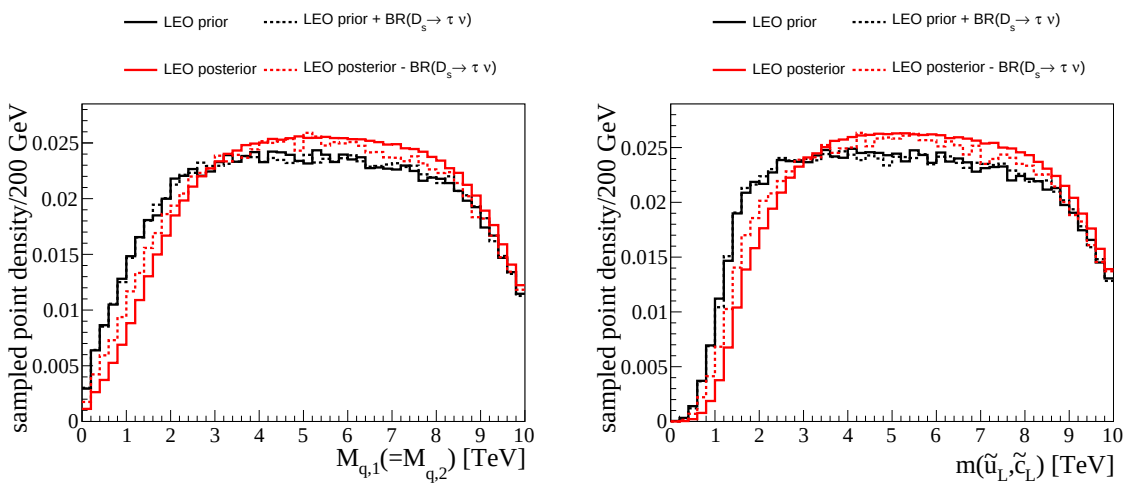

Figure 197: Distributions of the left-chiral first generation squark mass parameter $M_{q,1}$ (left) and the left-chiral sup mass $m(\tilde{u}_L, \tilde{c}_L)$ (right). The distributions are shown for the LEO prior (black), the LEO prior+BR($D_s \to \tau\nu$) (dashed black), the LEO posterior (red), and the LEO posterior-BR($D_s \to \tau\nu$) (dashed red). Note that the first two generations of sfermions are mass degenerate in the pMSSM, as well as the left-chiral up- and down-type squarks in the first two generations.

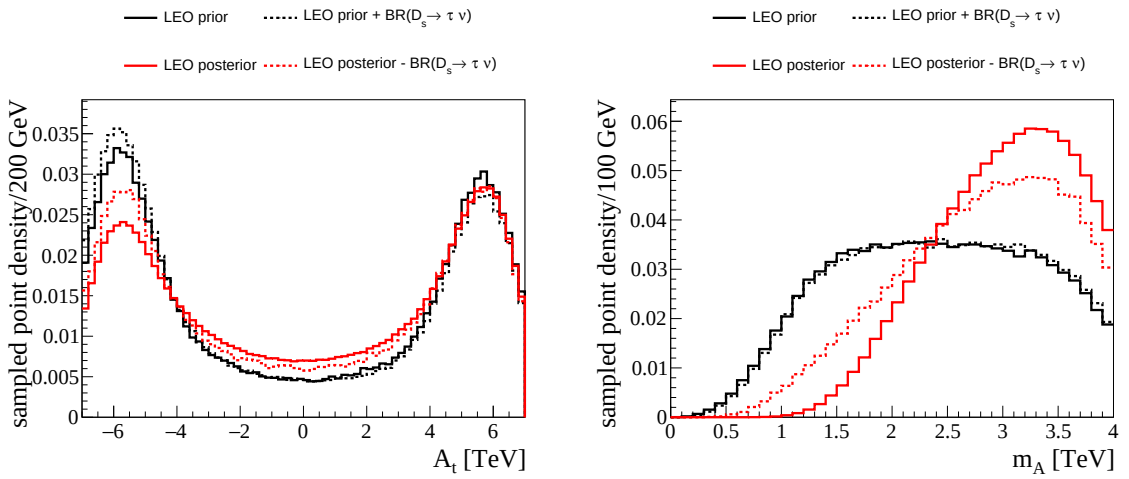

Figure 198: Distributions of the trilinear Higgs-stop coupling A_t (left), and the masses of the heavy Higgs bosons m_A (right). The distributions are shown for the LEO prior (black), the LEO prior+BR($D_s \to \tau\nu$) (dashed black), the LEO posterior (red), and the LEO posterior-BR($D_s \to \tau\nu$) (dashed red).

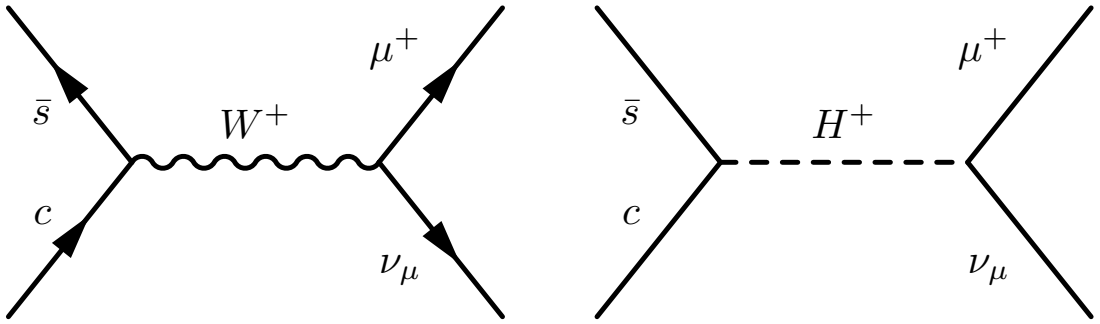

Figure 199: Feynman diagram for the leptonic decay of D_s-mesons into a muon final state for the SM (left) and an example contribution in the MSSM (right).

C.6 BR($D_s \to \mu\nu$)

The McMC includes measurements of the leptonic decay of D_S-mesons into a muon final state. Example Feynman diagrams for the principle SM process and a MSSM contribution are shown in Figure 199.

The measurement $BR(D_s \to \mu\nu) = (5.50 \pm 0.23) \times 10^{-3}$ [107] has similar impacts on the pMSSM as $BR(D_s \to \tau\nu)$, affecting the higgsinos, the first and third generation squarks, as well as the Higgs sector.

To begin, Figure 200 shows the impact of $BR(D_s \to \mu\nu)$ on the higgsino mass parameter, and the lightest neutralino and chargino. No significant impact is seen when only $BR(D_s \to \mu\nu)$ is used to constrain the pMSSM, as there is no significant difference between the distributions of the LEO prior and the LEO prior+$BR(D_s \to \mu\nu)$. If included alongside the other observables however, the small-$|\mu|$ region is further suppressed to the benefit of an increased probability density between $|\mu| \gtrsim 1.5\,\text{TeV}$ and $|\mu| \lesssim 2.5\,\text{TeV}$. These effects can be found in the change of the distributions of the for the lightest neutralino and chargino masses, where $m(\widetilde{\chi}_1^0)$ and $m(\widetilde{\chi}_1^\pm)$ are slightly suppressed at small masses, and $m(\widetilde{\chi}_1^\pm)$ experiences a small enhancement around $m(\widetilde{\chi}_1^\pm) \simeq 1.5\,\text{TeV}$. These effects on the particle masses are a direct consequence of the decreased and enhanced probability density in the different regions of $|\mu|$.

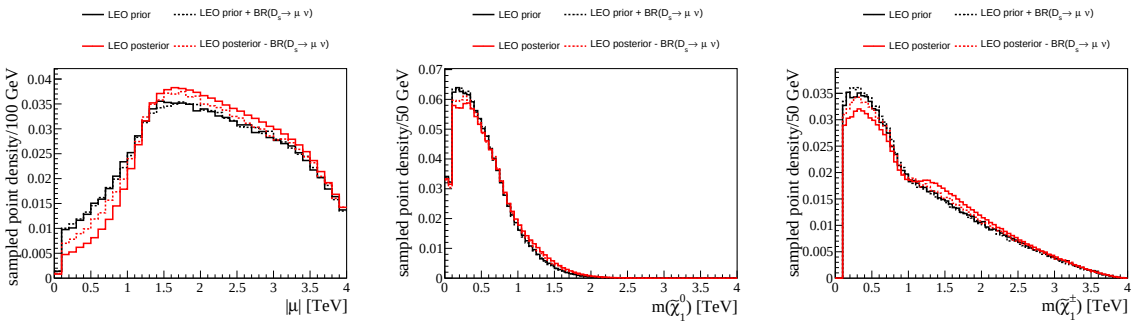

Figure 200: Distributions of the absolute value of the higgsino mass parameter $|\mu|$ (left), the mass of the lightest neutralino $m(\widetilde{\chi}_1^0)$ (center), and the mass of the lighter chargino $m(\widetilde{\chi}_1^\pm)$ (right). The distributions are shown for the LEO prior (black), the LEO prior+$BR(D_s \to \mu\nu)$ (dashed black), the LEO posterior (red), and the LEO posterior-$BR(D_s \to \mu\nu)$ (dashed red).

In the distributions of the third-generation squarks in Figure 201, we also see no impact of $BR(D_s \to \mu\nu)$ when it is the only LEO observable constraining the pMSSM. However, the third-generation squark and stop mass parameters $M_{q,3}$ and $M_{u,3}$, as well as the lighter stop mass $m(\widetilde{t}_1)$, are significantly suppressed at small to medium masses. In contrast, small values of the sbottom mass

parameter $M_{d,3}$ are enhanced when $BR(D_s \to \mu\nu)$ is included alongside the other LEO observables. Because the lighter sbottom mass is a mix of its left- and right-chiral components, both $M_{q,3}$ and $M_{d,3}$ determine the sbottom mass. The fact that small $M_{q,3}$ are disfavored and small $M_{d,3}$ enhanced leads to an overall suppression of small $m(\widetilde{b}_1)$, with a larger contribution of the right-chiral component in the full LEO posterior compared to the LEO posterior-$BR(D_s \to \mu\nu)$.

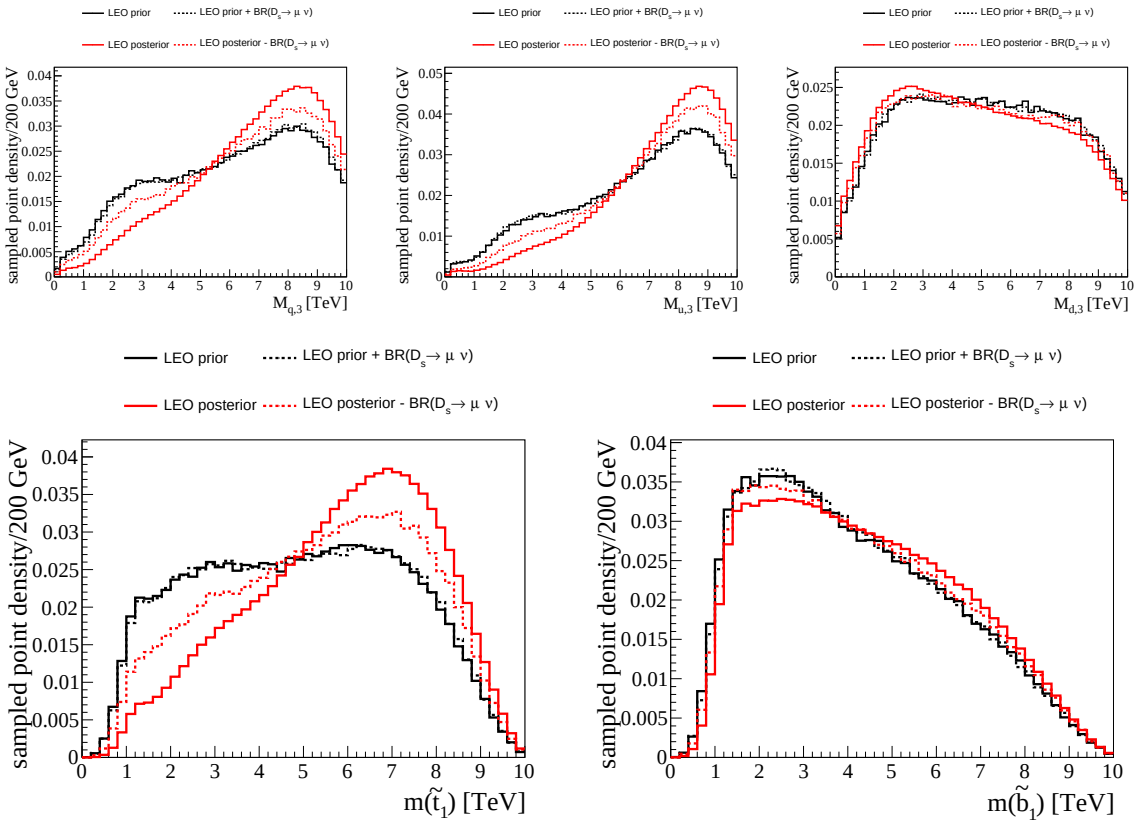

Figure 201: Distributions of the left-chiral third generation squark mass parameter $M_{q,3}$ (top left), the right-chiral stop mass parameter $M_{u,3}$ (top center), the right-chiral sbottom mass parameter $M_{d,3}$ (top right), and the resulting lighter stop mass $m(\widetilde{t}_1)$ (bottom left) and lighter sbottom mass $m(\widetilde{b}_1)$ (bottom right). The distributions are shown for the LEO prior (black), the LEO prior+$BR(D_s \to \mu\nu)$ (dashed black), the LEO posterior (red), and the LEO posterior-$BR(D_s \to \mu\nu)$ (dashed red).

The impact on the first generation squarks is shown in Figure 202. In addition to the suppression of small $M_{q,1}$ and $m(\widetilde{u}_L, \widetilde{c}_L)$ already seen in the impact of $BR(D_s \to \tau\nu)$, there is a slight enhancement of the right-chiral sdown mass parameter $M_{d,1}$ at small masses when $BR(D_s \to \mu\nu)$ is included alongside the other LEO observables. This has the surprising effect of creating a peculiar feature in the full LEO posterior between $m(\widetilde{d}_R, \widetilde{s}_R) \gtrsim 1.5\,\text{TeV}$ and $m(\widetilde{d}_R, \widetilde{s}_R) \lesssim 3\,\text{TeV}$. Here, the full posterior shows a soft peak in the distribution, whereas the LEO prior shows a flat plateau in the distribution of $m(\widetilde{d}_R, \widetilde{s}_R)$. However, the impact in the most interesting region, in terms of LHC phenomenology, at small $\widetilde{d}_R$ is minimal to non-existent in the marginalized distribution.

Finally, Figure 203 shows the impact on the Higgs sector. As with all the other parameters, the sole use of $BR(D_s \to \mu\nu)$ to constrain the pMSSM has no impact on the marginalized distributions here. If used alongside the other LEO observables, large negative A_t are significantly suppressed in favor of small $|A_t|$. Additionally, the asymmetry in A_t seen in the full LEO posterior is only present if $BR(D_s \to \mu\nu)$ is included in constraining the pMSSM. In addition to affecting A_t, the inclusion of $BR(D_s \to \mu\nu)$ with the other LEO observables further strongly suppresses the small m_A region, contributing to the fact that almost no posterior density remains for $m_A \lesssim 1\,\text{TeV}$

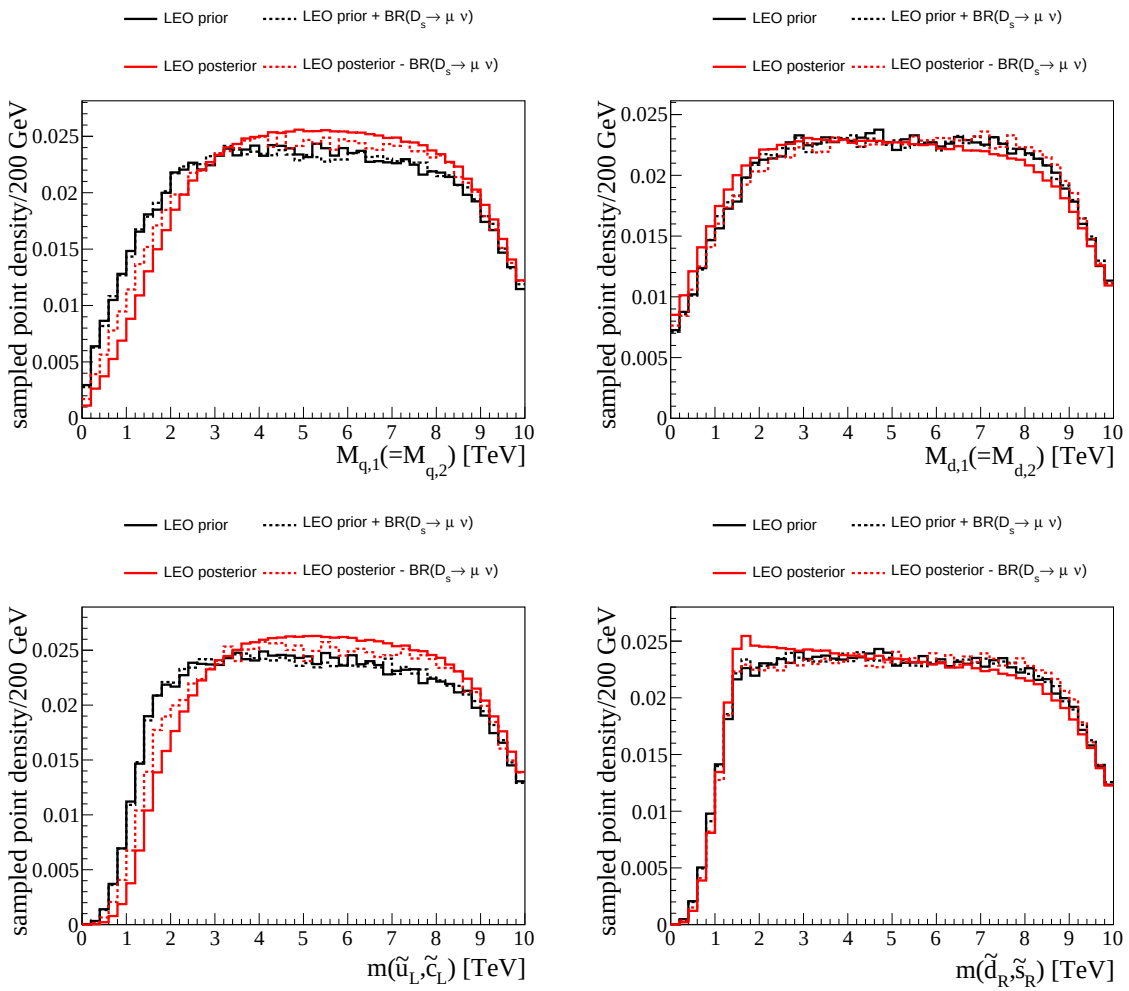

Figure 202: Distributions of the left-chiral first generation squark mass parameter $M_{q,1}$ (top left), the right-chiral sdown mass parameter $M_{d,1}$ (top right), as well as and the left-chiral sup mass $m(\tilde{u}_L, \tilde{c}_L)$ (bottom left), and the right-chiral sdown mass $m(\tilde{d}_R, \tilde{s}_R)$. The distributions are shown for the LEO prior (black), the LEO prior+BR($D_s \to \mu\nu$) (dashed black), the LEO posterior (red), and the LEO posterior-BR($D_s \to \mu\nu$) (dashed red). Note that the first two generations of sfermions are mass degenerate in the pMSSM, as well as the left-chiral up- and down-type squarks in the first two generations.

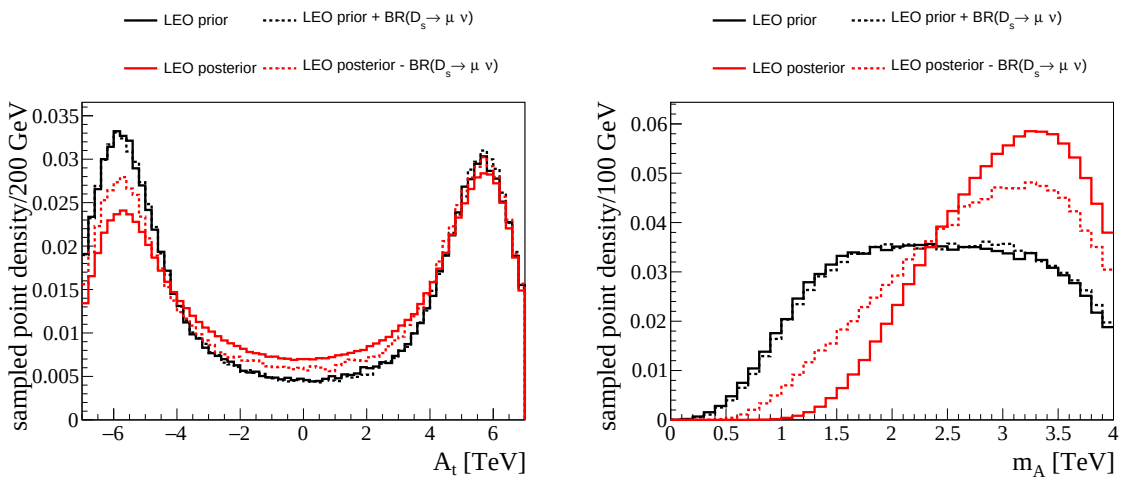

Figure 203: Distributions of the trilinear Higgs-stop coupling A_t (left), and the masses of the heavy Higgs bosons m_A (right). The distributions are shown for the LEO prior (black), the LEO prior+BR($D_s \to \mu\nu$) (dashed black), the LEO posterior (red), and the LEO posterior-BR($D_s \to \mu\nu$) (dashed red).

C.7 $\mathbf{BR(B_d \to \mu\mu)}$ and $\Delta_{0+}(\mathbf{K^*\gamma})$

Finally, the McMC contains measurements of the observables $\mathrm{BR}(\mathrm{B_d} \to \mu\mu)$ and $\Delta_{0+}(\mathrm{K^*}\gamma)$. Example Feynman diagrams for the $\mathrm{B_d} \to \mu\mu$ decay for the SM and the MSSM are shown in Figure 204. The

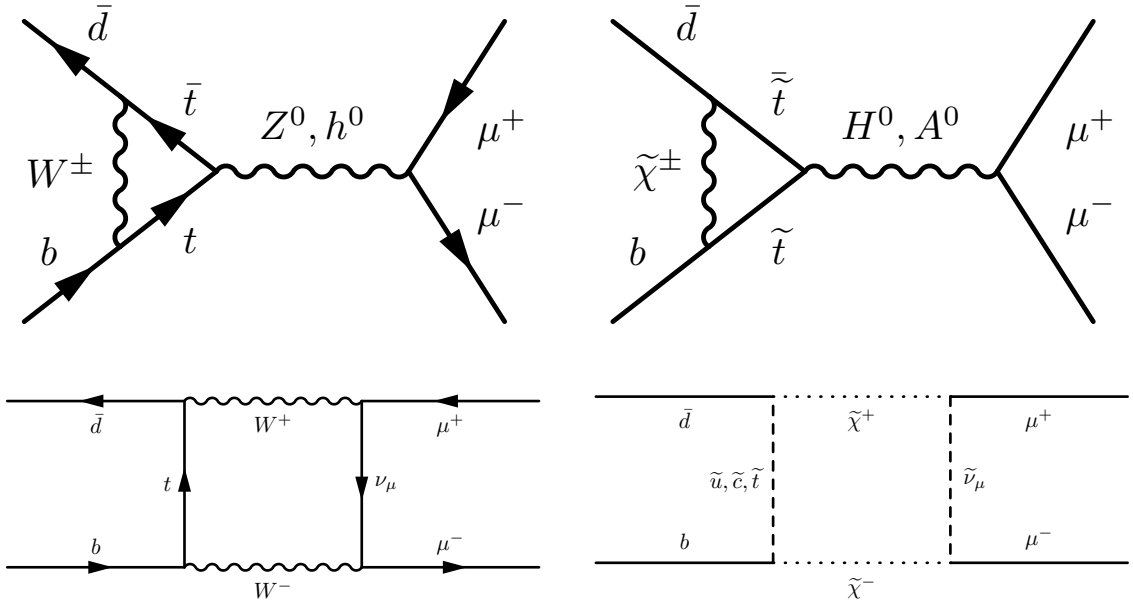

Figure 204: Feynman diagrams for the decay of $\mathrm{B_d}$-mesons into a di-muon final state for the SM (left) and example contributions in the MSSM (right).

observable $\Delta_{0+}(\mathrm{K^*}\gamma)$ is the isospin asymmetry in the decays of B-mesons into the neutral and charged $\mathrm{K^*}\gamma$ final states, measured by the difference of the decay widths of neutral and charged B-mesons into the $\mathrm{K^*}\gamma$ final state,

$$\Delta_{0\pm}(K^*\gamma) = \frac{\Gamma(\bar{B}^0 \to \bar{K}^{*0}\gamma) - \Gamma(B^\pm \to K^{*\pm}\gamma)}{\Gamma(\bar{B}^0 \to \bar{K}^{*0}\gamma) + \Gamma(B^\pm \to K^{*\pm}\gamma)} [162].$$

For the measurements $\mathrm{BR}(\mathrm{B_d} \to \mu\mu) = (3.6^{+1.6}_{-1.4}) \times 10^{-10}$ [96, 97, 98] and $\Delta_{0+}(\mathrm{K^*}\gamma) = (5.2 \pm 2.6) \times 10^{-2}$ (`SuperIso` internal combination of [103, 104, 105]), no significant impact is seen on the marginalized 1-dimension distributions for any of the pMSSM parameters or particles masses. It is possible that small corners of the pMSSM are affected, which are integrated out during the marginalization.

References

[1] The CMS collaboration. "Search for supersymmetry in proton-proton collisions at 13 TeV in final states with jets and missing transverse momentum". *Journal of High Energy Physics*, 2019(10), Oct 2019.

[2] Malte Mrowietz et al. "Implementation of the CMS-SUS-19-006 analysis in the MadAnalysis 5 framework (supersymmetry with large hadronic activity and missing transverse energy; 137 fb^{-1})". *Mod. Phys. Lett. A*, 36(01):2141007, 2021.

[3] The ATLAS collaboration. "Search for electroweak production of charginos and sleptons decaying into final states with two leptons and missing transverse momentum in $\sqrt{s} = 13\,\text{TeV}$ pp collisions using the ATLAS detector". *The European Physical Journal C*, 80(2), Feb 2020.

[4] The CMS collaboration. "Search for supersymmetry in final states with two or three soft leptons and missing transverse momentum in proton-proton collisions at $\sqrt{s} = 13$ TeV". *JHEP*, 2204:091, 2022.

[5] The ATLAS Collaboration. "Search for chargino-neutralino production with mass splittings near the electroweak scale in three-lepton final states in $\sqrt{s} = 13\,\text{TeV}$ pp collisions with the ATLAS detector". *Physical Review D*, 101(7), Apr 2020.

[6] Viktor Gerhard Kutzner. *"Search for exotic long-lived particles using disappearing tracks with the CMS experiment in proton-proton collisions at $\sqrt{s} = 13\,TeV$"*. PhD thesis, Universität Hamburg, 2023.

[7] The CMS Collaboration. "Search for supersymmetry in final states with disappearing tracks in proton-proton collisions at $\sqrt{s} = 13\,\text{TeV}$". Technical report, CERN, Geneva, 2023.

[8] Planck Collaboration. "Planck 2018 results - VI. Cosmological parameters". *A&A*, 641:A6, 2020.

[9] The CMS Collaboration. "Observation of a new boson at a mass of 125 GeV with the CMS experiment at the LHC". *Physics Letters B*, 716(1):30–61, 2012.

[10] The ATLAS Collaboration. "Observation of a new particle in the search for the Standard Model Higgs boson with the ATLAS detector at the LHC". *Physics Letters B*, 716(1):1–29, 2012.

[11] Rudolf Haag et al. "All possible generators of supersymmetries of the S-matrix". *Nuclear Physics B*, 88(2):257–274, 1975.

[12] Mark Thomson. *"Modern Particle Physics"*. Cambridge University Press, 2013.

[13] Lewis H. Ryder. *"Quantum Field Theory"*. Cambridge University Press, 2 edition, 1996.

[14] R. L. Workman et al. "Review of Particle Physics". *PTEP*, 2022:083C01, 2022.

[15] Cush. "Standard Model of Elementary Particles". Graphic on website: `https://upload.wikimedia.org/wikipedia/commons/thumb/0/00/Standard_Model_of_Elementary_Particles.svg/2140px-Standard_Model_of_Elementary_Particles.svg.png`, May 2023.

[16] F. Englert and R. Brout. "Broken Symmetry and the Mass of Gauge Vector Mesons". *Phys. Rev. Lett.*, 13:321–323, Aug 1964.

[17] Peter W. Higgs. "Broken Symmetries and the Masses of Gauge Bosons". *Phys. Rev. Lett.*, 13:508–509, Oct 1964.

[18] Marcela Carena et al. "Electroweak baryogenesis and new TeV fermions". *Nucl. Phys. B*, 716:319–351, 2005.

[19] Andrey Katz and Maxim Perelstein. "Higgs Couplings and Electroweak Phase Transition". *JHEP*, 07:108, 2014.

[20] Eibun Senaha. "Symmetry Restoration and Breaking at Finite Temperature: An Introductory Review". *Symmetry*, 12(5), 2020.

[21] Latham Boyle. "Standard Model Of Particle Physics–Most Complete Diagram". Graphic on website: `https://commons.wikimedia.org/wiki/File:Standard_Model_Of_Particle_Physics--Most_Complete_Diagram.png`, Dec 2015.

[22] Julien Billard et al. "Direct detection of dark matter—APPEC committee report". *Reports on Progress in Physics*, 85(5):056201, Apr 2022.

[23] Katherine Garrett and Gintaras Duda. "Dark Matter: A Primer". *Advances in Astronomy*, 2011:1–22, 2011.

[24] Andrei D Sakharov. "Violation of CP invariance, C asymmetry, and baryon asymmetry of the universe". *Soviet Physics Uspekhi*, 34(5):392, May 1991.

[25] V.A. Kuzmin et al. "On anomalous electroweak baryon-number non-conservation in the early universe". *Physics Letters B*, 155(1):36–42, 1985.

[26] M. C. Gonzalez-Garcia and Michele Maltoni. "Phenomenology with Massive Neutrinos". *Phys. Rept.*, 460:1–129, 2008.

[27] J. W. F. Valle. "Neutrino physics overview". *J. Phys. Conf. Ser.*, 53:473–505, 2006.

[28] D.I. Kazakov. "Supersymmetry on the Run: LHC and Dark Matter". *Nuclear Physics B - Proceedings Supplements*, 203-204:118–154, Jun 2010.

[29] Sidney Coleman and Jeffrey Mandula. "All Possible Symmetries of the S Matrix". *Phys. Rev.*, 159:1251–1256, Jul 1967.

[30] Rudolf Haag et al. "All possible generators of supersymmetries of the S-matrix". *Nuclear Physics B*, 88(2):257–274, 1975.

[31] STEPHEN P. MARTIN. "A SUPERSYMMETRY PRIMER". In *Perspectives on Supersymmetry*, pages 1–98. WORLD SCIENTIFIC, Jul 1998.

[32] Malte Mrowietz. "Identifying signatures of and designing searches for unexplored SUSY models with the CMS detector". Master's thesis, Universität Hamburg, 2018.

[33] A. H. Chamseddine et al. "Locally Supersymmetric Grand Unification". *Phys. Rev. Lett.*, 49:970–974, Oct 1982.

[34] R. Barbieri et al. "Gauge models with spontaneously broken local supersymmetry". *Physics Letters B*, 119(4):343–347, 1982.

[35] Luis Ibáñez. "Locally supersymmetric SU(5) grand unification". *Physics Letters B*, 118(1):73–78, 1982.

[36] Lawrence Hall et al. "Supergravity as the messenger of supersymmetry breaking". *Phys. Rev. D*, 27:2359–2378, May 1983.

[37] Nobuyoshi Ohta. "Grand Unified Theories Based on Local Supersymmetry". *Progress of Theoretical Physics*, 70(2):542–549, 08 1983.

[38] John Ellis et al. "Gaugino masses and grand unification". *Physics Letters B*, 155(5):381–386, 1985.

[39] Luis Alvarez-Gaumé et al. "Minimal low-energy supergravity". *Nuclear Physics B*, 221(2):495–523, 1983.

[40] Lisa Randall and Raman Sundrum. "Out of this world supersymmetry breaking". *Nuclear Physics B*, 557(1-2):79–118, Sep 1999.

[41] Gian F Giudice et al. "Gaugino mass without singlets". *Journal of High Energy Physics*, 1998(12):027–027, Dec 1998.

[42] Michael Dine and Willy Fischler. "A phenomenological model of particle physics based on supersymmetry". *Physics Letters B*, 110(3):227–231, 1982.

[43] Chiara R. Nappi and Burt A. Ovrut. "Supersymmetric extension of the SU(3)×SU(2)×U(1) model". *Physics Letters B*, 113(2):175–179, 1982.

[44] Luis Alvarez-Gaumé et al. "Low-energy supersymmetry". *Nuclear Physics B*, 207(1):96–110, 1982.

[45] Michael Dine and Ann E. Nelson. "Dynamical supersymmetry breaking at low energies". *Physical Review D*, 48(3):1277–1287, Aug 1993.

[46] Michael Dine et al. "Low energy dynamical supersymmetry breaking simplified". *Physical Review D*, 51(3):1362–1370, Feb 1995.

[47] Michael Dine et al. "New tools for low energy dynamical supersymmetry breaking". *Physical Review D*, 53(5):2658–2669, Mar 1996.

[48] Ben Moore et al. "Resolving the structure of cold dark matter halos". *Astrophys. J. Lett.*, 499:L5, 1998.

[49] Rafael Rebolo et al. "Cosmological parameter estimation using Very Small Array data out to l = 1500". *Mon. Not. Roy. Astron. Soc.*, 353:747–759, 2004.

[50] A. Djouadi et al. "The Minimal supersymmetric standard model: Group summary report". In *GDR (Groupement De Recherche) - Supersymetrie*, 12 1998.

[51] Howard Baer et al. "Electroweak versus high scale finetuning in the 19-parameter SUGRA model". *Phys. Rev. D*, 88:055026, 2013.

[52] Johan Alwall et al. "Simplified models for a first characterization of new physics at the LHC ". *Physical Review D*, 79(7), Apr 2009.

[53] Stefano Giagu. "WIMP dark matter searches with the ATLAS detector at the LHC". *Frontiers in Physics*, 7, 05 2019.

[54] E. Aprile et al. "Conceptual design and simulation of a water Cherenkov muon veto for the XENON1T experiment". *Journal of Instrumentation*, 9(11):P11006–P11006, Nov 2014.

[55] Michael Murra et al. "OUR DETECTOR". Website, 2022. accessible under `https://xenonexperiment.org/time-projection-chamber/`; accessed on 12th of June 2023.

[56] P. Agnes et al. "First results from the DarkSide-50 dark matter experiment at Laboratori Nazionali del Gran Sasso". *Physics Letters B*, 743:456–466, Apr 2015.

[57] A. H. Abdelhameed et al. "First results from the CRESST-III low-mass dark matter program". *Physical Review D*, 100(10), Nov 2019.

[58] PICO collaboration. "PICO-60". Website, 2019. accessible under `https://www.picoexperiment.com/pico-60/`; accessed on 13th of June 2023.

[59] C. Amole et al. "Dark matter search results from the complete exposure of the PICO-60 bubble chamber". *Physical Review D*, 100(2), Jul 2019.

[60] J. Aalbers et al. First dark matter search results from the lux-zeplin (lz) experiment. *Physical Review Letters*, 131(4), July 2023.

[61] Ciaran A. J. O'Hare. "New Definition of the Neutrino Floor for Direct Dark Matter Searches". *Physical Review Letters*, 127(25), Dec 2021.

[62] MAGIC collaboration. "Limits to dark matter annihilation cross-section from a combined analysis of MAGIC and Fermi-LAT observations of dwarf satellite galaxies". *Journal of Cosmology and Astroparticle Physics*, 2016(02):039, Feb 2016.

[63] Juan Cortina et al. "Technical Performance of the MAGIC Telescopes2. arXiv 0907.1211, 2009.

[64] W. B. Atwood et al. "THE LARGE AREA TELESCOPE ON THE *FERMI GAMMA-RAY SPACE TELESCOPE* MISSION". *The Astrophysical Journal*, 697(2):1071–1102, May 2009.

[65] J Grange et al. "Muon (g-2) Technical Design Report". Technical report, 2015.

[66] D. P. Aguillard et al. "Measurement of the Positive Muon Anomalous Magnetic Moment to 0.20 ppm". arXiv 2308.06230, 8 2023.

[67] A. J. Bevan et al. "The Physics of the B Factories". *The European Physical Journal C*, 74(11), Nov 2014.

[68] A. Augusto Alves, Jr. et al. "The LHCb Detector at the LHC". *JINST*, 3:S08005, 2008.

[69] LHCb collaboration. "Large Hadron Collider beauty experiment". Website, 2023. accessible under `https://lhcb-outreach.web.cern.ch/`; accessed on 1st of July 2023.

[70] I. Belyaev et al. "The history of LHCb". *Eur. Phys. J. H*, 46(1):3, 2021.

[71] The ALICE Collaboration. "The ALICE experiment at the CERN LHC". *Journal of Instrumentation*, 3(08):S08002, Aug 2008.

[72] The ATLAS Collaboration. "The ATLAS Experiment at the CERN Large Hadron Collider". *Journal of Instrumentation*, 3(08):S08003, Aug 2008.

[73] The CMS Collaboration. "The CMS experiment at the CERN LHC". *Journal of Instrumentation*, 3(08):S08004, Aug 2008.

[74] Philippe Mouche. "Overall view of the LHC. Vue d'ensemble du LHC", 2014. General Photo.

[75] CMS collaboration. "Detector". Website. accessible under `https://cms.cern/index.php/detector`; accessed on 4th of July 2023.

[76] Jason Nielsen. "Fundamentals of LHC Experiments". In *Theoretical Advanced Study Institute in Elementary Particle Physics: String theory and its Applications: From meV to the Planck Scale*, pages 127–152, 6 2011.

[77] W. Adam et al. "The CMS Phase-1 Pixel Detector Upgrade". *JINST*, 16(02):P02027, 2021.

[78] CMS collaboration. "CMS Tracker Detector Performance Results". Website, 2022. accessible under `https://twiki.cern.ch/twiki/bin/view/CMSPublic/DPGResultsTRK`; accessed on 4th of July 2023.

[79] Min Suk Kim for the CMS collaboration. "CMS reconstruction improvement for the muon tracking by the RPC chambers". *PoS*, RPC2012:045, 2012.

[80] Mia Tosi for the CMS collaboration. "The CMS trigger in Run 2". *PoS*, EPS-HEP2017:523, 2017.

[81] The ATLAS collaboration. "Operation of the ATLAS trigger system in Run 2". *Journal of Instrumentation*, 15(10):P10004–P10004, Oct 2020.

[82] C. R. Das and M. K. Parida. "New formulas and predictions for running fermion masses at higher scales in SM, 2 HDM, and MSSM". *Eur. Phys. J. C*, 20:121–137, 2001.

[83] W. K. Hastings. "Monte Carlo sampling methods using Markov chains and their applications". *Biometrika*, 57(1):97–109, 04 1970.

[84] Galin L. Jones. "on the markov chain central limit theorem". *Probability Surveys*, 1:299–320, 2004.

[85] H. Bahl et al. "Precision calculations in the MSSM Higgs-boson sector with FeynHiggs 2.14". *Comput. Phys. Commun.*, 249:107099, 2020.

[86] Henning Bahl et al. "Reconciling EFT and hybrid calculations of the light MSSM Higgs-boson mass". *The European Physical Journal C*, 78(1), Jan 2018.

[87] Henning Bahl and Wolfgang Hollik. "Precise prediction for the light MSSM Higgs-boson mass combining effective field theory and fixed-order calculations". *The European Physical Journal C*, 76(9), Sep 2016.

[88] T. Hahn et al. "High-Precision Predictions for the Light CP-Even Higgs Boson Mass of the Minimal Supersymmetric Standard Model". *Physical Review Letters*, 112(14), Apr 2014.

[89] Meikel Frank et al. "The Higgs boson masses and mixings of the complex MSSM in the Feynman-diagrammatic approach". *Journal of High Energy Physics*, 2007(02):047–047, Feb 2007.

[90] G. Degrassi et al. "Towards high-precision predictions for the MSSM Higgs sector". *The European Physical Journal C*, 28(1):133–143, May 2003.

[91] S. Heinemeyer et al. "The masses of the neutral CP-even Higgs bosons in the MSSM: Accurate analysis at the two-loop level". *The European Physical Journal C*, 9(2):343–366, Jun 1999.

[92] S. Heinemeyer et al. "FeynHiggs: a program for the calculation of the masses of the neutral CP-even Higgs bosons in the MSSM". *Computer Physics Communications*, 124(1):76–89, Jan 2000.

[93] Henning Bahl et al. "Theoretical uncertainties in the MSSM Higgs boson mass calculation". *The European Physical Journal C*, 80(6), Jun 2020.

[94] G. Bélanger et al. "Recasting direct detection limits within micrOMEGAs and implication for non-standard dark matter scenarios". *The European Physical Journal C*, 81(3), Mar 2021.

[95] E. Barberio et al. "Averages of $b-$hadron and $c-$hadron Properties at the End of 2007". arXiv 0808.1297, 8 2008.

[96] Serguei Chatrchyan et al. "Measurement of the $B_s^0 \to \mu^+\mu^-$ Branching Fraction and Search for $B^0 \to \mu^+\mu^-$ with the CMS Experiment". *Phys. Rev. Lett.*, 111:101804, 2013.

[97] R. Aaij et al. "Measurement of the $B_s^0 \to \mu^+\mu^-$ branching fraction and search for $B^0 \to \mu^+\mu^-$ decays at the LHCb experiment". *Phys. Rev. Lett.*, 111:101805, 2013.

[98] The CMS and LHCb collaborations. "Combination of results on the rare decays $B_{(s)}^0 \to \mu^+\mu^-$ from the CMS and LHCb experiments". Technical report, CERN, Geneva, 2013.

[99] M. Iwasaki et al. "Improved measurement of the electroweak penguin process $B \to X_s l^+ l^-$". *Phys. Rev. D*, 72:092005, 2005.

[100] J. P. Lees et al. "Measurement of the $B \to X_s l^+ l^-$ branching fraction and search for direct CP violation from a sum of exclusive final states". *Phys. Rev. Lett.*, 112:211802, 2014.

[101] R Aaij et al. "Measurement of Form-Factor-Independent Observables in the Decay $B^0 \to K^{*0}\mu^+\mu^-$". *Phys. Rev. Lett.*, 111:191801, 2013.

[102] Y. Amhis et al. "Averages of B-Hadron, C-Hadron, and tau-lepton properties as of early 2012". arXiv 1207.1158, 7 2012.

[103] Bernard Aubert et al. "Measurement of Branching Fractions and CP and Isospin Asymmetries in $B \to K^*\gamma$". In *34th International Conference on High Energy Physics*, 8 2008.

[104] M. Nakao et al. "Measurement of the $B \to K^*\gamma$ branching fractions and asymmetries". *Phys. Rev. D*, 69:112001, 2004.

[105] K. A. Olive et al. "Review of Particle Physics". *Chinese Physics C*, 38(9):090001, Aug 2014.

[106] Y. Amhis et al. "Averages of b-hadron, c-hadron, and τ-lepton properties as of 2021". *Phys. Rev. D*, 107:052008, 2023. We are using the tables from May 2018 for this work.

[107] M. Tanabashi et al. "Review of Particle Physics". *Phys. Rev. D*, 98:030001, Aug 2018.

[108] Werner Porod. "SPheno, a program for calculating supersymmetric spectra, SUSY particle decays and SUSY particle production at e+ e- colliders". *Comput. Phys. Commun.*, 153:275–315, 2003.

[109] W. Porod and F. Staub. "SPheno 3.1: Extensions including flavour, CP-phases and models beyond the MSSM". *Comput. Phys. Commun.*, 183:2458–2469, 2012.

[110] Peter Z. Skands et al. "SUSY Les Houches accord: Interfacing SUSY spectrum calculators, decay packages, and event generators". *JHEP*, 07:036, 2004.

[111] The LHCb Collaboration. "Test of lepton universality in beauty-quark decays". *Nature Physics*, 18(3):277–282, Mar 2022.

[112] R. Aaij et al. "Test of lepton universality with $B^0 \to K^{*0}\ell^+\ell^-$ decays". *JHEP*, 08:055, 2017.

[113] Elena Graverini. "Flavour anomalies: a review". *J. Phys. Conf. Ser.*, 1137(1):012025, 2019.

[114] C. Patrignani et al. "Review of Particle Physics". *Chinese Physics C*, 40(10):100001, Oct 2016.

[115] D. Giusti et al. "Strange and charm HVP contributions to the muon (g - 2) including QED corrections with twisted-mass fermions". *Journal of High Energy Physics*, 2017(10), Oct 2017.

[116] B. Abi et al. "Measurement of the Positive Muon Anomalous Magnetic Moment to 0.46 ppm". *Physical Review Letters*, 126(14), Apr 2021.

[117] M. Misiak et al. "Estimate of $\mathcal{B}(\bar{B} \to X_s\gamma)$ at $O(\alpha_s^2)$". *Phys. Rev. Lett.*, 98:022002, 2007.

[118] Mikolaj Misiak and Matthias Steinhauser. "NNLO QCD corrections to the anti-B $\to$ X(s) gamma matrix elements using interpolation in m(c)". *Nucl. Phys. B*, 764:62–82, 2007.

[119] Martin Beneke et al. "Power-enhanced leading-logarithmic QED corrections to $B_q \to \mu^+\mu^-$". *JHEP*, 10:232, 2019. [Erratum: JHEP 11, 099 (2022)].

[120] Dootika Vats and Christina Knudson. "Revisiting the Gelman–Rubin Diagnostic". *Statistical Science*, 36(4):518 – 529, 2021.

[121] Eric Conte and Benjamin Fuks. "Confronting new physics theories to LHC data with MADANALYSIS 5". *Int. J. Mod. Phys. A*, 33(28):1830027, 2018.

[122] B. Dumont et al. "Toward a public analysis database for LHC new physics searches using MADANALYSIS 5". *Eur. Phys. J. C*, 75(2):56, 2015.

[123] Eric Conte et al. "Designing and recasting LHC analyses with MadAnalysis 5". *Eur. Phys. J. C*, 74(10):3103, 2014.

[124] Eric Conte et al. "MadAnalysis 5, A User-Friendly Framework for Collider Phenomenology". *Comput. Phys. Commun.*, 184:222–256, 2013.

[125] B. C. Allanach. "SOFTSUSY: a program for calculating supersymmetric spectra". *Comput. Phys. Commun.*, 143:305–331, 2002.

[126] Federico Ambrogi et al. "SModelS v1.1 user manual: Improving simplified model constraints with efficiency maps". *Comput. Phys. Commun.*, 227:72–98, 2018.

[127] Federico Ambrogi et al. "SModelS v1.2: long-lived particles, combination of signal regions, and other novelties". *Comput. Phys. Commun.*, 251:106848, 2020.

[128] Sabine Kraml et al. "SModelS: a tool for interpreting simplified-model results from the LHC and its application to supersymmetry". *Eur. Phys. J. C*, 74:2868, 2014.

[129] Christian Bierlich et al. "A comprehensive guide to the physics and usage of PYTHIA 8.3". *arXiv 2203.11601*, 3 2022.

[130] Torbjorn Sjostrand et al. "PYTHIA 6.4 Physics and Manual". *JHEP*, 05:026, 2006.

[131] W. Beenakker et al. "Squark and gluino production at hadron colliders". *Nucl. Phys. B*, 492:51–103, 1997.

[132] A. Kulesza and L. Motyka. "Threshold resummation for squark-antisquark and gluino-pair production at the LHC". *Phys. Rev. Lett.*, 102:111802, 2009.

[133] A. Kulesza and L. Motyka. "Soft gluon resummation for the production of gluino-gluino and squark-antisquark pairs at the LHC". *Phys. Rev. D*, 80:095004, 2009.

[134] Wim Beenakker et al. "Soft-gluon resummation for squark and gluino hadroproduction". *JHEP*, 12:041, 2009.

[135] W. Beenakker et al. "Squark and Gluino Hadroproduction". *Int. J. Mod. Phys. A*, 26:2637–2664, 2011.

[136] W. Beenakker et al. "Stop production at hadron colliders". *Nucl. Phys. B*, 515:3–14, 1998.

[137] Wim Beenakker et al. "Supersymmetric top and bottom squark production at hadron colliders". *JHEP*, 08:098, 2010.

[138] W. Beenakker et al. "Squark and Gluino Hadroproduction". *Int. J. Mod. Phys. A*, 26:2637–2664, 2011.

[139] Wim Beenakker et al. "NLO+NLL squark and gluino production cross-sections with threshold-improved parton distributions". *Eur. Phys. J. C*, 76(2):53, 2016.

[140] Andy Buckley. "PySLHA: a Pythonic interface to SUSY Les Houches Accord data". *Eur. Phys. J. C*, 75(10):467, 2015.

[141] J. de Favereau et al. "DELPHES 3: a modular framework for fast simulation of a generic collider experiment". *Journal of High Energy Physics*, 2014(2), Feb 2014.

[142] Jack Y. Araz and Benjamin Fuks. "Implementation of the ATLAS-SUSY-2018-31 analysis in the MadAnalysis 5 framework (sbottoms with multi-bottoms and missing transverse energy; 139 fb^{-1})". *Mod. Phys. Lett. A*, 36(01):2141010, 2021.

[143] Paul Jackson et al. "Sparticles in motion: Analyzing compressed SUSY scenarios with a new method of event reconstruction". *Physical Review D*, 95(3), Feb 2017.

[144] Paul Jackson and Christopher Rogan. "Recursive jigsaw reconstruction: HEP event analysis in the presence of kinematic and combinatoric ambiguities". *Physical Review D*, 96(11), Dec 2017.

[145] Jack Y. Araz and Benjamin Fuks. "Implementation of the ATLAS-SUSY-2018-32 analysis (sleptons and electroweakinos with two leptons and missing transverse energy; 139 fb^{-1})". *Mod. Phys. Lett. A*, 36(01):2141005, 2021.

[146] The CMS collaboration. "Phenomenological MSSM interpretation of CMS searches in pp collisions at $\sqrt{s} = 7$ and and 8 TeV". *Journal of High Energy Physics*, 2016(10), Oct 2016.

[147] S. S. Wilks. "The Large-Sample Distribution of the Likelihood Ratio for Testing Composite Hypotheses". *The Annals of Mathematical Statistics*, 9(1):60 – 62, 1938.

[148] E. Aprile et al. "Dark Matter Search Results from a One Ton-Year Exposure of XENON1T". *Physical Review Letters*, 121(11), Sep 2018.

[149] P. Agnes et al. "Low-Mass Dark Matter Search with the DarkSide-50 Experiment". *Physical Review Letters*, 121(8), Aug 2018.

[150] Junji Hisano et al. "Direct detection of the Wino and Higgsino-like neutralino dark matter at one-loop level". *Physical Review D*, 71(1), Jan 2005.

[151] Paul Bergeron et al. "Theoretical uncertainties in the calculation of supersymmetric dark matter observables". *Journal of High Energy Physics*, 2018(5), May 2018.

[152] Junji Hisano et al. "Nonperturbative effect on dark matter annihilation and gamma ray signature from the galactic center". *Phys. Rev. D*, 71:063528, Mar 2005.

[153] Andrzej Hryczuk et al. "Relic densities including Sommerfeld enhancements in the MSSM". *Journal of High Energy Physics*, 2011(3), Mar 2011.

[154] Junji Hisano et al. "Unitarity and higher-order corrections in neutralino dark matter annihilation into two photons". *Physical Review D*, 67(7), Apr 2003.

[155] M. Aguilar et al. The alpha magnetic spectrometer (ams) on the international space station: Part ii — results from the first seven years. *Physics Reports*, 894:1–116, 2021.

[156] *Science with the Cherenkov Telescope Array*. WORLD SCIENTIFIC, Feb 2018.

[157] T. Aoyama et al. "The anomalous magnetic moment of the muon in the Standard Model". *Physics Reports*, 887:1–166, 2020.

[158] Sz. Borsanyi et al. "Leading hadronic contribution to the muon magnetic moment from lattice QCD". *Nature*, 593(7857):51–55, Apr 2021.

[159] Peter Athron et al. "GM2Calc: precise MSSM prediction for (g-2) of the muon". *The European Physical Journal C*, 76(2), Feb 2016.

[160] Peter Athron et al. "Two-loop prediction of the anomalous magnetic moment of the muon in the Two-Higgs Doublet Model with GM2Calc 2". *The European Physical Journal C*, 82(3), Mar 2022.

[161] M. Bona et al. "An Improved Standard Model Prediction Of BR(B $\to \tau\nu$) And Its Implications For New Physics". *Phys. Lett. B*, 687:61–69, 2010.

[162] F. Mahmoudi. "SuperIso v2.3: A program for calculating flavor physics observables in supersymmetry". *Computer Physics Communications*, 180(9):1579–1613, Sep 2009.

Eidesstattliche Versicherung
Declaration on oath

Hiermit versichere ich an Eides statt, die vorliegende Dissertationsschrift selbst verfasst und keine anderen als die angegebenen Hilfsmittel und Quellen benutzt zu haben.

Hamburg, den 29.08.2023

.....

Malte Mrowietz